The Internal Structure of Fault Zones

Implications for Mechanical and Fluid-Flow Properties

Edited by
C. A. J. Wibberley, W. Kurz, J. Imber,
R. E. Holdsworth and C. Collettini

Geological Society
Special Publication 299

The Internal Structure of Fault Zones

Implications for Mechanical and Fluid-Flow Properties

Edited by
C. A. J. Wibberley, W. Kurz, J. Imber,
R. E. Holdsworth and C. Collettini

Geological Society
Special Publication 299

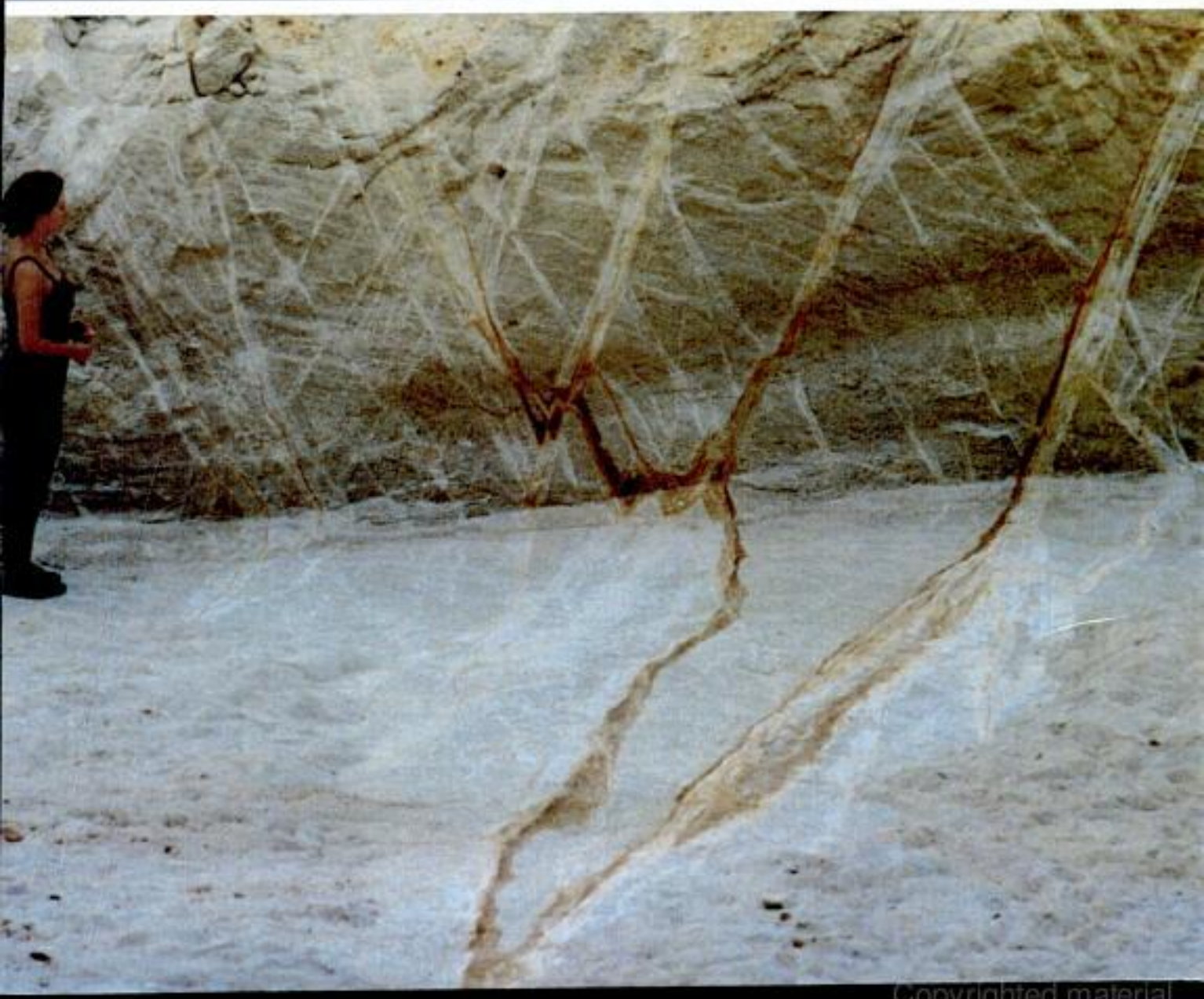

The Internal Structure of Fault Zones: Implications for Mechanical and Fluid-Flow Properties

Geological Society books refereeing procedures

The Society makes every effort to ensure that the scientific and production quality of its books matches that of its journals. Since 1997, all book proposals have been refereed by specialist reviewers as well as by the Society's Books Editorial Committee. If the referees identify weaknesses in the proposal, these must be addressed before the proposal is accepted.

Once the book is accepted, the Society Book Editors ensure that the volume editors follow strict guidelines on refereeing and quality control. We insist that individual papers can only be accepted after satisfactory review by two independent referees. The questions on the review forms are similar to those for *Journal of the Geological Society*. The referees' forms and comments must be available to the Society's Book Editors on request.

Although many of the books result from meetings, the editors are expected to commission papers that were not presented at the meeting to ensure that the book provides a balanced coverage of the subject. Being accepted for presentation at the meeting does not guarantee inclusion in the book.

More information about submitting a proposal and producing a book for the Society can be found on its web site: www.geolsoc.org.uk.

It is recommended that reference to all or part of this book should be made in one of the following ways:

WIBBERLEY, C. A. J., KURZ, W., IMBER, J., HOLDSWORTH, R. E. & COLLETTINI, C. (eds) 2008. *The Internal Structure of Fault Zones: Implications for Mechanical and Fluid-Flow Properties.* Geological Society, London, Special Publications, **299**.

FERRILL, D. A. SMART, K. J. & NECSOIU, M. 2008. Displacement-length scaling for single-event fault ruptures: insights from Newberry Springs fault zone and implications for fault zone structure. *In*: WIBBERLEY, C. A. J., KURZ, W., IMBER, J., HOLDSWORTH, R. E. & COLLETTINI, C. (eds) *The Internal Structure of Fault Zones: Implications for Mechanical and Fluid-Flow Properties.* Geological Society, London, Special Publications, **299**, 113–122.

GEOLOGICAL SOCIETY SPECIAL PUBLICATION NO. 299

The Internal Structure of Fault Zones: Implications for Mechanical and Fluid-Flow Properties

EDITED BY

C. A. J. WIBBERLEY
TOTAL, France

W. KURZ
Technische Universitaet Graz, Austria

J. IMBER
University of Durham, UK

R. E. HOLDSWORTH
University of Durham, UK

and

C. COLLETTINI
Università di Perugia, Italy

2008
Published by
The Geological Society
London

THE GEOLOGICAL SOCIETY

The Geological Society of London (GSL) was founded in 1807. It is the oldest national geological society in the world and the largest in Europe. It was incorporated under Royal Charter in 1825 and is Registered Charity 210161.

The Society is the UK national learned and professional society for geology with a worldwide Fellowship (FGS) of over 9000. The Society has the power to confer Chartered status on suitably qualified Fellows, and about 2000 of the Fellowship carry the title (CGeol). Chartered Geologists may also obtain the equivalent European title, European Geologist (EurGeol). One fifth of the Society's fellowship resides outside the UK. To find out more about the Society, log on to www.geolsoc.org.uk.

The Geological Society Publishing House (Bath, UK) produces the Society's international journals and books, and acts as European distributor for selected publications of the American Association of Petroleum Geologists (AAPG), the Indonesian Petroleum Association (IPA), the Geological Society of America (GSA), the Society for Sedimentary Geology (SEPM) and the Geologists' Association (GA). Joint marketing agreements ensure that GSL Fellows may purchase these societies' publications at a discount. The Society's online bookshop (accessible from www.geolsoc.org.uk) offers secure book purchasing with your credit or debit card.

To find out about joining the Society and benefiting from substantial discounts on publications of GSL and other societies worldwide, consult www.geolsoc.org.uk, or contact the Fellowship Department at: The Geological Society, Burlington House, Piccadilly, London W1J 0BG: Tel. +44 (0)20 7434 9944; Fax +44 (0)20 7439 8975; E-mail: enquiries@geolsoc.org.uk.

For information about the Society's meetings, consult *Events* on www.geolsoc.org.uk. To find out more about the Society's Corporate Affiliates Scheme, write to enquiries@geolsoc.org.uk.

Published by The Geological Society from:
The Geological Society Publishing House, Unit 7, Brassmill Enterprise Centre, Brassmill Lane, Bath BA1 3JN, UK

(*Orders*: Tel. +44 (0)1225 445046, Fax +44 (0)1225 442836)
Online bookshop: www.geolsoc.org.uk/bookshop

British Library Cataloguing in Publication Data

A catalogue record for this book is available from the British Library.

ISBN 978-1-86239-253-3

Typeset by Techset Composition Ltd, Salisbury, UK

Printed by MPG Books Ltd, Bodmin, UK

Distributors

North America
For trade and institutional orders:
The Geological Society, c/o AIDC, 82 Winter Sport Lane, Williston, VT 05495, USA
Orders: Tel. +1 800-972-9892
Fax +1 802-864-7626
E-mail gsl.orders@aidcvt.com

For individual and corporate orders:
AAPG Bookstore, PO Box 979, Tulsa, OK 74101-0979, USA
Orders: Tel. +1 918-584-2555
Fax +1 918-560-2652
E-mail bookstore@aapg.org
Website http://bookstore.aapg.org

India
Affiliated East-West Press Private Ltd, Marketing Division, G-1/16 Ansari Road, Darya Ganj, New Delhi 110 002, India
Orders: Tel. +91 11 2327-9113/2326-4180
Fax +91 11 2326-0538
E-mail affiliat@vsnl.com

Contents

Part III: **Fluid flow properties**

The internal structure of fault zones: fluid flow and mechanical properties

W. KURZ[1], J. IMBER[2], C. A. J. WIBBERLEY[3], R. E. HOLDSWORTH[4] & C. COLLETTINI[5]

[1]*Institut fuer Angewandte Geowissenschaften, Technische Geologie und Mineralogie, Technische Universitaet Graz, Rechbauerstrasse 12, A-8010 Graz, Austria*

[2]*Reactivation Research Group, Dept of Earth Sciences, University of Durham, South Road, Durham DH1 3LE, UK*

[3]*TOTAL, CSTJF, Avenue Larribau, 64018 PAU Cedex, France (e-mail: christopher.wibberley@total.com)*

[4]*Department of Earth Sciences, University of Durham, South Road, Durham, DH1 3LE, UK*

[5]*Dipartimento di Scienze della Terra, Universita di Perugia, Piazza dell'Universita 1, 06100, Perugia, Italy*

Faults are important controls on hydrocarbon migration and ore mineralization and, in areas of active deformation, are the most important source of seismic hazard. However, faults are rarely discrete surfaces and the internal structure of fault zones (e.g., the thickness, nature and continuity of the fault rocks, the distribution and segmentation of slip surfaces, and the orientation, distribution and connectivity of subsidiary faults and fractures) is a key control on their bulk fluid flow and mechanical properties. This Special Publication was inspired by two sessions held at the European Geosciences Union General Assembly in Vienna during 2005 and 2006 and contains 19 original papers divided into three sections. Part I addresses the controls on fault zone evolution, whilst Parts II and III focus, respectively, on the mechanical behaviour and fluid flow properties of fault zones.

The introductory paper (**Wibberley *et al.***) addresses each theme of the Special Publication: fault zone evolution, the permeability structure of ancient and active fault zones, the impact of faults on hydrocarbon sealing and migration, and the implications of fault zone geometry and material heterogeneity for seismogenic processes. In each section, Wibberley *et al.* identify important recent findings and suggest areas in which new conceptual advances in our understanding of fault zones are likely to occur.

A key theme highlighted by many of the papers in Part I is the importance of pre-existing mechanical heterogeneities (e.g., bedding, joints) in controlling the internal structure of faults in sedimentary sequences. **Johanssen & Fossen** consider the control of bed thickness and fault displacement on the geometry, orientation and distribution of minor fractures and deformation bands (i.e., the 'damage zone') that surround faults cutting aeolian sandstones, siltstones and shales in the western United States. They conclude that the highest concentrations of deformation bands occur close to the main faults, favouring fluid flow within the damage zone in a direction parallel to the principal fault surfaces. Next, **van der Zee *et al.*** examine the influence of layering and pre-existing joints on the internal structure of normal fault zones exposed in southern France. They show that fault zone complexity increases, first as fault displacement exceeds the thickness of the competent beds and second, in response to syn-faulting tilting of the strata. The role of mechanical anisotropy is also central to **Brosch & Kurz**'s study of brittle shear zones within layered marbles and foliated quartzites in the eastern Alps. These authors demonstrate that pre-existing fault-parallel fractures and foliation planes are important controls on the development of fault breccias. In the following paper, **Putz-Perrier & Sanderson** investigate how strain is partitioned between fault zones, minor faults and veins that cut a carbonate-mudstone sequence exposed in southern England. They show that faults and veins follow different scaling relationships, thus the observed heterogeneity of extensional strain appears to be scale dependent. The contribution by **Ferrill *et al.*** returns to the question of damage zone evolution. In a study of neotectonic ruptures in California, Ferrill *et al.* conclude that damage zone width is established early during fault propagation, although the active portion of the fault zone will likely

From: WIBBERLEY, C. A. J., KURZ, W., IMBER, J., HOLDSWORTH, R. E. & COLLETTINI, C. (eds) *The Internal Structure of Fault Zones: Implications for Mechanical and Fluid-Flow Properties*. **299**, 1–3.
DOI: 10.1144/SP299.1 0305-8719/08/$15.00

narrow as faulting continues and a through-going slip surface accommodates the bulk of the displacement. The final paper in this section (**Micarelli & Benedicto**) examines the role played by mechanical layering in accommodating strains at the tips of normal faults, and the implications for the fluid flow properties of normal faults. Echoing one of the conclusions reached by van der Zee *et al.*, Micarelli & Benedicto show that the ratio between displacement magnitude and bed thickness strongly influences fault tip architecture.

Part II deals with the mechanical consequences of fault zone architecture, with emphasis on the relationships between the mechanical behaviour, seismicity and internal structure of fault zones. **Faulkner *et al.*** present observations from two well-exposed strike-slip faults that have been passively exhumed from seismogenic depths. They demonstrate cases in which internal structures of these fault zones are consistent with the strain hardening or strain weakening behaviour of the country rock predicted by laboratory deformation experiments. In the following paper, **Imber *et al.*** review the geology of large displacement intra-plate faults exhumed from $<$15 km depth and conclude that many such faults display evidence for frictional–viscous deformation within foliated, phyllosilicate rich cores. Comparison with seismological data suggest that some faults with phyllosilicate rich cores are likely to generate large earthquakes, which is contrary to the findings of some previous rock deformation experiments. The study by **Collettini *et al.*** focuses on CO_2 degassing in the Northern Apennines. This region provides an important opportunity to investigate slip and microseismicity along an active low-angle normal fault, and to compare these geophysical data with geological observations of equivalent exhumed structures. Collettini *et al.* propose that over geological timescales, fluid–rock interaction within fault cores give rise to aggregates of weak, phyllosilicate rich fault rocks that deform by frictional–viscous creep at sub-Byerlee friction values ($\mu < 0.3$). Fluids can be stored in structural and stratigraphic traps (e.g., beneath mature fault cores and regionally extensive Triassic evaporites) giving rise to short-term cycles of fluid pressure build-up and release. In a study of strike-slip earthquake sequences in southern Italy, **Boncio** also highlights the role of rheological layering in allowing the build-up of fluid overpressures and in controlling the vertical extent of seismicity. The final paper in this section (**Wölfler *et al.***) presents a case study of structures produced during sinistral transpression along the southwestern margin of the Tauern Window. They consider the role of fluids in reducing fault shear strength and promoting shear localization on geological timescales.

The final section considers the fluid flow properties of fault zones. The first contribution (**Lunn *et al.***) uses numerical simulations of fluid flow through fault zones mapped in outcrop to demonstrate that across fault flow is controlled by tortuous high permeability pathways. Lunn *et al.* argue that predicting the bulk hydraulic properties of faults in the subsurface depends upon a statistical characterization of the likelihood and frequency of such pathways. In the following paper, **Zhang *et al.*** also use numerical modelling to explore the interactions between faulting, fluid flow and chemical processes in dilatant jogs. In these regions, the precipitation rates of gold and quartz depend on the local fluid velocity and chemical concentration gradients generated by fluid mixing. **Benedicto *et al.*** investigate changes in the nature of fluid–rock interactions during the growth of a major normal fault system on the southern margin of the Corinth rift, Greece. They show that the evolution from distributed deformation (brecciation) to localized slip during progressive exhumation of the footwall was accompanied by a change from a geochemically closed system characterized by fluid–rock equilibrium to a more open system characterized by influx of meteoric waters. Developing this focus on extensional faulting, **Agosta** examines the fluid flow properties of major (basin-bounding) faults within platform carbonates of the Fucino Basin, central Italy. He uses measurements of porosity, pore-throat radii and elastic moduli to compute the permeability of the host rocks and carbonate-rich fault cores to explain the combined conduit-barrier behaviour of the normal faults. In the following contribution, **Rolland *et al.*** highlight the application of syn-kinematic phyllosilicates (similar to those described by Imber *et al.* and Collettini *et al.*) to dating deformation and fluid-rock interaction within ductile shear zones under low-grade metamorphic conditions. Returning to the theme of near-surface fluid flow, **Baietto *et al.*** use three-dimensional thermohydraulic models to investigate the control of fault geometry on thermal circulation and fluid outflow at the tip of a major strike-slip fault in the western Alps. In the final paper, **Boutareaud *et al.*** examine the effect of secondary splay faults on the hydrodynamic behaviour of fault zones. They conclude that splaying of a rupture into surrounding microbreccias or into newly generated splay faults of higher permeability will release co-seismic fluid pressures, or inhibit the generation of excess fluid pressures by thermal pressurization.

Several points emerge from the contributions to this Special Publication, all of which illustrate the importance of the internal structure of fault zones to understanding the hydraulic, seismogenic and mechanical behaviour of faults. The first is the

critical role of mechanical anisotropy – in particular stratigraphic layering – in influencing not only the detailed structural evolution of fault zones, but also the distribution of fluid overpressure and fault-related seismicity (Boncio, 2008). These findings highlight the need to investigate the influence of mechanical stratigraphy on the development and scaling of fault zone structures such as stepovers (e.g., relay zones; Peacock 2003), which are known to be important controls on both the fluid-flow/sealing properties of faults (e.g., Childs *et al.* 1995; Zhang *et al.* 2008) and on earthquake rupture processes (e.g., Sibson 1989). Second, the results of laboratory deformation experiments appear to be consistent with field and microstructural observations of some, but not all natural large displacement faults. The possible mismatch between field and laboratory observations seems to arise where fluid–rock interaction within fault zones has a significant chemical in addition to mechanical effect (e.g., Axen 2004). Future laboratory studies should therefore investigate deformation under hydrothermal conditions where chemical and metamorphic processes may be of critical importance (e.g., Mariani *et al.* 2006; Niemeijer & Spiers 2007). Finally, it is clear that the hydrodynamic behaviour of fault zones is a major control on processes that operate on widely differing timescales and under different stress conditions. These include dynamic weakening during seismic slip (e.g., Wibberley & Shimamoto 2005), fluid flow in hydrocarbon reservoirs and aquifers (e.g., Manzocchi *et al.* 1999), ore mineralization and fault sealing (e.g., Yielding *et al.* 1997). The internal structure of faults is likely to evolve to a greater or lesser extent during each of these processes and future work should aim to better describe and quantify the temporal in addition to spatial variations in fault zone structure and permeability (e.g., Sheldon & Micklethwaite 2007). The breadth of topics discussed here has meant that we have relied heavily upon the expertise and professionalism of the peer reviewers. We are therefore grateful to the following colleagues for their timely and constructive reviews:

F. Agosta, S. Barba, A. Billi, P. Bonsio, C. Bonson, W. Brueckmann, C. Childs, P. Connolly, N. Davatzes, I. Davison, K. Decker, N. De Paola, O. Dor, J. Fairley, H. Fritz, N. Froitzheim, B. Fugenschuh, J. Genser, M. Handy, G. Hirth, J. Imber, K. de Jong, K. McCaffrey, T. Manzocchi, A. McCaig, S. Micklethwaite, S. Miller, T. Needham, E. Nelson, F. Neubauer, D. Peacock, G. Roberts, D. Sanderson, J. Selverstone, S. Shapiro, H. Sheldon, S. Sherlock, Z. Shipton, R. Soliva, A. Tsutsumi, P. Vanucchi, C. Vita-Finzi, S. Wilkins, R. Wilson, D. Wiltschko, N. Woodcock.

Finally, we would like to thank Angharad Hills and Jonathan Turner for handling this project on behalf of the Geological Society.

References

AXEN, G. J. 2004. Mechanics of low-angle normal faults. *In*: KARNER, G. D., TAYLOR, B., DRISCOLL, N. W. & KOHLSTEDT, D. L. (eds) *Rheology and Deformation of the Lithosphere at Continental Margins*. Columbia University Press, New York, 46–91.

BONCIO, P. 2008. Deep-crust strike–slip earthquake faulting in southern Italy aided by high fluid pressure: insights from rheological analysis. *In*: WIBBERLEY, C. A. J., KURZ, W., IMBER, J., HOLDSWORTH, R. E. & COLLETTINI, C. (eds) *The Internal Structure of Fault Zones: Implications for Mechanical and Fluid-Flow Properties*. Geological Society, London, Special Publications, **299**, 195–210.

CHILDS, C., WATTERSON, J. & WALSH, J. J. 1995. Fault overlap zones within developing normal fault systems. *Journal of the Geological Society, London*, **152**, 535–549.

MANZOCCHI, T., WALSH, J. J., NELL, P. & YIELDING, G. 1999. Fault transmissibility multipliers for flow simulation models. *Petroleum Geoscience*, **5**, 53–63.

MARIANI, E., BRODIE, K. H. & RUTTER, E. H. 2006. Experimental deformation of muscovite shear zones at high temperatures under hydrothermal conditions and the strength of phyllosilicate-bearing faults in nature. *Journal of Structural Geology*, **28**, 1569–1587.

NIEMEIJER, A. R. & SPIERS, C. J. 2007. A microphysical model for strong velocity weakening in phyllosilicate-bearing fault gouges. *Journal of Geophysical Research*, **112**, B10405, doi:10.1029/2007JB005008.

PEACOCK, D. C. P. 2003. Scaling of transfer zones in the British Isles. *Journal of Structural Geology*, **25**, 1561–1567.

SHELDON, H. A. & MICKLETHWAITE, S. 2007. Damage and permeability around faults: implications for mineralization. *Geology*, **35**, 903–906.

SIBSON, R. H. 1989. Earthquake faulting as a structural process. *Journal of Structural Geology*, **11**, 1–14.

WIBBERLEY, C. A. J. & SHIMAMOTO, T. 2005. Earthquake slip weakening and asperities explained by thermal pressurization. *Nature*, **436**, 689–692.

YIELDING, G., FREEMAN, B. & NEEDHAM, D. T. 1997. Quantitative fault seal prediction. *AAPG Bulletin*, **81**, 897–917.

ZHANG, Y., SCHAUBS, P. M., ZHAO, C., ORD, A., HOBBS, B. E. & BARNICOAT, A. C. 2008. Fault-related dilation, permeability enhancement, fluid flow and mineral precipitation patterns: numerical models. *In*: WIBBERLEY, C. A. J., KURZ, W., IMBER, J., HOLDSWORTH, R. E. & COLLETTINI, C. (eds) *The Internal Structure of Fault Zones: Implications for Mechanical and Fluid-Flow Properties*. Geological Society, London, Special Publications, **299**, 239–255.

Recent advances in the understanding of fault zone internal structure: a review

CHRISTOPHER A. J. WIBBERLEY[1,2], GRAHAM YIELDING[3] & GIULIO DI TORO[4,5]

[1]*Géosciences Azur, CNRS UMR6526, Université de Nice – Sophia Antipolis, 250 rue A. Einstein, 06560 Valbonne, France*

[2]*Present address: TOTAL, CSTJF, Av. Larribau, 64018 Pau, France (e-mail: christopher.wibberley@total.com)*

[3]*Badley Geoscience Ltd, North Beck House, North Beck Lane, Hundleby, Lincolnshire PE23 5NB, UK*

[4]*Università di Padova, Dipartimento di Geoscienze, Via Giotto 1, 35137 Padova, Italy*

[5]*Istituto Nazionale di Geofisica e Vulcanologia, Via di Vigna Murata 605, Roma, Italy*

Abstract: It is increasingly apparent that faults are typically not discrete planes but zones of deformed rock with a complex internal structure and three-dimensional geometry. In the last decade this has led to renewed interest in the consequences of this complexity for modelling the impact of fault zones on fluid flow and mechanical behaviour of the Earth's crust. A number of processes operate during the development of fault zones, both internally and in the surrounding host rock, which may encourage or inhibit continuing fault zone growth. The complexity of the evolution of a faulted system requires changes in the rheological properties of both the fault zone and the surrounding host rock volume, both of which impact on how the fault zone evolves with increasing displacement. Models of the permeability structure of fault zones emphasize the presence of two types of fault rock components: fractured conduits parallel to the fault and granular core zone barriers to flow. New data presented in this paper on porosity–permeability relationships of fault rocks during laboratory deformation tests support recently advancing concepts which have extended these models to show that poro-mechanical approaches (e.g., critical state soil mechanics, fracture dilatancy) may be applied to predict the fluid flow behaviour of complex fault zones during the active life of the fault. Predicting the three-dimensional heterogeneity of fault zone internal structure is important in the hydrocarbon industry for evaluating the retention capacity of faults in exploration contexts and the hydraulic behaviour in production contexts. Across-fault reservoir juxtaposition or non-juxtaposition, a key property in predicting retention or across-fault leakage, is strongly controlled by the three-dimensional complexity of the fault zone. Although algorithms such as shale gouge ratio greatly help predict capillary threshold pressures, quantification of the statistical variation in fault zone composition will allow estimations of uncertainty in fault retention capacity and hence prospect reserve estimations. Permeability structure in the fault zone is an important issue because bulk fluid flow rates through or along a fault zone are dependent on permeability variations, anisotropy and tortuosity of flow paths. A possible way forward is to compare numerical flow models using statistical variations of permeability in a complex fault zone in a given sandstone/shale context with field-scale estimates of fault zone permeability. Fault zone internal structure is equally important in understanding the seismogenic behaviour of faults. Both geometric and compositional complexities can control the nucleation, propagation and arrest of earthquakes. The presence and complex distribution of different fault zone materials of contrasting velocity-weakening and velocity-strengthening properties is an important factor in controlling earthquake nucleation and whether a fault slips seismogenically or creeps steadily, as illustrated by recent studies of the San Andreas Fault. A synthesis of laboratory experiments presented in this paper shows that fault zone materials which become stronger with increasing slip rate, typically then get weaker as slip rate continues to increase to seismogenic slip rates. Thus the probability that a nucleating rupture can propagate sufficiently to generate a large earthquake depends upon its success in propagating fast enough through these materials in order to give them the required velocity kick. This propagation success is hence controlled by the relative and absolute size distributions of velocity-weakening and velocity-strengthening rocks within the fault zone. Statistical characterisation of the distribution of such contrasting properties within complex fault zones may allow for better predictive models of rupture propagation in the future and provide an additional approach to earthquake size forecasting and early warnings.

From: WIBBERLEY, C. A. J., KURZ, W., IMBER, J., HOLDSWORTH, R. E. & COLLETTINI, C. (eds) *The Internal Structure of Fault Zones: Implications for Mechanical and Fluid-Flow Properties*. **299**, 5–33.
DOI: 10.1144/SP299.2 0305-8719/08/$15.00

Fault zones influence the mechanical properties and seismogenic behaviour of the crust, the migration and trapping of hydrocarbons and mineralizing fluids, regional hydrology and hydrogeology, and the morphology of the land surface (e.g., Handy *et al.* 2007). In particular, localization of shear within relatively narrow zones results in the formation of fault rocks, characterized by specific mechanical and hydrological properties dependent on a complex interplay between many factors. These fault rocks change during deformation, due to the operation of physico-chemical mechanisms related either directly or indirectly to deformation and often controlled by fluids. The resulting zone of fault rock is typically therefore highly heterogeneous, leading to large uncertainties in understanding and predicting the resulting mechanical and fluid flow behaviour of the fault. Nevertheless, the fact that faults are not discrete surfaces but zones, of finite width, of fault rock with different properties to surrounding host rocks has profound implications for the way in which we should assess the impact of faults on fluid migration and seismogenic behaviour in the Earth's crust.

Fault zone architecture and related permeability structures form primary controls on fluid flow in upper-crustal, brittle fault zones. Compacting and dilatant regions of the fault zone will lead to the establishment of distinct structural and hydrogeologic units (e.g., Chester & Logan 1986). These units reflect the material properties and stress conditions within a fault zone, and dictate whether a fault zone will act as a conduit, barrier or combined conduit–barrier system (e.g., Caine *et al.* 1996). The permeability of fault zones is an aspect of particular interest in the fields of economic geology and seismogenesis, being a key factor in determining fluid pressure distributions and the volume of fluid that can pass through a fault zone. The temporal and spatial evolution of permeability in fault zones depends on the host rock type, stress and strain rate, deformation mechanisms, fault architecture, and many other parameters. Numerical modelling is a powerful tool to investigate the effect of varying permeability on the fluid flow patterns in terms of the stress regime, which can provide useful constraints for mineral exploration when coupled with reactive transport simulation (e.g., Zhang *et al.* 2008), and for understanding the role of faults within petroleum systems in both exploration and production contexts. Field and laboratory studies provide the input for such models in terms of both data and the appropriate fluid flow and mechanical/rheological laws.

The seismogenic behaviour of a fault is also known to depend greatly on fault zone internal structure (Scholz 2002; Rice & Cocco 2007). At the large scale, the continued propagation or early arrest of ruptures depends largely upon the geometry of fault bends, dilational jogs and the connectivity or distance of step-over of individual strands in the fault system (King & Yielding 1984; Sibson 1985; Wesnousky 2006). Frictional properties of the fault materials, and their spatial variation, also control seismogenic behaviour and are key influences on whether the fault slips unstably or moves by steady slow creep. At smaller scales, more mature, evolved (higher displacement) fault zones are: (i) likely to have better developed smoother slip zones for localising rapid slip than rough slip planes of less-mature faults (e.g., Sagy *et al.* 2007); (ii) have larger overall fault zones of increasing complexity which may conversely encourage the diversion of the main rupture off the main slip zone onto a branch fault of different mechanical and permeability properties which may favour arrest (e.g., Shipton *et al.* 2006; Boutareaud *et al.* 2008*a*). These two competing factors may greatly impact on the frequency of the seismicity emitted, particularly in the early stages of earthquake slip, the repartition of the energy budget of the earthquake by different energy-sink mechanisms, and hence the operation and efficiency of various dynamic slip weakening mechanisms which govern the overall magnitude of the earthquake.

Experience shows that the complexity of a fault zone is strongly dependent on host rock lithology, displacement and pre-existing structure (including interactions with the mechanical layering of the host rocks). Depth (pressure and temperature) and stress regime and its evolution during the life of the fault can also play a role (e.g., Sibson 1977; Butler *et al.* 1995). Nevertheless, a single fault may also show strong changes in complexity along-strike or down-dip, even over relatively short distances (e.g., Childs *et al.* 1997; Schulz & Evans 1998). Despite such variation, careful documentation of the internal structure of a large number of faults, in terms of host lithology and displacement increase, is valuable in building up a general picture of the mechanisms of fault zone growth.

The purpose of this paper is to briefly critically review research into the heterogeneity of fault zone internal structure and fluid flow properties, how they may evolve during fault growth, and impact on improving our understanding and prediction of hydrocarbon migration and seismogenic behaviour of the crust. The emphasis is placed on recent and advancing concepts with suggestions for future work.

Fault zone evolution

Fault zone evolution has been examined for over two decades by comparing examples of fault

zones at different scales, the assumption being that small fault zones preserved in a population represent the early growth stages of the larger ones. Typically data on fault zone thickness, usually considered to be the thickness of highly deformed fault rock in which no original fabric is identifiable, have been compared for faults and shear zones – their deep crustal equivalents – of different displacement magnitudes in order to examine how a fault zone might develop with increasing offset (e.g., Robertson 1983; Wallace & Morris 1986; Scholz 1987; Hull 1988). Compilations of data over several orders of magnitude of displacement showed general linear trends of fault zone thickness increase with displacement (e.g., Fig. 1a), suggesting that continuous wear of the fault walls occurs as a function of increasing displacement (e.g., Scholz 1987), and that the fault therefore does not really change its rheology as it becomes larger. Numerous objections were raised to this kind of approach (e.g., Blenkinsop 1989; Evans 1990): definition of fault zone thickness is often difficult in highly heterogeneous zones with complex internal structure: comparing data over a range of scales necessarily requires log–log plots which mask the often large scatter; and datasets from different contexts (e.g., lithologies, tectonic settings, depths, etc.) were not always separated out, thus increasing the risk of irrelevant comparisons. Shipton *et al.* (2006) demonstrated the importance of separating out the fault zone 'width' into the thickness of different components such as fault zone core and damage zone (see Fig. 1a).

An increased awareness of these problems has led to more careful descriptions and data presentation/interpretation, such as describing faults in a single given field area and hence context, and separating out different components of the fault zone (e.g., Shipton *et al.* 2006). Nevertheless, the heterogeneity of fault zones, especially in cases where slip has localized onto several strands separating slivers of almost intact protolith means that interpretation of such data in terms of wear processes and fault mechanics should be done with caution. Furthermore, such an approach to examining fault zone evaluation depends on the assumption that the small faults observed in a given population are representative of the early stages of development of the large faults in the population.

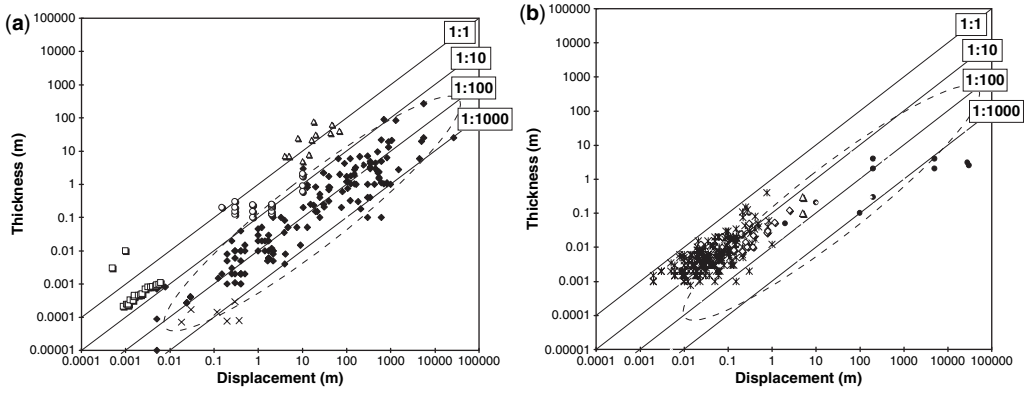

Fig. 1. Compilations of fault zone thickness–displacement data over a wide range of scales, illustrating a general linear data trend, typical scatter in this trend, and examples of particular situations where data lie a long way off this trend. Note the log–log scales. (**a**) Synthesis of data for fault gouge zones in siliclastic rocks (solid symbols) compared with measurements of the width of fault zones including zones of fracturing, and/or lens formation at linked segment relays (open symbols). Data from fault gouge zones are from Robertson (1983), Wallace & Morris (1986) and some unpublished field and microstructural data from the Lodève Basin in S. France measured by the first author. A general envelope of these data is shown as a dashed oval. Data from the fractured zones are small-scale (thin section and experimental rupturing) fault tip-related rupturing from Otsuki (1978), Amitrano & Schmittbuhl (2002) and field measurements in granite from the Pelvoux Massif, western Alps by the first author (squares), lenses formed by relays at segment linkage zones (circles) (van der Zee *et al.* 2008) and larger-scale damage zones in sandstones (triangles) (Fossen & Hesthammer 2000). Data from sliding on discrete pre-cut surfaces are also shown for comparison (crosses), from Tullis & Weeks (1986), Yoshioka (1986), Blanpied *et al.* (1987) and Power *et al.* (1988). (**b**) Data from faults in high-porosity Cretaceous sands from S. France (crosses and open symbols) (Wibberley *et al.* 2007) and phyllosilicate-rich faults in crystalline basement of cataclastic origin (solid circles) (Wibberley 2005) as two examples of data exhibiting relatively inhibited fault zone growth in comparison to the general envelope of data in (a). Small-scale cataclastic deformation bands (crosses) show evidence of work-hardening in the field and do not lie significantly off a linear relationship. However, localized cataclastic faults (diamonds) and clay-rich larger faults (triangles) do not increase thickness as a linear function of increasing displacement.

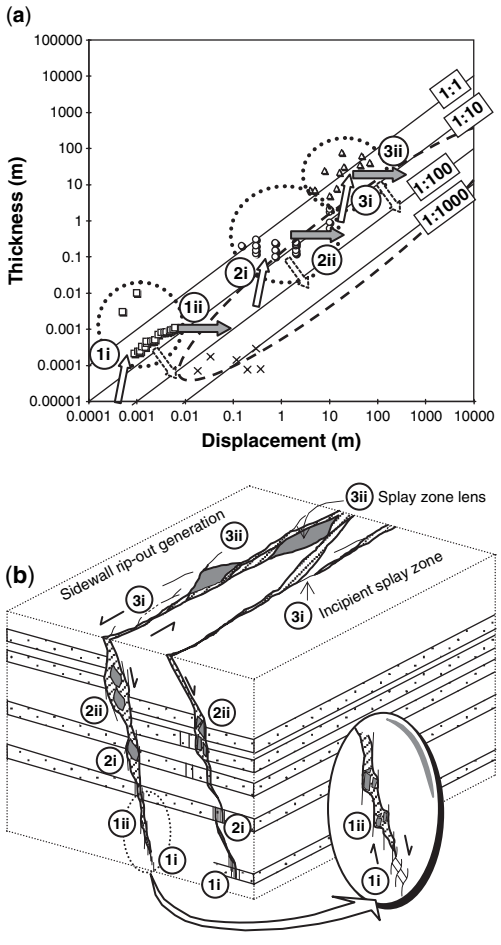

Fig. 2. Illustration of examples of different processes contributing to fault zone growth at different scales, and their effect on the evolution of fault zone growth as represented on a thickness–displacement plot. The thickness–displacement plot (**a**) summarizes data from Fig. 1a, with arrows suggesting possible evolution pathways as a result of different deformation processes. In the block diagram (**b**) the newly incorporated material in each process is indicated by dark shading, the pre-existing fault zone gouge denoted by diagonal shading. Each process first weakens the surrounding wall rock by fracturing (step i, open arrows on the graph), followed by incorporation of the fractured wall rock material into the fault zone during continued displacement (step ii, shaded arrows on the graph). The processes illustrated are tip-process zone microfracturing (1), segment linkage by relay breaching and lens formation (2) and splay-faulting and re-connection forming sidewall rip-outs (3). Note that each process increases the fault zone thickness above the general gouge trend during step (i), but the system strives to regain the general (wear?) trend as displacement continues during step (ii). The graph also attempts to illustrate the possible evolution of active slip bands or deformation zones (dotted arrows) during strain localization events, although the representation of this concept is dependent on the spatial and time-scales concerned.

Role of peripheral fracturing and host rock weakening

Emphasis in the last decade has been placed on the fault zone also often containing a zone of peripheral fracturing (often termed 'damage zone'; Caine *et al.* 1996) generated by a variety of mechanisms. Whether this is ignored or measured (if present) in a measurement of the thickness of the fault zone may have important impact on the interpretation of the data in terms of mechanical evolution of the fault zone during growth (Shipton *et al.* 2006). Dilatant fractures formed during initial rupture of low-porosity rocks may result in a fracture zone around the initial rupture fracture right from the outset (e.g., McGrath & Davison 1995; Moore & Lockner 1995; Wibberley *et al.* 2000*a*). Faults in fracture-dilatant rocks such as crystalline rocks and low-porosity sandstones are thought to be governed largely by the interaction between the generation of peripheral fractures and the main fault zone. Dilatant fractures formed, such as mode I cracks and synthetic and antithetic Riedel microfaults (e.g., Tchalenko 1970; Brosch & Kurz 2008), result in weakening of the host rock adjacent to the developing fault, so that fault zone widening may be controlled as much by evolving host rock properties as by fault rock rheology (Fig. 2).

In natural fault zones, much of the geometric complexity can be related to wall rock fracturing and is therefore likely to be inherited from such processes occurring early on in the life of the fault. A wealth of theoretical and experimental data suggest that shear fractures form due to the interaction and coalescence of numerous tensile mode I microcracks (e.g., Paterson 1978; Lockner *et al.* 1992). Healy *et al.* (2006) have shown that the elastic stress fields developed around tensile microcracks in three dimensions lead inevitably to mutual interactions that promote the development of brittle shear fractures – and shear fracture intersections – that lie significantly oblique to all three principal stresses. This accounts well for the development of anastomosing and coalescing polymodal faulting patterns observed in many natural fault zones, even at low strains, in which fractures lie in a wide range of orientations at angles of up to 25° or more relative to the σ_1 and σ_2 axes. The importance of such peripheral wall rock fracturing may extend to controlling the entire rheological behaviour of the fault at the large scale by inducing stress rotations due to contrasting elastic moduli of such

zones with respect to the surrounding country rock (e.g., Faulkner *et al.* 2006).

The continued development of the fault zone as displacement increases may incorporate the fractured material into the developing fault zone as a function of the original width of the fractured zone. Eventually the material becomes sufficiently comminuted to form a zone of ultracataclasite, which, if forming a continuous zone, will localize further deformation and inhibit further widening of the fracture 'damage' zone (e.g., Micarelli *et al.* 2006). Hence such dilatant fractures on the small scale will diminish in impact as the fault zone increases in thickness. Indeed, continued deformation may result in the localization of strain and consequent narrowing of the *active* slip zone, whilst the overall finite fault zone thickness remains constant (Fig. 2a). Nevertheless, the generation of larger-scale splay faults (such as Riedel faults), fracturing around fault intersection zones, and cutting of asperities at a wider range of scales, will also result in bulk weakening of the host rock and favour incorporation of blocks of wall rock material into the fault zone as it gets larger. Examples of these processes are the incorporation of 'sidewall rip-outs' (Swanson 2005) and short-cuts of bedding-parallel slip asperities in the fault zone (Watterson *et al.* 1998), often classed as tip-line and asperity bifurcations respectively (Childs *et al.* 1996). In limestones, dilatant fracturing may be also important in the early stages of faulting, but the high rates of dissolution–precipitation processes are likely to govern later behaviour (e.g., Benedicto *et al.* 2008).

Influence of segment linkage

Studies of fault linkage, particularly in stratified rocks such as interbedded sandstones and shales or limestones and marls, suggest that if faults link at dilational jogs they may form relays containing lenses of relatively undeformed protolith (e.g., Peacock & Sanderson 1992; Childs *et al.* 1995; van der Zee *et al.* 2008; Micarelli & Benedicto 2008). Thus the thickness of the fault increases suddenly as two initially narrow faults link and form a wider relay zone (step i in Fig. 2a and b). Increased displacement will result in these relay zones evolving to a lens surrounded by fault gouges or other high strain fault rocks, without the overall width of the zone having significantly increased (step ii in Fig. 2a and b). Different fault zones, and indeed perhaps even different parts of the same fault zone, will have ceased activity at different stages of this relay evolution. Hence this model evolution predicts variations in displacement – thickness statistics. The thickness of mechanical layered units such as competent sandstones or limestones is thought to be an important scale control on this process (e.g., Wilkins & Gross 2002; Soliva & Benedicto 2005), and hence is likely to also be an important scale-related control on fault zone thickness resulting from this process. Thus a number of processes may operate, possibly repeating themselves at different scales, which together contribute to generating the structure of the fault zone. Furthermore, due to this potentially large number of processes contributing to fracturing of wall rock at different scales, the stepped evolution of the thickness–displacement trend is likely to be much more complicated than is illustrated in Figure 2. This is particularly so because a fault may cease its activity as a particular process, at any one scale, is in an early, mid or late stage of its evolution and/or repetition, and this may also vary along the length of the fault. Thus the superposition of a number of 'stepped' thickness–displacement patterns would naturally give a general linear trend with also the two- to three- orders of magnitude scatter that these data typically show. Nevertheless, the scale-dependence of some of these damage processes on features such as bed or mechanical layer thickness may give rise to similar scaling patterns for different faults and fault systems.

Effect of changes in fault rock rheology

In high-porosity sandstones the widespread presence of 'deformation band' faults has attracted much interest as these structures are thought to influence fluid migration in many good quality sandstone reservoirs (e.g., Aydin & Johnson 1983; Underhill & Woodcock 1987; Fowles & Burley 1994; Antonellini & Aydin 1994; Fossen *et al.* 2007). They typically appear as one or several white strands on the order of 1 mm wide clustered in zones a few millimetres to centimetres wide, accommodating displacements on the order of a few millimetres to tens of centimetres. These features have often been interpreted as being due to 'work-hardening', i.e. that the fault rock becomes stronger with displacement, so that the system has to wear the adjacent host rock to accommodate further displacement (e.g., Aydin & Johnson 1983; Underhill & Woodcock 1987). Abutting relationships of later deformation bands against earlier formed ones also suggest that the material in the deformation bands is stronger than that of the high-porosity host sandstone (Wibberley *et al.* 2000*b*). Studies of overprinting also suggest that deformation band networks also act to strengthen the system in the bulk sense. This may cause widening of the deformation zone initially (e.g., Johansen & Fossen 2008), but localization of deformation onto fewer, larger faults is eventually favoured during later deformation. These patterns of behaviour are probably a feature specific to high-porosity materials because they typically compact under most stress conditions, to

reduce their porosity as they shear, becoming stronger in the process. Most examples of deformation bands in the literature are cataclasitic, with intragranular (hertzian) fracturing at grain–grain contacts resulting in the generation of angular fragments. The changing nature of the grains/fragments in the developing deformation band may contribute to increasing fault strength as well as to the operation of shear-enhanced compaction of the high-porosity material. Yet studies of deformation band populations and larger (greater than metre-scale displacement) faults in high-porosity sandstones suggest that this work-hardening does not continue indefinitely. Larger faults show narrower thickness/displacement ratios (e.g., Fig. 1b) and evidence of deformation localization in slip planes as displacement continues (e.g., Antonellini & Aydin 1995; Shipton & Cowie 2001; Davatzes *et al.* 2005; Wibberley *et al.* 2007). Fault rock material in these cases is usually a 'mature' ultracataclasite, with a large proportion of very fine-grained fragmented and comminuted matrix supporting a small number of nearly intact original sand grains. Thus 'large' faults are very different in character and microstructural properties to small faults in high-porosity sandstones.

Integrated field, microstructural and geochemical evidence suggests that weakening of the fault rock, such as by syn-kinematic alteration, may encourage localization of the deformation onto a narrowing part of the active fault zone (reaction-enhanced ductility, White & Knipe 1978; e.g., Fig. 1b). This is particularly favoured in crystalline basement fault zones, where syn-kinematic alteration of feldspars to phyllosilicates in granitic upper/middle crust or olivine to serpentine in the upper mantle may encourage such localization of deformation (e.g., Janecke & Evans 1988; Wintsch *et al.* 1995; Imber *et al.* 1997; Stewart *et al.* 2000; Handy & Stünitz 2002; Wibberley 2005; Jeffries *et al.* 2006). Nevertheless, care must be made in interpreting narrow fault zones in terms of absolute strength of the fault alone, because the localization of deformation is potentially related to the competence contrast between host rock and fault zone rather than in absolute changes in fault zone strength. However, the development of fine-grained phyllosilicate-rich fault rocks has been shown by both analogue experimental studies (e.g., Bos & Spiers 2002; Niemeijer & Spiers 2005) and field studies of natural weak fault zones such as low-angle normal faults (e.g., Collettini & Holdsworth 2004) to promote the operation of 'frictional-viscous' mechanisms where grain-scale slip is accommodated by pressure solution allowing faulting at significantly reduced friction coefficients (μ as low as 0.2), i.e. absolute weakening (see Imber *et al.* 2008).

Summary

A number of processes operate during the development of fault zones, both in the developing fault zone itself and in the surrounding host rock, which may encourage or inhibit further fault growth. The complexity of the evolution of a faulted system requires changes in the rheological properties of both the fault zone and the surrounding host rock volume, both of which impact on how the fault zone evolves with increasing displacement (Fig. 2). Processes encouraging fault zones to grow include tip zone rupturing, formation of relay zones and splay faulting, all of which weaken the wall rock in a relative sense and allow incorporation of fragments or lenses of material into the fault zone. Processes inhibiting fault zone growth include work-hardening of the host rock volume before localization of a through-going fault, and strain-weakening in the fault zone itself, often influenced by syn-kinematic metamorphic reactions in the fault zone. Studies of 'very large' faults, i.e. those likely to cut the entire upper crust, show that the thicknesses of high strain zones are usually much narrower in relation to displacement than for small faults (e.g., Wibberley, 2005), implying that further wear by generation of splays and their incorporation into the zone diminishes once this scale of layering has been reached. Nevertheless, 'large' faults at this scale often occur in a set such as duplexes or strike–slip arrays. If the entire array is included in the definition of width of the 'zone of faults' (different to a 'fault zone' of near-exclusively high-strain fault rock), then the interpretation drawn may be somewhat different. Indeed, the application of 'wear' concepts to faults in the Earth's crust seems to be a generalization of a wide range of mechanisms for weakening the surrounding host rock and incorporating it into the fault zone, most of which are scale dependent to some degree (Fig. 2), but when averaged out over a wide scale range, give an overall impression of scale-independence of fault zone growth processes.

Despite many studies into the internal structure of fault zones at different scales, evolution of the fault zone is usually inferred by comparison with smaller faults. Yet examination of the final structure can rarely distinguish whether deformation spread through time, or that the entire width was generated early on with later localization of deformation, or a combination of both (Means 1995). For large fault zones with complex internal structure and surrounding fracturing, a way ahead may be to look for methods of relative or absolute dating of the generation of structures around the high-strain part of the fault zone in order to resolve this question. This may be for example

by careful observation of the evolution of peripheral deformation with respect to reliable time markers around faults. In the case of recent alluvial deposits around seismogenic faults from California, Ferrill *et al.* (2008) suggest that the fault damage zone width is established early on in fault zone evolution, with the active portion of the fault zone narrowing with further displacement. Interestingly, a similar pattern in the evolution of deformation distribution is proposed from integrated structural, microthermometric and stable isotope data from hectometric-displacement fault zones in limestone in the Gulf of Corinth, which suggest localization of deformation onto narrow slip zones after relatively early distributed brecciation (Benedicto *et al.* 2008).

Fault zone permeability structure

Introduction to concepts

Since the recognition became widespread that faults are zones of deformed material rather than discrete surfaces, the need became apparent to understand the physical properties of the fault zone, especially the permeability and its heterogeneity. Relatively early studies focused on the low-permeability nature of clay-rich fault gouges from the centre of large strike–slip faults such as the San Andreas Fault (Chu *et al.* 1981; Morrow *et al.* 1984) and an exhumed ancient branch, the Punchbowl fault (Chester & Logan 1986). The latter case also documented high-permeability zones around the fault associated with the presence of peripheral fractures around the central zone. In siliclastic sedimentary settings, focus was placed on the moderate permeability reductions of deformation bands and cataclastic fault zones in high-porosity sandstones and the more significant reductions with increasing clay-to-sandstone proportion in the fault zone (e.g., Antonellini & Aydin 1994; Gibson 1994). Through the need to generalize such variability and fault zone complexity, a simple framework emerged for fault zone permeability structure by considering the presence or absence of two main elements modifying host rock properties: a low-permeability fault zone *core*, providing a barrier to across-fault flow, and a high-permeability fractured *damage zone* around the central core, providing a conduit or drain for along-fault flow (Caine *et al.* 1996). Whether or not each of these elements are present, and how important they are, depends upon various factors such as host lithology and displacement, which help to understand whether a given fault can act as a lateral barrier to fluid flow, a fault-parallel conduit, or both.

More complex permeability structure models

Several studies have shown that the simple core zone/damage zone model does not always adequately represent fault zone complexity, particularly the heterogeneous nature of the core zone, despite the overall usefulness of the concept. Core zone complexity becomes particularly important, for example, when considering the core zone behaviour during the onset of earthquake dynamic slip, particularly in the low-permeability slip zones governing dynamic slip weakening by thermal pressurization (Wibberley & Shimamoto 2005) and their branching (Boutareaud *et al.* 2008) or the distribution of velocity-strengthening and velocity-weakening fault rocks in the core (Faulkner *et al.* 2008). Two contrasting models of detailed core zone internal structure and permeability heterogeneity were based on very different lithosphere-scale strike-slip faults. The model of Faulkner *et al.* (2003), based on the Carboneras fault in southeast Spain, suggests that very wide (on the order of 1 km) fault gouge zones of low-permeability may contain large lenses of high-permeability fractured ('damage zone') host rock. Thus, while fluid escape from the fault zone is hindered by the low-permeability nature of the clay gouge perpendicular to foliation (Faulkner & Rutter 2001), the lateral (e.g., up-fault) permeability could be much higher given sufficient connectivity of the fractured host rock lenses. Wibberley & Shimamoto (2003) use a study from the much narrower Median Tectonic Line in Japan to show how the juxtaposition of host rocks of contrasting mechanical properties results both in an asymmetric permeability structure and in the intense localization of deformation into a narrow central slip zone (several millimetres to centimetres wide), probably generated by episodes of rapid slip, at the boundary between the fault rocks derived from the host rocks either side of the fault. The intense grain size reduction and very finely foliated clay-rich nature of this slip zone gouge results in it having the lowest permeability of all the fault rocks in this complex large scale fault zone.

Permeability structure and behaviour of active faults

The above studies on fault zone internal structure were carried out from field studies complemented by laboratory permeability measurements not subjected to deformation apart from isotropic confinement (inducing compaction). Seront *et al.* (1998) measured the permeability, during deformation

experiments, of fracture-dilatant cataclasites and breccias sampled from the core of a seismogenic active fault, and showed how their complex arrangement in the fault zone core may result in the irregular distribution of dilatancy-hardening and contribute to local fluid storage and rupture arrest during an earthquake, similar to fault jogs. The heterogeneous distribution in the fault core of fracture dilatant fault rocks (typically cemented cataclasites) and fault gouges which deform by shear-enhanced compaction is significant in controlling permeability changes in the fault zone during active faulting (Uehara & Shimamoto 2004), and can determine whether or not up-fault leakage occurs. During rapid slip, the permeability behaviour – which can also feedback to the dynamic slip behaviour – is therefore governed by the propagation path of the through-going rupture in this heterogeneous fault zone.

Field observations of mineralization localized in fault breccias and veins around high-angle reverse faults in mid-crustal crystalline basement motivated Sibson (1990, 1992) to propose a fault-valve model of transient fault zone permeability. This model necessitates a large vertical pressure gradient supported by a low-permeability mid-crustal seal in the fault, periodically broken by earthquake slip to allow pressure re-equilibrium by fast up-fault fluid flow. The rapidly decreasing temperature of the mineralising fluid induces precipitation, thereby sealing the transiently high permeability of the fault until the next slip cycle. This model assumes dilatancy and permeability increase by fracturing during rapid slip, likely to be the case in crystalline basement. As argued by Sibson (1995), such a fault valve behaviour is more likely to be valid in the case of reverse reactivation of high-angle faults (e.g., Cox 1995) than normal faulting, although case studies in normal fault zones show similar features to those predicted to be caused by fault-valve behaviour such as evidence for the seismic release of high-pressure fluid in the fault zone followed by interseismic sealing by mineralization (e.g., Bruhn *et al.* 1994).

Another approach to considering/modelling permeability of active faults is to draw on the assertion that fault gouges are fluid-saturated granular media of a given porosity. Despite the increasing wealth of permeability data from such fault rocks, truly coupled porosity–permeability data of fault gouges are rare because of the technical challenges of measuring both properties at the same time, particularly under a range of pressure and anisotropic stress conditions. Nevertheless, such porosity–permeability relationships are potentially extremely useful, because the framework of critical state soil mechanics provides a quantitative link between porosity changes and the evolution of differential stress and effective pressure for granular materials, and have already been used to explain the mechanical and porosity evolution of deformation bands and cataclastic fault zones in high porosity sandstones (Sheldon *et al.* 2006; Wibberley *et al.* 2007). Combined with porosity–permeability relationships, critical state soil mechanics should provide a new framework in predicting permeability changes during the evolution of fault activity and stress state in active fault zones. The validity of this approach needs to be evaluated with appropriate porosity–permeability data for fault rocks under a range of effective mean stress and differential stress conditions.

As an illustration, a previously unpublished series of experiments on a suite of phyllosilicate-rich (muscovite/illite and chlorite) gouges of different quartz clast content and grain size (collected from the Median Tectonic Line, Japan; Wibberley & Shimamoto 2003) were performed to evaluate porosity–permeability relationships of these fault rocks and their variation with mean effective stress and differential stress, using nitrogen gas as a pore fluid at a pore pressure of 50 MPa.

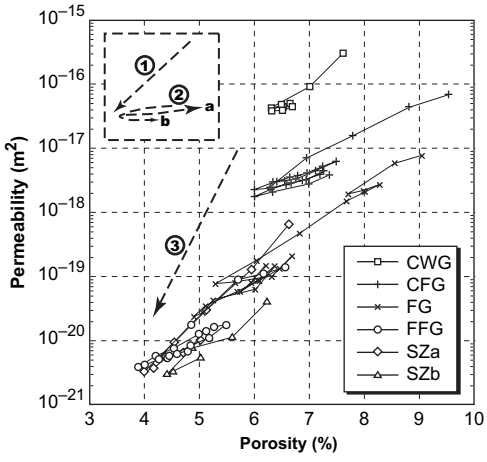

Fig. 3. Permeability v. porosity of a suite of clay-rich granular fault gouges from the Median Tectonic Line, measured under isotropic stress conditions with nitrogen gas as a pore fluid (pore pressure 50 MPa) with confining pressure ranging from 80 to 200 MPa. CWG = coarse white (quartzo-feldspathic) gouge, CFG = coarse foliated gouge, FG = foliated gouge, FFG = fine foliated gouge, SZ = narrow central slip zone gouge (two samples, denoted SZa and SZb). All permeability measurements are parallel to foliation, obtained using the pore pressure oscillation method. Porosity was measured from an initial pore volume measurement, followed by pore volume change measurements after each change in confining pressure. General trends in the data, as described in the text, are illustrated by the numbered dashed arrows.

Figure 3 shows the porosity–permeability relationships for the suite of gouge samples without axial loading, i.e., confining pressure changes only. The suite of samples shows porosities ranging from 10% down to 4% for the coarsest to the finest gouges, and permeabilities from 10^{-16} down to around 10^{-21} m^2 parallel to foliation. These results illustrate three pertinent findings:

1. Porosity and permeability diminish with increasing confining pressure during compaction with an approximately log–linear relationship (Fig. 3, trend 1).
2. The deconfining parts of the experiments, and any later pressure cycling not exceeding the maximum previous confining pressure, systematically show a different porosity–permeability relationship to the initial confining phase (Fig. 3, trends 2a and b respectively).
3. Porosity and permeability decrease with decreasing grain size working in towards the centre of the fault zone (Fig. 3, trend 3), yet the different samples have similar gradients of the porosity–permeability relationship.

These data show that, whilst porosity varies by a factor of 2–2.5, permeability varies by 4–5 orders of magnitude. Permanent compaction and later elastic decompaction have different effects on the relationship of the pore volume (porosity) and pore connectivity/tortuosity of flow paths (permeability).

Figure 4a shows porosity and permeability data for a foliated quartzo-feldspathic gouge sample first subjected to two confining pressure cycles

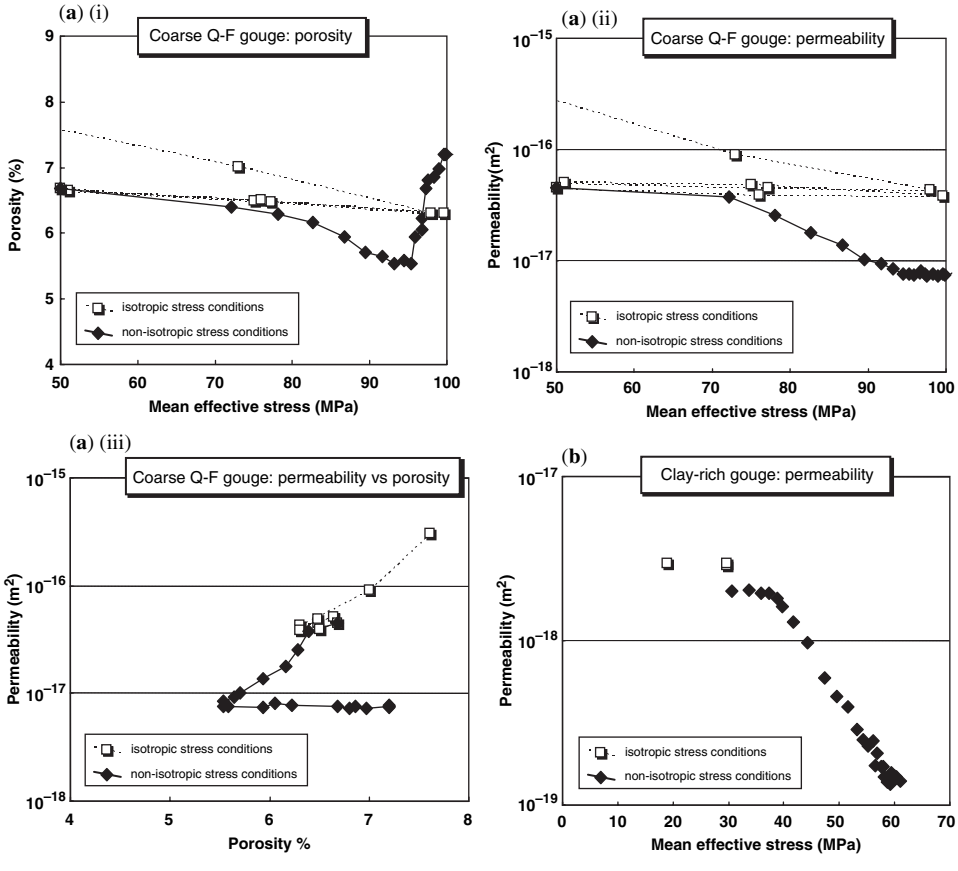

Fig. 4. The evolution of permeability and porosity with mean effective stress for cases of isotropic stress and non-isotropic stress (deformation experiments), measured with nitrogen gas as the pore fluid (50 MPa pore pressure). Permeability was measured using the pore pressure oscillation technique. (**a**) Experiment on a coarse quartzo-feldspathic (Q-F) gouge with two confining pressure cycles followed by axial shortening. (i) Porosity data; (ii) permeability data; (iii) permeability–porosity relationship. (**b**) Experiment on a clay-rich gouge after pre-confinement to a mean effective stress of 50 MPa. In the case of the clay-rich gouge, simultaneous measurement of porosity with permeability during deformation was not possible.

(i.e., no axial deformation, isotropic stress), followed by axial shortening by a constant piston displacement rate at constant confining pressure during which axial stress was measured. In the first case the mean effective stress $P' = (\sigma_1' + 2\sigma_3')/3$ is simply the difference between confining pressure (P_c) and pore pressure (P_p) where $\sigma_1' = \sigma_3' = (P_c - \alpha P_p)$ and assuming that the coefficient α equals 1. In the second case there is a significant deviatoric component to the stress regime. The data show that:

1. Both porosity and permeability have log–linear relationships with mean effective stress during axial deformation, at least while deformation remains relatively homogeneously distributed throughout the samples.
2. For a given mean effective stress, both porosity and permeability are significantly lower if there is a differential component to the stress regime.

The porosity kick (Fig. 4a i and iii) may be due to spaces being created at the slip zone – jacket interface during localised slip. This phenomenon was apparently never severe enough to short-cut flow and affect the sample bulk permeability measurement. Figure 4b shows that the permeability of a clay-rich foliated gouge sample has a log–linear dependence on mean effective stress during axial deformation (at constant confining pressure).

Care must be taken when applying these findings to foliated gouge behaviour in natural fault zone systems because the result depends largely on foliation orientation in the experiment. First, permeability is anisotropic, so porosity–permeability relationships will be different for permeability in different directions with respect to the foliation. Second, the mechanical response of the pore spaces, folia and flow pathways to axial loading may be different if the foliation is perpendicular to piston displacement direction or parallel to it. Healthy scepticism is also required for quantitative application of these data in modelling – both the role of pore fluid in the experiments (nitrogen gas rather than water) and the effect of barrelling of the samples during deformation need to be properly considered. Nevertheless, these findings show that fault gouge behaviour is consistent with behaviour predicted by critical state soil mechanics and that, with future carefully planned experiments, fault gouge permeability may also be predictable within this framework.

Summary of advancing concepts: active fault permeability structure

The original concept of a two-component fault zone system affecting host rock properties, the fault core and surrounding damage zone model has more recently been modified for large, potentially seismogenic or creeping lithosphere-scale fault zones with complex fault core structures. To understand and predict permeability behaviour during active deformation, a knowledge of the fault rocks and their response to (anisotropic) stress changes and deformation is critical. The basic two-component fault rock model is improved upon by using the above results on fault gouge, coupled with previous experiments on deformation of cemented cataclasites. Although the more recent models for permeability structure suggest that lenses of fractured fault rock with the low-permeability gouge core, or an asymmetric fractured cataclasite/gouge distribution with intense slip localization at the boundary, the same premise nevertheless runs that two fault rocks are present of contrasting poro-mechanical behaviours (e.g., Agosta 2008), namely:

1. a low-permeability granular material which can be modelled by critical state soil mechanics (possibly coupled with pressure solution);
2. a generally higher-permeability fracture-dilatant material which can be modelled by elastic-fracture permeability laws coupled if necessary with the effect of cyclic cementation.

Thus faults which contain predominantly clay gouge cores are likely to behave in a compaction-creep manner during steady low-deformation rate fault activity. During rapid slip they may nevertheless act as temporary conduits simply due to the irregular large-scale slip surface or slip zone geometry inducing dilatancy, although this is still an open question. Indeed, the three-dimensional structure of fault zones must be borne in mind when considering all the models described in this section, particularly as fracture–fault intersection zones and dilational jogs often provide localized vertical conduits for fluid flow or infiltration if sufficient pressure gradients are present (e.g., Sibson 1996; Baietto *et al.* 2008; Micarelli & Benedicto 2008).

Faults containing sufficient lenses of fracture-dilatant cataclasites may drain fluid more easily up the fault during deformation depending on whether or not these lenses are sufficiently connected. Poor connectivity between lenses may result in dilatancy hardening in the fault zone (e.g., Seront *et al.* 1998), depending on the rate of dilatancy with respect to fracture connectivity. Faults containing predominantly fracture-dilatant cataclasites in their cores are likely to behave in a mechanically more intermittent manner with fracture dilatancy inducing high fluid flow rates, cyclically sealed by cementation. These concepts may provide the basis for evaluating the dynamic slip v. continuous creep behaviour of faults independently

of (or in addition to) the velocity-strengthening/velocity-weakening behaviour which is currently only studied as a function of mineral composition by laboratory rotary shear experiments.

Impact on hydrocarbon sealing and migration

Fault zone internal structure has major implications in hydrocarbon exploration and production. Faults frequently form side-seals to petroleum traps, as well as providing conduits for fluid flow from deeper to shallow levels in basins. During hydrocarbon production, faults often act as barriers or baffles to fluid flow along the reservoir layers. Understanding these behaviours requires knowledge of fault-zone structure in the subsurface at an appropriate scale – a challenging task for the petroleum geoscientist.

A fault can provide a long-term seal (on geological time-scales) to hydrocarbon movement if the following conditions are met:

1. the reservoir rocks are juxtaposed against sealing lithologies across the fault, by virtue of the fault displacement;
2. or, reservoir–reservoir juxtapositions at the fault-zone are characterized by sealing fault-rock with high capillary threshold pressure;
3. and, the stress conditions on the fault do not promote flow up the fault plane.

Geometrical implications

To determine the first of these conditions requires a detailed mapping of the fault network and the sequence which it cuts. Typically such mapping is based primarily on the interpretation of 3D seismic reflection data. From the layer and fault interpretation, 'Allan diagrams' (named after Urban Allan who popularized these diagrams; Allan 1989) can be constructed. These are displays of the fault plane(s) showing the juxtaposition relationships between reservoir layers on the two sides of the fault. Allan diagrams provide the first-order control on the potential connection topology (plumbing) across faults. In simple circumstances, it is assumed that reservoirs juxtaposed against sealing lithologies will experience a side-seal at the fault, whereas reservoir–reservoir juxtapositions have the potential to provide a fluid pathway across the fault. Interpretational and structural integrity is critical to the creation of accurate Allan diagrams, and industry-standard mapping practice is often inadequate (e.g., auto-tracked horizons, no fault interpretation).

Detailed fault-zone structure also adds uncertainty to Allan diagrams because these details (<10 m size) are below the resolution of the seismic reflection technique (Hesthammer & Fossen 2000). They may include multiple fault planes within the fault zone, and local deformation (ductile or brittle) of the wall-rocks. A common occurrence (Childs *et al.* 1996, 1997) is for two or more separate slip planes to be present, sharing the total displacement that is seen on seismic data, with an intact sliver of rock between them (Fig. 5a). In such cases, individual reservoir layers which appear offset in the seismic image have the risk of being self-connected if their thickness is more than half of the total throw. Three-dimensional studies of fault zone internal structure (e.g., Childs *et al.* 1996) suggest that such a system of separate slip surfaces can be surprisingly variable along strike and up and down the fault (Fig. 5b). Hence such complexity is extremely difficult to predict, although it is likely that such heterogeneity is increased by the presence of strong mechanical layering in the host rock and tilting during deformation (e.g., van der Zee *et al.* 2008). A common wall-rock deformation is a small-scale (<100 m) 'drag' fold in one or both walls of the fault – in extreme cases, such folds may accommodate up to 90% of the total offset (e.g., Fossen & Hesthammer 1998).

Impact of fault rock composition

The sliding of wall rocks past each other creates new rock types within the fault zone, potentially having completely different hydraulic properties from the juxtaposed formations. The nature of fault rock depends on three key factors: the composition of faulted sequence, the stress conditions at the time of faulting, and the post-faulting burial history (especially temperature); (Antonellini & Aydin 1994; Fisher & Knipe 2001; Fulljames *et al.* 1997; Gibson 1998; Sperrevik *et al.* 2002). In clay-rich sequences (typically $>40\%$ clay beds), clay smears are a common component of the fault zone. They are characterized by a tapering wedge geometry, with clay being sheared into the fault zone from upthrown and downthrown halves of an offset clay layer (Weber *et al.* 1978; Aydin & Eyal 2002; Takahashi 2003; Eichhubl *et al.* 2005; van der Zee & Urai 2005). Thicker clay layers tend to be particularly effective at contributing clay into the fault zone, and examples observed at outcrop include smears up to 1 m thick continuous over 70×400 m of fault plane (Lehner & Pilaar 1997). In impure sands (15–40% clay content), faulting creates a 'clay gouge' (or shaly gouge), also known as a phyllosilicate-framework fault-rock (PFFR) (Gibson 1998; Fisher & Knipe 2001). PFFRs exhibit a deformation-induced mixing of clay and sand grains, often with a fabric

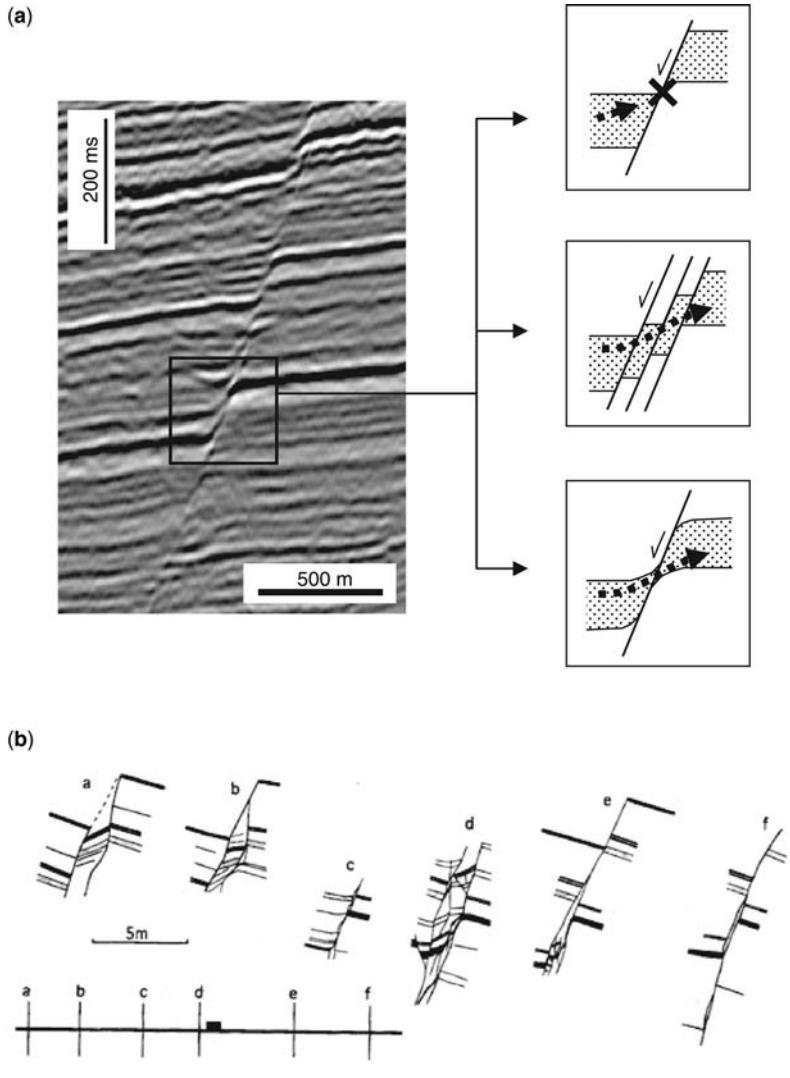

Fig. 5. The problem of resolution from seismically imaged faults and impact on across-fault reservoir connectivity and possible fluid flow pathways. (**a**) Fault zones more complicated than a single slip plane will have reservoir–reservoir connectivities and the potential for fluid migration (bold dashed arrows), which are difficult to predict, as a function of multiple slip planes and/or normal drag. (**b**) An example of along-strike changes in fault zone structure (from Childs *et al.* 1996).

aligned parallel to the fault plane. Faults cutting clean sands (<15–20% clay) show the greatest variety of fault rocks, dependent on the stress-temperature history (Fossen *et al.* 2007). Faulting of clean sand near to the surface results only in a local grain rearrangement, to produce a rock type called a disaggregation zone which has similar hydraulic properties to the host sandstone (Fisher & Knipe 2001). However, faulting the same sand at higher stresses (e.g., >1 km burial depth) results in grain fracturing (cataclasis), with the smaller grain fragments clogging the pore-space (Fowles & Burley 1994; Crawford 1998). With subsequent post-faulting burial, both disaggregation zones and cataclasites (but especially the latter) can be further modified by quartz dissolution and local reprecipitation – this thermally activated process becomes significant deeper than *c.* 3 km (for an average geothermal gradient), (Fisher *et al.* 2003). Severe quartz overgrowths can convert a cataclastic

deformation band to something resembling a 'sheet of glass' in the reservoir.

For fault seal prediction, the huge variety of fault-rocks, described above, may seem daunting. Which fault-rocks are relevant to a particular hydrocarbon prospect? A widely used methodology in the petroleum industry uses the Shale Gouge Ratio algorithm (SGR) to map out the main areas of different fault-rocks automatically on the Allan diagram. SGR is computed from the net clay content of the section sliding past each point on the fault, as this represents the material that can potentially be entrained into the fault zone (Yielding *et al.* 1997; Yielding 2002). Under conditions of perfect mixing, SGR would represent the upscaled composition of the fault rock, but in reality it does not represent the detailed internal structure (e.g., Fig. 6), where many different components (e.g., smears, cataclasites) might be present together (e.g., Foxford *et al.* 1998; van der Zee *et al.* 2008). Nevertheless, recent stochastic modelling of that detailed structure implies that at higher ratios of throw-to-bed thickness the SGR is an effective and pragmatic approximation (Childs *et al*. 2007).

In exploration contexts, fault hydrocarbon retention capacity is then usually evaluated by considering the capillary threshold pressure of the fault rock likely for any SGR value, supposing that the fault zone is saturated in water. In order to perform such an evaluation, a relationship between SGR and threshold pressure needs to be calibrated. SGR values have been calibrated using two different approaches:

1. empirical comparison with in-situ hydrocarbon and pre-production pore-pressure data at proven fault traps (Yielding 2002; Bretan *et al.* 2003; Bretan & Yielding 2005); and
2. analogy with small-scale samples recovered from simple fault zones (Sperrevik *et al.* 2002).

In the empirical approach, it is observed that an SGR of around 15–20% often represents a threshold for a leak-seal transition (e.g., Yielding *et al.* 1997; Gibson & Bentham 2003). This is consistent with fault-rock samples because it corresponds to the distinction between clay-poor fault rocks, such as disaggregation zones, and more clay-rich rocks such as PFFRs and smears. On a more quantitative basis, the SGR values can be calibrated by the *in situ* hydrocarbon buoyancy pressures in observed fault-bound traps, to indicate the strength of the fault seal in terms of the trapped column height (Bretan & Yielding 2005). Similar calibrations can be performed using fault-rock samples, but lab-derived Hg–air threshold pressures must then be converted to hydrocarbon-water values using uncertain fluid properties (O'Connor 2000; Nordgård Bolås *et al.* 2005). In a field development context, the relevant physical property is the fault-rock permeability, upscaled to the size of the cell–cell connections in a geocellular simulation model. The fault-rock property is typically input in terms of modifiers to the cell–cell transmissibilities across the fault – the transmissibility is simply the mean permeability of the juxtaposed cells, weighted by their cross-sectional contact area and the inverse of the distance between their centres (Manzocchi *et al.* 1999).

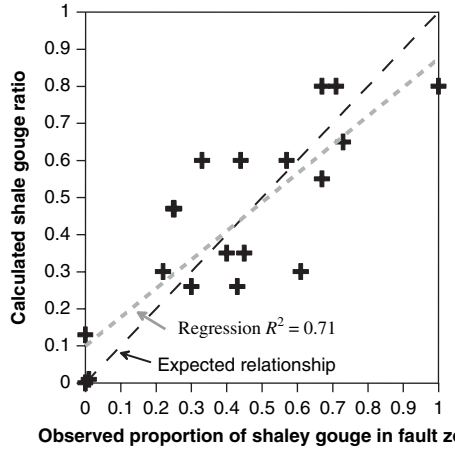

Fig. 6. Evaluation of heterogeneity in clay contents of fault zones as a function of clay content predicted by the shale gouge ratio method (from the Moab fault, Utah, Yielding 2002).

The impact of heterogeneity in structure and composition

The three-dimensional heterogeneity of fault zone internal structure becomes important in predicting hydrocarbon flow in a number of ways. Fault zone capillary threshold pressures vary down the fault plane as a function of juxtaposed stratigraphy (Yielding *et al.* 1997). A sandstone reservoir unit juxtaposed against a sand–shale cover series will have a higher SGR working up the fault plane to the top of the reservoir because a higher percentage of the juxtaposition history will have involved the more shaley cover. Thus capillary threshold pressure will increase up the fault plane accordingly, and such a threshold pressure profile will have to be compared with the buoyancy pressure profile of a possible hydrocarbon column to predict the leak point and hydrocarbon column height retained against the fault (Brown 2003; Bretan & Yielding 2005). Along-strike variations in throw will strongly alter reservoir–reservoir

juxtaposition connections as imaged on Allan diagrams, where reservoir self-juxtaposition becomes more important approaching fault tips and low-displacement segment connections, but also because the branching nature of fault strands can change drastically along strike as described above, strongly influencing reservoir juxtapositions (Hesthammer & Fossen 2000). In the third dimension, across the fault zone, heterogeneity in composition will result in a wide range of fault rock capillary threshold pressures and permeabilities even at the same 'point' on a two-dimensional Allan diagram. Thus treating a three-dimensional fault zone as a two-dimensional surface necessarily adds uncertainty by not taking into account such heterogeneity. For threshold pressures, the threshold pressure of the fault rock directly adjacent to the reservoir wall rock will initially control the hydrocarbon infiltration into the fault zone, followed by the geometry of percolating pathways within the internal structure of the fault zone. Nevertheless, various fault seal prediction studies have attested to the robustness of the SGR approach (at least in the hydrostatic regime), despite this uncertainty, suggesting that this third dimension heterogeneity somehow gets averaged out over the large scale (Yielding 2002; Childs *et al.* 2007).

For permeability, various algorithms have been proposed to predict fault rock permeability with respect to percentage clay content (e.g., Manzocchi *et al.* 1999; Sperrevik *et al.* 2002). These vary widely between each other and are mostly calibrated from samples taken from small (centimetre-offset) faults, although these may not have the same fabrics as more 'mature' faults. A heterogeneous composition across the fault zone will result in across-fault flow rates which are much harder to predict than for a single composition in a homogeneous fault zone. Here the large-scale 'bulk' permeability is unlikely to be the thickness-weighted average of the individual fault rock permeabilities in the fault zone, particularly when permeability anisotropy and tortuosity come into effect. One suggested way forward is to use stochastic flow simulations (e.g., Lunn *et al.* 2008) to model flow in heterogeneous fault zones composed of clay contents with a defined statistical variation both across and along the fault zone, coupled with a permeability-clay content algorithm taking into account permeability anisotropy, and compare the results with single-component systems. A second parallel route forward is to 'calibrate' fault zone permeability behaviour with large (e.g., field) scale examples where fault permeability has been estimated, such as from field tests like tracers or four-dimensional seismic, or production history matching, for example (see Jolley *et al.* 2007 for a comprehensive overview of current best practice).

Impact of stress state

Whatever the ability of the fault zone to act as a seal to across-fault flow, fluid flow *within* the fault zone may be promoted by the *in situ* stress state. A fundamental criterion for such flow is that the fault be critically stressed and close to frictional failure (Barton *et al.* 1995). Flow probably occurs in arrays of dilatant microfractures which are associated with the slipping (or near-slipping) fault surface (e.g., Losh *et al.* 1999). This behaviour was initially quantified by studies of fractured basement rocks, but has now been observed in seismic reflection studies of an actively slipping growth fault in the Gulf of Mexico, where a large pulse of overpressured fluid appears to be moving up the fault zone at >100 m per year (Haney *et al.* 2005). For predictions of whether such flow may occur, it is necessary to know the *in situ* stress state and pore-pressure, and the approximate strength of the fault zone (assumed to be weaker than the surrounding rock, but see Dewhurst & Jones 2003). Different parts of the fault network feel a different imposed stress according to their orientation in the stress field. The nearness to failure of a particular fault plane is assessed by parameters such as 'slip tendency' (ratio of shear stress to normal stress, Morris *et al.* 1996) and 'fracture stability' (a measure of the pore-pressure increase that would induce slip, Wiprut & Zoback 2000; Mildren *et al.* 2005). Such parameters may help in ranking different fault trends for potential seal breach, ranking different faults for stability during drilling, and understanding migration pathways from deep to shallow parts of the section (Mildren *et al.* 2002).

Implications for seismogenic processes

Earthquakes are the result of ruptures that nucleate, grow and terminate along, in most cases, pre-existing faults (Gilbert 1884; Koto 1893; Scholz 2002). Earthquake dynamics is concerned with both the behaviour of the volume around the fault, its accumulation of elastic strain energy and catastrophic release thereof (e.g., Reid 1910). The behaviour of the fault itself is a contact problem in which understanding fault friction (e.g., Scholz 1998) and shear fracture development (Ohnaka 2003) are key features. The recognition that most faults are in reality zones of complex and unpredictable internal structure and composition in which the rupture nucleates and through which it propagates (e.g., Sibson 1983), has deep-reaching implications for

our understanding of earthquake-related processes and how we model them. In this section we will briefly review some recent results of the role of rheology of fault materials and of geometry of faults in controlling earthquake nucleation, propagation and arrest.

Complexity of seismic fault zone structure

As the contributions to this Special Publication illustrate, faults are often very heterogeneous zones with respect to their structure and physical properties. In the case of strike–slip faults, for example, field investigation of fault zones exhumed from different depths in the crust reveal different architectures that vary with host lithology and grade of maturity of the fault (displacement, exhumation history and reactivation for example). In the case of shallow crustal deformation, the Punchbowl fault, exhumed from 2–5 km depth in the San Andreas Fault system, accommodated about 30 km of slip on a metre-scale wide cataclasite fault core surrounded by a fracture damage zone several hundreds of metres wide (e.g., Chester *et al.* 1993; Chester & Chester 1998). In this case it has been shown that most of the deformation is localized on individual 100 μm to centimetre-scale thick ultracataclasite slipping zones, so that only a small proportion of the highly deformed fault core was thought to have accommodated the most recent rapid slip events. Larger-displacement fault zones from similar depth, such as the main active strands of the San Andreas fault intersected at 3 km depth by SAFOD drilling (San Andreas Fault Observatory at Depth) project, have several creeping subparallel fault cores, cutting a wider, up to 1 km thick, damage zone (SAFOD phase III preliminary results, Hickman 2007). A spectacular example of the complexity of a mature plate-boundary fault zone exhumed from 1.5–4 km depth is the Carboneras Fault in Spain (Faulkner *et al.* 2003). The fault zone, which accommodates up to 40 km of displacement, consists of a 1 km thick fault zone composed of continuous and anastomosing strands of phyllosilicate-rich fault gouge bounding lenses of dolomite hundreds of meters long. The wide nature of the fault gouge and lack of evidence for localization of rapid slip deformation within the structure suggests that the fault operated as a stably creeping plate boundary fault (Faulkner *et al.* 2003, 2008).

With increasing depth, fault zone internal structure and the range of fault rocks vary with the degree of maturity of the fault (e.g., Holdsworth *et al.* 2001). For instance, long-lived active faults exhumed from about 10–15 km depth that accommodated hundreds of kilometres of slip, like the Median Tectonic Line in Japan, have complex fault cores, with mylonites and foliated cataclasites (representative of the deeper activity of the fault, see Jefferies *et al.* 2006) cut by phyllosilicate-rich foliated gouges and clay-rich cores produced by continued fault activity during exhumation to shallower levels (Wibberley & Shimamoto 2003). Less mature fault zones exhumed from similar depths (9–11 km), but with cumulated displacements of several kilometres at most, may consist of hundreds of centimetre-thick cataclasite–mylonite zones cutting a poorly developed damage zone (e.g., Gole Larghe Fault Zone, Italy, Di Toro & Pennacchioni 2005; Fort Foster Brittle Zone, Maine, Swanson 1988; Ikertorq Brittle Fault Zone, Greenland, Grocott 1981). In this latter case, the fault zone hosts abundant pseudotachylytes (usually less than 1 cm in thickness) within the fault rocks (a marker of ancient seismic activity, e.g., Cowan 1999), which are not found in the other faults. Thus for these examples of faults active at greater depths in the Earth's upper crust, the range of fault rocks and complexity of their distribution increases with fault displacement and degree of exhumation during activity. Though these field studies give a flavour of the complexity of natural fault zones as well as how difficult it is to determine and infer fault structure at depth, recent experimental and numerical modelling studies, based on field observations and seismological data, have helped greatly to understand the role of heterogeneity and complexity in fault zone internal structure on the seismogenic behaviour of fault zones.

Rupture nucleation

The nucleation of crustal earthquakes is generally thought to be the consequence of frictional instabilities along fault surfaces (Brace & Byerlee 1966) similar to stick–slip phenomena observed during sliding of metals (Bowden & Tabor 1950; Rabinowicz 1966). Although friction is the result of geometrical, chemical and atomic interactions (Coulomb 1785; Bowden & Tabor 1950; Rabinowicz 1965; Persson 2000; Gerde & Marder 2001; Urbakh *et al.* 2004), here we only consider rock friction as the result of the interaction of geometrical asperities or protuberance of the sliding surfaces; the importance of fault healing (e.g., Muhuri *et al.* 2004) being beyond the scope of this review. Roughness is typical of all fault surfaces over a wide scale range (Power *et al.* 1988; Power & Tullis 1992; Renard *et al.* 2006; Sagy *et al.* 2007). Fault irregularities may produce detectable pre-earthquake stress heterogeneities. The distribution of static stress drops during earthquakes suggests that fault surfaces are irregular and only

accumulate stresses over a small fraction of their area at a limited number of asperities, emphasizing the importance of the asperities in the rupture process (Bouchon 1997; Sammis *et al.* 1999; Fletcher & McGarr 2006).

Seismic ruptures can only nucleate in velocity-weakening rocks (see Scholz 2002 for a discussion). However, not all rocks are velocity-weakening for slip rates lower than 0.001 m s^{-1} (velocities considered to be appropriate to the nucleation zone of an earthquake). Fault gouges containing abundant clay minerals such as montmorillonite, chlorite and illite are consistently velocity strengthening (Marone *et al.* 2008), whereas smectite may show a complex dependence with slip rate, normal stress and temperature (e.g., Saffer *et al.* 2001). For $T < 200\ ^{\circ}C$, brucite, chrysotile- or antigorite-serpentinite gouges are velocity-strengthening or velocity-independent under drained conditions (e.g., Moore *et al.* 1996, 2001), thereby inhibiting dynamic instability and promoting stable creep (Moore *et al.* 2004). The direct extrapolation of these experimental observations to natural conditions implies that a heterogeneous distribution of different velocity-weakening and velocity-strengthening fault materials is one of the factors controlling earthquake nucleation (Marone & Scholz 1988). For example, in the case of the complex Carboneras Fault zone structure, this extrapolation predicts that earthquakes would nucleate in the dolomite patches (velocity-weakening) and arrest in the continuous clay-rich layers (velocity-strengthening) (Faulkner *et al.* 2003, 2008). The preliminary examination of the samples recovered from cuttings of the SAFOD borehole, located close to the northwestern end of the 2004 M5 Parkfield earthquake rupture zone, shows the presence of velocity-strengthening materials such as talc (derived from host rock serpentinite by alteration in the fault zone). Although further work is needed to better quantify how much talc is present, this could provide an explanation for the lack of large earthquakes on this portion of the San Andreas fault (Moore & Rymer 2007). Yet the fact that there are earthquakes at all, albeit small ones, suggests the presence of compositional heterogeneity with both velocity-strengthening and velocity-weakening materials (Wibberley 2007) similar to the behaviour suggested for the Carboneras fault as mentioned above. Indeed, recent borehole data (SAFOD, phase III preliminary results, Hickman 2007) show that aseismic creeping fault strands have a 1–2 m thick clay-, serpentinite- and talc-bearing central zones (Moore & Rymer 2007), whereas microseismicity is localized in metric to decametric scale patches (the so-called 'Hawaii Islands') located about 150 m below the cored faults. Though we might speculate that the 'Hawaii Island' microearthquakes are located inside velocity-weakening patches (e.g., sandstones lenses embedded in the creeping sections), further studies (and drilling) are necessary to solve the issue.

Rupture propagation

Dynamic weakening. The diversity of material-dependent frictional responses observed at subseismic slip rates (velocity-strengthening v. velocity-weakening), disappears approaching seismic slip rates ($V = 1$ m s^{-1}), as illustrated by the synthesis of laboratory rock friction data in Figure 7. In fact, *all* the rocks tested so far, including cohesive rocks (tonalite, diorite, gabbro, peridotite, serpentinite, limestone, marbles, siltstone, serpentinite: Hirose & Shimamoto 2005*a*, *b*; Spray 2005; Di Toro *et al.* 2006*a*, *b*; Hirose & Bystricky 2007; Han *et al.* 2007), and non-cohesive rocks (clay-rich fault gouges, Mizoguchi *et al.* 2007; Boutareaud *et al.* 2008*b*), have a low friction coefficient (on average, 0.2) and a strong velocity dependence at seismic slip rates, independently of the specific weakening mechanism involved (Figs 7 & 8). The experimental data are reliable, since (1) these low values for friction were obtained in different experimental configurations and apparatus (e.g., rotary torsion, rotary shears, torsion bars, Di Toro *et al.* 2004; Hirose & Shimamoto 2005*a*; Prakash & Yuan 2004) and (2) other materials, such as aluminium, in the same apparatus and under the same deformation conditions, are velocity-strengthening (Han, pers. comm.). In the case of frictional melting, field (Di Toro *et al.* 2006*a*) experimental (Hirose & Shimamoto 2005*a*; Spray 2005; Di Toro *et al.* 2006*a*) and theoretical analyses (Fialko & Khazan 2005; Nielsen *et al.* 2008) all indicate lubrication of fault surfaces in the presence of melts. Such a review of data from different velocity ranges shows that the low value for friction at $V = 1$ m s^{-1} is in contrast with the finding of the conventional experiments performed at $V < 0.01$ m s^{-1} and displacements of few centimetres at most, where μ is 0.6–0.8 (Fig. 7; Stesky *et al.* 1974; Byerlee 1978). The dramatic weakening found in these high-velocity experiments, might explain several seismological and geophysical observations, including: (i) why dynamic stress drops (the difference between initial stress and frictional stress while the fault is slipping) are larger than static stress drops (the difference between the average shear stress on the fault zone before and after the earthquake); (ii) the rupture propagation mode (see below); (iii) the increase in the ratio of radiated energy v. seismic moment with earthquake size (Mayeda & Walter 1996); and (iv) the production of heat during seismic slip (e.g., Lachenbruch 1980).

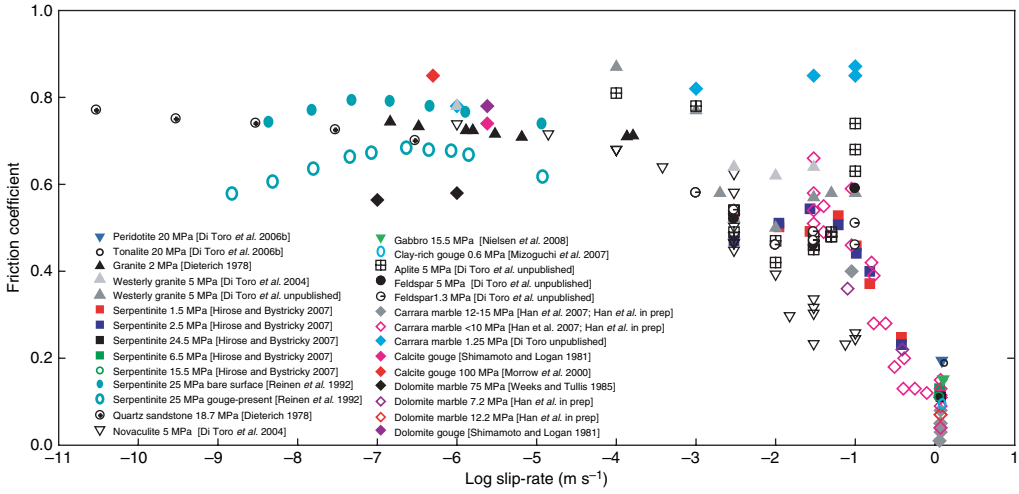

Fig. 7. Dependence of steady-state friction (black box in Fig. 8) on slip velocity. Data for aplite (Di Toro, Goldsby & Tullis unpublished data), calcite marble (Di Toro, Goldsby & Tullis unpublished data; Han *et al.* 2007), calcite gouge (Shimamoto & Logan 1981; Morrow *et al.* 2000), clay-rich gouge (Mizoguchi *et al.* 2007), dolomite (Weeks & Tullis 1985; Han *et al.* in preparation), feldspar (Di Toro, Goldsby and Tullis unpublished data), gabbro (Nielsen *et al.* 2008), granite (Di Toro *et al.* 2004; Di Toro, Goldsby and Tullis unpublished data; Dieterich 1978), peridotite (Di Toro *et al.* 2006*b*), quartz sandstone (Dieterich 1978), novaculite (100% quartz rock, Di Toro *et al.* 2004), serpentinite (Reinen *et al.* 1992; Hirose & Bystricky 2007) and tonalite (Di Toro *et al.* 2006*b*). At slip rates approaching 0.1 m s^{-1}, most rocks show an abrupt decrease in friction coefficient, independently of normal stress and rock type. The standard deviation at steady-state for each individual data point (namely, the standard deviation for the corresponding curve inside the black box shown in Fig. 8) is usually smaller than the plotted symbol, so it was eliminated to render the figure simpler. The diagram was made in collaboration with Raehee Han.

Another observation is that clay-rich gouges are also velocity-weakening at seismic slip rates (Fig. 7). This has important implications for the role played by the internal structure of the fault: earthquakes nucleating in velocity-weakening parts of the fault zone may propagate into and through zones such as clay gouges (or at greater depths, phyllonite) of velocity-strengthening (at low slip rates) behaviour if the rupture energy is sufficient to overcome the low-slip-rate barrier (Fig. 9). This will either bring this material into the high-velocity weakening regime and/or allow propagation through into another velocity-weakening region (Fig. 9c). Thus although a rupture tip propagating through a velocity-strengthening material will have more energy absorbed than it would do in a velocity-weakening material, the inference that the strengthening material will change the polarity of its velocity dependence at high velocity to that of weakening suggests that the dampening impact on propagation may not be as severe as previously thought (e.g., Scholz 2002). Such behaviour could be considered as 'conditionally stable' in a slightly different sense than that defined by Scholz (1998), but with the same outcome: a sufficient velocity kick will make it unstable, allowing rupture propagation. Whether or not the rupture tip can give the required velocity kick depends upon the slip rate behind the tip zone when it entered the velocity-strengthening material. This will be a function of the seismic moment up to this point, and hence rupture surface area in the velocity-weakening material, suggesting that there is a strong scale influence of heterogeneity on this process. Other key controls will be the rate of dampening during slip acceleration to the velocity-weakening state, and the relative and absolute sizes of 'nucleating' velocity-weakening zones and 'conditionally' stable zones, which are initially velocity-strengthening (Fig. 9c). The impact of other weakening processes such as those listed below can also affect the success of the rupture tip in continuing to propagate by absorbing less energy on the parts of the rupture surface already slipping at high velocity, thus retarding dampening. Hence, in many heterogeneous fault zones, ruptures may continue to propagate beyond velocity-weakening (at low slip rates) zones depending upon a variety of factors in which the spatial distribution of different fault zone materials plays an important part (Fig. 9c). This might in some cases reduce the degree of complexity of earthquake source physics.

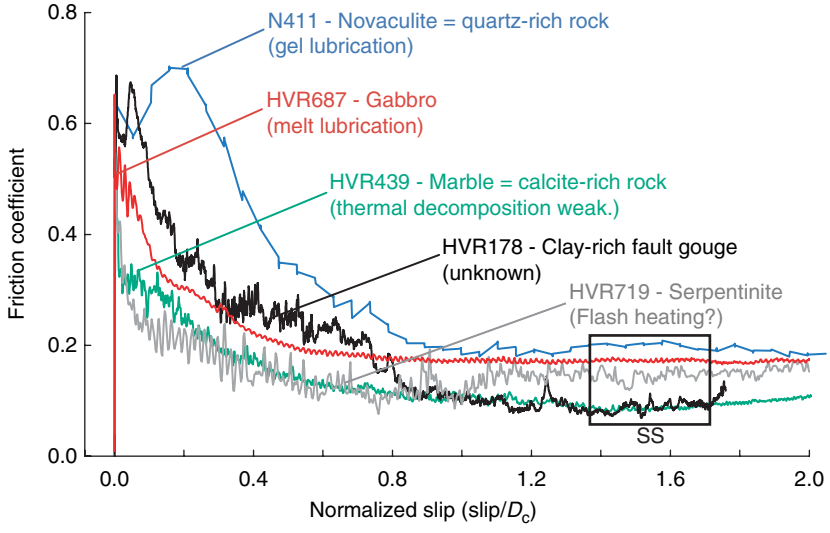

Fig. 8. Dependence of friction on slip displacement for gabbro (HVR687, $\sigma_n = 15.5$ MPa, $V = 1.14$ m s^{-1}, $D_c = 2.5$ m, Nielsen *et al.* 2008), novaculite (N411, $\sigma_n = 5$ MPa, $V = 0.1$ m s^{-1}, $D_c = 1.3$ m, Di Toro *et al.* 2004), serpentinite (HVR719, $\sigma_n = 2.5$ MPa, $V = 1.10$ m s^{-1}, $D_c = 1.8$ m, Hirose & Bystricky 2007), calcite marble (HVR439, $\sigma_n = 7.3$ MPa, $V = 1.18$ m s^{-1}, $D_c = 5.0$ m, Han *et al.* 2007) and clay-rich gouge (HVR178, $\sigma_n = 0.62$ MPa, $V = 1.03$ m s^{-1}, $D_c = 22.2$ m, Mizoguchi *et al.* 2007). The black box highlights the so called steady-state (SS) friction coefficient, reported in Figure 7. These experiments were performed under different normal stress and, in the case for novaculite, slip rate. To plot all the data in the same diagram, the slip displacement was normalized with respect to the critical slip distance D_c. All rocks shown in this diagram, independently of the weakening mechanism involved (which remains unknown for HVR178), have a low friction coefficient approaching seismic slip rates. The sharp decrease in friction coefficient (about 80–90% of the initial value) is one order of magnitude larger than the one observed in the same rocks but for $V < 1$ mm s^{-1} (few per cent of the initial value, e.g., Marone 1998) Original data are courtesy of Takehiro Hirose (HVR719), Raehee Han (HVR439) and Kazuo Mizoguhi (HVR178).

The weakening mechanisms activated in the laboratory at seismic slip rates share the strong dependence with temperature. Examples of such weakening mechanisms are: water pressurization and vaporization (e.g., Brantut *et al.* 2008; Boutareaud *et al.* 2008*b*); dehydration (Hirose & Bystricky 2007) and decarbonation (Han *et al.* 2007) reactions; gelification (Goldsby & Tullis 2002; Di Toro *et al.* 2004; Roig-Silva *et al.* 2004) of silica-bearing rocks; local (flash) heating and eventually melting of the asperity contacts (Goldsby & Tullis 2003; Beeler *et al.* 2008) or bulk melting (Hirose & Shimamoto 2005*a*; Spray 2005; Di Toro *et al.* 2006*a*, *b*) of the fault surfaces and materials. Given that frictional heating depends upon the shear strain rate and hence (coseismic) slip zone width, the typical narrowness of slip zones (a few hundreds of microns to a few centimetres at most, see Sibson 2003 for a review) makes coseismic temperature increase an important issue. Furthermore, frictional heat diffusion is typically limited to a few millimetres in the slipping zone due to the low thermal diffusivity of rocks, so that the localization of heat in the slipping zone means that earthquake mechanics and dynamic weakening mechanisms are mainly controlled by local temperatures (Rice 2006; Rice & Cocco 2007; Pittarello *et al.* 2008). The narrowest slip zones are often (but not always) those generated by the most extreme localization of deformation at competence contrast boundaries between different lithologies or different fault rock materials. Hence it is likely that the localization of rapid deformation at competence contrast boundaries within fault zones or at the fault zone/host rock boundaries will favour dynamic weakening.

In all these cases, the continuity of the fault zone material(s) giving rise to the particular dynamic weakening process is an important issue – without this continuity in the slipping zone, the weakening process cannot operate efficiently and the rupture propagation may terminate. For example, water-saturated gouge slip zones have sufficiently low permeability to trap frictionally-heated pore water and hence cause dynamic weakening by thermal pressurization, provided they are laterally

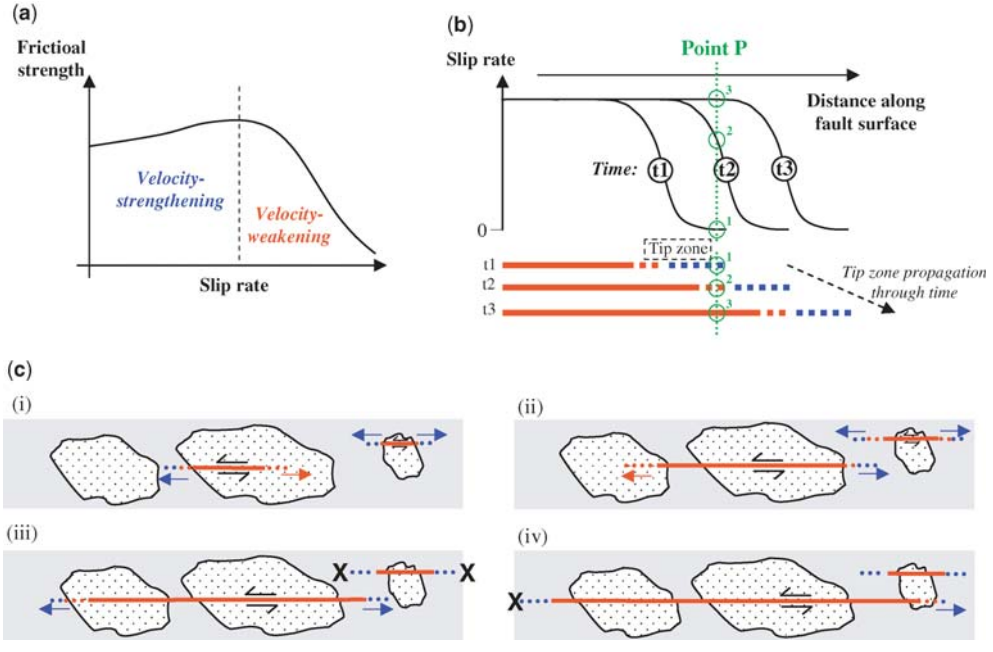

Fig. 9. The impact of material heterogeneities as velocity-behaviour heterogeneities in the fault zone on seismic rupture propagation. (**a**) Velocity behaviour of a material which is velocity-strengthening at low slip rates and velocity-weakening at high slip rates. The slip rate at the transition from one velocity regime to the other may vary from one material to another for those materials which behave in this way; (**b**) change in velocity behaviour at a point as a function of time as the rupture zone propagates through the point. The tip zone is represented as a dashed line. For propagation through a material which is velocity-strengthening at low slip rates, that part of the tip zone which is in the velocity-strengthening field is indicated in blue, the part which has already accelerated into the velocity-weakening field is indicated in red; (**c**) schematic cartoon illustrating the importance of the size of velocity-weakening (at low slip rate) zones (stippled) and the 'gaps' between them containing velocity-strengthening (at low slip rates) material (grey shading). (i)–(iv) represent phases through time. **X** denotes a rupture termination where the size of a velocity-strengthening (at low slip rate) material 'gap', in relation to the scale of velocity-weakening zones and rupture size, was too large to sustain continued rupture propagation and give the velocity kick necessary to bring it into the velocity-weakening field. The dotted lines indicate the tip zones, with blue arrows indicating rupture propagation despite velocity-strengthening at the front of the tip zone, and red arrows indicating velocity-weakening propagation.

and vertically continuous (Wibberley & Shimamoto 2005). Heterogeneity in permeability properties of the slip zone, such as could happen if the rupture front propagates onto a branch fault which splays into a higher-permeability damage zone, would diminish the efficiency of the dynamic weakening, leading to possible rupture termination and seismic asperities (Wibberley & Shimamoto 2005, Boutareaud *et al.* 2008*a*).

The critical slip distance Dc. One important parameter in earthquakes is the critical slip distance D_c over which strength drastically decreases because it controls the size of the rupture nucleation dimension, the magnitude of pre- and post-seismic slip and the length scale over which dynamic stress is concentrated at the rupture front (Marone 1998 for a review). In experiments performed at sub-seismic slip rates, D_c has a length comparable with the asperity diameter (*c.* 5–50 μm) of the bare surfaces. So D_c is related to the initial roughness of the sliding surface and is interpreted as the slip distance to renew the asperity contacts (Dieterich 1979). In the case of gouge in an experimental fault zone, D_c is controlled by the thickness of the zone of localized shear strain (Marone & Kilgore 1993). However, in nature, if a slip weakening distance exists, it is of the order of metres (Ide & Takeo 1997; Tinti *et al.* 2004; Ma *et al.* 2006). Simple upscaling of experimental data from drained gouge zones suggests that a deforming zone in the order of a hundred metres wide is needed to explain seismically-derived D_c

values (Marone & Kilgore 1993). Whilst gouge zones may indeed be this wide, field studies of fault zone internal structure suggest that typically much narrower slip zones are active during any one rapid slip event (Chester & Chester 1998; Sibson 2003; Wibberley & Shimamoto 2005; Di Toro *et al.* 2006*a*). The discrepancy between experimental and seismically-inferred D_c values might firstly be because in natural faults gouges are typically of low permeability causing undrained conditions during rapid shearing, so that thermal pressurization controls D_c (Wibberley & Shimamoto 2005), or by considering that asperities are larger in nature. This latter possibility requires the determination of fault roughness (Power *et al.* 1988; Power & Tullis 1992; Renard *et al.* 2006; Sagy *et al.* 2007) over a wide range of scales, particularly as geometric irregularities at larger scales than the thickness of the seismic slip zone are likely to be the most important. However, in high-velocity rock friction experiments, performed on smooth surfaces, the slip weakening distance is of the order of metres, and decreases with increasing normal stress, suggesting that it is the thermal history and the rheological evolution of the fault materials that controls D_c (Hirose & Shimamoto 2005*b*; Nielsen *et al.* 2008), as well as possibly its dependence on slip velocity in these experiments. Further studies are necessary to investigate the relationships between fault geometry and weakening mechanisms and their role in controlling D_c, as well as integrating the results of constant-velocity experiments into a real earthquake model for widely varying velocity regimes.

Type and speed of rupture propagation. The type of rupture propagation during earthquakes is strongly influenced by fault geometry and fault zone structure. The two end member models of rupture propagation are the expanding crack model and the self healing pulse model (e.g., Heaton 1990; Zhang & Rice 1998; Beeler & Tullis 1996; Nielsen *et al.* 2000). In the expanding crack model, the earthquake nucleation region slips for the duration of the earthquake, and slip ceases on the entire fault when the rupture arrests. The self-healing pulse considers that only a small patch of the fault slips at any one time. Quantitative models that produce self-healing pulses consider large dynamic stress drops (e.g., Heaton 1990), not included in the rate and state friction law (Dieterich 1979; Ruina 1983) that describes rock friction experiments conducted at slip rates <1 mm s^{-1}, but consistent with the large dynamic stress drops found in high-velocity rock friction experiments (Fig. 8), and with the presence of strong pre-rupture stress heterogeneity related, for instance, to fault geometry (Nielsen *et al.* 2000).

Preliminary field studies suggest that the rupture speed during earthquakes is controlled by fault geometry. For instance, though most earthquake ruptures propagate at velocities approaching the shear wave velocity (the so-called Rayleigh speed which is on average in most rocks 3 km s^{-1}), some ruptures propagate at supershear velocities (4.5–5 km s^{-1}) (Bouchon & Valleé 2003). Ongoing research suggests that supershear speed is achieved along straight fault segments, indicating that fault smoothness is one of the main parameters controlling rupture speed (Das 2007; Bouchon pers. comm.).

Asperities. High-velocity experiments indicate that the friction coefficient decreases at seismic slip rates to about 10–20% of its initial value (Fig. 7) and is slightly dependent on the normal stress (e.g., melt lubrication, Nielsen *et al.* 2008). Extrapolating these observations to natural conditions suggests: (1) the possibility of large coseismic stress drops in nature (up to 100–150 MPa at 10 km depth); and (2) that stress drop should increase with fault depth. Although *dynamic* stress drops as large as 100 MPa have been estimated for discrete fault segments of the ML 6.7 Loma Prieta earthquake (Bouchon 1997), and Fletcher & McGarr (2006) calculated an increase in the *static* stress drop with depth for some earthquakes, experimental results are at odds with the seismological observation that *static* stress drops are typically between 1 and 30 MPa, irrespective of earthquake size (e.g., Hanks 1977). One appealing explanation for the discrepancy – although not the only possible explanation – is the role of fault geometry. In the experiments, given the small size of the samples (usually less than 25 mm in diameter), it is not possible to reproduce the roughness of natural fault surfaces. The presence of geometrical asperities might impede the smooth sliding simulated in the laboratory, and experiments performed along pre-existing smooth surfaces underestimate the mechanical work expended (1) to override the asperities (dilatancy), and (2) to break the asperity junctions and short-cut the contractional jogs. The bulk effect of the introduction of surface roughness could be to increase the frictional resistance: roughness could buffer the dramatic decreases in strength suggested by the weakening mechanism discussed earlier. The problem could be tackled by numerical models which include the fault roughness and the constitutive laws of the new dynamic weakening mechanisms. The input roughness of the fault for the numerical model could be imported directly from the quantitative field reconstruction of the fault geometry (e.g., Sagy *et al.* 2007).

Rupture arrest

Looking at the larger scale, one of the most critical aspects of fault geometry is their action as barriers to earthquake propagation. For instance, the presence of kilometric scale dilational and contractional jogs and step-overs is one of the most reliable physical barriers to arrest the propagation of large earthquakes (King & Yielding 1984; Sibson 1985, 1986; Wesnousky 1988, 2006). However, 'barriers' are not only geometrical. For instance, several strike–slip earthquake ruptures stop along planar surfaces, suggesting that other mechanisms, such as the presence of velocity-strengthening materials (clays, serpentinites, etc.) might stop the propagation of the rupture. In the case of the repeated M5 earthquakes occurring in the Parkfield segment of the San Andreas Fault, one rupture tip could be associated with the southern fault bend where the 1857 M8.1 Fort Tejon earthquake, propagating from the south, stopped (geometrical barrier), whereas the north-western rupture end of the Parkfield segment could be explained by fault rheology (Bakun *et al.* 2005).

However, rupture arrest may also occur because the elastic strain energy released from the wall rocks is not able to sustain the propagation of the rupture in the slipping zone. This, for instance, could be the case in the lower crust, where (i) fault rocks are velocity-strengthening (e.g., at temperatures $>300\ ^{\circ}C$ in the case of granite), and (ii) crystal-plastic deformation in the shear zones releases the elastic strain energy stored in the host rocks which, by decreasing the rupture driving forces, progressively stops the propagation of the rupture at depth. As the presence of phyllosilicates such as talc, phengite and chlorite in large fault zones is extremely frequent, and these minerals show temperature-activated creep at much lower temperatures than most other silicates, the role of crystal plastic deformation in rupture arrest even at relatively shallow levels in the Earth's upper crust should be considered (Wibberley 2007; Imber *et al.* 2008). Alternatively, the energy loss in the damage zone (i.e., outside the slip zone) by fracturing the wall rocks and by absorbing the elastic strain energy released during rupture propagation may determine the arrest of the rupture (Andrews 2005).

A corollary stemming from findings into the role of fault geometric barriers in stopping earthquake propagation is that earthquakes therefore do not always know *a priori* if they are going to be small or large, and could be similar at least during their nucleation phase (e.g., Wesnousky 2006). Other than fault geometry, such earthquakes may differ only in the amount of elastic strain energy stored in the wall rocks and of its release during rupture propagation. Yet this suggestion conflicts with other studies that found much higher proportions of high-frequency radiated energy during the early stages of small earthquakes than large ones, suggesting that small and large earthquakes could be different from their very early initiation, perhaps due to differences in the initial stress (Olson & Allen 2005). The answer to this paradox may lie in considering the evolution of fault zone structure with growth of the fault, and in particular the roughness of the seismic slip zone (e.g., Dolan 2006). Small magnitude earthquakes, which may occur on small faults as well as large faults, often generate higher-frequency seismic waves in the early stages of the earthquake than do larger earthquakes, which necessarily occur on larger, more mature and probably 'smoother', faults. Hence the correlation of earthquake magnitude with proportion of early high frequency waves could simply be reflecting slip zone roughness within a complex fault zone structure. In particular, Sagy *et al.* (2007) found that fault surface roughness evolves with cumulated slip: parallel to the slip direction, small-slip faults are about one order of magnitude rougher than large-slip faults. The difference in geometry implies that the nucleation, growth and arrest of earthquakes should be different for small compared to large earthquakes and explains why the amount of high-frequency radiated energy should be smaller for large earthquakes. The way in which fault zone internal structure and heterogeneity in physical properties may control the final size of the rupture (and of the magnitude of an earthquake) is of great relevance in earthquake hazard mitigation such as early warning systems (e.g., Gasparini *et al.* 2007), and this necessitates further field, theoretical and experimental studies.

Concluding statements

Field studies of fault zones show a wide variety of internal structure depending on a number of geological variables such as displacement, lithology, depth and pre-existing fabric. A number of different mechanisms for incorporating wall rock material into the fault zone have been identified, each of them scale-dependent, and each relying on weakening of the surrounding host rock by a specific scale-dependent mechanism. The sum effect of these scale-dependent mechanisms in data complications over a wide range of scales may give the inaccurate impression that fault growth mechanisms are scale-independent. Nevertheless, whilst a certain amount may be gleaned from field studies of fault zones in terms of their growth mechanisms, relative chronological markers in the growth stages of a fault are not often

present. Hence inferences on growth patterns of fault zones from studying the final state alone must be treated with caution.

Concepts on permeability structure have advanced significantly in the past decade, but remain centred around the notion that two components can usually be identified in fault zones: a fracture-dilatant conducting component and a granular compacting barrier component. The relative distribution and properties, including anisotropy, of each component will govern the overall hydraulic behaviour of the fault. An advancing concept in this paper is that hydraulic and hydrodynamic behaviour of the fault during its activity may be predictable using concepts of critical state soil mechanics for the granular material and elastic crack mechanics for the fracture-dilatant component. Such advances have clear applications in considering the role of active faults in limiting hydrocarbon trap retention, evaluating the risk of slip instability during hydrocarbon production, and understanding the role of fluids in earthquake slip mechanics.

Field studies illustrate why faults cannot simply be treated as discrete surfaces when modelling mechanical and fluid flow behaviour. Yet the complexity and heterogeneity in fault zone internal structure makes predicting fluid flow and seismogenic behaviour an extremely difficult task. For applications to the hydrocarbon industry, across-fault reservoir juxtaposition or non-juxtaposition is a critical geometric property to define in fault analysis. Yet juxtaposition is largely controlled by the geometry of accommodation of overall throw in the complex fault zone and adjacent volume: normal 'drag' folds may reduce reservoir offsets, as may the distribution of throw over several sub-parallel fault strands. Thus the recognition of this at the scale of seismic resolution or incorporation of such possible complexity at the sub-seismic scale in uncertainty estimates is crucial to prediction of across-fault reservoir communication. The last decade has seen significant advances in the way fault zone properties are quantitatively evaluated for estimates of hydrocarbon retention and production-induced pressure differences. These relatively recent approaches use rules-of-thumb to predict general fault zone structure based on previous experience and field examples, often by predicting average properties at any one point on a fault and calculating the variation in these properties over the entire fault 'surface' of interest. Such pragmatic approaches average out the complexity across the fault zone. Whilst such approaches have met with success up to a point, a next natural step is to evaluate the uncertainties induced in these averaging approaches by modelling statistical variations in properties across the fault zone and what impact they would have on the predicted outcome.

Linking fault zone internal structure characteristics to various aspects of seismogenic behaviour such as those described in this paper requires a leap of scientific imagination only possible by integrating structural observations with seismological data and laboratory frictional and petrophysical measurements on relevant fault rocks. The complexity of fault zones strongly influences a number of processes occurring during the lifetime of an earthquake rupture, particularly by the distribution of materials of contrasting mechanical and frictional behaviours. Indeed, recent findings suggest that whether the fault deforms by unstable earthquake slip at all, or suffers slow steady creep instead, is controlled at least partly by the contrast in velocity behaviours of different materials in the fault zone. Despite the recent increase in available laboratory data, the limits of scale, particularly in fault surface geometry, should never be neglected.

The authors would like to thank Bob Holdsworth for a very efficient and effective review of the paper. C. W. thanks the Geological Society publishing staff and book committee for encouraging this Special Publication to come to fruition. Data for Figures 3 and 4 were measured in a high-pressure gas deformation apparatus at Kyoto University in the laboratory of T. Shimamoto, who is thanked for his guidance. G. D. T. thanks M. Bouchon and S. Nielsen for discussions, T. Hirose, R. Han and K. Mizoguchi for sending their original data for preparing Figure 8 and R. Han for helping in assembling Figure 7. The costs of the work by G. D. T. were covered by grants from the Università degli Studi di Padova (Progetto di Ateneo 2007) and Progretti di Eccellenza Fondazione CARIPARO (CAassa di RIsparmio di PAdova e ROvigo).

References

AGOSTA, F. 2008. Fluid flow properties of basin-bounding normal faults in platform carbonates, Fucino basin, central Italy. *In*: WIBBERLEY, C. A. J., KURZ, W., IMBER, J., HOLDSWORTH, R. E. & COLLETTINI, C. (eds) *The Internal Structure of Fault Zones.* Geological Society, London, Special Publications, **299**, 277–291.

ALLAN, U. S. 1989. Model for hydrocarbon migration and entrapment within faulted structures. *American Association of Petroleum Geologists Bulletin*, **73**, 803–811.

AMITRANO, D. & SCHMITBUHL, J. 2002. Fracture roughness and rouge distribution of a granite shear band. *Journal of Geophysical Research*, **107**, 2357 doi:10.1029/2002JB001761.

ANDREWS, D. J. 2005. Rupture dynamics with energy loss outside the slip zone. *Journal of Geophysical Research*, **110**, doi:101029/2004JB003191.

ANTONELLINI, M. A. & AYDIN, A. 1994. Effect of faulting on fluid flow in porous sandstones: petrophysical properties. *American Association of Petroleum Geologists Bulletin*, **78**, 355–377.

ANTONELLINI, M. A. & AYDIN, A. 1995. Effect of faulting on fluid flow in porous sandstones: geometry and spatial distribution. *American Association of Petroleum Geologists Bulletin*, **79**, 642–671.

AYDIN, A. & EYAL, Y. 2002. Anatomy of a normal fault with shale smear: implications for fault seal. *American Association of Petroleum Geologists Bulletin*, **86**, 1367–1381.

AYDIN, A. & JOHNSON, A. M. 1983. Analysis of faulting in porous sandstones. *Journal of Structural Geology*, **5**, 19–31.

BAIETTO, A., CADOPPI, P., MARTINOTTI, G., PERELLO, P., PERROCHET, P. & VUATEZ, F.-D. 2008. Assessment of termal circulations in strike-slip fault systems: the Terme di Valdieri case (Italian Western Alps). *In*: WIBBERLEY, C. A. J., KURZ, W., IMBER, J., HOLDSWORTH, R. E. & COLLETTINI, C. (eds) *The Internal Structure of Fault Zones*. Geological Society, London, Special Publications, **299**, 317–339.

BAKUN, W. H., AAGAARD, B. *ET AL*. 2005. Implications for prediction and hazard assessment from the 2004 Parkfield Earthquake – Parkfield, *Nature*, **437**, 969–974.

BARTON, C. A., ZOBACK, M. D. & MOOS, D. 1995. Fluid flow along potentially active faults in crystalline rock. *Geology*, **23**, 683–686.

BEELER, N. M. & TULLIS, T. E. 1996. Self-healing slip pulse in dynamic rupture models due to velocity dependent strength. *Bulletin of the Seismological Society of America*, **86**, 1130–1148.

BEELER, N. M., TULLIS, T. E. & GOLDSBY, D. L. 2008. Constitutive relationships and physical basis of fault strength due to flash heating. *Journal of Geophysical Research*, **113**, B01401, doi:10.1029/2007JB004988.

BENEDICTO, A., PLAGNES, V., VERGÉLY, P., FLOTTÉ, N. & SCHULTZ, R. A. 2008. Fault and fluid interaction in a rifted margin: integrated study of calcite-sealed fault-related structures (southern Corinth margin). *In*: WIBBERLEY, C. A. J., IMBER, J., HOLDSWORTH, R. E. & COLLETTINI, C. (eds) *The Internal Structure of Fault Zones*. Geological Society, London, Special Publications, **299**, 257–275.

BLANPIED, M. L., TULLIS, T. E. & WEEKS, J. D. 1987. Frictional behaviour of granite at low and high sliding velocities. *Geophysical Research Letters*, **14**, 554–557.

BLENKINSOP, T. G. 1989. Thickness–displacement relationships for deformation zones: discussion. *Journal of Structural Geology*, **11**, 1051–1053.

BOS, B. & SPIERS, C. 2002. Frictional-viscous flow of phyllosilicate-bearing fault rock: microphysical model and implications for crustal strength profiles. *Journal of Geophysical Research*, **107**, 2028, doi:10.1029/2001JB000301.

BOUCHON, M. 1997. The state of stress on same faults of the San Andreas system inferred from near-field strong motion data. *Journal of Geophysical Research*, **102**, 11731–11744.

BOUCHON, M. & VALLÉE, M. 2003. Observation of long supershear rupture during the magnitude 8.1 Kunlunshan earthquake. *Science*, **301**, 824–826.

BOUTAREAUD, S., WIBBERLEY, C. A. J., FABBRI, O. & SHIMAMOTO, T. 2008*a*. Permeability structure and co-seismic thermal pressurization on fault branches: insights from the Usukidani fault, Japan. *In*: WIBBERLEY, C. A. J., KURZ, W., IMBER, J., HOLDSWORTH, R. E. & COLLETTINI, C. (eds) *The Internal Structure of Fault Zones*. Geological Society, London, Special Publications, **299**, 341–361.

BOUTAREAUD, S., CALUGARU, D.-G., HAN, R., FABBRI, O., MIZOGUCHI, K., TSUTSUMI, A. & SHIMAMOTO, T. 2008*b*. Clay-clast aggregates: a new textural evidence for seismic fault sliding? *Geophysical Research Letters*, **35**, doi:10.1029/2007GL032554.

BOWDEN, F. P. & TABOR, D. 1950. *The Friction and Lubrication of Solids: Part I.* Oxford, Clarendon Press.

BRACE, W. F. & BYERLEE, J. D. 1966. Stick slip as a mechanism for earthquakes. *Science*, **168**, 990–992.

BRANTUT, N., SCHUBNEL, A., ROUZAUD, J.-N., BRUNET, F. & SHIMAMOTO, T. 2008. High velocity frictional properties of a natural clay bearing fault gouge. *Journal of Geophysical Research*, submitted.

BRETAN, P. & YIELDING, G. 2005. Using buoyancy pressure profiles to assess uncertainty in fault seal calibration. *In*: BOULT, P. & KALDI, J. (eds) *Evaluating Fault and Cap Rock Seals*. AAPG Hedberg Series, no. 2, 151–162.

BRETAN, P., YIELDING, G. & JONES, H. 2003. Using calibrated shale gouge ratio to estimate hydrocarbon column heights. *American Association of Petroleum Geologists Bulletin*, **87**, 397–413.

BROSCH, F.-J. & KURZ, W. 2008. Fault damage zones dominated by high-angle fractures within layer-parallel brittle shear zones: examples from the eastern Alps. *In*: WIBBERLEY, C. A. J., KURZ, W., IMBER, J., HOLDSWORTH, R. E. & COLLETTINI, C. (eds) *The Internal Structure of Fault Zones*. Geological Society, London, Special Publications, **299**, 75–95.

BROWN, A. 2003. Capillary effects on fault-fill sealing. *American Association of Petroleum Geologists Bulletin*, **87**, 381–395.

BRUHN, R. L., PARRY, W. T., YONKEE, W. A. & THOMPSON, T. 1994. Fracturing and hydrothermal alteration in normal fault zones. *Pure and Applied Geophysics*, **142**, 609–644.

BUTLER, C. A., HOLDSWORTH, R. E. & STRACHAN, R. A. 1995. Evidence for Caledonian sinistral strike-slip motion and associated fault zone weakening, Outer Hebrides Fault Zone, Scotland. *Journal of the Geological Society, London*, **152**, 743–746.

BYERLEE, J. D. 1978. Friction of rocks. *Pure and Applied Geophysics*, **116**, 615–626.

CAINE, J. S., EVANS, J. P. & FORSTER, C. B. 1996. Fault zone architecture and permeability structure. *Geology*, **24**, 1025–1028.

CHESTER, F. M. & CHESTER, J. S. 1998. Ultracataclasite structure and friction processes of the Punchbowl fault, San Andreas system, California. *Tectonophysics*, **295**, 199–221.

CHESTER, F. M. & LOGAN, J. M. 1986. Implications for mechanical properties of brittle faults from observations of the Punchbowl Fault, California. *Pure and Applied Geophysics*, **124**, 79–106.

CHESTER, F. M., EVANS, J. P. & BIEGEL, L. R. 1993. Internal structure and weakening mechanism of the San Andreas Fault. *Journal of Geophysical Research*, **98**, 771–786.

CHILDS, C., WALSH, J. J. *ET AL.* 2007. Definition of a fault permeability predictor from outcrop studies of a faulted turbidite sequence, Taranaki, New Zealand. *In*: JOLLEY, S. J., BARR, D., WALSH, J. J. & KNIPE, R. J. (eds) *Structurally Complex Reservoirs*, Geological Society, London, Special Publications, **292**, 235–258.

CHILDS, C., WATTERSON, J. & WALSH, J. J. 1995. Fault overlap zones within developing normal fault systems. *Journal of the Geological Society of London*, **152**, 535–549.

CHILDS, C., WATTERSON, J. & WALSH, J. J. 1996. A model for the structure and development of fault zones. *Journal of the Geological Society of London*, **153**, 337–340.

CHILDS, C., WATTERSON, J. & WALSH, J. J. 1997. Complexity in fault zone structure and implications for fault seal prediction. *In*: MØLLER-PEDERSEN, P. & KOESTLER, A. G. (eds) *Hydrocarbon Seals: Importance for Exploration and Production.* Norwegian Petroleum Society (NPF) Special Publications, **7**, 61–72. Elsevier, Singapore.

CHU, C. L., WANG, C. Y. & LIN, W. 1981. Permeability and frictional properties of San Andreas fault gouges. *Geophysical Research Letters*, **8**, 565–568.

COLLETTINI, C. & HOLDSWORTH, R. E. 2004. Fault zone weakening and character of slip along low-angle normal faults: insights from the Zuccale fault, Elba, Italy. *Journal of the Geological Society, London*, **161**, 1039–1051.

COULOMB, C. A. 1785. The theory of simple machines [in French]. *Mémoires de Mathématique et de Physique présenté à l'Académie Royale des Sciences*, **10**, 161–331.

COWAN, D. S. 1999. Do faults preserve a record of seismic faulting? A field geologist's opinion. *Journal of Structural Geology*, **21**, 995–1001.

COX, S. F. 1995. Faulting processes at high fluid pressures: an example of fault valve behavior from the Wattle Gully Fault, Victoria, Australia. *Journal of Geophysical Research*, **100**, 12841–12860.

CRAWFORD, B. R. 1998. Experimental fault sealing: shear band permeability dependency on cataclastic fault gouge characteristics. *In*: COWARD, M. P., DALTABAN, T. S. & JOHNSON, H. (eds) *Structural Geology in Reservoir Characterization.* Geological Society, London, Special Publications, **127**, 27–47.

DAS, S. 2007. The need to study speed. *Science*, **317**, 905–906.

DAVATZES, N. C., EICHHUBL, P. & AYDIN, A. 2005. The structural evolution of fault zones in sandstone by multiple deformation mechanisms; Moab fault, SE Utah. *Geological Societey of America Bulletin*, **117**, 135–148.

DEWHURST, D. N. & JONES, R. M. 2003. Influence of physical and diagenetic processes on fault geomechanics and reactivation. *Journal of Geomechanical Exploration*, **78–79**, 153–157.

DIETERICH, J. H. 1978. Time-dependent friction and the mechanics of stick–slip. *Pure and Applied Geophysics*, **116**, 790–806.

DIETERICH, J. H. 1979. Modeling of rock friction 1. Experimental results and constitutive equations, *Journal of Geophysical Research*, **84**, 2161–2168.

DI TORO, G. & PENNACCHIONI, G. 2005. Fault plane processes and mesoscopic structure of a strong-type seismogenic fault in tonalites (Adamello batholith, Southern Alps). *Tectonophysics*, **402**, 54–79.

DI TORO, G., GOLDSBY, D. L. & TULLIS, T. E. 2004. Friction falls towards zero in quartz rock as slip velocity approaches seismic rates. *Nature*, **427**, 436–439.

DI TORO, G., HIROSE, T., NIELSEN, S., PENNACCHIONI, G. & SHIMAMOTO, T. 2006*a*. Natural and experimental evidence of melt lubrication of faults during earthquakes. *Science*, **311**, 647–649.

DI TORO, G., HIROSE, T., NIELSEN, S. & SHIMAMOTO, T. 2006*b*. Relating high-velocity rock friction experiments to coseismic slip in the presence of melts. *In*: ABERCROMBIE, R., MCGARR, A., DI TORO, G. & KANAMORI, H. (eds) *Radiated Energy and the Physics of Faulting*. American Geophysical Union Monograph Series, **170**, 121–134.

DOLAN, J. F. 2006. Greatness thrust upon them. *Nature*, **444**, 276–278.

EICHHUBL, P., D'ONFRO, P. S., AYDIN, A., WATERS, J. & MCCARTY, D. K. 2005. Structure, petrophysics, and diagenesis of shale entrained along a normal fault at Black Diamond Mines, California – Implications for fault seal. *American Association of Petroleum Geologists Bulletin*, **89**, 1113–1137.

EVANS, J. P. 1990. Thickness-displacement relationships for fault zones. *Journal of Structural Geology*, **12**, 1062–1065.

FAULKNER, D. R. & RUTTER, E. H. 2001. Can the maintenance of overpressured fluids in large strike-slip fault zones explain their apparent weakness? *Geology*, **29**, 503–506.

FAULKNER, D. R., LEWIS, A. C. & RUTTER, E. H. 2003. On the internal structure and mechanics of large strike–slip fault zones: field observations of the Carboneras fault in southeastern Spain. *Tectonophysics*, **367**, 235–251.

FAULKNER, D. R., MITCHELL, T. M., HEALY, D. & HEAP, M. J. 2006. Slip on 'weak' faults by the rotation of regional stress in the fracture damage zone. *Nature*, **444**, 922–925.

FAULKNER, D. R., MITCHELL, T. M., RUTTER, E. H. & CEMBRANO, J. 2008. On the structure and mechanical properties of large strike-slip faults. *In*: WIBBERLEY, C. A. J., KURZ, W., IMBER, J., HOLDSWORTH, R. E. & COLLETTINI, C. (eds) *The Internal Structure of Fault Zones*. Geological Society, London, Special Publications, **299**, 139–150.

FERRILL, D. A., SMART, K. J. & NECSOIU, M. 2008. Displacement–length scaling for single-event fault ruptures: insights from the Newberry Springs Fault Zone and implications for fault zone structure. *In*: WIBBERLEY, C. A. J., KURZ, W., IMBER, J., HOLDSWORTH, R. E. & COLLETTINI, C. (eds) *The Internal Structure of Fault Zones*. Geological Society, London, Special Publications, **299**, 113–122.

FIALKO, Y. & KHAZAN, Y. 2005. Fusion by the earthquake fault friction: stick or slip? *Journal of Geophysical Research*, **110**, doi.org/10.1029/2005JB003869.

FISHER, Q. J. & KNIPE, R. J. 2001. The permeability of faults within siliciclastic petroleum reservoirs of the

North Sea and Norwegian Continental Shelf. *Marine & Petroleum Geology*, **18**, 1063–1081.

FISHER, Q. J., CASEY, N., HARRIS, S. D. & KNIPE, R. J. 2003. Fluid-flow properties of faults in sandstone: the importance of temperature history. *Geology*, **31**, 965–968.

FLETCHER, J. B. & MCGARR, A. 2006. Distribution of stress drop, stiffness, and fracture energy over earthquake rupture zones. *Journal of Geophysical Research*, **111**, doi:10.1029/2004JB003396.

FOSSEN, H. & HESTHAMMER, J. 1998. Structural geology of the Gullfaks Field, northern North Sea. *In*: COWARD, M. P., DALTABAN, T. S. & JOHNSON, H. (eds) *Structural Geology in Reservoir Characterization.* Geological Society, London, Special Publications, **127**, 231–261.

FOSSEN, H. & HESTHAMMER, J. 2000. Possible absence of small faults in the Gullfaks field, northern North Sea: implications for downscaling faults in some porous sandstones. *Journal of Structural Geology*, **22**, 851–863.

FOSSEN, H., SCHULTZ, R. A., SHIPTON, Z. K. & MAIR, K. 2007. Deformation bands in sandstone: a review. *Journal of the Geological Society of London*, **164**, 755–769.

FOWLES, J. & BURLEY, S. 1994. Textural and permeability characteristics of faulted, high porosity sandstones. *Marine & Petroleum Geology*, **11**, 608–623.

FOXFORD, K. A., WALSH, J. J., WATTERSON, J., GARDEN, I. R., GUSCOTT, S. C. & BURLEY, S. D. 1998. Structure and content of the Moab Fault Zone, Utah, USA, and its implications for fault seal prediction. *In*: JONES, G., FISHER, Q. J. & KNIPE, R. J. (eds) *Faulting, Fault Sealing and Fluid Flow in Hydrocarbon Reservoirs.* Geological Society, London, Special Publications, **147**, 87–103.

FULLJAMES, J. R., ZIJERVELD, L. J. J. & FRANSSEN, R. C. M. W. 1997. Fault seal processes: systematic analyses of fault seals over geological and production time scales. *In*: MØLLER-PEDERSEN, P. & KOESTLER, A. G. (eds) *Hydrocarbon Seals: Importance for Exploration and Production*. NPF Special Publications, **7**, 51–59. Elsevier, Singapore.

GASPARINI, P., MANFREDI, G. & ZSCHAU, J. 2007. *Earthquake Early Warning Systems*. Springer, Berlin.

GERDE, E. & MARDER, M. 2001. Friction and fracture. *Nature*, **413**, 285–288.

GIBSON, R. G. 1994. Fault-zone seals in siliclastic strata of the Columbus Basin, offshore Trinidad. *AAPG Bulletin*, **78**, 1372–1385.

GIBSON, R. G. 1998. Physical character and fluid-flow properties of sandstone-derived fault gouge. *In*: COWARD, M. P., DALTABAN, T. S. & JOHNSON, H. (eds) *Structural Geology in Reservoir Characterzation.* Geological Society, London, Special Publications, **127**, 83–97.

GIBSON, R. G. & BENTHAM, P. A. 2003. Use of fault-seal analysis in understanding petroleum migration in a complexly faulted anticlinal trap, Columbus Basin, offshore Trinidad. *American Association of Petroleum Geologists Bulletin*, **87**, 465–478.

GILBERT, G. K. 1884. A theory of the earthquakes of the Great Basin, with a practical application. *American Journal of Science*, **xxvii**, 49–54.

GOLDSBY, D. L. & TULLIS, T. E. 2002. Low frictional strength of quartz rocks at subseismic slip rates. *Geophysical Research Letters*, **29**, 10.1029/2002GL01240.

GOLDSBY, D. L. & TULLIS, T. E. 2003. Flash heating/melting phenomena for crustal rocks at (nearly) seismic slip rates. *SCEC Annual Meeting Proceedings and Abstracts*, Palm Springs, CA.

GROCOTT, J. 1981. Fracture geometry of pseudotachylyte generation zones: a study of shear fractures formed during seismic events. *Journal of Structural Geology*, **3**, 169–178.

HAN, R., SHIMAMOTO, T., HIROSE, T., REE, J-H. & ANDO, J. 2007. Ultralow friction of carbonate faults caused by thermal decomposition. *Science*, **316**, 878–881.

HANDY, M. R. & STÜNITZ, H. 2002. Strain localization by fracturing and reaction weakening – a mechanism for initiating exhumation of subcontinental mantle beneath rifted margins. *In*: DE MEER, S., DRURY, M. R., DE BRESSER, J. H. P. & PENNOCK, G. M. (eds) *Deformation Mechanisms, Rheology and Tectonics: Current Status and Future Perspectives*. Geological Society, London, Special Publications, **200**, 387–407.

HANDY, M. R., HIRTH, G. & HOVIUS, N. 2007. Tectonic faults: agents of change on a dynamic Earth. *In*: HANDY, M. R., HIRTH, G. & HOVIOUS, N. (eds) *The Dynamics of Fault Zones*, 1–8. MIT Press, Cambridge, MA.

HANEY, M. M., SNIEDER, R., SHEIMAN, J. & LOSH, S. 2005. A moving fluid pulse in a fault zone. *Nature*, **437**, 46.

HANKS, T. C. 1977. Earthquake stress drops, ambient tectonic stresses and stresses that drive plate motions. *Pure and Applied Geophysics*, **143**, 441–458.

HEALY, D., JONES, R. R. & HOLDSWORTH, R. E. 2006. Three-dimensional brittle shear fracturing by tensile crack interaction. *Nature*, **439**, 64–67.

HEATON, T. H. 1990. Evidence for and implications of self healing pulses of slip in earthquake rupture. *Physics of Earth and Planetary Interiors*, **64**, 1–20.

HESTHAMMER, J. & FOSSEN, H. 2000. Uncertainties associated with fault sealing analysis. *Petroleum Geoscience*, **6**, 37–45.

HICKMAN, S. 2007. Structure and properties of the San Andreas fault at seismogenic depths: recent results from the SAFOD experiment. *Euro-conference of Rock Physics and Geomechanics on Natural hazards: Thermo-hydro-mechanical Processes in Rocks, 29th Course of the International School of Geophysics*, Erice.

HIROSE, T. & SHIMAMOTO, T. 2005*a*. Growth of molten zone as a mechanism of slip weakening of simulated faults in gabbro during frictional melting. *Journal of Geophysical Research*, **110**, doi:10.1029/2004JB003207.

HIROSE, T. & SHIMAMOTO, T. 2005*b*. Slip-weakening distance of faults during frictional melting as inferred from experimental and natural pseudotachylytes. *Bulletin of the Seismological Society of America*, **95**, 1666–1673.

HIROSE, T. & BYSTRICKY, M. 2007. Extreme dynamic weakening of faults during dehydration by coseismic

shear heating. *Geophysical Research Letters*, **34**, doi:10.1029/2007GL030049.

HOLDSWORTH, R. E., STEWART, M., IMBER, J. & STRACHAN, R. A. 2001. The structure and rheological evolution of reactivated continental fault zones: a review and case study. *In*: MILLER, J. A., HOLDSWORTH, R. E., BUICK, I. S. & HAND, M. (eds) *Continental Reactivation and Reworking*. Geological Society, London, Special Publications, **184**, 115–137.

HULL, J. 1988. Thickness-displacement relationships for deformation zones. *Journal of Structural Geology*, **10**, 431–435.

IDE, S. & TAKEO, M. 1997. Determination of the constitutive relation of fault slip based on wave analysis. *Journal of Geophysical Research*, **102**, 27379–27392.

IMBER, J., HOLDSWORTH, R. E., BUTLER, C. A. & LLOYD, G. E. 1997. Fault-zone weakening processes along the reactived Outer Hebrides Fault Zone, Scotland. *Journal of the Geological Society, London*, **154**, 105–109.

IMBER, J., HOLDSWORTH, R. E., SMITH, S. A. F., JEFFERIES, S. P. & COLLETTINI, C. 2008. Frictional-viscous flow, seismicity and the geology of weak faults: a review and future directions. *In*: WIBBERLEY, C. A. J., KURZ, W., IMBER, J., HOLDSWORTH, R. E. & COLLETTINI, C. (eds) *The Internal Structure of Fault Zones*. Geological Society, London, Special Publications, **299**, 151–173.

JANECKE, S. U. & EVANS, J. P. 1988. Feldpsar-influenced rock rheologies. *Geology*, **16**, 1064–1067.

JEFFERIES, S. P., HOLDSWORTH, R. E., WIBBERLEY, C. A. J., SHIMAMOTO, T., SPIERS, C. J., NIEMEIJER, A. R. & LLOYD, G. E. 2006. The nature and importance of phyllonite development in crustal-scale fault cores: an example from the Median Tectonic Line, Japan. *Journal of Structural*, **28**, 220–235.

JOHANSEN, T. E. S. & FOSSEN, H. 2008. Internal geometry of fault damage zones in interbedded siliclastic sediments. *In*: WIBBERLEY, C. A. J., KURZ, W., IMBER, J., HOLDSWORTH, R. E. & COLLETTINI, C. (eds) *The Internal Structure of Fault Zones*. Geological Society, London, Special Publications, **299**, 35–56.

JOLLEY, S. J., DIJK, H., LAMENS, J. H., FISHER, Q. J., MANZOCCHI, T., EIKMANS, H. & HUANG, Y. 2007. Faulting and fault sealing in production simulation models: Brent Province, northern North Sea. *Petroleum Geoscience*, **13**, 321–340.

KING, G. & YIELDING, G. 1984. The evolution of a thrust fault system: process of rupture initiation, propagation and termination in the 1980 El Asnam (Algeria) earthquake. *Geophysical Journal International*, **77**, 915–933.

KOTO, B. 1893. On the cause of the Great Earthquake in Central Japan. *Journal of the College of Science, Imperial University of Tokyo*, **5**, 294–353.

LACHENBRUCH, A. H. 1980. Frictional heating, fluid pressure, and the resistance to fault motion. *Journal of Geophysical Research*, **85**, 6249–6272.

LEHNER, F. K. & PILAAR, W. F. 1997. The emplacement of clay smears in synsedimentary normal faults: inferences from field observations near Frechen, Germany. *In*: MØLLER-PEDERSEN, P. & KOESTLER, A. G. (eds) *Hydrocarbon Seals: Importance for Exploration and Production*, NPF Special Publications, **7**, 39–50. Elsevier, Singapore.

LOCKNER, D. A., BYERLEE, J. D., KUKSENKO, V., PONOMAREV, A. & SIDERON, A. 1992. Observations of quasi-static fault growth from acoustic emissions. *In*: EVANS, B. & WONG, T.-F. (eds) *Fault Mechanics and Transport Properties of Rocks*, 3–31. Academic Press, San Diego, CA.

LOSH, S., EGLINTON, L., SCHOELL, M. & WOOD, J. 1999. Vertical and lateral fluid flow related to a large growth fault, South Eugene Island Block 330 Field, offshore Louisiana. *American Association of Petroleum Geologists Bulletin*, **83**, 244–276.

LUNN, R. J., SHIPTON, Z. K. & BRIGHT, A. M. 2008. How can we improve estimates of bulk fault zone hydraulic properties? *In*: WIBBERLEY, C. A. J., KURZ, W., IMBER, J., HOLDSWORTH, R. E. & COLLETTINI, C. (eds) *The Internal Structure of Fault Zones*. Geological Society, London, Special Publications, **299**, 231–237.

MA, K. F., SONG, S. R. *ET AL*. 2006. Slip zone and energetics of a large earthquake from the Taiwan Chelungpu-fault Drilling Project (TCDP). *Nature*, **444**, 473–476.

MANZOCCHI, T., WALSH, J. J., NELL, P. A. R. & YIELDING, G. 1999. Fault transmissibility multipliers for flow simulation models. *Petroleum Geoscience*, **5**, 53–63.

MARONE, C. 1998. Laboratory-derived friction laws and their application to seismic faulting. *Annual Reviews in Earth and Planetary Sciences*, **26**, 643–696.

MARONE, C. & KILGORE, B. 1993. Scaling of the critical slip distance for seismic faulting with shear strain in fault zones. *Nature*, **362**, 618–621.

MARONE, C. & SCHOLZ, C. H. 1988. The depth of seismic faulting and the upper transition from stable to unstable slip regimes. *Geophysical Research Letters*, **15**, 621–624.

MARONE, C., SAFFER, D., IKARI, M. J. & HAINES, S. 2008. Frictional properties and hydromechanical processes in clay-rich fault gouge. *EGU General Assembly*, abstract EGU2008-A-06272.

MAYEDA, K. & WALTER, W. R. 1996. Moment, energy, stress drop, and source spectra of western United States earthquakes from regional coda envelopes. *Journal of Geophysical Research*, **101**, 11195–11208.

MCGRATH, A. G. & DAVISON, I. 1995. Damage zone geometry around fault tips. *Journal of Structural Geology*, **17**, 1011–1024.

MEANS, W. D. 1995. Shear zones and rock history. *Tectonophysics*, **247**, 157–160.

MICARELLI, L. & BENEDICTO, A. 2008. Normal fault terminations in limestones from the SE-Basin (France): implications for fluid flow. *In*: WIBBERLEY, C. A. J., KURZ, W., IMBER, J., HOLDSWORTH, R. E. & COLLETTINI, C. (eds) *The Internal Structure of Fault Zones* Geological Society, London, Special Publications, **299**, 123–138.

MICARELLI, L., BENEDICTO, A. & WIBBERLEY, C. A. J. 2006. Structural evolution and permeability of normal fault zones in highly porous carbonate rocks. *Journal of Structural Geology*, **28**, 1214–1227.

MILDREN, S., HILLIS, R. & KALDI, J. 2002. Calibrating predictions of fault seal reactivation in the Timor Sea. *APPEA Journal*, **42**, 187–202.

MILDREN, S. D., HILLIS, R. R., DEWHURST, D. N., LYON, P. J., MEYER, J. J. & BOULT, P. J. 2005. FAST: a new technique for geomechanical assessment of the risk of reactivation-related breach of fault seals. *In*: BOULT, P. & KALDI, J. (eds) *Evaluating Fault and Cap Rock Seals*. AAPG Hedberg Series, no. 2, 73–85.

MIZOGUCHI, K., HIROSE, T., SHIMAMOTO, T. & FUKUYAMA, E. 2007. Reconstruction of seismic faulting by high-velocity friction experiments: an example of the 1995 Kobe earthquake. *Geophysical Research Letters*, **34**, doi:10.1029/2006GL027931.

MOORE, D. E. & LOCKNER, D. A. 1995. The role of microcracking in shear-fracture propagation in granite. *Journal of Structural Geology*, **17**, 95–114.

MOORE, D. E. & RYMER, M. J. 2007. Talc-bearing serpentinite and the creeping section of the San Andreas Fault. *Nature*, **448**, 795–797.

MOORE, D. E., LOCKNER, D. A., IWATA, K., TANAKA, H. & BYERLEE, J. D. 2001. *How Brucite may Affect the Frictional Properties of Serpentinite*. U.S. Geological Survey Open File Reports, **01–320**.

MOORE, D. E., LOCKNER, D. A., SUMMERS, R., MA, S. & BYERLEE, J. D. 1996. Strength of chrysotile-serpentinite gouge under hydrothermal conditions: can it explain a weak San Andreas fault? *Geology*, **24**, 1041–1044.

MOORE, D. E., LOCKNER, D. A., TANAKA, H. & IWATA, K. 2004. The coefficient of friction of chrysotile gouge at seismogenic depths. *International Geology Review*, **46**, 385–398.

MORRIS, A., FERRILL, D. A. & HENDERSON, D. B. 1996. Slip-tendency analysis and fault reactivation, *Geology*, **24**, 275–278.

MORROW, C. A., MOORE, D. E. & LOCKNER, D. A. 2000. The effect of mineral bond strength and adsorbed water on fault gouge frictional strength. *Geophysical Research Letters*, **27**, 815–818.

MORROW, C. A., SHI, L. Q. & BYERLEE, J. D. 1984. Permeability of fault gouge under confining pressure and shear stress. *Journal of Geophysical Research*, **89**, 3193–3200.

MUHURI, S. K., DEWERS, T. A., SCOTT, T. E. & RECHES, Z. 2004. Interseismic fault strengthening and earthquake-slip instability: friction or cohesion? *Geology*, **31**, 881–884.

NIELSEN, S., CARSLON, J. & OLSEN, K. 2000. Influence of friction and fault geometry on earthquake rupture. *Journal of Geophysical Research*, **105**, 6069–6088.

NIELSEN, S., DI TORO, G., HIROSE, T. & SHIMAMOTO, T. 2008. Frictional melt and seismic slip. *Journal of Geophysical Research*, **113**, doi:10.1029/2007JB005122.

NIEMEIJER, A. R. & SPIERS, C. J. 2005. Influence of phyllosilicates on fault strength in the brittle-ductile transition: insights from rock analogue experiments. *In*: BRUHN, D. & BURLINI, L. (eds) *High Strain Zones: Structure and Physical Properties*. Geological Society, London, Special Publications, **245**, 303–327.

NORDGÅRD BOLÅS, H. M., HERMANRUD, C. & TEIGE, G. M. G. 2005. Seal capacity estimation from subsurface pore pressures. *Basin Research*, **17**, 583–599.

O'CONNOR, S. J. 2000. Hydrocarbon–water interfacial tension values at reservoir conditions: inconsistencies in the technical literature and the impact on maximum oil and gas column height calculations. *American Association of Petroleum Geologists Bulletin*, **84**, 1537–1541.

OHNAKA, M. 2003. A constitutive scaling law and a unified comprehension for frictional slip failure, shear fracture of intact rock, and earthquake rupture. *Journal of Geophysical Research*, **108**, doi:10.1029/2000JB000123.

OLSON, E. L. & ALLEN, R. M. 2005. The deterministic nature of earthquake rupture. *Nature*, **438**, 212–215.

OTSUKI, K. 1978. On the relationship between the width of shear zone and the displacement along fault. *Journal of the Geological Society of Japan*, **84**, 661–669.

PATERSON, M. S. 1978. *Experimental Rock Deformation – the Brittle Field. Springer, Berlin.*

PEACOCK, D. C. P. & SANDERSON, D. J. 1992. Effects of layering and anisotropy on fault geometry. *Journal of the Geological Society*, **149**, 793–802.

PERSSON, B. N. J. 2000. *Sliding Friction: Physical Principles and Applications*. Springer, Heidelberg.

PITTARELLO, L., DI TORO, G., BIZZARRI, A., PENNACCHIONI, G., HADIZADEH, J. & COCCO, M. 2008. Energy partitioning during seismic slip in pseudotachylyte-bearing faults (Gole Larghe Fault, Adamello, Italy). *Earth and Planetary Science Letters*, **269**, 131–139.

POWER, W. L. & TULLIS, T. E. 1992. The contact between opposing fault surfaces at Dixie Valley, Nevada, and implications for fault mechanics. *Journal of Geophysical Research*, **97**, 15425–15435.

POWER, W. L., TULLIS, T. E. & WEEKS, J. D. 1988. Roughness and wear during brittle faulting. *Journal of Geophysical Research*, **93**, 15268–15278.

PRAKASH, V. & YUAN, F. 2004. Results of a pilot study to investigate the feasibility of using new experimental techniques to measure sliding resistance at seismic slip rates. *Eos Transactions, AGU*, **85**, Fall Meeting Supplement, abstract T21D-02.

RABINOWICZ, E. 1965. *Friction and Wear of Materials.* Wiley, New York.

REID, H. F. 1910. The mechanism of the earthquake. *In*: *The California Earthquake of Arpil 18, 1906, Report of the State Earthquake Investigation Commission,* 2. Carnegie Institution, Washington, DC.

REINEN, L. A., TULLIS, T. E. & WEEKS, J. D. 1992. Two-mechanism model for frictional sliding of serpentinite. *Geophysical Research Letters*, **19**, 1535–1538.

RENARD, F., VOISIN, C., MARSAN, D. & SCHMITTBUHL, J. 2006. High resolution 3D laser scanner measurements of a strike–slip fault quantify its morphological anisotropy at all scales. *Geophysical Research Letters*, **33**, doi:10.1029/2005GL025038.

RICE, J. R. 2006. Heating and weakening of faults during earthquake slip. *Journal of Geophysical Research*, **111**, doi:10.1029/2005JB004006.

RICE, J. R. & COCCO, M. 2007. Seismic fault rheology and earthquake dynamics. *In*: HANDY, M. R.,

HIRTH, G. & HOVIOUS, N. (eds) *The Dynamics of Fault Zones*, 99–137. MIT Press, Cambridge, MA.

ROBERTSON, E. C. 1983. Relationship of fault displacement to gouge and breccia thickness. *Mining Engineering*, **35**, 1426–1432.

ROIG-SILVA, C., GOLDSBY, D. L., DI TORO, G. & TULLIS, T. E. 2004. The role of silica content in dynamic fault weakening due to gel lubrication. *Southern California Earthquake Center Annual Meeting, Proceedings and Abstracts Volume*, **XIV**, 150.

RUINA, A. 1983. Slip instability and state variable friction laws. *Journal of Geophysical Research*, **88**, 10359–10370.

SAFFER, D. M., FRYE, K., MARONE, C. & MAIR, K. 2001. Laboratory results indicating weak and potentially unstable frictional behaviour of smectite clay. *Geophysical Research Letters*, **28**, 2297–2300.

SAGY, A., BRODSKY, E. & AXEN, G. J. 2007. Evolution of fault-surface roughness with slip. *Geology*, **35**, 283–286.

SAMMIS, C. G., NADEAU, R. M. & JOHNSON, L. R. 1999. How strong is an asperity? *Journal of Geophysical Research*, **104**, 10609–10619.

SCHOLZ, C. H. 1987. Wear and gouge formation in brittle faulting. *Geology*, **15**, 493–495.

SCHOLZ, C. H. 1998. Earthquakes and friction laws. *Nature*, **391**, 37–42.

SCHOLZ, C. H. 2002. *The Mechanics of Earthquakes and Faulting*. Cambridge University Press, Cambridge.

SCHULZ, S. E. & EVANS, J. P. 1998. Spatial variability in microscopic deformation and composition of the Punchbowl fault, southern California: implications for mechanisms, fluid-rock interaction, and fault morphology. *Tectonophysics*, **295**, 223–244.

SERONT, B., WONG, T.-F., CAINE, J. S., FORSTER, C. B., BRUHN, R. L. & FREDRICH, J. T. 1998. Laboratory characterization of hydrodynamic properties of a seismogenic normal fault system. *Journal of Structural Geology*, **20**, 865–881.

SHELDON, H. A., BARNICOAT, A. C. & ORD, A. 2006. Numerical modelling of faulting and fluid flow in porous rocks: an approach based on critical state soil mechanics. *Journal of Structural Geology*, **28**, 1468–1482.

SHIMAMOTO, T. & LOGAN, J. M. 1981. Effects of simulated fault gouge on the sliding behavior of Tennessee sandstone: nonclay gouges. *Journal of Geophysical Research*, **86**, 2902–2914.

SHIPTON, Z. K. & COWIE, P. A. 2001. Damage zone and slip-surface evolution over μm to km scales in high-porosity Navajo sandstone, Utah. *Journal of Structural Geology*, **23**, 1825–1844.

SHIPTON, Z. K., SODEN, A. M., KIRKPATRICK, J. D., BRIGHT, A. M. & LUNN, R. J. 2006. How thick is a fault? Fault displacement–thickness scaling revisited. *In*: ABERCROMBIE, R., MCGARR, A., DI TORO, G. & KANAMORI, H. (eds) *Radiated Energy and the Physics of Faulting*. American Geophysical Union Monograph Series, **170**, 193–198.

SIBSON, R. H. 1977. Fault rocks and fault mechanisms. *Journal of the Geological Society, London*, **133**, 191–213.

SIBSON, R. H. 1983. Continental fault structure and the shallow earthquake source. *Journal of the Geological Society, London*, **140**, 741–767.

SIBSON, R. H. 1985. Stopping of earthquake ruptures at dilational fault jogs. *Nature*, **316**, 248–251.

SIBSON, R. H. 1986. Brecciation processes in fault zones: inference from earthquake rupturing. *Pure and Applied Geophysics*, **124**, 159–175.

SIBSON, R. H. 1990. Conditions for fault-valve behaviour. *In*: KNIPE, R. J. & RUTTER, E. H. (eds) *Deformation Mechanisms, Rheology and Tectonics*. Geological Society, London, Special Publications, **54**, 15–28.

SIBSON, R. H. 1992. Implications of fault-valve behaviour for rupture nucleation and recurrence. *Tectonophysics*, **211**, 283–293.

SIBSON, R. H. 1995. Selective fault reactivation during basin inversion: potential for fluid redistribution through fault-valve action. *In*: BUCHANAN, J. G. & BUCHANAN, P. G. (eds) *Basin Inversion*. Geological Society, London, Special Publications, **88**, 3–19.

SIBSON, R. H. 1996. Structural permeability of fluid–driven fault-fracture meshes. *Journal of Structural Geology*, **18**, 1031–1042.

SIBSON, R. H. 2003. Thickness of the seismic slip zone. *Bulletin of the Seismological Society of America*, **93**, 1169–1178.

SOLIVA, R. & BENEDICTO, A. 2005. Geometry, scaling relations and spacing of vertically restricted normal faults. *Journal of Structural Geology*, **27**, 317–325.

SPERREVIK, S., GILLESPIE, P. A., FISHER, Q. J., HALVORSEN, T. & KNIPE, R. J. 2002. Empirical estimation of fault rock properties. *In*: KOESTLER, A. G. & HUNSDALE, R. (eds) *Hydrocarbon Seal Quantification*, 109–125. NPF Special Publications, **11**. Elsevier, Amsterdam.

SPRAY, J. G. 2005. Evidence for melt lubrication during large earthquakes. *Geophysical Research Letters*, **32**, doi:10.1029/2004GL022293.

STESKY, R. M., BRACE, W. F., RILEY, D. K. & ROBIN, P.-Y. F. 1974. Friction in faulted related rock at high temperature and pressure. *Tectonophysics*, **23**, 177–203.

STEWART, M., HOLDSWORTH, R. E. & STRACHAN, R. A. 2000. Deformation processes and weakening mechanisms within the frictional-viscous transition zone of major crustal-scale faults: insights form the Great Glen Fault Zone, Scotland. *Journal of Structural Geology*, **22**, 543–560.

SWANSON, M. T. 1988. Pseudotachylyte-bearing strike-slip duplex structures in the Fort Foster Brittle Zone, S. Maine. *Journal of Structural Geology*, **10**, 813–828.

SWANSON, M. T. 2005. Geometry and kinematics of adhesive wear in brittle strike-slip fault zones. *Journal of Structural Geology*, **27**, 871–887.

TAKAHASHI, M. 2003. Permeability change during experimental fault smearing. *Journal of Geophysical Research*, **108**, doi:10.1029/2002JB001984.

TCHALENKO, J. S. 1970. Similarities between shear zones of different magnitudes. *Bulletin of the Geological Society of America*, **81**, 1625–1640.

TINTI, E., BIZZARRI, A., PIATANESI, A. & COCCO, M. 2004. Estimates of slip weakening distance for different dynamic rupture models. *Geophysical Research Letters*, **31**, doi:10.1029/2993GL018811.

TULLIS, T. E. & WEEKS, J. D. 1986. Constitutive behaviour and stability of frictional sliding of granite. *Pure and Applied Geophysics*, **124**, 383–414.

UEHARA, S. & SHIMAMOTO, T. 2004. Gas permeability evolution of cataclasite and fault gouge in triaxial compression and implications for changes in fault-zone permeability structure through the earthquake cycle. *Tectonophysics*, **378**, 183–195.

UNDERHILL, J. R. & WOODCOCK, N. H. 1987. Faulting mechanisms in high-porosity sandstones; New Red Sandstone, Arran, Scotland. *In*: JONES, M. E. & PRESTON, M. F. (eds) *Deformation of Sediments and Sedimentary Rocks*. Geological Society, London, 91–105.

URBAKH, M., KLAFTER, J., GOURDON, D. & ISRAELACHVILI, J. 2004. The non linear nature of friction. *Nature*, **430**, 525–530.

VAN DER ZEE, W. & URAI, J. L. 2005. Processes of fault evolution in a siliciclastic sequence: a case study from Miri, Sarawak, Malaysia. *Journal of Structural Geology*, **27**, 2281–2300.

VAN DER ZEE, W., WIBBERLEY, C. A. J. & URAI, J. L. 2008. The influence of layering and pre-existing joints on the development of internal structure in normal fault zones: the Lodève Basin, France. *In*: WIBBERLEY, C. A. J., KURZ, W., IMBER, J., HOLDSWORTH, R. E. & COLLETTINI, C. (eds) *The Internal Structure of Fault Zones*. Geological Society, London, Special Publications, **299**, 57–74.

WALLACE, R. E. & MORRIS, H. T. 1986. Characteristics of faults and shear zones in deep mines. *Pure and Applied Geophysics*, **124**, 107–125.

WATTERSON, J., CHILDS, C. & WALSH, J. J. 1998. Widening of fault zones by erosion of asperities formed by bed-parallel slip. *Geology*, **26**, 71–74.

WEBER, K. J., MANDL, G., PILAAR, W. F., LEHNER, F. & PRECIOUS, R. G. 1978. The role of faults in hydrocarbon migration and trapping in Nigerian growth fault structures. *10th Annual Offshore Technology Conference Proceedings* **4**, 2643–2653.

WEEKS, J. D. & TULLIS, T. E. 1985. Frictional sliding of dolomite: a variation in constitutional behavior. *Journal of Geophysical Research*, **90**, 7821–7826.

WESNOUSKY, S. G. 1988. Seismological and structural evolution of strike–slip faults. *Nature*, **335**, 340–343.

WESNOUSKY, S. G. 2006. Predicting the endpoints of earthquake ruptures. *Nature*, **444**, 358–360.

WHITE, S. H. & KNIPE, R. J. 1978. Transformation and reaction-enhanced ductility in rocks. *Journal of the Geological Society, London*, **135**, 513–516.

WIBBERLEY, C. A. J. 2005. Initiation of basement thrust detachments by fault-zone reaction weakening. *In*: BRUHN, D. & BURLINI, L. (eds) *High Strain Zones: Structure and Physical Properties*. Geological Society, London, Special Publications, **245**, 347–372.

WIBBERLEY, C. A. J. 2007. Talc at fault. *Nature*, **448**, 756–757.

WIBBERLEY, C. A. J. & SHIMAMOTO, T. 2003. Internal structure and permeability of major strike–slip fault zones: the Median Tectonic Line in W. Mie Prefecture, S. W. Japan. *Journal of Structural Geology*, **25**, 59–78.

WIBBERLEY, C. A. J. & SHIMAMOTO, T. 2005. Earthquake slip weakening and asperities explained by thermal pressurization. *Nature*, **436**, 689–692.

WIBBERLEY, C. A. J., PETIT, J.-P. & RIVES, T. 2000*a*. Micromechanics of shear rupture and the control of normal stress. *Journal of Structural Geology*, **22**, 411–427.

WIBBERLEY, C. A. J., PETIT, J.-P. & RIVES, T. 2000*b*. Mechanics of cataclastic 'deformation band' faulting in high-porosity sandstone, Provence. *Comptes Rendus de l'Academie des Sciences, Serie II. Sciences de la Terre et des Planetes*, **331**, 419–425.

WIBBERLEY, C. A. J., PETIT, J.-P. & RIVES, T. 2007. The mechanics of fault distribution and localization in high-porosity sands, Provence, France. *In*: LEWIS, H. & COUPLES, G. D. (eds) *The Relationship between Damage and Localization.* Geological Society, London, Special Publications, **289**, 19–46.

WILKINS, S. J. & GROSS, M. R. 2002. Normal fault growth in layered rocks at Split Mountain, Utah: influence of mechanical stratigraphy on dip linkage, fault restriction and fault scaling. *Journal of Structural Geology*, **24**, 1413–1429.

WINTSCH, R. P., CHRISTOFFERSON, R. & KRONENBERG, A. K. 1995. Fluid–rock reaction weakening of fault zones. *Journal of Geophysical Research*, **100**, 13021–13032.

WIPRUT, D. & ZOBACK, M. D. 2000. Fault reactivation and fluid flow along a previously dormant normal fault in the northern North Sea. *Geology*, **7**, 595–598.

YIELDING, G., 2002. Shale gouge ratio – calibration by geohistory. *In*: KOESTLER, A. G. & HUNSDALE, R. (eds) *Hydrocarbon Seal Quantification*, 1–15 NPF Special Publications, **11**, Elsevier, Amsterdam.

YIELDING, G., FREEMAN, B. & NEEDHAM, T. 1997. Quantitative fault seal prediction. *American Association of Petroleum Geologists Bulletin*, **81**, 897–917.

YOSHIOKA, N. 1986. Fracture energy and the variation of gouge and surface roughness during the frictional sliding of rocks. *Journal of the Physics of the Earth*, **34**, 335–355.

ZHANG, G. & RICE, J. R. 1998. Conditions under which velocity-weakening friction allows a self-healing versus a cracklike mode of rupture. *Bulletin of the Seismological Society of America*, **88**, 1466–1483.

ZHANG, Y., SCHAUBS, P. M., ZHAO, C., ORD, A., HOBBS, B. E. & BARNICOAT, A. C. 2008. Fault-related dilation, permeability enhancement, fluid flow and mineral precipitation patterns: numerical models. *In*: WIBBERLEY, C. A. J., KURZ, W., IMBER, J., HOLDSWORTH, R. E. & COLLETTINI, C. (eds) *The Internal Structure of Fault Zones*. Geological Society, London, Special Publications, **299**, 239–255.

Internal geometry of fault damage zones in interbedded siliciclastic sediments

TORD ERLEND SKEIE JOHANSEN[1] & HAAKON FOSSEN[2]

[1]*StatoilHydro, Post Office Box 7200, 5020 Bergen, Norway (e-mail: tesj@statoilhydro.com)*

[2]*Centre of Integrated Petroleum Research, University of Bergen, Allégaten 41, N-5007 Bergen, Norway*

Abstract: The geometry, orientation and distribution of deformation bands and fractures in eolian sandstones, siltstones and shales of the San Rafael Desert and Moab Fault area have been investigated. The results show that deformation bands, which are cataclastic in eolian sandstones and disaggregation structures in siltstones, are unevenly distributed throughout the damage zone in the form of individual bands, deformation band zones and deformation band clusters. The density of bands increases with increasing grain size. In thin (<3 m) eolian sandstones deformation band frequency is significantly lower than in thicker eolian sandstones, whereas above this thickness the frequency seems not to be related to layer thickness. Furthermore, large faults do not develop higher concentrations of deformation bands. Somewhat simplified, this suggests that damage zone growth occurs by expansion into its hanging wall and footwall. Still, the highest concentrations of deformation bands occur close to the main fault, which is of importance when considering their effect on fluid flow. Their general fault-parallel conjugate arrangements favour intra-damage zone flow parallel to rather than perpendicular to the fault.

Faults and fault-related structures and processes in porous sandstone have received growing attention during the last couple of decades (e.g., Underhill & Woodcock 1987; Fowles & Burley 1994; Antonellini & Aydin 1995; Davis 1999; Beach *et al.* 1999; Wibberley *et al.* 2000; see Fossen *et al.* 2007 for a review). It has been shown that the process of faulting is different in siliciclastic rocks compared with non-porous crystalline rocks. In particular, sandstones tend to undergo a phase of deformation band nucleation and growth prior to faulting. The hydromechanical properties of the deformation bands in many cases are such as to prohibit or restrict fluid flow. Hence, understanding the orientation, sizes, geometry, spatial distribution and properties of deformation bands around faults is of major interest, in particular to the petroleum industry (e.g., Hesthammer & Fossen 2000).

Faults in siliciclastic sediments consist of two main architectural elements that include a central fault core and an enveloping fault damage zone (Caine *et al.* 1996). The fault core absorbs most of the deformation and may contain cataclastic rocks, deformation bands, slip surfaces, lens-shaped bodies of host-rock and clay/shale smears (e.g., Shipton & Cowie 2001, 2003). The fault damage zone includes the population of brittle, fault-related deformation structures outside the fault core and may include different types of deformation bands, shear fractures and joints. Strain within the damage zone is considerably lower than in the fault core.

Deformation bands are millimetre-wide structures that characterize small-scale strain localization in porous granular media, notably in porous sandstones. Deformation bands differ from faults or slip surfaces in that they lack a discrete fracture surface. Furthermore, most deformation bands maintain or increase cohesion, while cohesion is lost across classical fractures. Formation of deformation bands normally involves compaction and reduction of porosity, whereas dilation may occur along restricted sections of the bands, such as in the tip region (Antonellini *et al.* 1994). Only in rare cases do dilational bands occur (Du Bernard *et al.* 2002). Deformation bands are classified based on kinematics (Aydin *et al.* 2006) or deformation mechanisms (Fossen *et al.* 2007). Disaggregation bands form by grain boundary sliding and granular flow and accommodate minor reduction in porosity (Fisher & Knipe 1998; Hesthammer & Fossen 2001). Formation of cataclastic deformation bands involves grain comminution, which in turn results in reduction of grain size and porosity relative to the host rock (Antonellini *et al.* 1994; Marone and Scholz 1989; Menéndez *et al.* 1996; Hadizadeh & Johnson 2003). In mica-, chlorite- and clay-bearing sandstones, phyllosilicate grains reorient and align with the deformation bands, forming a framework structure in the sandstone across which fluid flow is restricted. These

From: WIBBERLEY, C. A. J., KURZ, W., IMBER, J., HOLDSWORTH, R. E. & COLLETTINI, C. (eds) *The Internal Structure of Fault Zones: Implications for Mechanical and Fluid-Flow Properties*. **299**, 35–56.
DOI: 10.1144/SP299.3 0305-8719/08/$15.00

structures are known as framework phyllosilicate bands (Knipe *et al.* 1997; Fisher & Knipe 1998). In addition, temperature history is an important control on the dissolution and cementation of quartz and other minerals and may influence the sealing potential of faults and deformation bands (Hesthammer *et al.* 2002; Fisher *et al.* 2003).

Granular flow dominates at shallow burial depths (<1 km) and low confining pressure in poorly consolidated sands (Owen 1987; Fisher & Knipe 1998). Grain comminution and quartz dissolution/cementation dominate in consolidated sands at deeper burial depths (>1 km) and higher confining pressures, although studies have shown that cataclasis may also occur under low confining pressure in unconsolidated sediments (Cashman & Cashman 2000; Rawling & Godwin 2003). Lithological factors, such as sorting, roundness, grain size and composition, are also important in controlling the deformation mechanisms under given boundary conditions.

Aydin (1978) and Aydin & Johnson (1978) presented the now widely accepted model that faults in porous sandstones typically grow from swarms of deformation bands, which result from strain hardening during the growth history of single deformation bands (Schultz & Siddharthan 2005, cf. Harper & Lundin 1997). This model explains why deformation bands never accumulate more than centimetre-scale displacements before interlocking of grains and related strain hardening cause strain to relocalize by the formation of a new band(s) in their vicinity. The faulted deformation band model has been supported by other field studies (Antonellini & Aydin 1995; Fossen & Hesthammer 1997; Shipton & Cowie 2003) as well as experimental work (Mair *et al.* 2000).

In this paper we revisit the field area in the San Rafael Desert of SE Utah (Fig. 1a), where faulting in porous sandstones was first explored in detail (Aydin 1978; Aydin & Johnson 1978, 1983), and we examine a system of small normal faults and fault-related structures (<15 m throw) that offset interbedded sandstones, siltstones and shales of the Entrada and Carmel Formations. In addition, field data from a major (about 200 m throw) fault segment related to the Moab Fault (Fig. 1b) (Foxford *et al.* 1996) in the Paradox Basin are presented. The objective of the current study is to identify internal geometrical characteristics of fault damage zones in multi-layered siliciclastic rocks. Seven fault zones that offset interbedded eolian sandstones, siltstones and shales have been examined and mapped in detail using surface grids and fault-perpendicular scanlines.

Geological setting

The San Rafael Desert area

The San Rafael Desert study area (Fig. 1a) is situated off the SE flank of the San Rafael Swell, one of several Late Cretaceous–early Tertiary Laramide-related contractional uplift structures on the Colorado Plateau (e.g., Bump & Davis 2003). The Jurassic stratigraphic framework of the San Rafael Desert study area (Fig. 1c) is dominated by interlayered fluvial, tidal and sand dune deposits (Milligan 2000) assigned to the Upper Member of the Carmel Formation and the Middle Jurassic Entrada Formation. The Upper Member of the Carmel Formation contains alternating red siltstone to silty, very fine sandstone, shales, and light-coloured, medium grained quartz arenites resting on top of thick alabaster gypsum interbedded with shale. The Entrada Formation is 76–160 m thick and sub-horizontal across most of the San Rafael Desert study area. Four sub-units have been discerned in ascending stratigraphic order: e_1, e_2, e_3 and e_4. Sub-units e_1 and e_3 and e_4 are dominated by light-coloured massive or cross-laminated, medium-grained quartz arenites (dune deposits), whereas sub-unit e_2 constitutes red-brown siltstone to very fine-grained sandstone in alteration with thin shales. The siltstones, shales and sandstones of the Carmel Formation are texturally similar to those of the Entrada Formation. Layer-internal variation in grain-size from that of the siltstones to the very fine-grained sandstones is common. For convenience, however, these lithologies are referred to as siltstones in the remainder of this paper.

The faults examined belong to a regional system of NW–SE-oriented normal faults (Aydin & Johnson 1978, 1983) that accommodate minor NE–SW extension and cut across the San Rafael Swell (Milligan 2000). The general fault pattern locally defines orthorhombic fault blocks in plan view (Aydin & Reches 1982).

The cross-cutting relationship between the extensional faults and the San Rafael Swell indicates that the extension postdates the Laramide contraction. During this period the Jurassic units in the Paradox Basin, about 90 km to the east, were buried at about 2 km depth (Nuccio & Condon 1996; Garden *et al.* 2001).

The Moab area and the Moab fault

In the Moab area, about 90 km east of the San Rafael Desert study area, the Entrada Formation is represented by the approximately 60 m thick Slickrock Member (Fig. 1b). The Slickrock Member is a fine-grained, cross-laminated eolian sandstone with local silty to very fine-grained interdunes. The

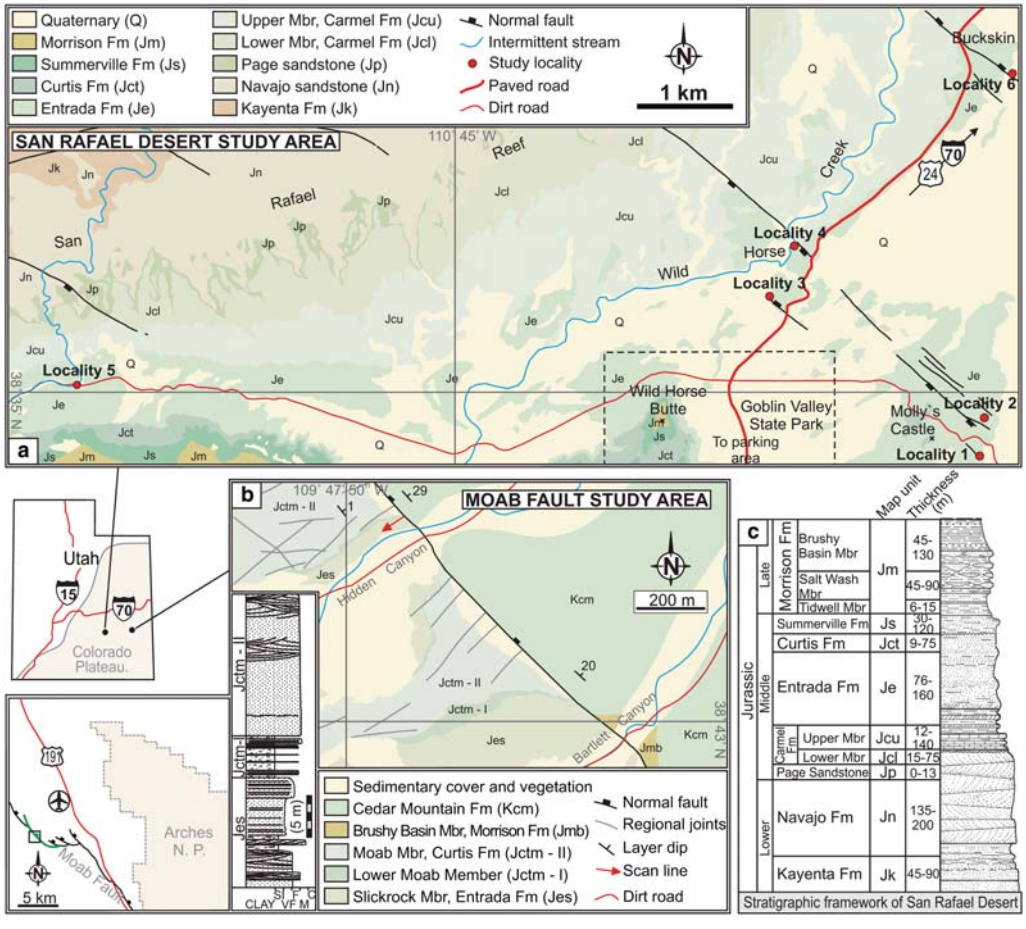

Fig. 1. Overview of study areas. (**a**) San Rafael Desert. (**b**) The Bartlett Fault (solid green line) comprises one of several fault segments connected to the northwestern end of the Moab Fault. Only the most significant regional joints are shown. (**c**) Stratigraphic column of the San Rafael Desert. Modified from Doelling (2001, 2002).

Slickrock Member is overlain by the Moab Member of the Curtis Formation (Doelling 2000). The Moab Member is 25–30 m thick and consists of a light-coloured, massive, medium-grained eolian sandstone unit, underlain by a few-metres-thick siltstone. These and other units are locally affected by the Moab Fault (Fig. 1b), which is structurally located within the Paradox Fold and Fault Belt (Doelling 1988). The Moab Fault defines a major NW-striking, salt-related normal fault with a total outcrop length of about 45 km and a maximum throw of about 950 m (Foxford *et al.* 1996). The northern part of the Moab Fault splays into a series of west-stepping, hard-linked fault strands which will be discussed below.

Salt diapirism in the Moab area was triggered by reactivation of basement lineaments in the Permian–Triassic, which also caused the creation of the Moab Fault in sediments overlying the Paradox salt (Foxford *et al.* 1996). The age of the Moab Fault itself is uncertain, but K–Ar (Pevear *et al.* 1997) and Ar/Ar dating (Solum *et al.* 2005) indicate that much of its present offset accumulated during the late Cretaceous–early Tertiary (Laramide) time period. This was also the time of maximum burial, implying that faulting of the Entrada Sandstone occurred at burial depths of approximately 2.2 km (Nuccio & Condon 1996; Garden *et al.* 2001).

Outline of structural data

Deformation structures

Faults in the eolian sandstones of the study region are associated with abundant cataclastic

deformation bands (Fig. 2a & b) with offset and width in the order of 0–40 and 0.5–2 mm, respectively. At the microscale, these deformation bands show evidence of extensive grain comminution accompanied by reduced grain size and collapse of pore space (Aydin 1978; Aydin & Johnson 1978; Antonellini *et al.* 1994). The deformation bands appear as isolated bands or define densely

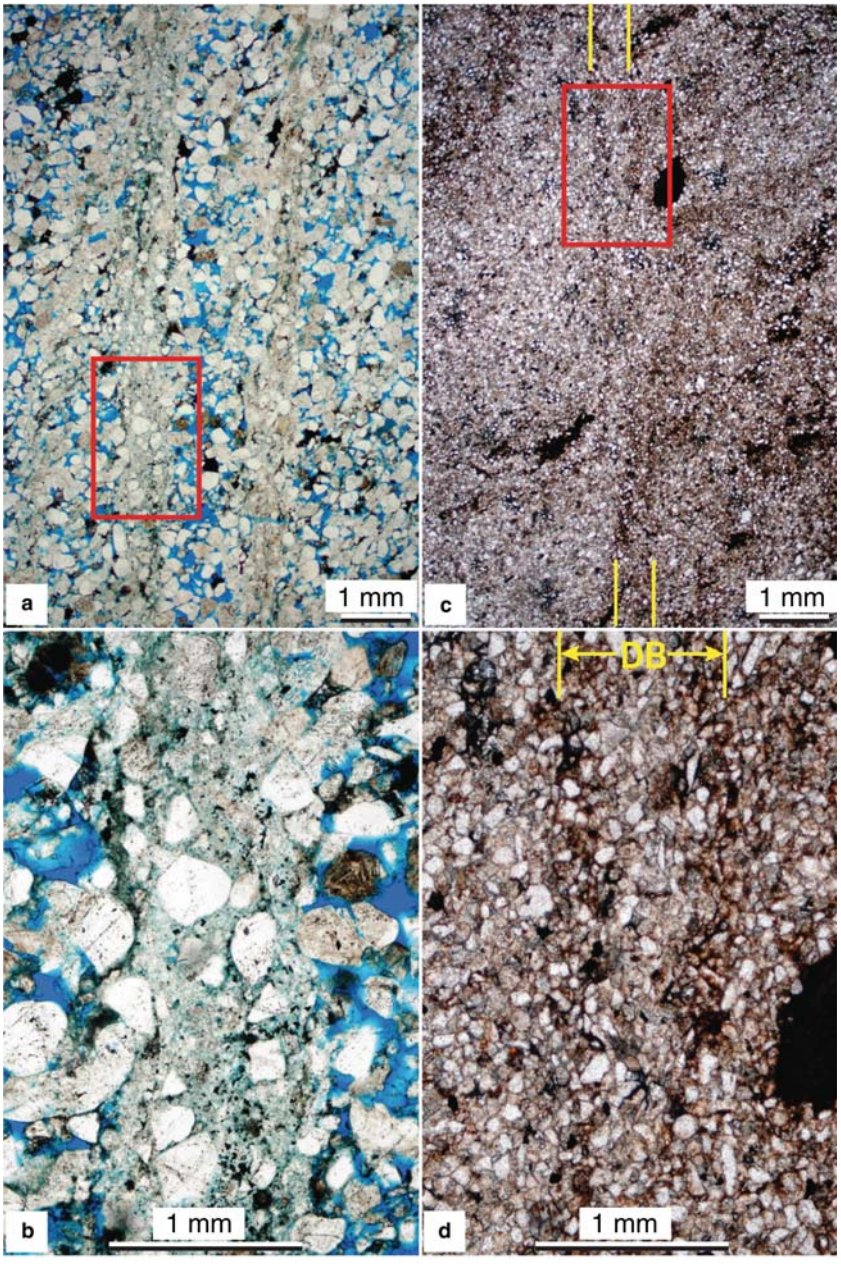

Fig. 2. Deformation bands in the study area. (**a**) Cataclastic deformation band where grain crushing (cataclasis) has resulted in grain-size reduction and a dense, low-porosity band about 1mm thick. (**b**) Magnification of the field indicated in (a). (**c**) Disaggregation band in siltstone. Deformation occurred by grain reorganization (granular flow), and no grain-size reduction is seen and the deformation occurred by grain reorganization (granular flow). (**d**) Magnification of the field indicated in (c).

packed tabular zones of bands. Bands within the decimetre-thick zones show anastomosing arrangement along strike. Deformation bands and deformation band zones may also be concentrated at larger scales as clusters 1–10 m wide. Such concentrations are here referred to as deformation band clusters and represent concentrations within fault damage zones.

Deformation bands in the siltstones of the study region have widths of less than 0.5 mm (Fig. 2c & d) and offsets of up to several tens of centimetres. Their microstructure reveals generally fine-grained, well-sorted and quartz-rich gouge with minor phyllosilicate content. Grain comminution and reduction in grain size is weak or absent, i.e., cataclasis appears much less prominent as compared with deformation bands in the eolian sandstones (Fig. 2a & b). Deformation bands in the siltstones thus classify as disaggregation bands.

In the shales the deformation bands are replaced by shale smears or slip surfaces, which can be hard to detect in outcrop. Those observed occur close to major slip surfaces or along the vertical continuation of thick zones of deformation bands in the eolian sandstones. None of these non-cohesive structures were sampled.

Slip surfaces occur in all three lithologies. In the eolian sandstones they are associated with tabular zones of densely packed deformation bands (Aydin 1978; Aydin & Johnson 1978; Antonellini *et al.* 1994), while in the siltstones they may occur as more or less isolated structures or accompanied by a few disaggregation bands. Slip surface represents the main structure type in the shales.

San Rafael Desert study localities

The San Rafael Desert study area is situated close to the Goblin Valley State Park and features an array of small-scale, NW–SE-oriented steeply (65–80°) dipping normal faults with throw up to 15 m (Fig. 1a). Fault damage zones were mapped at six localities in the Entrada and Carmel Formations (Figs 3–6).

Locality 1 (Fig. 3a) shows a vertical section across a minor normal fault which offsets two thick eolian sandstone beds separated by a 0.5 m thick shale, all assigned to the Entrada Formation, by 1.7 m. The fault core displays a throughgoing slip surface mantled by 10–20 cm thick deformation band zones. The slip surface is oriented at 144/69 (right-hand rule used throughout this paper) and shows dip–slip striations with a minor sinistral component (pitch: 77°E). Scan-line data were recorded across the fault in the shale and the lower eolian sandstone bed. The results are rendered in Figures 7a, b & 8a.

Locality 2 (Fig. 3b) features two sub-parallel normal faults (Faults 1 and 2) that penetrate sandstones, siltstones and shales of the Entrada Formation, all surrounded by deformation bands of synthetic and antithetic dips. Fault 1 defines a geometrically coherent and sub-planar slip surface oriented at 121/80, whereas Fault 2 consists of several hard-linked slip surface segments with strike in the range of 099–128° and about 80° dip. Segment interaction has resulted in metres-wide deformation band networks in unit e_3 (Fig. 3b), each containing hundreds of deformation bands and several minor slip surfaces. Structural data were sampled along a fault-perpendicular exposure to the NW and include two scanlines in eolian sandstone (units e_1 and e_3), two scanlines in siltstone (e_2) and two scanlines in shale (e_2). The results are shown in Figures 7c–h & 8b–f. Here, the offsets of Faults 1 and 2 approximate the maximum offsets, estimated to 3.1 and 5.4 m, respectively. Throw decreases toward the SE, where all structures disintegrate into an array of deformation bands (unit e_3).

The normal fault in Locality 3 (Fig. 4a) was examined by Schultz & Fossen (2002) and offsets siltstones and shales of the uppermost Carmel Formation (Upper Member) as well as a thick, light-coloured and medium grained eolian sandstone of the lowermost Entrada Formation (e_1). The fault core is associated with a throughgoing, striated slip surface and centimetres-thick gouge, which is mantled by a sub-parallel deformation band zone in the Entrada Formation The main slip surface is oriented at 313/69 and has about 6 m offset in the examined cross-section. Structural data were acquired from fault-perpendicular scanlines in the three lithologies. The results are shown in Figures 7i–k & 8g–h.

Locality 4 (Fig. 4b) exposes a steep, SE-striking (133/78) normal fault with a fault core comprising centimetres-thick, dark-coloured gouge and a throughgoing striated slip surface with about 15 m offset. The outcrop lithology is similar to that of Locality 3 and features a light yellow, medium-grained eolian sandstone of the Entrada Formation (e_1) resting on top of alternating sandstones, siltstones and shales of the Carmel Formation. More heterolithic sequences of evaporates, siltstones and shales (Doelling 2002) characterize the stratigraphically deepest exposures of the Carmel Formation. Here, the fault passes into a monoclinal flexure associated with steep minor reverse and normal faults. Structural scanline data were recorded from two separate sandstones and a siltstone, about 5 m into the hanging wall. The results are provided in Figures 7l–n & 8i–k.

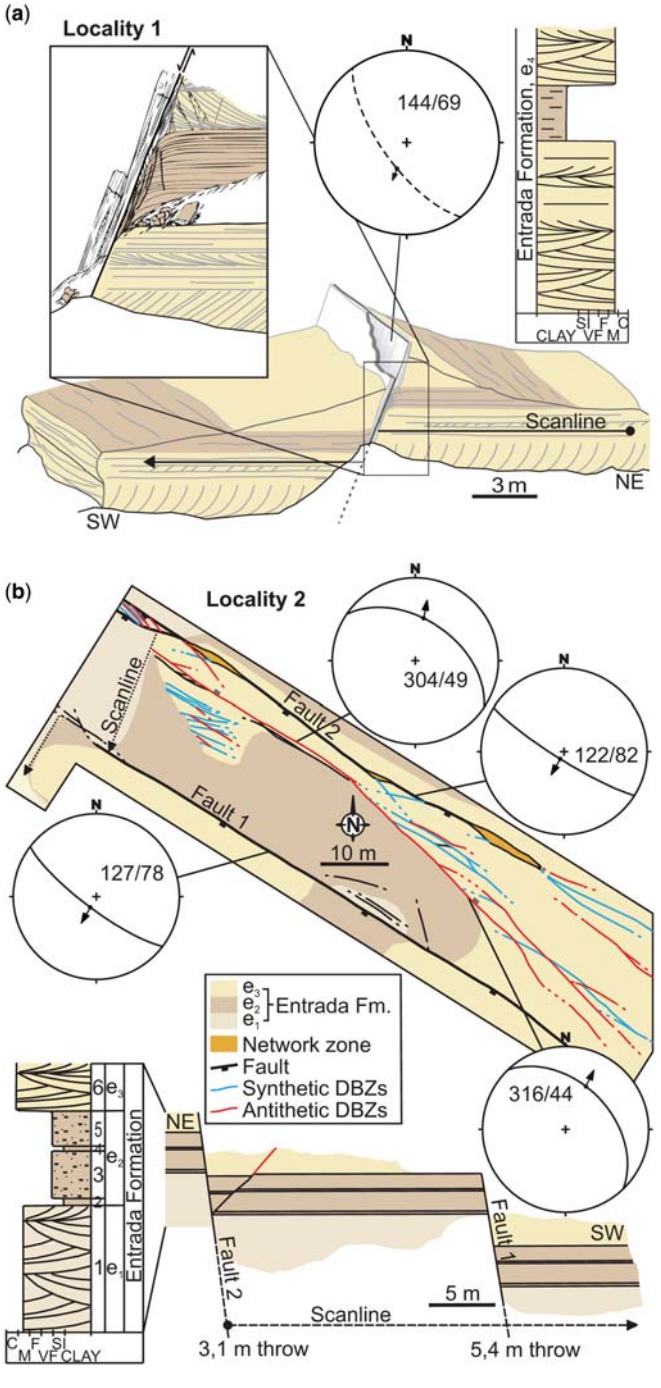

Fig. 3. Outcrops of faults in the Entrada Formation close to the Molly's Castle in the southeastern part of the San Rafael Desert study area. (**a**) Locality 1 features an isolated normal fault offsetting eolian sandstone and shale by about 1.7 m. Deformation bands and fractures were recorded along indicated scanline. (**b**) Locality 2 shows two sub-parallel normal faults that cut across sandstones, siltstones and shales. Fault orientations and pitch of striations are projected in equal area stereoplots (lower hemisphere). Structural data were recorded in all lithologies along scanlines and from surface grids (unit e_3). Synthetic (blue) and antithetic (red) deformation band zones (DBZs) are outlined in the upper sandstone (e_3), and the colour code corresponds to that of Figure 8c. The largest deformation band zones continue as slip surfaces in the siltstones and shales.

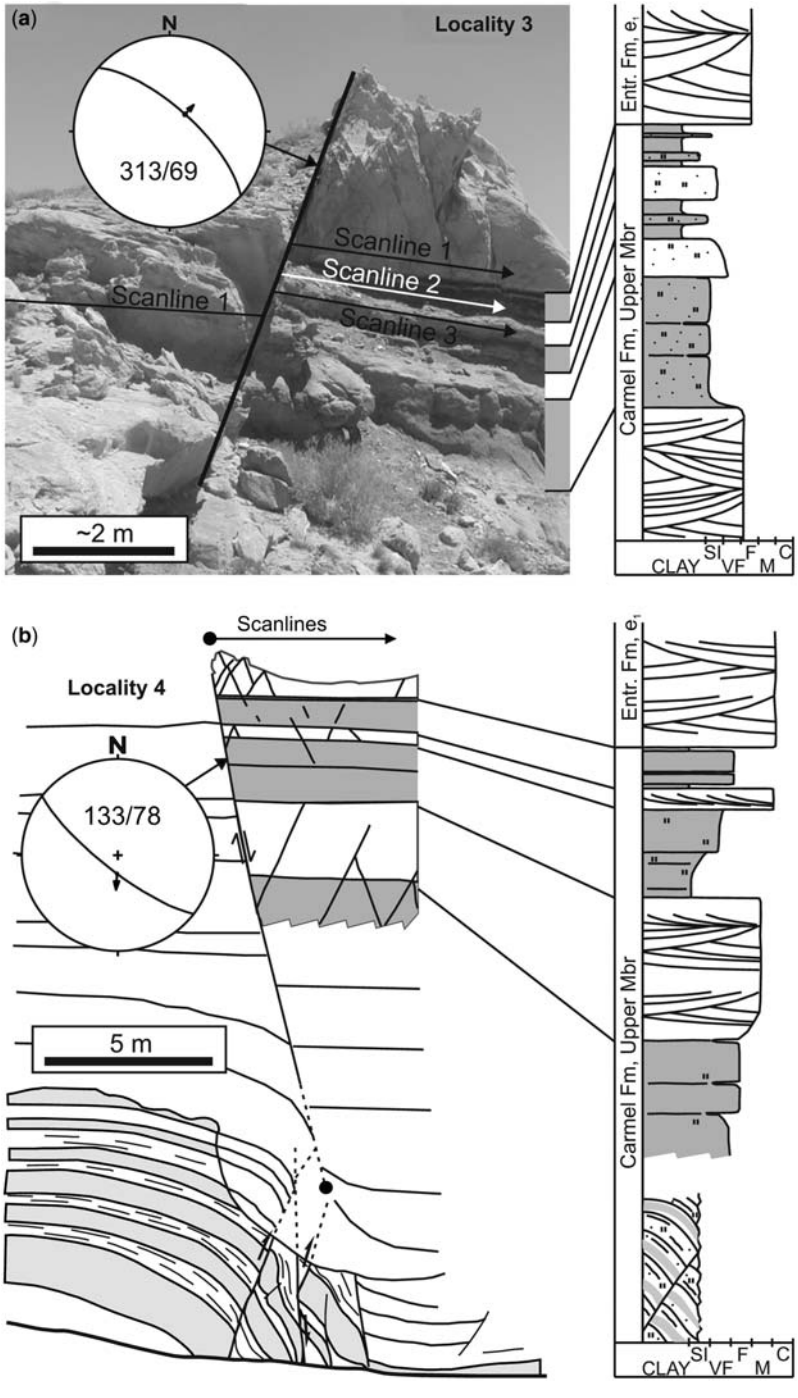

Fig. 4. Localities near the Wild Horse Creek in the San Rafael Desert study area showing faults in the Entrada and Carmel Formations. (**a**) Normal fault in Locality 3 with offset of about 6 m. Structural data were recorded along three scanlines in eolian sandstone, siltstone and shale. (**b**) Normal fault in Locality 4 with about 15 m offset. Fault-related structures were mapped in similar lithologies as in Locality 3 along scanlines extending about 5 m into the hanging wall. Fault orientations and pitch of striations are projected in equal area stereoplots (lower hemisphere).

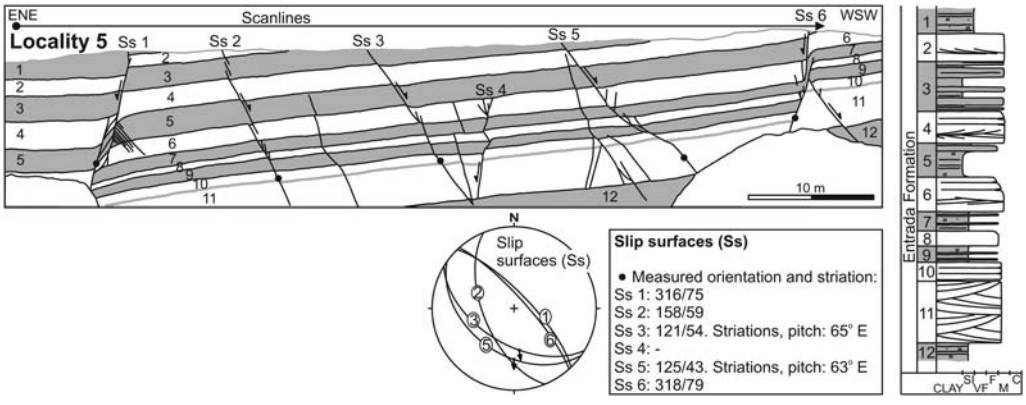

Fig. 5. Locality 5 at the Little Wild Horse Canyon trailhead in the San Rafael Desert. Several small faults (slip surfaces = Ss) with offset in the range 0.1–1.9 m crop out in 70 m wide and 10 m high ENE–WSW oriented vertical cross-section. The orientation of the faults and associated slickenline striations are shown in the stereoplot, whereas the respective sample locations are indicated in the cross-section (black dots). Deformation bands and slip surfaces were mapped in eight separate lithological units, constituting interbedded sandstone, siltstone and shale of the Entrada Formation.

Locality 5 (Fig. 5) features an array of small faults that crop out in the Entrada Formation along a 70 m wide and 10 m high ENE–WSW oriented vertical cross-section. These faults exhibit a NW–SE orientation and have offset in the range of 0.1–1.9 m. Data were sampled along scanlines in eight separate lithological units, constituting layers of sandstone, siltstone and shale (Fig. 9).

Locality 6 (Fig. 6) exposes two overlapping NE-striking faults, which penetrate the Entrada and Carmel Formations. The largest fault (Fault 1) is mainly dip–slip with an orientation of about 300/70 and maximum offset of approximately 12 m. Fault 2 is near vertical and oriented at 292/80. Slip surface striations demonstrate prominent dextral slip with pitch in the range of 10–49°E (31°E average). The overlap zone covers a 100 by 250 m area, breached by abundant oblique faults. Slickenside striations were measured on slip surfaces within the overlap zone, and deformation bands along one of the breaching faults were mapped in detail. In addition, scanline data were sampled in unit e_3 perpendicular to Fault 1, SE of the overlap zone (Figs 7o & 8l).

The Moab Fault

Structural analyses of the Moab Fault area were carried out along one of the major NW-striking fault segments connected to its northwestern end (Fig. 1b), known as the Bartlett Fault (Fossen *et al.* 2005). Fault-perpendicular canyons, such as the Hidden Canyon, expose outstanding sections through the fault segment. The fault displacement is close to 200 m in the Hidden Canyon area, and the fault core is locally up to 5 m wide and defines a composite extensional duplex of cataclastic fault rocks, major fault-bounded lenses of host rock and numerous slip surfaces. Strata in the hanging wall are affected by a 200–300 m wide syncline with a maximum layer dip of 20–30° adjacent to the fault core. The layering in the footwall is sub-horizontal.

Deformation band distribution and orientations were sampled in the footwall from the Moab Member and Slickrock Member in Hidden Canyon (Figs 10 & 11). In the Slickrock Member two sub-layers were examined, including a medium-to coarse-grained eolian sandstone layer and a fine-grained to silty interdune layer, both with thicknesses of 0.5–1.0 m. Deformation bands in these lithologies are similar to those of corresponding lithologies in the San Rafael Desert study area (Aydin 1978). Light-coloured, 1–2 mm wide cataclastic bands reside in the eolian sandstone units, whereas narrow (<0.5 mm), dark-coloured disaggregation bands are seen in the interdune deposits. The dark brownish colour of the disaggregation bands is related to iron (hydr)oxides rather than to phyllosilicates (which are absent or scarce in the interdune siltstones). In addition to deformation bands, all lithologies contain a small number of slip surfaces. Sub-vertical, regional joints cut across and postdate the damage zone, but do not significantly bias deformation band frequencies associated with the Bartlett Fault due to their wide spacing (5–30 m).

Although not fully covered by the scanline, the total width of the damage zone in the Moab

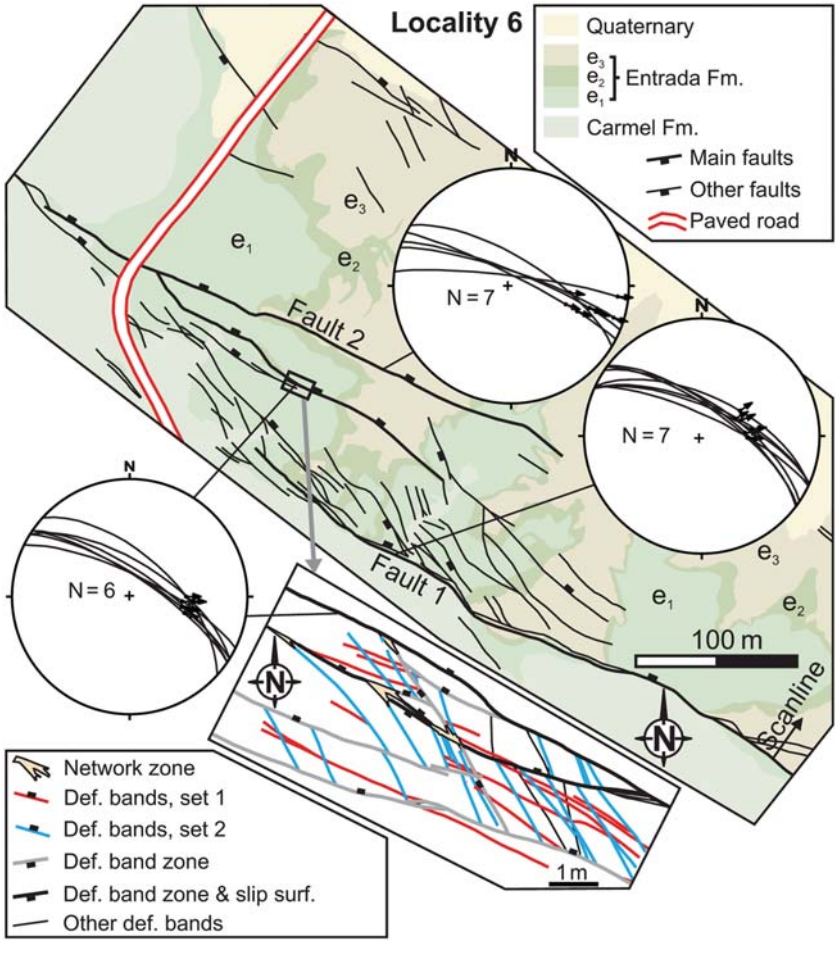

Fig. 6. Locality 6 in the San Rafael Desert show two overlapping faults (Faults 1 and 2) in the Entrada and Carmel Formations. The largest fault (Fault 1) is mainly dip–slip and has offset of approximately 12 m. Slip surface striations on Fault 2 demonstrate prominent dextral slip with pitch in the range of 10–49°E. Fault orientations are shown in stereoplots (equal area, lower hemisphere). Slip surface striations were also measured on slip surfaces within the overlap zone. Further, deformation bands along one of the breaching faults were mapped in detail (field indicated in map), and the colour code of Set 1 (red) and Set 2 (blue) corresponds to that in Figure 18c. Scanline data were sampled perpendicular to Fault 1 in unit e_3.

Member in Hidden Canyon approximates 70 m. Here, the deformation band frequency is at its maximum of about 100 m^{-1} close to the fault core, and decreases toward the margin of the damage zone (Fig. 10a). High-frequency deformation band clusters (>20–30 m^{-1}) typically envelop a throughgoing slip surface. The damage zone is much narrower in the interdune units (about 13 m wide; Fig. 10b). Deformation band frequencies are high (>70 m^{-1}) adjacent to the fault core, but decline rapidly to less than 18 m^{-1} toward the peripheral part of the damage zone. The width of the damage zone in the Slickrock Member dune is similar to that of the interdune, but the deformation band frequencies are higher (about 5 m^{-1}) on the whole (Fig. 10c). Despite significant scatter in the orientation data, the vast majority of the structures follow the trend of the main fault (318/62) (Fig. 11). Synthetic structures with sample mean orientation (316/62) close to the main fault orientation prevail in the Moab Member (Fig. 11a), while the less frequent yet abundant antithetic structures (143/75) have about 10° steeper dip on average (Fig. 11b).

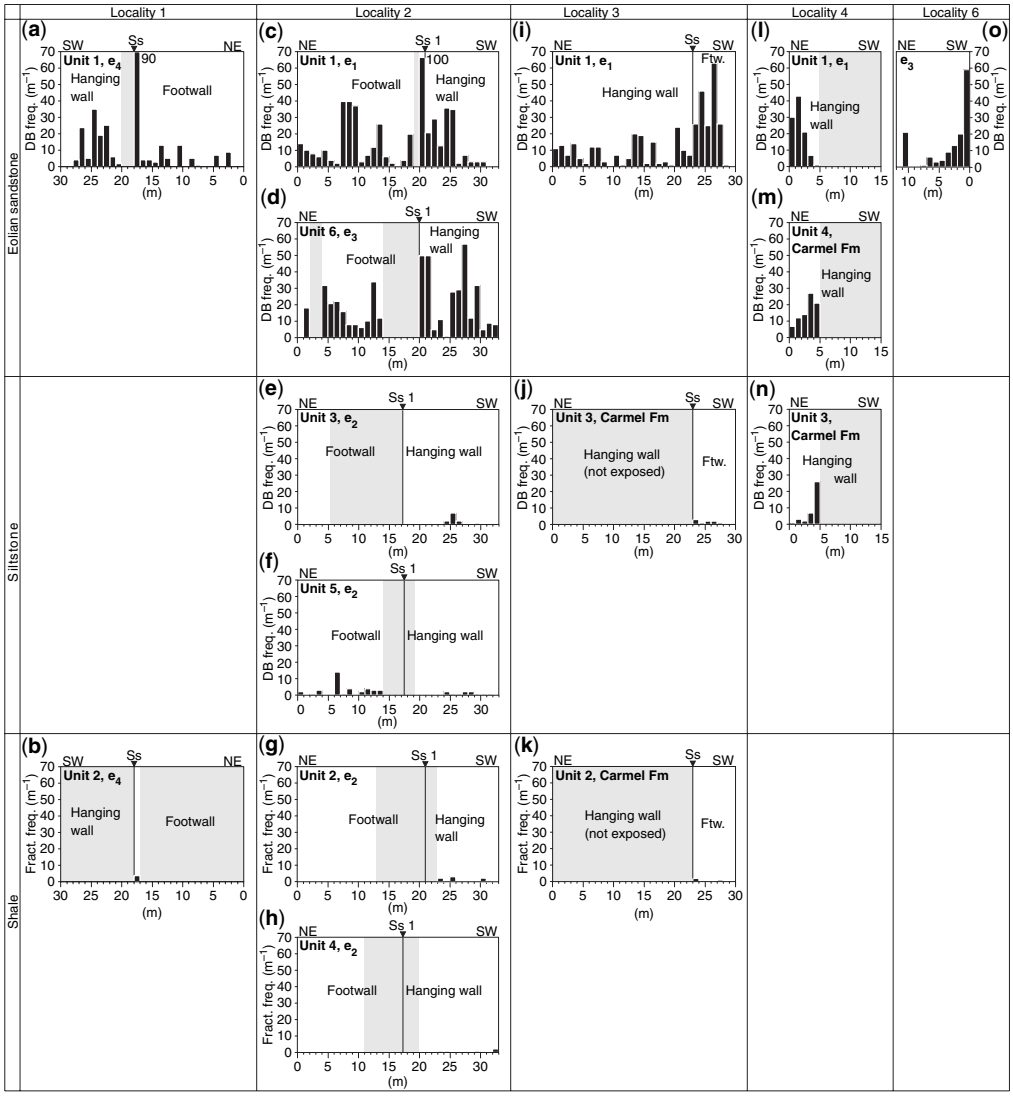

Fig. 7. The spatial distribution of deformation bands and fractures in the damage zone of faults in the San Rafael Desert area was recorded along fault-perpendicular scanlines in eolian sandstones, siltstones and shales. The resulting deformation band (DB) and fracture frequency profiles have been arranged according to lithology and locality. Grey areas indicate unexposed sections. Throughgoing slip surfaces (Ss) are indicated in the profiles. Ss 1 in Locality 2 corresponds to Fault 1 in Figure 3b.

Sub-vertical structures (dip $>80^\circ$) parallel to the main fault (Fig. 11b) are also frequent. The Slickrock Member dune and interdune units show similar deformation band orientations with two distinct sets (Fig. 11c & d). Sub-vertical deformation bands are frequent in both lithologies, but antithetic deformation bands are about 10° steeper in the interdune than in the dune units. However, synthetic deformation bands were not recorded.

Results and discussion

Deformation band frequency v. lithology

The spatial distribution of deformation bands has been recorded along 29 fault-perpendicular scanlines in porous eolian sandstones, siltstones, and shales, as shown in Figure 7 (San Rafael Desert), Figure 9 (San Rafael Desert, Little Wild Horse Canyon trailhead) and Figure 10 (Bartlett

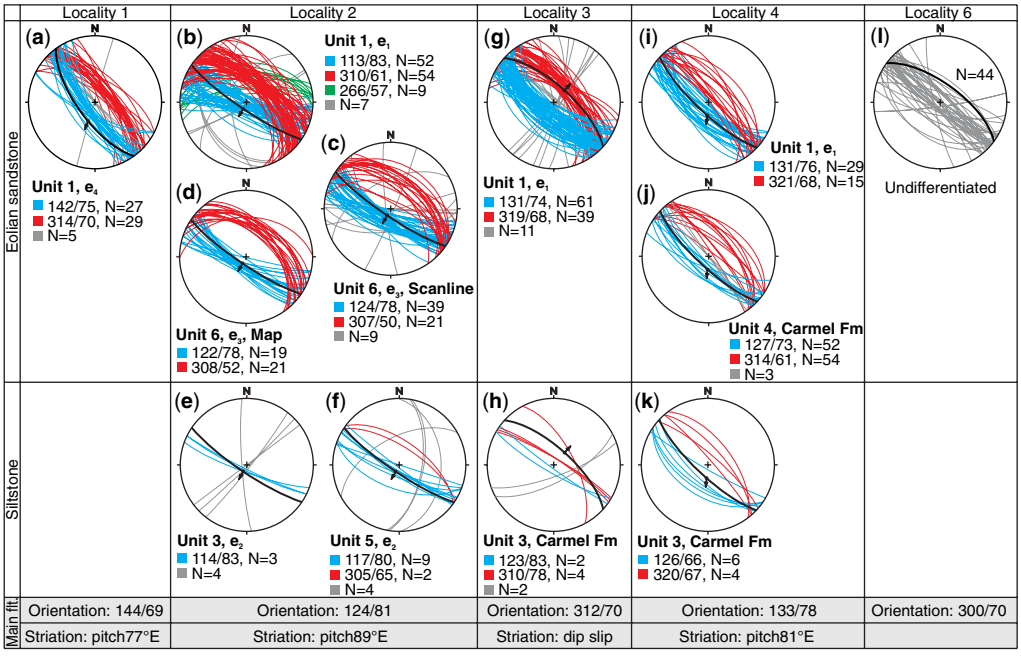

Fig. 8. Stereoplots (equal area, lower hemisphere) of deformation bands in eolian sandstones and siltstones in fault damage zones of the San Rafael Desert area. The thick black line (great circle) represents associated main fault (slip surface) orientation. Main fault orientation and pitch of striations are noted at the base of the figure. The stereoplots have been arranged with respect to location and lithology. The colour code represents the dominant sets, and their respective average orientation is as indicated.

Fault). Among several characteristic features revealed by this data set is the clustered distribution of deformation bands in the fault damage zones. The most prominent clusters appear in the eolian sandstones, manifest as up to 10 m wide zones with several tens or hundreds of deformation bands and typically also deformation band zones with opposing dips (Fig. 12). Most of these deformation band clusters, however, range in width from 2 to 7 m (Fig. 13a). Deformation band frequencies tend to reach their maxima near the centre of the clusters. Typically, the maximum deformation band frequencies are in the range $5–40\ m^{-1}$, but may locally approach $100\ m^{-1}$ (Fig. 13b). The clusters have been determined qualitatively from deformation band frequency profiles, as indicated in Figure 10a. It should be noted, however, that these data reflect concentration per measured metre, and that the concentration for instance at the 10 cm scale can be considerably higher when crossing a deformation band cluster.

An important finding is the lithological control on deformation band and fracture frequency. Clearly, the maximum deformation band frequency of clusters in the eolian sandstones is generally much higher and shows significantly greater scatter compared with that of deformation band clusters in the siltstones (Fig. 14). In the shales discrete fractures in the form of slip surfaces dominate, but fracture clusters are nearly absent. Such lithology-dependent contrasts in fault damage zones are probably attributed to contrasting fault growth mechanisms in the different lithologies. It is generally thought that sequential growth of deformation bands in response to strain hardening of gouge precedes faulting, i.e., nucleation of slip surfaces, in porous sandstones (Aydin & Johnson 1978, 1983; Jamison & Stearns 1982; Underhill & Woodcock 1987; Antonellini & Aydin 1994; Mair *et al.* 2000; Wibberley *et al.* 2000; Shipton & Cowie 2001, 2003; Rawling & Goodwin 2003; Schultz & Siddhartha 2005). Strain hardening of gouge within a deforming band results in loading of the more compliant sidewalls, in which new deformation bands may form. This model can explain the extensive deformation band zones and clusters observed in the eolian sandstones.

The thinner zones and larger offsets of disaggregation bands in siltstones suggest that strain hardening is less important or absent here. Strain hardening seems to be related to deformation

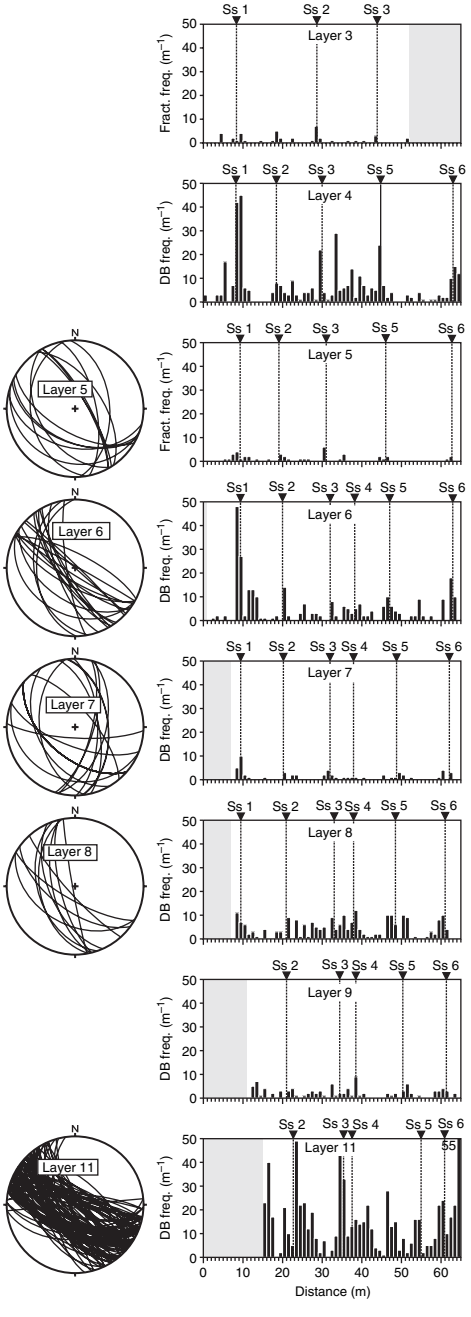

Fig. 9. Results from Locality 5. Deformation band and fracture frequencies were recorded in eight layers, including eolian sandstones, siltstones and shales. Grey areas indicate lack of exposure. Deformation bands (DB) dominate the eolian sandstones and siltstones, whereas fractures (slip surfaces) dominate the shales. Note high deformation band frequencies in the sandstones relative to that of siltstones and shales. Orientation data were recorded only in sandstones and siltstones. Stereoplots (equal area, lower hemisphere) demonstrate a relatively complex pattern, but the main trend is sub-parallel to that of the slip surfaces (Ss). The numbering of the slip surfaces as well as the layers is in accordance with Figure 5.

mechanism in this case. The disaggregation bands do not involve significant grain fracturing, probably because of the finer grain size and the resulting lower grain-contact stresses (Schultz & Siddharthan 2005; Fossen *et al.* 2007). There is no reason to believe that the reorganization of grains itself would cause significant strain hardening (Harper & Lundin 1997), although the formation of grain bridge structures may result in temporal stress fluctuations (Mandl *et al.* 1977). However, the cataclastic grain size reduction, porosity reduction and the change from rounded to angular grain shapes seen in the cataclastic deformation bands in the eolian sandstones (Fig. 2a & b) cause locking of grain contacts and thereby promote strain hardening, wider deformation band zones, and smaller offsets of deformation bands in these sandstones.

Shale layers show no evidence of sequential deformation band growth, which can probably be explained by the presence of phyllosilicates (Fisher & Knipe 1998), in addition to the fine grain size. Phyllosilicates tend to align along the shear fracture and seem to have a smearing and weakening effect as offset accumulates. Thus, strain softening and early slip surface formation occur.

Growth of deformation band clusters

The maximum deformation band frequency of the deformation band clusters in the eolian sandstones decreases non-linearly with distance to the main fault core or slip surface (Fig. 15). Hence, clusters located close to the main fault can be expected to contain considerably higher concentrations of deformation bands than more peripheral clusters. Comparing the damage zone data from the small ($<$15 m throw) faults in the San Rafael Desert area with the 200 m throw Bartlett fault reveals similar concentrations of deformation bands very close to the fault core, but higher concentrations of deformation bands in the peripheral part of the Bartlett fault damage zone relative to the San Rafael Desert faults. These characteristics indicate that new clusters form peripherally while the established clusters continue to grow. However, because clusters adjacent to the main fault have similar maximum deformation band frequencies in both wide and narrow damage zones, there seems to be

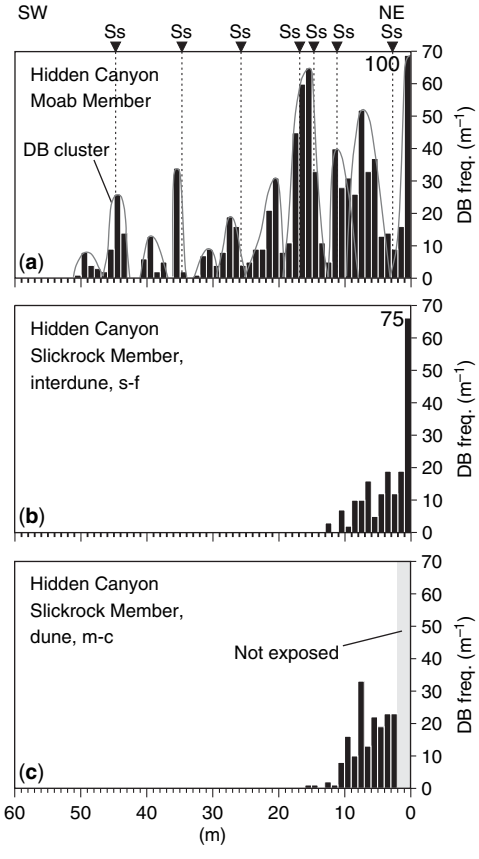

Fig. 10. Distribution of deformation bands (DB) in the footwall damage zone of the Bartlett Fault in Hidden Canyon. (**a**) Profile in Moab Member. Throughgoing slip surfaces (Ss) are indicated, and deformation band clusters are outlined. Close to the main fault the clusters tend to overlap. (**b**) Profile in Slickrock Member interdune and (**c**) dune. The deformation band and fracture frequencies in the Slickrock Member are generally lower and the fault damage zone is narrower compared with the Moab Member.

a critical strain level at which the clusters become saturated with deformation bands. Based on the plot in Figure 15, this critical strain level corresponds to a deformation band frequency of about 100 m^{-1} in the study area.

In the eolian sandstones the maximum deformation band frequency associated with slip surfaces is typically about 25–60 m^{-1}, but may be as high as 100 m^{-1}. The largest clusters are frequently associated with a throughgoing slip surface. For example, slip surfaces in the San Rafael Desert are commonly centred within the largest clusters (Fig. 7), and several of the subsidiary slip surfaces in the footwall of the Bartlett fault are mantled by major deformation band clusters (Fig. 10a). If, as suggested by Aydin & Johnson (1978), deformation band formation involves strain hardening and faulting implies strain softening in these rocks, then there is no mechanical reason why deformation bands should form after the establishment of a continuous slip surface. However, the variation in deformation band density around slip surfaces is considerable. Whether this variation is related to local lithological changes or stress perturbations, or whether deformation band growth occurs near the slip surface at a later stage, is not evident from our data. Renewed deformation band growth could be related to incorporation of fault lenses or geometrical asperities along the slip surface. However, it is unclear why higher deformation band concentrations should be obtained during faulting preferentially to forming new slip surfaces in the wall rock. Hence, it seems likely that the maximum concentration of deformation bands near slip surfaces for the most part is established prior to faulting of the deformation band zone.

Several studies have shown a positive correlation between damage zone width and main fault offset for porous sandstones (e.g., Beach *et al.* 1999; Shipton & Cowie 2001). The widths of the damage zones are generally not well constrained in the current study, owing to limited exposure or interference of damage zones of adjacent faults. Accordingly, such correlations have not been possible to study directly, although Figure 15 may suggest a positive correlation. Field observations do, however, show that the width of damage zones is prone to considerable variation along strike even within the same lithology.

There is a non-linear correlation between the total number of deformation bands within the clusters and their respective widths (Fig. 16). More precisely, the density of deformation bands within the clusters appears to have increased as the clusters matured, suggesting progressive strain localization with increasing throw. Deformation band zones are expected to absorb most of the offset, and typically there is a limited number of deformation band zones within mature clusters compared with the number of single deformation bands.

Deformation band frequency v. layer thickness

Whereas spacing of joints typically is inversely proportional to the thickness of the fractured layer (e.g., Huang & Angelier 1989; Narr & Suppe 1991), Heynekamp *et al.* (1999) found that thick sandstones have wider damage zones with more deformation bands than thin sandstones. Motivated

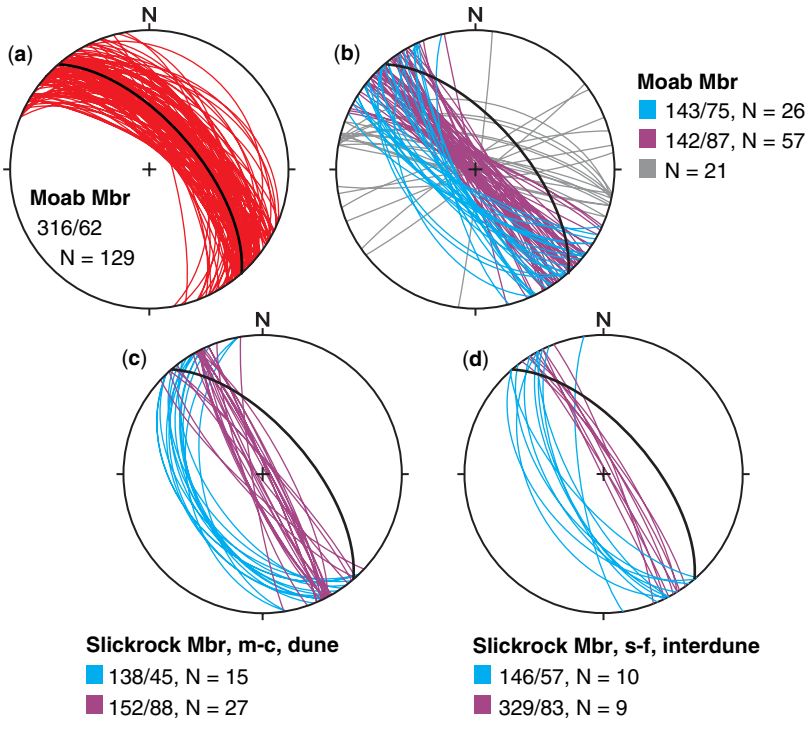

Fig. 11. Stereoplots (equal area, lower hemisphere) of deformation band orientations in the damage zone of the Bartlett Fault in Hidden Canyon, based on scanline data from the (**a** and **b**) Moab Member, (**c**) Slickrock Member dune, and (**d**) Slickrock Member interdune. The main fault (thick black line) is oriented at 318/62.

by this finding we compared the maximum deformation band frequency of deformation band clusters in the eolian sandstones with thickness in the range of about 1–25 m, based on data from 12 different scanlines. The results (Fig. 17a) demonstrate distinctly lower maximum deformation band frequency of clusters in the thinnest (1.3–1.8 m) layers compared with that of clusters in layers thicker than 3 m. Further, the maximum deformation band frequency of clusters in layers thicker than 3 m appears to be more or less unrelated to layer thickness.

These observations indicate an overall positive nonlinear or bilinear correlation between layer

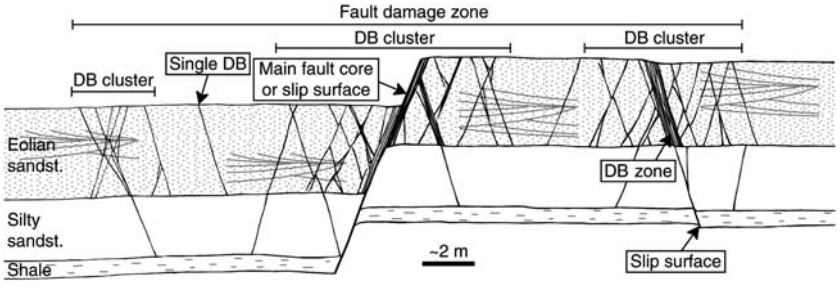

Fig. 12. Conceptual sketch of fault damage zones in the examined lithologies. Deformation bands dominate damage zones in eolian sandstones and appear as 1–2 mm wide isolated deformation bands or centimetres-wide tabular deformation band zones with densely packed deformation bands. Deformation bands and deformation band zones may also be concentrated at a larger (1–10 m) scale, here referred to as deformation band clusters. Fault damage zones may consist of several deformation band clusters. Deformation band clusters are nearly absent in the siltstones and shales.

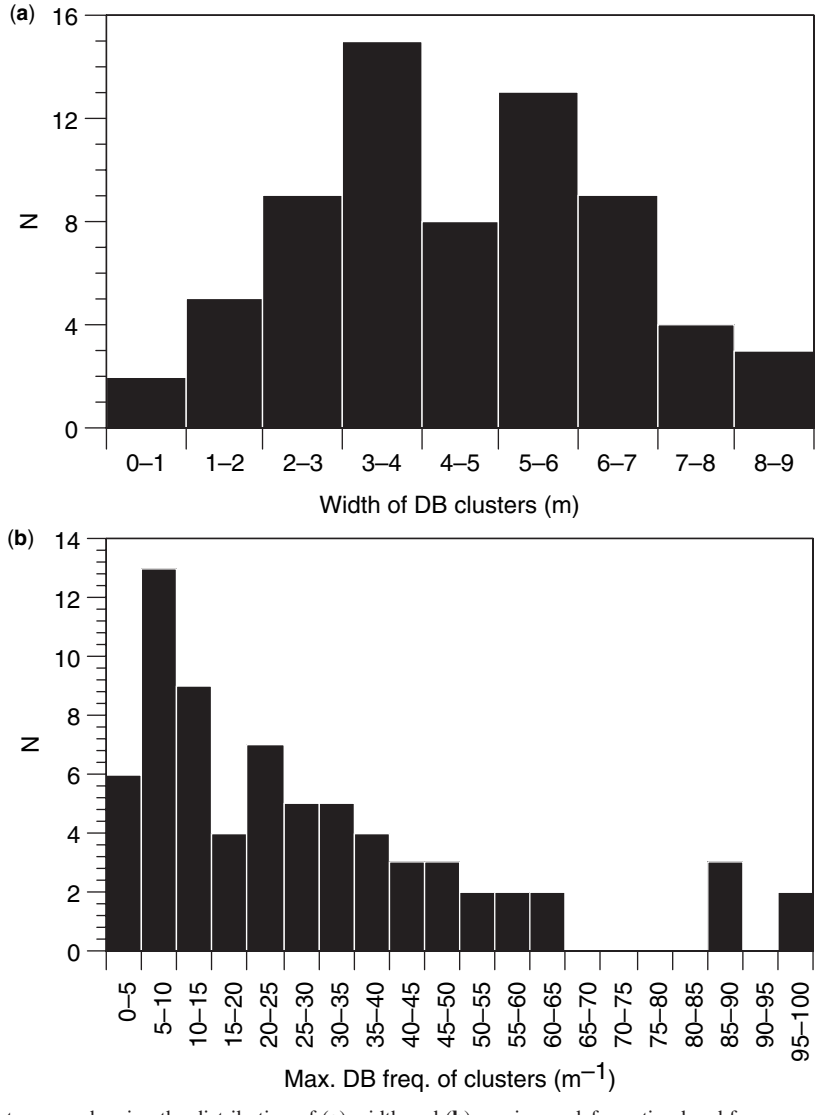

Fig. 13. Histograms showing the distribution of (**a**) width and (**b**) maximum deformation band frequency of deformation band clusters in the eolian sandstones. The maximum deformation band frequency denotes the highest concentration of bands (m^{-1}) within the deformation band clusters as recorded along the scanline.

thickness and maximum deformation band frequency, which can be attributed to the process of faulting in these and similar eolian sandstones. Growth of deformation band clusters in the eolian sandstones results mainly from strain hardening of gouge prior to faulting, but is expected to cease when slip surfaces nucleate. Deformation band zones represent the main contribution to high deformation band frequencies within deformation band clusters. Cluster growth in the eolian sandstones inevitably requires that the layers remain structurally coherent across the future fault plane (slip surface) so that strain hardening and thus cluster growth may continue. Where offset exceeds layer thickness so that the sandstone layer is cut off and juxtaposed against a weaker lithology, such as a siltstone or shale, clusters may cease to develop before slip surface nucleation takes place within the sandstone. Field observations show that the largest deformation band zones typically have

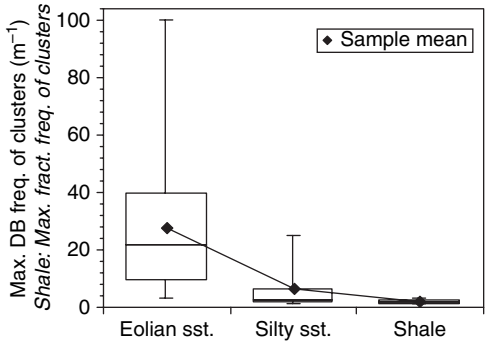

Fig. 14. Box plot with sample means showing the distribution of maximum deformation band (shale: fracture) frequency (m^{-1}) of deformation band clusters in eolian sandstones and siltstones, in addition to maximum fracture frequencies of fracture clusters in shales. The bottom and top of the boxes show the 25 and 75 percentiles, respectively, whereas the central horizontal lines show the median. Horizontal lines joined to the boxes by solid vertical lines represent the maximum and minimum values of the data set.

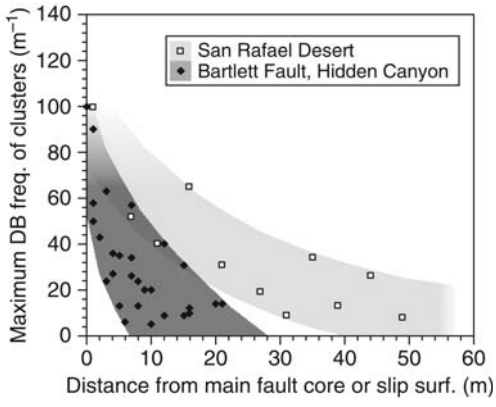

Fig. 15. Maximum deformation band (DB) frequency (m^{-1}) of deformation band clusters as a function of the distance from the main fault core or slip surface. The wide damage zone of the *c*. 200 m throw Bartlett Fault is compared with the narrower damage zones of the relatively small (<15 m throw) faults in the San Rafael Desert. Proximal to the main fault the deformation band frequency reaches a maximum of about 100 m^{-1}, suggesting a critical strain level where clusters become saturated with deformation bands and which seems independent of main fault offset. Together with cluster maturation close to the main fault, new clusters may form peripherally and increase the width of the damage zone.

accumulated decimetre-scale offset, and those associated with throughgoing slip surfaces have a total offset of the order of 0.5 m. Accordingly, growth of deformation band zones and clusters should not be affected by layer thickness in sandstone layers thicker than about 0.5 m. However, Figure 17a shows that the maximum deformation band frequency is low also for the 1.3–1.8 m thick sandstone layers, suggesting that the sandstone layers need not necessarily be cut off in order for cluster growth to cease.

Strain hardening and deformation band formation only continue as long as there is sand–sand contact across a deformation band zone. Where sand is juxtaposed against shale, i.e., in the upper and lower parts of the sand layer, strain is expected to localize in the shale or along the shale-sandstone interface in the form of an overlying and an underlying slip surface. Because of the short distance between these slip surfaces, they are likely to connect through the thin sandstone before the deformation band zones becomes very thick. As such, stress concentration within the thin (1.3–1.8 m) sandstone layers induced by the interacting slip surface tips may have facilitated localization of deformation through more intensive grain size reduction and early slip surface formation compared with thick (<3 m) layers. Deformation band frequency profiles in Figure 9 support this assumption. Here, clusters in the thin sandstone layers have lower maximum deformation band frequencies than those in the thickest layer (Layer 11). Nonetheless, clusters in both thin and thick sandstone layers are associated with slip surfaces. The significance and implications of these differences with respect to microstructure and micromechanical behaviour have not been explored in the current study.

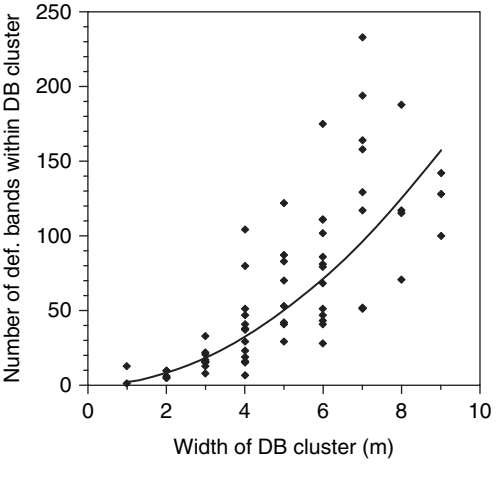

Fig. 16. Correlation of the total number of deformation bands (DBs) within the clusters against their respective widths indicates progressive localization of deformation with increasing offset.

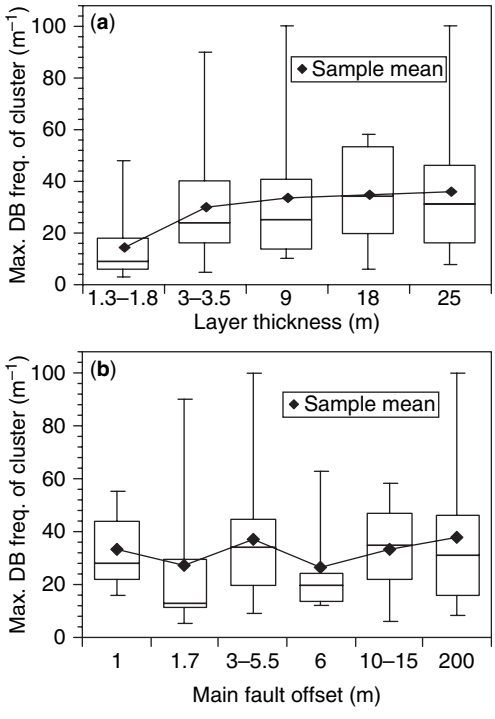

Fig. 17. Box plot of the maximum deformation band (DB) frequency of deformation band clusters in eolian sandstones correlated against (**a**) layer thickness and (**b**) main fault offset. Note that only sandstone layers thicker than 3 m were included in (**b**) to avoid influence of layer thickness on DB frequency. Eolian sandstone layers thinner than 2–3 m have less concentration of deformation bands compared with thicker layers. However, there is no strong correlation between deformation band frequency and layer thickness for layers thicker than 2–3 m in this lithology. Further, there is no apparent correlation between the maximum deformation band frequency of the deformation band clusters and main fault offset. See main text for discussion.

Deformation band frequency v. offset of main fault

The box plot in Figure 17b reveals no apparent correlation between the maximum deformation band frequency of the deformation band clusters in the eolian sandstones and main fault (slip surface or fault core) offset. Faults with offsets of about 1–200 m were incorporated. In order to isolate the effect of fault offset on the maximum deformation band frequency of the deformation band clusters, and because the deformation band frequency in thinner (<3 m) layers is affected by layer thickness (Fig. 17a), only data from layers with ≥ 3 m thickness were considered. The distribution of maximum deformation band frequencies associated with deformation band clusters is consistently skewed toward the lower values, regardless of main fault offset. In keeping with Figure 15, this finding indicates that formation of new clusters and maturation of existing clusters within the developing damage zone is more or less coeval. Thus, the lack of correlation between the maximum deformation band frequency and main fault offset points to a scale-invariant damage zone growth, where the accumulation of new deformation bands is approximately balanced by widening of the damage zone so that the distribution of the maximum deformation band frequency of the deformation band clusters remains more or less constant.

Deformation band and fracture orientation

In agreement with observations made by Aydin (1978) and Johnson (1995), the vast majority of the fault-related structures are oriented sub-parallel to their associated main fault (Figs 8–10). The fault-parallel deformation bands typically form two sets with opposing dip directions. These sets are either symmetric or slightly asymmetric about the vertical and mutually intersecting, suggesting that they originated as conjugate pairs. The dip is in the range of 50–80°. Sub-vertical deformation bands and shear fractures aligned with the main fault trend are also common. Conjugate, fault-parallel sets prevail in damage zones of isolated faults (e.g., Locality 1, San Rafael Desert) or isolated sections of faults where no significant mechanical fault interaction is evident.

There is a tendency for deformation bands to become more complexly oriented within sections of the damage zone that has the highest deformation band frequencies. Sets of deformation bands in the damage zone of the Bartlett Fault in Hidden Canyon show a wider range of orientations compared with deformation band sets in most of the damage zones of the small faults in the San Rafael Desert. Furthermore, sets of damage zone structures in the siltstones and shales are generally more distinct than sets in the eolian sandstones. Dense spacing of deformation bands, such as in mature deformation band clusters, may result in stress perturbations and mechanical interaction between deformation bands within the clusters, which in turn influence the orientation and geometry of the deformation bands (e.g., Fossen & Hesthammer 1997).

Mechanical interaction associated with fault branch points, fault overlap zones, and fault intersections may also result in stress perturbations and increased structural complexity (e.g., Cruikshank *et al.* 1991; Childs *et al.* 1995; Davatzes *et al.*

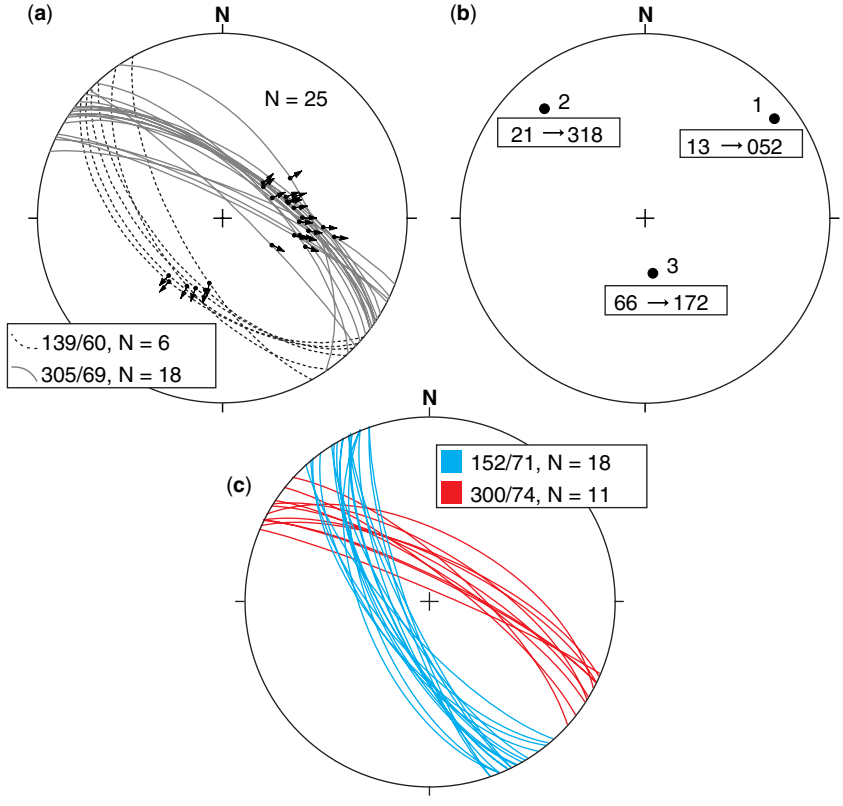

Fig. 18. (**a**) Orientation and slip lineation data of slip surfaces that breach the overlap zone in Locality 6, San Rafael Desert. (**b**) Palaeostress analysis indicates the maximum principal stress inclined at 25° from the vertical to the south (172°), whereas the least principal stress is oriented at 13/032 (Fig. 18). (**c**) Detailed mapping of deformation bands in unit e_1 along one of the breaching faults (Fig. 6) revealed similar orientations as the breaching faults, indicating that slip surfaces and associated deformation bands experienced a uniform stress field.

2005; Johansen *et al.* 2005) in order to accommodate differences in orientation and kinematics of the interacting faults. Locality 6 (Fig. 6) in the San Rafael Desert study area features an overlap zone, which is breached by numerous slip surfaces and associated deformation bands (Fossen *et al.* 2005). The breaching faults define two conjugate sets oriented at 139/60 and 305/69, obliquely to the overlapping faults (Fig. 18a). Palaeostress analysis of slip surface striations (P and T dihedral method, Angelier & Mechler 1977) internally in the overlap zone suggest that the maximum principal stress was inclined by 25° from the vertical to the south (172°), whereas the least principal stress was oriented at 13/032 (Fig. 18b). Detailed mapping of deformation bands in unit e_1 along one of the breaching faults (Fig. 6) revealed two sets of bands oriented sub-parallel to the oblique faults (Fig. 18c). This indicates that a uniform stress field prevailed during the formation of both the slip surfaces and associated deformation bands.

Accordingly, both stress perturbations resulting from mechanical interaction of faults as well as increasing structure density, such as in mature deformation band clusters proximal to the main fault or slip surface, seem to promote orientation heterogeneity within the damage zones examined.

Implications for fluid flow

Most deformation bands, and particularly those involving cataclasis, represent zones of reduced porosity and permeability (Pitman 1981; Antonellini & Aydin 1994; Gibson 1998; Heynekamp *et al.* 1999; Antonellini *et al.* 1999; Taylor & Pollard 2000; Lothe *et al.* 2002; Shipton *et al.* 2005; Sample *et al.* 2006). While deformation bands may locally reduce permeability by as

much as 5–6 orders of magnitude (e.g., Fisher & Knipe 2001), their effect on fluid flow in a petroleum reservoir is strongly dependent on their vertical and horizontal continuity and on their geometrical arrangement. Because transmissibility across the fault damage zone is a function of thickness and permeability only (e.g., Manzocchi *et al.* 1998), the number of deformation bands is an important parameter when considering cross-fault flow. However, where a producer or an injector is placed within the damage zone, the geometry and arrangement of the deformation bands become important. The conjugate sets mapped in the present study would favour fault-parallel flow controlled by deformation band clusters. Because the clusters are more well-developed close to the fault (Fig. 15), the location of the well with respect to the fault is important. Minor slip surfaces with low permeability perpendicular to strike (Antonellini & Aydin 1994) near the main fault, as observed in the damage zone of the Bartlett Fault (Fig. 10a), add to the low-permeable structure of the inner damage zone. However, slip surfaces often have significantly higher along-strike permeability, and may enhance transmissibility if the slip surfaces are interconnected and accessible to fluids.

The fact that the deformation bands are more frequent in the sandstones than in the more silty (still porous) layers may in some cases have a positive effect on reservoir performance. If present, deformation bands are likely to reduce the sweep in the most permeable sandstone layers and thereby counteract the expected early water-breakthrough in such intervals. One would expect this effect to increase with increasing amount of strain in the reservoir.

Conclusion

Detailed analyses of fault zones in interbedded porous sandstones, siltstones and shales have been conducted in order to examine internal fault zone geometry with emphasis on orientation and spatial distribution of fault-related deformation bands. Data from 29 scanlines were analyzed. The following conclusions were reached.

Deformation bands in fault damage zones in the sandstones are heterogeneously distributed in the form of individual bands, densely packed zones and clusters consisting of several zones. Conjugate sets of both bands and zones are common, but additional sets and increasing orientation heterogeneity occur close to the fault core and in complexly faulted areas. The maximum deformation band frequency of the deformation band clusters appears to decrease non-linearly away from the fault core so that clusters located near the fault must be expected to contain the highest concentrations of deformation bands. The data are consistent with the model that the maximum deformation band frequency in the damage zone is mainly established at the onset of faulting and that the syn-faulting increase in number of deformation bands is balanced by the widening of the damage zone.

Deformation bands zones and clusters are both thicker and more common in sandstones than in siltstones and are replaced by rare slip surfaces in shale layers. This difference is probably related to strain hardening: cataclastic deformation in the sandstone deformation bands involves significant strain hardening while granular flow in the siltstone deformation bands does not. However, thin (metres-thick) sandstone layers contain fewer deformation bands than thicker ones. This relation breaks down for a layer thickness of around 3 m in the study areas.

The authors are grateful to C. Childs and N. Davatzes for constructive and helpful reviews on an earlier version of this paper. Thanks also to Richard Kluge for assistance and company in the field. Richard Allmendinger's FaultKin program was used for the palaeostress analysis. The authors are thankful to StatoilHydro for funding the publication of this research.

References

ANGELIER, J. & MECHLER, P. 1977. Sur une methode graphique de recherche des contraintes principales egalement utilisable en tectonique et en seismologie: la methode des diedres droits. *Bulletin dela Societe Geologique de France*, **7**, 1309–1318.

ANTONELLINI, M. A. & AYDIN, A. 1994. Effect of faulting on fluid flow in porous sandstones: petrophysical properties. *American Association of Petroleum Geologists Bulletin*, **78**, 355–377.

ANTONELLINI, M. A. & AYDIN, A. 1995. Effect of faulting on fluid flow in porous sandstones: geometry and spatial distribution. *American Association of Petroleum Geologists Bulletin*, **79**, 642–671.

ANTONELLINI, M. A., AYDIN, A. & POLLARD, D. D. 1994. Microstructure of deformation bands in porous sandstones at Arches National Park, Utah. *Journal of Structural Geology*, **16**, 941–959.

ANTONELLINI, M. A., AYDIN, A. & ORR, L. 1999. Outcrop aided characterization of a faulted hydrocarbon reservoir: Arroyo Grande oil field, California, USA. *In*: HANEBERG, W. C., MOZLEY, P. S., MOORE, C. J. & GOODWIN, L. B. (eds) *Faults and Subsurface Fluid Flow*. American Geophysical Union Geophysical Monographs **113**, 7–26.

AYDIN, A. 1978. Small faults formed as deformation bands in sandstone. *In*: BYERLEE, J. D. & WYSS, M. (eds) *Rock Friction and Earthquake Prediction*. Birkhaeuser, Basel, 913–930.

AYDIN, A. & JOHNSON, A. M. 1978. Development of faults as zones of deformation bands and as slip surfaces in sandstone. *In*: BYERLEE, J. D. & WYSS, M. (eds) *Rock Friction and Earthquake Prediction*. Birkhaeuser, Basel, 931–942.

AYDIN, A. & JOHNSON, A. M. 1983. Analysis of faulting in porous sandstones. *Journal of Structural Geology*, **5**, 19–31.

AYDIN, A. & RECHES, Z. 1982. Number and orientation of fault sets in the field and in experiments. *Geology*, **10**, 107–112.

AYDIN, A., BORJA, R. I. & EICHHUBL, P. 2006. Geological and mathematical framework for failure modes in granular rock. *Journal of Structural Geology*, **28**, 83–98.

BEACH, A., WELBON, A. I., BROCKBANK, P. & MCCALLUM, J. E. 1999. Reservoir damage around faults: outcrop examples from the Suez rift. *Petroleum Geoscience*, **5**, 109–116.

BUMP, A. P. & DAVIS, G. H. 2003. Late Cretaceous–early Tertiary Laramide deformation of the northern Colorado Plateau, Utah and Colorado. *Journal of Structural Geology*, **25**, 421–440.

CAINE, J. S., EVANS, J. P. & FORSTER, C. B. 1996. Fault zone architecture and permeability structure. *Geology*, **24**, 1025–1028.

CASHMAN, S. & CASHMAN, K. 2000. Cataclasis and deformation-band formation in unconsolidated marine terrace sand, Humboldt County, California. *Geology*, **28**, 111–114.

CHILDS, C., WATTERSON, J. & WALSH, J. J. 1995. Fault overlap zones within developing normal fault systems. *Journal of the Geological Society of London*, **152**, 535–549.

CRUIKSHANK, K. M., ZHAO, G. & JOHNSON, A. M. 1991. Analysis of minor fractures associated with joints and faulted joints. *Journal of Structural Geology*, **13**, 865–886.

DAVATZES, N. C., EICHHUBL, P. & AYDIN, A. 2005. The structural evolution of fault zones in sandstone by multiple deformation mechanisms; Moab fault, SE Utah. *Geological Societey of America Bulletin*, **117**, 135–148.

DAVIS, G. H. 1999. *Structural Geology of the Colorado Plateau Regional of Southern Utah, with Special Emphasis on Deformation Bands*. Geological Society of America Special Papers, **342**.

DOELLING, H. H. 1988. Geology of Salt Valley Anticline and Arches National Park, Grand County, Utah. *In*: DOELLING, H. H., OVIATT, C. G. & HUNTOON, P. W. (eds) *Salt Deformation in the Paradox Region*. Utah Geological and Mineral Survey, Salt Lake City, UT, 1–58.

DOELLING, H. H. 2000. Geology of Arches National Park, Grand County, Utah. *In*: SPRINKEL, D. A., CHIDSEY, T. C. JR & ANDERSON, P. B. (eds) *Geology of Utah's Parks and Monuments*. Utah Geological Association, Salt Lake City, UT, 11–36.

DOELLING, H. H. 2001. *Geologic Map of the Moab and Eastern Part of the San Rafael Desert 30′ × 60′ Quadrangles, Grand and Emery Counties, Utah, and Mesa County, Colorado*. Geologic Map **180**. Utah Geological Survey, Salt Lake City, UT.

DOELLING, H. H. 2002. *Geologic Map of the Fisher Towers 7.5′ Quadrangle, Grand County, Utah*. Utah Geological Survey, Salt Lake City, UT, 22, 1 Sheet.

DU BERNARD, X., EICHHUBL, P. & AYDIN, A. 2002. Dilation bands: a new form of localized failure in granular media. *Geophysical Research Letters*, **29**, 2176–2179.

FISHER, Q. J. & KNIPE, R. J. 1998. Fault sealing processes in siliciclastic sediments. *In*: FISHER, Q. J. & KNIPE ROBERT, J. (eds) *Faulting, Fault Sealing and Fluid Flow in Hydrocarbon Reservoirs*. The Geological Society of London, Special Publications, **147**, 117–134.

FISHER, Q. J. & KNIPE, R. J. 2001. The permeability of faults within siliciclastic petroleum reservoirs of the North Sea and Norwegian Continental Shelf. *Marine and Petroleum Geology*, **18**, 1063–1081.

FISHER, Q. J., CASEY, M., HARRIS, S. D. & KNIPE, R. J. 2003. Fluid flow properties of faults in sandstone: the importance of temperature history. *Geology*, **31**, 965–968.

FOSSEN, H. & HESTHAMMER, J. 1997. Geometric analysis and scaling relations of deformation bands in porous sandstone from the San Rafael Desert, Utah. *Journal of Structural Geology*, **19**, 1479–1493.

FOSSEN, H., JOHANSEN, T. S. E., HESTHAMMER, J. & ROTEVATN, A. 2005. Fault interaction in porous sandstone and implications for reservoir management; examples from southern Utah. *American Association of Petroleum Geologists Bulletin*, **89**, 1593–1606.

FOSSEN, H., SCHULZ, R. A., SHIPTON, Z. K. & MAIR, K. 2007. Deformation bands in sandstone – a review. *Journal of the Geological Society of London*, **164**, 755–769.

FOWLES, J. & BURLEY, S. 1994. Textural and permeability characteristics of faulted, high porosity sandstones. *Marine and Petroleum Geology*, **11**, 608–623.

FOXFORD, K. A., GARDEN, I. R., GUSCOTT, S. C., BURLEY, S. D., LEWIS, J. L. L., WALSH, J. J. & WATTERSON, J. 1996. The Field Geology of the Moab Fault. *In*: HUFFMAN, A. C., LUND, W. R. J. & GODWIN, L. H. (eds) *Geology and Resources of the Paradox Basin*. Utah Geological Association, Salt Lake City, UT, 265–283.

GARDEN, I. R., GUSCOTT, S. C., BURLEY, S. D., FOXFORD, K. A., WALSH, J. J. & MARSHALL, J. 2001. An exhumed palaeo-hydrocarbon migration fairway in a faulted carrier system, Entrada Sandstone of SE Utah, USA. *Geofluids*, **1**, 195–213.

GIBSON, R. G. 1998. Physical character and fluid-flow properties of sandstone-derived fault zones. *In*: COWARD, M. P., JOHNSON, H. & DALTABAN, T. S. (eds) *Structural Geology in Reservoir Characterization*. Geological Society, London, Special Publications, **127**, 83–97.

HADIZADEH, J. & JOHNSON, W. K. 2003. Estimating local strain due to comminution in experimental cataclastic textures. *Journal of Structural Geology*, **25**, 1973–1979.

HARPER, T. R. & LUNDIN, E. R. 1997. Fault seal analysis: reducing our dependence on empiricism. *In*: MÖLLER-PEDERSEN, P. & KOESTLER, A. G. (eds)

Hydrocarbon Seals – Importance for Exploration and Production. 7. Norwegian Petroleum Society Special Publications, **7**, 149–165.

HESTHAMMER, J. & FOSSEN, H. 2000. Uncertainties associated with fault sealing analysis. *Petroleum Geoscience*, **6**, 37–45.

HESTHAMMER, J. & FOSSEN, H. 2001. Structural core analysis from the Gullfaks area, northern North Sea. *Marine and Petroleum Geology*, **18**, 411–439.

HESTHAMMER, J., BJØRKUM, P. A. & WATTS, L. 2002. The effect of temperature on sealing capacity of faults in sandstone reservoirs; examples from the Gullfaks and Gullfaks Sør fields, North Sea. *American Association of Petroleum Geologists Bulletin*, **86**, 1733–1751.

HEYNEKAMP, M. R., GOODWIN, L. B., MOZLEY, P. S. & HANEBERG, W. C. 1999. Controls on fault-zone architecture in poorly lithified sediments, Rio Grande Rift, New Mexico; implications for fault-zone permeability and fluid flow. *In*: HANEBERG, W. C., MOZLEY, P. S., MOORE, J. C. & GOODWIN, L. B. (eds) *Faults and Subsurface Fluid Flow in the Shallow Crust*. American Geophysical Union, Washington, DC, 27–49.

HUANG, Q. & ANGELIER, J. 1989. Fracture spacing and its relation to bed thickness. *Geological Magazine*, **126**, 355–362.

JAMISON, W. R. & STEARNS, D. W. 1982. Tectonic deformation of Wingate Sandstone, Colorado National Monument. *American Association of Petroleum Geologists Bulletin*, **66**, 2584–2608.

JOHNSON, A. M. 1995. Orientations of faults determined by premonitory shear zones. *Tectonophysics*, **247**, 161–238.

JOHANSEN, T. E. S., FOSSEN, H. & KLUGE, R. 2005. The impact of syn-faulting porosity reduction on damage zone architecture in porous sandstone; an outcrop example from the Moab Fault, Utah. *Journal of Structural Geology*, **27**, 1469–1485.

KNIPE, R. J., FISHER, Q. J. *ET AL*. 1997. Fault seal analysis: successful methodologies, application and future directions. *In*: MØLLER-PEDERSEN, P. & KOESTLER, A. G. (eds) *Hydrocarbon Seals: Importance for Exploration and Production*. Norwegian Petroleum Society Special Publications, **7**. Elsevier, Singapore, 15–40.

LOTHE, A. E., GABRIELSEN, R. H., BJØRNEVOLL-HAGEN, N. & LARSEN, B. T. 2002. An experimental study of the texture of deformation bands; effects on the porosity and permeability of sandstones. *Petroleum Geoscience*, **8**, 195–207.

MAIR, K., MAIN, I. & ELPHICK, S. 2000. Sequential growth of deformation bands in the laboratory. *Journal of Structural Geology*, **22**, 25–42.

MANDL, G., DE JONG, L. N. J. & MALTHA, A. 1977. Shear zones in granular material. *Rock Mechanics*, **9**, 95–144.

MANZOCCHI, T., RINGROSE, P. S. & UNDERHILL, J. R. 1998. Flow through fault systems in high-porosity sandstones. *In*: COWARD, M. P., JOHNSON, H. & DALTABAN, T. S. (eds) *Structural Geology in Reservoir Characterization*. The Geological Society of London, Special Publications, **127**, 65–82.

MARONE, C. & SCHOLZ, C. H. 1989. Particle-size distribution and microstructures within simulated fault gouge. *In*: SPRAY, J. G. & HUDLESTON, P. J. (eds) *Friction Phenomena in Rock*. Pergamon, Oxford, 799–814.

MENÉNDEZ, B., ZHU, W. & WONG, T. F. 1996. Micromechanics of brittle faulting and cataclastic flow in Berea Sandstone. *Journal of Structural Geology*, **18**, 1–16.

MILLIGAN, M. R. 2000. Geology of Goblin Valley State Park, Utah. *In*: SPRINKEL, D. A., CHIDSEY, T. C., JR. & ANDERSON, P. B. (eds) *Geology of Utah's Parks and Monuments*. Utah Geological Association, Salt Lake City, UT, 11–36.

NARR, W. & SUPPE, J. 1991. Joint spacing in sedimentary rocks. *Journal of Structural Geology*, **13**, 1037–1048.

NUCCIO, V. F. & CONDON, S. M. 1996. *Burial and Thermal History of the Paradox Basin, Utah and Colorado, and Petroleum Potential of the Middle Pennsylvanian Paradox Basin*. US Geological Survey, Reston, VA.

OWEN, G. 1987. Deformation processes in unconsolidated sands. *In*: JONES, M. E. & PRESTON, R. M. (eds) *Deformation of Sediments and Sedimentary Rocks*. The Geological Society of London, Special Publications, **29**, 11–24.

PEVEAR, D. R., VROLIJK, P. J. & LONGSTAFFE, F. J. 1997. Timing of Moab fault displacement and fluid movement integrated with burial history using radiogenic and stable isotopes. *In*: HENDRY, J. P., CAREY, P. F. & PARNELL, J. (eds) *Geofluids II '97, Contributions to the Second International Conference on Fluid Evolution, Migration and Interaction in Sedimentary Basins and Orogenic Belts*. 10–14 March 1997, Belfast: Queen's University of Belfast, 42–45.

PITTMAN, E. D. 1981. Effect of fault-related granulation on porosity and permeability of quartz sandstones, Simpson Group (Ordovician) Oklahoma. *American Association of Petroleum Geologists Bulletin*, **65**, 2381–2387.

RAWLING, G. C. & GOODWIN, L. B. 2003. Cataclasis and particulate flow in faulted, poorly lithified sediments. *Journal of Structural Geology*, **25**, 317–331.

SAMPLE, J. C., WOODS, S., BENDER, E. & LOVEALL, M. 2006. Relationship between deformation bands and petroleum migration in an exhumed reservoir rock, Los Angeles Basin, California, USA. *Geofluids*, **6**, 105–112.

SCHULTZ, R. A. & FOSSEN, H. 2002. Displacement-length scaling in three dimensions; the importance of aspect ratio and application to deformation bands. *Journal of Structural Geology*, **24**, 1389–1411.

SCHULTZ, R. A. & SIDDHARTHAN, R. 2005. A general framework for the occurrence and faulting of deformation bands in porous granular rocks. *Tectonophysics*, **411**, 1–18.

SHIPTON, Z. K. & COWIE, P. A. 2001. Damage zone and slip-surface evolution over μm to km scales in high-porosity Navajo sandstone, Utah. *Journal of Structural Geology*, **23**, 1825–1844.

SHIPTON, Z. K. & COWIE, P. A. 2003. A conceptual model for the origin of fault damage zone structures in high-porosity sandstone. *Journal of Structural Geology*, **25**, 333–344.

SHIPTON, Z. K., EVANS, J. P. & THOMPSON, L. B. 2005. The geometry and thickness of deformation-band fault core and its influence on sealing characteristics of

deformation-band fault zones. *American Association of Petroleum Geologists Memoir*, **85**, 181–195.

SOLUM, J. G., VAN DER PLUIJM, B. A. & PEACOR, D. R. 2005. Neocrystallization, fabrics and age of clay minerals from an exposure of the Moab Fault, Utah. *Journal of Structural Geology*, **27**, 1563–1576.

TAYLOR, W. L. & POLLARD, D. D. 2000. Estimation of in situ permeability of deformation bands in porous sandstone, Valley of Fire, Nevada. *Water Resources Research*, **36**, 2595–2606.

UNDERHILL, J. R. & WOODCOCK, N. H. 1987. Faulting mechanisms in high-porosity sandstones; New Red Sandstone, Arran, Scotland. *In*: JONES, M. E. & PRESTON, M. F. (eds) *Deformation of Sediments and Sedimentary Rocks*. The Geological Society, London, 91–105.

WIBBERLEY, C. A. J., PETIT, J. P. & RIVES, T. 2000. Mechanics of cataclastic 'deformation band' faulting in high-porosity sandstone, Provence. *Comptes Rendus de l'Academie des Sciences, Serie II. Sciences de la Terre et des Planetes*, **331**, 419–425.

The influence of layering and pre-existing joints on the development of internal structure in normal fault zones: the Lodève basin, France

WOUTER VAN DER ZEE[1], CHRISTOPHER A. J. WIBBERLEY[2,3] & JANOS L. URAI[4]

[1]*GeoMechanics International Inc, Emmerich-Josef-Str., 55116, Mainz, Germany*

[2]*Géosciences Azur, CNRS UMR6526, Université de Nice – Sophia Antipolis, 250 rue A. Einstein, 06560 Valbonne, France*

[3]*Present address: TOTAL, CSTJF, Av. Larribau, 64018 Pau, France (e-mail: christopher.wibberley@total.com)*

[4]*Geologie-Endogene Dynamik, RWTH Aachen, Lochnerstrasse 4-20, 52056 Aachen, Germany*

Abstract: This paper examines the role of mechanical stratigraphy on the evolution of normal fault geometry and fault zone internal structure, using a well-exposed normal fault system from the Permian Lodève Basin, southern France. Faults formed early during the syn-deformation tilting history of the basin tend to have steeper segments in the competent sandstone layers due to refraction, assisted by pre-existing early bedding-perpendicular joints, where displacement remained on the order of bed thickness. Faults which continued to slip during tilting have a more complex structure of splays due both to the space incompatability problem of slip at fault bends of this irregular geometry, and because tilting favours the generation of new splays at a different angle to the earlier faults experiencing rotation. Continued deformation between faults and their splays often causes both distributed deformation in between the two, and reconnection of splays to the main fault forming isolated lenses. Thus, fault zone complexity increases greatly as slip exceeds competent bed thickness, owing both to the presence of the mechanical layering, and the fact that this layering is being tilted.

Faults in the upper crust evolve in relation to changes in the structure of the effective stress field and the mechanical properties of the rocks. For example, basin-wide tilting during ongoing deformation can rotate faults to an unfavourable orientation for further slip, and cause faults to splay or even initiate new faults (cf. Jaeger & Cook 1976; Sibson 1985; Buck 1993; Agnon & Reches 1995; Wibberley *et al.* 2007). Mechanical heterogeneity (e.g., sedimentary layering, pre-existing faults or joints) has a strong influence on fault propagation through the system (Peacock & Sanderson 1992; Bürgmann & Pollard 1994; Childs *et al.* 1996; Gross *et al.* 1997; Martel 1999; Wilkins & Gross 2002; Soliva & Benedicto 2005). The interplay of all these processes can be expected to produce a variety of fault geometric irregularities at all length scales. During slip on a non-planar fault additional deformation of the wall rock must occur. The deformation of asperities is thought to cause widening of the fault zone (such as those caused by the interaction with bedding-parallel slip planes (Watterson *et al.* 1998), leading to the suggestion that there is a universal relationship between displacement on a fault and fault zone thickness (e.g., Scholz 1987; Hull 1988). The likely operation of these processes implies that the internal structure will evolve to become generally more complex through time during deformation. However, the influence of such mechanical heterogeneity and the generation of asperities on fault zone complexity is poorly understood. Furthermore, the feasibility of directly comparing data sets from different fault systems formed in different geological and tectonic settings has been questioned (e.g., Blenkinsop 1989; Evans 1990).

In this paper, we use outcrop data of faults in a sand–shale sequence to better understand the evolution of normal faults in a layered medium. We investigate the influence of layering and pre-existing joints on the fault zone width, fault throw, and the internal structure of normal fault

From: WIBBERLEY, C. A. J., KURZ, W., IMBER, J., HOLDSWORTH, R. E. & COLLETTINI, C. (eds) *The Internal Structure of Fault Zones: Implications for Mechanical and Fluid-Flow Properties*. **299**, 57–74.
DOI: 10.1144/SP299.4 0305-8719/08/$15.00

zones. The faults studied are related to the Mas d'Alary–Saint Jean fault zone in the Permian Lodève Basin in the South of France, and crop out in the Tréviels open-cast mine from which the observations presented in this paper are taken. The outcrop is situated near the hamlet of Mas d'Alary, 3 km SSE of Lodève in the eastern part of the Lodève Basin, southern France (Fig. 1).

Geological setting

The 15 × 25 km Lodève basin is situated 50 km west of Montpellier, south of the Massif Central (Lopez 1992). It is a half-graben which formed during the Permian. The Palaeozoic strata dip 15–30° southward and consist of Permian sediments concordantly deposited on a Cambrian basement, in turn covered by horizontal Mesozoic sediments (Fig. 1). The Mesozoic cover is almost completely eroded, exposing both the Permian sediments and basement. The Permian sediments comprise a combination of continental, detrital and bioclastic sediments representing a lacustrine to floodplain succession, and related to a progressive change from a humid-tropical to semi-arid climate.

The rocks exposed in the Treviels open-cast mine comprise a layered shale-sandstone sequence of 30–35% sandstone (low-porosity, calcite-cemented arkose) and 65–70% shale. The bed thickness of the sandstone varies from 10 cm to 1 m, whereas the bed thickness of the shale ranges from very thin laminae (5 mm) to thick beds (2 m). The shale is hard and weathers to a flaky aggregate, which can be related to overconsolidation during burial to approximately 5 km maximum depth (pers. comm., J. P. Petit). Most of the geologic boundaries of the Permian Lodeve basin are formed by faults. During the early- to middle-Permian, the regional Cambrian structure was eroded and the valleys filled with conglomerates, causing the non-uniform thickness of the conglomerate sequence. At the end of this period the major basement faults were reactivated.

During the late Permian the basin was tilted 15–20° to the south by reactivation of older basement faults, interpreted by Lopez (1992) as a roll-over anticline involving the Permian half-graben and its Cambrian basement above a late orogenic listric fault, the Aires fault. Also during this tectonic event, the *Mas d'Alary–Saint Jean fault zone* formed, presumably in the collapsed crest of the roll-over anticline. Thus the faults examined in this paper are thought to be early Saxonian in age, and active before the main burial by the remaining Upper Permian sediments. This is compatible with a recent interpretation that these faults started forming at the onset of tilting and continued to evolve during tilting of the Permian strata as the listric Lodève Basin evolved (Wibberley *et al.* 2007). Although the exact depth at which the faults formed is not known, it is therefore likely to be less than 1000 m based on correlated thicknesses of the Upper Autunian and Lower Saxonian (syn-rift) strata.

The opening of Neotethys during the Jurassic time caused marine sedimentation and syn-sedimentary deformation. Inside the basin this period is only marked by rotated blocks in the Mesozoic cover. The Pyrenean shortening (*c.* 40 Ma) caused strong deformation east of the Cevennes fault (northwards thrusting and east–west trending folds), but only minor deformation in the Lodève basin. The deformation styles found in the Lodève basin are slight inversions of normal faults, strike–slip reactivation of the Permian fault and some bedding-parallel slip at the base of the sedimentary sequences. The large extensional deformation in the Oligocene (opening of the Camargue trough) only had an influence east of the Cévennes fault, and caused a reactivation of the Cévennes fault itself (normal movement). Therefore, although the tectonic history of the basin is rather complex, the structures found in the Mas d'Alary–Saint Jean fault zone investigated in this study are essentially extensional and of Permian age with a small overprint of the Pyrenean compression (manifested at the outcrop scale by slight reverse-sense bedding-parallel slip).

Field study of the Mas d'Alary–Saint Jean fault zone

The Tréviels pit-mine exposes a large variety of normal fault structures in lower Permian rocks. The outcrop face is approximately 140 m long and 25 m high. The bedding is tilted 30° southwards and crosscut by mostly north-dipping normal faults and some nearly vertical and south-dipping faults (Fig. 2).

Methods

The total outcrop face was photographed in detail with a 300 mm objective to prevent distortion as much as possible. The overview angle from north to south is 40° and from top to bottom 15° (photos are taken level with the half-height of the outcrop). The interesting structures in the lower part of the outcrop (up to *c.* 6 m) were examined in more detail from ground level. Care was taken to take photographs parallel to fault strike where possible, to avoid distortion. Structures were investigated with the help of detailed sketches and interpretation of photographs. Orientation data and

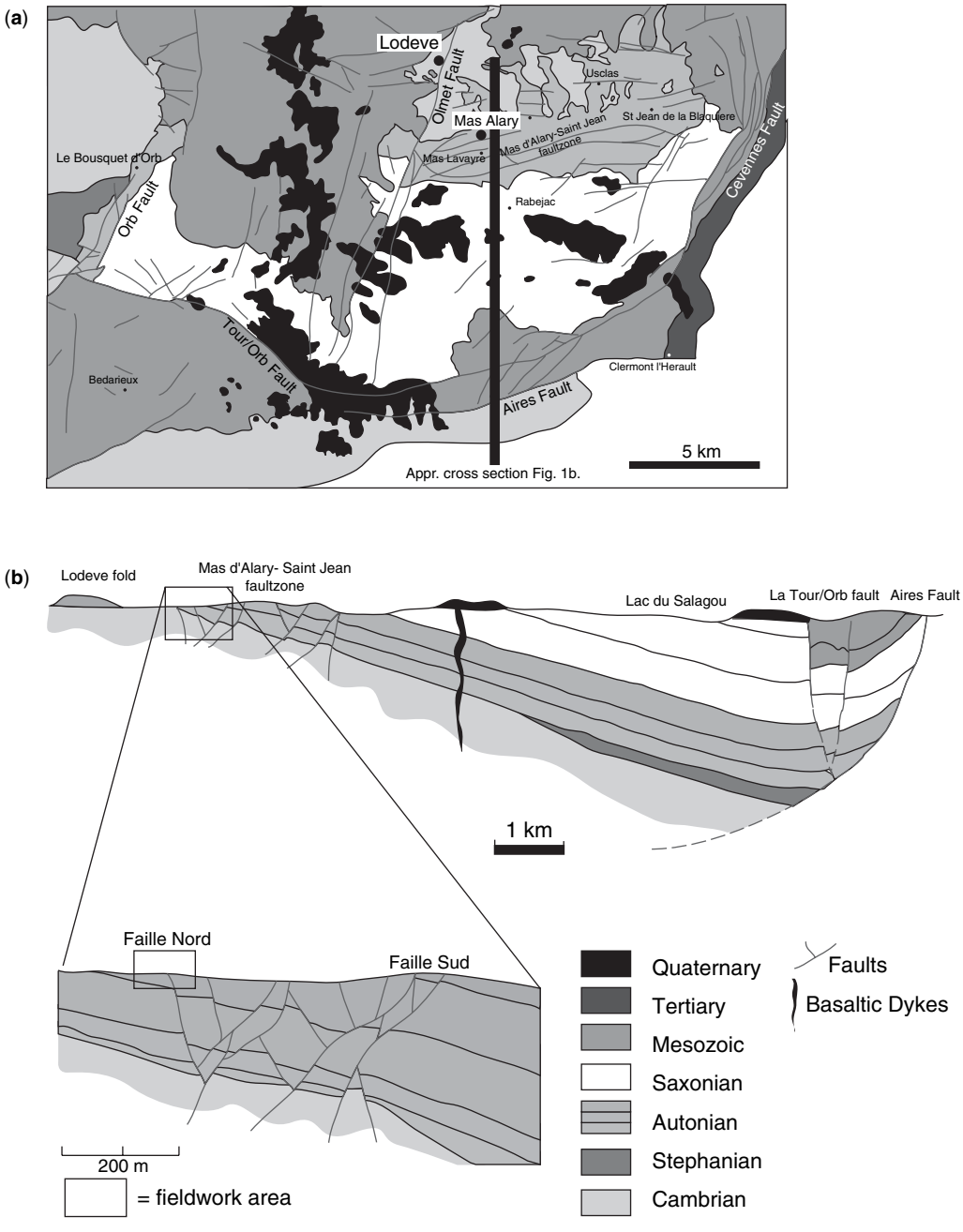

Fig. 1. (**a**) Schematic geological map of the Lodève Basin. North is towards the top of the page. UTM coordinates of the outcrop are: E3°20′27″ longitude and N43°42′11″ latitude. (**b**) Schematic geological cross section north (left) to south (right), both after Lopez (1992).

structural observations were collected along a scanline at the bottom part of the outcrop (ground level).

Samples were collected after on-site impregnation with a very low viscosity epoxy, which was poured on the outcrop before extracting the samples. After extraction from the outcrop, the sample was impregnated from all sides, and stabilized with a gypsum collar. For microstructural

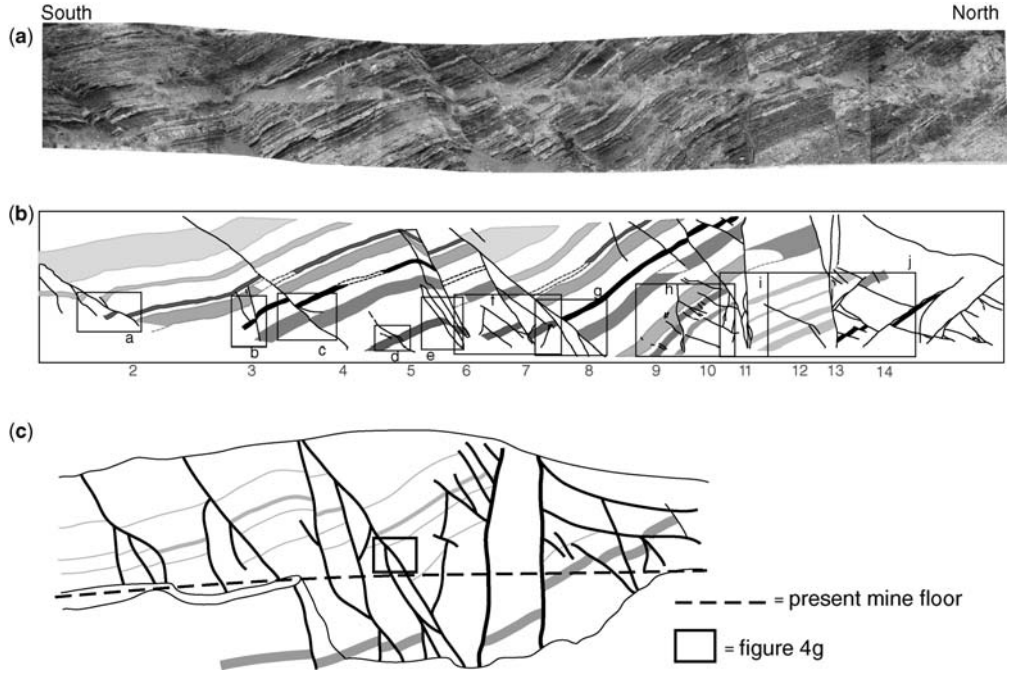

Fig. 2. (**a**) Profile of the Tréviels pit-mine with main faults indicated and numbered. Outcrop length is 140 m. (**b**) Interpretation of the fault structures; the positions of the enlargements of Figure 4 are indicated. The shaded beds are sandstones, the most prominent of which are highlighted in darker shades as marker beds. White represents shale. In (a) and (b) the outcrop heights are 20 m and lengths 120 m. (**c**) Profile of the Treviels pit-mine outcrop after Bruel (1997). This profile was drawn while the mine was still being actively operated, before it was partially filled; please note that this profile is therefore slightly different from the one above. The rectangle indicates the enlargement in Figure 4g.

analysis, the sample was cut perpendicular to the fault plane, to allow high resloution photography.

Characteristics of individual faults

The strike of the faults is perpendicular to the outcrop face. Fault offset ranges from 10 cm to 25 m. The structure as seen in the outcrop is shown in the profile of Figure 2. Although the faulting took place during the Permian, no evidence for syn-sedimentary faulting of Permian beds is found. Significant features are the larger number of normal faults which dip 40–60° to the north and the few larger normal faults which down-throw to the south (very steep, sometimes overturned). The measured fault orientations (Fig. 3) are biased towards the steeper faults, because measurable fault surfaces were mostly found in the sandstone beds due to outcrop quality, and these faults tend to be steeper. In the northern part of the outcrop, bedding-parallel slip is evidenced by bedding-parallel offset of the steep normal faults.

Low displacement ($d < 1.5$ m) north-dipping normal faults are bedding-oblique and have dips of 20–50°. Their orientation with respect to bedding is between 50 and 80°. Although they are irregular in nature, the faults are consistently steeper in the sandstone beds than in the shale beds (e.g., Fault 2, Fig. 4a; Fault 12, Fig. 4j), a point also borne out by separating the orientation statistics of sandstone fault contacts from shale-shale juxtaposition contacts (Wibberley *et al.* 2007). In the sandstone beds the fault surfaces follow pre-existing joints, which are perpendicular to bedding. Where these faults coincide with joint surfaces, the faults are often splayed and the area between the two splays is filled with shale (e.g. Fig. 4a). Step-over geometries often form restraining bends which either partly or fully transfer the offset (e.g., Fig. 4c & d).

Low-displacement ($d < 1.5$ m) south-down-throwing faults are vertical or slightly overturned, at angles of 65–80° to bedding. They are irregular, following bedding-perpendicular joints in the sandstone beds and have splays and/or conjugates which form small graben structures in the hanging walls of the faults. Irregularity is also expressed by the generation of lens structures

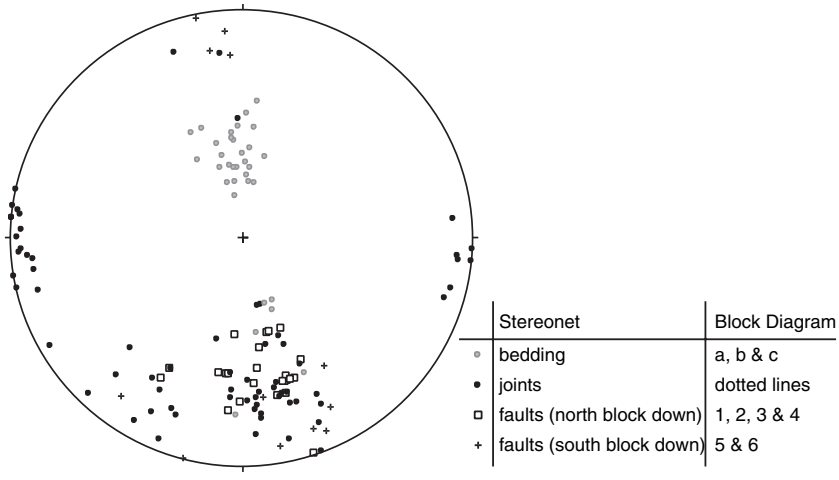

Fig. 3. Lower hemisphere equal area stereographic projection with the orientations of the bedding, joints and faults denoted as poles to planes.

bounded by splays (Figs 4h & 5a) or at step-overs (Fig. 4b).

A single high-displacement north-downthrowing fault, Fault 8 (Fig. 4g), has a large offset (10 m). This fault splays in the middle of the outcrop, which is the top part of a large lens. The full lens geometry of this structure was sketched by Bruel (1997) before the open-cast mine was recultivated and partially filled (Fig. 2c). The overall dip of the fault above the lens is 45°. Detailed observation showed a relatively undisturbed wall rock, and a severely faulted and folded interior of the lens (Fig. 4g). There is a remarkable absence of deformation in the hanging wall of this fault.

High-displacement south-downthrowing faults, Faults 11 and 13, are vertical and have offsets of 25 and 5 m respectively. Both fault zones have splays branching off the main fault, but the higher-displacement fault, Fault 11, shows a much more complicated internal structure with splays re-connecting to the main fault and consequent lenses inside the fault zone in which rotated bedding is still recognizable. Both fault zones contain shale-rich gouge, but Fault 11 also has cemented breccia within the gouge.

Bedding-perpendicular faults (Faults 6 & 7, Fig. 2b) are north-downthrowing normal faults interpreted to have formed as the system rotates during regional tilting of the basin (Wibberley *et al.* 2007). They dip 60° to the north and have offsets of approximately 5 m and 2 m respectively. They both consist of two parallel strands separated by weakly deformed rock in which bedding is still visible (Figs 4e, f & 5b). In the case of Fault 7, the strands anastomose and widening of the fault zone by divergence of the splays is observed where bedding-parallel slip surfaces interact with the fault during movement (Fig. 5b): here, fault gouge thickness varies from 1 to 15 cm. The edges of the fault zone cut the sandstone bed in a clean break identical in appearance to joint surfaces, and indeed bedding-perpendicular joints in the vicinity often have small (millimetre to centimetre) amounts of slip on them (Fig. 6a), suggesting that these bedding-perpendicular faults propagated along joints in the sandstone beds. Similar reactivated bedding-parallel joints are present elsewhere in the outcrop and suggest that this is a general phenomenon (e.g., Fig. 6b). In the case of Fault 6, one of the strands terminates halfway up the outcrop (Fault 6a in Fig. 4f) in a zone of continuous deformation (folding) of the wall rock so that total displacement (a + b) stays constant (Fig. 4e). Anomalous bedding rotation to the north in the overlap zone between strands a and b, facilitated by bedding-parallel slip, attests to the transfer of displacement from one strand to the other (Fig. 4e). Striations are visible on the exposed fault surfaces, showing a purely down-dip movement (Wibberley *et al.* 2007). A very thin coating of clay is present on parts of the fault surfaces.

A system of bedding-parallel faults makes up a complex structure in the northern part of the outcrop adjacent to Fault 13 (Fig. 4j). The tilted bedding functions as a slip plane for low-angle 'normal-sense' south-dipping faults. These bedding-parallel slip planes are amongst the youngest faults in the entire outcrop, offsetting the older north-dipping faults in this region. The evolution of this network is described in more detail in Wibberley *et al.* (2007).

Joints

Two joint sets are recognized in the outcrop. The joints are typically only visible in the sandstone layers. The joint surfaces cross cut the sand layers at high angles to bedding. The strikes of the two joint sets are perpendicular and parallel to that of the faults. The fault-parallel joint set is often reactivated (Fig. 7), as mentioned above, particularly in the generation of bedding-perpendicular faults. The combination of the lower angle faults in the shale and the slip-reactivated joints in the sandstone bed give the faults an irregular geometry (e.g., Fig. 8).

Fault zone internal structure

The fault zones consist mostly of clay with quartz and/or sandstone blocks present in places, as may

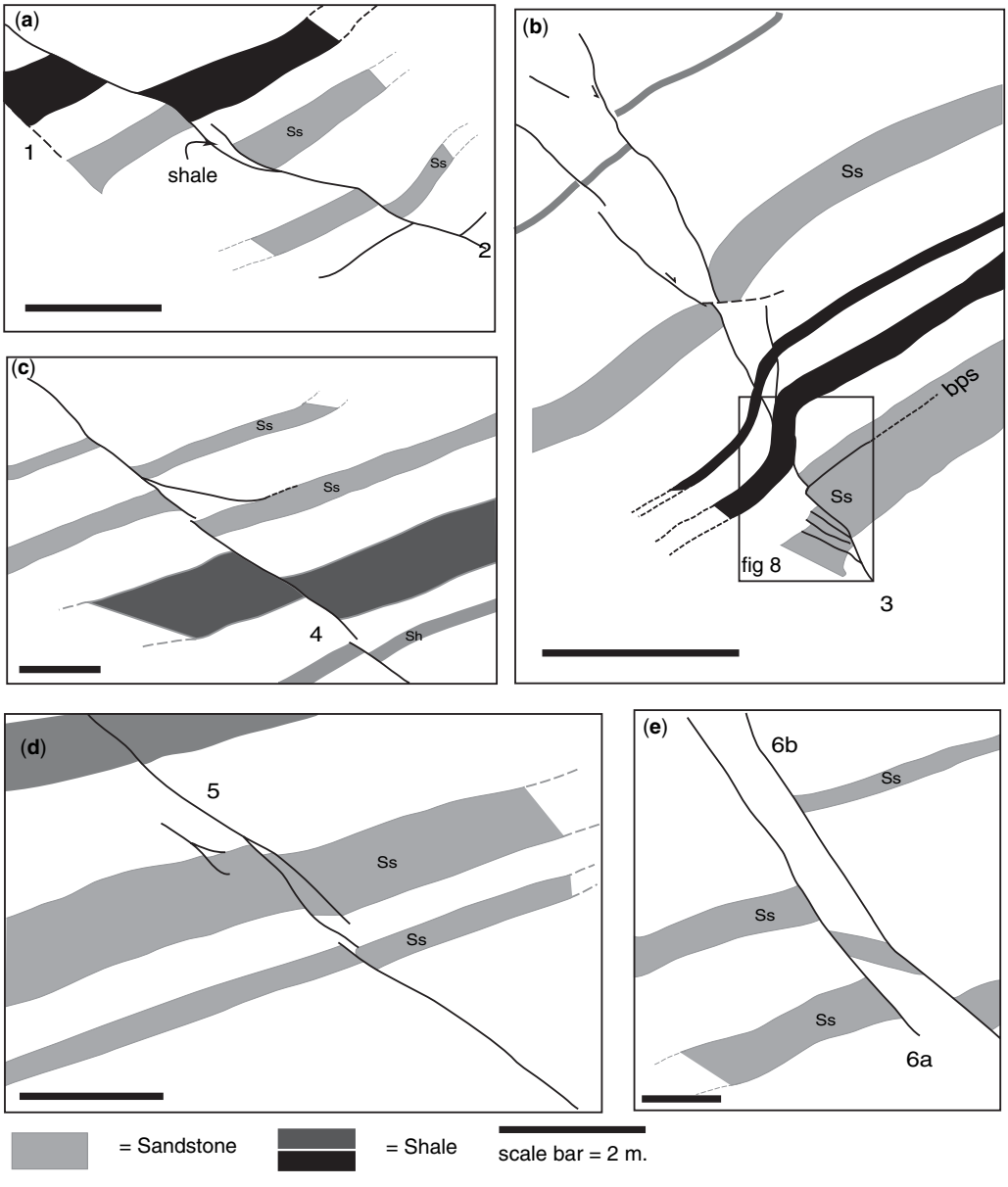

Fig. 4. Overview of the main fault structures found in the lower part of the outcrop (continued on next page). The location of each structure is indicated in Figure 2. Locations of more detailed figures are indicated. The lithology colour code is as per Figure 2b.

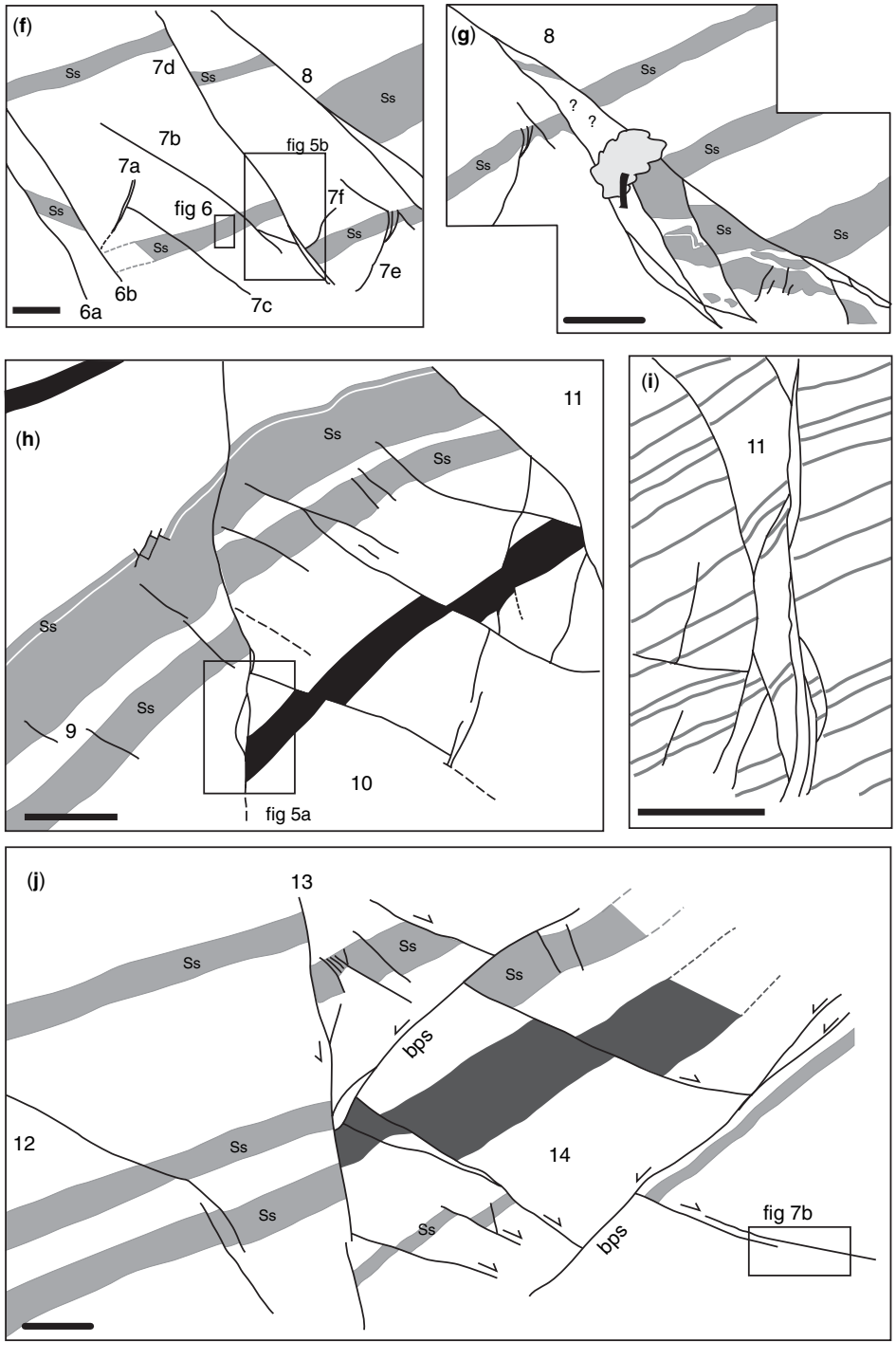

Fig. 4. (*Continued*).

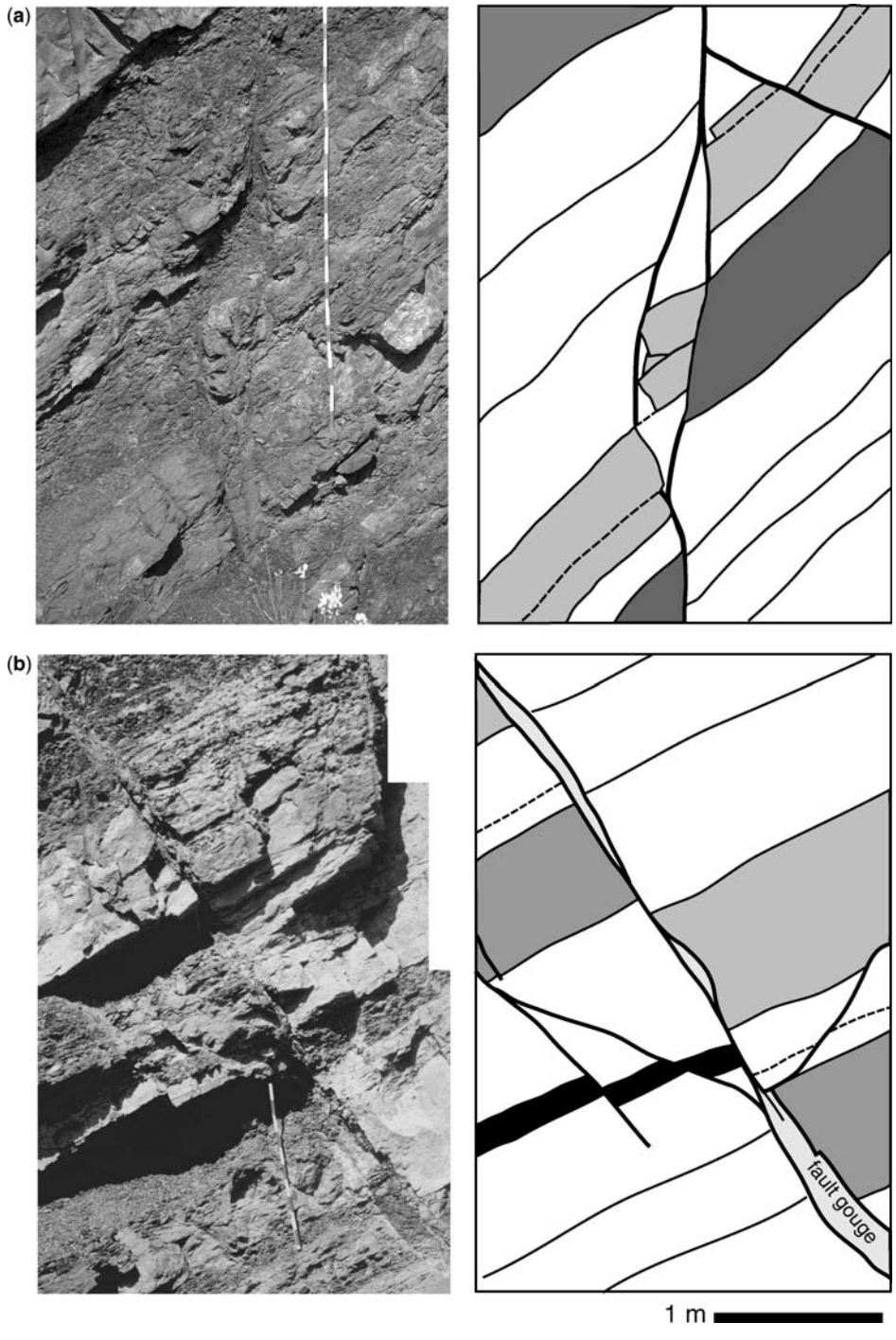

Fig. 5. (**a**) Lens structure in the lower part of fault zone 10. Measuring tape = 2 m. (**b**) Detail of Fault 7d. Note the strong variation in fault gouge thickness.

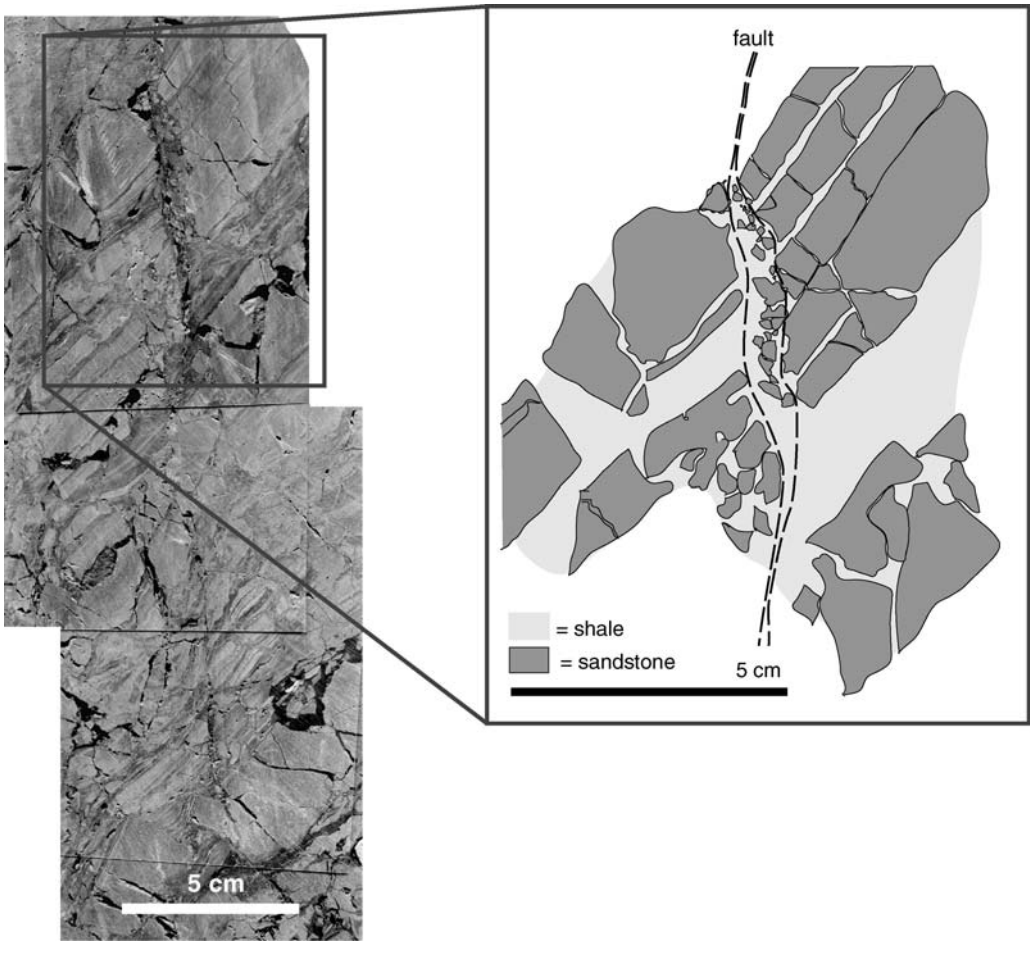

Fig. 6. Microstructures of a faulted sandstone–shale sequence in Fault 7a. The deformation of the more competent sandstone beds results in sandstone clasts floating in a clay matrix. Even on this small scale the fault gouge shows considerably thickness variations.

be expected from the composition of the wall rock (65–70% shale and 30–35% sandstone). In all cases of sand–sand juxtapositions (and throw > bed thickness), a continuous clay layer is found on the fault surfaces. The thickness of the shale-rich zones ranges from a thin coating of clay on the fault surfaces of the sandstone beds, to a zone of clay gouge or shale-rich deformation bands 10–20 cm thick in the larger faults and in oblique pull-aparts. Microstructural analyses show that the sandstone layers are deformed in a brittle manner whereas the shale was 'ductile', resulting in angular sandstone clasts floating in a clay matrix (Fig. 6), and this style appears to be consistent for earlier (rotated) and later faults. The sandstone layers are cross-cut by little faults which separate the sandstone layer into blocks. The space between these blocks is filled with clay. This suggests that during deformation the sand was much stronger than the clay, indicating that the clay was very weak (probably water-rich) during the faulting. Supporting evidence for this is found in the scaly microfabrics of the clay-rich gouge (Fig. 9), which are identical to those reported from active overpressured décollements in mud-rich accretionary prisms (e.g., Agar *et al.* 1989). Evidence for the brittle deformation of the sandstone and the ductile deformation of the shale is also observed at larger scales. Fault 3 (Fig. 8) shows folded shale layers (although some localization is present), above a sharply faulted sandstone bed originating from a pre-existing joint. Thus the deformation style and fault zone structure are strongly influenced by the contrasting mechanical properties of the sandstone and shale.

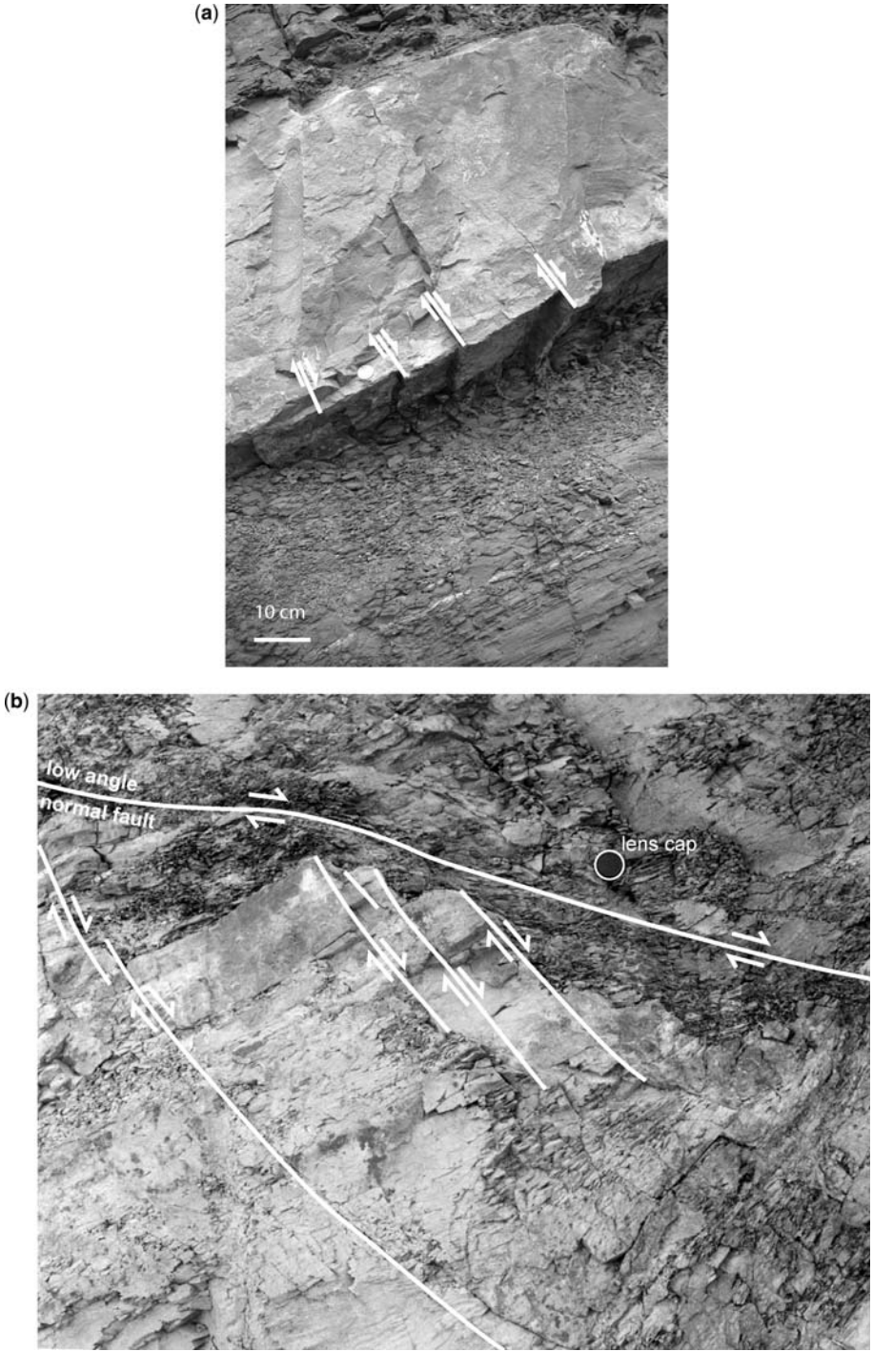

Fig. 7. (**a**) Reactivated joints in a rigid sandstone bed. (**b**) Example of reactivated joints in Fault zone 14.

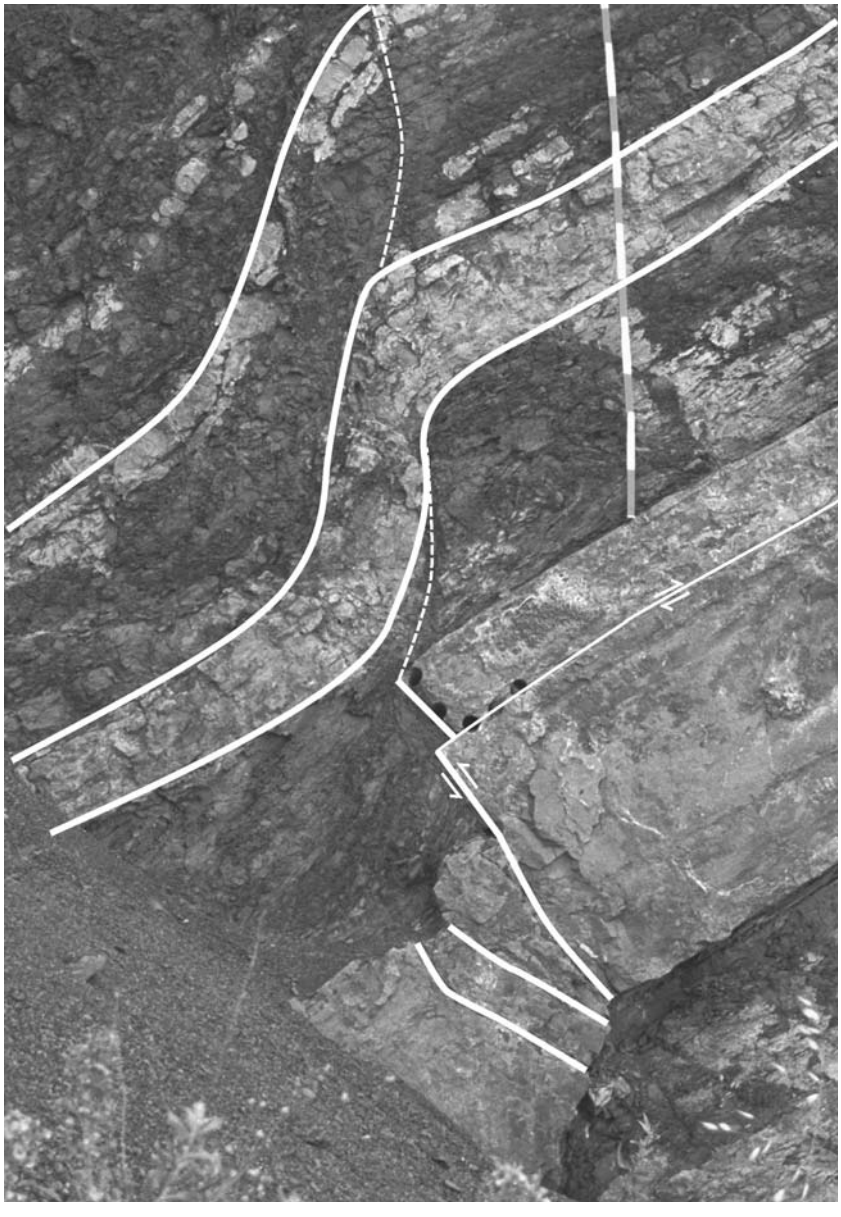

Fig. 8. Detail of the lower part of Fault 3 showing folded shale layers and a sandstone layer with discrete faults. The measuring tape is approximately 1 m.

Where faults have formed splays and lens-shaped structures, we observe a higher degree of deformation inside the lens (or between the splays) than outside, implying a very wide overall zone of deformation. An example is the large lens of Fault 8, where folding and faulting inside the lens tip were observed (Figs 2c & 4g), and the right splay forming the lens contains lens-shaped bodies which are strongly deformed themselves. The phenomenon of lens generation and deformation in fault zones is analyzed in more detail in van der Zee & Urai (2005). Other examples are the faults with large offsets (e.g., Fault 11, 'Faille Nord' in Figs 2b & 4i) which consist of different (sub) parallel fault strands separating zones with different degrees of deformation. Subsequent

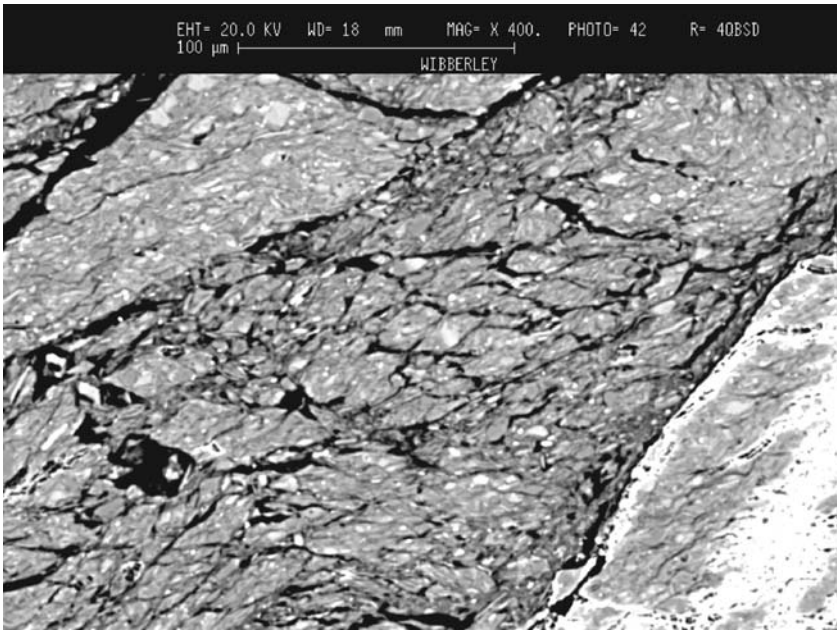

Fig. 9. SEM image of shale gouge in Fault zone 14.

continued movement incorporates the lesser-deformed zones into the fault zone.

Several authors have discussed the existence of a uniform displacement-thickness ratio for faults (Scholz 1987; Hull 1988; Blenkinsop 1989; Evans 1990; Knott *et al.* 1996). Yet fault gouge thickness can vary greatly along a fault. The thickness of a single fault strand in the Tréviels open-cast pit ranges from <1 mm in the reactivated joints in sandstone beds, which did not slip further than the sandstone bed thickness, to 30–40 cm in the shaly intervals. Fault 7, for example, shows a much thicker fault gouge in areas where shale is juxtaposed against shale than the areas where the sandstone is juxtaposed against sandstone. This variation in thickness of 1–1.5 orders of magnitude is often observed and is clearly a problem in defining a simple and accurate relationship. Large thickness variations along strike are also observed are reported by other authors (Foxford *et al.* 1998; van der Zee & Urai 2005).

The definitions and interpretations of fault thickness are problematic, because:

- a single fault has a variable thickness along strike and down-dip;
- the definition of the edges of a fault zone is very subjective.

To define the thickness of a fault zone, the edges of the fault have to be identified. This definition is mostly very subjective and will vary between different authors (Blenkinsop 1989). Some authors (e.g., Knott *et al.* 1996) prefer to sum the thicknesses of individual strands, thereby discarding the (supposedly undeformed) material between these strands. The problem of this method is that in sequences without marker horizons it is hard to determine if the material is deformed or not, which makes the thickness determination lithology-dependent, which is unwanted. In the case of the normal faults in the Lodève basin, lenses of relatively undeformed material were commonly imbricated into the fault zones by sequential displacement on successive fault strands. Thus, a practical solution was to measure the widths of highly deformed fault strands, and also of the overall fault zone width including lenses of less-deformed material and zones of rotated bedding, i.e., an overall fault zone width. Nevertheless, distinguishing 'highly deformed' state in the shales is often subjective because the destruction of bedding may not be recognized if a shaley foliation is generated in the shale-rich shear zone. Hence the distinction should be treated with caution.

The fault zone thickness of a single fault strand in the Tréviels pit-mine ranges from <1 mm in the slip-reactivated joints, which did not move further than a sandstone bed thickness, to 30–40 cm in the shaley intervals. Along with the two different types of fault zone width measurement, fault zone offset at the point of width measurement was also made. The measurements were performed at

different points along the fault trace because the fault gouge thickness can vary strongly along the fault. The displacement-thickness data are plotted together with data from the Airport road outcrop, Miri, Malaysia (van der Zee & Urai 2005) and literature data of Evans (1990) and Foxford *et al.* (1998) (Fig. 10). The data illustrate the large variation in thickness even along a single fault, highlighting the danger in using an average displacement–thickness relationship for predicting fault zone thicknesses, as well as the difference between highly deformed zone thickness and 'total' fault zone thickness. Nevertheless, such data can be used in probabilistic estimates of the uncertainties in estimating fault zone thickness from throw, for example.

Discussion

Fault orientations

We interpret our data to show that the faults in the sandstone beds originated as slip-reactivated joints. We conclude this because on many occasions the orientation of the fault planes in the sandstone is the same as the orientation of the joint surfaces in the same unit (Fig. 3). Further, these faults typically have little or no damage in the wall rock, and in the case of the smallest faults, segments generated as slip-reactivated joints have low displacement–length ratios in the sandstone beds in comparison with typical data in the literature, and in such cases, the sandstone beds have demonstrably lower displacement gradients along any one fault than the shale-rich portions of the stratigraphy (Wibberley *et al.* 2007).

There are several possible reasons for the range of normal fault orientations found in the outcrop. In a heterogeneous stress field, the fault could initiate in different orientations. Such a heterogeneous stress field may be caused by interaction between the regional stress field and a basement fault below the outcrop. Another possibility is that the lower-angle faults initiated while the bedding was close to horizontal, and they reached their present orientation after basin-wide tilting (Agnon & Reches 1995). After, or in the late stages of, the tilting the steeper faults initiate and therefore their dips equal those predicted by Anderson (1942). Such a fault distribution pre- and post-rotation is illustrated in Wibberley *et al.* (2007).

Although the data do not allow a definite test of the different models, we favour the model of faulting during progressive tilting (Wibberley *et al.* 2007). In the outcrop described here, the large normal faults with their southern block moving downwards are very steep or overturned, suggesting

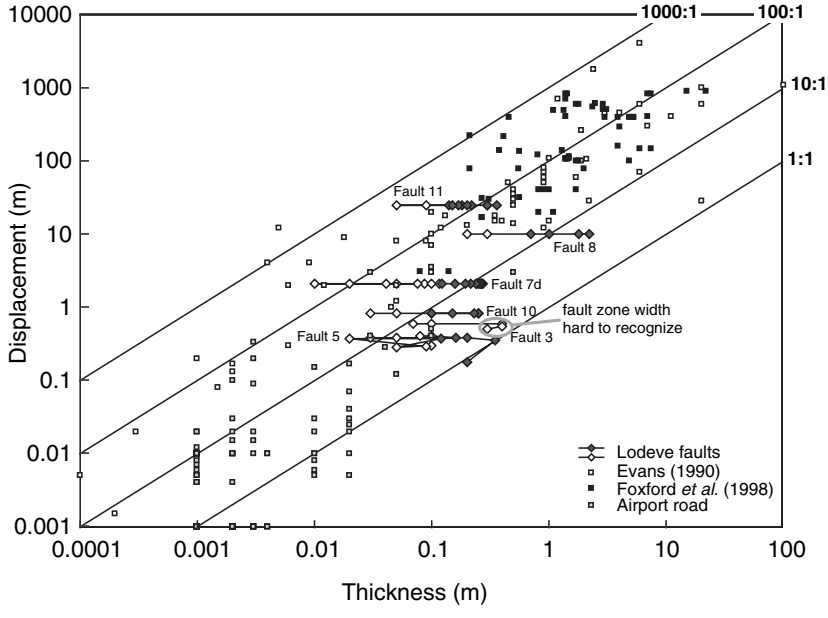

Fig. 10. Fault displacement v. fault gouge thickness graph for several faults of the Treviels pit-mine, combined with data from the Airportroad outcrop (van der Zee & Urai 2005), Evans (1990) and Foxford *et al.* (1998). See text for discussion. For the Lodève faults, the open symbols represent cumulative thicknesses of the high strain deformation zones, and the solid symbols represent the overall thickness including low strain material in the fault zone.

that these formed before the tilting and reached their present orientation after tilting. In the northern part of the outcrop some low-angle normal faults are present. These faults are bedding parallel and are probably using the weak bedding interfaces as slip planes. These faults are interpreted to have initiated after tilting, because (i) they offset other faults, and (ii) the dip of these faults before tilting would be too low to act as slip planes.

Relationship between faults and bedding orientation

A schematic block diagram (Fig. 11) illustrates the relationships between the structures of different orientations. In the outcrop, the bedding mostly dips 30° to the south (case a in the block diagram Fig. 11). However, in areas close to faults some north-dipping bedding can be found. The two cases observed for this are:

- The bedding is rotated by simple shear between two faults, such as the bedding in the top of the lens of Fault 8, or between Faults 6a and 6b. This is case b in the block diagram (Fig. 11).
- A fault termination below a layer causes bending of the layer over the fault tip, such as above Fault 6a. This is represented by case c in the block diagram (Fig. 11).

Fault trace geometry

Most of the faults observed in the Treviels pit mine often have an irregular, strongly non-planar geometry. We interpret this appearance as being caused largely by the difference in orientation of the fault in the sandstone beds compared with the shale beds (e.g., Fault 3, Figs 4b & 8). In the sandstone beds, the fault is very often perpendicular to bedding, because it is a reactivated joint, whereas in the shale it is a link between these reactivated joints. This illustrates how the fault shape and orientation is controlled by the distribution and orientation of the initial discontinuities (the joints) in the sandstone and the contrasting material properties between the shale and the sandstone. The present day dip of the fault in the shale intervals can be lower than it was during faulting due to compaction of the shales during burial (Davison 1987; Wang 1995).

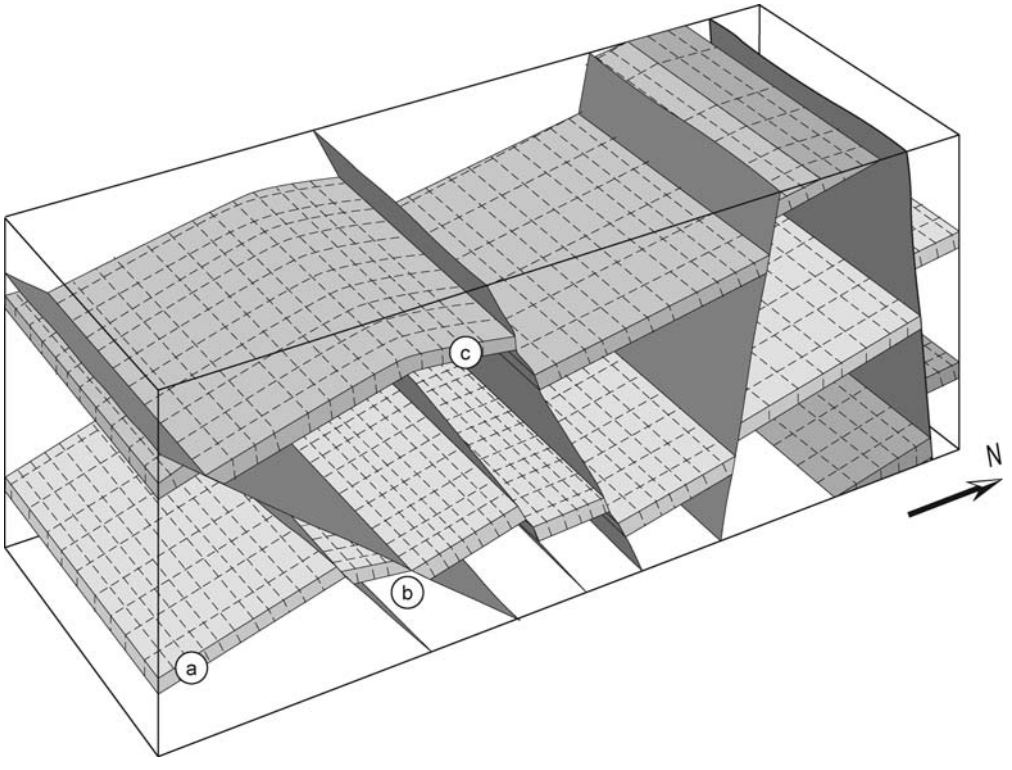

Fig. 11. Schematic block diagram not representing the reality in detail, but a model geometry to understand the observed structures and orientations. The letters are key features referred to in the text.

The movement of the reactivated joints parallel to the joint surface can cause problems for large fault displacements because a space problem occurs in the shale. We note that we did not observe separated joint surfaces as long as the throw was smaller than the sand layer thickness (cf. Ramsay & Huber 1987; Peacock & Sanderson 1992; McGrath & Davison 1995). The commonly observed splays of the fault inside the shale beds just above sandstone beds are probably in response to this space problem (e.g., Fault 2, Fig. 4a). A possible evolution of the fault structure around a reactivated joint is shown in Figure 12.

Fault gouge thickness and composition

The displacement–thickness data for the Tréviels outcrop show a similar scatter to the global trend taken from the literature (Fig. 10). It is noticeable that, even if the same definition of fault thickness is used across the whole outcrop, a wide spread in throw–thickness ratios is observed. This is due to the thickness variations along dip, and an abrupt step in the fault thickness related to the throw–bed thickness ratio between:

- small displacement faults (<bed thickness);
- medium-large displacement faults (> to >> bed thickness).

Small displacement. Sandstone–sandstone contacts are very thin (*c*. 1 mm), and are often reactivated joints. *Shale–sandstone* contacts show a narrow deformation zone. The lithological difference and competence contrast between the sandstone and shale favours the deformation in the weak shale layer towards the contact. *Shale–shale* contacts are 1–2 cm thick, and are recognized by the lining up of clay flakes or folding of the shale layers causing a broader zone of deformation.

Medium-large displacement. Sandstone–sandstone contacts have the same range of thickness as the other contacts after slip further than the sandstone bed thickness. The contacts of *sandstone–shale*

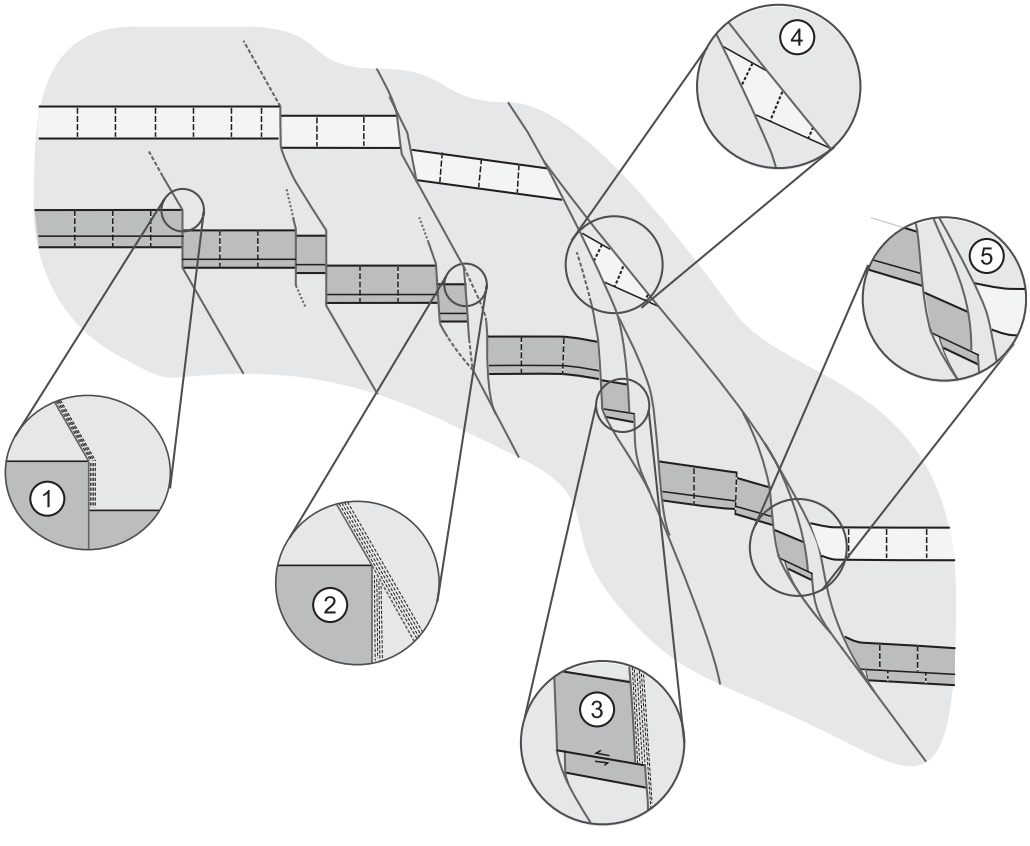

Fig. 12. Schematic cartoon showing the reactivation of a joint as observed in the Tréviels pit-mine. The observed foliation in the shale is indicated. An example of such a shale-filled pull-apart structure is observed in Fault 2 (Fig. 4a).

show a narrow zone of deformation along the sandstone, but also often a shortcutting structure, which will widen the fault zone. *Shale–shale* contacts merely consist of an anastomosing network of slip planes with variable width and degree of deformation (Fig. 4i).

In all cases of sand–sand juxtapositions and throw of more than the bed thickness, a consistent seal of clay is found on the fault surfaces. This coating resembles the clay smear structures as described by Lindsay *et al.* (1993) in which a thin veneer of clay coats the fault surface of the sandstone bed, and shale has often either been injected or imbricated into the fault zone between juxtaposed sandstone blocks. Places in the fault zone with very thick clay material are mostly related to multiple strands ('pseudo gouge', see van der Zee & Urai 2005). For example, where a fault offsets a sandstone bed more than its bed thickness, a pull-apart structure is formed (e.g., Fault 2; Fig. 4a). This opening is filled with shale, forming a locally thick, shale-rich fault zone. An example is the Faille Nord (Fig. 4i), in which the fault zone consists of shale and fault breccia. In the breccia parts the original bedding is recognizable, albeit with difficulty in places, suggesting that ongoing movement incorporated the lesser-deformed zones into the more highly deformed part of the fault zone.

In previous articles (e.g., Wojtal & Mitra 1986) the importance of strain hardening in widening or localizing the active zone of deformation and strain softening in the fault zone is discussed. We think that the laboratory-derived data on this behaviour are not very suitable to simulate a natural fault gouge, because laboratory fault surfaces are not rough enough. Our data on medium to large displacement faults show that the fault roughness plays an important role in the fault gouge development.

Fault gouge generation and coupled localization in a fault is described by Tullis (1999). He reports that movement on a rough fault plane causes asperities to be sheared off and that a localized (shortcutting) slip zone develops in the generated fault gouge. Watterson *et al.* (1998) also describes this process of fault gouge generation by fault roughness caused by bedding parallel slip, oblique to a normal fault. In our case the roughness is largely caused by pre-existing joints (see fault shape section) and splays, as illustrated in Figure 12, leading to a fault zone of variable thickness due to the generation of lenses of less-deformed material bounded by high-deformation fault strands.

It is argued by several authors (e.g., Hull 1989) that the fractal roughness of the fault would generate a constant throw-thickness ratio because, with further throw, an asperity with a larger amplitude and wavelength would be sheared off. This is not necessarily true, because fault planes can be self-affine instead of self-similar (Power & Tullis 1991); this means that, with increasing displacement, the wavelength–amplitude ratio does not stay constant (Develi & Babadagli 1998). The result of this is that the shearing of larger wavelength asperities does not automatically cause a linear increase in gouge thickness.

We can conclude that a global displacement–thickness relationship is not appropriate for the details of this outcrop. As reviewed by others (e.g., Evans 1990; Knott *et al.* 1996) this relationship is more an artefact of the log–log presentation than the result of a physical process. The thickness definition is very subjective, and is dependent on authors, lithology and resolution of observation. Down-dip thickness variations of 1–2 orders of magnitude will also cause a large scatter of the throw–thickness ratios.

Conclusions

The faults exposed in the Tréviels pit-mine have different orientations because of the different timings of the faulting relative to the tilting of the bedding. Many of the faults follow bedding-perpendicular joints in the sandstone beds. Hence those faults generated oblique to bedding, typically early on in the tilting history, have irregular stepped geometries due to different orientations in the sandstone and in the shale beds. However, those faults that propagated perpendicular to bedding after bedding tilt by 25–30° tend to be planar, and were assisted by the pre-existing joints. The operation of bedding-parallel slip during faulting can also increases the complexity of the fault zones and fault surface geometry.

The complicated fault shape (pre-existing joints and bedding parallel slip), particularly of the earlier faults formed oblique to bedding and rotated by regional tilting during their continued activity, causes extra deformation of the wall rock during ongoing deformation. The less competent shales between the rigid sandstone layers deform to overcome space problems by initiating splays at irregularities in the fault surface which reconnect to leave isolate lenses within the fault zone. These lenses may be of broken sandstone beds, or weak shale that has flowed into pull-aparts between separated sandstone blocks. Microstructural evidence suggests that during faulting the sandstone deformed by brittle fracturing whereas the shale deformed by ductile mechanisms, being much weaker than the sandstone and probably water-rich.

The global gouge thickness–throw relationship does not hold for this outcrop. For a single fault, the fault zone thickness often varies widely up- and down-dip. This variation in thickness is

partially lithology-controlled, and is greatly increased due to splay initiation and the formation of lenses in the fault zone.

Jean Pierre Petit is acknowledged for his help with field work and for the numerous discussions on the geology and structures in the Treviels Pit mine. Financial support to W.v.d.Z. and J.L.U. from the Deutsche Forschungsgemeinschaft (Project UR 64-2) and ExxonMobil Upstream Research Company is gratefully acknowledged, as is financial support to C.A.J.W. from Elf Aquitaine. Scott Wilkins and Roger Soliva are thanked for their thorough reviews.

References

AGAR, S. M., PRIOR, D. J. & BEHRMANN, J. H. 1989. Back-scattered electron imagery of the tectonic fabrics of some fine-grained sediments: implications for fabric nomenclature and deformation processes. *Geology*, **17**, 901–904.

AGNON, A. & RECHES, Z. 1995. Frictional rheology: hardening by rotation of active normal faults. *Tectonophysics*, **247**, 239–254.

ANDERSON, E. M. 1942. *The Dynamics of Faulting and Dyke Formation with Applications to Britain*. Oliver and Boyd, Edinburgh.

BLENKINSOP, T. G. 1989. Thickness–displacement relationships for deformation zones: discussion. *Journal of Structural Geology*, **11**, 1051–1053.

BRUEL, T. 1997. *Caractérisation des circulations des fluides dans un réseau fracturé et rôle des contraintes in situ. Une étude de cas dans le bassin permien de Lodève*. Doctorate thesis, Université Montpellier 2.

BUCK, W. R. 1993. Effect of lithospheric thickness on the formation of high- and low-angle normal faults. *Geology*, **21**, 933–936.

BÜRGMANN, R. & POLLARD, D. 1994. Strain accommodation about strike–slip fault discontinuities in granitic rock under brittle-to-ductile conditions. *Journal of Structural Geology*, **16**, 1655–1674.

CHILDS, C., WATTERSON, J. & WALSH, J. J. 1996. A model for the structure and development of fault zones. *Journal of the Geological Society of London*, **153**, 337–340.

DAVISON, I. 1987. Normal fault geometry related to sediment compaction and burial. *Journal of Structural Geology*, **9**, 393–401.

DEVELI, K. & BABADAGLI, T. 1998. Quantification of natural fracture surfaces using fractal geometry. *Mathematical Geology*, **30**, 971–998.

EVANS, J. P. 1990. Thickness-displacement relationships for fault zones. *Journal of Structural Geology*, **12**, 1062–1065.

FOXFORD, K. A., WALSH, J. J., WATTERSON, J., GARDEN, I. R., GUSCOTT, S. C. & BURLEY, S. D. 1998. Structure and content of the Moab Fault Zone, Utah, USA, and its implications for fault seal prediction. *In*: JONES, G., FISHER, Q. & KNIPE, R. J. (eds) *Fault Sealing and Fluid Flow in Hydrocarbon Reservoirs*. Geological Society, London, Special Publications, **147**, 87–103.

GROSS, M. R., GUTTIERREZ-ALONSO, G., BAI, T., WACKER, A. & COLLINSWORTH, K. B. 1997. Influence of mechanical stratigraphy and kinematics on fault scaling relations. *Journal of Structural Geology*, **19**, 171–183.

HULL, J. 1988. Thickness–displacement relationships for deformation zones. *Journal of Structural Geology*, **10**, 431–435.

HULL, J. 1989. Thickness–displacement relationships for deformation zones: reply. *Journal of Structural Geology*, **11**, 1053–1054.

JAEGER, J. C. & COOK, N. G. W. 1976. *Fundamentals of Rock Mechanics*. Chapman & Hall, London, 585.

KNOTT, S. D., BEACH, A., BROCKBANK, P. J., BROWN, J. L., MCCALLUM, J. E. & WELBON, A. I. 1996. Spatial and mechanical controls on normal fault populations. *Journal of Structural Geology*, **18**, 359–372.

LINDSAY, N. G., MURPHY, F. C., WALSH, J. J. & WATTERSON, J. 1993. *Outcrop Studies of Shale Smears on Fault Surfaces*. Special Publications of the International Association of Sedimentology, **15**, 113–123.

LOPEZ, M. 1992. *Dynamique du passage d'un appareil terrigène à une plate-forme carbonatée en domaine semi-aride: le Trias de Lodève, sud de la France*. Doctorate thesis, Université Montpellier 2.

MARTEL, S. J. 1999. Mechanical controls on fault geometry. *Journal of Structural Geology*, **21**, 585–596.

MCGRATH, A. G. & DAVISON, I. 1995. Damage zone geometry around fault tips. *Journal of Structural Geology*, **17**, 1011–1024.

PEACOCK, D. C. P. & SANDERSON, D. J. 1992. Effects of layering and anisotropy on fault geometry. *Journal of the Geological Society*, **149**, 793–802.

PEACOCK, D. C. P. & SANDERSON, D. J. 1994. Strain and scaling of faults in the chalk at Flambourgh Head, U.K. *Journal of Structural Geology*, **16**, 97–107.

POWER, W. L. & TULLIS, T. E. 1991. Euclidean and fractal models for the description of rock surface roughness. *Journal of Geophysical Research*, **96**, 415–424.

RAMSAY, J. G. & HUBER, M. I. 1987. *The Techniques of Modern Structural Geology. Volume 2: Folds and Fractures*. Academic Press, London, 391.

SCHOLZ, C. H. 1987. Wear and gouge formation in brittle faulting. *Geology*, **15**, 493–495.

SIBSON, R. H. 1985. A note on fault reactivation. *Journal of Structural Geology*, **7**, 751–754.

SOLIVA, R. & BENEDICTO, A. 2005. Geometry, scaling relations and spacing of vertically restricted normal faults. *Journal of Structural Geology*, **27**, 317–325.

TULLIS, T. E. 1999. Shear localization, slip- and velocity-weakening, and earthquake slip: expectations for faults from laboratory friction experiments and measurements of natural roughness. *EOS Transactions, AGU*, **80**(46, supplement), F728.

VAN DER ZEE, W. & URAI, J. L. 2005. Processes of normal fault evolution in a siliciclastic sequence: a case study from Miri, Sarawak, Malaysia. *Journal of Structural Geology*, **27**, 2281–2300.

WANG, X. 1995. Estimation of the variation in apparent displacement along normal fault traces refracted by differential compaction. *Journal of Structural Geology*, **17**, 1789–1792.

WATTERSON, J., CHILDS, C. & WALSH, J. J. 1998. Widening of fault zones by erosion of asperities formed by bed-parallel slip. *Geology*, **26**, 71–74.

WIBBERLEY, C. A. J., PETIT, J.-P. & RIVES, T. 2007. The effect of tilting on fault propagation and network development in sandstone–shale sequences: a case study from the Lodève Basin, S. France. *Journal of the Geological Society of London*, **164**, 599–608.

WILKINS, S. J. & GROSS, M. R. 2002. Normal fault growth in layered rocks at Split Mountain, Utah: influence of mechanical stratigraphy on dip linkage, fault restriction and fault scaling. *Journal of Structural Geology*, **24**, 1413–1429.

WOJTAL, S. & MITRA, G. 1986. Strain hardening and strain softening in fault zones from foreland thrusts. *Geological Society of America Bulletin*, **97**, 674–687.

Fault damage zones dominated by high-angle fractures within layer-parallel brittle shear zones: examples from the eastern Alps

FRANZ-JOSEF BROSCH & WALTER KURZ

Institute of Applied Geosciences, Graz University of Technology, Rechbauerstr. 12, A-8010 Graz, Austria (e-mail: brosch@tugraz.at)

Abstract: In this study, we focus on the transition from the host rock to the damage zone within brittle shear zones in order to document the structures forming during the initial phases of deformation, i.e., the fractures that formed prior to the formation of fault breccias and cataclasites. Structural analyses of rock samples from sites of the Talhof– and Palten–Liesing faults in the eastern Alps show that in these cases well-known R- and P-fracture patterns do not play a dominant role in the early stages of the generation of brittle fracture zones. In the studied layered marble and foliated impure quartzite samples, the boundary between the host rock and the damage zone is characterized by the formation of closely spaced fractures at high angles (70–90°) to the shear zone boundaries, being parallel to pre-existing layering/foliation planes. These fractures bound and define slender slab-like or columnar rock elements, here being termed lamellae. It is assumed that subsequent rotation of these lamellae in the bookshelf and domino modes associated with impeded dilation across the actual shear zone boundaries leads to kinking, splitting and final granulation of the lamellae to generate breccias of later fault core zones parallel to the shear zone boundary. In some cases, the observed bending and buckling of lamellae indicate additional ductile deformation subsequent to the development of the dominant lamellar structures formed by brittle fracturing.

A brittle fault or fault zone in structural geological terms may be defined as an assemblage of discontinuities (sets of shear planes) along which there has been displacement of rocks parallel to the shear planes (e.g., Brodie *et al.* 2002). These relative displacements are accompanied by disintegration and fracturing of the adjacent host rocks (the process being termed cataclasis), and the formation of fault rocks, particularly fault gouges and cataclasites. This may result in the devolopment of fault zones as structurally complex zones of localized fractional and frictional wear, referred to as brittle deformation. Brittle shear zones generally show a spatio-temporal evolution from the protolith to the fully developed fault with a zoned internal architecture (e.g., Chester & Logan 1986).

In the past decades, a better understanding of the internal structure of brittle fault zones has been achieved from both field work (e.g., Anderson 1951; Tchalenko 1970; Sibson 1986; Hancock *et al.* 1987; Chester & Logan 1987; Chester *et al.* 1993; Caine *et al.* 1996; Billi *et al.* 2003; Wibberley & Shimamoto 2003; Billi & Storti 2004; Flodin & Aydin 2004; Berg & Skar 2005; Billi 2005; Tarasewicz *et al.* 2005), laboratory fracture experiments, and numerical models (e.g., Reches 1978, 1983; Reches & Dietrich 1983; Sagy *et al.* 2001; Katz *et al.* 2003). Generally, the following structural elements may be discriminated across brittle fault zones (following Chester & Logan 1986; Caine *et al.* 1996; Billi *et al.* 2003; Faulkner *et al.* 2003):

1. The protolith or host/country/parent rock consisting of the rock mass bounding the fault-related structures, and being characterized by a certain background value of deformation intensity which is considerably lower than in the fault zone proper.
2. The damage zone, characterized by minor faults, veins and fracture networks; these structures are generally related to the processes of fault zone formation and fault growth. Generally, the transition from the host rock to the damage and brecciation zone is gradual. Therefore, the width of a damage zone can be structurally defined as the region that bound the fault core and in which fracture density is above a certain threshold value (Cello *et al.* 2001).
3. The fault core, where shear displacement with grinding, particle rotation and grain size diminution is localized. Fault rocks within the fault core may obtain a characteristic grain size distribution (Billi *et al.* 2003; Billi & Storti 2004; Billi 2005), being particularly dependent on normal and shear stresses, displacement and strain rate.
4. Another structural element, which plays a significant role in describing the growth processes

From: WIBBERLEY, C. A. J., KURZ, W., IMBER, J., HOLDSWORTH, R. E. & COLLETTINI, C. (eds) *The Internal Structure of Fault Zones: Implications for Mechanical and Fluid-Flow Properties*. **299**, 75–95.
DOI: 10.1144/SP299.5 0305-8719/08/$15.00

of a single discrete fracture is the 'process zone'. Following the definition of Vermilye & Scholz (1998), the process zone comprises those features that result directly from propagation of the fault tip.

This internal structure of fault zones may be either symmetric (with predominating slip surfaces within the center core), or asymmetric, with shear localization at the boundary between fault core rocks and the damage zone. The spatial zonation from the protolith to the core zone, including the development of fault rocks, corresponds to the evolution during time. Thus, these structural elements may also be seen as representing the evolutionary steps in the temporal development of a fault zone.

A nomenclature of R-, R′ and T fractures (Fig. 1) has classically applied to structures observed in shear zones developed in unconsolidated granular materials (typically clays) in experiments and in the field, in order to describe their kinematic relationships to the overall shear zone (e.g., Cloos 1928; Riedel 1929; Morgenstern & Tchalenko 1967; Mandl *et al.* 1977; Logan *et al.* 1979; Chester & Logan 1986; Rutter *et al.* 1986; Shimamoto 1986; Moore *et al.* 1989; Power *et al.* 1989). This framework has more recently been used to describe kinematically similar structures in brittle shear zones in other lithologies (e.g., Tchalenko 1970; Barlett *et al.* 1981; Petit 1987; Chester & Logan 1986, 1990; Mandl 1988; Sylvester 1988; Chester *et al.* 1993; Schulz & Evans 2000; Chester 2003; Wilson *et al.* 2003; Kim *et al.* 2004; Katz *et al.* 2004), with the recognition that additional classes of secondary structures such as X-, P- or Y-fractures may also be present (Fig. 1). Experiments designed to monitor the generation of different structures during shear zone development show that the latter are generally formed in later stages (e.g., Logan *et al.* 1979, 1992). Therefore, assuming the validity of the Coulomb fracture theory, the orientation of distinct fractures can be taken as a rule, but does not depend on material composition (i.e., lithology) for homogenous isotropic materials at linear-elastic to frictional-plastic (generally termed as brittle) behaviour.

In the course of deformation, T- and R′-bounded slabs in particular are forced either to break up or to rotate towards the shear direction in a bookshelf- or domino-style mode, resulting in an incremental increase of the angle between the shear zone boundary and the T- and R′-fractures as well as antithetic displacement along the latter (e.g., Hancock 1972, 1985; Pollard *et al.* 1982; Rothery 1988; Aydin & Schulz 1990; Olson & Pollard 1991). Consequently, bookshelf- or domino-style arrays may be generated and subsequently deformed in a complex sequence, so that the origin and history of the structure cannot be unambiguously interpreted from the kinematics of the structures or the angle of lithons (e.g., Mandal & Chattopadhyay 1995).

Within a completely developed brittle shear zone ('completely' in terms of the occurrence of a well developed fault core and corresponding fault rocks) the fractures mentioned above may still be observed within the damage zone as shown in a number of field studies (e.g., Rutter *et al.* 1986; Chester & Logan 1987; Schulz & Evans 2000).

Objectives

In this study, we focus on the transition from the host rock to the damage zone, in order to document the structures formed during the initial phases of

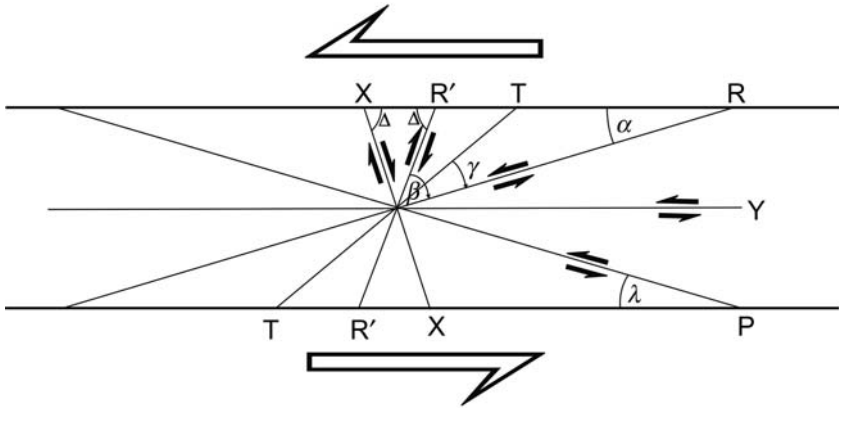

Fig. 1. Fracture array and geometrical relationships forming in a sinistral shear zone during triaxial compression (after Logan *et al.* 1992); $\alpha = \lambda = \phi/2$; $\beta = (90 - \phi)^\circ$; $\gamma = (45 - \phi/2)^\circ$; $\Delta = (90 - \phi/2)^\circ$; ϕ, angle of internal friction in Mohr–Coulomb terms.

fracturing and subsequent fault zone evolution. These include the fractures that formed prior to the full development of cataclasites, fault breccias and gouges concerning the evolution in time, and the transitional structures concerning the evolution in space. Some macroscopic as well as microscopic observations on the fracture pattern and the inferred kinematics shall be discussed on the basis of phenomena detected in serial sections of samples from meso-scale incipient shear zones. In particular, we want to draw the attention on the remarkable importance of high-angle fractures in certain rock types with a particular pre-existing structure and deformation-related geometry. Moreover, we focus on the assumed role of these structures in the development of brittle shear zones and brecciation, regardless of a quantitative mechanical analysis. Therefore, the model presented in this study is a kinematic concept based on field and lab observations; it describes an evolutionary scheme from initial high-angle fracture formation toward the development of fault rocks, in particular fault breccias.

Geological/tectonic setting

For a case study we selected two sites within fault zones in the Eastern Alps (Fig. 2): the Talhof fault (Gmeindl 1999) being a segment of the Salzach–Ennstal–Mariazell–Puchberg (SEMP) fault system (Ratschbacher *et al.* 1989, 1991; Decker *et al.* 1993; Decker & Peresson 1996; Wang & Neubauer 1998; Frisch *et al.* 2000), and the NW–SE trending Palten–Liesing fault.

At the locations studied along the Talhof and Palten–Liesing fault the individual shear zones as parts of the main fault follow for the large part pre-existing layers and foliation planes, with subsequent high-angle fractures forming between the moderately wide spaced layers. Therefore the latter can be termed the shear zone boundaries (SZB). In this study, SZB is used as the obvious confining planar fabric element that high-angle fractures diverge from.

The subvertical, approximately east–west-striking Talhof fault shows left-lateral displacement and separates Triassic fine grained layered marbles from quartzites of the Lower Austro-Alpine unit (Fig. 2). These lithological units are characterized by contrasting deformational and rheological behaviour during faulting. Within the quartzites the protolith is almost totally disintegrated up to the formation of incoherent fault gouges, forming the fault core zone. Within the marbles, the fault-bound deformation has obviously been accommodated by multiple strike–slip shears along the nearly vertical discontinuities defined by a composite metamorphic foliation and sedimentary bedding, acting as slip planes (Fig. 3). At a smaller scale, brittle structures within the carbonates are generally characterized by shear and extensional fractures at high angles to the SZB, and cemented tectonic breccia.

The Palten–Liesing fault (Fig. 2) is a regional element with dextral sense of displacement (Linzer *et al.* 2002). At the sites of investigation the prevailing rocks are chlorite-bearing foliated quartzite with minor intercalations of chloritic quartz phyllites, both attributed to the Rannach Formation (Flügel & Neubauer 1984). These rocks form the Permian to Mesozoic cover sequences above Middle Austro-Alpine basement units. Samples were taken from brittle shear zones extending parallel to the foliation dipping moderately steep to NNW (Fig. 4). A general SE-directed oblique reverse displacement can be inferred from prominent sets of fractures and lamellae (a main set 1 and a subordinate set 2) with approximate R′-, T- and X-orientations (Figs 4 & 5).

All faults mentioned may be detected in the field as assemblages of sub-parallel shear zones ranging from the centimetre to the decimetre scale in width, with a distributed displacement pattern and occasional shear localization including the formation of fault core structures and fault rocks. All site positions and the sample locations are given in Appendix 1.

Methods

In order to obtain an insight into structures that had developed within damage zones, oriented samples were isolated from domains confined by layer-parallel shear planes. The extremely broken and friable field rock samples had to be stabilized by epoxy resin impregnation in the laboratory. These impregnated blocks were saw-cut into serial sections parallel to the plane of shear, i.e., both parallel to the local (and inferred global) shear direction and perpendicular to the shear zone boundaries. Fracture decoration was achieved by staining of the dry, coarsely ground surfaces of the cut slabs by a permanent black marker pen and subsequent finishing. This procedure enabled the visualization of the traces of the existing subtle internal fracture network, voids and pores.

The angular geometry of these fractures relative to the SZB (in all cases planes of foliation or compositional layering) was assessed and analysed both manually at an adopted plotting board and by using the program package CorelDraw 12 (© 2003 Corel Corporation). Orientation distributions of distinct fracture sets and geometrical relationships were analysed by using the program package Tectonics FP 1.6.2, a 32-bit Windows™-Software for Structural Geology (Reiter & Acs 2002).

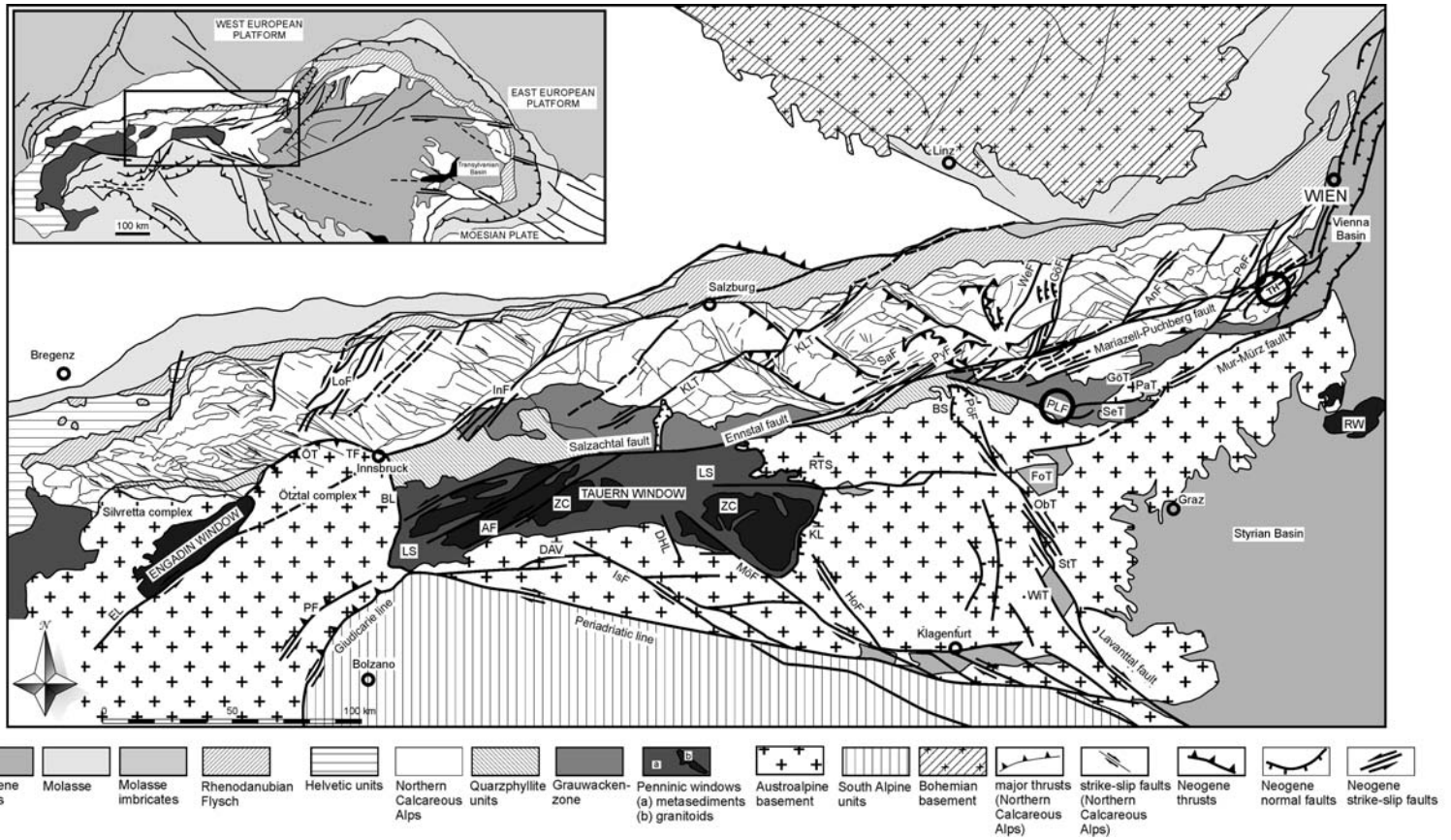

Fig. 2. Tectonic map of the eastern Alps displaying major and minor Paleogene to Neogene fault systems (after Linzer *et al.* 2002). The sites discussed in this contribution are located along the Salzach–Ennstal–Mariazell–Puchberg fault (SEMP), and the Palten–Liesing fault. AF = Ahrtal fault; AnF = Annaberg fault; BL = Brenner line; DHL = Döllach–Heiligenblut line; EL = Engadine line; GöF = Göstling fault; HoF = Hochstuhl fault; InF = Inntal fault; IsF = Iseltal fault; KL = Katschberg line; KLT = Königssee–Lammertal–Traunsee fault; LoF = Loisach fault; LS = Lower Schieferhülle; MöF = Mölltal fault; ÖT = Ötztal thrust; PF = Peijo fault; PeF = Pernitz fault; *PLF (encircled) = Palten–Liesing fault*; PöF = Pöls fault; PyF = Pyhrn fault; RTS = Radstadt thrust system; RW = Rechnitz window; SaF = Salzsteig fault; *TH (encircled) = Talhof fault segment of the Salzach–Ennstal–Mariazell–Puchberg fault system*; TF = Telfs fault; WeF = Weyer fault; WGF = Windischgarsten fault; Z = Zell pull-apart structure; ZC = Zentralgneiss core. GöT = Göriach basin; PaT = Parschlug basin; SeT = Seegraben basin; FoT = Fohnsdorf basin; ObT = Obdach basin; WiT Wiesenau basin; StT = St. Stefan basin.

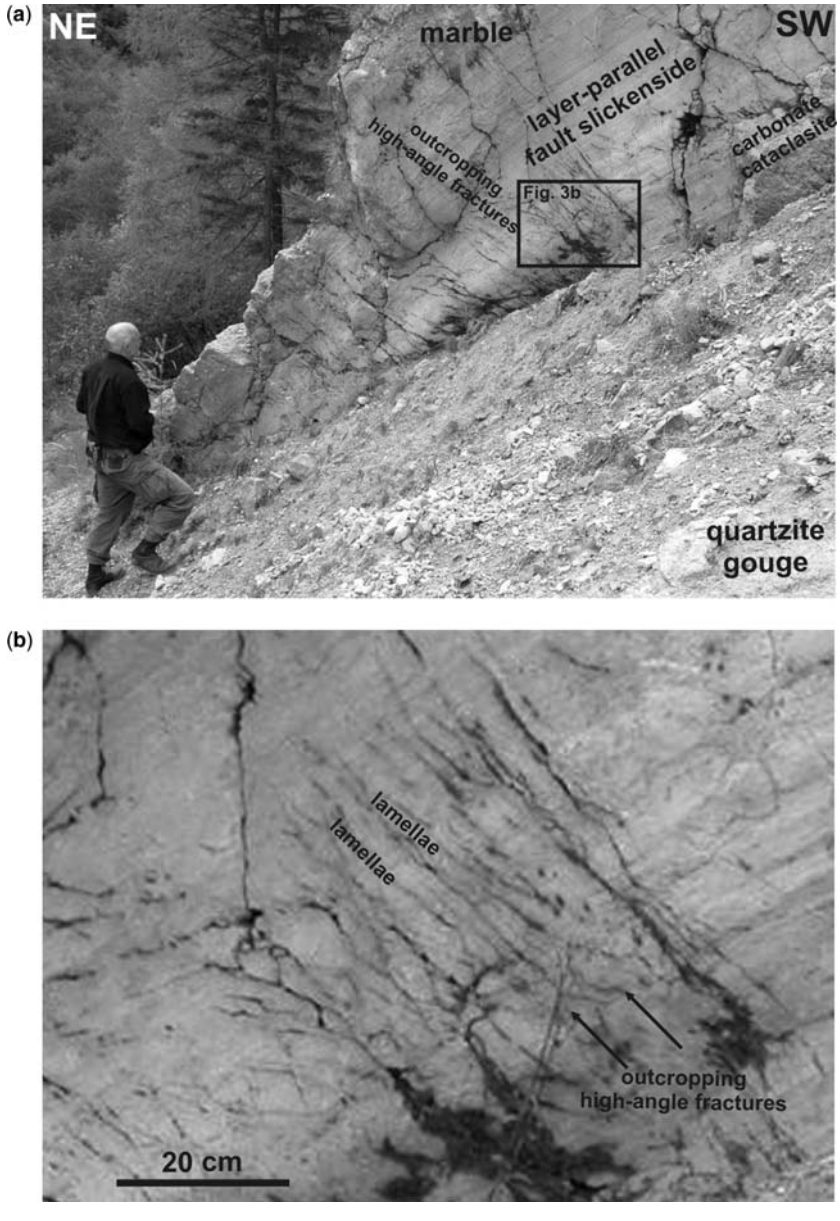

Fig. 3. (**a**) Exposure of the Talhof segment of the Salzach–Ennstal–Mariazell–Puchberg fault system, site 'Stiegerinhütte'. The fault slickenside runs parallel to the subvertical bedding of carbonates; note the outcrops of oblique fractures at the fault surface displaying the traces of closely spaced fractures (R′ or T) at high angles to the fault slickenside. (**b**) Close view of outcropping high-angle fractures and rock lamellae shown in (a); site positions and the sample locations are given in Appendix 1.

The terminology used for the (orientation) identification of fractures in this study remains 'conventional' in the way it is generally used in structural geology. However, by this labelling we do not claim a strict applicability of the Coulomb failure criterion, and an according fracture geometry and kinematic characteristics (as may be derived from two-dimensional stress field Mohr circle presentations). We are aware that material anisotropy (e.g., Paterson 1978; Jaeger & Cook 1979; Peacock & Sanderson 1992), and repeated activation of discontinuities may obliterate the

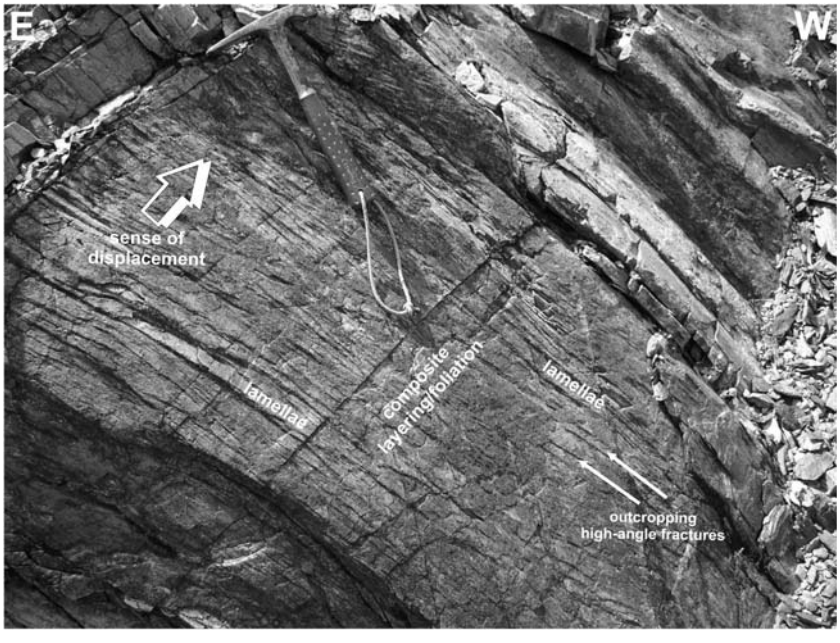

Fig. 4. Exposure of the Palten–Liesing fault, site 'Mautern'. The fault slickenside runs parallel to the composite bedding/foliation of schistose quartzites; note the outcrops of oblique fractures at the fault surface displaying the traces of closely spaced fractures (R′ or T) at high angles to the foliation; site position is given in Appendix 1.

original fracture-mechanical properties, change the kinematic function and modify the angular relationships of generated fractures. Thus, we avoid to use genetic terms (joint, shear, etc.), but do characterize the fracture pattern in the first place by the orientation of elements with respect to the overall shear directions.

Mesoscale structures

Macroscopically, a pronounced asymmetrically stepped surface morphology (in parts with prominent saw-tooth or cockscomb morphology) is characteristic for the SZB surfaces (Fig. 6a). These are parallel to existing bedding and foliation planes. The step traces at the SZB surface are slightly sinuous, sub-parallel and cut by short, abutting transverse fractures. Along the Palten–Liesing fault occasionally occurring chlorite–sericite layers display a coarse lineation consisting of asymmetric furrows and ridges instead of steps (Fig. 6b). In a few sections slip surfaces parallel to the existing foliation/layering can be observed, indicating a card-deck-mode of sliding.

Mesoscale structures along the Talhof fault

The internal macro-fracture fabric in fine-grained banded marble is dominated by a set of sub-parallel, rarely straight discontinuities at high angles to the SZB (approximate R′-orientation) (Figs 7 & 8). Consequently, the general structure is characterized as an array of roughly prismatic rock slices or lithons termed 'lamellae' in this study. These show varying thickness and are inclined against the shear direction with a frequency mode of bounding fracture traces at *c*. 65° anticlockwise from the reference line (SZB). Owing to variations in dip and curvature of bounding discontinuity traces, cross-sectional shapes of lamellae may vary considerably and show prismatic/rhombohedral, triangular, phacoidal/sigmoidal or lozenge-shapes (Figs 8–12).

The thickness of the lamellae varies between 2 and 25 mm, the height between approximately 20 and 160 mm. Generally, most lamellae exhibit reverse (antithetic) displacements, displayed by an offset of markers related to a 'bookshelf'-style tilting. This results in a distinct 'saw-tooth' morphology at the SZB (foliation) planes. Features of the shear displacements along the fracture surfaces, however, have commonly been obliterated by pressure solution phenomena, e.g. stylolites.

Frequently, triangular fragments, evidently split off from the acute edges of the lamellae, can be observed at the steps along the SZB. These structures can be observed at several scales from outcrop to thin section, being characteristic for

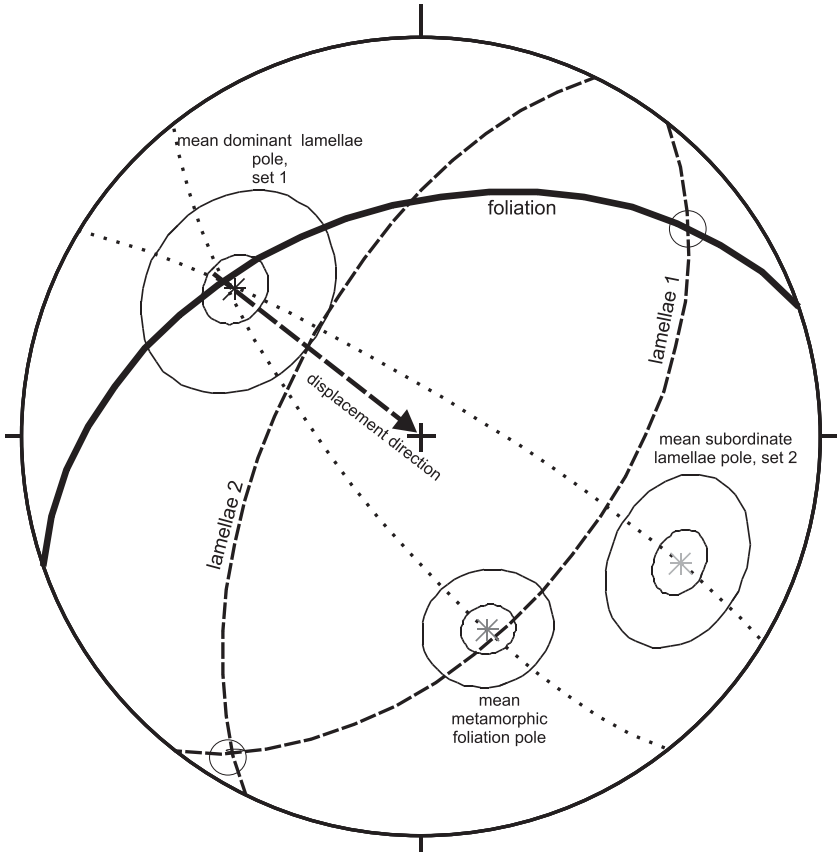

Fig. 5. Geometry and analysis of the main structural elements and construction of displacement direction at the Mautern site along the Palten–Liesing fault. Both the normal planes (dotted great circles) to the intersection axis of lamellae orientations (sets 1, 2; dashed great circles) and the intersection of the main lamellae with the foliation uniquely define the attitude of the displacement direction by their intersection with the foliation (dashed arrow and bold great circle, respectively); equal area lower hemisphere projection; pole point distributions are represented as statistical parameters (centre of gravity, cone of confidence, spherical aperture; see Wallbrecher 1986). The constructed displacement direction coincides with the one observed in the field (see Fig. 5).

lamellae with obvious antithetic shearing displacements (Fig. 12). Face contacts of fragments are predominantly stylolithic, in particular when interfaces include low angles with the SZB.

Low-angle fractures (in R-, or P-orientation) play a subordinate role in the trace orientation spectrum (Figs 7 & 8). Calcite-filled veins, open cracks or other fracture sets exhibiting local extensional deformation are oriented predominantly at angles $<45^\circ$ to the SZB, with a small submaximum at quite high angles (Fig. 9). Aspect ratios (slenderness) of lamella sections display a markedly skewed distribution with most frequent values between 2 and 6 and a mode at approximately 3 (Fig. 10).

Features of assumed enhanced deformation intensity contain open fractures, irregular fragmentation, with both sub-rounded and angular, approximately isometric fragments and distinct particle displacements (i.e., filled gashes at particle interfaces). Additionally, stylolithic fragment contacts can be observed along single fragment boundaries (Figs 11 & 12). Locally, completely developed matrix-supported fault breccia characterized by fragment wear, attrition and noticeable rotation of fragments has developed within and between the domains built up from fracture-bound lamellae (Figs 8 & 11). Here encrusted voids and vein swarms are common phenomena. The matrix consists of ground, fine-grained carbonate and partly residual material in the clay/silt grain size fractions.

It must be noted that all these features of brittle deformation described above can be found in close

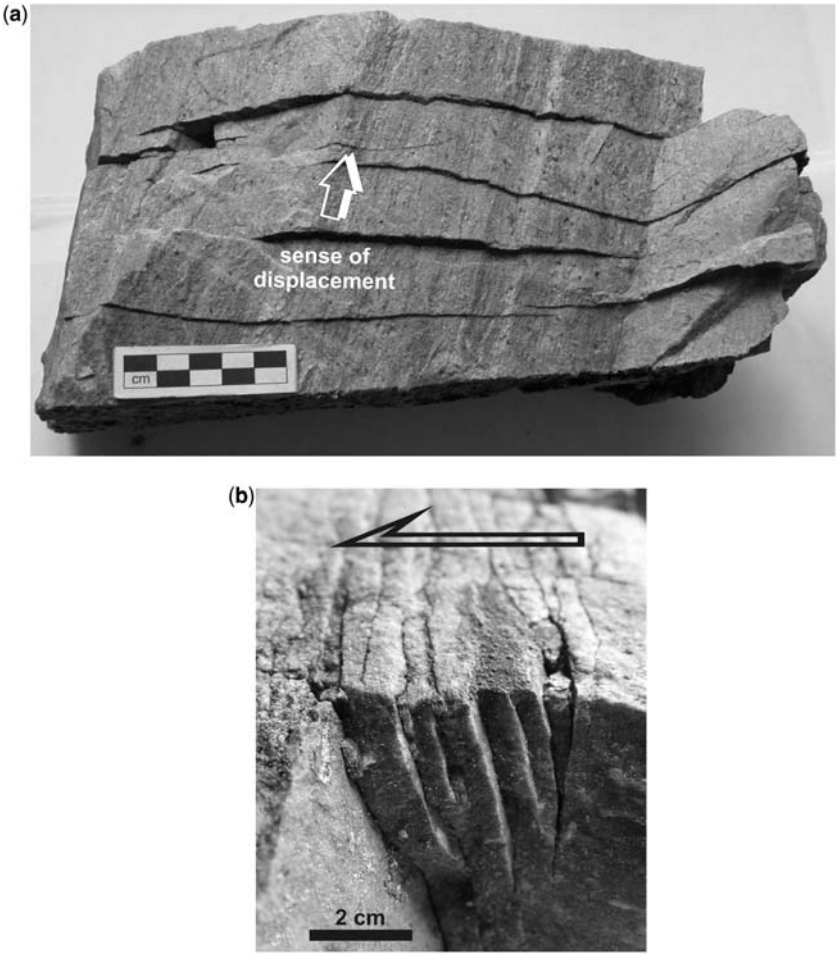

Fig. 6. (**a**) View onto the foliation plane forming the shear zone boundary of a chlorite-bearing quartzite from the Palten–Liesing fault. The step traces on the foliation plane are formed by fractures at high angle to the fault zone boundary. (**b**) View perpendicular to the shear zone boundary, showing slightly bent lamellae confined by subvertical fractures. Both samples are from the site 'Mautern' (see Appendix 1).

spatial relationship from the scales of several centimetres up to several metres within one individual shear zone.

Mesoscale structures along the Palten–Liesing fault

The dominant structure consists of fracture arrays initiating at the foliation planes defining the SZB. These fracture sets (and hence the generated lamellae) are oriented almost perpendicular to the foliation and may even attain an X-orientation (see Fig. 1). Thus, the maxima of fracture traces are concentrated in the angular range of approximately 80–110° anticlockwise from a horizontal reference line representing the SZB within the projection area (Fig. 13). Displacement of markers clearly indicates the activation of high-angle fractures as shear planes in a domino-style rotational deformation (Figs 6 & 13). The thickness of the lamellae varies between 2 and 40 mm, the height between 15 and 160 mm. The distribution of aspect ratios is asymmetric and skewed, altogether broader than that of the marbles along the Talhof fault, with highest counts of aspect ratios between 3 and 10, and a mode in the class of 5 (Fig. 14).

In some cases, the persistent development of inter-fingering very slender, triangular wedges (with highly fragmented vertices at the SZB) replacing the regular lamellae structure can be

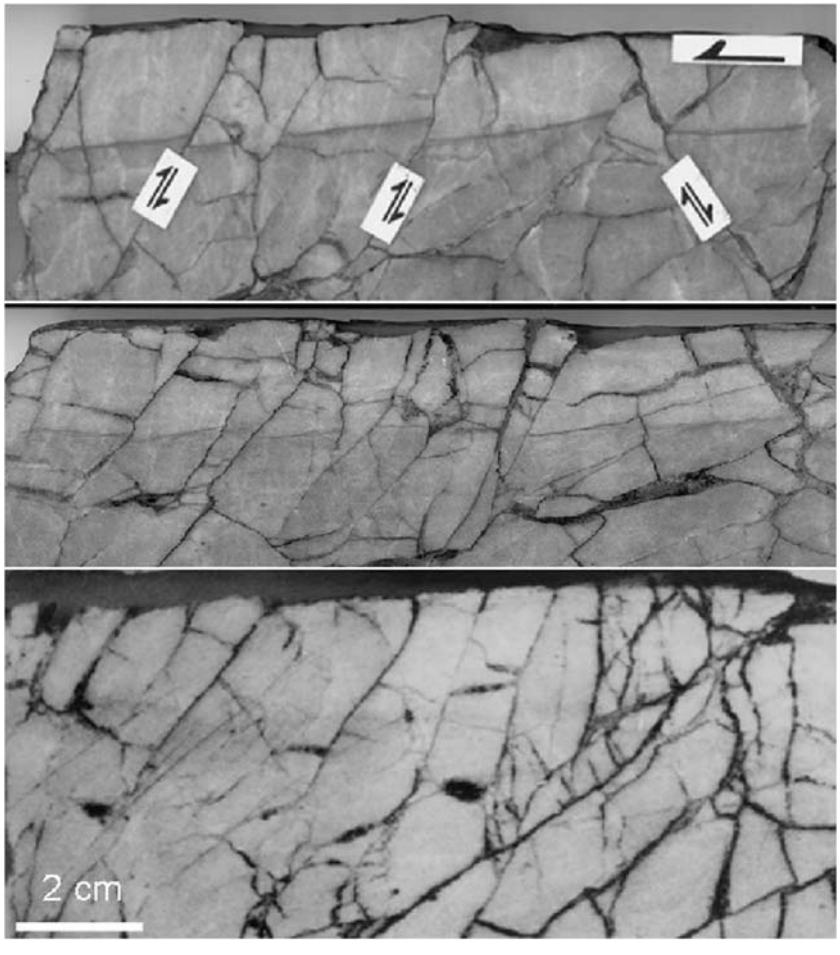

Fig. 7. Sequence of cut sample sections at right angle to the shear zone boundary, parallel to the displacement direction; predominant high-angle fractures with antithetic and minor synthetic displacement, resulting in the formation of lamellae displaying bookshelf-mode rotation; Talhof fault, site 'Kalte Rinne'; site positions and the sample locations are given in Appendix 1.

documented. Partially mineralized voids are frequently left between the acute splinters or rhombohedra, being related to fragment displacements (wedging and rotation; Fig. 15).

Frequently, the slender lamellae are seen to be bent and have attained irregular S-shaped fold-like cross sectional profiles (Fig. 16). Accordingly, the displacements differ in relation to curvature and inclination of lamellae; highest curvatures occur near, but not directly at the SZB traces. In consequence of the bending of lamellae into the assumed general shear direction, portions of their boundaries may acquire acute angle positions to the SZB. Submaxima of trace directions at approximately 140° anticlockwise from a horizontal reference line are related to these warped and rotated lamellae (Fig. 13).

Discussion

The general high-angle relationships of fractures shown in this study (see also Petit 1988) call for an explanation. These fractures are assumed to have been formed at an early stage of deformation. In many studies the fracture patterns and orientations within damage and core zones of faults have been interpreted in terms of favouring the early origin and activity of low-angle shears, particularily of R-, P- and Y-orientation (see Fig. 1). This generally would give way to an interlacing mesh of sliding planes, thus pre-forming the core zone (Riedel 1929; Skempton 1966; Morgenstern & Tchalenko 1967; Tchalenko 1970; Logan *et al.* 1979, 1992; Bartlett *et al.* 1981; Hancock 1985; Naylor *et al.* 1986; Harding & Tuminas 1989).

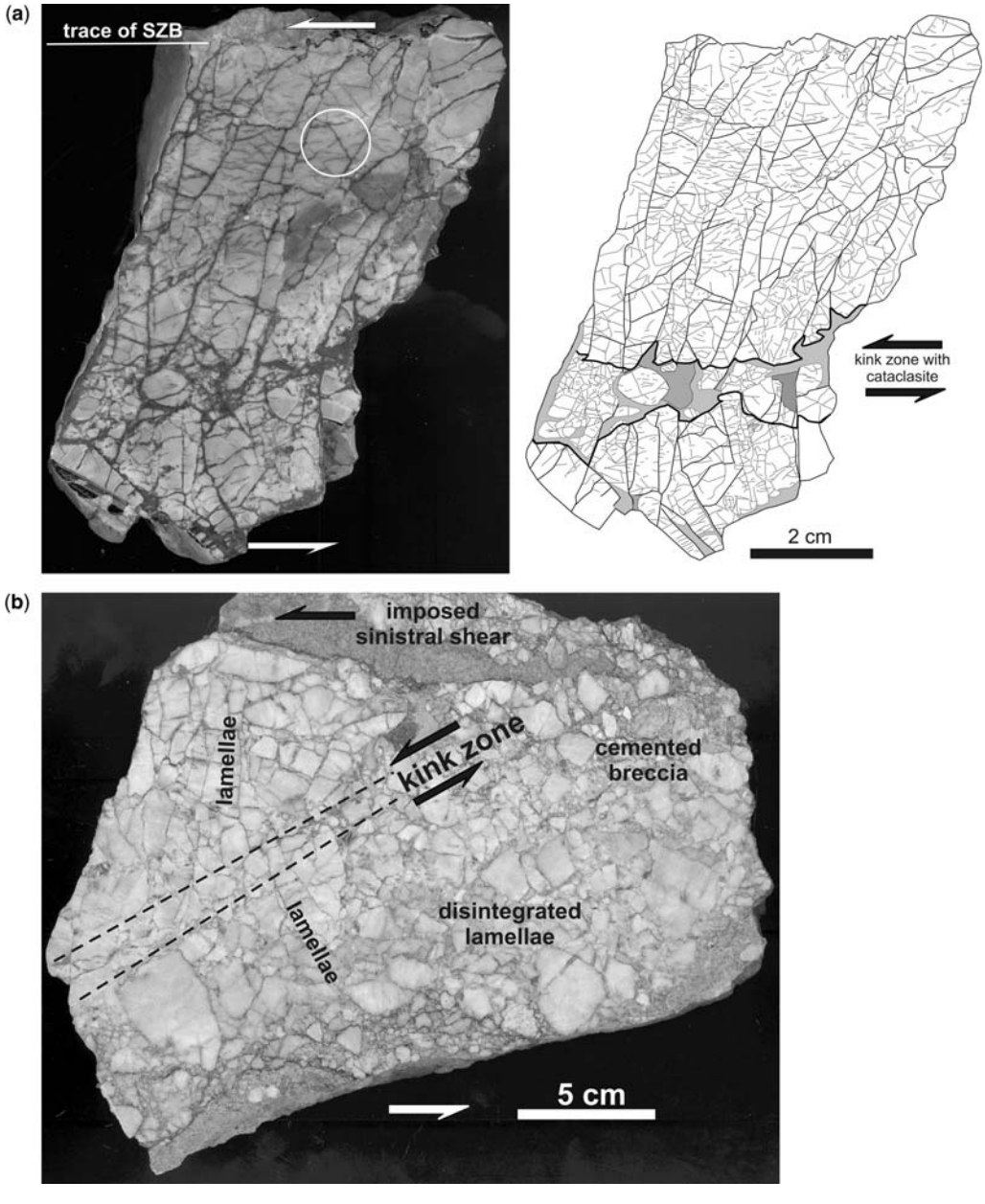

Fig. 8. (**a**) Fracture pattern within carbonates along the Talhof fault, site 'Stiegerinhütte'. The shear zone boundary (SZB) runs parallel to the bedding/foliation. Slabs with a thickness of *c*. 1 cm are bordered by subvertical major fractures formed at high angles to the SZB. Minor fractures in the internal parts of the slabs either run sub-parallel to the SZB or occur as probably conjugate sets (encircled). The slabs are kinked related to a sinistral sense of shear along the SZB; the kink zone is characterized by the formation of slab-derived fragments embedded within a finer-grained carbonate matrix; shear sense within the kink zone is assumed to coincide with the general sense of shear along the SZB. (**b**) Structural style at an advanced state of a cataclastic shear zone evolution within layered carbonates; lamellar precursor structures including the development of a kink zone (left); disintegrated clusters of lamellae remnants within a brecciated fault zone (right). Sample from site 'Stiegerinhütte' (see Appendix 1).

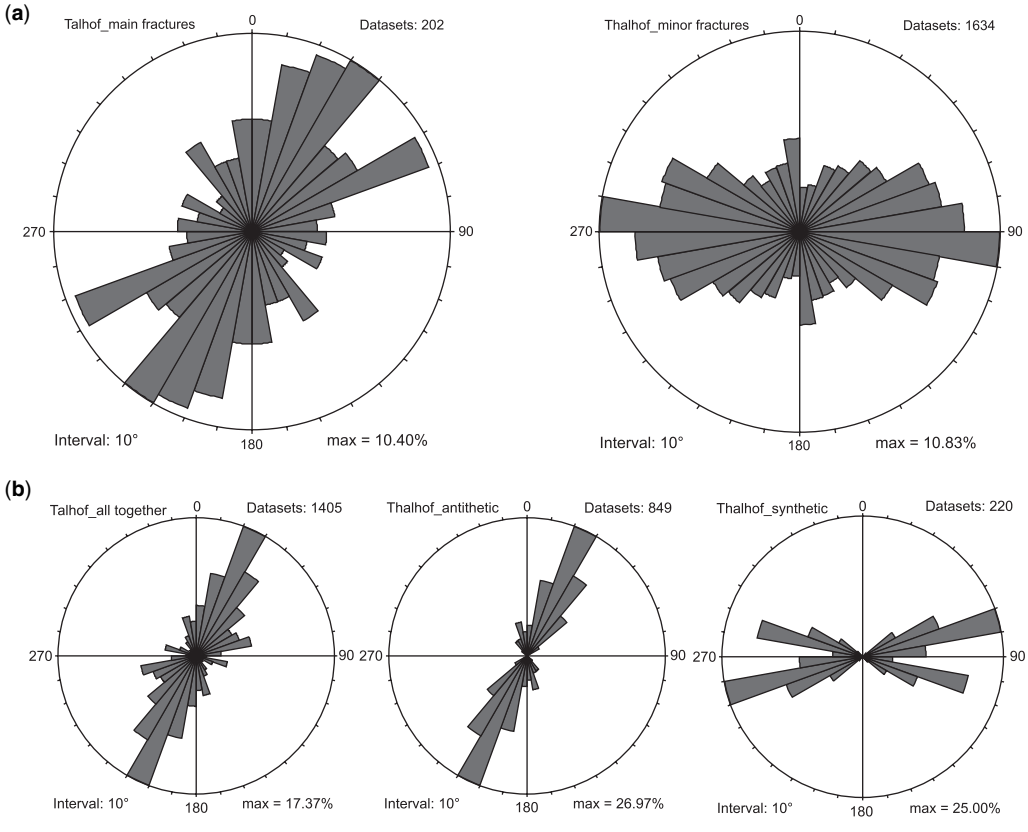

Fig. 9. (**a**) Orientation distribution of slab-forming major and minor fractures shown in Figure 8. The rose diagrams display the angular distribution and frequency of lamella-bounding fractures with respect to SZB; all diagrams are arranged to refer to a sinistral sense of shear (top to the left); the trace of the SZB is parallel to a horizontal reference line; azimuth intervall 10°. The scale is linear with maximum directional count as full radius. (**b**) Orientation distribution of slab-forming fractures from sample data and field data along the Talhof segment, also separated into syn- and antithetic sets.

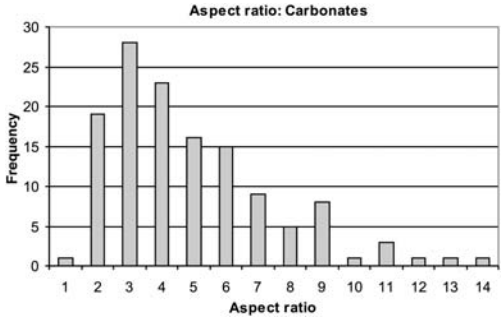

Fig. 10. Frequency diagram of aspect ratios of lamellae (length/width) within marbles along the Talhof fault segment. The width was determined within the longest straight portion of distinct lamellae at right angles to the bounding fractures.

One of the chief characteristics of a Riedel shear system is an overstepping, en échelon array of synthetic shears (called 'R-shears') oriented theoretically at $(\phi/2)^\circ$ anticlockwise to the general trace of strike–slip shear (assuming a left-lateral sense of displacement, Fig. 1; Davis *et al.* 1999). In particular, across transfer zones these may be connected by another en échelon array of (antithetic) shears (called 'R′-shears'; e.g., Naylor *et al.* 1986; Wibberley *et al.* 2000; Katz *et al.* 2004; Kim *et al.* 2004). In cross section these R′-shears have their fracture traces oriented at approximately $(90 - \phi/2)^\circ$ anticlockwise to the trace of the shear zone boundary. Both shear fracture orientations have the same potential of being developed (as derived from the Mohr diagram); in reality, their activation depends on stress and kinematic boundary conditions.

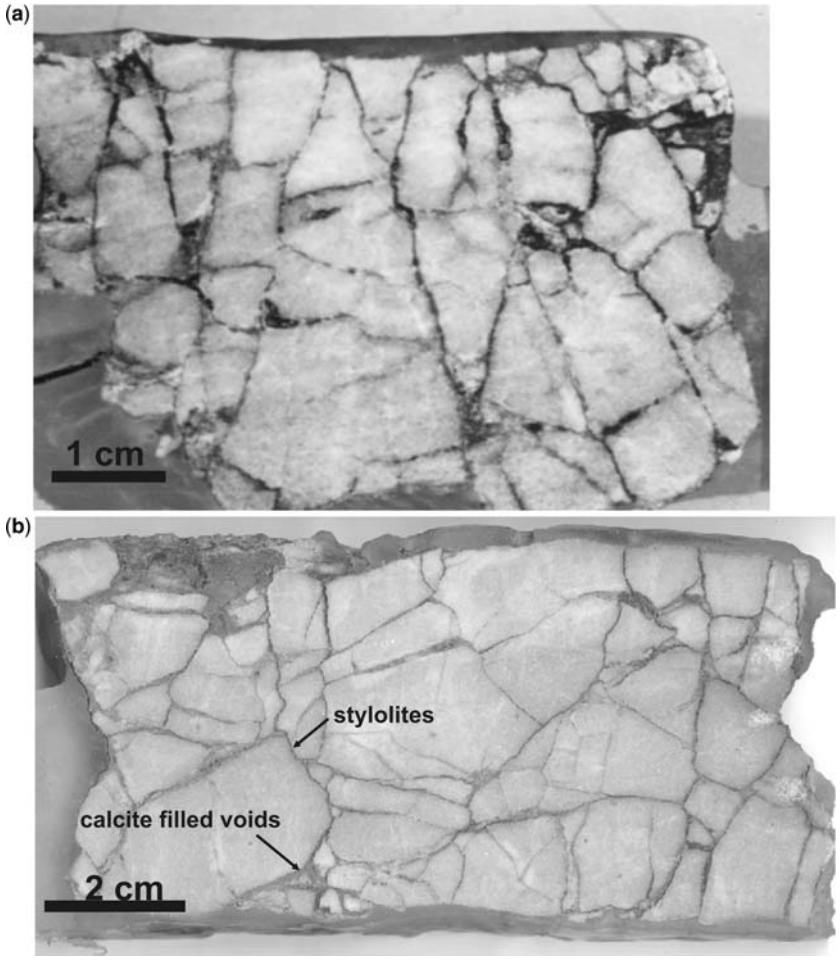

Fig. 11. (**a**) Development of interfingering triangular wedges. (**b**) Almost irregular fragmentation based on a complex fracture configuration within marbles, with curved, in parts stylolithic fractures pre-forming subrounded fragments; onset of particle rotation which opened calcite filled voids. Samples from site 'Kalte Rinne' (see Appendix 1).

With reference to the predominance of high-angle fractures in the observed shear zones, we argue that:

1. The presence of discontinuities parallel to the general shear direction (layering, foliation) within a rock mass provides that the generation of new Y-fractures is not immediately required; in other words, easy slip along the anisotropy eliminates the mechanical need for R- or P-fractures, leading to the prefential development of high-angle sets.
2. Large strains may have been accommodated by 'card-deck' sliding along SZB (foliation planes) without much fracturing and disintegration.

Therefore, our considerations can be focused on the sequence of generation of fractures within single layers which are bounded by pre-existing parallel planes of Y-orientation.

Regarding the geometrical fracture configuration and angular relationships, we have to consider various influences, in particular the (local) stress tensor orientation, relative stress magnitudes and the effects of rock anisotropy. Generally the magnitude ratio between the effective normal stress acting parallel to the externally imposed general shear direction ($\sigma_{||}$) and the normal stress acting

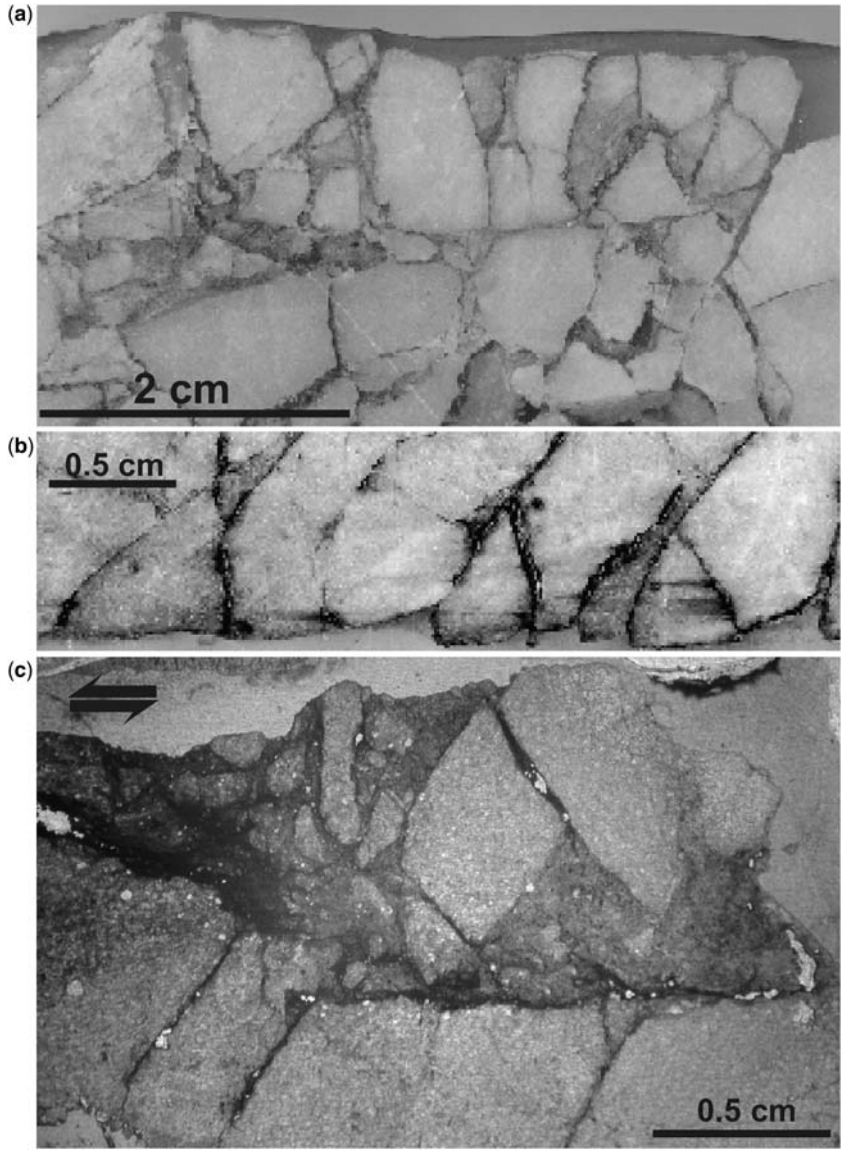

Fig. 12. (**a**) Intensified fragmentation near the SZB: Fragmentation into isometric particles of limited range in size, noticeable fragment rotation generating stylolithic contacts and/or calcite-filled voids (dark grey, lower part); conjugate fractures in an X- shaped array generate fragments of triangular sectional shape (upper right). (**b**) Splitting-off of fragments with triangular sectional shape from slender rock slabs at the SZB is typical for rotated lamellae allowing for accommodation of the stress peaks at the edges during rotation in the case that the dilation across the shear zone is impeded. The structure can be observed at several scales from outcrop to thin section. (**c**) Remnants of cataclasite (fault breccia) with anticlockwise rotated fragments due to bookshelf-rotation of the sheared lamellae along the SZB; anticlockwise rotation of fragments is assumed to b related to left-lateral general sense of shear. Samples from site 'Kalte Rinne' (see Appendix 1).

perpendicular to that direction ($\sigma_{\perp}$) governs which of the potential shear plane orientations (R, R′, or even higher angles) will be generated or activated (see e.g., Mandl 1988, 2000; Wibberley *et al.* 2000). Accordingly, high- to very high-angle shear planes (and associated bookshelf- or domino-mode displacement kinematics) are to be expected in all cases of low to very low $\sigma_{||}$ as compared to the

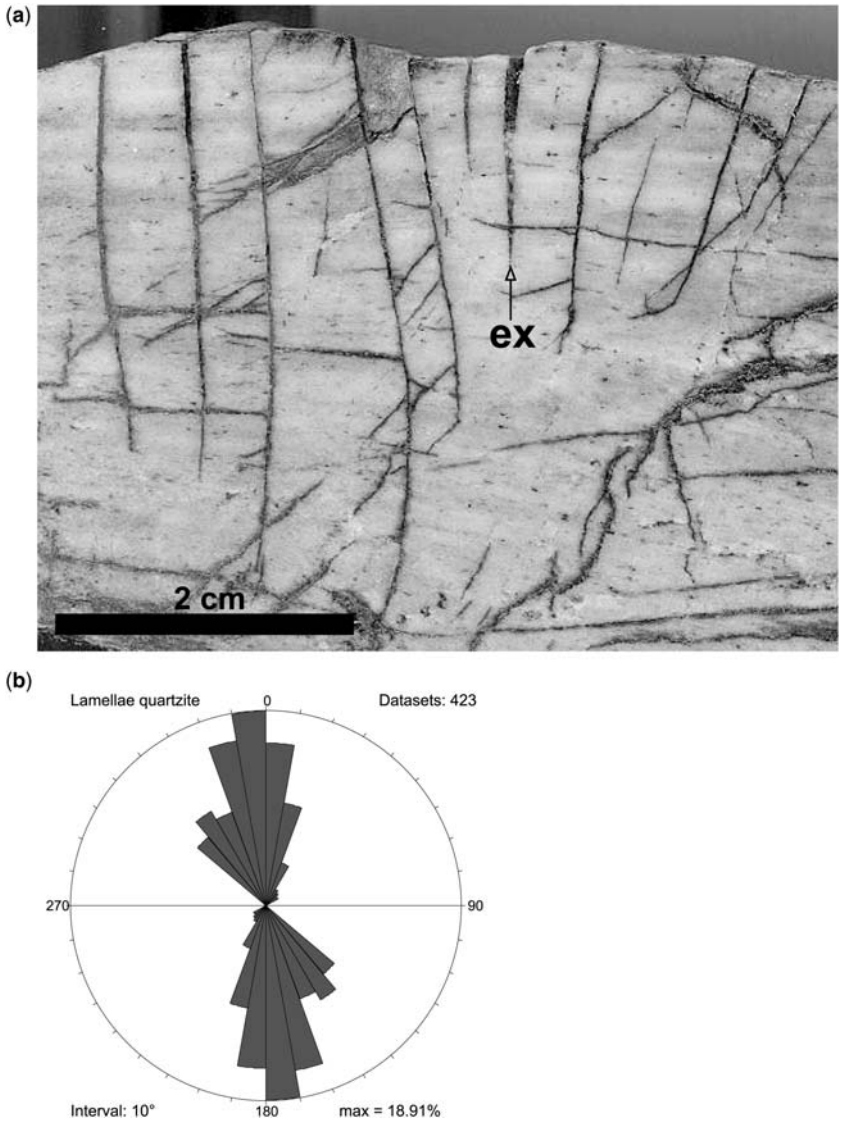

Fig. 13. (**a**) Fracturing within foliated quartzite showing slight bending and breaking of lamellae; gently dipping fractures often abutting against steep (extensional) fractures (ex), in cases displaced by the latter; note the unequal and for the most parts low persistence of lamellae-bounding fractures. The displayed structures are not due to tectonic buckling/folding of the host rock layer. Sample from site 'Mautern' (see Appendix 1). (**b**) Orientation distribution of slab-forming major and minor fractures within quartzites along the Palten–Liesing fault. The rose diagrams display the angular distribution and frequency of lamella bounding fractures with respect to SZB; all diagrams are arranged to refer to a sinistral sense of shear (top to the left); the trace of the SZB is parallel to a horizontal reference line; azimuth intervall 10°, scale is linear with maximum directional count as full radius. The high frequency of trace orientations within the NW and SE quadrants of the projection is related to the bending and overturning of lamellae.

relative magnitude of $\sigma_{\perp}$, i.e., in a distinctly transpressional deformation regime. Present observations confirm a corresponding interpretation:

1. We find signs of high normal stress across the shear zone (buckling, kinking, splitting and crushing of lamellae, low-angle stylolithic contacts) associated with indications of low lateral confinement ($\sigma_{||}$), like extensional structures (open cracks, veins), the formation of voids, and breccias showing dilational fabrics (Figs 17 & 18).

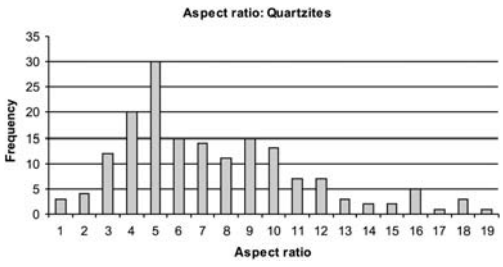

Fig. 14. Frequency diagram of aspect ratios of lamellae (length/width) within quartzites along the Palten–Liesing fault segment.

2. For the Palten–Liesing Fault zone the observed structures (overturned, folded lamella portions, split–crushed lamellae; Figs 15 & 16) also must be attributed to high stresses across the shear zone ($\sigma_{\perp}$). The maximum principal stress is therefore assumed to be oriented at very high angles to the SZB. Thus the related shear stress along the SZB was low, the pre-formed slender lamellae (ready to act in a domino-mode kinematics) predominantly were compressed axially, and the kinematically required widening of the shear zone was inhibited (e.g., Means 1995; Fig. 18).

From field observations and evidence from the prepared samples we assume that the structures described above represent common initial states in the development of brittle shear zones in rocks with spaced bedding or foliation, and the imposed shear deformation is roughly parallel to these primary structures. Additionally, this may be forced by a stress vector orientation at very high angles to the SZB.

It is noteworthy that all described structures and hence inferred stages of structural development exist in close spatial relationship within one individual shear zone in the field (or even one sample). This obviously simultaneous development of different deformation styles and intensities along the shear zone extent is interpreted as being in the first place the consequence of variations in shear zone width (layer thickness, as in the marble samples) and hence differing stress and strain conditions to be accommodated.

Our conceptual model for brittle fault zone development in the observed rock types starts with the generation of broad bands of concentrated shear-imposed deformation by the development of fracture zones with an internal lamellae structure (see discussion in, e.g., Wilcox *et al.* 1973; Paterson 1978; Naylor *et al.* 1986; Olson & Pollard 1991; Katz *et al.* 2004; Mandl 2005). These fracture zones probably combine R′, T and mixed-mode fracture components and may be assumed to evolve initially from transfer zones between parallel pre-formed large-scale shears of higher order (see, e.g., Naylor *et al.* 1986; Davis *et al.* 1999; Kim *et al.* 2004). The consequent synthetic rotation of lamellae results in the first place in the development of a pervasive bending or kink zone with an axial plane subparallel to the pre-existing planar discontinuities (the SZB) (Figs 8 & 17). Kinking results

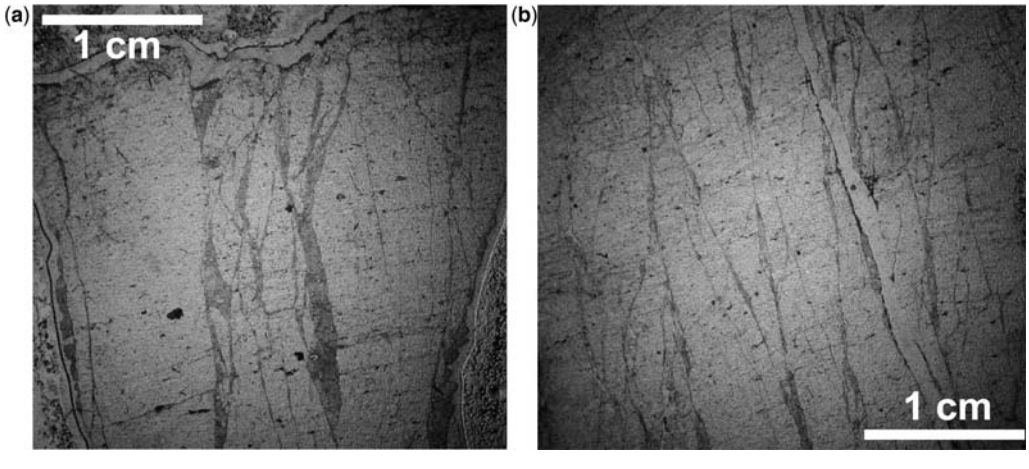

Fig. 15. (**a**) Intensified fragmentation within narrow sub-vertical, funnel-like structures. Rock pillars to the left and right display only minor signs of axial splitting. (**b**) Slender triangular rock lamellae generated by acute-angled intersections of fractures. Vertical shortening is accommodated by lateral dilation, thus giving space to opening of voids (calcite-healed pull-apart structures, dark) and increasing axial fragmentation. Samples from site 'Mautern' (see Appendix 1).

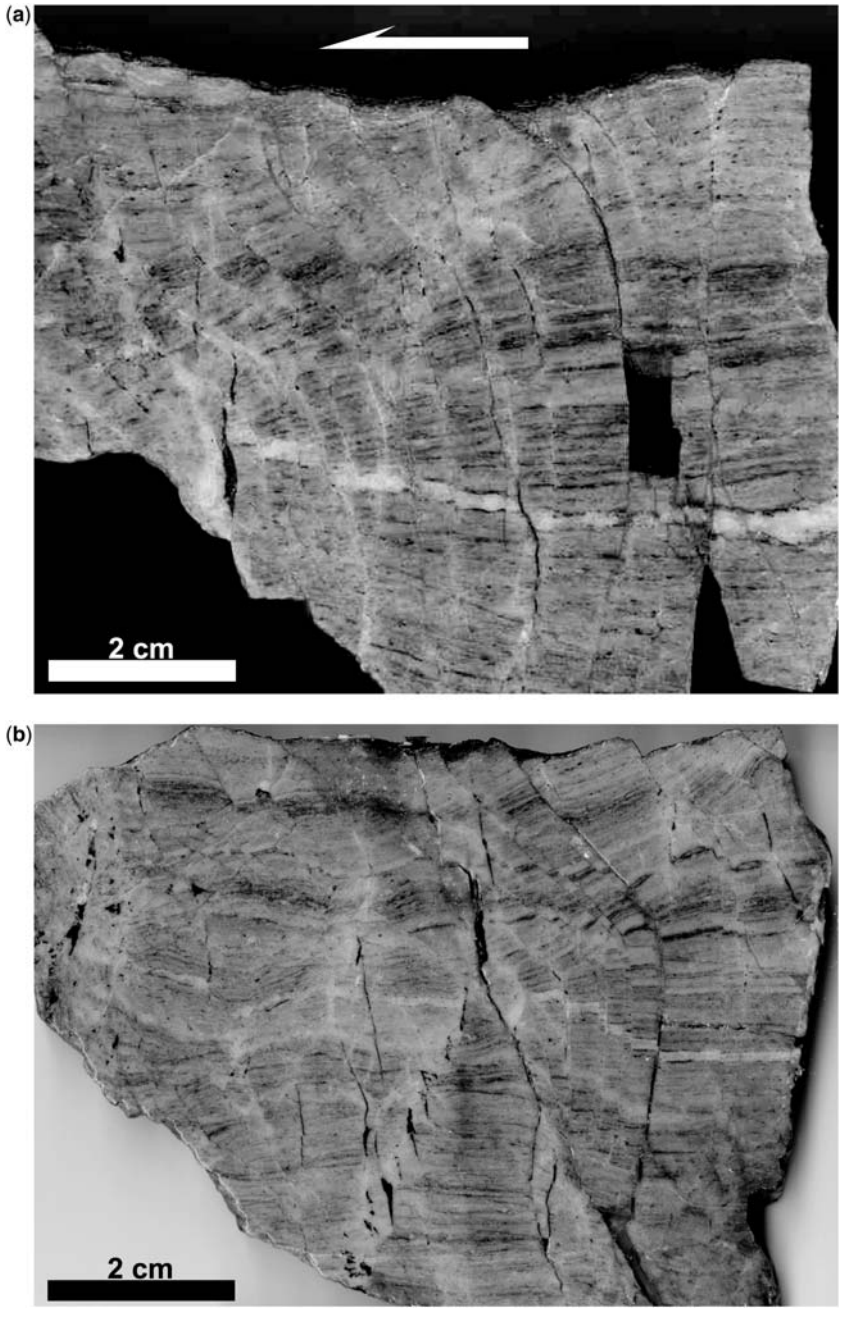

Fig. 16. Consequences of compression across the foliation resulting in multi-bent lamellae; (**a**) ductile–semiductile buckling and bending of initially straight lamellae (in parts to S-shaped structures) with tilting of markers and increasing displacement with inclination angle of lamellae; (**b**) development of horst–graben structures in the central part of the sample and subsequent formation of conjugate brittle fractures – in parts as en echelon vein arrays. Sample from site 'Mautern' (see Appendix 1).

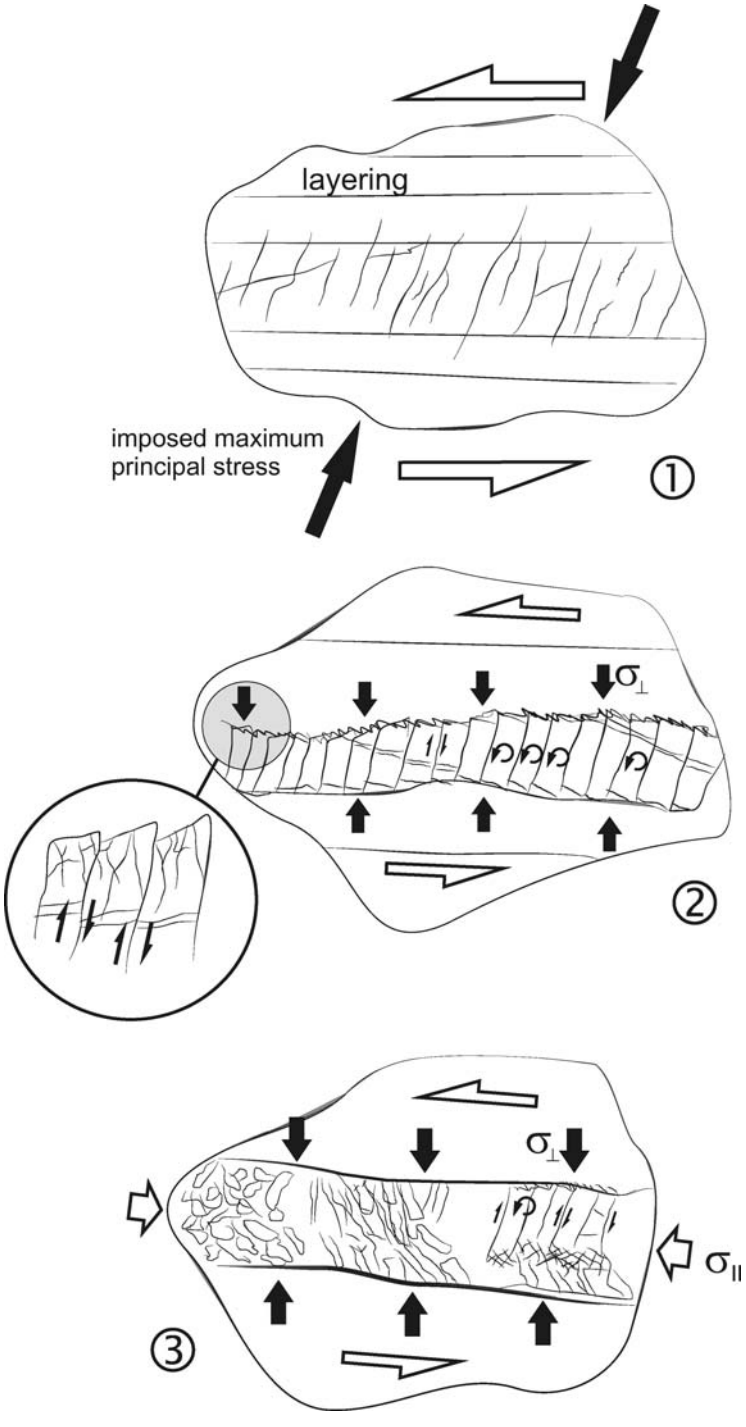

Fig. 17. Inferred qualitative scheme of shear zone evolution due to layer-parallel shear along the Talhof fault deduced from field and sample observations: 1, formation of distinct fractures at high angle to the pre-existing bedding/foliation planes; 2, formation of fracture-bound lamellae, rotation of lamellae and formation of secondary fractures at the tips of lamellae; widening of the fault zone is inhibited due to external compressive stresses; 3, kinking and disintegration of lamellae and formation of a kink zone, developing into a cataclastic shear zone at advanced stages of displacement.

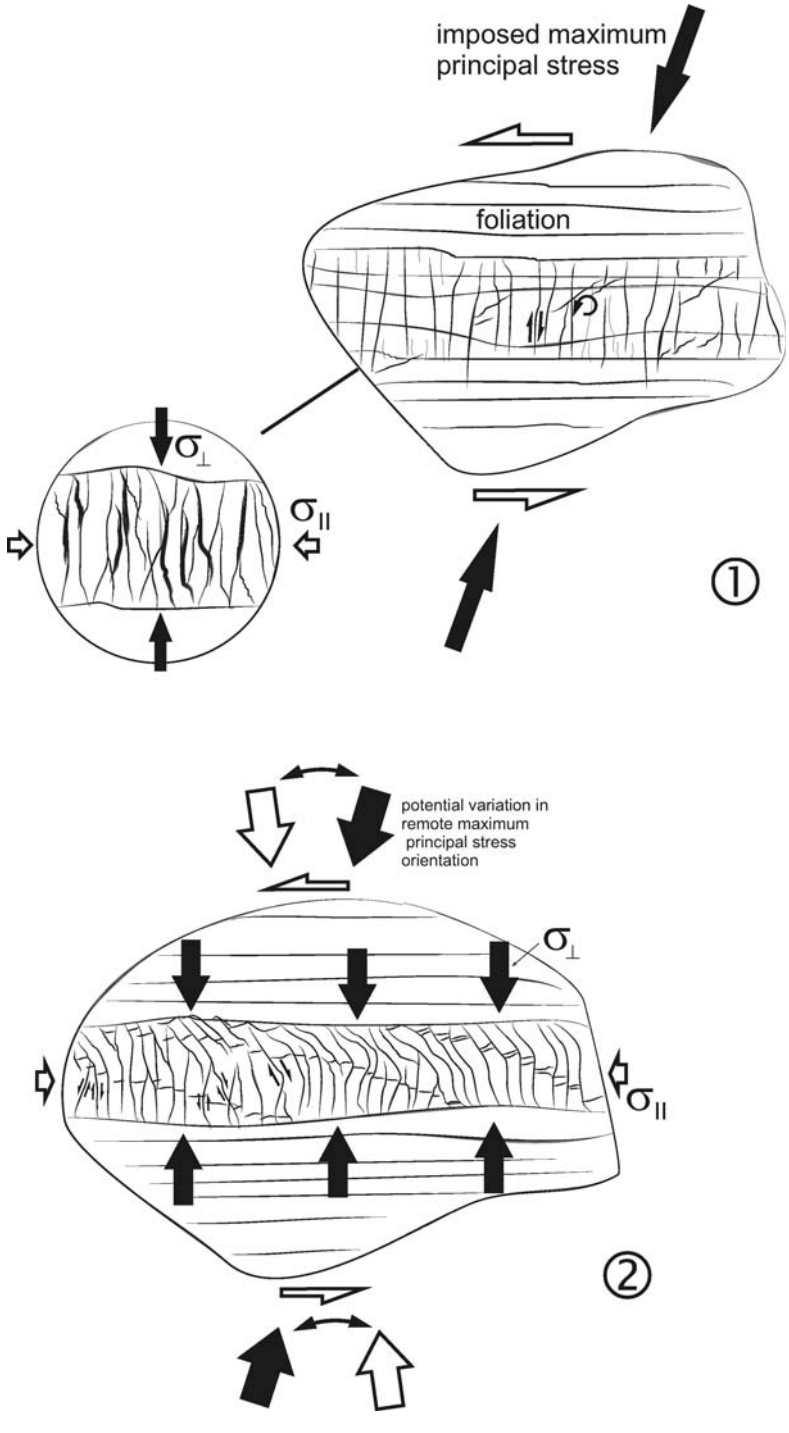

Fig. 18. Inferred qualitative scheme of fault zone evolution due to layer-parallel shear along the Palten–Liesing fault deduced from field and sample observations; 1, formation of distinct fractures at very high angle to the pre-existing bedding/foliation planes and of fracture-bound lamellae; rotation of lamellae into an overturned position; 2, ductile bending and folding of lamellae; widening of the fault zone is inhibited due to external compressive stresses.

from the longitudinal constraint of lamellae associated by reduced lateral confinement as well. The kinking and overturning of lamellae, their breakdown due to the assumed impeded shear zone widening (required initially in a bookshelf-mode rotation) and their cracking along the pre-formed shear zone boundary (e.g., a foliation plane) altogether will cooperate in the formation of distinct zones of shear accommodation. Rupturing along kink bands developing within the lamellae array and breaking up to smaller fragments with independent rotational and translational displacement may mark the transition to the formation of cataclastic fault rocks (Figs 8 & 17). Subsequent shear is assumed to be localized along these brecciated zones, eventually ending up with the formation of bands of fine-grained fault gouges, and the evolution of a fault core with slip planes of local influence (Figs 8 & 17).

This perception is corroborated by the inferred further stages of fault zone evolution. These examples illustrate the interpretation that, with the overturning of broken lamellae, bringing the fabric elements into the extensional quadrant of the incremental strain ellipsoid, and with breakup and kinking of lamellae, the evolution of cataclastic zones is triggered off. Only remnants and increasingly isolated rotated clusters of initial lamellae (torn apart, partially interacting in a domino-style kinematics) may survive during advancing stages of cataclastic deformation, thereby documenting the preceding stages of structural evolution (Fig. 8).

These processes, including the development of associated structures, may proceed repeatedly in the case that earlier-formed breccias get cemented and subsequently undergo continuous brittle shear deformation – a cylic process of cementation healing and refracturing that might be termed 'fault rock recycling'.

Conclusions

Within brittle shear zones different evolutionary stages and structures of different local modes of strain accommodation may co-exist. From the examples presented in this study, this fact can be corroborated by the observed close spatial connection of regions dominated by a regular pattern of shear fracture sets and irregularly crushed, brecciated domains of apparently contemporaneous formation.

The examples in our study show that well-known R-, P- (and Y-) fracture patterns may not always play a dominant role in the early stages of the generation of fault zones. The presence of discontinuities parallel to the general shear direction (layering, foliation) within a rock means that the generation of new Y-fractures is not immediately required. In rocks with a spaced foliation (bedding/layering) and in which shear is parallel to these fabric element, shear zone formation and fault rock generation may start with the development of kink zones with a characteristic internal structure:

1. Lamellae bounded by en echelon fractures of R′-orientation or even higher angles and of possible mixed-mode origin. The formation of these structures can be explained by the impeded formation of low-angle fractures due to the pre-existing discontinuities, and the influence of the ratio of normal stresses acting across as well as parallel to the SZB. Subsequent rotation of the rock lamellae (in particular in the bookshelf style) associated with inhibited dilatancy and widening of the shear zone leads to kinking of lamellae and subsequent cataclastic deformation. The final fragmentation of the lamellae generates fault breccias, accumulating in fault core zones.
2. The occurrence of ductile deformation features (bends, folds) in lamellae within impure, schistose quartzites, subsequent to the formation of high-angle brittle fractures may be attributed to particular lithological and exhumation conditions (e.g., elevated confining stresses).

This study was carried out during a research project (P-17697-N10) granted by the Austrian Science Fund (FWF). We highly appreciate the fieldwork support by H. Gaich, E. Kiechl, R. Rabitsch and G. Winkler. The reviews by F. Agosta and N. Woodcock contributed a lot to the improvement of the manuscript. Chris Wibberley is thanked for his thorough editorial comments.

Appendix 1: Sites and sampling locations described in the text

'Stiegerinhütte': Austrian map, 1:50 000, sheet no. 104 (Mürzzuschlag); 15° 44′ 29″ E; 47° 39′ 17″ N.

'Kalte Rinne': Austrian map, 1:50 000, sheet no. 104 (Mürzzuschlag); 15° 47′ 23″ E; 47° 39′ 28″ N.

'Mautern': cut slope along the A9 freeway (Pyhrnautobahn): Austrian map, 1:50 000, sheet no. 132 (Trofaiach); 14° 50′ 57″ E; 47° 23′ 41″ N.

References

ANDERSON, E. M. 1951. *The Dynamics of Faulting*. Oliver & Boyd, Edinburgh.

AYDIN, A. & SCHULTZ, R. 1990. Effect of mechanical interaction on the development of strike-slip faults with echelon patterns. *Journal of Structural Geology*, **12**, 123–129.

BARTLETT, W. L., FRIEDMAN, M. & LOGAN, J. M. 1981. Experimental folding and faulting of rocks under confining pressure. Part IX: wrench faults in limestone layers. *Tectonophysics*, **79**, 255–277.

BERG, S. S. & SKAR, T. 2005. Controls on damage zone asymmetry of a normal fault zone: outcrop analyses of a segment of the Moab fault, SE Utah. *Journal of Structural Geology*, **27**, 1803–1822.

BILLI, A. 2005. Grain size distribution and thickness of breccia and gouge zones from thin (<1 m) strike–slip fault cores in limestone. *Journal of Structural Geology*, **27**, 1823–1837.

BILLI, A. & STORTI, F. 2004. Fractal distribution of particle size in carbonate cataclastic rocks from the core of a regional strike-slip fault zone. *Tectonophysics*, **384**, 115–128.

BILLI, A., SALVINI, F. & STORTI, F. 2003. The damage zone–fault core transition in carbonate rocks: implications for fault growth, structure and permeability. *Journal of Structural Geology*, **25**, 1779–1794.

BRODIE, K., FETTES, D., HARTE, B. & SCHMID, R. 2002. *Structural terms including fault rock terms*. IUGS Subcommission on the Systematics of Metamorphic Rocks.

CAINE, J. S., EVANS, J. P. & FORSTER, C. B. 1996. Fault zone architecture and permeability structure. *Geology*, **24**, 1025–1028.

CELLO, G., INVERNIZZI, C., MAZZOLI, S. & TONDI, E. 2001. Fault properties and fluid flow patterns from Quaternary faults in the Apennines, Italy. *Tectonophysics*, **336**, 63–78.

CHESTER, F. M. & LOGAN, J. M. 1986. Implications for mechanical properties of brittle faults from observations of the Puchbowl Fault, California. *Pure and Applied Geophysics*, **124**, 79–106.

CHESTER, F. M. & LOGAN, J. M. 1987. Composite planar fabric of gouge from the Punchbowl Fault, California. *Journal of Structural Geology*, **9**, 621–634.

CHESTER, F. M. & LOGAN, J. M. 1990. Frictional faulting in polycrystalline halite: correlation of microstructure, mechanism of slip and constitutive behaviour. *American Geophysical Monographs*, **56**, 49–56.

CHESTER, F. M., EVANS, J. P. & BIEGEL, R. L. 1993. Internal structure and weakening mechanisms of the San Andreas. *Journal of Geophysical Research*, **98**, 771–786.

CHESTER, J. S. 2003. Mechanical stratigraphy and fault-fold interaction, Absaroka thrust sheet, Salt River Range, Wyoming. *Journal of Structural Geology*, **25**, 1171–1192.

CLOOS, H. 1928. Experimente zur Inneren Tektonik. *Beiträge zur Mineralogie, Geologie, und Paläontologie*, **B**, 609–621.

DAVIS, G. A., BUMP, A. P., GARCIA, P. E. & AHLGREN, S. G. 1999. Conjugate Riedel deformation band shear zones. *Journal of Structural Geology*, **22**, 169–190.

DECKER, K. & PERESSON, H. 1996. Tertiary kinematics in the Alpine–Carpathian–Pannonian system: links between thrusting, transform faulting and crustal extension. *In*: WESSELY, G. & LIEBL, W. (eds) *Oil and Gas in Alpidic Thrustbelts and Basins of Central and Eastern Europe*. EAGE Special Publications, **5**, 69–77.

DECKER, K., MESCHEDE, M. & RING, U. 1993. Fault slip analysis along the northern margin of the Eastern Alps (Molasse, Helvetic nappes, North and South Penninic flysch, and Northern Calcareous Alps). *Tectonophysics*, **223**, 291–312.

FAULKNER, D. R., LEWIS, A. C. & RUTTER, E. H. 2003. On the internal structure and mechanics of large strike-slip fault zones: field observations of the Carboneras fault in southeastern Spain. *Tectonophysics*, **367**, 235–251.

FLODIN, E. & AYDIN, A. 2004. Faults with asymmetric damage zones in sandstone, Valley of Fire State Park, southern Nevada. *Journal of Structural Geology*, **26**, 983–988.

FLÜGEL, H. W. & NEUBAUER, F. 1984. Erläuterungen zur Geologischen Karte der Steiermark 1:200 000. *Geologie der Österreichischen Bundesländer in kurzgefassten Darstellungen–Steiermark (Geologische Bundesanstalt)*.

FRISCH, W., DUNKL, I. & KUHLEMANN, J. 2000. Post-collisional orogen-parallel large-scale extension in the Eastern Alps. *Tectonophysics*, **327**, 239–265.

GMEINDL, M. 1999. Diploma Thesis, Institute of Applied Geology, University for Natural Resources and Life Sciences, Vienna.

HANCOCK, P. L. 1972. The analyses of en echelon veins. *Geology Magazine*, **109**, 269–276.

HANCOCK, P. L. 1985 Brittle microtectonics: principles and practice. *Journal of Structural Geology*, **7**, 437–457.

HANCOCK, P. L., AL-KHADI, A., BARKA, A. A. & BEVAN, T. G. 1987. Aspects of analysing brittle structures. *Annales Tectonicae*, **1**, 5–19.

HARDING, T. P. & TUMINAS, A. C. 1989. Structural interpretation of hydrocarbon traps sealed by basement normal block faults at stable flanks of foredeep basins and rift basins. *American Association of Petroleum Geologists Bulletin*, **73**, 812–840.

JAEGER, J. C. & COOK, N. G. W. 1979. *Fundamentals of Rock Mechanics*, 3rd edn. Methuen, London, 593 S.

KATZ, O., RECHES, Z. & BAER, G. 2003. Faults and their associated host rock deformation: Part I. Structure of small faults in a quartz-syenite body, southern Israel. *Journal of Structural Geology*, **25**, 1675–1689.

KATZ, Y., WEINBERGER, R. & AYDIN, A. 2004. Geometry and kinematic evolution of Riedel shear structures, Capitol Reef National Park, Utah. *Journal of Structural Geology*, **26**, 491–501.

KIM, Y.-S., PEACOCK, D. C. P. & SANDERSON, D. 2004. Fault damage zones. *Journal of Structural Geology*, **26**, 503–507.

LINZER, H.-G., DECKER, K., PERESSON, H., DELL'-MOUR, R. & FRISCH, W. 2002. Balancing lateral orogenic float of the Eastern Alps. *Tectonophysics*, **354**, 211–237.

LOGAN, J. M., FRIEDMAN, M., HIGGS, M., DENGO, C. & SHIMAMOTO, T. 1979. Experimental studies of simulated gouge and their application to studies of natural fault zones. *Proceedings of Conference VIII, Analysis of Actual Fault Zones in Bedrock*, 305–343.

LOGAN, J. M., DENGO, C. A., HIGGS, N. G. & WANG, Z. Z. 1992. Fabrics of experimental fault zones: their development and relationship to mechanical behaviour. *In*: EVANS, B. & WONG, T. (eds) *Fault Mechanics and Transport Properties of Rocks*. Academic Press, San Diego, CA, 33–67.

MANDAL, N. & CHATTOPADHYAY, A. 1995. Modes of reverse reactivation of domino-type normal faults: experimental and theoretical approach. *Journal of Structural Geology*, **17**, 1151–1163.

MANDL, G. 1988. *Mechanics of Tectonic Faulting; Models and Basic Concepts*. Elsevier, Oxford.

MANDL, G. 2000. *Faulting in Brittle Rocks*. Springer, Berlin.

MANDL, G. 2005. *Rock Joints, the Mechanical Genesis*. Springer, Berlin.

MANDL, G., DE JONG, L. N. & MALTHA, A. 1977. Shear zones in granular material. *Rock Mechanics*, **9**, 95–144.

MEANS, W. D. 1995. Shear zones and rock history. *Tectonophysics*, **247**, 157–160.

MOORE, D. E., SUMMERS, R. & BYERLEE, J. 1989. Sliding behaviour and deformation textures of heated illite gouge. *Journal of Structural Geology*, **11**, 329–342.

MORGENSTERN, N. R. & TCHALENKO, J. S. 1967. Microscopic structures in kaolin subjected to direct shear. *Geotechnique*, **17**, 309–328.

NAYLOR, M. A., MANDL, G. & SEIJPENSTEIJN, C. H. 1986. Fault geometries in basement-induced wrench faulting under different initial stress states. *Journal of Structural Geology*, **8**, 737–752.

OLSON, J. E. & POLLARD, D. D. 1991. The initiation and growth of en echelon veins. *Journal of Structural Geology*, **13**, 595–609.

PATERSON, M. S. 1978. *Experimental Rock Deformation – The Brittle Field*. Springer, Berlin, 254 S.

PEACOCK, D. C. P. & SANDERSON, D. J. 1992. Effects of layering and anisotropy on fault geometry. *Journal of the Geological Society of London*, **149**, 792–802.

PETIT, J.-P. 1987. Criteria for the sense of movement on fault surfaces in brittle rocks. *Journal of Structural Geology*, **9**, 597–608.

PETIT, J.-P. 1988. Normal stress dependent rupture morphology in direct shear tests on sandstone with application to some natural fault surface features. *International Journal of Rock Mechanics, Mining Sciences and Geomechanics Abstracts* **25**, 411–419.

POLLARD, D. D., SEGALL, P. & DELANEY, T. P. 1982. Formation and Interpretation of dilatant echelon cracks. *Geological Society of America Bulletin*, **93**, 1291–1303.

POWER, W. L., TULLIS, T. E. & WEEKS, J. D. 1989. The relationship between slickenside surfaces in fine-grained quartz and the seismic cycle. *Journal of Structural Geology*, **11**, 879–893.

RATSCHBACHER, L., FRISCH, W., NEUBAUER, F., SCHMID, S. M. & NEUGEBAUER, J. 1989. Extension in compressional orogenic belts: the eastern Alps. *Geology*, **17**, 404–407.

RATSCHBACHER, L., FRISCH, W., LINZER, H.-G. & MERLE, O. 1991. Lateral extrusion in the eastern Alps. Part 2: structural analyses. *Tectonics*, **10**, 257–271.

RECHES, Z. 1978. Analyses of faulting in three-dimensional strain field. *Tectonophysics*, **47**, 109–129.

RECHES, Z. 1983. Faulting of rocks in three-dimensional strain fields; II: theoretical analyses. *Tectonophysics*, **95**, 133–156.

RECHES, Z. & DIETRICH, J. H. 1983. Faulting of rocks in three-dimensional strain fields; I. Failured rocks in poly-axial, servo-control experiments. *Tectonophysics*, **95**, 111–132.

REITER, F. & ACS, P. 2002. Tectonics FP 1.6.2, a 32-bit Windows^{TM}-Software for Structural Geology.

RIEDEL, W. 1929. Zur Mechanik geologischer Brucherscheinungen. *Zentralblatt für Mineralogie, Geologie und Paläontologie*, **1929B**, 354–368.

ROTHERY, E. 1988. En echelon vein array development in extension and shear. *Journal of Structural Geology*, **10**, 63–71.

RUTTER, E. H., MADDOCK, R. H. & HALL, S. H. 1986. Comparative microstructures of natural and experimentally produced clay-bearing fault gouges. *Pure and Applied Geophysics*, **124**, 3–30.

SAGY, A., RECHES, Z. & ROMAN, I. 2001. Dynamic fracturing: field and experimental observations. *Journal of Structural Geology*, **23**, 1223–1239.

SCHULZ, S. E. & EVANS, J. P. 2000. Mesoscopic structure of the Punchbowl Fault, Southern California and the geologic and geophysical structure of active strike–slip faults. *Journal of Structural Geology*, **22**, 913–930.

SHIMAMOTO, T. 1986. A transition between frictional slip and ductile flow for halite undergoing large shearing deformation at room temperature. *Science*, **231**, 711–714.

SIBSON, R. H. 1986. Brecciation processes in fault zones: inference from earthquake rupturing. *Pure and Applied Geophysics*, **124**, 159–175.

SKEMPTON, A. W. 1966. Some observations on tectonic shear zones. *Proceedings of the 1st Congress International Society of Rock Mechanics, Lisboa*, **I**, 329–335.

SYLVESTER, A. G. 1988. Strike-slip faults. *Geological Society of America Bulletin*, **100**, 1666–1703.

TARASEWICZ, J. P. T., WOODCOCK, N. H. & DICKSON, J. A. D. 2005. Carbonate dilation breccias: Examples from the damage zone to the Dent Fault, northwest England. *Geological Society of America Bulletin*, **117**, 736–745.

TCHALENKO, J. S. 1970. Similarities between shear zones of different magnitudes. *Geological Society of America Bulletin*, **81**, 1625–1640.

VERMILYE, J. M. & SCHOLZ, C. H. 1998. The process zone: a microstructural view of fault growth. *Journal of Geophysical Research*, **103**, 12223–12237.

WALLBRECHER, E. 1986. *Tektonische und gefügeanalytische Arbeitsweisen*. Enke, Stuttgart.

WANG, X. & NEUBAUER, F. 1998. Orogen-parallel strike–slip faults bordering metamorphic core complexes: the Salzach–Enns fault zone in the eastern Alps, Austria. *Journal of Structural Geology*, **20**, 799–818.

WIBBERLEY, C. A. A. & SHIMAMOTO, T. 2003. Internal structure and permeability of major strike-slip fault zones: the Median Tectonic Line in Mie Prefecture, Southwest Japan. *Journal of Structural Geology*, **25**, 59–78.

WIBBERLEY, C. A. A., PETIT, J.-P. & RIVES, T. 2000. Micromechanics of shear rupture and the control of normal stress. *Journal of Structural Geology*, **22**, 411–427.

WILCOX, R. E., HARDING, T. P. & SEELY, D. R. 1973. Basic wrench tectonics. *American Association of Petroleum Geologists Bulletin*, **57**, 74–96.

WILSON, J. E., CHESTER, J. S. & CHESTER, F. M. 2003. Microfracture analysis of fault growth and wear processes, Punchbowl Fault, San Andreas system, California. *Journal of Structural Geology*, **25**, 1855–1873.

The distribution of faults and fractures and their importance in accommodating extensional strain at Kimmeridge Bay, Dorset, UK

MARTIN W. PUTZ-PERRIER & DAVID J. SANDERSON

Department of Earth Science and Engineering, Imperial College London, Exhibition Road, London SW7 2AZ, UK (e-mail: m_putz@hotmail.com)

Abstract: The spatial distribution of extensional strain in interbedded mudstones and carbonates from around Kimmeridge Bay in southern England is examined using a variety of line samples. Normal faults and tensile fractures (veins) from the same deformation event show displacements ranging over 6 orders of magnitude. The relative contribution of these structures to the overall extension varies, with large faults (>10 m heave) accommodating about 65%, smaller faults (1–10 m heave) about 25% and veins less than 10% of the overall extension. The heterogeneity of fracture density and strain can be quantified from cumulative plots by applying a non-parametric method based on Kuiper's test. Both the degree and statistical significance of strain heterogeneity can be determined and are shown to be scale-dependent. Thin veins accommodate a fairly constant background strain across the region, whilst thick veins and small faults take up localized higher strains in damage zones around larger faults. Fault-strain is relatively homogenously distributed across the region. The faults and veins do not share the same scaling relationship. Thus, this study shows that it is not possible to simply extrapolate fracture frequencies and strain from fault scale to vein scale, and that the heterogeneity of extensional strain is scale dependent.

Extension in the upper crust is largely accommodated by slip and opening on fractures, producing faults, joints and veins. This brittle deformation occurs over a wide range of scales from the grain-scale up to major fault zones with kilometre displacements.

Fault zones are commonly composed of a fault core, where most of the displacement is accommodated, and an associated damage zone that is mechanically related to the growth of the fault zone (e.g., Caine *et al.* 1996; Billi *et al.* 2003). These higher strain zones are surrounded by lower strain regions.

The aim of this study is to measure the displacement and extension accommodated on a range of structures belonging to a single deformation phase, varying from faults with displacements of several 100 m to small veins with openings of <0.1 mm. From these measurements we address a number of important questions regarding the deformation:

1. What is the relative importance of faults and veins in accommodating the total strain?
2. What are the spatial relationships between localized and distributed deformation?
3. Is strain accommodated in a scale-invariant or scale-dependent manner across the structures in an extensional region?

We selected a set of extensional faults from around Kimmeridge Bay in southern England for the study. The area displays a series of north–south trending normal faults and associated fractures that intersect the generally east–west trending coastline at a high angle, with cliffs providing two continuous sections several kilometres in length. The competent carbonate beds within the Kimmeridge Clay have thicknesses of 0.1–2 m and are very useful marker-beds as they can be traced and correlated across the entire study area (Morgans-Bell *et al.* 2001). This allows displacements to be accurately measured on faults over a wide range of scales (Hunsdale & Sanderson 1998). Fault displacements of up to 5 m can be directly measured in the cliffs and larger displacements can be inferred using stratigraphic separation across faults and fault orientation measurements. Associated veins have openings that can be measured to <1 mm. In addition there is a high-resolution seismic section available (Hunsdale *et al.* 1998) that runs parallel to the cliff section (Fig. 1).

Geological overview

The type section of the Upper Jurassic Kimmeridge Clay at Kimmeridge Bay consists mainly of mudrocks with some intercalated white coccolithic limestones and minor grey and yellow limestones and dolostones (Morgans-Bell *et al.* 2001). The shale:carbonate ratio of the exposed section is about 13:1. The rocks form part of the Wessex Basin and the Kimmeridge Clay has long been recognized as a major source rock for North Sea

From: WIBBERLEY, C. A. J., KURZ, W., IMBER, J., HOLDSWORTH, R. E. & COLLETTINI, C. (eds) *The Internal Structure of Fault Zones: Implications for Mechanical and Fluid-Flow Properties*. **299**, 97–111.
DOI: 10.1144/SP299.6 0305-8719/08/$15.00

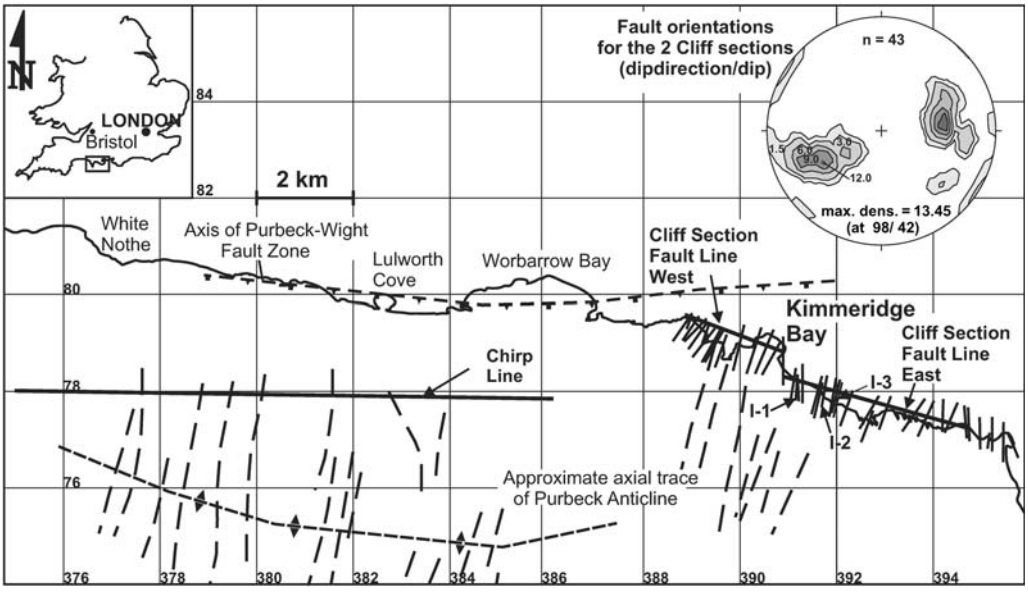

Fig. 1. Map of the study area around Kimmeridge Bay, Dorset. Long dashed lines show fault traces mapped by Donovan & Stride (1961). Short dashed lines indicate approximate positions of the Purbeck–Wight Fault Zone and the axial trace of the Purbeck Anticline. Mapped faults along the cliff sections east of Kimmeridge Bay are shown as short black lines. Positions of the Chirp line, the two fault lines and the three integrated lines are shown. Coordinates refer to the British National Grid.

oil, although, at its type locality in Dorset, the succession is immature, having experienced only modest burial (Farrimond *et al.* 1984).

The Wessex Basin underwent north–south extension from Permian to mid-Cretaceous times, leading to the development of a series of normal faults, sometimes reactivating basement structures (Chadwick 1985; Karner *et al.* 1987; Lake & Karner 1987; Underhill & Stoneley 1998). Major basin-bounding and intra-basinal faults strike east–west and all major faults dip to the south. Active crustal extension ceased in the Aptian, and the region underwent widespread subsidence, presumed to result from thermal relaxation after the Jurassic and Early Cretaceous crustal stretching (Chadwick 1993). Across the Wessex Basin a thick, flat-lying post-rift sequence of marine sandstones, shales and chalk was deposited during Aptian to Danian.

There is evidence for a change of structural style in the Wessex Basin in the lower Tertiary. The east–west striking normal faults were reactivated in response to north–south compression (Chadwick 1993), leading to widespread inversion structures, such as the Purbeck Anticline that lies just to the north of the sections examined in this paper.

During Oligocene–Miocene times, the north–south compression led to the development of conjugate strike–slip faults in some areas (e.g., north Somerset, Peacock & Sanderson 1998; Lyme Bay, Harvey & Stewart 1998) and to conjugate, north–south striking extensional faults in the Weymouth Bay region (Hunsdale & Sanderson 1998). This late extensional event produced the normal faults and veins that are the subject of this study.

Hunsdale & Sanderson (1998) analysed the frequency of fault throws (vertical component of separation) over four orders of magnitude (1 mm to 11 m) by integrating map and field data from the coast around Kimmeridge Bay. They found that the faults in the area obey power-law distributions, with a change in scaling exponent from -0.96 for faults with throws >2 m to -0.67 for small faults (throw <1 m). They attributed this change to variations in lithology and layer thickness that influenced the small more than the large displacement faults.

The present paper aims to take these fracture population studies a step further. Instead of analysing fault-size populations, we focus on the accommodation and spatial variation of strain at different scales across the region, and examine the relative importance of extensional fractures and faults in taking up the regional strain. Compared with Hunsdale & Sanderson (1998), we extend the sampled range of displacements from 4 to over 6 orders of magnitude and include extensional fractures (veins) in addition to normal faults.

Methods

In this study extension is measured as the one-dimensional (longitudinal), bed-parallel increase in length of a marker layer compared with its initial length. As the beds are flat-lying at Kimmeridge, the extension accommodated by discrete structures is easily quantified by summing the bed-parallel components of fault displacements (heaves) and the bed-parallel thicknesses (apertures) of steeply dipping veins. To do this in a consistent manner, over the entire scale-range and across different structures, data were collected along straight lines oriented at high angles to the regional trend of the faults. For each fracture encountered along a traverse we measured its distance from the origin of the line, its heave (for faults) or thickness (for veins), and its dip and strike. Errors due to oblique sampling were corrected for by applying the methods described by Terzaghi (1965) and Peacock & Sanderson (1993).

The data can be visualized by plotting cumulative heave against the corrected distance (Figs 2 & 3, solid lines). Throughout this paper we use the term 'heave' to include the aperture of the veins. As the ratio of heave:distance is the one-dimensional extension, the cumulative heave diagrams show the distribution of extension along each sample

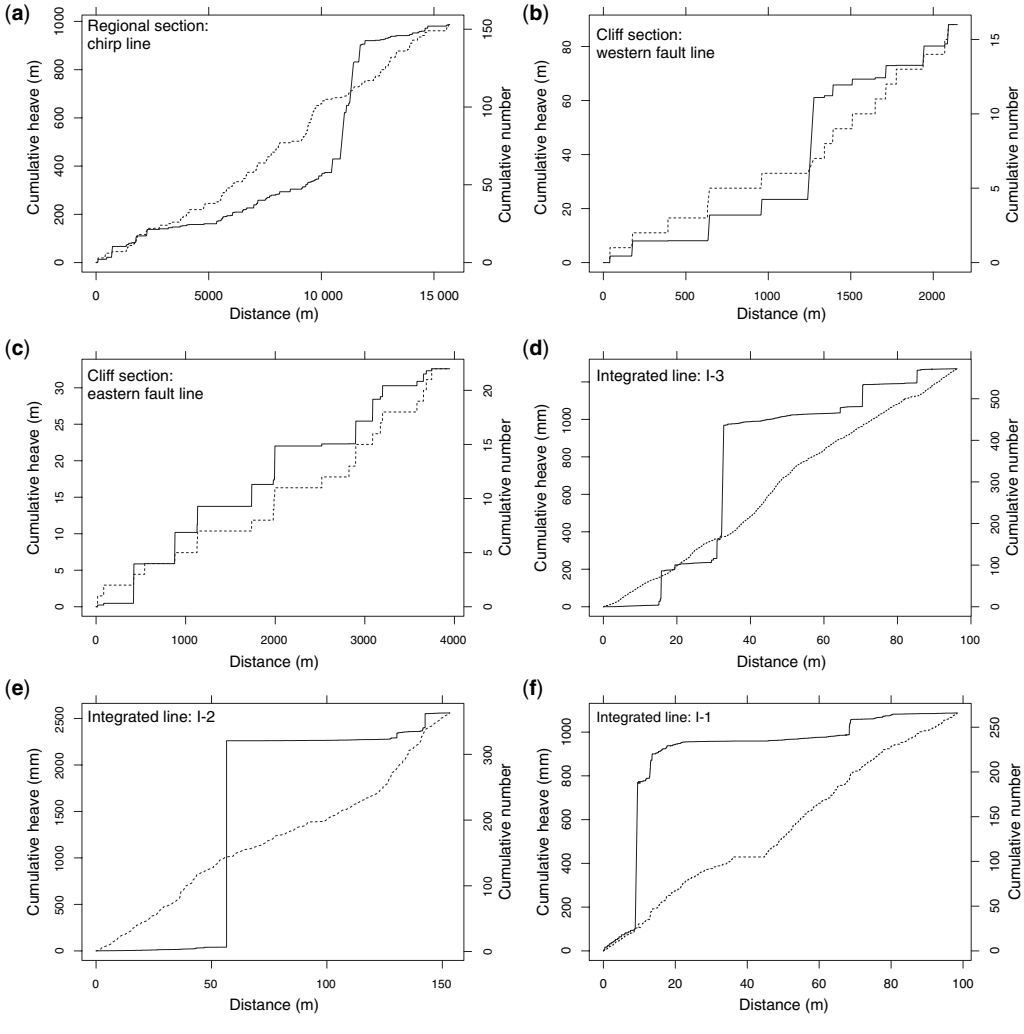

Fig. 2. Cumulative heaves (solid lines) and numbers (dashed lines) plotted against corrected distance (traverse length) for the Chirp line (**a**), the two fault lines (**b**, **c**) and the three integrated lines (**d**–**f**). Left vertical axes show the cumulative heave, right vertical axes show the cumulative number of encountered structures along each line.

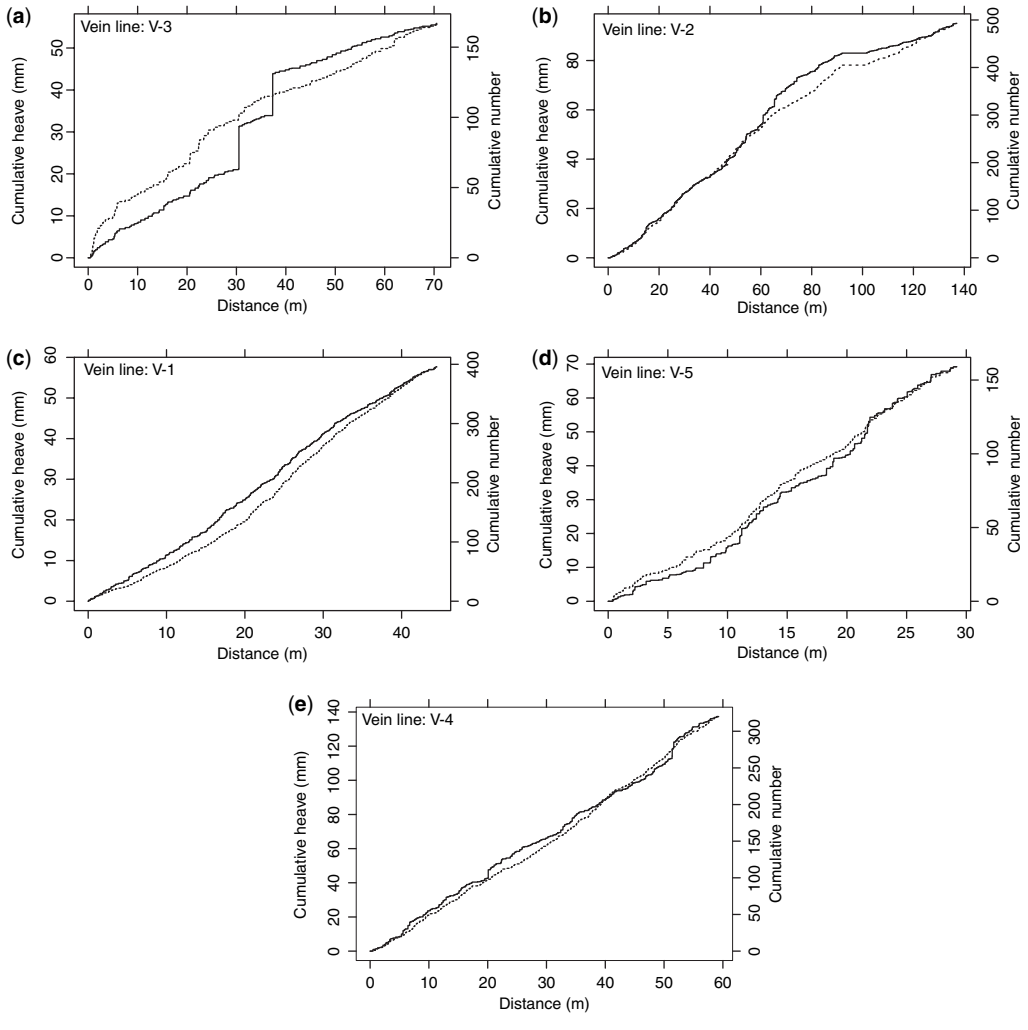

Fig. 3. Cumulative heaves (solid lines) and numbers (dashed lines) plotted against corrected distance (traverse length) for the five vein lines. Left vertical axes show the cumulative heave, right vertical axes show the cumulative number of encountered structures along each line.

line. Low gradients represent smaller extensions, whilst steep slopes represent larger extensions. Constant gradients indicate homogeneously distributed deformation whilst large steps and gradient changes indicate localized deformation.

On plots of cumulative number versus distance (Figs 2 & 3, dashed lines) the gradients represent the fracture frequency. Low gradients indicate low frequencies whilst steep slopes represent high frequencies. Constant gradients indicate homogenously distributed fractures whilst varying gradients indicate heterogeneously spaced fractures.

A compilation of all data are shown in Figure 4 and Table 1 summarizes locations and observations of the data sets. The combination of seismic and field data covers a size-range of more than 6 orders of magnitude. Thin sections locally add another 2–3 orders to the lower end of this scale-range. The sampled scale-range is close to the total scale-range to be expected in an extensional setting of the dimensions of our study area.

Results

The data from the Kimmeridge area can be separated into four groups based on their spatial extend and the type of structures sampled. Throughout this section we describe observations from the

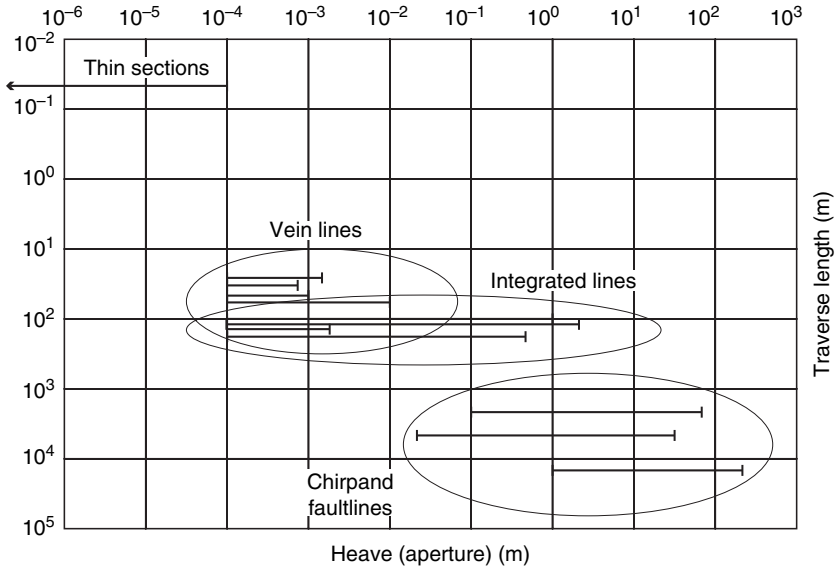

Fig. 4. Plot of sampled range of heaves (compare with Table 1) against traverse length for all line samples. Chirp and fault lines sample faults with $0.1 <$ heave < 200 m over distances of about 2.1–15.7 km. Vein lines trace single beds at great distance from faults encountering only veins with a heave-range of 0.1–10 mm with traverse lengths ranging from about 30 to 140 m. Integrated lines sample both veins and faults as they trace single beds through fault zones. Thin sections locally add >2 orders of magnitude to the lower end of the scale range.

various sample lines in terms of the respective scale and resolution of the line. Although strain is discontinuous, being accommodated by displacement on discrete fractures, it may be regarded as continuous at length scales $>>1$ m if the cumulative heave v. distance graph is close to a straight line trend (Fig. 2). A more rigorous attempt to quantify the heterogeneity of extension and its scale dependency follows in the next sections. Here we discuss the observations in a qualitative (descriptive) manner.

Regional line

The high resolution seismic section was acquired using a Chirp system (Hunsdale *et al.* 1998), hereafter referred to as the *Chirp line*. This runs parallel to the Dorset Coast and is oriented at a high angle to the main fault trend (Fig. 1). It has a length of 15.7 km and intersects 153 resolvable faults with displacements ranging from 221 to 0.5 m. The vertical separation of prominent reflectors is used to determine fault throw, which was converted to heave (bedding parallel displacement component) using the fault dip.

The cumulative heave plot (Fig. 2a, solid line) for these data shows a total resolved fault-extension of 6.7%. The section is dominated by a high strain zone between 10.5 and 12 km that takes up about two-thirds of the extension. The rest of the extension appears to be continuously distributed along the line at length scales $>>100$ m. The 10 km section to the west of the high strain zone shows a resolved extension of about 4% whereas to the east, closer to Kimmeridge Bay, it is lower at $<2\%$. The fault-frequency graph (Fig. 2a, dashed line) shows that fault-spacing is relatively homogenous with an average spacing of about 100 m.

Fault lines

Two cliff sections were measured for 2.14 and 3.95 km to the west and east of Kimmeridge Bay, respectively. These lines record all faults along the sections and are hereafter referred to as *fault lines*. Fault heaves were directly measured where displacements are small (≤ 5 m) and calculated from stratigraphic separation and fault dip where displacements are high (≥ 5 m). The stratigraphic separation is defined as the stratigraphic thickness between horizons on either side of a fault that were brought next to each other due to the displacement on the fault. By using the detailed graphic logs of Morgans-Bell *et al.* (2001), fault displacements can be estimated with accuracies of about ± 0.2 m. The continuous exposure along the sampled sections permits recording of all faults with displacements ≥ 0.2 m (Fig. 2b & c).

Table 1. *Summary of field observations and positions of the 11 line samples*

Name of line	Distance (m)	Sample size (1)	Minimum heave (m)	Maximum heave (m)	· Heaves (m)	Bed thickness (m)	Average fracture spacing (m)	Positive start (m)	Positive end (m)
Chirp	15 700	153	0.33	192	987	×	102.61	E: 374974, N: 77999	E: 390898, N: 77995
Fault E	3947.9	22	0.02	5.4	32.6	×	179.45	E: 394738, N: 77282	E: 390938, N: 78350
Fault W	2144.2	16	0.09	37.76	88.12	×	134.01	E: 390948, N: 78862	E: 388939, N: 79611
I-1	98.33	267	1.00×10^{-4}	0.666	1.088	0.4	0.332	E: 391197, N: 78249	E: 391103, N: 78310
I-2	153.21	363	1.00×10^{-4}	2.22	2.56	1.7–2.0	0.402	E: 391899, N: 77891	E: 391661, N: 78037
I-3	96.21	572	1.00×10^{-4}	0.58	1.2704	0.09–0.11	0.168		E: 391968, N: 77749
V-1	44.484	396	1.00×10^{-4}	6.00×10^{-4}	5.77×10^{-2}	0.56 (0.92)	0.112	E: 393738, N: 77475	E: 393699, N: 77494
V-2	137.02	493	1.00×10^{-4}	1.00×10^{-3}	9.51×10^{-2}	0.3	0.257	E: 392424, N: 77577	E: 392232, N: 77642
V-3	70.58	167	1.00×10^{-4}	1.00×10^{-2}	1.34×10^{-1}	0.2 (0.4)	0.423	E: 394141, N: 77293	E: 394077, N: 77224
V-4	60.2	321	1.00×10^{-4}	4.00×10^{-3}	5.59×10^{-2}	0.55–0.65	0.188	E: 399785, N: 76954	E: 399726, N: 76969
V-5	29.2	160	1.00×10^{-4}	2.00×10^{-3}	6.92×10^{-2}	0.35 (0.55)	0.184	E: 398456, N: 398427	E: 398427, N: 76629

The positions are given as start and end points of each line in BNG coordinates.

The two *fault lines* show lower total extension than the *Chirp line*, due mainly to them not crossing any major fault zones. The largest faults encountered have heaves of about 40 m (western fault line) and 5.4 m (eastern fault line), compared with the maximum heave of 192 m on the Chirp line. However, the average fault spacing and extensions recorded for the *fault lines* compare well with the lower strain zones (0–10 km and 12 km to end) surrounding the high strain zone in the Chirp data set.

The western fault line has a length of 2.14 km and a total resolved fault extension of 4.3%, which is comparable to the western portion of the Chirp line (0–10 km). It encounters 16 faults over a distance of about 2.14 km, i.e. an average fault spacing of 134 m. Both strain distribution and fault spacing (Fig. 2b) appear heterogeneous on this scale of observation with one fault in the centre of the line accounting for about two-fifths of the total resolved extension.

The eastern fault line (Fig. 2c) encounters 22 faults over a distance of 3.95 km, i.e., an average fault spacing of 180 m. The total resolved extension along this section is only 0.8%. Both strain and fault spacing are fairly homogenously distributed along the line.

Bed-scale sections

Eight data-sets were collected by tracing single beds over distances of 30–150 m, sampling all structures observable with the naked eye (thickness $\geq$ 0.1 mm). To cover the entire variability in strain we aimed to sample both low-strain zones, deformed almost exclusively by veins (*vein lines*), and deformation zones that comprise both faults and veins (*integrated lines*), as well as transitions between these. Vein apertures were measured using a 10× magnifier with an integrated 0.1 mm scale.

Integrated lines. The three *integrated lines* cover a total length of about 350 m. All of them trace single beds across small fault zones with heaves between 1.1 and 2.5 m. The wall-rock deformation adjacent to the faults is represented by zones of slightly increased strain compared with the background extension, and can be seen as a change in slope of the heave-distance graph (Fig. 2d–f). The increase in strain is mainly accommodated by greater dilation of veins rather than by nucleation of additional veins, as can be seen from the cumulative number v. distance graphs. Line I-3 shows a damage zone extending for about 20 m from the fault into hanging wall and footwall, with the footwall showing more intense deformation than the hanging wall (Fig. 2d). Line I-2 (Fig. 2e) shows

asymmetric wall-rock deformation with most of the fault-related strain accommodated in its footwall within a zone of about 15 m. Line I-1 displays symmetric wall-rock deformation extending about 15 m into the hanging wall and footwall of the fault (Fig. 2f).

The fracture spacing along each line is fairly constant, as can be seen in the cumulative number v. distance graphs (Fig. 2d–f) that are close to straight line trends. The extensional fractures in these lines display a positive correlation between fracture-spacing and layer-thickness (Table 1). The average fracture spacing increases from 0.17 m in a 0.1 m thick bed (line I-3) to 0.4 m in a 2 m thick bed (line I-2).

Vein lines. The five *vein lines* sample a total length of about 340 m (Fig. 3). They trace single beds within un-faulted regions at distances of at least 50 m from the closest fault. Extension along these lines is accommodated by veins with apertures between 0.1 and 10 mm, but most commonly these are between 0.1 and 0.5 mm. Line V-3 (Fig. 3a) shows the widest range of vein thicknesses (10^{-4}–10^{-2} m) and relatively high variation in fracture spacing. All other *vein lines* show more regular distributions of both extension and fractures, with average fracture spacings between 0.1 and 0.3 m and cumulative extensions between 0.07 and 0.24%. No direct relationship between fracture spacing and layer thickness was found. The observed variation may be related to varying distances from the closest fault zone and/or may be due to different lithologies (different rheological behaviour) of the sampled beds.

Thin sections. Twelve samples for thin sectioning were taken from the bed-scale sections, both within fault damage zones and far from faults. The aim was to investigate the contribution of microfractures (with thicknesses $\leq$0.1 mm). No fractures with apertures that could not be resolved with naked eye were observed in thin section. We conclude that veins with apertures $<$0.1 mm are rare in the Kimmeridge Clay, and that field observations in good outcrops record virtually all of the significant discrete deformation. This result is supported by the absence of deformation of ammonites, even close to faults. If there was a measurable 'microscale' component of extension, it would be recorded by shape changes of bedding parallel ammonites. Based on these observations, a lower limit for the displacement scale range in our study area can be given with 0.1 mm thickness (heave). It should, however, not be assumed that this lower limit will apply to other rock units and locations.

Damage zones around faults

Field observations and the *integrated lines* (Fig. 2d–f) show that extension increases adjacent to most of the faults. For this study we define damage zones as regions of increased strain (usually $>>$0.1%) compared with the observed background extension of $\sim$0.1%. Damage zones were found to extend typically for 10–20 m on either side of the fault. The width of the damage zone is largely independent of the displacement on the fault for heaves between 0.1 and 40 m. Within the damage zones there is no consistent increase in the fracture density. The observed range of fracture spacing lies between 0.17 and 0.4 m, and is largely independent of the local strain.

Thus the higher extensional strains in the damage zones are accommodated by increased opening of existing fractures rather than by the nucleation of new fractures. In the carbonate beds, this opening often leads to the development of pull-aparts (Peacock & Sanderson 1995) linked to small faults splaying from the main fault.

Spatial heterogeneity of fracturing and extension

Two simple tests have been used to assess the heterogeneity of fracturing and strain from the line samples. The first is the calculation of the coefficient of variation of the fracture spacing; the second involves use of a non-parametric test for the cumulative curves (as in Figs 2 & 3) that can be applied to both the fracture frequency and extension.

The *coefficient of variation* is the ratio of the standard deviation (s) to the mean (m) of the fracture spacings, i.e. $C_V = s/m$. For small samples, it is better to use $C_V^* = C_V[(n+1)/(n-1)]^{1/2}$, where n is the sample size (Gillespie *et al.* 2001; Gillespie 2003). A random sample from a uniform distribution should have a negative exponential distribution of fracture spacings, in which case the standard deviation is the same as the mean ($s = m$), hence $C_V = 1$. Traverses in which the fractures are clustered should have $s > m$ and $C_V > 1$, whereas for more regularly spaced (anticlustered) fractures $s < m$ and $C_V < 1$. This way of characterizing fracture spacing has been discussed by Ackermann *et al.* (2001), Gillespie *et al.* (2001) and Gillespie (2003). The values for C_V^* are listed in Table 2. Most lines show $0.7 < C_V^* \leq 1$, suggesting that the fracture distribution is close to random (uniform), apart from the Chirp line, where the faults seem to be slightly clustered ($C_V^* = 1.4$). This test is useful for analysing fracture

Table 2. *Summary of statistical data of the 11 line samples*

Name of line	Chirp	Fault E	Fault W	I-1	I-2	I-3	V-1	V-2	V-3	V-4	V-5
Sample size	153	22	16	267	363	572	396	493	167	321	159
Overall extension	6.7	0.8	4.3	1.12	1.7	1.3	0.13	0.07	0.08	0.23	0.24
C_V^*	1.4	1.02	0.74	0.82	0.84	0.71	0.88	0.82	1.01	0.81	0.79
V'	0.459	0.261	0.411	0.691	0.853	0.572	0.096	0.136	0.311	0.086	0.172
V^*	5.68	1.22	1.84	11.29	11.97	13.68	1.91	2.42	4.02	1.53	2.18
Statistical significance	***	n.s.	*	***	***	***	**	***	***	n.s.	***
Bin strains (%)											
300–100 m	2.391	×	×	×	×	×	×	×	×	×	×
100–30 m	1.179	0	1.837	×	×	×	×	×	×	×	×
30–10 m	1.157	0	0	×	×	×	×	×	×	×	×
10–3 m	1.112	0.362	2.116	×	×	×	×	×	×	×	×
3–1 m	0.667	0.356	0.221	×	×	×	×	×	×	×	×
1–0.3 m	0.203	0.076	0.095	×	×	×	×	×	×	×	×
0.3–0.1 m	×	0.035	0.009	×	×	0.277	×	×	×	×	×
10–3 cm	×	×	0.009	0.041	0	0.176	0	0	0	0	0
3–1 cm	×	×	×	0.098	0	0.112	0	0	0	0	0
10–3 mm	×	×	×	0.152	0.011	0.032	0	0	0.028	0.021	0
3–1 mm	×	×	×	0.082	0.007	0.020	0	0.107	0.001	0.030	0.069
1–0.3 mm	×	×	×	0.036	0.012	0.052	0.018	0.257	0.012	0.117	0.108
0.3–0.1 mm	×	×	×	0.013	0.011	0.030	0.047	0.380	0.027	0.050	0.045
≤0.1 mm	×	×	×	0.008	0.007	0.023	0.065	0.240	0.010	0.015	0.016

C_V^* is the modified coefficient of variation of fracture spacing after Ackermann *et al.* (2001) and Gillespie (2003). V' and V^* are the test results for Kuiper's non-parametric test applied to the cumulative heave data for all lines. V' is a measure of the departure from a uniform distribution with $0 < V' < 1$. Asterisks indicate statistical significance at probabilities of 0.005 (***), 0.01 (**) and 0.05 (*) respectively. 'n.s.' stands for 'not significant'. Bin strains for each data set are in percentage extension. '×' means that the scale range of the respective data set does not cover this heave-bin.

spacing but cannot be easily adapted to investigate the strain distribution.

As already noted, a uniform distribution of fracture density or extension would be represented on a cumulative plot by a straight line (Fig. 5). The extent to which the observed data conform to a uniform distribution can be tested using non-parametric Kolmogorov–Smirnov tests (K–S tests). The simplest of these is based on the maximum deviation (D^{max}) of the observed values from the straight line cumulative curve (Conover 1980). The value of D^{max} is strongly dependent on its position (distance) on the cumulative plot. For this reason, Kuiper (1960) developed a variant of the K–S test that utilizes D^+ and D^-, which represent the maximum deviation above and below a cumulative distribution function (see Fig. 5). Kuiper's test uses the quantity $V = |D^+| + |D^-|$. To allow comparison of cumulative heave data over different lengths and scale ranges, the quantity V (or D^+ and D^-) needs to be normalized by dividing by the cumulative total (T), $V' = V/T$, where $T =$ number of fractures (n) or $T = \Sigma$(heaves) for fracture frequency or extension, respectively.

V' is a measure of the departure from a uniform distribution, hence a measure of heterogeneity. Values of V' vary from 0 (homogeneous) to 1 (heterogeneous). One important property of Kuiper's test is that it is as sensitive in the tails as near the median of the cumulative curve, a feature not shared by tests based on D^{max}. This means that the values of V' are less dependent on the starting point of the traverse in relation to the greatest concentration of fractures or extension.

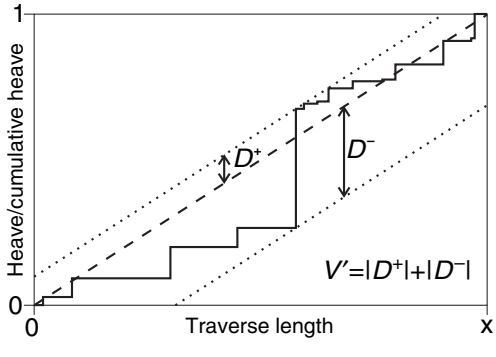

Fig. 5. Diagram to illustrate the application of Kuiper's test. The straight dashed line shows the uniform distribution and the solid line the observed cumulative heave (normalized). The two dotted lines indicate an 'envelope' defined by the maximum deviations from the uniform distribution above (D^+) and below (D^-) the uniform distribution. The test statistic in Kuiper's test is the quantity $V' = |D^+| + |D^-|$, which varies between 0 (homogenous) and 1 (heterogeneous).

Before discussing this variation in heterogeneity further, we should seek to establish that the suggested heterogeneity is statistically significant, taking into account the magnitude of V' and the sample size, n. To do this, Stephens (1965) (see also Mardia 1972) proposed a parameter $V^* = n^{1/2}V'$ for Kuiper's test, and tabulated critical values for rejection of the null hypothesis of the uniform distribution. For large n, say >50, the critical value is $V^* \approx 1.7$ at the 0.05 (5%) level. Values of V^* are listed in Table 2 together with an indication of the statistical significance. Only the Eastern fault line and line V-4 are not significantly different from a uniform distribution (at the 0.05 level), with all other lines showing a heterogeneous strain distribution.

Having established that the determined heterogeneities are statistically significant, we can now discuss the results of Kuiper's test applied to the 11 cumulative heave curves (Fig. 6). V' values for all lines are plotted against the maximum heave included in each data set. In the *vein lines*, strain is accommodated by opening extensional fractures (veins), with apertures in the range 0.1–10 mm. The heterogeneity is weak ($V' < 0.2$), but the large sample sizes make these values statistically significant (Table 2). In the *integrated lines* that cross the damage zones of one or more small faults, strain is mainly accommodated by small faults and pull-aparts with heaves of 10–100 mm. These show much higher heterogeneity ($V' > 0.5$), with the large sample sizes making these results highly significant. On the *Chirp line* and the two *fault lines*, most of the strain is accommodated on faults with heaves of >1 m. These show some heterogeneity ($0.2 < V' < 0.5$), but the small sample sizes of the fault lines make these estimates less certain and we cannot reject a uniform model for the Eastern fault line. There is some suggestion that heterogeneity may also be increasing for the larger faults (>100 m heave), with localization of strain onto the largest faults.

Frequency/extension at different scales

The lines were designed to sample structures across different scales ranges, allowing the strains accommodated in different heave intervals to be determined. The data from each line were binned using steps of half an order of magnitude (*c*. $\log_{10}3$) and the results are shown in Table 2 and Figure 7a. This shows that higher strains are associated with faults that have heaves in excess of 0.5 m and that data consisting dominantly of veins (i.e., heaves <0.01 m) show extensions of 0.1% or less.

An interesting observation from the Chirp and fault lines is that, almost independent of the total

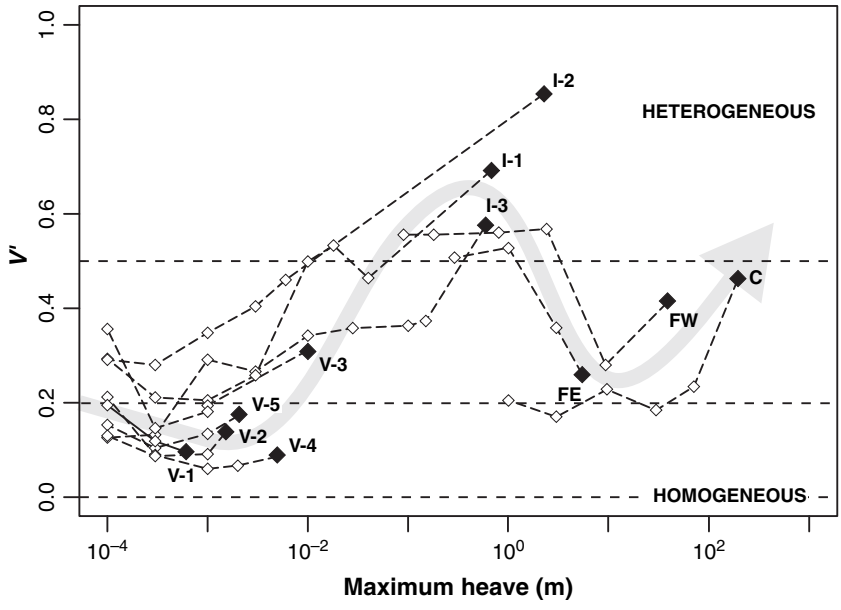

Fig. 6. V' values plotted against the maximum heave for each sample line. The values for complete data sets are shown as solid diamonds for the Chirp line (C), western (FW) and eastern (FE) fault lines, integrated lines (I-1 to I-3) and vein lines (V-1 to V-5). The 'tails' (open diamonds connected by dashed lines) to the left of each solid diamond were derived by successively removing the largest structures (heaves) from the complete data sets – see text for further explanation. The grey arrow emphasizes the observed scale dependence of heterogeneity.

strain in each section, faults with heaves <3 m accommodate $<1\%$ extension. On the other hand, the larger the encountered faults, the higher the total extensions. This clearly shows that extension is localized by concentrating slip on large faults rather than by increasing the number of small fractures. This has also been observed for faults on seismic sections (e.g., Meyer *et al.* 2002).

To assess the proportion of the total strain that is accommodated by structures of a certain size range, cumulative heave v. distance plots for the Chirp and fault lines have been constructed, with successive removal of the higher heave structures (Fig. 7b–d). The uppermost curve in each diagram includes all sampled structures. The other lines are cumulative heave plots excluding faults above certain displacement values in steps of half an order of magnitude. The left-hand vertical axes show the cumulative heaves, whilst the right-hand vertical axes show the total resolved extensions. The successive removal of the larger heave faults reduces the overall extension, especially down to about 10 m. The cumulative curves also become smoother, suggesting that the smaller-scale structures are more homogenous.

The heterogeneity for each data set has also been analysed for the cumulative plots by successively removing the largest binned heave values. The derived V' values are plotted against maximum heave for each data set (Fig. 6) as a series of 'tails' to the left of the complete datasets. One interesting feature is that the 'tails' tend to link the different type of sample line. Thus, elimination of the larger faults in the *Chirp line* reduces the heterogeneity towards that of the *fault lines* and elimination of the faults in the *integrated lines* reduces the heterogeneity towards that of the *vein lines*. There is even some suggestion that elimination of larger faults in the *fault lines* leads to increasing heterogeneity (towards that of the *integrated lines*), but the reduction in sample size from the already small values of the fault lines increases the uncertainty in the values of V'.

Strain scaling

Having assessed the spatial and scale heterogeneity of fracturing in each sample line, we are now in a position to analyse the relative contribution of smaller and larger structures to the total brittle strain of the region over the entire scale range. To do this we need to develop methods of combining and comparing data from the different lines. A key to achieving this is to assess if faults, damage zones and background strains between faults have

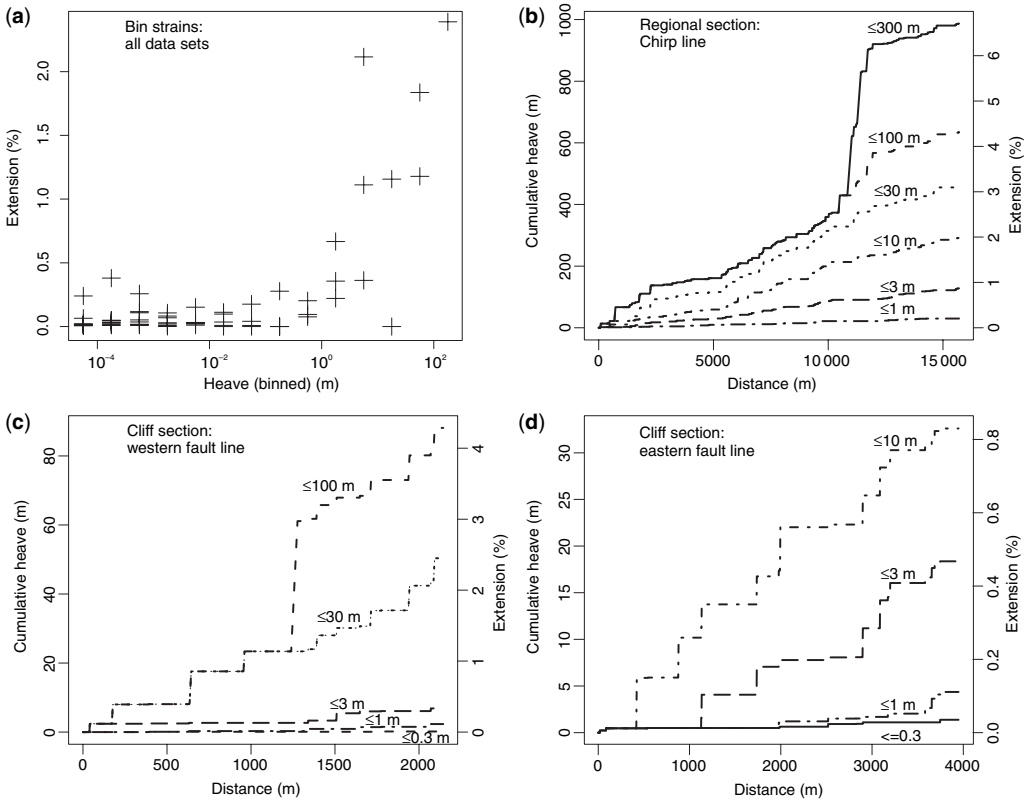

Fig. 7. (**a**) Extensions plotted for half-order-of-magnitude bins (+). Cumulative heave v. corrected distance plots for the Chirp (**b**) and fault lines (**c**, **d**) with successive removal of the higher heave structures in half-order-of-magnitude steps. The uppermost curve in each diagram includes all sampled structures of the respective line. Labels on the graphs indicate the included heave-ranges.

been sampled in a way that is representative of the population.

The fault-data (Chirp and fault lines) cover a total sampled distance of 21.9 km. Based on these data, the average fault spacing at Kimmeridge Bay is about 115 m and is similar on both types of line. The Chirp line and the two fault lines also cover a similar heave range. Hence, we treat each of these as an independent sample of the faulting and simply add together the data from each to provide estimates of the fault density and strain.

Field observations along the cliff sections and integrated lines (Fig. 2d–f) show that wall-rock deformation adjacent to faults typically extends for about 10–20 m (average observed extent: 15 m) into the footwall and hanging wall and that the extent of these deformation zones is largely independent of the fault size. Based on these observations, the expected ratio of damage zones to background-strain regions can be estimated as 30 m: (115–30 m) ≈ 1:3 (Fig. 8). Within the Kimmeridge area, the small-scale deformation (veins and joints) was sampled in eight traverses over a total distance of 690 m. This comprises about 180 m within damage zones with extensions >0.1% and 510 m with background strains (≤0.1% extension), giving a ratio of damage zone:background strain of *c*. 1:3. Thus, at least approximately and quite fortuitously, we appear to have sampled the high-strain and low-strain regions between large faults in about the correct proportions, and simply combine these data to get a representative sample of the bed-scale fractures.

The extensions for each half-order-of-magnitude bin are listed in Table 2, and plotted against heave-intervals in Figure 9 (crosses). This shows the range of observed extension values accommodated by structures of differing sizes. The solid lines in Figure 9 represent the average extension values per bin. These plots show that the extension in each heave interval is low (*c*. 0.1%) up to a heave of about 0.1 m, and is accommodated entirely by the opening of veins. The data are scattered,

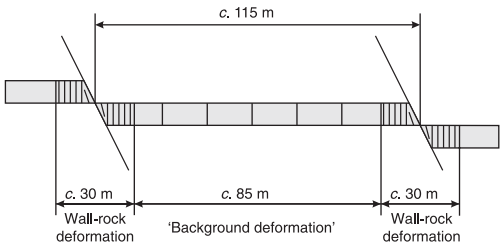

Fig. 8. Schematic section showing typical dimensions of damage and inter-fault zones at Kimmeridge Bay. The average fault spacing (derived from Chirp and fault lines) is about 115 m, with damage zones typically extending for about 15 m into footwalls and hanging walls, leaving a zone of background deformation of about 85 m in between two faults.

reflecting the varying contributions of veins to the background strain and to the development of damage zones around faults. Above about 0.3 m, the extension is accommodated by faults and increases in each bin with increasing heave. The data are much less scattered, indicating that the faults show a fairly well-ordered scaling, with larger faults contributing more to the overall strain.

Similarly the number of structures within half-order-of-magnitude bins can be plotted for the heave-intervals (Fig. 10). These show a rapid decrease from a few fractures per meter at the millimetre-scale heaves to <1 per 100 m for metre-scale faults. From these data we calculate that about 500 extensional fractures might be expected for each observed fault. If we only consider large faults, such as would be observable on a commercial seismic line (say 10–20 m throw), we might expect 10–30 'sub-seismic faults' and 5000–15 000 extensional fractures for each fault. These numbers are probably strongly dependent on the lithology and thus can only be taken as estimates for interbedded mudstones and limestones similar to the Kimmeridge Clay.

These data appear to conform to a power-law distribution (Fig. 10), as reported widely for faults and fractures (Walsh *et al.* 1991; Jackson & Sanderson 1992; Marrett & Allmendinger 1992; Pickering *et al.* 1994). In Figure 10b the average number of fractures in each bin is plotted on a log–log scale. The large faults ($\geq$10 m) conform to a power-law distribution, as do the veins ($<$0.1 m), both having scaling exponents of $\sim$0.95, with correlation coefficients $R^2 > 0.98$. Note that these plots are for discrete bins and not the more conventional cumulative plots where the ranking of the data always generates high R^2 values (Pickering *et al.* 1995). The veins and faults are clearly separated by a transitional region at heaves of between 0.1 and 10 m, and do not form part of the same power-law distribution. A similar transition was found by Hunsdale & Sanderson (1998) in their study of the scaling of fault frequencies at Kimmeridge, but this was between faults cutting many beds and micro-faults confined to a single carbonate bed (the Whitestone Band). The vein population in the present study represents opening mode fractures that are developed in most of the carbonate beds and has a different scaling exponent (0.98) to that for the layer-confined micro-faults (Hunsdale & Sanderson, 1998). These results support the transition in the scaling of the strain discussed previously.

Extrapolation of the fault frequencies to the millimetre-scale would predict about 10 faults per

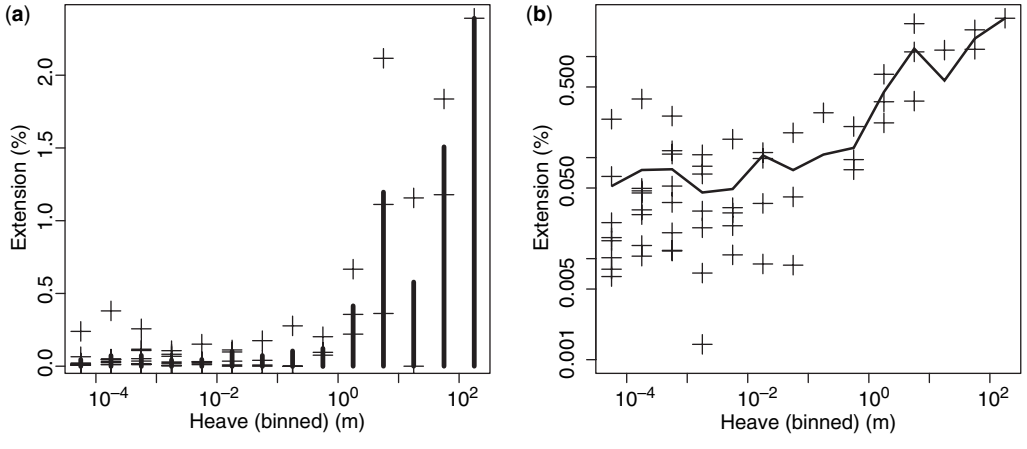

Fig. 9. Extensions for half-order-of-magnitude bins (+) plotted against heave-intervals in log–linear space (**a**) and log–log space (**b**). The solid lines represent the average extension values plotted as a histogram in (a) and as a moving average in (b).

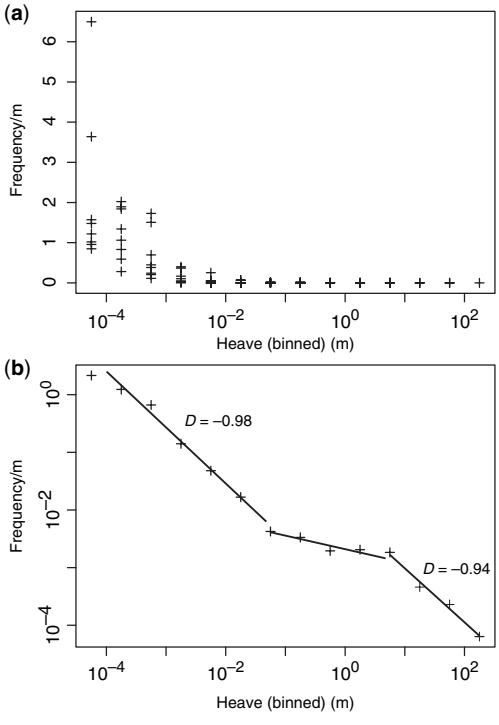

Fig. 10. Frequency (number/m) of structures (+) plotted against heave in half-order-of-magnitude bins in log–linear (**a**) and log–log (**b**) space. In (b) the average frequency for each bin is plotted. The three solid lines are best fit power-law trends through the data for different scale ranges.

metre. Such high densities are not generally observed in our study area, even in damage zones, and deformation at this scale is accommodated by one to three veins per metre. Again, these observations may be typical for interbedded mudstones and limestones but may not apply to other lithologies.

Conclusions

Fractures are responsible for producing an extension of about 7% in the rocks at Kimmeridge Bay. This is accommodated by both slip on faults and opening of extension fractures to produce veins. The relative contribution of these structures to the overall extension in this inter-bedded mudstone–limestone sequence varies, as follows:

- Large faults, with heaves of >10 m, accommodate about 65% of the total extension, which would be resolvable by high-quality commercial seismic surveys.
- Smaller faults, with heaves of 0.1–10 m, accommodate about 25% of the total extension.
- Opening mode fractures (veins) are very numerous, but account for less than 10% of the overall extension.

For the analysis of cumulative plots of heave (bed-parallel extension) along line samples, a simple non-parametric method, based on Kuiper's test, is used to assess both the degree and statistical significance of heterogeneity. This, together with the scale-dependence of strain, allows us to recognize three different patterns of strain distribution:

1. Extensional fractures are widely distributed, with fracture spacing in carbonate beds varying between 0.1 and 0.4 m with an average of about 0.3 m. The variation is probably caused by differences in lithologies and thicknesses between the beds. Opening of these produces thin veins, usually $\leq$0.5 mm in aperture, accommodating a background extension of about 0.1% across the area. This strain can be neglected in terms of the overall extension, but might be of interest for interpretation of the early deformation history and the permeability of the rock units. Extension is fairly homogenously distributed ($0.1 \leq V' \leq 0.3$) across the 0.1–10 mm range of vein opening.
2. Extension increases in the damage zones around faults, with only a small increase of fracture density. The damage zones typically extend 10–20 m into the wall-rock, which appears to be largely independent of the fault heave. Deformation in these zones is mainly achieved by opening (dilation) of fractures to produce veins with apertures of 0.1–10 mm. Pull-apart structures are common in the damage zones and produce veins with up to 100 mm thickness. In interbedded mudstones and limestones, the interaction of faulting and opening-mode fractures produces very heterogeneous strain distributions ($V' > 0.5$) in damage zones around faults. This behaviour may not apply in other lithologies, such as porous sandstones, where strain hardening may lead to nucleation of new faults rather than to opening of veins.
3. Faults with heaves of 1–100 m are developed at a spacing that usually exceeds 100 m. They produce only weak to moderate heterogeneity ($0.2 \leq V' \leq 0.4$) in the strain distribution. There is some evidence of heterogeneity increasing with increasing fault heave, suggesting that strain is localized into large faults at the basin-scale.

Thus the brittle deformation in at least this part of the upper crust occurred over a wide range of

scales and was accommodated by both slip on faults and opening of extension fractures to produce veins. Power-law scaling of the frequency of both veins and faults is found, but these do not share a single power-law relationship. A major change in scaling occurs at the transition between extensional (mode I) and shear (mode II/III) deformation. Thus, it is not possible to simply extrapolate extensions and fracture frequency from one scale-range to the other across structures with differing spatial organization and mechanical significance.

Martin Putz-Perrier acknowledges a Janet Watson PhD Scholarship from Imperial College London. The authors would like to thank Tim Needham and Andrea Billi for constructive reviews of this paper.

References

ACKERMANN, R. V., SCHLISCHE, R. W. & WITHJACK, M. O. 2001. The geometric and statistical evolution of normal fault systems: an experimental study of the effects of mechanical layer thickness on scaling laws. *Journal of Structural Geology*, **23**, 1803–1819.

BILLI, A., SALVINI, F. & STORTI, F. 2003. The damage zone-fault core transition in carbonate rocks: implications for fault growth, structure and permeability. *Journal of Structural Geology*, **25**, 1779–1794.

CAINE, J. S., EVANS, J. P. & FORSTER, C. B. 1996. Fault zone architecture and permeability structure. *Geology*, **24**, 1025–1028.

CHADWICK, R. A. 1985. Permian, Mesozoic and Cenozoic structural evolution of England and Wales in relation to the principles of extension and inversion tectonics. *In*: WHITTAKER, A. (ed.) *Atlas of Onshore Sedimentary Basins in England and Wales: Post Carboniferous Tectonics Stratigraphy*. Blackie, New York, 9–25.

CHADWICK, R. A. 1993. Aspects of basin inversion in southern Britain. *Journal of the Geological Society London*, **150**, 311–322.

CONOVER, W. J. 1980. *Practical Nonparametric Statistics*. Wiley, New York.

DONOVAN, D. T. & STRIDE, A. H. 1961. An acoustic survey of the sea floor south of Dorset and its geological interpretation. *Philosophical Transactions of the Royal Society of London*, **44**, 299–330.

FARRIMOND, P., COMET, P., EGLINTON, G., HALL, M. A., PARK, D. W. & WARDROPER, A. M. K. 1984. Organic geochemical study of the Upper Kimmeridge Clay of the Dorset type area. *Marine and Petroleum Geology*, **1**, 340–354.

GILLESPIE, P. 2003. Comment on 'The geometric and statistical evolution of normal fault systems: an experimental study of the effects of mechanical layer thickness on scaling laws' by R. V. Ackermann, R. W. Schlische and M. O. Withjack. *Journal of Structural Geology*, **25**, 819–822.

GILLESPIE, P. A., WALSH, J. J., WATTERSON, J., BONSON, C. G. & MANZOCCHI, T. 2001. Scaling relationships of joint and vein arrays from The Burren, Co. Clare, Ireland. *Journal of Structural Geology*, **23**, 183–201.

HARVEY, M. J. & STEWART, S. A. 1998. Influence of salt on the structural evolution of the Channel Basin. *In*: UNDERHILL, J. R. (ed.) *Development, Evolution and Petroleum Geology of the Wessex Basin*, Geological Society, London, Special Publications, **133**, 241–266.

HUNSDALE, R. & SANDERSON, D. J. 1998. Fault size distribution analysis – an example from Kimmeridge Bay, Dorset, U.K. *In*: UNDERHILL, J. R. (ed.) *Development, Evolution and Petroleum Geology of the Wessex Basin*, Geological Society, London, Special Publications, **133**, 299–310.

HUNSDALE, R., BULL, J. M., DIX, J. K. & SANDERSON, D. J. 1998. The use of high-resolution seismic reflection profiles for fault analysis in the near-shore environment, Weymouth Bay, Dorset, England, United Kingdom. *Journal of Geophysical Research*, **103**, 15409–15422.

JACKSON, P. & SANDERSON, D. J. 1992. Scaling of fault displacements from the Badajoz Cordoba shear zone, SW Spain. *Tectonophysics*, **210**, 179–190.

KARNER, G. D., LAKE, S. D. & DEWEY, J. F. 1987. The thermo-mechanical development of the Wessex Basin, southern England. *In*: HANCOCK, J. F., DEWEY, J. F. & COWARD, M. P. (eds) *Continental Extension Tectonics*, London, Geological Society, 517–536.

KUIPER, N. H. 1960. Tests concerning random points on a circle. *Proceedings Koninklijke Nederlandse Akademie van Wetenschappen*, **A63**, 38–47.

LAKE, S. D. & KARNER, G. D. 1987. The structure and evolution of the Wessex Basin, southern England: an example of inveresion tectonics. *Tectonophysics*, **137**, 347–378.

MARDIA, K. V. 1972. *Statistics of Directional Data*. Academic Press, London.

MARRETT, R. & ALLMENDINGER, R. W. 1992. Amount of extension on small faults: an example from the Viking graben. *Geology*, **20**, 47–50.

MEYER, V., NICOL, A., CHILDS, S., WALSH, J. J. & WATTERSON, J. 2002. Progressive localisation of strain during the evolution of a normal fault population. *Journal of Structural Geology*, **24**, 1215–1232.

MORGANS-BELL, H. S., COE, A. L. *ET AL.* 2001. Integrated stratigraphy of the Kimmeridge Clay Formation (Upper Jurassic) based on exposures and boreholes in south Dorset, UK. *Geological Magazine*, **138**, 511–539.

PEACOCK, D. C. P. & SANDERSON, D. J. 1993. Estimating strain from fault slip using a line sample. *Journal of Structural Geology*, **15**, 1513–1516.

PEACOCK, D. C. P. & SANDERSON, D. J. 1995. Pull-aparts, shear fractures and pressure solution. *Tectonophysics*, **241**, 1–13.

PEACOCK, D. C. P. & SANDERSON, D. J. 1998. Deformation history and basin-controlling faults in the Mesozoic sedimentary rocks of the Somerset coast. *Proceedings of the Geologists' Association*, **110**, 41–52.

PICKERING, G., BULL, J. M., SANDERSON, D. J. & HARRISON, P. V. 1994. Fractal fault displacements: a case study from the Moray Firth, Scotland. *In*: KRUHL, J. H. (ed.) *Fractals and Dynamic Systems in Geoscience*. Berlin, Springer, 105–120.

PICKERING, G., BULL, J. M. & SANDERSON, D. J. 1995. Sampling power-law distributions. *Tectonophysics*, **248**, 1–20.

STEPHENS, M. 1965. The goodness-of-fit statistic VN: distribution and significance points. *Biometrika*, **52**, 309–321.

TERZAGHI, R. D. 1965. Sources of errors in joint trace surveys. *Geotechniques*, **15**, 287–304.

UNDERHILL, J. G. & STONELEY, R. C. 1998. Introduction to the development, evolution and petroleum geology of the Wessex Basin. *Special Publication of the Geological Society*, **133**, 1–18.

WALSH, J., WATTERSON, J. & YIELDING, G. 1991. The importance of small-scale faulting in regional extension. *Nature*, **351**, 391–393.

Displacement-length scaling for single-event fault ruptures: insights from Newberry Springs Fault Zone and implications for fault zone structure

DAVID A. FERRILL, KEVIN J. SMART & MARIUS NECSOIU

Department of Earth, Material, and Planetary Sciences, Southwest Research Institute®, 6220 Culebra Road, San Antonio, TX 78238-5166, USA (e-mail: dferrill@swri.org)

Abstract: The Newberry Springs Fault Zone experienced slip associated with the 1992 Landers earthquake in the Mojave Desert of California, USA. Detailed analysis of scaling relationships from single-event ground ruptures in the Newberry Springs Fault Zone mapped in the field shows an average maximum displacement to length (D_{max}/L) relationship for fault segments (rupture lengths in the range of 100–1000 m) of 8×10^{-5}–consistent with previously published D_{max}/L ratios for normal fault earthquake ground ruptures (rupture lengths in the range of 1–100 km) of 7×10^{-5}. To explore the ability of remote sensing (interferometric synthetic aperture radar or InSAR) to map small-displacement single-event fault ruptures and add constraints on segment displacements, we applied established interferometry methods with phase unwrapping to produce maps of line-of-sight displacement and displacement gradient. These maps highlight fault traces that experienced displacement during the time between collection of the synthetic aperture radar images. Comparison of published 1992 single-event ground rupture maps with mapping based on photogeologic interpretation of 1950s vintage aerial photographs indicates that most of the 1992 ruptures occurred as reactivation of pre-existing slip surfaces. In general, D_{max}/L for total fault displacement is approximately 100 times D_{max}/L for single-event ruptures. Evidence from the Newberry Springs Fault Zone indicates that, since the Pleistocene, at least 10–20 Landers-like slip events have occurred, reactivating the Newberry Springs Fault Zone. Evidence of wide damage zones and reactivation of individual segments developed in alluvial floodplain deposits, at relatively small (order of metres) fault displacements, supports a conceptual model of fault damage zone width being established early, during fault propagation. With continued displacement by accumulation of additional slip events, fault zone damage intensifies. The fault zone width may remain relatively stable, although the active portion of the fault zone will likely narrow as faulting continues and a throughgoing slip surface develops and accumulates the bulk of displacement.

The past several decades have seen an explosion of effort to characterize the scaling relationships of total displacement for faults. Much of this work has focused on normal faults spanning many orders of magnitude of displacement and fault trace length (e.g., Walsh & Watterson 1988; Cowie & Scholz, 1992*a*, *b*; Dawers *et al.* 1993; Dawers & Anders, 1995; Walsh *et al.* 2002). These scaling relationships address fault displacement that is the product of many slip events. In contrast, work on maximum displacement to length (D_{max}/L) scaling relationships for single-event fault ruptures is more limited (e.g., Bonilla *et al.* 1984; Wells & Coppersmith, 1994; Walsh *et al.* 2002). Understanding characteristics of ground ruptures associated with seismic fault slip is of growing importance to seismic hazard assessment and probabilistic fault displacement hazard assessment. Few detailed studies of single-event fault ground rupture, however, are available for use as inputs to such analyses. These studies have focused primarily on ground rupture dimensions associated with earthquakes, and thus have concentrated on fault ruptures with lengths of *c*. 10–100 km. Resulting scaling relationships (e.g., Wells & Coppersmith 1994) are a primary component of many probabilistic seismic hazard assessments in the western United States, with more limited application elsewhere (e.g., Roberts & Michetti 2004; Roberts *et al.* 2004).

Little work has been performed to explore these scaling relationships below the 10–100 km length scale of principal earthquake ruptures. However, smaller-scale distributed fault ruptures have been investigated, including the density of such distributed fault ruptures (Waiting *et al.* 2003), for purposes of probabilistic fault displacement hazard assessment (Youngs *et al.* 2003) to evaluate direct rupture effects (e.g., fault offset and related fracturing rather than seismic ground motion) of fault slip. Additional data to inform such investigations are still needed.

In this paper we explore the displacement to length scaling of single-event distributed normal

From: WIBBERLEY, C. A. J., KURZ, W., IMBER, J., HOLDSWORTH, R. E. & COLLETTINI, C. (eds) *The Internal Structure of Fault Zones: Implications for Mechanical and Fluid-Flow Properties*. **299**, 113–122.
DOI: 10.1144/SP299.7 0305-8719/08/$15.00

fault ruptures at a range of rupture lengths from 100 to 1000 m. We compare scaling relationships (comparing maximum displacement and fault length) for these short ruptures and the principal normal fault earthquake ruptures compiled by Wells & Coppersmith (1994), and explore single-event ruptures v. cumulative fault displacements. The goal is an improved understanding of the roles of fault propagation v. displacement accumulation during earthquake-related fault slip. The paper includes analysis of field maps of ground ruptures in the Mojave Valley east of Barstow, California, USA (Hart 1994; Unruh *et al.* 1994) along a fault zone north and east of Newberry Springs (hereafter referred to as the Newberry Springs Fault Zone). The Newberry Springs Fault Zone was not recognized prior to the 1992 Landers earthquake, and ruptured coevally with the Landers earthquake. InSAR-derived displacement gradient mapping presented here confirms the timing and extends the field-based interpretations by providing independent confirmation of overall rupture network morphology and displacement values for two ruptures that were previously mapped but for which displacement was not measured. The InSAR-based analyses also reveal evidence for previously unmapped ground ruptures and demonstrate that this InSAR-based approach is capable of mapping small-displacement (*c.* 2 cm) ruptures in remote areas where direct measurements are not available. Implications of these processes associated with repeated fault slip for the resulting fault zone structure are discussed.

Background on Newberry Springs Fault Zone

Studies of the 1992 Newberry Springs Fault Zone ruptures provide the basis for assessment of displacement/length scaling of single-event fault ruptures, reactivation of rupture segments and implications for fault zone deformation. The large magnitude (M_w 7.3) and *c.* 80 km rupture length of the Landers earthquake on 28 June 1992 surprised the scientific community (Fig. 1). Although the main dextral fault segments that ruptured during the earthquake had been documented previously in the Mojave Desert region of southern California, a throughgoing fault of sufficient length to produce such a large earthquake had not been recognized (Monastersky 1993; Sieh *et al.* 1993). Previous estimates of maximum magnitude based on mapped fault lengths were $M = 6.9$ (Wesnousky 1986; Sieh *et al.* 1993). The primary surface rupture occurred along a series of five mapped faults with new ruptures on previously unmapped or non-existent linking faults (Hart *et al.* 1993). Because most earthquakes occur on pre-existing single faults or linked fault networks, as demonstrated by the Landers earthquake, detailed mapping of existing fault ruptures is a key element of earthquake source characterization and magnitude estimation. In California, the 'Alquist Priolo Earthquake Fault Zoning Act' and 'Earthquake Fault Zones' (renamed from 'Alquist Priolo Special Studies Zones Act' and 'Special Studies Zones') of 1972 require characterization of such active fault ruptures and a construction setback of human-occupied structures away from active fault ruptures (Hart, 1992). Therefore, it is important that active faults be characterized in detail.

An area 16–25 km northeast of the northwestern termination of the Landers rupture experienced localized extensional deformation forming a system of north and northeast striking ground ruptures (Fig. 2a). These normal fault ruptures were mapped from aerial photographs and field measurements, and constitute the Newberry Springs Fault Zone (Hart *et al.* 1993; Hart 1994; Unruh *et al.* 1994). Hart (1994) describes the Newberry Springs Fault Zone as an active but 'very messy' fault that appears to be a branch of the Calico Fault. The fault system consists of multiple discontinuous traces, which Hart presumed to be simplified and more continuous at depth. This system of ruptures occurs in late Pleistocene flood plain deposits of the Mojave river that are locally covered by a thin veneer of Holocene eolian sand and alluvium (Dibblee & Bassett 1966; Hart 1994).

The Landers earthquake has served as the type example for interferometric synthetic aperture radar (InSAR) analysis of earthquake-related ground deformation (Massonnet *et al.* 1993, 1994). InSAR investigations of the Landers displacement pattern include analysis of coseismic deformation by Massonnet *et al.* (1993) and numerous follow-up studies (e.g., Peltzer *et al.* 1994; Massonnet *et al.* 1994; Zebker *et al.* 1994; Price & Sandwell 1998; Michel *et al.* 1999; Price & Burgmann 2002; Fialko 2004).

InSAR analysis of Newberry Springs Fault Zone

InSAR analysis is the process by which a pair of synthetic aperture radar images (master and slave) collected at different times from the same orbital position are coregistered, filtered and compared to develop an interference pattern. Documentation of deformation patterns is possible by analysing appropriate pairs for an area collected over a time period during which surface displacement (e.g., subsidence, uplift, fault slip) has occurred. InSAR investigations commonly result in fringe patterns

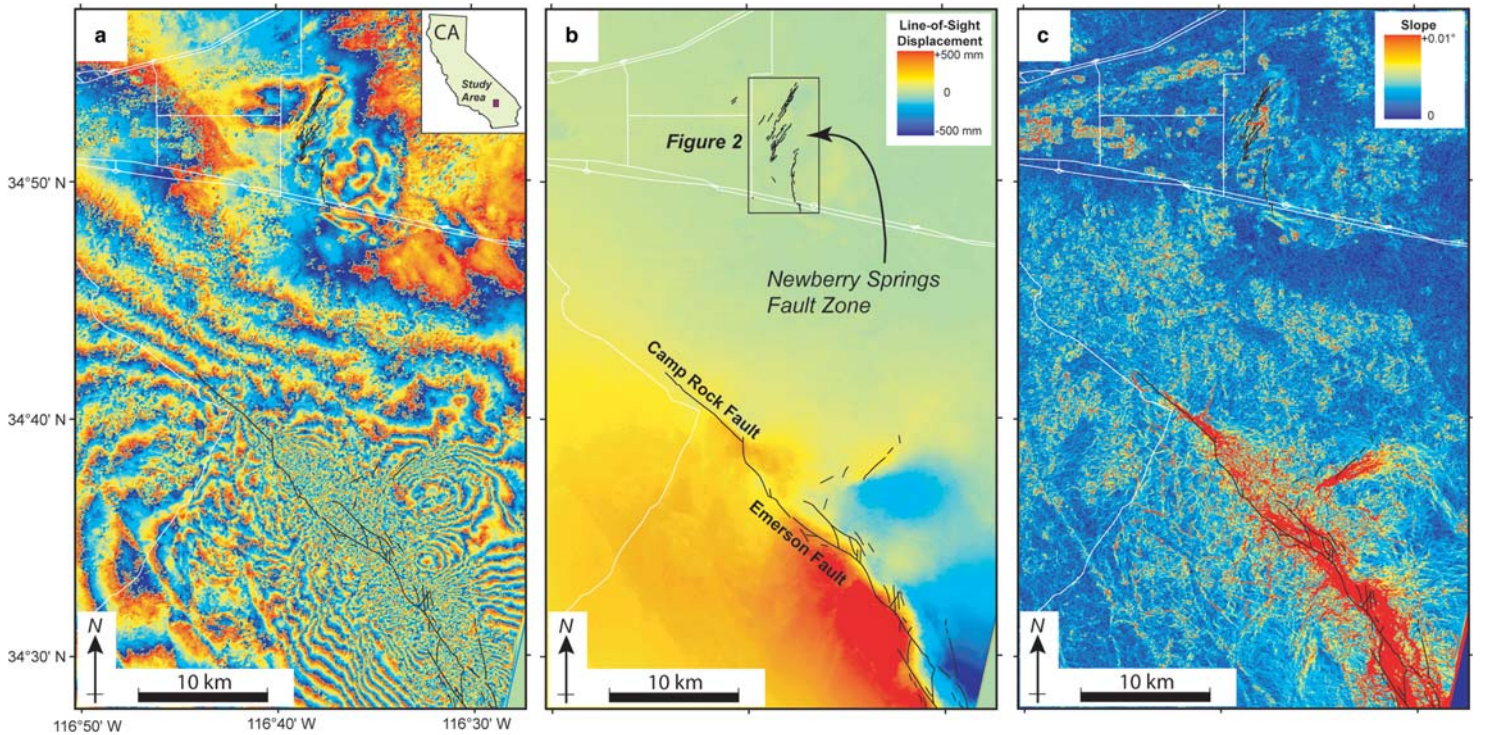

Fig. 1. (**a**) Interferogram or wrapped fringe map derived for the SAR image pair from ERS-1 Track 399, Frame 2907, collected on 24 April 1992 [ERS-1: 4051 (D)] and 7 August 1992 [ERS-1: 5554 (D)]. Each cycle represents 28 mm of displacement. The inset map shows location of study area in southern California. (**b**) Unwrapped interferogram line-of-sight displacement map for same period as (a). Positive displacement values (yellow to red colours) indicate motion away from the satellite whereas negative displacement values (green to blue colours) indicate motion towards the satellite. The network of fault ruptures labelled Camp Rock Fault and Emerson fault are the northern part of the primarily right lateral strike slip ground rupture produced by the 1992 Landers Earthquake (after Hart *et al.* 1993). Faulting in the Newberry Springs Fault Zone also formed as a product of the Landers earthquake. (**c**) Displacement gradient (slope) map for same period as (a) and (b).

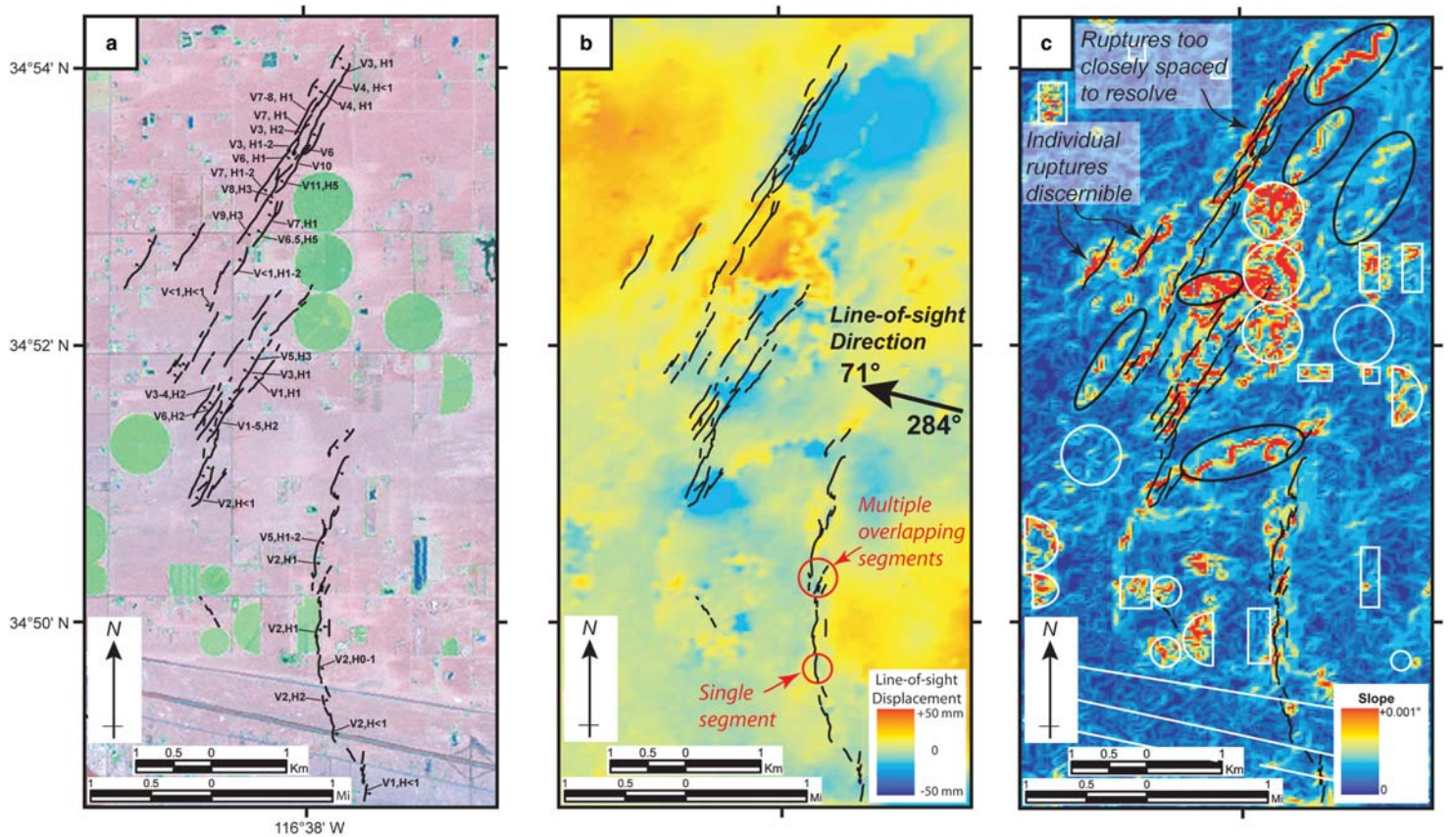

Fig. 2. Detailed study area in vicinity of the Newberry Springs Fault Zone. (**a**) Landsat 7 Enhanced Thematic Mapper plus image (acquired on 24 April 2000; image courtesy of Global Land Cover Facility, University of Maryland) showing small fault ruptures and measured throw (labelled V) and heave (labelled H) values in cm (0.01 m; after Hart 1994). (**b**) Enlargement of line-of-sight displacement map showing satellite look direction (azimuth of 284°, plunge of 71°). Positive values (yellow to red colours) indicate motion away from the satellite. (**c**) Enlargement of displacement gradient map (c). Fault rupture traces are from Hart 1994). Cultural and agricultural anomalies (e.g., highway, centre pivot irrigation circles, ponds) are outlined in white. Suspected fault ruptures are indicated by black ellipses.

where each cycle relates to surface displacement as a function of the radar signal wavelength. Price & Sandwell (1998) calculated phase gradients to identify anomalies in displacement phase as a method for identifying fault ruptures.

Methodology

We have developed a different approach for identifying fault ruptures that involves unwrapping the displacement phase (fringe) maps to generate surface displacement maps. From the displacement map we calculate a slope or displacement gradient map, using the 3DAnalyst module of ArcGIS™. Values of displacement are calculated as the maximum rate of change in 'elevation' (in this case displacement) over each *c*. 60 m cell and its eight neighbours. The resulting displacement gradient map highlights localized changes in displacement magnitude, thus highlighting features such as fault ruptures. Resulting displacement and displacement gradient maps are ideal for mapping ruptures and contain additional information on overall ground deformation patterns.

A pair of focused synthetic aperture radar single look complex (SAR SLC) images (collected on 24 April 1992 and 7 August 1992) was used to analyse seismic ground deformation. The Delft object-oriented radar interferometric software (DORIS) provided the computational framework (Kampes 1999), several public domain utilities were used to visualize/analyse intermediate products (Kampes & Usai 1999), and commercial off-the-shelf software was used for interpolation and map analysis (e.g., ENVI, ArcGIS). The first interferogram-producing steps (i.e., coregistration, resampling, interferogram generation and phase unwrapping) follow standard InSAR methodology (e.g., Kampes & Usai 1999). Spectral filtering was unnecessary because of small differences in Doppler centroid frequencies ($<$20 Hz) and low decorrelation in the data (Necsoiu *et al.* 2006).

The products of amplitude and phase difference were obtained by multiplication of the master and complex conjugated slave images. A multilook averaging factor (10×2) was applied to obtain an estimate of the phase data, and the resulting interferometric phase was corrected for the Earth phase (i.e., flat Earth correction) and topography. The topography contribution was removed using synthetic phase data extracted from a mosaic of nine digital elevation models and the coherence image was computed and used in the unwrapping process. A statistical-cost, network-flow algorithm for phase unwrapping (SNAPHU; Chen & Zebker 2000) was used to unwrap the interferogram. This algorithm has an interactive optimization procedure that improved the quality of unwrapped interferograms when compared with the results of unwrapping methods based on traditional residue-cut algorithms (Goldstein *et al.* 1988). The final geocoding step used a modified DORIS ambiguity routine to georeference the coherence, wrapped and unwrapped interferograms. ENVI was used for interpolation, reprojection and normalization. In-house generated process-control scripts were developed to control the production of the InSAR displacement maps (Ferrill *et al.* 2005*b*; Necsoiu *et al.* 2006). Geocoded displacement maps were generated with displacement in the line-of-sight direction (in both radians and mm).

Results

Interference fringe (Fig. 1a) and line-of-sight displacement (Fig. 1b) maps of the northern part of the Landers earthquake illustrate broad regions of $>$10 cm uplift and subsidence adjacent to the main rupture. Displacement gradient (Fig. 1c) maps illustrate anomalies in the displacement field (high displacement gradients) indicative of fault ruptures or other surface processes (Ferrill *et al.* 2005*b*). An area 16–25 km NE of the northwestern termination of the Landers rupture experienced localized extensional deformation, forming a system of north and northeast striking ground ruptures (Fig. 2a). These normal fault ruptures were mapped from aerial photographs and field measurements, and constitute the Newberry Springs Fault Zone (Hart *et al.* 1993; Hart 1994; Unruh *et al.* 1994). The line-of-sight displacement direction (satellite image look direction) for the InSAR maps in the vicinity of the Newberry Springs Fault Zone has an azimuth of 284° and inclination of 71° down from horizontal (Fig. 2b). The displacement gradient map illustrates both cultural and fault rupture anomalies (Fig. 2c). Cultural anomalies associated with irrigation probably reflect surface changes related to variations in vegetation height, soil swelling or shrinking related to soil moisture, or changes in soil character (e.g., harvesting or plowing).

Other prominent displacement anomalies show close correspondence to mapped ruptures of the Newberry Springs Fault Zone (Fig. 2c). Where ruptures are highly segmented and closely spaced, individual rupture segments are not discernible on the displacement gradient map because of the large ground-cell resolution (*c.* 60 m) with respect to the locally small spacing (approximately 0–100 m) between rupture segments. Where ruptures are more isolated, however, individual rupture segments are discernible. The InSAR-derived displacement gradient map (Fig. 2c) clearly illustrates the main rupture segments, while the line-of-sight displacement map (Fig. 2b) provides a sense of fault slip and credible measurements of

actual displacements for discrete ruptures. This approach provided D_{max} for two ruptures (labelled 'individual ruptures discernible' in Fig. 2c) that were previously mapped but lacked displacement measurements. Comparison of detailed rupture mapping with InSAR analysis shows that our InSAR-based methodology can identify ground ruptures with displacements of 2–10 cm, although discerning individual rupture traces within closely spaced rupture swarms is not possible due to limited data resolution.

D_{max}/L scaling of Newberry Springs Fault Zone ruptures

Ground ruptures in the Newberry Springs Fault Zone reflect a broad pattern of distributed deformation. While some discrete faults are related to easily discernible line-of-sight displacement patterns and display the correct sense of displacement compared with independently mapped ruptures, other sets of segmented ruptures appear to coincide with relatively large areas that were associated with either coseismic uplift or subsidence (Fig. 2b). These broad upwardly or downwardly displaced warps may reflect distributed deformation related to fault-tip displacement in the extensional region associated with the right-lateral strike–slip motion on the main Landers fault rupture.

The detailed mapping of the Newberry Springs Fault Zone (Hart 1994) offers the opportunity to analyse the maximum displacement/length (D_{max}/L) scaling relationships for single-event fault ruptures and to compare these results with InSAR-derived displacement gradient maps. Plotting throw (vertical component of fault displacement) v. heave (horizontal component of fault displacement) for mapped ruptures of the Newberry Springs Fault Zone (derived from mapping of Hart 1994) illustrates that displacement directions are approximately evenly distributed between down-to-the-SE and down-to-the-NW displacement (Fig. 3a). Displacement directions, presumably related to fault dips at depth, generally plunge 45–90° and displacement magnitudes range from 0 to 12 cm. The line-of-sight direction for InSAR data in the area of the Newberry Springs Fault Zone approximately parallels, and thus is nearly ideal to accurately measure, the down-to-the-NW displacement for the steep NW-dipping normal fault segments.

D_{max}/L ratios for *total* displacement on natural normal faults, regardless of rock type, range between 10^{0} and 10^{-3}, and primarily between 10^{-1} and 10^{-2} (Schultz & Fossen 2002). In contrast, D_{max}/L ratios for single-event normal fault ruptures or rupture segments range between 10^{-3} and 10^{-5} (Wells & Coppersmith 1994; Fig. 3b). Plotting D_{max} v. L for the measured segments of the Newberry Springs Fault Zone ruptures demonstrates that these ruptures exhibit positive correlation between displacement and fault length. The D_{max}/L distributions from Newberry Springs Fault Zone rupture segments have a similar range of D_{max}/L ratios to that derived by Wells & Coppersmith (1994) for normal-fault earthquake ruptures, as shown in Figure 3b. The Newberry Springs Fault Zone rupture segment data, with an average D_{max}/L ratio of 8×10^{-5}, have nearly the same displacements with respect to their lengths as the general relationship for normal-fault earthquake ruptures defined by Wells & Coppersmith (1994; average D_{max}/L ratio of 7×10^{-5}).

Discussion

Fault reactivation and displacement accumulation

Our observations concerning scaling of single event fault ruptures associated with the Newberry Springs Fault Zone support the observations and interpretations of Walsh *et al.* (2002) that faults may not grow by systematic increases in both length and displacement, but instead by early propagation followed by progressive increase in displacement. If we take the general scaling relationships for single-event fault ruptures and total fault ruptures at face value, then the typical total displacement profile could be produced by rapid propagation of a fault fracture with $D/L = 10^{-4}$, followed by 99 additional individual characteristic slip events that rupture along the entire fault trace length but do not cause lateral propagation of the fault (Fig. 4). In reality, the total displacement profile may be the product of more slip events, including many smaller rupture events that do not reactivate the entire fault (Walsh *et al.* 2002; Manzocchi *et al.* 2006). Perhaps this implies that a steady-state total fault displacement profile develops and a critical displacement gradient must be generated to cause propagation of the fault, increasing the fault length.

For the Newberry Springs Fault Zone, Unruh *et al.* (1994) reported that 'fractures border the margins of several preexisting en echelon elongate depressions 1 to 2 m deep, associated with normal-fault bounded grabens, suggesting that similar deformations have occurred repeatedly in the past'. Extrapolating from this information, Hart (1994) noted that, if the Landers event was assumed to be characteristic of displacement on the Newberry Springs Fault Zone, then 10–20 rupture events with 10 cm throw each would be needed to produce the observed 1–2 m deep

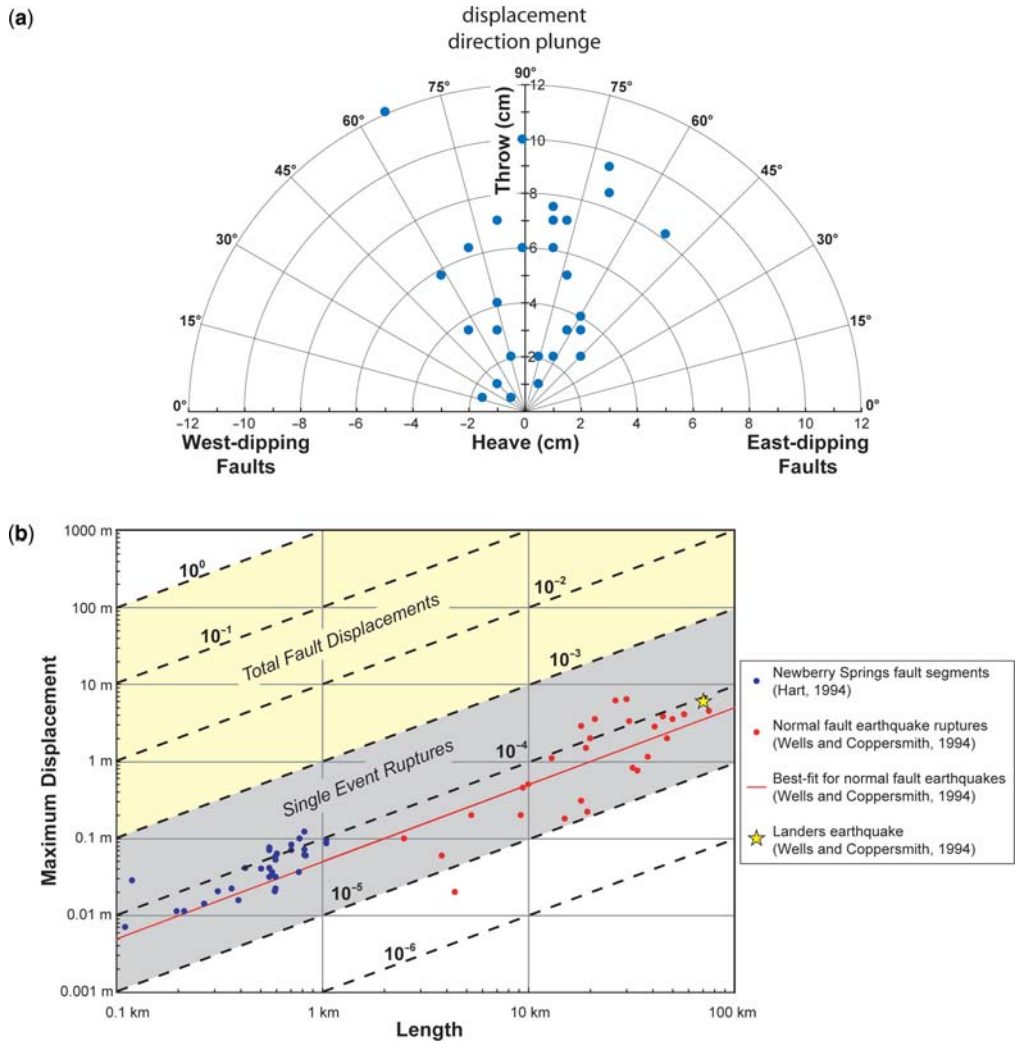

Fig. 3. (**a**) Throw v. heave for mapped surface ruptures in the Newberry Springs Fault Zone (data from mapping of Hart 1994). Concentric lines of equal displacement magnitude and radial lines of equal displacement direction are superimposed. (**b**) Comparison of maximum measured displacement (D_{max}) v. rupture length (L) for fault ruptures of the Newberry Springs Fault Zone as well as other single-event normal fault ruptures from Wells & Coppersmith (1994). The primary Landers strike–slip rupture is also plotted for comparison.

graben depressions, going on to say that, if the surface is assumed to be 10 000 years old, then this would equate to one slip event every 500–1000 years. Hart (1994) mapped photogeologic lineaments on 1952–1953 vintage aerial photographs. Although coregistration of this mapping with 1992 ruptures is imperfect, it is clear that the 1950s lineament pattern – including rupture segments and intervening relays – closely matches ruptures associated with the 1992 event, providing strong evidence of segment reactivation, rather than indicating that the 1992 ruptures were newly formed.

Implications for fault zone processes

Although relatively simple isolated ruptures do exist in the Newberry Springs Fault Zone, most rupture segments are elements of complex arrays that in the northern part of the zone form a complex en echelon graben system, and in the southern part of the zone form a curved, segmented,

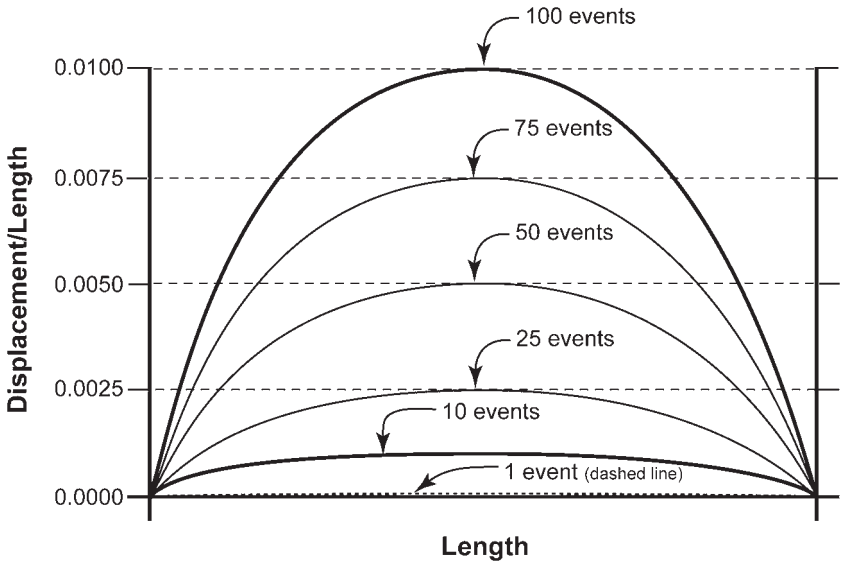

Fig. 4. Illustration shows schematic displacement profile for total fault displacement and curves showing one model for accumulation of the total displacement profile by 100 individual slip events that rupture the entire fault.

down-to-the-east normal fault system (cf. Fig. 2a & b). The conjugate normal faults in the northern portion of the Newberry Springs Fault Zone define 200–300 m wide grabens bounded by conjugate normal faults with displacement direction plunges (parallel to fault dips) of 45–90°. Based on the pattern of mapped ruptures shown in Figure 2b, the southern east-dipping segmented fault zone ranges in width from the width of a single segment (a few metres or less) to >200 m wide where segmentation manifested by multiple overlapping fault segments exists. Given the apparently small total displacement of the Pleistocene flood plain deposits in this fault system, it is interesting to the note that the width of the fault zone tends to be large even at small total fault displacements. The implication of this is that fault zone width appears to be established early at small total fault displacements. Increasing total displacement on the fault zone will lead to increasing strain and may involve increasing strain localization, effectively narrowing the active portion of the fault zone width. This is in contrast to the clear relationship of increasing damage zone width with increasing displacement in the Navajo Sandstone demonstrated by Shipton & Cowie (2001). Our interpretation may help to explain the orders of magnitude variation in fault zone width at a given fault displacement, or conversely the orders of magnitude variation in displacement for a particular fault zone width observed by Evans (1990). Other factors such as lithology and structural setting also probably play a significant role in controlling fault zone width, as these probably control timing and mechanisms of fault related deformation during damage zone evolution (e.g., Ferrill *et al.* 2005*a*).

Conclusions

The D_{max}/L ratios for fault segments (rupture lengths in the range of 0.1–1 km) in the Newberry Springs Fault Zone average 8×10^{-5} – consistent with previously published D_{max}/L ratios for normal fault earthquake ground ruptures (rupture lengths in the range of 1–100 km) of 7×10^{-5}. Evidence of wide damage zones and reactivation of individual segments developed in alluvial floodplain deposits, at relatively small (order of metres) fault displacements, supports a conceptual model of fault damage zone width being established early, during fault propagation. This observation, along with the variable development of overlapping fault segments, helps to explain the orders of magnitude variation in fault displacement associated with a given fault zone width. With continued displacement – additional slip events – we envision that displacement accumulates and fault zone damage intensifies, but the fault zone width may remain relatively stable. Consequently, the active portion of the fault zone may tend to narrow as faulting continues. InSAR-derived line-of-sight displacement and displacement gradient maps provide images of fault ruptures with displacements of *c.* 2 cm in the line-of-sight direction

mappable. Although individual ruptures are not distinguishable in closely spaced rupture swarms, linear zones of high displacement gradient illustrate the location and orientation of possible ruptures and can be used to map ruptures in remote areas for characterizing distributed rupture zones and informing fault displacement hazards investigations.

D_{max}/L scaling relationships for single-event ruptures can be used to estimate rupture length, or, conversely, the apparent rupture length can be used to help constrain displacement. The InSAR-based approach to produce displacement gradient maps provides a powerful tool to assist with interpreting and measuring ground rupture, and provides an independent tool for characterization of potential seismic sources in remote regions.

Financial support for this research was provided by the Southwest Research Institute Advisory Committee on Research (IR&D project no. 20.R9423). The SAR SLC data used in this study were produced by the European Space Agency (ESA) and distributed by Eurimage. We thank A. Morris, G. Walter, L. McKague and J. Russell for their careful reviews of the manuscript. The review comments of G. Roberts and J. Imber were particularly helpful for guiding the final revisions of the manuscript. We appreciate the formatting and editorial assistance of C. Patton.

References

BONILLA, M. G., MARK, R. K. & LIENKAEMPER, J. J. 1984. *Statistical Relations among Earthquake Magnitude, Surface Rupture Length, and Surface Fault Displacement.* US Geological Survey, Open-File Reports, **84-256**.

CHEN, C. W. & ZEBKER, H. A. 2000. Network approaches to two-dimensional phase unwrapping: intractability and two new algorithms. *Journal of the Optical Society of America*, **14**, 401–414.

COWIE, P. A. & SCHOLZ, C. H. 1992*a*. Displacement–length scaling relationship for faults: data synthesis and discussion. *Journal of Structural Geology*, **14**, 1149–1156.

COWIE, P. A. & SCHOLZ, C. H. 1992*b*. Physical explanation for displacement–length relationship for faults using a post-yield fracture mechanics model. *Journal of Structural Geology*, **14**, 1133–1148.

DAWERS, N. H. & ANDERS, M. H. 1995. Displacement-length scaling and fault linkage. *Journal of Structural Geology*, **17**, 607–614.

DAWERS, N. H., ANDERS, M. H. & SCHOLZ, C. H. 1993. Growth of normal faults: displacement–length scaling. *Geology*, **21**, 1107–1110.

DIBBLEE, T. W., JR. & BASSETT, A. M. 1966. *Geologic Map of the Newberry Quadrangle, San Bernardino, California*. U.S. Geological Survey Miscellaneous Geologic Investigations Map, **I-461**.

EVANS, J. P. 1990. Thickness–displacement relationships for fault zones. *Journal of Structural Geology*, **12**, 1061–1065.

FERRILL, D. A., MORRIS, A. P., SIMS, D. W., WAITING, D. J. & HASEGAWA, S. 2005*a*. Development of synthetic layer dip adjacent to normal faults. *In*: SORKHABI, R. & TSUJI, Y. (eds) *Faults, Fluid Flow, and Petroleum Traps.* American Association of Petroleum Geologists, Tulsa, OK, Memoirs, 125–138.

FERRILL, D. A., NECSOIU, M. & SMART, K. J. 2005*b*. Earthquake-induced ground-rupture mapping with InSAR-derived displacement gradiometry. *EOS Transactions of the American Geophysical Union*, **86**, Fall Meeting Supplement, abstract S51D-1042.

FIALKO, Y. 2004. Probing the mechanical properties of seismically active crust with space geodesy: study of the coseismic deformation due to the 1992 Mw 7.3 Landers (southern California) earthquake. *Journal of Geophysical Research*, **109**, B03307.

GOLDSTEIN, R. M., ZEBKER, H. A. & WERNER, C. L. 1988. Satellite radar interferometry: two-dimensional phase unwrapping. *Radio Science*, **23**, 713–720.

HART, E. 1992. *Fault-rupture Hazard Zones in California: Alquist Priolo Special Studies Zones Act of 1972 with Index to Special Studies Zones Maps.* California Department of Conservation, Division of Mines and Geology Special Publications, **42**, 32.

HART, E. 1994. *Calico Fault and Adjacent 1992 Surface Ruptures near Newberry Springs, San Bernardino County*. California Division of Mines and Geology Fault Evaluation Report, **238**, California Geological Survey CD 2002-02.

HART, E. W., BRYANT, W. A. & TREIMAN, J. A. 1993. Surface faulting associated with the June 1992 Landers earthquake, California. *California Geology*, **46**, 10–16.

KAMPES, B. 1999. *Delft Object-Oriented Radar Interferometric Software User's Manual and Technical Documentation*, 42–44.

KAMPES, B. & USAI, S. 1999. Doris: the Delft Object-Oriented Radar Interferometric Software, *Proceedings of ITC, 2nd ORS Symposium.*

MANZOCCHI, T., WALSH, J. J. & NICOL, A. 2006. Displacement accumulation from earthquakes on isolated faults. *Journal of Structural Geology*, **28**, 1685–1693.

MASSONNET, D., ROSSI, M., CARMONA, C., ADRAGNA, F., PELTZER, G., FEIGL, K. & RABAUTE, T. 1993. The displacement field of the Landers earthquake mapped by radar interferometry. *Nature*, **364**, 138–142.

MASSONNET, D., FEIGL, K., ROSSI, M. & ADRAGNA, F. 1994. Radar interferometric mapping of deformation in the year after the Landers earthquake. *Nature*, **369**, 227–230.

MICHEL, R., AVOUAC, J.-P. & TABOURY, J. 1999. Measuring near-field coseismic displacements from SAR images: application to the Landers earthquake. *Geophysical Research Letters*, **26**, 3017–3020.

MONASTERSKY, R. 1993. Lessons from Landers. *Earth*, **2**, 41–47.

NECSOIU, M., SMART, K. J. & FERRILL, D. A. 2006. High-resolution ground-rupture mapping using SAR data and public domain interferometric software. *American Society of Photogrammetry and Remote Sensing Annual Conference*, Reno, NV.

PELTZER, G., HUDNUT, K. & FEIGL, K. 1994. Analysis of coseismic surface displacement gradients using radar interferometry: new insights into the Landers

earthquake. *Journal of Geophysical Research*, **99**, 21971–21981.

PRICE, E. J. & BURGMANN, R. 2002. Interactions between the Landers and Hector Mine, California, earthquakes from space geodesy, boundary element modeling and time-dependent friction. *Bulletin of the Seismological Society of America*, **92**, 1450–1469.

PRICE, E. J. & SANDWELL, D. T. 1998. Small-scale deformation associated with the 1992 Landers, California, earthquake mapped by synthetic aperture radar interferometry phase gradients. *Journal of Geophysical Research*, **103**, 27001–27016.

ROBERTS, G. P. & MICHETTI, A. M. 2004. Spatial and temporal variations in growth rates along active normal fault systems: an example from the Lazio–Abruzzo Apennines, central Italy. *Journal of Structural Geology* **26**, 339–376.

ROBERTS, G. P., COWIE, P. P., PAPANIKOLAOU, I. & MICHETTI, A. M. 2004. Fault scaling relationships, deformation rates and seismic hazards: an example from the Lazio–Ambruzzo Apennines, central Italy. *Journal of Structural Geology*, **26**, 377–398.

SCHULTZ, R. A. & FOSSEN, H. 2002. Displacement–length scaling in three dimensions: the importance of aspect ratio and application to deformation bands. *Journal of Structural Geology*, **14**, 1389–1411.

SHIPTON, Z. K. & COWIE, P. A. 2001. Damage zone and slip-surface evolution over μm to km scales in high-porosity Navajo sandstone, Utah. *Journal of Structural Geology*, **23**, 1825–1844.

SIEH, K., JONES, L. *ET AL*. 1993. Near field investigation of the Landers earthquake sequence, April to July 1992. *Science*, **260**, 171–176.

UNRUH, J. R., LETTIS, W. R. & SOWERS, J. M. 1994. Kinematic interpretation of the 1992. Landers earthquake. *Bulletin of the Seismological Society of America*, **84**, 537–546.

WAITING, D. J., STAMATAKOS, J. A., FERRILL, D. A., SIMS, D. W., MORRIS, A. P., JUSTUS, P. S. & IBRAHIM, A. B. K. 2003. Methodologies for the Evaluation of Faulting at Yucca Mountain, Nevada. *10th International High-Level Radioactive Waste Management (IHLRWM) Conference*, Las Vegas, NV, 30 March to 2 April 2003, 377–387.

WALSH, J. J. & WATTERSON, J. 1988. Analysis of the relationship between the displacements and dimensions of faults. *Journal of Structural Geology*, **10**, 239–247.

WALSH, J. J., NICOL, A. & CHILDS, C. 2002. An alternative model for the growth of faults. *Journal of Structural Geology*, **24**, 1669–1675.

WELLS, D. L. & COPPERSMITH, K. J. 1994. New empirical relationships among magnitude, rupture length, rupture width, rupture area, and surface displacement. *Bulletin of the Seismological Society of America*, **84**, 974–1002.

WESNOUSKY, S. G. 1986. Earthquakes, Quaternary faults, and seismic hazards in California. *Journal of Geophysical Research*, **91**, 12587–12631.

YOUNGS, R. R., ARABASZ, W. J. *ET AL*. 2003. A methodology for probabilistic fault displacement hazard analysis (PFDHA). *Earthquake Spectra*, **19**, 191–219.

ZEBKER, H., ROSEN, P., GOLDSTEIN, R., GABRIEL, A. & WERNER, C. 1994. On the derivation of coseismic displacement fields using differential radar interferometry: the Landers earthquake. *Journal of Geophysical Research*, **99**, 19617–19634.

Normal fault terminations in limestones from the SE-Basin (France): implications for fluid flow

L. MICARELLI[1,2] & A. BENEDICTO[1]

[1]*Département de Science de la Terre, Groupe Dyn. Syst. Faillés, UMR, 7072, Université Paris Sud XI, 91405 Orsay, France (e-mail: lucamic@inwind.it)*

[2]*Present address: BEICIP-FRANLAB, 232, Av. Napoléon Bonaparte, BP 213, 92502 Rueil-Malmaison, France*

Abstract: The geometry and evolution of normal fault terminations were studied in Tithonian limestones exposed on a vertical cliff in the French SE-Basin. The rocks consist of mainly limestone layers alternated with thin clayey interlayers. All studied fault zones die out vertically into bed-perpendicular veins striking approximately parallel to the fault. Displacement decreasing to zero towards the fault tip is accommodated horizontally by bed-parallel opening of calcite veins, and vertically by bed-perpendicular localized compaction. The latter mechanism leads the clayey interlayers to be thinned and in places completely pushed out, and enhances pressure solution in bed-parallel seams. The respective thicknesses of the limestone layers and clayey interlayers, and the ratio between local displacement amount and bed thickness influence the geometries of the fault termination and of the steps between slip surfaces. Relatively thick clayey interlayers localize low-angle slip surfaces and may impede the vertical propagation of the slip surface. Vertical fault restriction is also related to thick limestone layers, which are deflected and affected by outer arc extensional fractures, localized pressure solution and dilational jogs connecting adjacent propagating slip surfaces. However, beds keep their continuity if thicker than the local displacement amount. Where the local displacement is larger than the layer thickness, limestone beds are disconnected and clayey interlayers are completely cut but the slip surfaces. Tip-point veins, as well as outer arc veins, do not cross the clayey interlayers and fluid flow is local and confined within one limestone layer. In contrast, dilational jogs in places cut through several layers, and the breaking of clayey interlayers causes an increase in fluid flow. Conduits can be opened along the fault zone and fluids are driven into the jog, so slip surfaces may communicate separate reservoirs, until dilational jogs are sealed by mineral precipitation.

Fault-related fracturing in damage zones may result from (i) the initiation of faults (e.g., Reches & Lockner 1994), (ii) the processes occurring at fault tips during fault propagation (e.g., McGrath & Davison 1995) and (iii) the interaction and build-up of slip along faults (e.g., Davison 1995; McGrath & Davison 1995; Kim *et al.* 2004). The features that result directly from propagation of the fault tip comprise the process zone (e.g., Ingraffea 1987; Vermilye & Scholz 1998), which commonly consists of an area of extensional fractures at the fault tip that enhances propagation (Reches & Lockner 1994; Vermilye & Scholz 1998). The process zone moves with the fault tip, leaving damaged rock in its wake. The location and geometry of damage zones are important as they may contribute to compartmentalization, or provide fracture-controlled fluid flow pathways in addition to the master fault in a reservoir (e.g., Knott *et al.* 1996; Micarelli *et al.* 2003). In particular, the development of normal fault tips is of interest in permeability studies, because fractures may be initially isolated, with linkage occurring during evolution (e.g., Kelly *et al.* 1998).

Field studies show that many faults in the upper crust commonly develop from earlier-formed joints (mode I fractures), veins (filled mode I fractures) or pressure solution surfaces (mode −I features). In particular, veins have been often suggested to dominate fault initiation and fault tip propagation (e.g., Peacock 2001; Mazzoli & Di Bucci 2003; Crider & Peacock 2004; Micarelli *et al.* 2005), whereas shear fractures are unlikely to play an important role in the initiation of most faults (Petit & Barquins 1988; Willemse *et al.* 1997). Once faults are formed, cumulated displacement obliterates the evidence of the initial stages of faulting. One way to get valuable information about fault propagation and growth (Vermilye & Scholz 1998; Kim *et al.* 2004; Micarelli *et al.* 2006*a*) and fluid flow (Sibson 1996; Micarelli *et al.* 2005; Micarelli *et al.* 2006*b*) is to study the development of different structures within damage zones and in particular fault tips. We focus on termination zones of faults with small amounts of displacement, to illustrate the style of the early stages of fault development (Crider & Peacock 2004; Mazzoli *et al.* 2004), and its consequences for fluid flow.

From: WIBBERLEY, C. A. J., KURZ, W., IMBER, J., HOLDSWORTH, R. E. & COLLETTINI, C. (eds) *The Internal Structure of Fault Zones: Implications for Mechanical and Fluid-Flow Properties*. **299**, 123–138.
DOI: 10.1144/SP299.8 0305-8719/08/$15.00

In this paper we specifically describe fault terminations of normal fault zones in Tithonian limestone rocks, in the SE-Basin of the French Alps. The studied faults are exposed on a natural vertical cliff face that allows the study of vertically segmented normal faults and their terminations. Faults are hosted in well-bedded, low-porosity, fine-grained limestones, showing thin marly/clayey interlayers. Fault tips are characterized by arrays of calcite-filled veins. Detailed analysis of areas around fault terminations gives information about how faults initiate, and the factors that influence the style of fault propagation and associated fluid flow.

Geological setting

The French South East Basin was part of the Mesozoic Tethyan passive margin (Dercourt *et al.* 1993; De Graciansky *et al.* 1993). A shelf marl–limestone thick succession characterizes the Kimmeridgian and Tithonian times. In the centre of the basin, the uppermost part of the succession commonly forms a 20–200 m high cliff and is informally called the 'Barre Tithonique' (Fig. 1a; Gignoux & Moret 1938). This is composed of coarse carbonate breccia bodies, interbedded with calcarenites and marl-lime mudstones. Some calcarenites are interpreted as tempestites, resulting from transport and deposition of carbonate sands under wave-induced combined flow (Bouchette *et al.* 2001; Séguret *et al.* 2001). The base of the 'Barre Tithonique' is either Late Kimmeridgian or Tithonian in age, with the uppermost part of this unit being Late Tithonian to Early Berriasian (Bouchette *et al.* 2001).

The 'Barre Tithonique' is affected by a system of normal faults with throws of up to few tens of metres. This system is related to a weak extensional phase with a general WNW–ENE direction of extension, as shown by palaeostress analysis (Fig. 1b). The fault dip angles are consistent with one extensional phase affecting the limestone series before the Alpine (i.e., ante-Miocene) thrusting and folding. The age of this fault system is not well constrained but stratigraphic data suggest it is Upper Cretaceous. The faults studied in this work do not show any evidence of reactivation during the Alpine compression.

We focused our study on several fault zones cropping out at the La Remuque site (location in Fig. 1; 44°26′46N, 5°16′37E), and affecting the 'Barre Tithonique' at a level consisting of mainly micritic limestones alternated with fine calcarenites. Clayey/marly interlayers, few millimetres to tens of millimetres thick, are present between most, but not all, layers. The 'Barre Tithonique' dips approximately 10–20° to the SE. The faults show strike directions between N020° and N060° and are normal dip–slip. P–T conditions in existence during the fault zones development were mostly controlled by the burial history, which indicates maximum burial of the SE-Basin series at about 120 Ma (Cros *et al.* 1993; Roure *et al.* 1994). During the Late Cretaceous to cenozoic episodes of compression, a regional uplift occurred, inducing 1.5–2 km of erosion in the Cretaceous sequences (Guilhaumou *et al.* 1996 and references therein). Maximum homogenization temperatures from primary inclusions in vein calcite display mean values around 75 °C with peak temperatures of 100 °C, and testify to P–T conditions remaining constant during the different stages of normal fault initiation and growth (Micarelli *et al.* 2005).

Fault terminations

Types of fault terminations and fault geometries

Eleven normal fault zones were analysed in detail. They are exposed vertically over lengths of a few metres and show one (lower or upper) or both mode 2 fault tips. All fault zones are characterized by the presence of fault-related, calcite-filled structures. Particular attention was paid to the cross-cutting relationships between the calcite-filled fractures and the other structures characterizing the fault zones, such as solution seams and slip planes, to determine the chronology of deformation. Time-relationships not recognizable at the macro-scale analysis, mineralogy, texture and paragenesis of the microstructures, were studied by means of transmitted light microscopy on thin sections. Cathodoluminescence microscopy (CL) was used to identify compositional zoning (Marshall 1988; Pagel *et al.* 2000) and cross-cutting relations between vein minerals not apparent in transmitted light. In the following paragraphs we describe in detail some of the studied fault zones, chosen as selected samples.

Fault 1

Fault 1 (Fig. 2) has a maximum displacement of 9 cm and a vertical length of approximately 2.5 m, completely exposed. Both vertical tip points are visible but the outcrop allows only the lower fault termination to be studied in detail. This is characterized by calcite veins perpendicular to the bedding and striking parallel to the fault. They cut through several limestone layers with no or very thin clayey interlayers, and commonly stop where thicker interlayers are present. Displacement

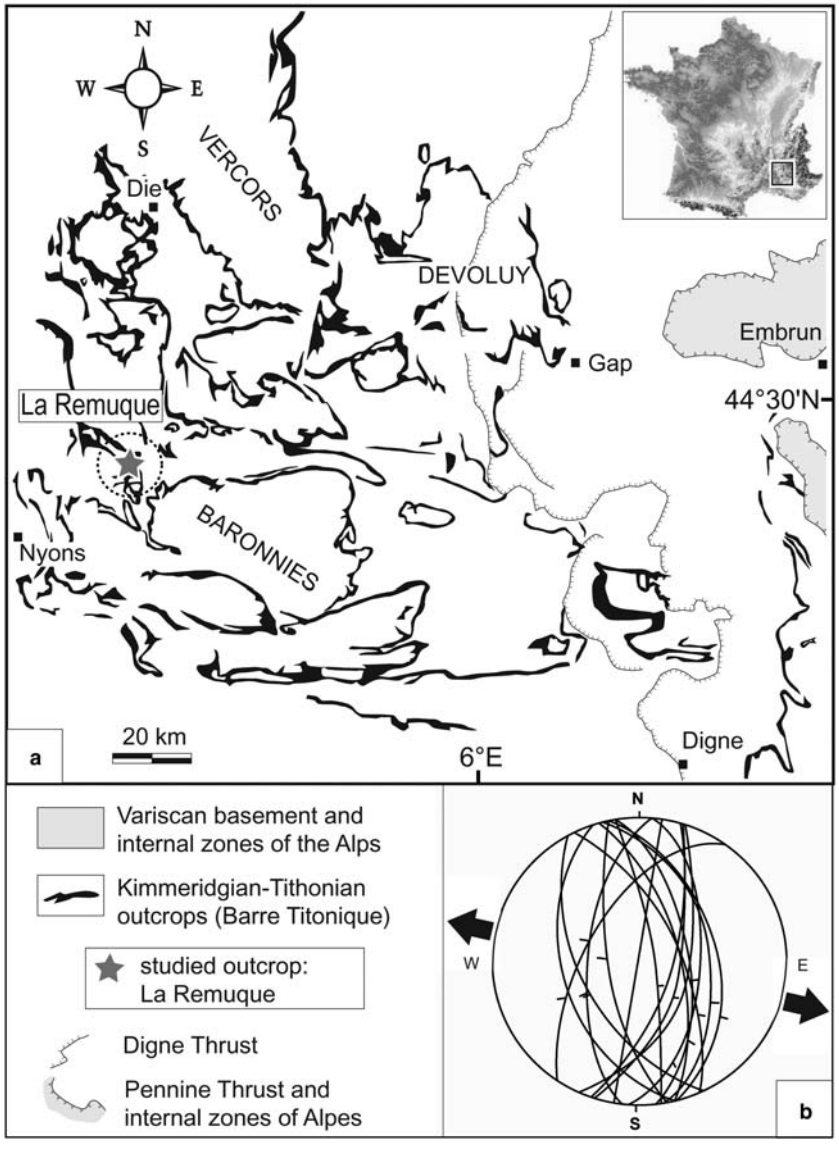

Fig. 1. (**a**) Simplified geological map of the central part of the South East Basin in France (from Séguret *et al.* 2001), showing the outcrops of the Kimmeridgian–Tithonian 'Barre Titonique.' The La Remuque outcrop is highlighted. Inset indicates the study area. (**b**) Stereogram (Schmidt projection, lower hemisphere) of the normal faults affecting the 'Barre Titonique' and palaeostress orientation analysis. Arrows indicate the direction of extension.

decreases progressively towards the fault lower tip. The fault slip surface cuts through the bedding obliquely, and the displacement decrease is accommodated by both bed-parallel and bed-perpendicular components of displacement. The bed-parallel slip component relates to the opening of calcite-filled veins, which cut perpendicular to the limestone layers and are simply extensional or slightly transtensional, as in places shown by displaced markers. The bed-perpendicular slip component is mostly accommodated by localized compaction of the clay-rich interlayer in the contractional quadrant of the fault. The interlayers are thus thinned in the fault hanging wall (near the lower tip), which in places leads to the complete disappearance of the clayey material that is completely pushed out. This is accompanied by the presence of stylolitic surfaces in the limestone layers that are locally slightly

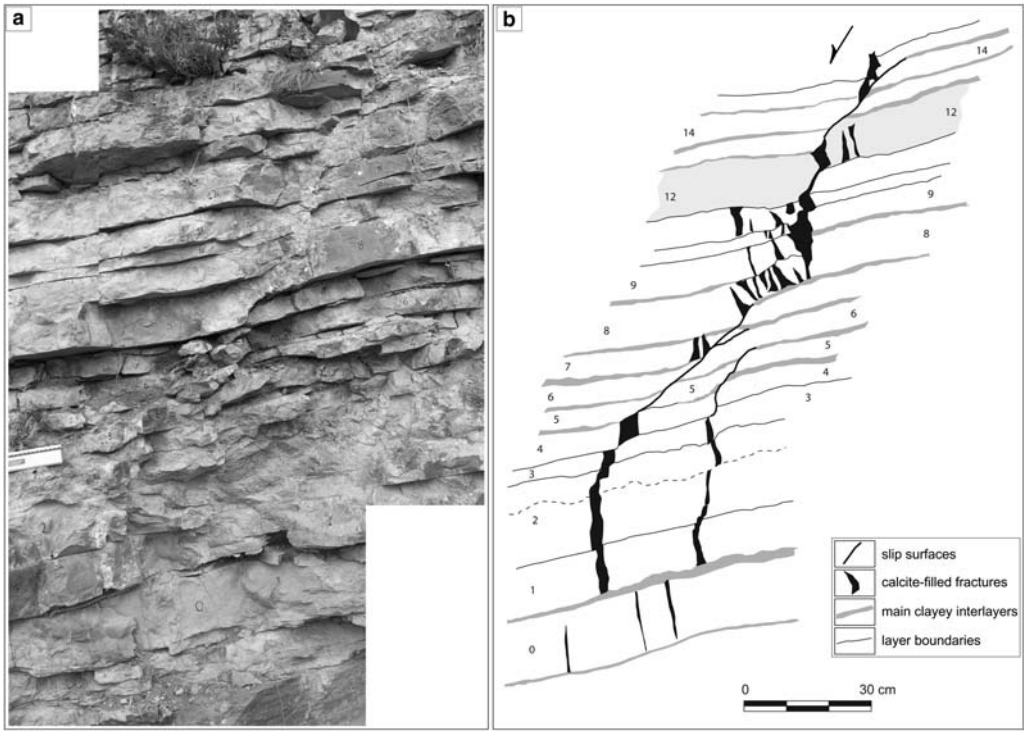

Fig. 2. (**a**) Photograph of the lower termination of Fault 1, characterized by calcite veins perpendicular to the bedding and striking parallel to the fault. (**b**) Interpretative sketch highlighting the main features and the geometry of the fault tip. The different kinds of calcite-filled features, i.e., tip-point veins outer arc veins and dilational jogs (see the text for explanation) are not distinguished. The fault has a measured maximum displacement of 9 cm, which decreases to 0 at the fault tip point.

thinned, which testifies for bed-perpendicular pressure solution (e.g., Pollard & Segall 1987).

The fault propagated from the tip-point extensional fractures into the limestone series (toward the central part of the fault zone in Fig. 2) by discrete, segmented slip surfaces, which display different cut-off angles with respect to the bedding (see also Peacock & Zhang 1994). In limestone beds 3–5 cm thick alternated with clayey interlayers with thickness of 3–10 mm (e.g., layers 4–7 in Fig. 2), slip surfaces form angles of 30–35° with respect to the bedding. In this case the slip surface shows no or little calcite. The multi-layer consisting of limestone and clayey alternated beds localizes thus gently dipping slip surfaces. The amount of slip accumulated on these segments is accommodated in the adjacent parts of the fault zone by bed-parallel opening, enhancing vein calcite mineralization. On the other hand, in the thickest limestone layers, or where clay-rich interlayers have small thickness (0–2 mm) compared with that of limestone beds (e.g., layers 9–12 in Fig. 2), slip surfaces are steeper, with angles of about 55–60° to the layer boundaries. They are usually associated with abundant calcite mineralizing the surface, filling the steps between slip surfaces, or localized within the most deformed limestone layers. Steps between overlapping slip surfaces consist of calcite-filled dilational jogs (Sibson 1989; Crider & Peacock 2004; Micarelli *et al.* 2005). Therefore, limestone layers may be either disconnected sharply by a simple slip surface, or in places apparently connected by dilational jogs (e.g., layers 9–11). Limestone layers thicker than the local displacement amount appear in places deflected (e.g., layer 8), and can be strongly affected by outer arc veins. These veins, acting as flexural extensional fractures (Micarelli *et al.* 2005), commonly have a triangular shape and are bounded by the clayey interlayers. Their opening implies flexural slip occurring between adjacent layers.

Fault 2

The lower fault termination of Fault 2 is exposed (Fig. 3). The displacement measured at a distance

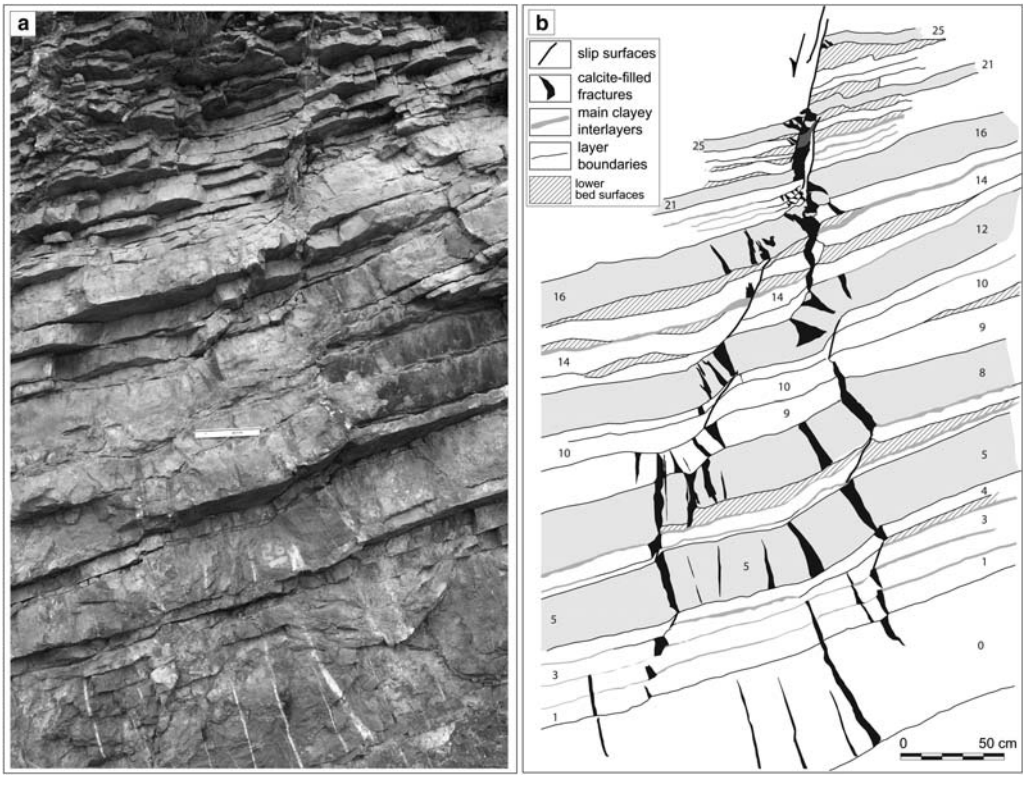

Fig. 3. (**a**) Photograph of the lower termination of Fault 2. The fault dies out in limestone layers 50–60 cm thick. (**b**) Interpretative sketch showing the main features of the fault tip. The thick limestone layers act as propagation-related precursory monoclinal folds. Slip surfaces have low cut-off angles with respect to bedding, where they affect thin limestone layers alternated with relatively thick clayey interlayers. Calcite-filled dilational jogs develop between stepped adjacent slip surfaces.

of approximately 4 m away from the tip point is 35–40 cm but does not represent the fault maximum displacement. The fault termination consists of sub-parallel, bed-perpendicular large calcite veins, so appears similar to Fault 1. However, the limestone layers where the fault dies out are significantly thicker (up to 50–60 cm) than in Fault 1, and most of them are bounded by relatively thick (10–15 mm) clayey interlayers. Interlayers appear to play a role in deformation style when their thickness is comparable with that of the limestone layers. Bed-perpendicular veins are thus systematically bed-bounded. In particular, the role played by the interlayers is important in decreasing fault displacement towards the fault tip (e.g., Muraoka & Kamata 1983). Displacement decrease on the slip surface is accommodated by bed-parallel vein opening, indicating also inter-layer slip, and by bed-perpendicular localized compaction and push-out of the clayey materials in the interlayers. Thinning by pressure solution of some limestone layers in the hanging wall of the fault also participates in the progressive accommodation of the fault displacement.

The thickest limestone layers are slightly bent and appear as propagation-related precursory monoclinal folds (e.g., Crider & Peacock 2004; layers 5, 8 and 12 in Fig. 3). The layer flexure is accommodated by brittle fracturing accompanied by pressure solution and crystallization processes. The most evident features are outer arc veins. Pressure solution takes place mostly either in the interlayers or on bed-parallel solution seams. As seen in Fault 1, low-angle slip surfaces localise in thin limestone layers with relatively thick clayey interlayers (e.g., layers 6–7 and 13–15). Low-angle slip surfaces usually do not cross thick limestone layers and in general are not associated with calcite.

Fault 3

Fault 3 has a maximum displacement of 2.3 cm and is about 1.7 m long. Both tip points are exposed

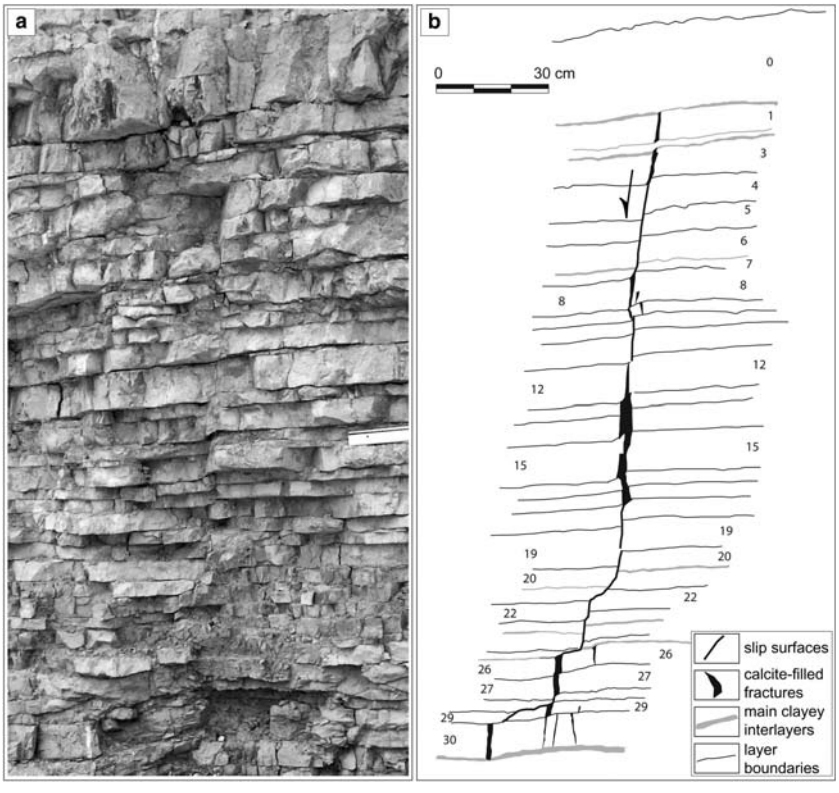

Fig. 4. (**a**) Photograph of the entire length of Fault 3, exposing both upper and lower fault terminations. (**b**) Interpretative sketch. The fault affects a relatively uniform limestone series and has a displacement of up to 2.3 cm. Clayey interlayers are thin and rare. The fault zone has a simple geometry, displaying straight slip surfaces with few calcite veins and not much deformed layers.

(Fig. 4). The displaced limestone layers have quite constant thickness (5–10 cm) and show rare clayey interlayers, a few millimetres thick. Owing to the small displacement amount, the fault is likely to show structures related to a very early stage in the evolution of the studied faults. Slip surface geometry is simple without important segment relays, and thus the fault plane is straight for most of its length. Calcite veins are few and perpendicular to the layers.

The upper fault termination displays few bed-perpendicular, bed-bounded calcite veins. Layer 3 (in Fig. 4) is sharply cut, whereas layer 1, the upper boundary of which is not faulted, is only slightly bent. The fault dies out against a 25 cm thick limestone layer. The lower fault termination shows similar characteristics, but with more calcite veins. Layers 20–26 have clayey interlayers and the slip surface is systematically less dipping. The fault dies out in a slightly bent layer, about 15 cm thick. Such slightly deformed layers, in places cut by few calcite veins with no or little vertical displacement, are likely to act as precursory monoclinal folds (Crider & Peacock 2004).

Fault 4

Fault 4 has a maximum displacement of 12.5 cm, with only the upper termination accessible. The fault affects limestone layers with quite constant thickness (some tens of centimetres; Fig. 5), with rare clayey interlayers few millimetres thick. In places, layer boundaries do not display any clay-rich interlayers, and consist of stylolitized surfaces. This lithology probably act as a massive layer, compared to the more heterogeneous layering involved in Faults 1 and 2 in which limestone and clayey layer thicknesses are comparable.

The fault dies out in limestone layers 30–50 cm thick, without significant clayey interlayers. The fault termination displays few bed-perpendicular, bed-bounded calcite veins, less than 10–15 mm wide. Owing to the small vein thickness, oblique vein opening is not sufficient to accommodate the

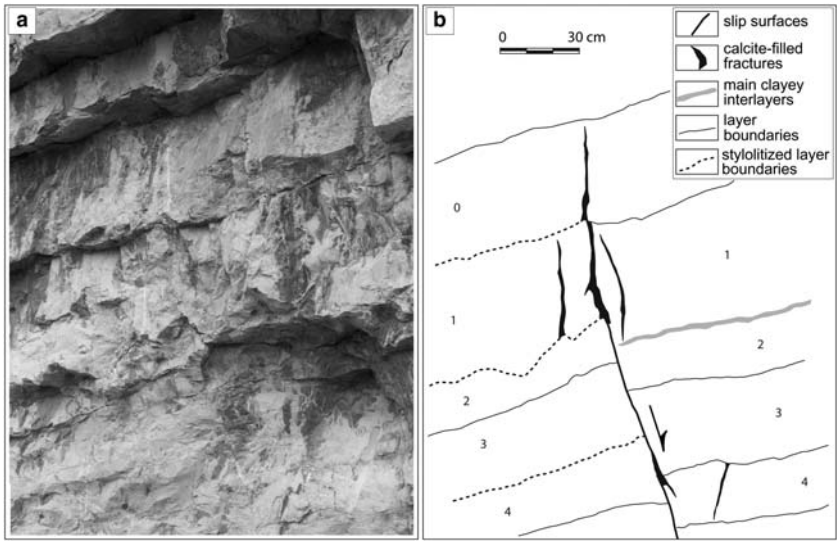

Fig. 5. (**a**) Photograph of the upper termination of Fault 4. (**b**) Interpretative sketch. The fault affects uniform thick limestone layers with relatively thin clayey interlayers or stylolitized layer boundaries. Tip-point calcite veins are narrow and accommodate a relatively high component of shear. Owing to the small thickness of clayey interlayers, displacement decrease is accommodated by significant pressure solution, mostly localized on the layer boundaries.

layer offset, and therefore some slip has to take place across the veins, or on their boundaries. The fault surface appears in general straight for most of its length, especially where it cuts thick layers. Dilational jogs are rare and small, and occur only where limestone layers are relatively thin (10–15 cm) and alternated with clayey interlayers some millimetres thick. Displacement decrease toward the upper tip point is accommodated, in the fault contractional quadrant, by clay push-out, on the bottom of layer 1 (in Fig. 5), and pressure solution mostly localized on the layer boundaries, leading the layers to be significantly thinned.

Fault 5

The tips of Fault 5 are not exposed, but the fault provides examples of different geometries of steps between overlapping slip surfaces (Fig. 6). This fault has a displacement increasing from 40 to 80 cm in the visible part, and thus is likely to show relatively more mature features compared with the faults described above (e.g., Knott *et al.* 1996; Shipton & Cowie 2001). Three dilational jogs are exposed. The lower dilational jog (J1 in Fig. 6) is confined within one limestone layer, the thickness of which is approximately the same as the local amount of displacement (about 40 cm). The two slip surfaces bounding the dilational jog die out into the clayey interlayers at the top and the bottom of the limestone layer, which appears to be sharply cut and is slightly dragged and locally thinned by progressive brittle fracturing accompanied by pressure solution localized in bed-parallel solution seams.

The central dilational jog (J2 in Fig. 6) develops through several layers with different thicknesses, but always smaller than the local displacement amount (about 52 cm). Clayey interlayers are present and their thickness is comparable to that of the limestone layers. Some layers are dragged toward the slip surface, mainly by brittle fracturing and mineralization. The upper dilational jog (J3 in Fig. 6) cuts through thin limestone layers alternated with clayey interlayers. The local fault displacement (about 80 cm) is significantly higher than the layer thickness. The dilational jog geometry is roughly similar to that of jog J2. The three dilational jogs coexist along the same fault zone and the differences in geometry between the first (J1) and the other two (J2 and J3) appear thus to depend on the respective ratios between displacement amount and layer thickness.

Fracture characteristics and microstructural observations

A common characteristic of all the faults described in this paper, independent of their displacement magnitude, is that they die out vertically into veins that strike parallel to the fault. Tip-point

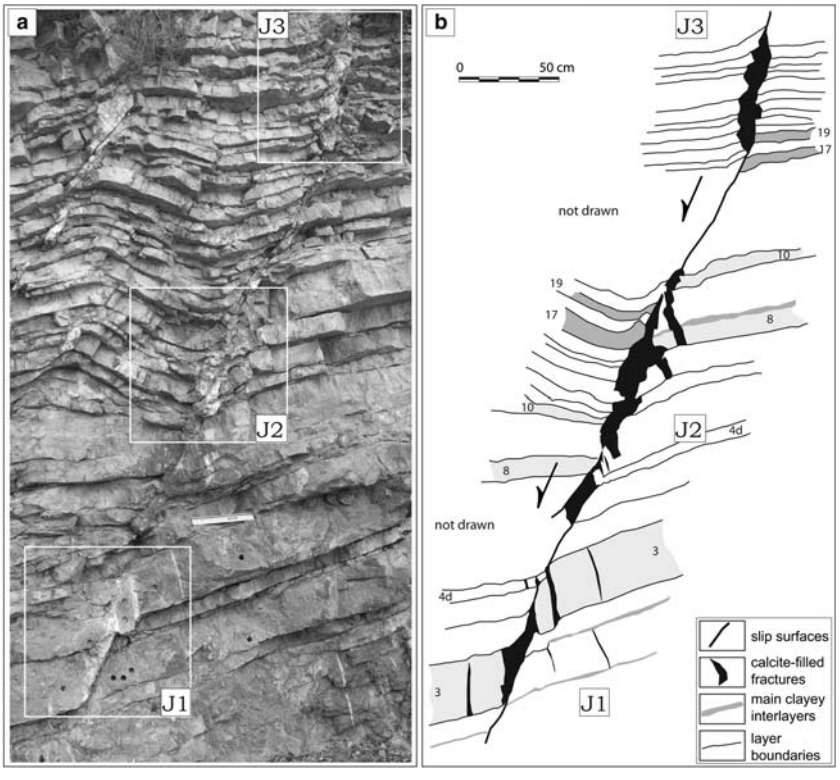

Fig. 6. (**a**) Photograph of Fault 5. (**b**) Interpretative sketch. The exposed fault zone displays three dilational jog structures developing in steps between overlapping slip surfaces. The dilational jogs (J1, J2 and J3, see the text for explanation) show different geometries depending on the ratio between local displacement amount and layer thickness. J1 is confined within one limestone layer, whereas J2 and J3 cut through several limestone and clayey beds. Note that only few very thick clayey interlayers have been drawn. The observable displacement amount varies between 40 and 80 cm.

veins are 5–40 mm wide, and generally tens of centimetres long, commonly depending on layer thickness. They are perpendicular to the layer boundaries and usually do not cross them. However, where the clayey interlayers are very thin (less than 1 mm) or absent, veins may cross them. Veins are planar and have straight boundaries. In places, they show a thicker central portion that tapers off into narrow tails. More commonly, veins end on layer boundaries, appearing as truncated by the clay-reach interlayers. Veins are mostly filled by subhedral calcite crystals (500 μm to 5 mm wide; Fig. 7a) that are weakly or not twinned, with straight grain boundaries. They commonly opened perpendicularly or slightly obliquely to their walls, as testified by displaced older stratigraphic or stylolite markers. Under CL microscopy, calcite filling tip-point veins show uniform red-rose or dull-orange luminescence, a little stronger (lighter) than the limestone host-rocks (Fig. 7b).

Away from the fault tips, toward the central part of most fault zones, outer arc veins occur in the most deflected limestone layers close to the slip surfaces (Fig. 7c). These veins are bounded by the clayey interlayers and have in places a triangular shape. They display complex filling (Fig. 7d) that consists of several generations of calcite related to successive crack-seal events taking place during progressive layer dragging. Calcite crystals are usually large, euhedral or slightly elongated, but also small drusy. Under CL microscopy, calcite filling the outer arc veins is red-rose luminescent, a little lighter than the limestone host-rocks.

Dilational jogs occur within steps between overlapping slip surfaces. Contrary to the tip-point veins and the outer arc veins, they commonly cut through one or more limestone layers. They are filled by thinly twinned, euhedral–subhedral, large blocky calcite crystals up to 10 mm wide, showing strongly zoned luminescence, which highlights different crystal growth steps and defines the individual

facets of grains (Fig. 7e). Slight chemical variations have been highlighted by stable isotope analysis in a previous study (Micarelli *et al.* 2005).

Fault slip surfaces are usually straight, several tens of centimetres long, and cut through several adjacent limestone layers and clay-rich interlayers. They are characterized by slip-parallel beds a few millimetres thick showing calcite fibres (Fig. 7f), and in places by abundant clay and/or dolomite. In places stylolitic peaks testify to combined shear and pressure solution processes (Peacock & Sanderson 1995).

Interpretation and discussion

Fault termination model

All the studied fault terminations are characterized by bed-perpendicular veins roughly striking parallel to the fault, which are usually filled by euhedral large calcite crystals. Veins are clustered along the fault zones, but they do not follow an en-échelon pattern defining shear zones (e.g., Willemse *et al.* 1997; Mazzoli & Di Bucci 2003; Micarelli *et al.* 2005), and do not show a sigmoidal shape, which suggests that no rotation affected them (Ramsay & Graham 1970). They opened perpendicularly or slightly obliquely to their walls.

As displacement decreases toward the fault tip to zero, fault offset has to be accommodated in the fault termination. Even if some contribution of intracrystalline deformation cannot be excluded (Mazzoli *et al.* 2004), the offset accommodation is essentially of frictional type accompanied by pressure solution/crystallization. Slip surfaces cut the limestone layers obliquely, and the displacement amount is systematically accommodated (i) horizontally by vein opening and (ii) vertically by localized compaction of the clayey interlayers in the contractional quadrant of faults (Fig. 8). Localized compaction leads interlayers to be significantly thinned and in places the clay is completely pushed out. Where limestone layers do not have interlayers, solution seams can either develop parallel to bedding or reactivate pre-existing bed-parallel stylolites surfaces.

The described fault termination structure illustrates how normal faults propagate vertically through layered limestone rocks. The observed features result directly from the propagation of the fault tip and constitute the process zone enhancing progressive fault propagation (Reches & Lockner 1994). With regard to the time relationships between fault-related structures, it is observed that all the studied faults die out vertically into only bed-perpendicular calcite veins. Besides, no slip surface has been observed alone, without associated veins. This suggests that in the studied normal fault terminations, layer-perpendicular veins developed before slip planes (e.g., Petit & Barquins 1988; Peacock 2001; Crider & Peacock 2004) and the other kinds of calcite-filled features (e.g., Peacock & Sanderson 1992; Willemse *et al.* 1997).

Influence of layer thickness and role of clayey interlayers on fault evolution and geometry

Slip surfaces have different angles with respect to layering (Fig. 9a). High cut-off angles characterize relatively thick limestone layers, whereas low angles characterize thinner layers alternated with clayey interlayers with comparable limestone/clay thicknesses (e.g., Peacock & Zhang 1994). The thickest limestone layers or relatively thick clayey interlayers may inhibit or restrict vertical propagation of the fault tip across the sequence (Gross *et al.* 1997; Cooke & Underwood 2001; Wilkins & Gross 2002; Soliva & Benedicto 2005). Restriction of fault propagation induces bending of limestone layers at the tips of incipient slip surfaces, which enhances opening of outer arc extensional fractures, and pressure solution localized in the clay-rich interlayers (Fig. 9b). As deformation continues, a single slip surface can cross the preventing interface/bed or connect to an adjacent slip surface by the formation of a calcite-filled dilational jog, as a result of the breakage and dislocation of the layer between the adjacent slip surfaces (Fig. 9c). Therefore, bed-perpendicular veins and dilational jogs usually do not have the same structural position in the fault zone. Dilational jogs develop within steps between slip surfaces, eventually from outer arc veins in the most deformed layers, even if their evolution from early tip-point veins is possible.

Limestone layer thickness appears to be the primary control on the fault tip geometry (Muraoka & Kamata 1983). Faults commonly die out vertically in relatively thick beds, rarely in thinner ones. In thin limestone layers that usually have relatively thick clayey interlayers, tip-point veins are tens of millimetres wide and open perpendicular to their walls (e.g., Fault 1 in Fig. 2). In thick layers, with thin or no interlayers, tip-point veins are commonly narrower (a few millimetres wide) and slip is necessary across them to accommodate deformation (e.g., Fault 4 in Fig. 5). This confirms the fundamental role played by relatively thick clayey interlayers in accommodating deformation by localized compaction.

Layer thickness also plays a role in the geometry of steps between adjacent slip surfaces. Layers thicker than the local fault displacement are dragged between the slip surface tips and can be highly fractured by outer arc veins and dilational

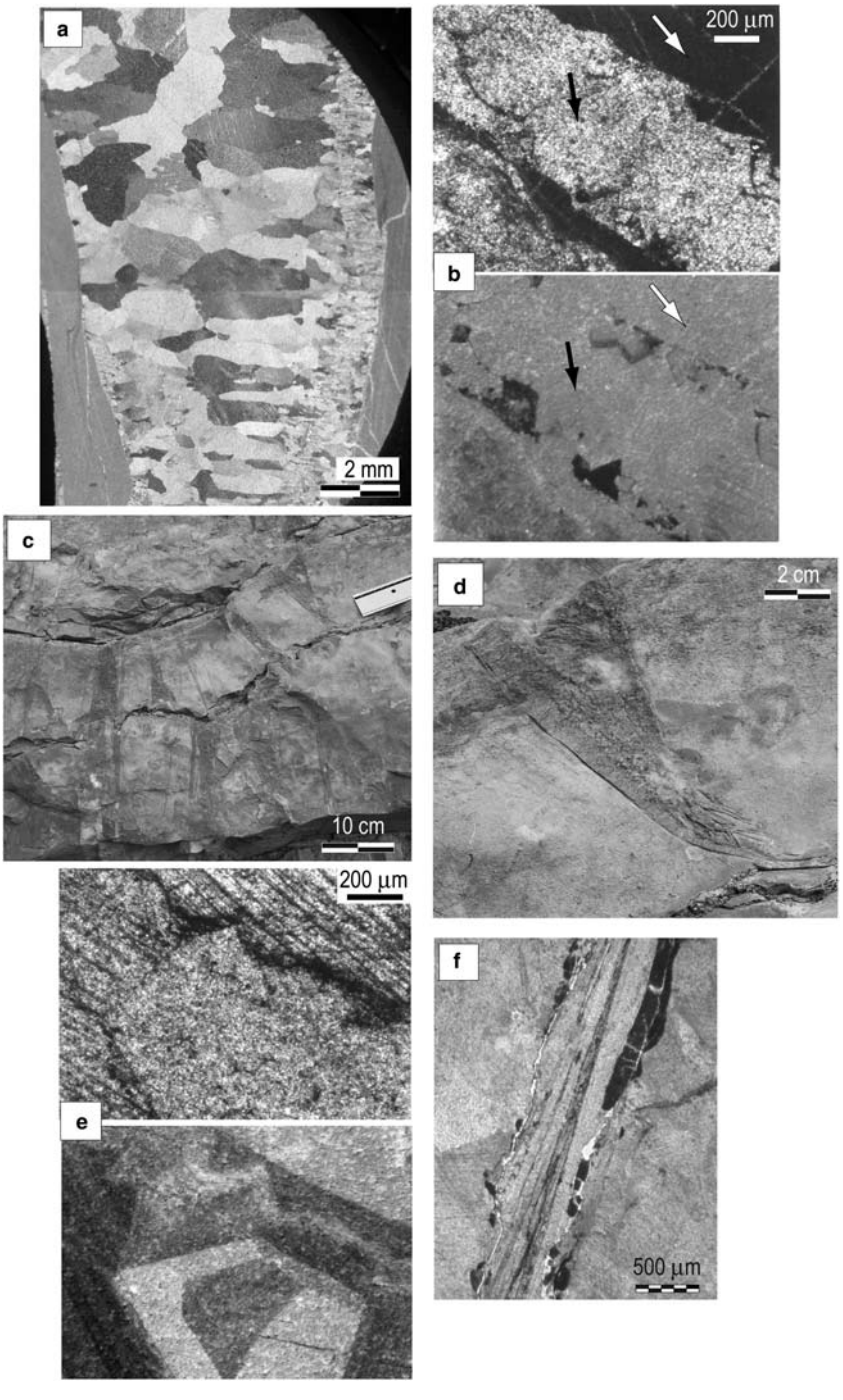

Fig. 7. Selected samples of the different kinds of calcite-filled features characterizing the studied fault terminations and fault zones. (**a**) Tip-point veins display large subhedral, weakly twinned crystals. Usually, they opened roughly perpendicularly or slightly obliquely to their walls (crossed polarized photomicrograph). (**b**) Calcite filling tip-point veins (black arrows) shows cathodoluminescence colours similar to the limestone host-rock (white arrows), suggesting fluid in chemical equilibrium with the host-rock (CL microscopy). (**c**) Outcrop picture of a detail of Fault 2. Continuous thick limestone layers are folded and affected by outer arc veins, showing a typical triangular

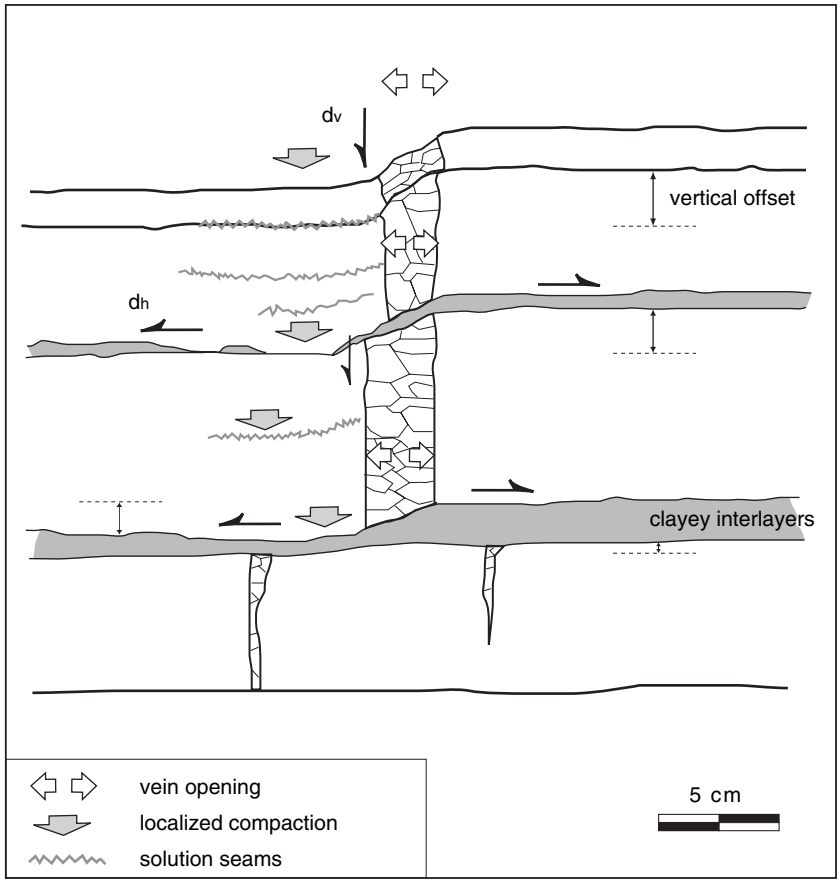

Fig. 8. Schematic diagram showing how fault displacement is accommodated at fault terminations in well-layered, fine-grained limestones alternated with thinner clayey interlayers. The main acting mechanisms are bed-parallel vein opening and bed-perpendicular clay compaction, accompanied by localized pressure solution. d_v and d_h are the vertical and horizontal components of displacement, respectively.

jogs (Fig. 9b), but usually are not completely disconnected. Moreover, the clayey interlayers bounding the limestone beds are sheared but usually keep their continuity. On the other hand, layers thinner than the local displacement are disconnected, although in places appear to be connected by dilational jogs. In this case, the clayey interlayers are cut by the propagating slip surfaces (Fig. 9c). Therefore, connected/disconnected beds within jogs between stepped slip surfaces may either constitute two successive steps of deformation in the fault evolution (Micarelli *et al.* 2005), or coexist in the same fault as a function of the bed thickness/local displacement ratio (Fig. 9, and Fault 5 in Fig. 6).

It appears that the role of clayey interlayers is important where they have thickness comparable with that of the limestone layers. In particular, interlayers (i) contribute to the decrease in fault displacement, which is accommodated by bed-perpendicular compaction, (ii) localize bed-parallel slip, allowing tip-point veins to open, (iii) inhibit vertical propagation of the fault tip across the

Fig. 7. (*Continued*) shape in places. (**d**) Detail of the previous picture: outer arc veins are in places constituted by several generations of calcite related to successive crack-seal events. (**e**) Thinly twinned, large, euhedral calcite crystals filling dilational jogs display strongly zoned luminescence, which suggests slight variations in fluid chemistry (CL microscopy). (**f**) Fault slip surfaces are commonly characterized by a thin layer constituted by slip-parallel calcite fibres (plain light photomicrograph).

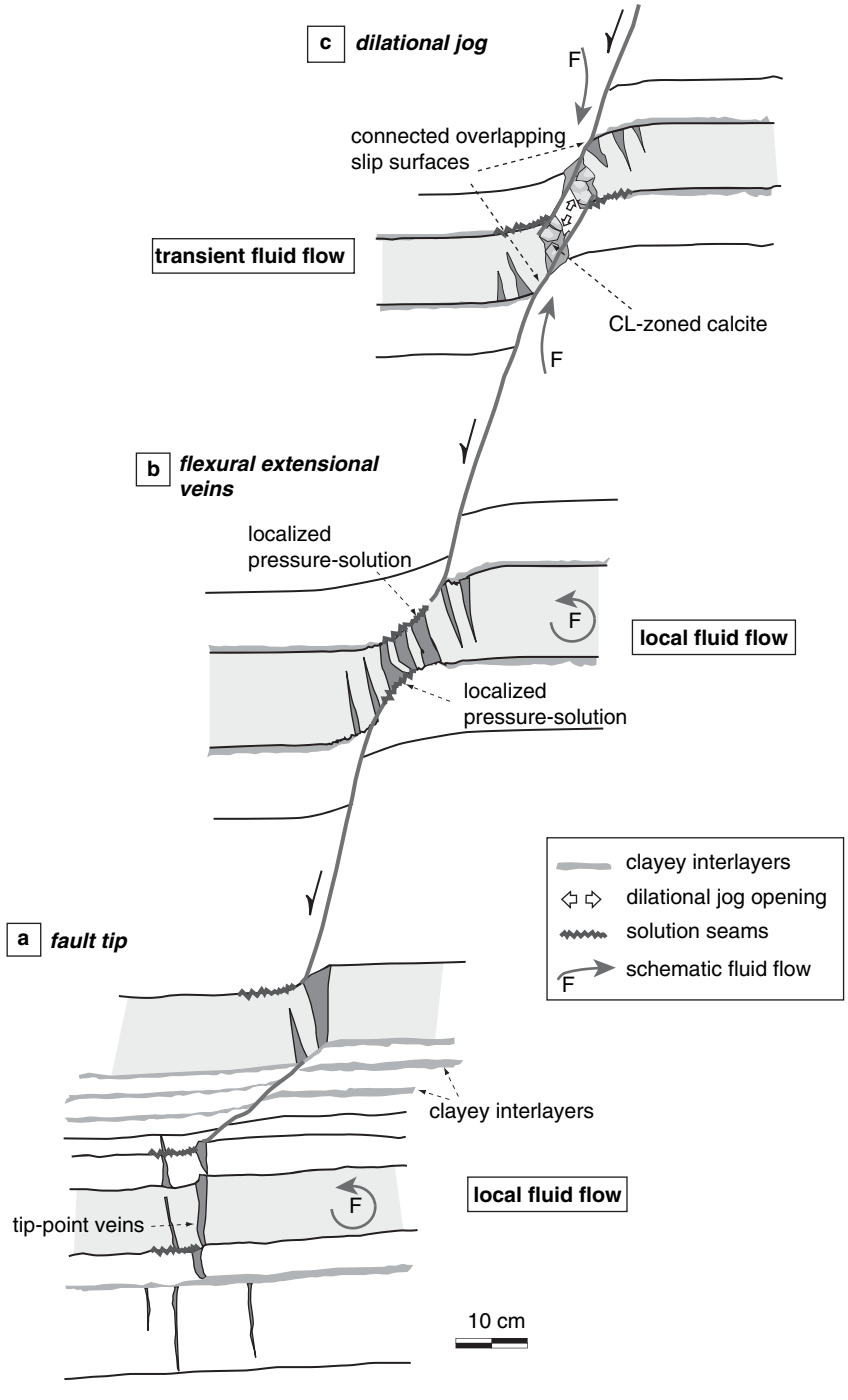

Fig. 9. Model for the different structures observed at increasing distances from the fault tip. Displacement amount increases away from the fault tip (sketch scale is approximate). (**a**) The fault tip is mostly characterized by bed-perpendicular, calcite-filled veins. Fluid circulation is local. Slip surfaces have different cut-off angles depending on the presence and thickness of clayey interlayers. In places, dilational jogs may occur within steps between adjacent slip surfaces. (**b**) Vertical propagation of fault slip surfaces may be inhibited by thick limestone layers and/or clayey interlayers, which leads the limestone layers to be bent and fractured by outer arc veins and dilational jogs. The local

limestone sequence, enhancing outer arc vein and dilational jog development and (iv) localize low-angle slip surfaces, where alternated with relatively thin limestone layers.

Influence on fluid flow properties

The series affected by the studied fault zones consists of limestone layers alternated with thinner clayey interlayers. The two lithologies are likely to have different permeabilities. A distinct vertical anisotropy in a sub-horizontally layered series is the major requirement for potential horizontal fluid flow (e.g., Bredehoeft *et al.* 1988). Most of the tip-point veins are bed-confined, and cross the layer boundaries only where clayey interlayers are very thin (commonly less than 1mm) or absent (Fig. 9a). Vein-filling calcite consists of large, euhedral crystals that filled a cavity that probably opened at a high rate of displacement (Gratier & Gamont 1990; Canole *et al.* 1997). However, calcite shows cathodoluminescence colours similar to that of the limestone host-rock, confirming that fluid circulation was local, confined by the clayey interlayers. This implies limited horizontal mass transfer, probably from bed-parallel solution seams to the fractures opening within the same limestone layer.

Restriction of propagating fault slip surfaces through the limestones, related to the presence of thick limestone layers or clayey interlayers, induced opening of outer arc extensional fractures and dilational jogs (Fig. 9b). If confined within the limestone layers, these structures show the same cathodoluminescence characteristics as the tip-point veins. Fluid circulation remained local again, confined by clayey interlayers.

Where dilational jogs connecting adjacent slip surfaces cut through one or more limestone beds because occurring in layers thinner than the local displacement, they are filled by calcite showing cathodoluminescence gradients outlining the facets of individual grains (Figs 9c & 7e). This suggests crystals growing in free fluid, with fluctuations in fluid chemistry (Sommer 1972; ten Have & Heijnen 1985; Dromgoole & Walter 1990; Travé *et al.* 1998), as also shown by stable isotope analysis in a previous study (Micarelli *et al.* 2005). Relatively increased fluid circulation is caused by the fact that limestone beds are completely disconnected, and in particular the clayey interlayers are cut by the slip surfaces. Moreover, slip surfaces meeting in the dilational jog lead the mean stress to decrease inside the jog in response to fault slip, which can drive fluids into the jog (Sibson 1985; Connoly & Cosgrove 1999; Nemčok *et al.* 2002). Transient fluid flow along the slip surfaces is documented by the presence of multiple layers a few millimetres thick showing thin calcite fibres (e.g., Fig. 7f), each precipitated during a different slip event. Slip surfaces cutting through several layers and the breakage of the confining clayey interlayers create thus a migration pathway between adjacent jogs, allowing communication between separated fluid reservoirs. Dilational jogs could remain open until either they are sealed by mineral precipitation, or their aperture is reduced when fluid pressure is decreased by fluid discharge (Sibson 1990; Knipe 1993).

Conclusions

This paper describes the geometry and evolution of normal fault terminations in limestones from the French SE-Basin. The affected series consists of limestone layers alternated with thin clayey interlayers. We provide a model for displacement accommodation at fault tips and discuss implications for related fluid flow.

Fault zones die out vertically into bed-perpendicular, commonly bed-bounded calcite veins. Slip surfaces cut obliquely through the limestone series. Displacement decreasing progressively towards the fault tip is accommodated by (i) bed-parallel vein opening and (ii) bed-perpendicular localized compaction of clayey interlayers, accompanied by pressure solution localized on bed-parallel seams in the contractional quadrants of faults.

Slip surfaces propagating vertically are usually steeper in more brittle limestone layers than in limestone/clay alternated layers with comparable relative thicknesses. The thickest limestone layers or relatively thick clayey interlayers may inhibit vertical propagation of the fault tip across the sequence, inducing bending of limestone layers, opening of outer arc extensional fractures and localized pressure solution, and formation of dilational jogs within steps between adjacent slip surfaces. If the local fault displacement is larger than the layer thickness, dilational jogs may cut through

Fig. 9. (*Continued*) displacement amount is smaller than the layer thickness. Fluid flow remains confined by the clayey interlayers. (**c**) As deformation continues, the slip surface crosses the preventing interface and the displacement becomes larger than the layer thickness. Limestone layers are disconnected and the confining clayey interlayers are sharply cut. Dilational jogs cutting through one or more limestone layers are filled by CL-zoned calcite, which indicates fluid chemistry fluctuation and thus relatively increased fluid flow (see text for explanation).

several limestone beds that are thus disconnected, and clayey interlayers are cut by the propagating slip surfaces. Different geometries may coexist in the same fault zone, due to the ratio between local displacement and layer thickness.

Tip-point vein opening induced formation of voids, as testified by the cement crystal characteristics indicating free-fluid growth, but the fluid circulation remained local. As the veins commonly stop at clayey interlayers, fluid flow is likely to be confined within the limestone layer, with limited mass transfer from bed-parallel solution seams to the veins.

In contrast, where limestone beds and clayey interlayers are disconnected by the propagating slip surfaces, the characteristics of the calcite crystals cementing dilational jogs indicate free-fluid growth with fluctuations in fluid chemistry. Relatively increased fluid circulation is caused by the breakage of the sealing clayey interlayers, and the opening of dilational jogs, which forms potential pressure gradient to suck fluid flow into the jogs. This leads fluid to migrate between adjacent jogs and along the fault during the interval between its failure and the complete cementation of dilational jogs.

This work has been carried out in the frame of a research convention TOTAL-Université Paris XI (DGEP/TDO/CA/RD no. (12806A1/UPS no. 6052 1/CNRS no. 041.1883.01). We thank S. Delisle and J.-L. Montenat (Total) for the facilities and the helpful discussions. We thank Jean-Pierre Villotte (Université Paris XI) for the preparation of thin sections. We also thank C. Invernizzi, Y. Missenard, B. Saint-Bezar and P. Vergely for the friendly help and useful suggestions on the fieldwork and interpretations. The very constructive reviews of I. Davison and D. Peacock considerably improved the manuscript.

References

BOUCHETTE, F., SÉGURET, M. & MOUSSINE-POUCHKINE, A. 2001. Coarse carbonate breccia as the result of water-wave cyclic loading (uppermost Jurassic–South East Basin, France). *Sedimentology*, **48**, 767–789.

BREDEHOEFT, J. D., DJEVANSHIR, R. D. & BELITZ, K. R. 1988. Lateral fluid flow in a compacting sand-shale sequence: South Caspian Basin. *American Association of Petroleum Geologists Bulletin*, **72**, 416–424.

CANOLE, P., ODONNE, F. & POLVE, M. 1997. Heterogeneous strain associated with normal faulting: evidence of mass transfer by pressure solution associated with fault displacement. *Tectonophysics*, **283**, 129–143.

CONNOLY, P. T. & COSGROVE, J. W. 1999. Prediction of fracture-induced permeability and fluid flow in the crust using experimental stress data. *American Association of Petroleum Geologists Bulletin*, **83**, 757–777.

COOKE, M. L. & UNDERWOOD, C. A. 2001. Fracture termination and step-over at bedding interfaces due to frictional slip and interface opening. *Journal of Structural Geology*, **23**, 223–238.

CRIDER, J. G. & PEACOCK, D. C. P. 2004. Initiation of brittle faults in the upper crust: a review of field observation. *Journal of Structural Geology*, **26**, 691–707.

CROS, P., LANAU, P., VINCHON, C., BONHOMME, M. G., BOULÈGUE, L., CULA, P. & GIOT, D. 1993. Sandstone diagenesis and evolution of the porosity in a potential Triassic source rock (Privas area, Ardèche). *Bullettin de la Société Géologique de France*, **164**, 631–647.

DAVISON, I. 1995. Fault slip evolution determined from crack-seal veins in pull-aparts and their implications for general slip models. *Journal of Structural Geology*, **17**, 1025–1034.

DE GRACIANSKY, P. C., DARDEAU, G., DUMONT, T., JACQUIN, T., MARCHAND, D., MOUTERDE, R. & VAIL, P. R. 1993. Depositional sequence cycles, transgressive–regressive facies cycles, and extensional tectonics: examples from the southern Subalpine Jurassic basin, France. *Bullettin de la Société Géologique de France*, **16**, 709–718.

DERCOURT, J., RICOU, L. E. & VRIELYNCK, B. E. 1993. *Atlas Téthys Palaeoenvironmental Maps*. Gauthiers-Villars, Paris.

DROMGOOLE, E. L. & WALTER, L. M. 1990. Iron and manganese incorporation into calcite: effects of growth kinetics, temperature and solution chemistry. *Chemical Geology*, **81**, 311–336.

GIGNOUX, M. & MORET, J. 1938. *Géologie dauphinoise*, 1st edn., Masson, Paris.

GRATIER, J. P. & GAMOND, J. F. 1990. Transition between seismic and aseismic deformation in the upper crust. *In*: KNIPE, R. J. & RUTTER, E. H. (eds) *Deformation Mechanisms, Rheology and Tectonics*. Geological Society, London, Special Publications, **54**, 461–473.

GROSS, M. R., GUTIERREZ-ALONZO, G., BAI, T., WACKER, M. A., COLLINSWORTH, K. B. & BEHL, R. J. 1997. Influence of mechanical stratigraphy and kinematics on fault scaling relations. *Journal of Structural Geology*, **19**, 171–183.

GUILHAUMOU, N., TOURAY, J. C., PERTHUISOT, V. & ROURE, F. 1996. Palaeocirculation in the basin of southeastern France sub-alpine range: a synthesis from fluid inclusions studies. *Marine and Petroleum Geology*, **13**, 695–706.

INGRAFFEA, A. D. 1987. Theory of crack initiation and propagation in rock. *In*: ATKINSON, B. K. (ed.) *Fracture Mechanics of Rocks*. Academic Press, San Diego, CA, 71–108.

KELLY, P. G., SANDERSON, D. J. & PEACOCK, D. C. P. 1998. Linkage and evolution of conjugate strike-slip fault zones in limestones of Somerset and

Northumbria. *Journal of Structural Geology*, **20**, 1477–1493.

KIM, Y.-S., PEACOCK, D. C. P. & SANDERSON, D. J. 2004. Fault damage zones. *Journal of Structural Geology*, **26**, 503–517.

KNIPE, R. J. 1993. The influence of fault zone processes and diagenesis on fluid flow. *In*: HORBURY, A. D. & ROBINSON, A. (eds) *Diagenesis and Basin Development*. American Association of Petroleum Geologists Studies in Geology, **36**, 135–151.

KNOTT, S. D., BEACH, A., BROCKBANK, P. J., BROWN, J. L., MCCALLUM, J. E. & WELBON, A. I. 1996. Spatial and mechanical controls on normal fault populations. *Journal of Structural Geology*, **18**, 359–372.

MARSHALL, D. J. 1988. *Cathodoluminescence of Geologic Materials*. Unwin Hyman, Boston, MA.

MAZZOLI, S. & DI BUCCI, D. 2003. Critical displacement for normal fault nucleation from en-échelon vein arrays in limestones: a case study from the southern Apennines (Italy). *Journal of Structural Geology*, **25**, 1011–1020.

MAZZOLI, S., INVERNIZZI, C., MARCHEGIANI, L., MATTIONI, L. & CELLO, G. 2004. Brittle–ductile shear zone evolution and fault initiation in limestones, Monte Cugnone (Lucania), southern Apennines, Italy. *In*: ALSOP, G. I., HOLDSWORTH, R. E., MCCAFFREY, K. J. W. & HAND, M. (eds) *Flow Processes in Faults and Shear Zones*. Geological Society, London, Special Publications, **224**, 353–373.

MCGRATH, A. G. & DAVISON, I. 1995. Damage zone geometry around fault tips. *Journal of Structural Geology*, **17**, 1011–1024.

MICARELLI, L., MORETTI, I. & DANIEL, J. M. 2003. Structural properties of rift-related normal faults: the case study of the Gulf of Corinth, Greece. *Journal of Geodynamics*, **36**, 275–303.

MICARELLI, L., BENEDICTO, A., INVERNIZZI, C., SAINT-BEZAR, B., MICHELOT, J. L. & VERGELY, P. 2005. Influence of P/T conditions on the style of normal fault initiation and growth in limestones from the SE-Basin, France. *Journal of Structural Geology*, **27**, 1577–1598.

MICARELLI, L., BENEDICTO, A. & WIBBERLEY, C. A. J. 2006*a*. Structural evolution and permeability of normal fault zones in highly porous carbonate rocks. *Journal of Structural Geology*, **28**, 1214–1227.

MICARELLI, L., MORETTI, I., JAUBERT, M. & MOULOUEL, H. 2006*b*. Fracture analysis in the southwestern Corinth rift (Greece) and implications on fault hydraulic behaviour. *Tectonophysics*, **426**, 31–59.

MURAOKA, H. & KAMATA, H. 1983. Displacement distribution along minor fault traces. *Journal of Structural Geology*, **5**, 483–495.

NEMČOK, M., HENK, A., GAYER, R. A., VANDYCKE, S. & HATHAWAY, T. M. 2002. Strike–slip fault bridge fluid pumping mechanism: insights from field-based palaeostress analysis and numerical modelling. *Journal of Structural Geology*, **24**, 1885–1901.

PAGEL, M., BARBIN, V., BLANC, P. & OHNENSTETTER, D. 2000. *Cathodoluminescence in Geosciences*. Springer, Berlin.

PEACOCK, D. C. P. 2001. The temporal relationship between joints and faults. *Journal of Structural Geology*, **23**, 329–341.

PEACOCK, D. C. P. & SANDERSON, D. J. 1992. Effects of layering and anisotropy on fault geometry. *Journal of the Geological Society of London*, **149**, 793–802.

PEACOCK, D. C. P. & SANDERSON, D. J. 1995. Pull-aparts, shear fractures and pressure solution. *Tectonophysics*, **241**, 1–13.

PEACOCK, D. C. P. & ZHANG, X. 1994. Field examples and numerical modelling of oversteps and bends along normal faults in cross-section. *Tectonophysics*, **234**, 147–167.

PETIT, J. P. & BARQUINS, M. 1988. Can natural faults propagate under mode II conditions? *Tectonics*, **7**, 1243–1256.

POLLARD, D. D. & SEGALL, P. 1987. Theoretical displacements and stresses near fractures in rock: with application to faults, joints, veins, dikes, and pressure solution surfaces. *In*: ATKINSON, B. K. (ed.) *Fracture Mechanics of Rock*. Academic Press, London, 277–349.

RAMSAY, J. G. & GRAHAM, R. H. 1970. Strain variations in shear belts. *Canadian Journal of Earth Sciences*, **7**, 783–813.

RECHES, Z. & LOCKNER, D. A. 1994. Nucleation and growth of faults in brittle rocks. *Journal of Geophysical Research*, **99**, 18159–18174.

ROURE, F., BRUN, J. P., COLLETTA, B. & VIALLY, R. 1994. Multiphase extensional structures, fault reactivation and petroleum plays in the alpine foreland basin of south eastern France. *In*: MASCLE, A. (ed.) *Hydrocarbon and Petroleum Geology of France.* Springer, Berlin, 245–248.

SÉGURET, M., MOUSSINE-POUCHKINE, A., RAJA GABAGLIA, G. & BOUCHETTE, F. 2001. Storm deposits and storm-generated coarse breccias on a pelagic outer-shelf (South East Basin, France). *Sedimentology*, **48**, 231–254.

SHIPTON, Z. K. & COWIE, P. A. 2001. Damage zone and slip-surface evolution over μm to km scales in high-porosity Navajo sandstone, Utah. *Journal of Structural Geology*, **23**, 1825–1844.

SIBSON, R. H. 1985. Stopping of earthquake ruptures at dilational fault jogs. *Nature*, **316**, 248–251.

SIBSON, R. H. 1989. Earthquake faulting as a structural process. *Journal of Structural Geology*, **11**, 1–14.

SIBSON, R. H. 1990. Conditions for fault-valve behaviour. *In*: KNIPE, R. J. & RUTTER, E. H. (eds) *Deformation Mechanisms, Rheology and Tectonics*. Geological Society, London, Special Publications, **54**, 15–28.

SIBSON, R. H. 1996. Structural permeability of fluid-driven fault-fracture meshes. *Journal of Structural Geology*, **18**, 1031–1042.

SOLIVA, R. & BENEDICTO, A. 2005. Geometry, scaling relations and spacing of vertically restricted normal faults. *Journal of Structural Geology*, **27**, 317–325.

SOMMER, S. E. 1972. Cathodoluminescence in carbonates, 1. Characterization of cathodoluminescence

from carbonate solid solution. *Chemical Geology*, **9**, 257–273.

TEN HAVE, T. & Heijnen, W. 1985. Cathodoluminescence activation and zonation in carbonate rocks: an experimental approach. *Geologie en Mijnbouw*, **64**, 297–310.

TRAVÉ, A., CALVET, F., SOLER, A. & LABAUME, P. 1998. Fracturing and fluid migration during Palaeogene compression and Neogene extension in the Catalan Coastal Ranges, Spain. *Sedimentology*, **45**, 1063–1082.

VERMILYE, J. M. & SCHOLZ, C. H. 1998. The process zone: a microstructural view of fault growth. *Journal of Geophysical Research*, **103**, 12223–12237.

WILKINS, S. J. & GROSS, M. R. 2002. Normal fault growth in layered rocks at Split Mountain, Utah. *Journal of Structural Geology*, **24**, 1413–1429.

WILLEMSE, E. J. M., PEACOCK, D. C. P. & AYDIN, A. 1997. Nucleation and growth of strike–slip faults in limestones from Somerset, U. K. *Journal of Structural Geology*, **19**, 1461–1477.

On the structure and mechanical properties of large strike-slip faults

D. R. FAULKNER[1], T. M. MITCHELL[1], E. H. RUTTER[2] & J. CEMBRANO[3]

[1]*Rock Deformation Laboratory, Department of Earth and Ocean Sciences, University of Liverpool, Liverpool, UK (e-mail: faulkner@liverpool.ac.uk)*

[2]*Rock Deformation Laboratory, School of Earth, Environment and Atmospheric Sciences, University of Manchester, Manchester, UK*

[3]*Departamento de Ciencias Geologicas, Universidad Catolica del Norte, Antofagasta, Chile*

Abstract: Elucidation of the internal structure of fault zones is paramount for understanding their mechanical, seismological and hydraulic properties. In order to observe representative brittle fault zone structures, it is preferable that the fault be passively exhumed from seismogenic depths and the exposure must be in arid or semi-arid environments where the fragile rocks are not subject to extensive weathering. Field observations of two such faults are used to constrain their likely mechanical properties. One fault is the Carboneras fault in southeastern Spain, where the predominant country rocks are phyllosilicate-rich lithologies, and the other is part of the Atacama fault system in northern Chile, where faults pass through crystalline rocks of acidic to intermediate composition. The Carboneras fault is a left lateral fault with several tens of kilometres offset exhumed from approximately 4 km depth, and displays multiple strands of clay-bearing fault gouge, each several metres wide, that contain variably fractured lenses of protolithic mica schists. The strain is evenly distributed across the gouge layers, in accordance with the measured laboratory mechanical behaviour which shows predominantly strain hardening characteristics. The overall width of the fault zone is several hundred metres. Additionally, there are blocks of dolomitic material that are contained within the fault zones that show extremely localized deformation in the form of faults several centimetres wide. These are typically arranged at an angle of *c*. 20° to the overall fault plane. These differing types of fault rock products allow for the possibility of 'mixed mode' seismicity, with fault creep occurring along the strands of velocity strengthening clay-rich gouge, punctuated by small seismic events that nucleate on the velocity weakening localized faults within the dolomite blocks. The Caleta Coloso fault in northern Chile has a left-lateral offset of at least 5 km and was exhumed from 5–10 km depth. The fault core is represented by a 200–300 m wide zone of hydrothermally altered protocataclasite and ultracataclasite. This is surrounded by a zone of micro and macro-fractures on the order of 150 m thick. The fault core shows a heterogeneous distribution of strain, with alternate layers of ultracataclasite and lower strain material. The strain-weakening behaviour of crystalline rocks might be expected to produce highly localized zones of deformation, and thus the wide core zone must be a result of additional process such as precipitation strengthening or geometric irregularities along the fault plane.

Understanding the structure of fault zones is essential in order to help interpret their mechanical, hydraulic and seismological properties. Faults are key structures in the Earth's upper crust that control the strength of the lithosphere (Kusznir & Bott 1977; Kohlstedt *et al.* 1995; Townend & Zoback 2000), the flow of fluids (Knipe 1992; Caine *et al.* 1996) and the nucleation and propagation of earthquakes. Often we want to describe the structure of faults at depth in the crust (for example at seismogenic depths), but these regions can only be accessed by remote geophysical methods, unless deep drilling is an option (Ohtani *et al.* 2001; Zoback *et al.* 2006) or observation from deep mines. Even where drillholes are present, a one-dimensional view of a fault zone is obtained, where a two- or three-dimensional view is necessary in order to understand fully the fault properties.

Field studies of exhumed fault zones can aid in the understanding of fault zone structure at depth, but must be approached with caution. Often, fault zones are active during the exhumation process and as such have a full range of structures that overprint those that formed at the depth of interest. The primary structures (those formed at depth) and the overprinting structures may not be easily distinguishable. Consequently structures formed under near-surface conditions may be wrongly interpreted as key features in exhumed

From: WIBBERLEY, C. A. J., KURZ, W., IMBER, J., HOLDSWORTH, R. E. & COLLETTINI, C. (eds) *The Internal Structure of Fault Zones: Implications for Mechanical and Fluid-Flow Properties*. **299**, 139–150.
DOI: 10.1144/SP299.9 0305-8719/08/$15.00

surface-exposed fault zones. For the above reasons field studies on fault zones are often made on passively exhumed fault zones where it can be demonstrated that little or no displacement and structural overprinting occurred during exhumation either from the regional tectonics or from the nature and mineralogy of the fault rocks.

Faults that are not well exposed can present problems as key parts of the fault zone may be disregarded solely because they are not observable at the surface. Another potential problem with using natural faults for study concerns collection of material from surface exposures for laboratory testing or analysis. Near-surface weathering can significantly alter the mineralogy, microstructure and physical properties of rocks, as demonstrated by Morrow & Lockner (1994). Again, incomplete exposure may lead to the over-emphasis of laboratory results obtained from material collected from the exposed material, whereas the mechanical and hydraulic properties may well be primarily controlled by unexposed or poorly exposed parts of the fault zone.

Given the difficulties of studying large faults in the field, it is hardly surprising that few detailed studies exist of their structure. Exceptions to this include work by Chester *et al.* (1993), Schulz & Evans (2000), Wibberley & Shimamoto (2003), Faulkner *et al.* (2003), Cembrano *et al.* (2005) and Jefferies *et al.* (2006). All of these examples study faults with variable exposure levels, varying constraints on their exhumation histories and as such give different degrees of confidence when interpreting the structure of faulting at depth.

In this work, we aim to contribute to the database on the internal structure of large strike-slip faults, and infer some aspects of the mechanical properties of faults from observations of their internal structure. First we describe the structure of two major strike–slip faults that cut through very different country rocks. Aspects of the structure of the Carboneras fault in southeastern Spain are described, then those from the Caleta Coloso fault in northern Chile. The likely mechanical properties of the two faults are inferred from the macroscopic structure of the two faults in the discussion.

Fault zone structure

Both the Carboneras and the Caleta Coloso faults have been largely passively exhumed from depth, and they are excellently exposed in semi- and hyper-arid environments. The mineralogy of the fault rock in the Carboneras fault and the Caleta Coloso fault indicates fault activity at *c*. 4 and *c*. 6 km depth respectively. The depth range from which the Carboneras fault was exhumed is estimated from the present height of uplifted basement rocks and Pliocene reef complexes and the temperatures at which the neocrystallized clay phases contained within the fault gouges formed (assuming an average geothermal gradient). This yields values of exhumation between 4 and 1.5 km (Faulkner *et al.* 2003), which is consistent with recent uplift rates estimated from marine terraces on the order of 0.05–0.1 mm a^{-1} (Bell *et al.* 1997). The fault accommodates several tens of kilometres of movement across it (Rutter *et al.* 1986). On the Caleta Coloso fault, fission track dating of fault-related fracturing has shown that the presently exposed fault rocks formed at a temperature of at least 100 °C, interpreted to indicate a minimum of 3 km depth (Herrera *et al.* 2005). The Caleta Coloso fault has undergone more recent movements, although these are limited in extent, and are in response to large subduction zone earthquakes associated with the offshore trench (Gonzalez & Carrizo 2003). These movements are easily recognized in the field and expressed as very localized, narrow fault planes that form small fault scarps at the surface. The Caleta Coloso fault has at least 5 km of strike–slip offset (Cembrano *et al.* 2005).

The results of the above analyses indicate that the structures of both faults can be taken to be representative of faulting at depth. Both faults, by virtue of their offset, are crustal-scale structures. The constituent structures of each fault are now described in turn, and the interpretation of the mechanical significance of these is analysed later in the discussion.

Carboneras fault, SE Spain

The macroscopic structure of the Carboneras fault has been described in detail previously in Faulkner *et al.* (2003). Here some key aspects of the structure are summarized. The fault cuts through Alpine age (Palaeogene) metamorphic rocks, Miocene age marine sediments and volcanic rocks. In the area of study (see Fig. 1) the fault cuts predominantly through the metamorphic basement rocks that consist largely of graphitic mica schist. The southern edge of the fault is obscured somewhat by later volcanic rocks (lava flows and lahars), but along-strike observations suggest that very little of the total fault width is unexposed. The igneous rocks contained within the fault zone are dolerites and show intrusive relationships with very little deformation. They have been interpreted previously as feeder systems for the later volcanics (Rutter *et al.* 1986). The fault initiated in the early Miocene (Scotney *et al.* 2000) and, as stated previously, ceased significant activity between 5 and 10 Ma ago. The fault has left-lateral offset on it, as

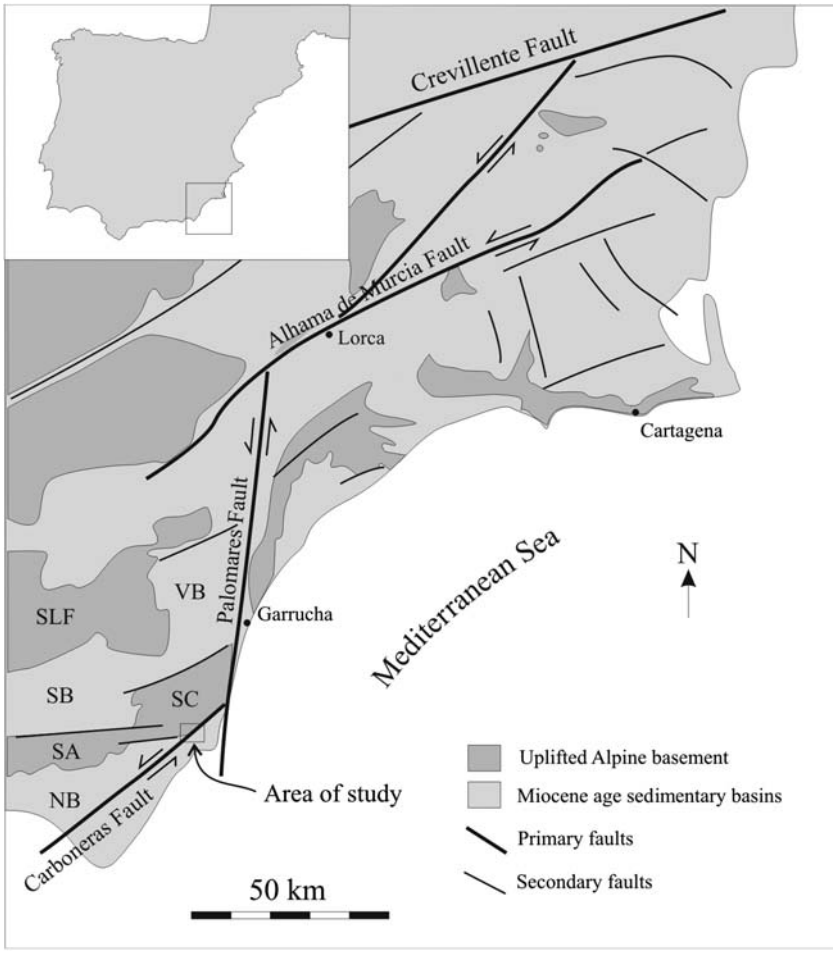

Fig. 1. Regional map showing the location of the Carboneras fault within the tectonic framework of southeastern Spain. SLF = Sierra de Los Filabres, SA = Sierra Alhamilla, SC = Sierra Cabrera, NB = Níjar Basin, SB = Sorbas Basin, VB = Vera Basin.

determined from slickenlines and movements indicators constructed from the measurement of the orientation of P foliations and R_1 Riedel shears present within the gouge layers.

The macroscopic fault zone structure is that of a fault consisting of multiple, anastomosing strands of fault gouge that contain variably fractured lenses of the country rock (Fig. 2). Overall the width of the zone of deformation is on the order of several hundred metres. As the fault cuts through mica-rich schists, the fault rocks within the gouge layers are phyllosilicate-rich, clay-bearing fault gouges. The typical mineralogical assemblage in these gouges includes muscovite/illite, chlorite, quartz with minor amounts of gypsum, albite and graphite. The layers of fault gouge are typically on the order of several metres wide and the distribution of strain within the gouge layers is very homogeneous (Fig. 3a & b).

Large blocks of dolomite are also included within the fault zone, and these display a completely different style of faulting to that developed within the mica-rich rocks. Instead of wide layers of deformed rock with an even distribution of strain across them, the faults in the dolomite are very localized, narrow features. Figure 3c shows one of these localized fault planes, that has a slickenlined mechanical wear surface. The orientation of these fault planes is typically oblique to the general strike of the Carboneras fault; they are arranged in an en echelon pattern and make an angle of 10–25° measured anticlockwise from the strike of the main fault zone (Fig. 2). Thus these faults are in a R_1 Riedel orientation.

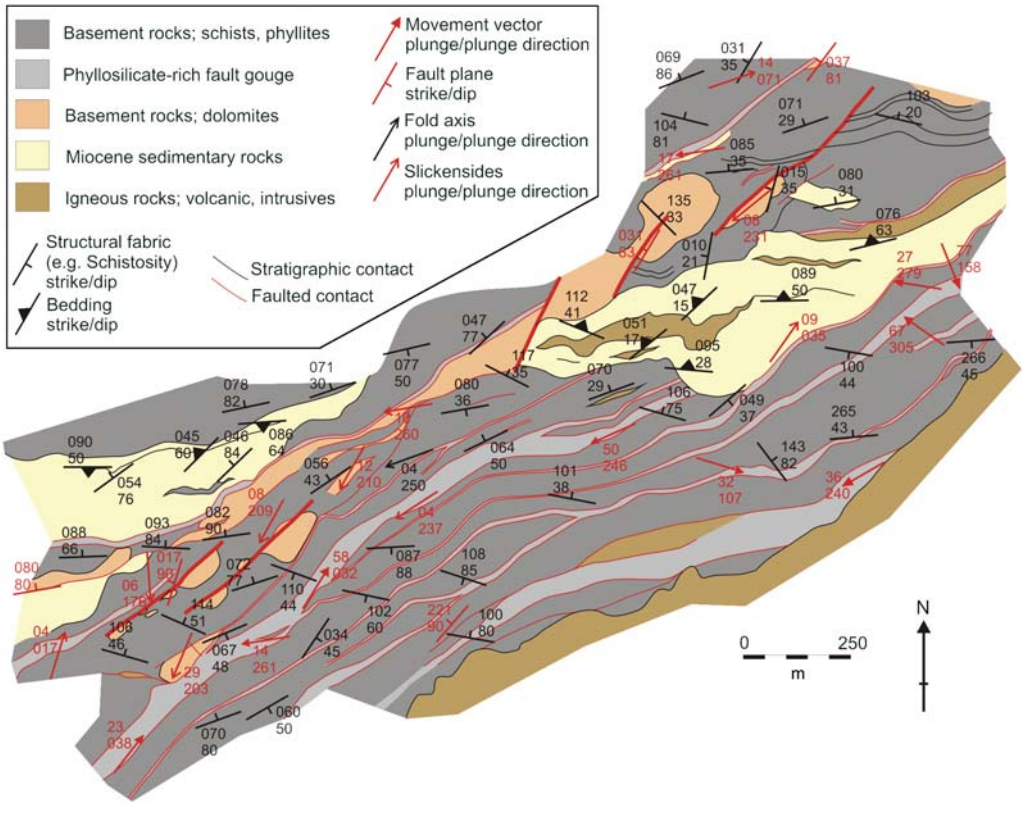

Fig. 2. Summary geological map of the Carboneras fault zone to the area immediately northeast of the village of El Saltador, southeastern Spain. The anastomosing layers of fault gouge are highlighted, as are the very localized narrow fault planes developed within the blocks of dolomite contained within the fault zone (after Faulkner *et al.* 2003).

Caleta Coloso fault, N. Chile

The large-scale structure of the Caleta Coloso fault in northern Chile has previously been described by Cembrano *et al.* (2005). The fault zone is part of the Atacama fault system, which is an arc-parallel strike–slip structure that accommodated some of the oblique convergence between the Nazca and South American plates (Fig. 4). Presently the Atacama fault system is largely passive, with transcurrent plate motions occurring on fault systems much further to the east (e.g., Falla Oeste). In this work, we describe the results of some new detailed fault zone mapping conducted on part of the Caleta Coloso fault surrounding Quebrada Isabel (Fig. 5). In the area of study, the fault zone cuts through plutonic rocks of predominantly granodioritic composition. It has a left-lateral sense of shear determined from the orientation of slickenlines and offset planar markers (e.g., dykes) within the fault zone.

The fault core structure is approximately 200–300 m wide and is characterized by zones of fractured protolith, cataclasite and ultracataclasite. Hydrothermal precipitation of chlorite and epidote within the fault core has led to a characteristic green colouration that is restricted to the fault core (Fig. 6). Geothermometry conducted on chlorite contained within veins, some of which have been affected by later fault movements, shows temperatures around 250 °C. Assuming that the fluids that deposited these veins had not travelled a great distance, their temperature gives an additional constraint on the maximum depth of faulting, if a reasonable geothermal gradient is used. For a magmatic arc this gradient may be up to 40 °C, indicating a depth of around 6 km.

The distribution of strain within the zones of cataclasite (Fig. 7a) and ultracataclasite (Fig. 7b) is not as clear as within the gouge layers of the Carboneras fault zone. There are angular blocks of granodiorite contained within an ultracataclasite matrix containing hydrothermally precipitated chlorite and epidote (Fig. 7a, c & e). At the edge of the cataclasite zones, strain is often localized

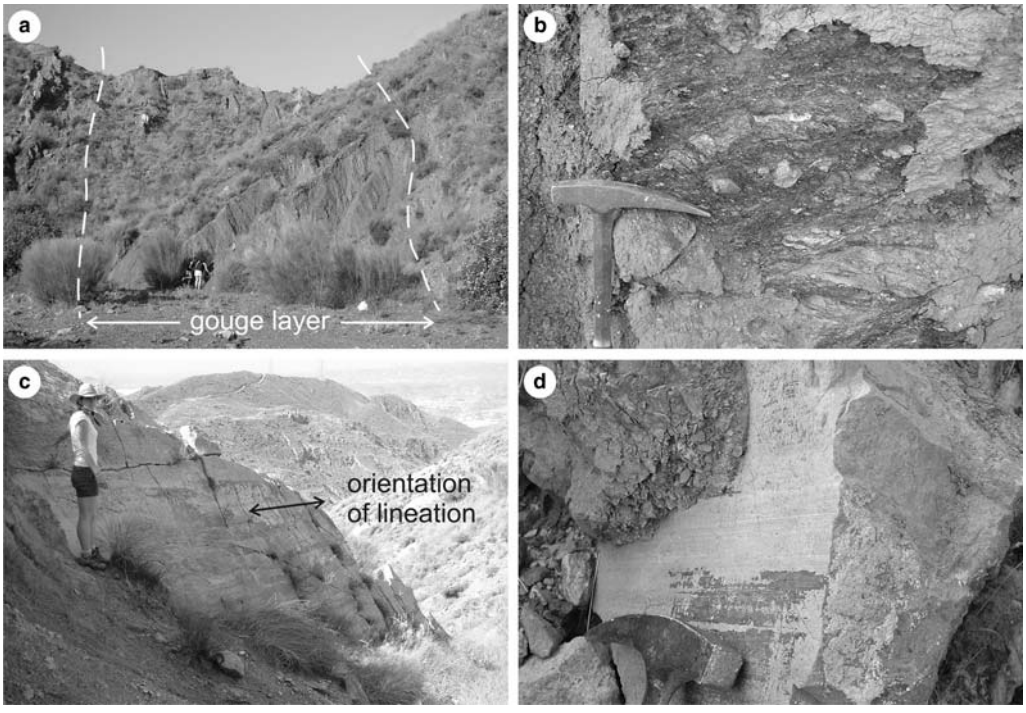

Fig. 3. Photographs of meso-scale deformation structures within the Carboneras fault zone. (**a**) Phyllosilicate-rich fault gouge layer developed within the graphitic mica schist. (**b**) Homogeneous distribution of strain within each phyllosilicate-rich gouge layer. The hammer head is approximately 20 cm in length. (**c**) Localized, polished fault plane developed within one of the dolomite blocks contained within the Carboneras fault zone. (**d**) Detail of one of the localized faults within the dolomite. The hammer head is approximately 20 cm in length.

into a very narrow plane (Fig. 7c & d). The damage zone consists of macro- and microscopic fracturing that decays with distance from the fault core (Faulkner *et al.* 2006).

Discussion

The structures of the fault zones of the Carboneras and Caleta Coloso faults are, at first glance, quite similar. Both have a wide fault core (on the order of several hundred metres) that consists of multiple strands of fault-related rocks. However, there are key differences between the faults and these are discussed below. First, we concentrate on what might be the general controls on fault zone structure. Second, the mechanical significance of the macroscopic structure of the two faults is discussed.

Controls on fault zone architecture

The primary controls on fault zone architecture are (a) the depth of faulting, (b) the protolith, (c) the fault displacement and (d) the interaction with other faults and/or pre-existing structures. In the case of crustal, plate boundary-scale faults, their angle with the local plate motion vector can also have an effect on the structure. One other possible control on fault zone structure is the mode of faulting itself. Recent work on the San Andreas fault has shown that seismic rupture may have produced 'pulverization' of the surrounding rock although this has yet to be shown to occur at significant depth (Wilson *et al.* 2005; Dor *et al.* 2006).

In this work we have described the fault rocks of the Carboneras and Caleta Coloso faults that formed at *c*. 4 and *c*. 6 km depth, respectively. The difference between these depths is not large, and hence the control exerted by depth [control (a)] on the relative structure of the two faults should not be a major factor. We consider the protolith to be an important factor in the development of the structure of the two faults [control (b)] and this is considered in more detail later in the discussion. With regard to displacements across the two faults [control (c)], they have *c*. 40 (Carboneras) and >5 km (Caleta Coloso) accumulated displacement. They are both crustal-scale features. Although the displacements

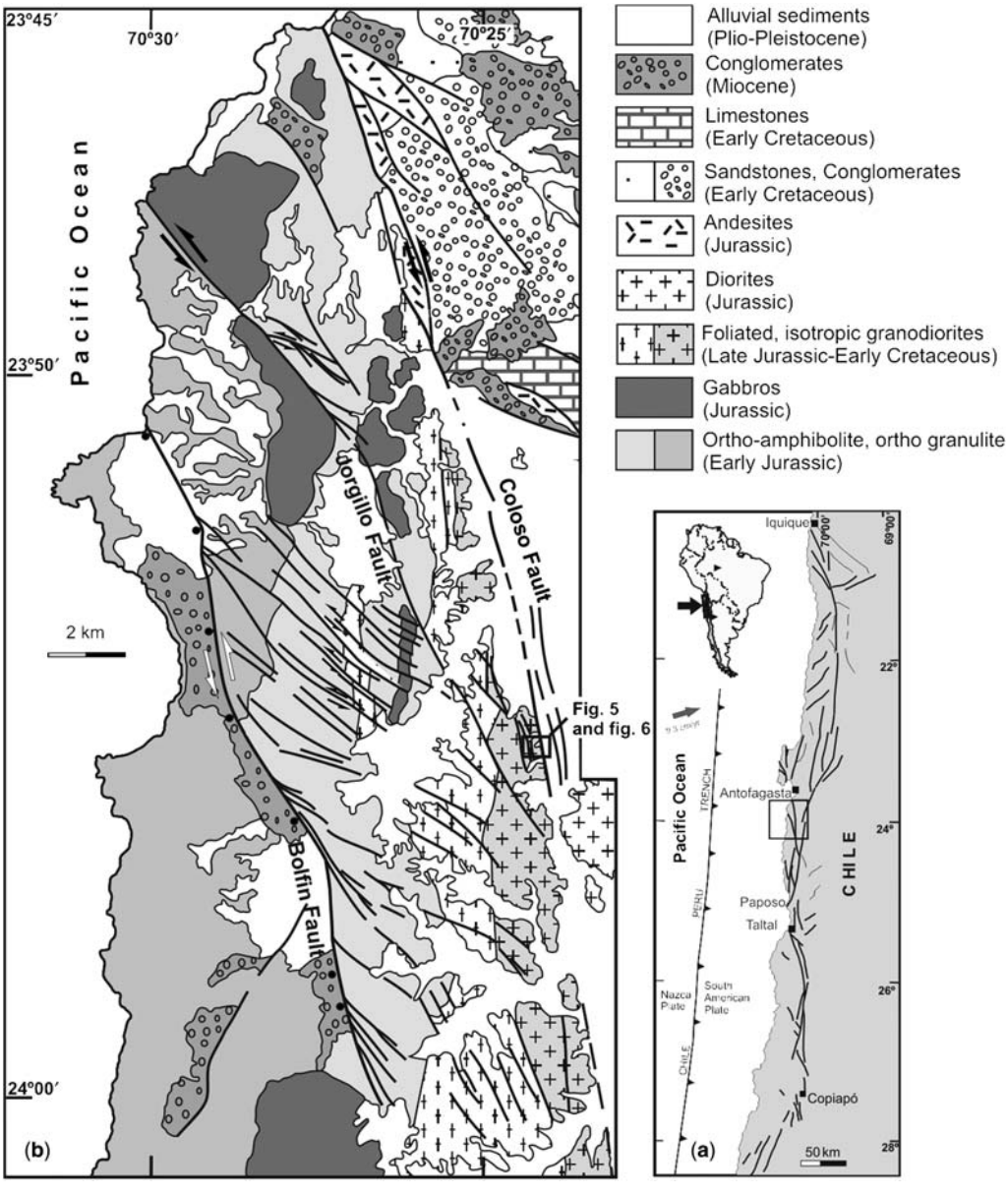

Fig. 4. Regional tectonic framework of the Caleta Coloso fault in northern Chile. It is part of the Atacama fault system. The Nazca and South American plates are labelled.

of the two faults are different, we consider that displacements of greater than a few kilometres will produce a macroscopic structure that is fairly typical of the depth and protolith, unless geometric factors or interactions with other faults occur. The view of Ben-Zion & Sammis (2003) that fault zones evolve towards simplicity does not adequately explain the complexity of high strain features seen across the Carboneras fault zone, for example (some of which must have developed outside of the fault's early history). The structure of the Carboneras fault can be compared with that of the Punchbowl fault, a trace of the San Andreas fault exhumed from similar depth and with a comparable displacement (Chester *et al.* 1993), where almost all of the strain was accommodated within

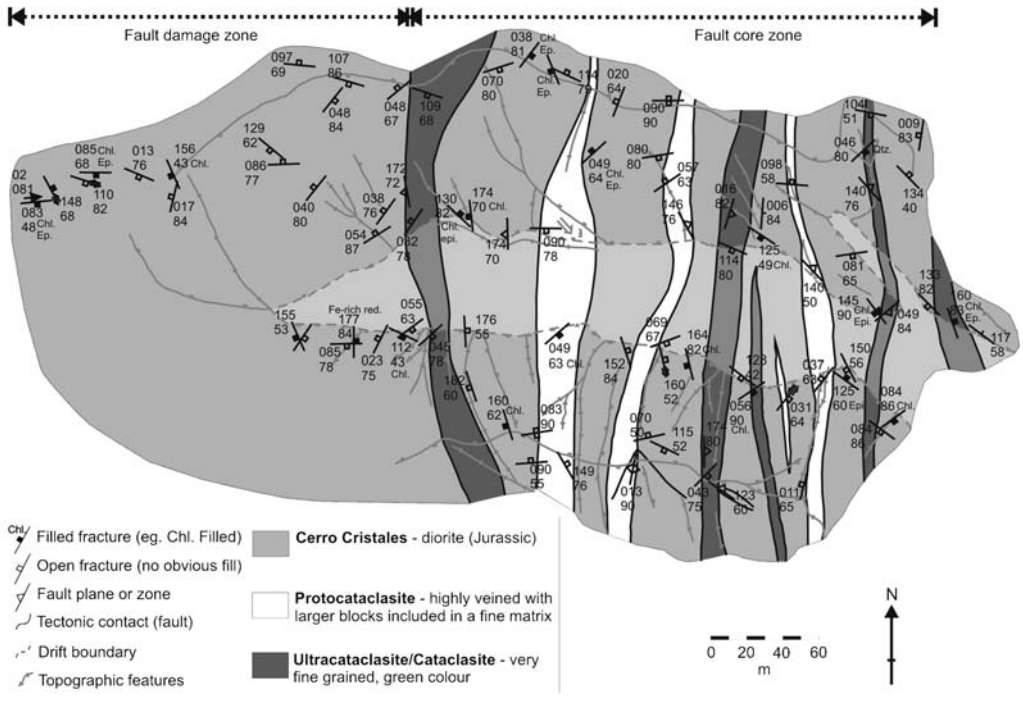

Fig. 5. Detailed map of the Caleta Coloso fault around Quebrada Isabel within the Coastal Cordillera to the south of Antofagasta. Drift deposits are indicated by a lighter shading of the solid geology deposits. The specific location of the field study area is shown by the latitude/longitude GPS position (S23°55.280 W070°24.809) on the map.

a fault core of 20–30 cm width. Clearly, factors in addition to fault displacement play a role in determining fault zone structure.

On the subject of interactions with other faults [control (d)], the observations in this work were made in areas that were some distance from other faults with any significant displacement on them. However, approximately 4 km to the NE of where observations and mapping of the Carboneras fault were made, the fault is cut by the Palomares fault, another many-kilometre-offset regional strike–slip fault (see Fig. 1). However, the activity on this fault is thought to post-date movements on the Carboneras fault (Faulkner *et al.* 2003) and consequently should have little effect on the development of the structure of the fault.

Fig. 6. Photograph of the part of the Caleta Coloso fault to the south of Quebrada Isabel. The fault core (indicated) is characterized in the field by a green colouration related to the precipitation of chlorite and epidote. The length of the arrow indicating the fault core is approximately 150 m long.

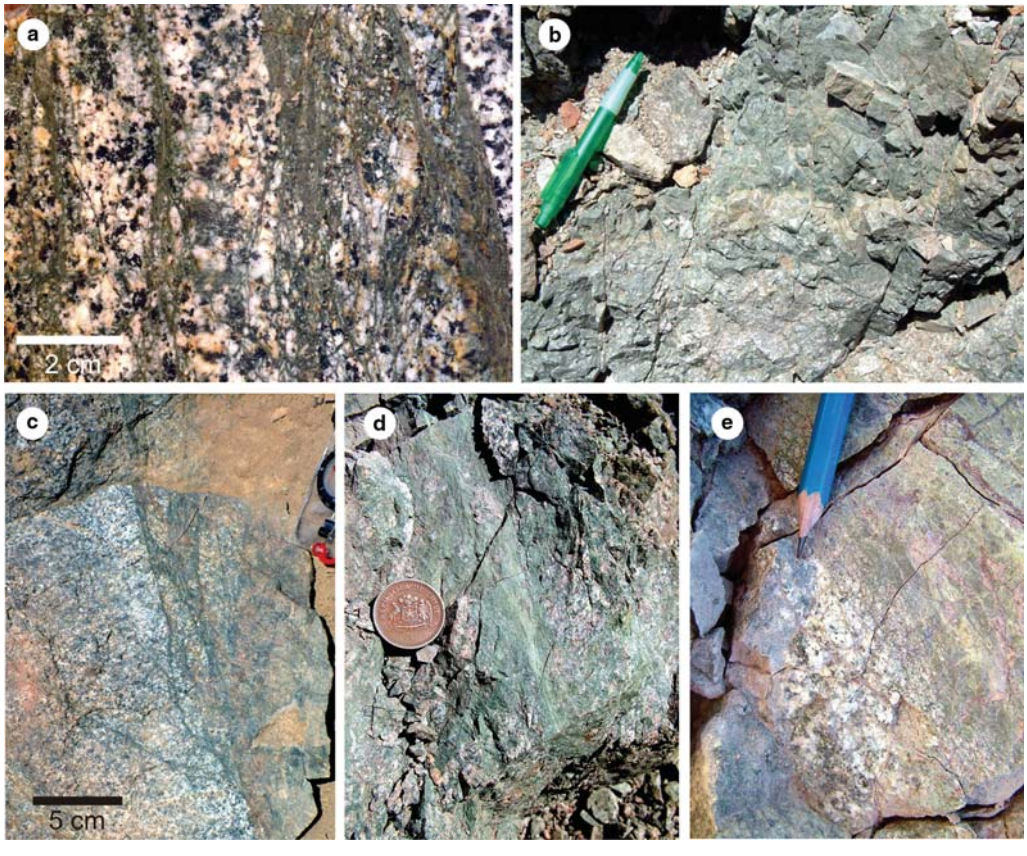

Fig. 7. Photographs showing characteristic meso-scale structures associated with the Caleta Coloso fault. (**a**) 'Network' zone showing angular blocks of granodiorite contained within a cataclasite and ultracataclasite matrix containing hydrothermally precipitated chlorite and epidote. (**b**) Ultracataclasite zone. (**c** and **d**) Localization of strain on the boundary of one of the strands of cataclasite. (**e**) Gradation of strain into a cataclasite layer.

We interpret the differences in the structure of the two faults arising from variations in depth, displacement and interactions with other faults to be of secondary importance. Hence we compare the structures of the two faults in terms of the protolith (and its mechanical response to deformation) from which they formed and post-formation processes. We first review briefly the factors responsible for changes in the mode of failure of rocks before considering in more detail the protolith and consequent mechanical response leading to variations in structure of each fault.

As depth increases in the crust, so the strength of brittle rocks also increases. As confining pressure increases, the mode of deformation of rocks can change from localized to distributed (Rutter 1986). At low temperatures, localized deformation is often associated with a mechanical response whereby the rock loses the ability to support as much differential stress once the failure stress has been exceeded. This is seen as the development of a fault plane in experiments (Fig. 8). In contrast, distributed deformation is commonly associated with a mechanical response in which the rock retains the ability to support differential stress on the same order as the failure stress after this has been reached (Fig. 8). However, it is worth noting that localized behaviour can develop in a strain hardening regime (Hobbs *et al.* 1990), although it is more usually the case that distributed deformation will occur. When we consider the mode of failure of rocks, nothing is implied about the *mechanism* of failure.

For rocks deforming by brittle deformation mechanisms, a transition between localized and distributed deformation can occur as a result of increasing effective pressure (Bernabe & Brace 1990) and would indicate that the strength of the intact rock is approximately equal to that of the resulting fault rock. This change can also be

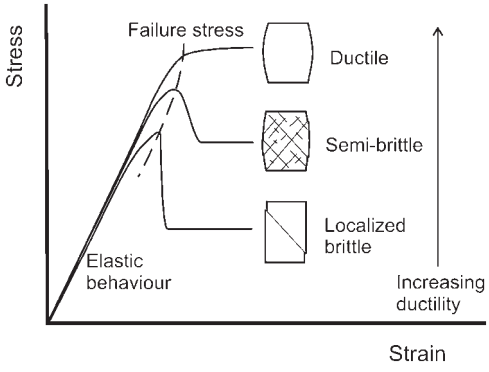

Fig. 8. The comparative appearance of experimentally compressed cylindrical rock samples and how these commonly relate to stress–strain curves under moderate- to low-temperature conditions. Thus ductile (distributed) deformation is often not related to a post-failure drop in flow stress, whereas localized brittle deformation is usually associated with a stress drop and continued focusing of deformation into the fault zone.

accommodated by the collapse of porosity within the intact rock (Rutter & Hadizadeh 1991), the presence of a 'weak' second phase (Byerlee 1968) or a contribution from some crystal plastic mechanism (Fredrich *et al.* 1989).

If we relate the mechanical data back to the fault zones studied, we may make the following observations. First, all fault zones are likely indicative of strain weakening, and the fact they exist as discrete structures within the surrounding country rock indicates that they continue to be weak relative to the country rock. However, the structure of the fault zone may give some idea as to the 'ductility' of the fault zone, i.e., the relative strength between the country rock and its faulted equivalent within the fault core. The greater the contrast between the strength of the intact rock and its faulted equivalent, the more localized the fault zone. In the examples considered in this paper, the fault zones are relatively wide, and contain multiple zones of fault gouge or cataclasite. We now seek to explain the structure of these faults by consideration of the mechanical properties of the faults and the protolith from which they are formed.

Carboneras fault structure; mechanical interpretation

In the case of the Carboneras fault, the mechanical strength contrast between the mica schist country rock and the phyllosilicate-rich fault gouge produced from it can be inferred to be small, given the width of the fault zone. If the strength of the country rock was much greater than the fault gouge, then a much more localized, and hence narrow, zone of deformation might be expected.

The apparently even distribution of strain within the individual fault gouge layers can be explained by the mechanical characteristics of phyllosilicate-rich fault gouge. In experiments, strain hardening behaviour is typically seen (Morrow *et al.* 1982, 1992; Rutter *et al.* 1986; Logan & Rauenzahn 1987), although velocity weakening has been noted in some phyllosilicates, notably serpentinites (Reinen 2000) and under very low effective stress (Saffer *et al.* 2001). The strength increase with strain within fault gouge layers may also be partly responsible for the width of the fault zone (Faulkner *et al.* 2003).

Other explanations for the wide nature of the fault zones studied can be considered. If a restraining or releasing bend occurs along the fault, then this also may spread the deformation over a much wider zone (giving rise to positive or negative flower structures). However, in the case of both the Carboneras fault and the Caleta Coloso fault, regional mapping of the fault zones shows no such restraining bend (as discussed previously), and qualitative observations along strike for several kilometres along both faults indicate that the fault structure mapped in detail is not unique and is characteristic of the fault zones along strike.

The predominant type of fault motion one might expect from a fault zone containing the materials found within the Carboneras fault is fault creep. The mechanical characteristics of phyllosilicate-rich fault gouge and the lack of any localization within the gouge layers suggest that the fault was strain hardening, which would preclude any periods of instability. The presence of the dolomitic blocks within the fault zone, with their contrasting, localized style of faulting, opens up the possibility of 'mixed mode' palaeo-seismicity on the Carboneras fault. These types of fault rock indicate strain weakening behaviour, and might well have been seismogenic. Hence one could envisage predominantly aseismic creep on a fault such as the Carboneras fault, punctuated by seismic events. It is interesting to note that this type of behaviour is the same as is seen on the San Andreas fault around the area of Parkfield, and recent results from the SAFOD borehole indicate that the fault zone at 3 km depth consists of multiple fault strands, similar to that of the Carboneras fault (Zoback *et al.* 2006). A fuller discussion of the similarities between the Carboneras fault zone structure and the San Andreas fault structure at depth around the area of Parkfield (from geophysical observations) is presented in Faulkner *et al.* (2003). The size of earthquake that could arise from faulting on included brittle blocks contained within a creeping fault depends on the size of the block. In the

case of the dolomites in the Carboneras fault zone, earthquake size would be small $<M_w$ 4 (Wells & Coppersmith 1994).

Caleta Coloso fault structure; mechanical interpretation

Low temperature faulting in granites at any crustal depth is localized. It is sometimes initiated on pre-existing joint planes, as has been interpreted by Martel *et al.* (1988) for the Mount Abbott quadrangle faults in the Sierra Nevada, or the Gole Larghe fault within the Adamello batholith (Di Toro & Pennacchioni 2005) in the Italian Alps. In laboratory experiments, low temperature faulting produced in intact crystalline rocks at any confining pressures such as would be encountered within the brittle crust displays localized behaviour (e.g., Lockner 1998). Strain rate would also play a role, but the strain rate in typical geological processes is such that the deformation mode is expected to be localized brittle. Given the body of evidence from the field and laboratory, faulting in crystalline rocks deformed within the brittle crust might be expected to be highly localized in the absence of geometrical irregularities. However, the nature of the faulting seen on the Caleta Coloso fault displays, at first glance, a similar mesoscale structure to that on the Carboneras fault, that of a wide fault zone consisting of multiple strands of fault rocks.

The character of the fault core seen on the Caleta Coloso fault, with large scale precipitation of predominantly chlorite and epidote, indicates a high flux of hydrothermal fluids (see Fig. 6). These fluids may perhaps be a result of the fault being a part of the Mesozoic Andean magmatic arc, where geothermal gradients were elevated and devolatilization of magmatic products may have led to enhanced fluid movements. Other present-day strike–slip faults in geothermally active areas such as the Dead Sea Transform or the Salton Sea cannot be compared with the Caleta Coloso fault as the seismogenic parts of the fault have not been exposed at the surface. The near-surface structure of these faults may not be representative of the structure of the deeper parts of the fault zone.

The fluids in the Caleta Coloso fault do not appear to have reacted significantly with the host rock as little phyllosilicate material or alteration is observed on the mesoscale. We interpret the structure of the fault to be influenced strongly by precipitation hardening of the fault zone leading to strengthening and subsequent failure along a new plane parallel to the fault zone. There are experimental data that support the idea of rapid mineral precipitation and strengthening in quartz-rich fault gouges at hydrothermal conditions (Olsen *et al.* 1998; Tenthorey *et al.* 2003; Yashuhara *et al.* 2005), and over time periods commensurate with the interseismic period, processes such as these are very likely to happen.

The nature of the strands of fault rocks within the Caleta Coloso fault zone are also very different to those seen on the Carboneras fault. The distribution of strain is very heterogeneous, with very localized planes of comminution, typically confined to the edges of the strands of cataclasite (Fig. 7c). This observation is consistent with the notion of strengthening of cataclasite layers due to precipitation, with later movements accommodated on new fault gouge strands confined to the boundary of the strengthened old cataclasite layers.

Conclusions

We have studied in detail the internal structure of two large strike–slip faults; the Carboneras fault in southeastern Spain and the Caleta Coloso fault in northern Chile. The protoliths for each fault are very different. The Carboneras fault cuts through predominantly phyllosilicate-rich metamorphic rocks, whereas the Caleta Coloso fault affects igneous crystalline rocks. Both faults have been largely passively exhumed from depth so that their present day surface structure can be viewed as representative of the structure of the faults while active at depth. Both faults are very well exposed in arid environments, ensuring the fault rocks have minimal degradation from surface weathering effects.

The Carboneras fault displays multiple strands of phyllosilicate-rich fault gouge in a fault zone with a total width approaching 750 m. The anastomosing fault gouge strands are typically less than 10 m thick and they contain lenses of variably fractured protolith between them. The strain is apparently evenly distributed within each gouge strand. We interpret the structure of the fault to represent a small strength contrast between the protolith and the resultant fault gouge (semibrittle or ductile behaviour in the mechanical sense). The strain hardening characteristics of phyllosilicate-rich fault gouge may also contribute towards the bulk structure and the uniform distribution of strain across the gouge layers.

The Caleta Coloso fault incorporates multiple strands of variably deformed rock including protocataclasite and ultracataclasite in a zone at least 200 m wide. The fault core zone is characterized by a green colouration produced by the precipitation of chlorite and epidote in veins and also in the fault rock. Localization of slip is seen typically on the boundaries of ultracataclasite layers.

The mechanical behaviour of these low-porosity crystalline rocks would be expected to be very localized and brittle, and hence we interpret the wide nature of the fault zone to be a product of precipitation healing of the fault zone leading to spatially and temporally localized strengthening that spreads the deformation over a wider zone.

This work was supported by NERC grant NE/C001117/1 (to D.R.F.). E. Jensen Siles and N. Reyes are thanked for field assistance.

References

BELL, J. W., AMELUNG, F. & KING, G. 1997. Preliminary late quaternary slip history of the Carboneras fault, southeastern Spain. *Journal of Geodynamics*, **24**, 51–66.

BEN-ZION, Y. & SAMMIS, C. G. 2003. Characterization of fault zones. *Pure and Applied Geophysics*, **160**, 677–715.

BERNABE, Y. & BRACE, W. F. 1990. Deformation and fracture of Berea sandstone. *In*: DUBA, A. G., DURHAM, W. S., HANDIN, J. W. & WANG, H. F. (eds) *The Brittle–Ductile Transition in Rocks – The Heard Volume*. American Geophysical Union Monographs, **56**, 91–101.

BYERLEE, J. D. 1968. Brittle–ductile transition in rocks. *Journal of Geophysical Research*, **73**, 4741–4750.

CAINE, J. S., EVANS, J. P. & FORSTER, C. B. 1996. Fault zone architecture and permeability structure. *Geology*, **24**, 1025–1028.

CEMBRANO, J., GONZÁLEZ, G., ARANCIBIA, G., AHUMADA, I., OLIVARES, V. & HERRERA, V. 2005. Fault zone development and strain partitioning in an extensional strike–slip duplex: a case study from the Atacama Fault System, northern Chile. *Tectonophysics*, **400**, 105–125.

CHESTER, F. M., EVANS, J. P. & BIEGEL, R. L. 1993. Internal structure and weakening mechanisms of the San Andreas fault. *Journal of Geophysical Research*, **98**, 771–786.

DI TORO, G. & PENNACCHIONI, G. 2005. Fault plane processes and mesoscopic structure of a strong-type seismogenic fault in tonalites (Adamello batholith, Southern Alps). *Tectonophysics*, **402**, 55–80.

DOR, O., BEN-ZION, Y., ROCKWELL, T. K. & BRUNE, J. N. 2006. Pulverized rocks in the Mojave section of the San Andreas fault zone. *Earth and Planetary Science Letters*, **245**, 642–654, doi:10.1016/j.epsl.2006.03.034.

FAULKNER, D. R., LEWIS, A. C. & RUTTER, E. H. 2003. On the internal structure and mechanics of large strike–slip faults: field observations from the Carboneras fault, southeastern Spain. *Tectonophysics*, **367**, 235–251.

FAULKNER, D. R., MITCHELL, T. M., HEALY, D. & HEAP, M. J. 2006. Slip on 'weak' faults by the rotation of regional stress in the fracture damage zone. *Nature*, **444**, 922–925, doi:10.1038/nature05353.

FREDRICH, J. T., EVANS, B. & WONG, T.-F. 1989. Micromechanics of the Brittle to Plastic Transition in Carrara Marble. *Journal of Geophysical Research*, **94**, 4129–4145.

GONZALEZ, G. & CARRIZO, D. 2003. Segmentación, cinemática y cronología relativa de la deformación tardía de la Falla Salar del Carmen, Sistema de Fallas de Atacama, (23°40'S), norte de Chile. *Revista Geológica de Chile*, **30**, 223–244.

HERRERA, V., CEMBRANO, J., OLIVARES, V., KOJIMA, S. & ARANCIBIA, G. 2005. Precipitación por despresurización y ebullición en vetas hospedades en un dúplex de rombo extensional: evidencias microestructurales y microtermométricas. *Revista Geológica de Chile*, **32**, 207–228.

HOBBS, B. E., MUHLHAUS, H. B. & ORD, A. 1990. Instability, softening and localization of deformation. *In*: KNIPE, R. J. & RUTTER, E. H. (eds) *Deformation Mechanisms, Rheology and Tectonics*. Geological Society, London, Special Publications, **54**, 143–165.

JEFFERIES, S. P., HOLDSWORTH, R. E. *ET AL*. 2006. The nature and importance of phyllonite development in crustal-scale fault cores: an example from the Median Tectonic Line, Japan. *Journal od Structural Geology*, **28**, 220–235.

KNIPE, R. J. 1992. *Faulting Processes and Fault Seal*. Norwegian Petroleum Society (NPF) Special Publications, **1**, 325–342.

KOHLSTEDT, D. L., EVANS, B. & MACKWELL, S. J. 1995. Strength of thelithosphere: constraints imposed by laboratory experiments. *Journal of Geophysical Research*, **100**, 17587–17602.

KUSZNIR, N. J. & BOTT, M. H. P. 1977. Stress-concentration in upper lithosphere caused by underlying viscoelastic creep. *Tectonophysics*, **43**, 247–256.

LOCKNER, D. A. 1998. A generalised law for brittle deformation of Westerly granite. *Journal of Geophysical Research*, **103**, 5107–5123.

LOGAN, J. M. & RAUENZAHN, K. A. 1987. Velocity-dependent behaviour of mixed quartz-montmorillonite gouge. *Tectonophysics*, **144**, 87–108.

MARTEL, S. J., POLLARD, D. D. & SEGALL, P. 1988. Development of simple strike-slip fault zones, Mount Abbotquadrangle, Sierra Nevada, California. *Geological Society of America Bulletin*, **100**, 1451–1465.

MORROW, C. A. & LOCKNER, D. A. 1994. Permeability differences between surface-derived and deep drillhole core samples. *Geophysical Research Letters*, **21**, 2151–2154.

MORROW, C. A., SHI, L. Q. & BYERLEE, J. D. 1982. Strain hardening and the strength of clay-rich fault gouges. *Journal of Geophysical Research*, **87**, 6771–6780.

MORROW, C. A., RADNEY, B. & BYERLEE, J. D. 1992. Frictional strength and the effective pressure law of montmorillonite and illite clays. *In*: EVANS, B. & WONG, T.-F. (eds) *Fault Mechanics and Transport Properties of Rocks*. Academic Press, London, 69–88.

OHTANI, T., TANAKA, H., FUJIMOTO, K., HIGUCHI, T., TOMIDA, N. & ITO, H. 2001. Internal structure of the Nojima Fault zone from the Hirabayashi GSJ drill core. *The Island Arc*, **10**, 392, doi:10.1046/j.p1440–1738.2001.00337.x.

OLSEN, M. P., SCHOLZ, C. H. & LÉGER, A. 1998. Healing and sealing of a simulated fault gouge under hydrothermal conditions: implications for fault

healing. *Journal of Geophysical Research*, **103**, 7421–7430, doi:10.1029/97JB03402.

REINEN, L. 2000. Slip styles in a spring-slider model with a laboratory-derived constitutive law for serpentinite. *Geophysical Research Letters*, **27**, 2037–2040.

RUTTER, E. H. 1986. On the nomenclature of mode of failure transitions in rocks. *Tectonophysics*, **122**, 381–387.

RUTTER, E. H. & HADIZADEH, J. 1991. On the influence of porosity on the low-temperature brittle–ductile transition in siliciclastic rocks. *Journal of Structural Geology*, **13**, 609–614.

RUTTER, E. H., MADDOCK, R. H., HALL, S. H. & WHITE, S. H. 1986. Comparative microstructures of natural and experimentally produced clay-bearing fault gouges. *Pure and Applied Geophysics*, **124**, 3–30.

SAFFER, D. M., FRYE, K. M., MARONE, C. & MAIR, K. 2001. Laboratory results indicating complex and potentially unstable frictional behaviour of smectite clay. *Geophysical Research Letters*, **28**, 2297–2300.

SCHULZ, S. E. & EVANS, J. P. 2000. Mesoscopic structure of the Punchbowl Fault, Southern California and the geologic and geophysical structure of active strike–slip faults. *Journal of Structural Geology*, **22**, 913–930.

SCOTNEY, P., BURGESS, R. & RUTTER, E. H. 2000. 40Ar/39Ar age of the Cabo de Gata volcanic series and displacements on the Carboneras fault zone, SE Spain. *Journal of the Geological Society, London*, **157**, 1003–1008.

TENTHOREY, E., COX, S. F. & TODD, H. F. 2003. Evolution of strength recovery and permeability during fluid-rock reaction in experimental fault zones. *Earth and Planetary Science Letters*, **206**, 161–172.

TOWNEND, J. & ZOBACK, M. D. 2000. How faulting keeps the crust strong. *Geology*, **28**, 399–402.

WELLS, D. L. & COPPERSMITH, K. J. 1994. New empirical relations among magnitude, rupture length, rupture width, rupture area and surface displacement. *Bulletin of the Seismic Society*, **84**, 974–1002.

WIBBERLEY, C. A. J. & SHIMAMOTO, T. 2003. Internal structure and permeability of major strike–slip fault zones: the Median Tectonic Line in Mie Prefecture, Southwest Japan. *Journal of Structural Geology*, **25**, 59–78.

WILSON, B., DEWERS, T., RECHES, Z. & BRUNE, J. 2005. Particle size and energetics of gouge from earthquake rupture zones. *Nature*, **434**, 749–752.

YASUHARA, H., MARONE, C. & ELSWORTH, D. 2005. Fault zone restrengthening and frictional healing: the role of pressure solution. *Journal of Geophysical Research*, **110**, B06310, doi:10.1029/2004JB003327.

ZOBACK, M. D., HICKMAN, S. H. & ELLSWORTH, W. 2006. Preliminary results from the SAFOD experiment. *Geophysical Research Abstracts*, **8**, 02474.

Frictional–viscous flow, seismicity and the geology of weak faults: a review and future directions

J. IMBER[1], R. E. HOLDSWORTH[1], S. A. F. SMITH[1], S. P. JEFFERIES[1] & C. COLLETTINI[2]

[1]*Reactivation Research Group, Department of Earth Sciences, University of Durham, South Road, Durham, DH1 3LE, UK (e-mail: jonathan.imber@durham.ac.uk)*

[2]*Geologia Strutturale e Geofisica, Dipartimento di Scienze della Terra, Università degli Studi di Perugia, Piazza dell'Università 1, 06100, Perugia, Italy*

Abstract: Previously hypothesized fault weakening mechanisms include faults lined by low-friction clay gouges, elevated pore pressures within fault cores and/or the operation of dynamic weakening during seismic slip. Geological studies to support dynamic weakening are still in their infancy and there is little geological evidence for the widespread occurrence of low-friction gouges. The cores of some ancient faults exhumed from <5 km depth contain sheared syntectonic mineral veins. This observation is consistent with elevated pore pressures, but the implications for long-term fault weakening are unclear. Experimental data and microphysical modelling suggest that frictional–viscous flow within phyllosilicate-rich fault rocks (phyllonites, some foliated cataclasites) can cause sufficient weakening of crustal faults to satisfy published heat flow constraints. These predictions are consistent with the common occurrence of phyllonite in the cores of large-displacement faults exhumed from >5 km depth. Comparison with seismological data suggests that some faults with phyllonitic cores are likely to generate large earthquakes. Future studies should establish the geological evidence for seismic slip within phyllonitic fault cores and quantify the partitioning between seismic slip and frictional–viscous flow. Further geological observations are also required to test the hypothesized mechanisms by which earthquakes can nucleate and propagate along phyllosilicate-rich faults.

The state of stress within the lithosphere is of fundamental importance to the mechanism of plate tectonics. In particular, constraints on the strengths of plate boundary faults are critical to determining the origins of forces that either drive or resist the motion of lithospheric plates (Scholz *et al.* 1979). However, the magnitude of shear stress required to produce slip on plate boundary faults has been a matter of intense debate for three decades. The argument centres on whether plate boundary faults support crustal-average shear stresses consistent with laboratory-derived friction coefficients (μ) of between 0.6 and 1.0 (e.g., Byerlee 1978; Townend & Zoback 2000) – or whether such faults are in fact much weaker, moving under crustal-average shear stresses of $\leq$20 MPa, consistent with a friction coefficient $\mu \leq 0.2$ (e.g., Lachenbruch & Sass 1992; Scholz 2000; Zoback 2000; Fig. 1).

Many of the observations used to support the 'weak fault' hypothesis were originally made in western California, adjacent to the San Andreas Fault (SAF), a continental transform fault that accommodates the right-lateral component of oblique convergence between the Pacific and North American plates, with a cumulative slip rate of *c*. 40 mm/year. Two lines of evidence have been used to argue that the SAF is weak. First, conduction-only models of frictional shear heating using a Byerlee friction coefficient predict a narrow, positive heat flow anomaly centred on the steeply dipping SAF (Brune *et al.* 1969). Although the California Coast and Transverse ranges are characterized by high regional heat flow, Lachenbruch and Sass (1980) found that the heat flow appears to be no greater near the fault trace than in the surrounding terranes, thus limiting the average shear stress on the SAF to $\leq$20 MPa (Lachenbruch & Sass 1992). Second, measurements of principal stress directions in western California show that the maximum horizontal stress (S_{Hmax}) is oriented nearly perpendicular to the trace of the SAF (Mount & Suppe 1987; Zoback *et al.* 1987). The SAF therefore appears to be close to a principal stress plane, consistent with the notion that it supports a small shear stress and is weak relative to the surrounding rock.

Molnar (1992) has questioned the relevance of the Mount & Suppe's (1987) stress measurements to constraining the relative strength or weakness of the SAF. He argued that, if the continental lithosphere behaves as a viscous continuum, upper crustal stress orientations 'merely take on the orientations necessary to accommodate the regional displacement field' (Molnar 1992). Thus, the fault-normal stresses reported by Mount & Suppe (1987)

From: WIBBERLEY, C. A. J., KURZ, W., IMBER, J., HOLDSWORTH, R. E. & COLLETTINI, C. (eds) *The Internal Structure of Fault Zones: Implications for Mechanical and Fluid-Flow Properties*. **299**, 151–173.
DOI: 10.1144/SP299.10 0305-8719/08/$15.00

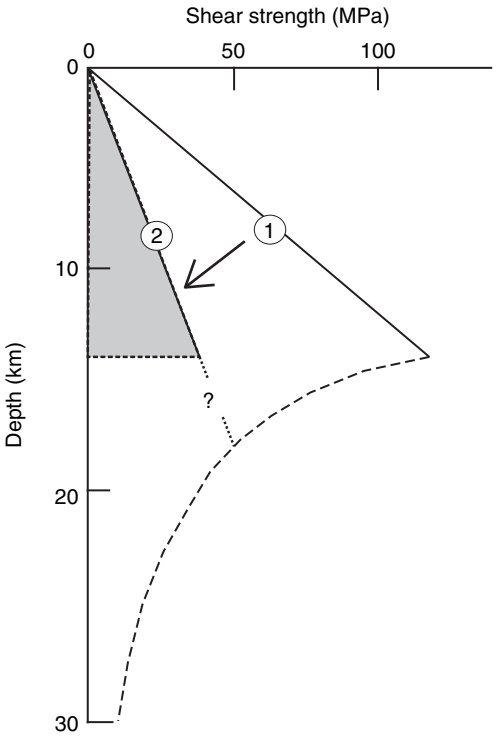

Fig. 1. Schematic strength profile for a crustal strike–slip fault, from Lachenbruch & Sass (1992). The thick dashed line is based on laboratory determinations of the creep strength of Westerly granite. Sold line (1) represents Byerlee friction for a dry fault. Solid line (2) approximately represents the maximum fault strength constrained by heat flow measurements along the San Andreas Fault. Increasing fluid pressure will result in a decrease in frictional strength, towards line (2). Frictional strength following line (2) could also result from a fault lined by low-friction clay gouge. According to Lachenbruch & Sass (1992), heat flow measurements (see text) constrain only the area under the friction curve (shaded) and it is not certain how the 'low friction' curve is joined to the creep strength curve, hence this section is shown dashed.

might arise from the kinematic requirement to accommodate the horizontal shortening component of the oblique convergence between the Pacific and North American plates. Furthermore, Scholz (2000) pointed out that the near fault-perpendicular stress orientations reported by Mount & Suppe (1987) could be the result of active compression within folds that initiated at 20–30° of the fault trace and have been progressively sheared clockwise from their original orientations. The reported stress orientations appear to have been induced by the folding and hence provide no information on the strength of the SAF. Further analysis by Hardebeck & Hauksson (1999) shows that, away from the folds, S_{Hmax} makes an angle of *c*. 50–60° with the fault strike – a prediction of the 'strong fault' hypothesis (Scholz 2000). The heat flow data are also open to reinterpretation. Scholz & Hanks (2004) pointed out that the excess regional heat flow in the California Coast and Transverse ranges is large enough to contain the frictional heat expected to be generated by a strong SAF. They went on to argue that heat advection by groundwater flow is likely to be important in this region and that therefore the basic assumption of the heat flow argument (the application of a conduction-only model) could be invalid. Thus, the strength of plate boundary faults in general and the SAF in particular remains open to debate.

Central to the weak fault hypothesis is a plausible mechanism that is capable of explaining the postulated low shear stresses along the SAF (Zoback *et al.* 1987; Zoback 2000). The nature of the supposed weakening mechanism remains enigmatic owing to the difficulties in sampling the active fault at seismogenic depths (Holdsworth 2004). In fact, Scholz (2000) and Scholz & Hanks (2004) have argued that, since the geophysical observations are, in their opinion, either inconclusive or consistent with the strong fault hypothesis, they see no compelling reason to suppose that the strength of the SAF should obey anything other than Byerlee friction. This use of Occam's razor would be consistent with worldwide stress measurements in intraplate regions and a large number of laboratory friction experiments (Byerlee 1978; Brudy *et al.* 1997; Townend & Zoback 2000; Rutter *et al.* 2001).

These fundamental uncertainties have stimulated an international project – the San Andreas Fault Observatory at Depth (SAFOD; Dalton 1999) – to drill at seismogenic depths (*c*. 3 km) across the Parkfield segment of the SAF, which moves through a combination of aseismic creep and repeating microearthquakes. The aim is to test rock and fluid samples from the fault zone in the laboratory, and to integrate these results with *in situ* observations of earthquake activity, strain and fluid pressure within the fault core. SAFOD is already providing unprecedented insights into the physical and chemical processes controlling faulting and earthquake generation within major plate bounding faults (e.g., see Hickman *et al.* 2004 and associated papers in the special section 'Preparing for the San Andreas Fault Observatory at Depth', *Geophysical Research Letters*, **31**). Nevertheless, direct geological observations of the *c*. 1300 km long SAF will be limited to the boreholes and associated side tracks, whilst *in situ* measurements will continue for a period of *c*. 20 years – a vanishingly small period of geological time during which

the fault is likely to slip a distance equivalent to 0.0001% of its total displacement.

These considerations have prompted us to review the geology of exhumed, large-displacement faults that are inferred to have been weak at the time they were active. Exposures of these faults provide direct access to well-developed fault cores that were active at seismogenic depths and capture the time-integrated effects of many kilometres of offset in two to three dimensions across a wide range of length scales (microscopic to regional scale). Studies of these ancient structures are therefore complementary to the *in situ* geophysical 'snapshots' and core samples obtained from SAFOD and can, potentially, provide improved geological constraints on otherwise speculative fault weakening mechanisms.

Outline

First, we examine the (currently limited) geological evidence for dynamic weakening along seismogenic faults. In the next section, we summarize the weakening mechanisms that have been proposed to operate along large-displacement, crustal-scale faults. Where appropriate, we compare these proposals with preliminary findings from SAFOD. The following section reviews the geology of large-displacement faults. The first part deals with faults that have been exhumed from depths of 5 km or less, i.e., within the approximate depth range of the SAFOD drilling project. The second part deals with faults that have been exhumed from greater depths, below the penetration of the SAFOD boreholes. Throughout this review, we emphasize the possible role of frictional–viscous deformation (sensitive to both normal stress *and* temperature/strain rate – see below) in controlling fault weakening, particularly at depths >5 km within the crust. This possibility has previously received less attention than weakening due to the presence of clay gouge or elevated pore fluid pressures within fault cores. Finally, we compare geological and seismological observations with conceptual and microphysical models of frictional–viscous slip along presumed weak faults to highlight uncertainties in current understanding and to suggest specific objectives for future research into the geology of weak faults.

Geological evidence for dynamic weakening along seismogenic faults

Dynamic weakening mechanisms temporarily reduce fault strength (friction) during seismic slip, thus potentially allowing slip to occur with little heat generation. Dynamic weakening mechanisms can operate alongside the processes discussed in the following section, but research into the geological expression of dynamic weakening is still in its infancy. Such research is likely to become increasingly important as new experimental work provides new hypotheses to test against observations from natural faults.

A commonly cited dynamic weakening mechanism is thermal pressurization of pore fluids. In such models, the first increments of frictionally generated heat increase fluid pressures to near-lithostatic values, thereby reducing the effective normal stress to near-zero (Sibson 1980). Alternatively, Melosh (1996) has advocated acoustic fluidization, in which the high frequency elastic waves emitted during seismic slip temporarily reduce the normal stresses within fault cores. Mora & Place (1998) have proposed a further mechanism. Numerical models of slip within high porosity gouge-filled shear zones suggest that slip can be accommodated with minimal heat generation through jostling and rolling of gouge particles. Increasing frictional resistance between the simulated gouge particles promotes particle rolling rather than sliding, so that heat production is observed to decrease as friction increases (Mora & Place 1998). According to Mora & Place (1998), this mechanism is likely to be effective during both seismic *and* aseismic creep, meaning it is 'dynamic' in the sense that low heat generation is a consequence of the way in which the particles move and interact, as opposed to the intrinsic weakness of the particles themselves.

Geological evidence to support these mechanisms is only just starting to be documented. These include outcrop observations of narrow (millimetre- to centimetre-thick) continuous gouge-filled slip zones, which are considered to expressions of earthquake slip (e.g., Wibberley & Shimamoto 2003). The low permeability of such slip zone gouges permit trapping of high fluid pressure over short (e.g., earthquake duration) timescales, with stress drops and slip weakening distances in the same order of magnitude as those inferred for natural large earthquakes (Wibberley & Shimamoto 2005). Han *et al.* (2006) showed that co-seismic frictional heating and thermal decomposition of siderite within experimental carbonate-bearing faults produces ultrafine grained magnetite. The low frictional strength of the ultrafine decomposition products at seismic slip rates may be responsible for dramatic dynamic weakening. Decomposition products such as magnetite could, potentially, be preserved in the geological record (Han *et al.* 2007).

A possible geological indication of dynamic weakening caused by acoustic fluidization has been reported from the active Nojima Fault, Japan

by Otsuki *et al.* (2003). Here, each seismic slip event produced a thin layer of fine gouge, pseudotachylyte or a composite layer of both materials. The narrow width of the layers is compatible with slip weakening. Otsuki *et al.* (2003) suggested that fluidization and melting of the gouge may have allowed nearly frictionless slip to take place. This conclusion is consistent with more recent field and experimental studies, which suggest that lubrication by friction-induced melt significantly reduces the dynamic strength of seismogenic faults compared with the predictions of Byerlee friction (Di Toro *et al.* 2006).

Weakening mechanisms within large-displacement faults

The apparent weakness of the SAF and other large-displacement faults has most commonly been attributed to the presence of low friction clay gouges (e.g., Wang 1984; Morrow *et al.* 1992) and/or the generation and maintenance of high pore fluid pressures within the fault core (e.g., Byerlee 1990; Rice 1992; Faulkner & Rutter 2001). The operation of frictional–viscous deformation mechanisms has also been proposed (e.g., Chester 1995), and may be particularly effective within phyllosilicate-rich fault cores (e.g., Holdsworth 2004). The first two weakening mechanisms have been described in detail elsewhere and so will be summarized before we go on to consider frictional–viscous deformation in more detail.

Low friction phyllosilicate gouge

According to Lachenbruch & Sass (1992), the heat flow data require the SAF to contain material with a coefficient of friction $\mu \leq 0.2$. Experimental studies suggest that certain water-swelling clays or serpentinite minerals are the only materials likely to fulfil this criterion (Morrow *et al.* 2000). However, a key issue with this weakening mechanism is that such materials are velocity strengthening, i.e., they deform by stable sliding (e.g., Scholz 1998), and as such may explain the steady creeping portion of the SAF in Central California. More recent velocity-stepping direct shear experiments on pure Ca-smectite gouge by Saffer *et al.* (2001) show that smectite can be both weak ($\mu < 0.25$) *and* velocity weakening at low sliding velocities and low effective pressures. Based on these results, Saffer *et al.* (2001) proposed that localized zones of high pore fluid pressure could be important in controlling sites of earthquake nucleation at seismogenic depths along weak, smectite-filled faults.

Washed drill cuttings obtained from the SAFOD main borehole (e.g., Schleicher *et al.* 2006) show that smectite and other clay minerals are present in variable amounts ($<$62–69 wt%) within sampled fault zones, and that trace amounts of serpentinite ($<$2–3 wt%) are associated with the active strand of the SAF centred at 3303 m measured depth (Solum *et al.* 2006). The rheological significance of these minerals is still unclear, but preliminary mechanical tests on hand-sorted fault rock cuttings from the SAFOD main borehole suggest that friction coefficients for clay-rich and serpentine grains that carry slickensides are between 0.3–0.5 and 0.4–0.45, respectively (Morrow *et al.* 2007).

Moore & Rymer (2007) reported the presence of talc in serpentinite cuttings obtained from the probable active trace of the SAF encountered at *c*. 3 km vertical depth within the SAFOD borehole. Talc is formed by a metamorphic reaction between serpentinite and silica-bearing pore fluids and has very low shear strength over the temperature range 100–400 °C. According to Moore & Rymer (2007), talc may be the only mineral capable of satisfying the requirement for a weak SAF over the entire range of seismogenic depths, without needing to invoke another weakening mechanism such as fluid overpressure. However, our current knowledge of the distribution of serpentinite cut by the SAF, from which the talc is derived, suggests that it is far from certain that talc is present below *c*. 7 km depth along this segment of the SAF.

High pore fluid pressures

High pore fluid pressures within fault cores reduce the effective normal stress, thereby reducing the shear strength. The fluid pressures required to reactivate a severely misoriented fault such as the SAF are difficult to maintain due to the onset of hydrofracturing. However, in a landmark paper, Rice (1992) demonstrated that high pore pressures can be sustained because the increased principal stresses (with respect to the surrounding crust) in the impermeable core of a mature fault are sufficient to prevent hydrofracturing. More recently, Faulkner *et al.* (2006) used a combination of field observations, laboratory experiments and numerical modelling to show that the changes in elastic parameters caused by microfracturing adjacent to major faults allow high pore pressures to be sustained within the narrow core without inducing hydrofracturing. In this case, the modification to the stress field occurs within the damage zone rather than the fault core as proposed in the model of Rice (1992). Thus, stress changes within the damage zone would still allow pore pressure weakening without hydrofracture even if stresses within weak fault core were modified by processes such as extrusion (e.g., Scholz 2000). Nevertheless, preliminary results from the SAFOD main borehole

have found no indications of anomalous fluid pressures within the fault core, although stress and heat flow measurements in the main hole and pilot hole appear to indicate that the SAF is weak fault relative to the surrounding crust (Hickman & Zoback 2004; Williams *et al.* 2004; Zoback *et al.* 2006).

Frictional–viscous deformation

Chester & Higgs (1992) argued that cataclasis and solution-precipitation aided cataclasis in the presence of a chemically active fluid may be operative during coseismic (high strain rate) and interseismic (low strain rate) periods, respectively. Such 'multi-mechanism' (or 'frictional–viscous' in the sense of Bos *et al.* 2000*a*) behaviour is dependent on both normal stress and strain rate/temperature (e.g., table 1 of Chester 1995). Chester (1995) has shown that multi-mechanism friction could significantly reduce the strength of crustal-scale strike–slip faults with respect to predictions based on Byerlee's law friction.

Spiers and co-workers at Utrecht University have attempted to quantify the effects of solution-precipitation and phyllosilicate content on fault strength. The significance of this work is that phyllosilicates are likely to be highly influential in fault zones at seismogenic depths (e.g., Wintsch *et al.* 1995, see below). In a series of innovative rotary shear experiments, the Utrecht group deformed brine-saturated halite–kaolinite or halite–muscovite rock analogues to ultrahigh strains at room temperatures and pressures (Bos & Spiers 2000, 2001, 2002; Bos *et al.* 2000*a*, *b*; Niemeijer & Spiers 2005, 2006). Pressure solution and cataclasis are known to predominate over dislocation creep in halite under these conditions. The experiments demonstrate that pressure solution only leads to frictional–viscous flow where both phyllosilicates (kaolinite or muscovite) *and* a chemically active fluid phase (brine) are present (Bos & Spiers 2000; cf. Blanpied *et al.* 1998).

Bos & Spiers (2001) showed that experiments conducted at low sliding velocities display significant strain weakening, with a transition towards more rate-sensitive and less normal stress-sensitive behaviour with increasing strain. A key finding has been that the onset of strain weakening is accompanied by a textural change from purely cataclastic microstructures to highly foliated, apparently mylonitic fabrics. These experimental 'mylonites' comprise elongate, asymmetric halite clasts in a contiguous, anastomosing kaolinite matrix (Bos & Spiers 2001). Bos & Spiers (2002) and Niemeijer & Spiers (2005) used their experimental results to derive microphysical models of frictional–viscous flow in phyllosilicate-bearing rocks (Fig. 2a), from which they constructed strength profiles for large-displacement, phyllosilicate-rich fault zones (Fig. 2b). The Bos & Spiers (2002) model predicts that steeply dipping

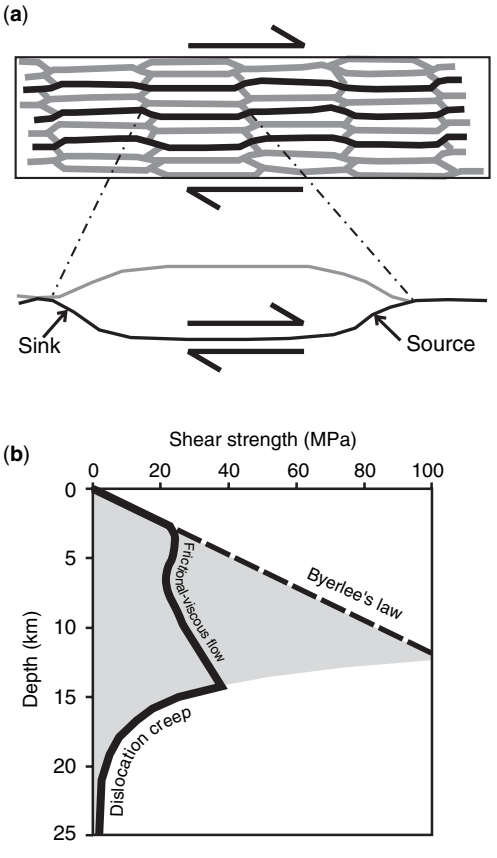

Fig. 2. (**a**) Microphysical model of Bos & Spiers (2002) to explain frictional–viscous flow in phyllosilicate-bearing fault rocks. Frictional slip along wavy phyllosilicate foliae (upper diagram: thick black lines = actively sliding foliation planes; thick grey lines = inactive foliation planes; uncoloured polygons = halite porphyroclasts) gives rise to incompatibilities at the leading edges of porphyroclasts. Material is removed by pressure solution (lower diagram; source) to accommodate these incompatibilities and diffuses through fluid-filled porphyroclast–phyllosilicate grain boundaries to be precipitated in at the trailing edges of porphyroclasts (lower diagram; sink). (**b**) Schematic strength profile for a transcurrent fault zone that widens with depth, based on the microphysical model in (a). The heavy line shows predictions of the microphysical model for diffusion-controlled pressure solution at strain rates of 10^{-10} and 10^{-12} s^{-1} (see Bos & Spiers 2002 for details). The shaded area gives the total strength predicted by traditional the two-mechanism strength profile based on Byerlee's law and dislocation creep in wet quartz.

transcurrent faults (such as the SAF) will be characterized by Byerlee's law behaviour at the shallowest depths (for a strain rate of 10^{-10} s^{-1} this corresponds to no more than 3 km depth; i.e. the approximate range of the SAFOD borehole), below which there is a transition to pressure solution-controlled creep, where mechanical behaviour is strongly rate- as well as normally stress-sensitive. Below about 15 km depth, the temperature increases sufficiently for strength to be controlled by dislocation creep in quartz. Such profiles show a reduction in upper crustal strength of 50–70% compared with standard calculations based solely on Byerlee friction and dislocation creep in wet quartz aggregates (Fig. 2b; Niemeijer & Spiers 2005). Significantly, several other workers have demonstrated that enhanced diffusion rates can give rise to significant reductions in the viscous strength of polymineralic rocks with respect to monomineralic rocks comprising end-member phases (e.g., Wheeler 1992; Bruhn *et al.* 1999). In particular, Robin (1979) highlighted the role played by phyllosilicates in catalysing silica diffusion and mobility.

The results of the Utrecht experiments and this previous work seem to provide elegant explanations for the apparent weakness of the SAF. A key test of their validity is whether the experiments are consistent with geological and seismological observations of exhumed, and active large-displacement faults. We return to this important question later on.

Geological observations of exhumed large-displacement faults

The following sections focus on case studies of two well-documented strike–slip fault systems: the Punchbowl/North Branch San Gabriel Faults (PF/NBSGF), CA, which have been exhumed from less than 5 km depth, and the Median Tectonic Line (MTL), Japan, which contains fault rocks that are inferred to have developed at 5–10 km depth. The kinematics and scale of these faults make them appropriate field analogues for the active San Andreas Fault. In both cases, a geologically based approach to understanding fault weakening has combined theoretical and experimental modelling with detailed field and microstructural observations and geochemical data. We compare results from the PF/NBSGF and MTL with findings from other exhumed faults in different geological settings. In each case, we summarize key aspects of the fault zone architectures, evidence for frictional–viscous deformation and the inferred mechanical behaviour of each fault.

Faults exhumed from ≤5 km depth

The internal structure, composition and properties of two exhumed, now inactive strands of the SAF – the Punchbowl and North Branch San Gabriel Faults – have been extensively described (Chester & Logan 1986; Chester *et al.* 1993; Evans & Chester 1995; Chester & Chester 1998; Wilson *et al.* 2003). These faults have been exhumed from 2–5 km depth, thereby potentially providing excellent field analogues for the active strands of the SAF encountered within the SAFOD borehole (although note the caveats below). The NBSGF was active during the Miocene and has accommodated *c*. 21 km dextral strike–slip. The PF was active during the Miocene and Pliocene and has accommodated *c*. 44 km right-lateral slip (Chester *et al.* 2004).

The PF and NBSGF both juxtapose a variety of quartzo-feldspathic protoliths and are characterized by wide damage zones (*c*. 10^2 m thick) containing one (NBSGF) or two (PF) narrow (<1 m thick), high strain fault cores. The damage zones which bound the ultracataclasite cores comprise narrow tabular zones of foliated cataclasite (Chester *et al.* 1985) within a much wider damage zone of fractured country rock (Chester *et al.* 1993; Fig. 3). The orientations of minor faults and other fabric elements suggest that strain was partitioned between simple shear in the fault cores and nearly fault-normal shortening in the damage zones (Chester *et al.* 1993). These findings appear to reflect the regional stress orientations described by Mount & Suppe (1987), leading Chester *et al.* (1993) to propose that the Punchbowl and North Branch San Gabriel Faults were weak and similar to the modern SAF.

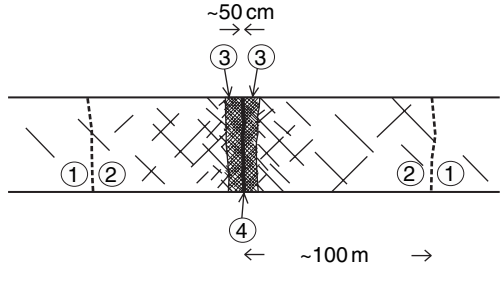

Fig. 3. Schematic profile through an exhumed segment of the San Andreas Fault (North Branch San Gabriel Fault), after Chester *et al.* (1993), showing narrow, ultracataclasite fault core (4) surrounded by an inner damage zone of foliated cataclasite (3) and an outer damage zone of fractured country rock (2). (1) is undeformed host rock; dashed vertical lines mark the approximate extent of the fault zone.

Whole-rock geochemical analyses of fault rocks from two localities (Bear Creek and Pacoima Canyon) along the San Gabriel Fault display evidence for limited fluid-rock interaction in a closed-system environment (Bear Creek) or cataclastic deformation in a dry environment (Pacoima Canyon; Evans & Chester 1995). However, analyses of fault rocks from the North Fork site (NBSGF) suggest that the fault core was an open system to fluid circulation. Dissolution and transport of silica resulted in a *c*. 37% fluid-assisted volume loss (Evans & Chester 1995). These data are consistent with the textural observations of Chester *et al.* (1993), who showed that the cores of the PF/NBSGF display pervasive evidence for syn-tectonic alteration of country rock to clays and zeolites, and for the widespread occurrence of sheared laumonite, albite, calcite and quartz veins. Mineralogical analysis of cuttings from the SAFOD pilot hole, however, led Solum & van der Pluijm (2004) to conclude that clay minerals within the ultracataclasite core of the Punchbowl Fault are likely to have formed at shallow depths (<2 km), as a result of post-faulting alteration. Despite these caveats in interpreting the mineralogy of exhumed faults, the presence of sheared veins within the cores of the PF/NBSGF is consistent with structural reworking of the fault cores at low effective stresses (Chester *et al.* 1993). These authors proposed that high pore fluid pressures were probably maintained by upward migration of fluids along fault cores (cf. Rice 1992). They attributed slip localization within the fault cores to a positive feedback between comminution and transformation weakening (i.e., the development of weak, water-swelling clays) during the initial stages of faulting. However, they made it clear that low friction clays are *not* present in sufficient quantities to be the primary means of lowering the frictional strength of the SAF across the entire brittle crust (Chester *et al.* 1993).

The ultracataclastic cores of both the PF and NBSGF contain a so-called 'prominent fracture surface' (PFS, e.g., Chester & Chester 1998). This is a sub-planar surface that cuts across or merges with all other mesostructures (e.g., layering, lithological boundaries and fracture surfaces) exposed within the fault cores. Chester *et al.* (2004) stated that the roughness of the PFS is smaller in slip-parallel compared with slip-perpendicular exposures. The PFS separates lithologically distinct cataclastic fault rocks that are believed to have been derived from the wall rocks located on either side of the fault zone. Chester & Chester (1998) used these observations to conclude that the PFS is a slip surface that developed during extreme and prolonged slip localization within the narrow fault cores, with little evidence for mixing of fault rock lithologies across the PFS. They argued that slip localization along a PFS is consistent with velocity weakening behaviour necessary for earthquake nucleation (e.g., Marone 1998). They further suggested that, if dynamic weakening was operative, the geological observations are more consistent with thermal pressurization rather than acoustic fluidization, arguing that the latter mechanism is likely to have given rise to liquefaction and mixing of material within the core (Chester & Chester 1998). The inference of seismic slip along the PF/NBSGF is supported by fault rock samples from a borehole through the seismically active Nojima Fault, Japan. According to Chester *et al.* (2004), the patterns of deformation and alteration associated with this fault are similar to the PF/NBSGF (e.g., Tanaka *et al.* 2001; Ohtani *et al.* 2000).

These observations from two exhumed segments of the SAF contrast with Faulkner *et al.*'s (2003) study of the Carboneras Fault (CF), southeastern Spain. The CF has been exhumed from between 1.5 and 4 km depth. It constitutes part of the diffuse plate boundary between Africa and Iberia and has accommodated *c*. 40 km sinistral strike–slip offset during the Miocene. The fault cuts phyllosilicate-rich basement rocks and is a *c*. 1 km wide zone comprising continuous strands of phyllosilicate-rich fault gouge that bound lenses of variably deformed protolith (Fig. 4). In contrast to the PF/NBSGF, the gouge zones are characterized by distributed deformation, from which Faulkner *et al.* (2003) inferred the gouge zones to have strain-hardening and/or velocity strengthening behaviour. Faulkner *et al.* attributed these differences in fault zone structure and inferred mechanical behaviour to the nature of the country rock: the PF/NBSGF cut mainly quartzo-feldspathic rocks, which in laboratory experiments typically display velocity weakening behaviour, whilst the CF cuts mainly phyllosilicate rich rocks – experimental data suggest that phyllosilicate-rich gouges generally display velocity strengthening behaviour. Faulkner *et al.* (2003) suggested that creep/strain hardening within the gouge layers was punctuated by seismic slip due to earthquake nucleation and localized slip along en-echelon fault surfaces within blocks of variably deformed dolomite entrained within the fault zone (Fig. 4). Faulkner *et al.* (2003) pointed out that their field observations from the CF are reminiscent of the en-echelon patterns of microseismicity in the M6 earthquake nucleation zone recorded at depth along the SAF near Parkfield, CA.

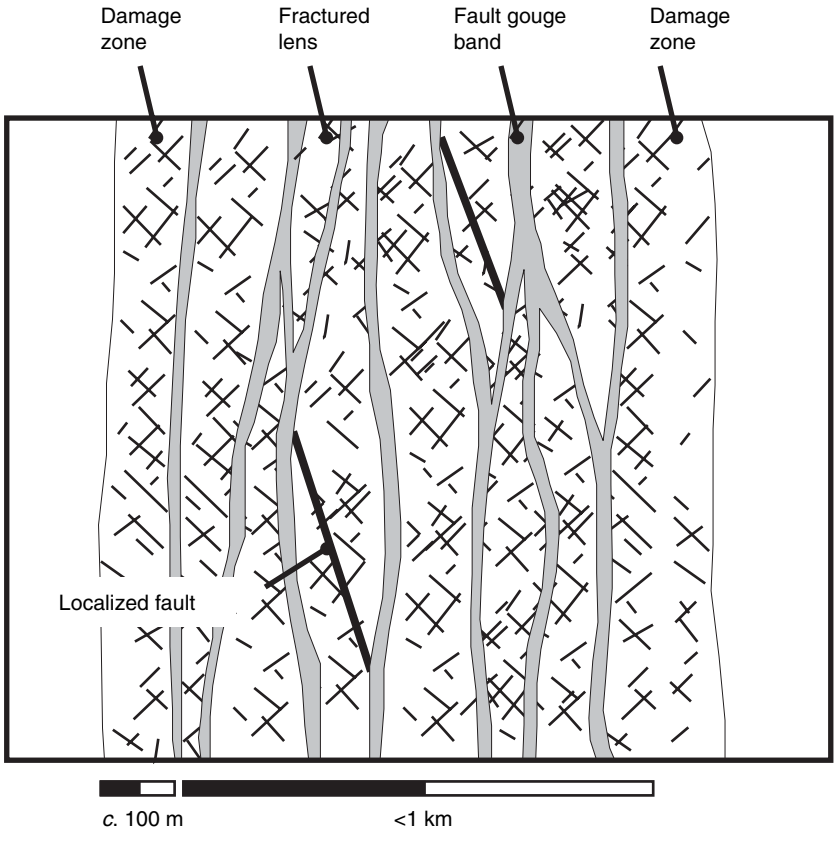

Fig. 4. Schematic profile through an exhumed segment of a crustal fault (such as the Carboneras Fault), which contains a large proportion of phyllosilicate-rich material. After Faulkner *et al.* (2003).

Summary. Geological studies of large-displacement faults exhumed from the uppermost 5 km of the seismogenic crust suggest that fault structure and mechanical behaviour are strongly controlled by protolith and fault rock lithology (Figs 3 & 4), in agreement with laboratory friction experiments. The geological observations support the hypotheses of elevated pore pressures within fault cores and/or the operation of dynamic weakening mechanisms such as thermal pressurization. However, low friction clay gouges are not present in sufficient quantities to control the rheology of the studied faults. There is evidence at some localities for significant fluid-related alteration, dissolution and volume loss. These conditions could favour the operation of frictional–viscous/multi-mechanism friction mechanisms (e.g., Chester & Higgs 1992; Bos & Spiers 2000). Yet, it is clear from the heterogeneous spatial distribution of fluid–rock interaction along the NBSGF that such mechanisms did not operate uniformly along the entire length of the fault, at least within the 2–5 km depth range.

Faults exhumed from >5 km depth

Geological characterization of large-displacement faults that, in general, have been exhumed from greater depths than the faults described in the previous section, often display evidence for frictional–viscous flow within phyllosilicate-rich fault cores. The MTL is a typical structure of this type, and has been active as a strike–slip fault since the late Cretaceous. Displacement estimates are poorly constrained, but are probably in the order of hundreds of kilometres minimum (Ichikawa 1980). The fault dips northwards 60° at the surface, although there is geological evidence that the MTL initiated as a shallowly dipping structure during the mid-Cretaceous. The MTL has an onshore trace of at least 1000 km and separates the Ryoke granitoid metamorphic rocks from Sambagawa metasediments (Fig. 5a). Recent studies have provided convincing textural evidence for the operation of frictional–viscous deformation mechanisms within macroscopically ductile fault

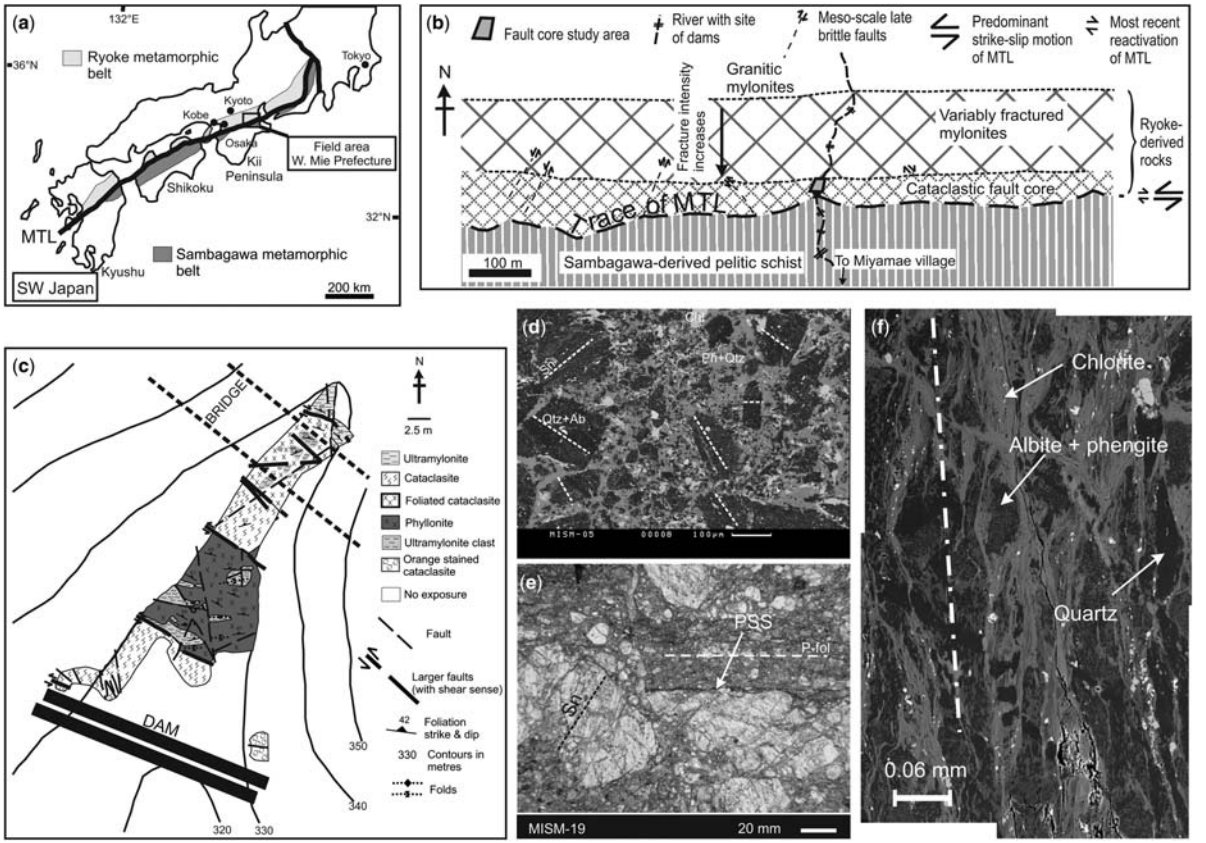

Fig. 5. (**a**) Map of SW Japan showing the MTL, Ryoke and Sambagawa metamorphic belts and the location of the study area in Mie Prefecture after Jefferies *et al.* (2006*a*). (**b**) Simplified geological map of the MTL near Miyamae village, Mie Prefecture. (**c**) Geological map of the fault core exposed in the Fukaya river section. Microstructures shown in (d–f) are from fault rock samples collected from this section. (**d**) Backscatter SEM image of cataclasite. Sn = ultramylonitic foliation, preserved in randomly oriented ultramylonite clasts; Chl = chlorite; Qtz + Ab = quartz + albite; Ph + Qtz = phengite + quartz. (**e**) Photomicrograph of a foliated cataclasite, viewed in plane polarised light. PSS = pressure solution seam; P-fol = phyllosilicate foliation; Sn = ultramylonitic foliation, preserved in randomly oriented ultramylonite clasts. (**f**) Backscatter SEM image of phyllonite. Dark areas are quartz and feldspar porphyroclasts; paler grey aggregates are chlorite. Note contiguity of aligned phyllosilicate aggregates, which are oriented parallel to the macroscopic foliation (dashed line).

rocks (phyllonites and foliated cataclasites) exposed at a number of localities along the MTL in SW Japan. These fault rocks are inferred to have developed at between 5 and 10 km depth (Jefferies *et al.* 2006*b*, fig. 10).

Previous studies suggest that the MTL has accommodated mainly sinistral strike–slip displacements, with some evidence for a later phase of dextral reactivation accommodated mainly by slip within incohesive gouges adjacent to the narrow central slip surface (Wibberley & Shimamoto 2003). Above Miyamae village in Mie Prefecture, the northern (Ryoke) side of the MTL is characterized by a highly deformed and locally foliated cataclastic fault core, *c*. 50 m wide, which contains the central slip surface (Fig. 5a, b). A damage zone of variably fractured and faulted Ryoke granitoid mylonites, which formed during late Cretaceous–early Tertiary shearing, continues for a further 200–250 m northwards before passing into a 5 km wide zone of largely intact Ryoke mylonites (Fig. 5b). The mylonites developed during exhumation from 18 to 11 km depth. According to Takagi (1986), the later MTL core and damage zone developed during a protracted phase of sinistral strike–slip deformation at progressively shallower crustal levels.

Continued strike–slip shearing during steady regional exhumation has juxtaposed a variety of fault-bounded cataclastic and mylonitic fault rocks within the core of the MTL. The core is well-exposed in the Fukaya river section near Miyamae village and comprises distinct packages of quartzofeldspathic ultramylonite, cataclasite, foliated cataclasite and phyllonite. Jefferies *et al.* (2006*a*) showed that the cataclasites, foliated cataclasites and phyllonites contain variably deformed and altered ultramylonite clasts. Thus, all the fault rocks within the core were derived from pre-existing mylonitic protoliths (Fig. 5c). Within the foliated cataclasites and phyllonites, the shallowly east- and north-plunging mineral lineation is defined by white mica and chlorite aggregates and is everywhere associated with sinistral shear sense criteria. The phyllonites have been subjected to an additional phase of deformation, producing centimetre- to metre-scale folds with predominantly dextral vergence, which suggests that away from the central slip zone late dextral movements were also preferentially focussed into the phyllonites.

In thin section and backscattered SEM images, the cataclasites comprise angular blocks of randomly oriented, fractured ultramylonite set within a matrix of white mica and comminuted quartz (Fig. 5d). The modal abundance of hydrous minerals (chlorite and white mica) increases to nearly 60% in packages of foliated cataclasite. Here, the foliation is defined by dissolution seams, aligned phyllosilicate minerals and ultramylonite clasts that have become deformed and elongated by distributed microfracturing (Fig. 5e). Jefferies *et al.* (2006*a*) reported that the degree of alteration is most intense within fine-grained, ultracataclasitic units and adjacent to pre-existing brittle fractures. These observations suggest that retrogression and the development of a macroscopically ductile fabric within the phyllonites and foliated cataclasites were triggered by the influx of hydrous fluids into the fault core. Fluid flow was focussed into those parts of the fault core most affected by macroscopic fracturing and cataclastic deformation (Jefferies *et al.* 2006*a*).

The phyllonites are also characterized by pervasive microstructural evidence for hydrous alteration and fluid-assisted diffusive mass transfer, such as the presence of pressure solution seams and fibrous overgrowths of white mica. The foliation is defined by neomineralized aggregates of chlorite and white mica, which wrap around relict lenses of cataclastically deformed ultramylonite (Fig. 5f). Microprobe analyses show that chlorite grains within the phyllonite are significantly enriched in MgO and depleted in FeO compared with chlorite grains preserved in the ultramylonites, cataclasites or foliated cataclasistes. These observations led Jefferies *et al.* (2006*a*) to propose there was a distinct, late phase of fluid influx and chlorite growth associated with the development of phyllonite within the fault core. They argued that the fault rock sequence cataclasite → foliated cataclasite → phyllonite results from progressively increasing fluid influx and phyllosilicate precipitation within the fault core. A corollary of this argument is that, prior to fluid influx and alteration, the MTL may have been characterized by an architecture similar to that of the exposed Punchbowl and North Branch San Gabriel Faults – that is, a narrow cataclastic fault core surrounded by a broad damage zone (although we note the greater width of the MTL core and damage zone compared with PF/NBSGF).

A similar characteristic fault rock sequence has been documented within the core of the MTL exposed at Anko in Nagano prefecture, *c*. 200 km along strike to the northeast (Jefferies *et al.* 2006*b*). Here, early brittle fractures are locally overprinted by foliated cataclasites and ultracataclasites in which the foliation is defined by aligned aggregates of fibrous chlorite and white mica that developed due to chemical alteration of feldspar, biotite and garnet. Sinistral strike–slip became progressively localized within the foliated cataclasites. These foliated units contain foliation-parallel and cross-cutting carbonate veins, which suggests that at least some of the veining and carbonate mineralisation was synchronous with

macrosopically ductile shear within the foliated cataclasite layers. Jefferies *et al.* (2006*b*) argued that the absence of well-developed phyllonite in the Anko section compared with the section at Miyamae reflects the shallower exhumation depth (*c*. 5 km) compared with Miyamae (*c*. 10 km). Thus, the two sections preserve fault rock assemblages that formed at different depths along the MTL at more or less the same time (Jefferies *et al.* 2006*b*).

Jefferies *et al.* (2006*a*, *b*) used two independent lines of evidence to argue that fluid-assisted deformation caused weakening of the MTL. First, the localization of deformation within phyllonites and foliated cataclasites in the Fukaya river section and at Anko, respectively, suggests that these highly altered fault rocks were weak relative to surrounding fault and country rocks. Second, the association between cataclasis and carbonate mineralization at Anko points to the periodic development of high pore fluid pressures in the fault core, which could also weaken the fault. To explain these observations, Jefferies *et al.* (2006*a*, *b*) proposed that fluid influx into the cataclastic fault core triggered the onset of solution-precipitation and growth of weak phyllosilicates at the expense of strong feldspar and hornblende grains, leading to reaction softening and frictional–viscous flow (cf. Janecke & Evans 1988; Tourigny & Tremblay 1997; Guermani & Pennacchioni 1998, who described examples of this phenomenon from along smaller-displacement structures). Developing this argument, they suggested that the operation of such processes along the pre-existing, interconnected network of brittle fractures in the cataclastic fault core would lead to the rapid establishment of a crustal-scale 'interconnected weak layer' (IWL; Handy 1994; Fusseis *et al.* 2006; Fig. 6). Thus, the effects of grain-scale weakening (reaction softening, frictional–viscous flow) triggered by the influx of chemically active fluids (cf. Chester & Higgs 1992; Bos & Spiers 2000) could be transmitted upwards to the crustal scale (Jefferies *et al.* 2006*b*).

Axen (2004) reached a qualitatively similar conclusion about the importance of syntectonic chemical changes in a discussion of the geological constraints on the initiation and slip along low-angle normal faults (LANFs) in the western US. LANFs are problematic because standard fault mechanical theory does not allow such orientations (Anderson 1942) and large earthquakes on LANFs are rare (Jackson & White 1989; Collettini & Sibson 2001). Axen (2004) demonstrated that, at most depths within the extending brittle crust, LANF slip can only occur if pore fluid pressures are unusually high (90% of lithostatic), or if the fault rocks are characterized by very low

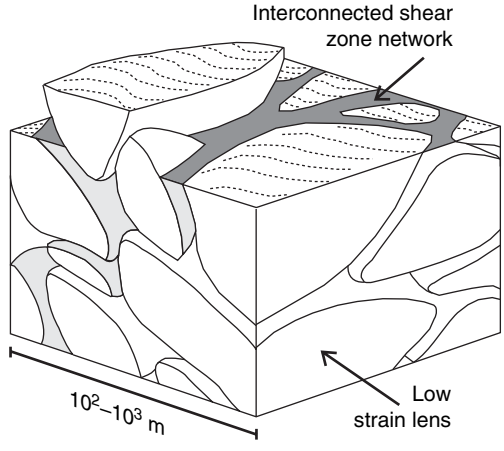

Fig. 6. Schematic diagram showing a crustal-scale interconnected weak layer, after Imber *et al.* (1997).

coefficients of sliding friction. He concluded that 'the difficulty in explaining LANF formation and slip suggest that our understanding of crustal mechanics is lacking a key ingredient, *possibly related to spatial, temporal and/or chemical changes that are not addressed in standard rock mechanical theory*' (our italics).

Collettini & Holdsworth (2004) showed that the core of the Zuccale Fault (ZF) – an ancient, eastward-dipping LANF exhumed from no deeper than 6 km (but perhaps as shallow as 3 km; Collettini *et al.* 2006*a, b*) and now exposed on the island of Elba, Italy (Fig. 7a–c) – is associated with five distinct cataclastic and foliated fault rock assemblages (e.g., Fig. 7d). They showed that most of the foliated fault rocks contain relict cataclastic textures that have become 'smeared out' by later ductile deformation. In addition, deformed carbonate veins preserved within the core of the ZF attest to hydrofracturing caused by cyclic build up of fluid overpressure beneath the low-permeability, phyllosilicate-rich fault core (Collettini *et al.* 2006*b*). Thin section observations show that syn-tectonic alteration of strong phases to fine-grained aggregates of weak hydrous minerals (chlorite and clays) triggered collapse of the initial 'load-bearing framework' microstructure (LBF; Handy 1994), explaining why the earlier cataclastic fabrics have been 'smeared out' parallel to the macroscopic foliation. The asymmetric character of many fibrous overgrowths (Fig. 7e) demonstrates that solution-precipitation occurred during top-to-the-E shear along the ZF (Collettini & Holdsworth 2004), whilst the presence of discordant and foliation-parallel (i.e., reworked) veins points to transient embrittlement due to cyclic increases in fluid overpressure (Fig. 7f; Collettini & Barchi

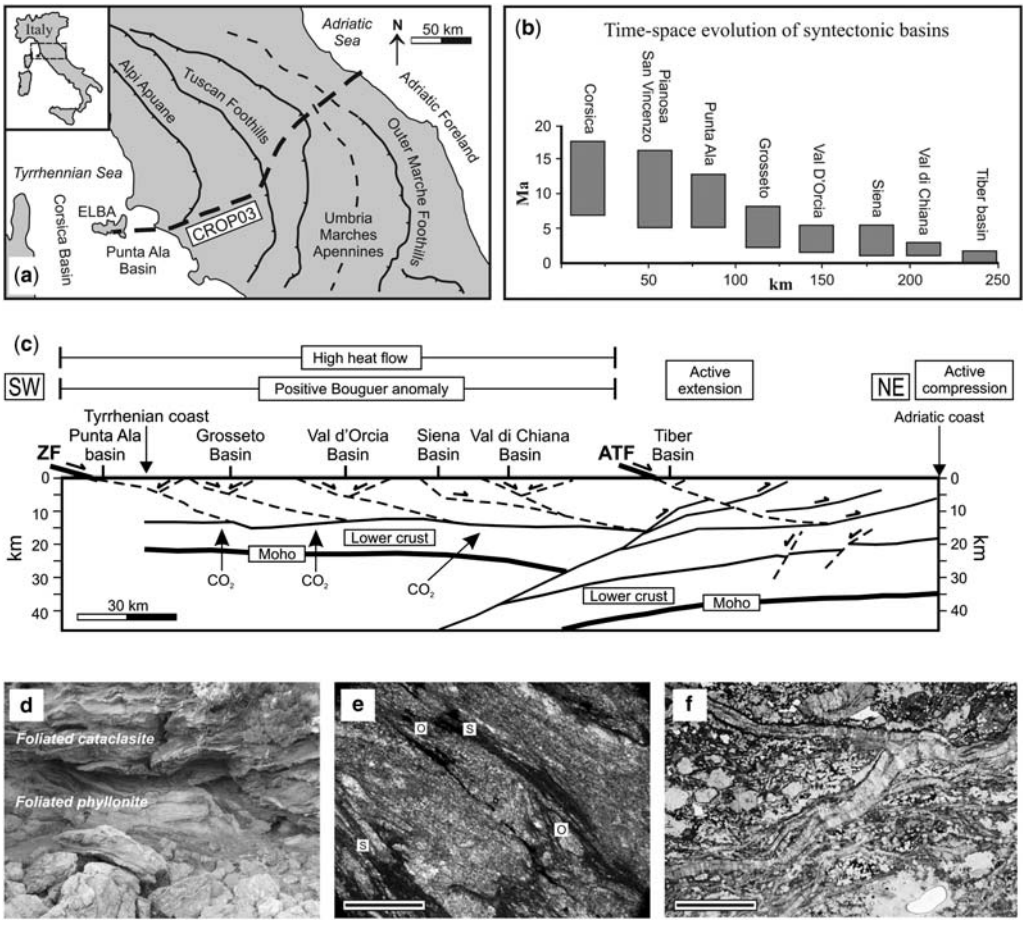

Fig. 7. (**a**) Map showing the regional tectonic setting of the Tyrrhenian–Apennine region of Italy, including the island of Elba and the location of the cross-section shown in (c). (**b**) Graph showing the inferred spatial and temporal evolution of syntectonic basins shown in (c). These basins are developed in the hanging walls of eastward-younging LANFs. (**c**) Crustal-scale cross-section from Elba to the Adriatic coast based on the CROP 03 regional seismic reflection profile. ZF is the Zuccale Fault; ATF is the active Altotiberina Fault. The exhumed ZF is believed to be an analogue for the active ATF. (**d**) Outcrop photograph showing the foliated core of the Zuccale Fault at Punta di Zuccale. (**e**) Photomicrograph of dissolution seams (S) and fibrous overgrowths (O) of tremolite, talc and calcite surrounding a carbonate clast. (**f**) Photomicrograph of discordant and foliation-parallel veins from the fault core, viewed in plane-polarized light. Modified from Collettini & Holdsworth (2004).

2004). Thus, there is clear field and microstructural evidence for the influx of chemically active hydrous fluids into the precursory cataclastic fault zone. Collettini & Holdsworth (2004) went on to argue that strain localization within the foliated fault core is evidence that reaction softening and frictional–viscous deformation caused weakening of the fault zone, a conclusion similar to that reached in the case of the MTL by Jefferies *et al.* (2006*a*, *b*) and consistent with Axen's (2004) predictions concerning the controls on the mechanical behaviour of LANFs.

Summary. The MTL and ZF display a characteristic sequence of fabric evolution in which early brittle deformation products (fractured host rock, cataclasites and ultracataclasites) are overprinted by macroscopically ductile foliated cataclasites and phyllonites. In each case, the development of the foliation was controlled by an influx of chemically active fluids along a pre-existing brittle fault zone. Fluid–rock interaction allowed growth of phyllosilicates and a switch from brittle to frictional–viscous deformation. In both cases, the inferred weakening results from transiently high pore

pressures and the operation of frictional–viscous deformation mechanisms.

The MTL and ZF are by no means unique. Foliated cataclasites and phyllonites that overprint earlier brittle fabrics have been reported along several exhumed, large-displacement faults from different tectonic settings worldwide, including: Great Glen Fault, Scotland (Stewart *et al.* 1999, 2000; Holdsworth *et al.* 2001); Moine Thrust Belt, Scotland (Wibberley 2005); Outer Hebrides Fault Zone, Scotland (Butler *et al.* 1995; Imber *et al.* 1997, 2001); Ser Barbier Thrust in the western external Alps (Wibberley 2005); Err Detachment, eastern Switzerland (Manatschal 1999); Nordfjord–Sogn Detachment, Norway (Braathen & Osmundsen 2004); and possibly the Siberia Fault Zone, New Zealand (White 2001) and Wasatch Fault, Utah (Parry *et al.* 1988). This apparently characteristic brittle-to-macroscopically ductile fabric evolution is strikingly similar to the sequence of microstructures observed by Bos & Spiers (2000, 2001) in a series of high-strain experiments on halite–kaolinite aggregates. On this basis, Collettini & Holdsworth (2004), Holdsworth (2004) and Jefferies *et al.* (2006*a*, *b*) proposed that microphysical models of frictional–viscous deformation in the presence of phyllosilicates (Bos & Spiers 2002; Niemeijer & Spiers 2005) can be used to quantify the strength of large-displacement faults with phyllonitic cores.

Discussion and future work

Based on these geological observations, previous authors have proposed a simple rheological model for large-displacement (mature) faults. In this model, the uppermost 3–5 km deforms in the frictional regime, presumably by seismic slip or aseismic creep, depending on the host rock lithology. Below 3–5 km depth, the fault deforms by frictional–viscous flow (Holdsworth 2004; Neimeijer & Spiers 2005; Jefferies *et al.* 2006*a*, *b*; Fig. 8). Similar models have been developed to explain the apparent weakness of low-angle normal faults (Collettini & Holdsworth 2004). The establishment of frictional–viscous flow requires a precursor brittle fault zone, followed by influx of hydrothermal fluid into the permeable fault core. As noted previously, microphysical models that describe the deformation of quartz–phyllosilicate aggregates (e.g., Bos & Spiers 2002) can be used to quantify the strength of such faults. For example, the model of Niemeijer & Spiers (2005), as formulated for the case of a vertical transcurrent fault assuming a geothermal gradient of 25 °C km^{-1} and a strain rate of 10^{-10} s^{-1}, predicts a 30–70% reduction in steady-state strength at midcrustal levels compared with conventional crustal strength profiles based on Byerlee friction in the upper crust, plus a dislocation creep law for wet quartz to describe plastic flow in the middle crust (Jefferies *et al.* 2006*b*; e.g., Figs 2b & 8). According to Niemeijer & Spiers (2005), the strength predicted by this steady-state microphysical model is 'roughly consistent with the low values [of shear stress] for the San Andreas Fault inferred from heat flow measurements and stress orientation data'. However, the model also suggests that large-displacement faults with phyllontic cores will be aseismic below 3–5 km depth. This prediction is

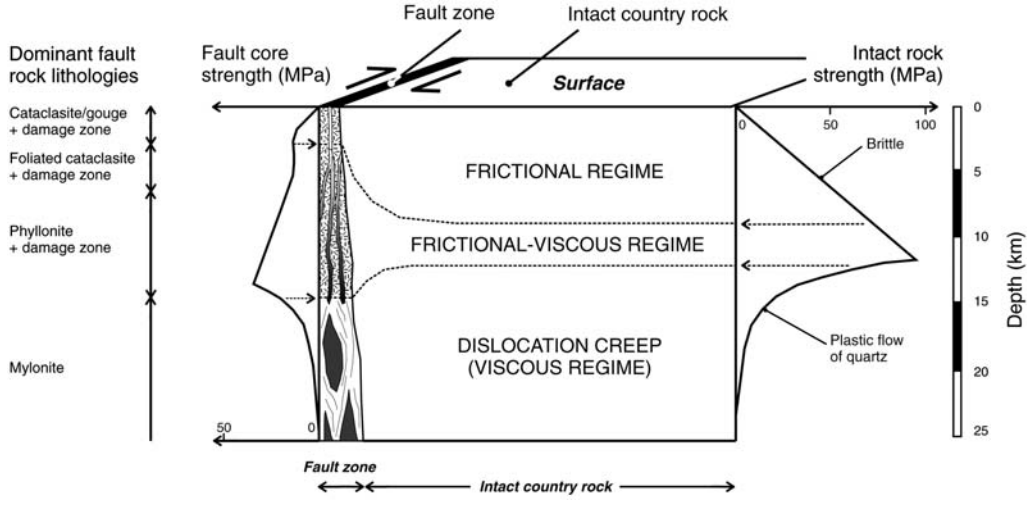

Fig. 8. Conceptual model and strength profile for a large-displacement strike–slip fault with a weak phyllonitic core, modified from Holdsworth (2004) and Jefferies *et al.* (2006*b*). The boundaries between different fault core lithologies are likely to be gradational. Fault slip within the frictional–viscous and viscous regimes is predicted to be aseismic.

consistent with the velocity strengthening behaviour of phyllosilicate gouges reported in most laboratory friction experiments (e.g., Morrow *et al.* 1992), but is at odds with geophysical observations of seismicity on many mature faults (Scholz 1990; Niemeijer & Spiers 2005).

Are faults with phyllonitic cores seismically active?

Seismological studies of active large-displacement faults in continental crust demonstrate that seismicity extends to depths of 10–15 km and that the largest earthquakes tend to nucleate near the base of the seismogenic layer (e.g., Sibson 1983; Scholz 1988). Quantitative comparison of geodetic strain rates with strain rate fields deduced from earthquake moment tensors suggests that faults move either by seismic slip (high seismic coupling) or aseismic creep (low seismic coupling; e.g., Scholz 1990; Masson *et al.* 2005; Sue *et al.* 2007). Aseismic creep accompanied by abundant microseismic activity, occurs along the Parkfield–San Juan Bautista segment of the San Andreas Fault in central California, whilst the segments to the north and south are currently locked having ruptured (slipped) during the great 1906 and 1857 earthquakes, respectively (Scholz 1990). Masson *et al.* (2005) have reported significant spatial variations in the degree of seismic coupling across Iran, a continent–continent collision zone. In northern and eastern Iran, seismic slip accounts for between 30 and 100% of the measured geodetic strain rate, but comprises less than 5% in the Zagros further to the south. In general, regions characterized by high seismic coupling are associated with the largest magnitude earthquakes (Masson *et al.* 2005), an observation that is consistent with the notion of stick–slip behaviour. In contrast, no earthquakes larger than $M > 5.5$ have been reported on unambiguously identified low-angle normal fault planes (dip $< 30^{\circ}$; Collettini & Sibson 2001; but cf. Axen 1999). Instead, it has been suggested that LANFs deform by aseismic creep. Abundant microseismic activity along the active low angle Altotiberina Fault, Italy cannot account for the calculated 1 mm per year slip rate and has been attributed to short-lived fluid overpressure events along small portions of the fault surface. These events are believed to give rise to localized hydrofracturing and veining, consistent with field observations from the exhumed Zuccale Fault (Collettini 2002; Collettini & Holdsworth 2004) and consistent with the predictions of the Utrecht models.

The simplest explanation for the observation that faults may creep or slip is that creeping faults have weak phyllonitic cores that deform by aseismic frictional–viscous flow, whilst stick–slip faults contain high abundances of materials that exhibit velocity weakening behaviour and have long-term strengths that can (in the absence of other weakening mechanisms) be approximated by traditional two-mechanism strength profiles (e.g., Fig. 2). Nevertheless, two lines of reasoning suggest that the relationship between fault rock distribution and seismicity may be more complicated. First, the metamorphic (P–T–fluid) conditions within the middle crust are such that prehenite–pumpellyite/greenschist/lower amphibolite facies hydration reactions leading to the development of macroscopically ductile phyllonites are likely to be widespread within the cores of (most?) active large-displacement faults that cut continental basements (e.g., Wintsch *et al.* 1995; Holdsworth 2004). This prediction is borne out by the geological studies of exhumed large-displacement faults summarized in the previous sections. For example, Imber *et al.* (2001) have shown that phyllonite can form repeatedly over wide depth ranges throughout the life of a large-displacement fault. Direct application of classic laboratory results (e.g., Morrow *et al.* 1992) therefore implies we should observe a large number of creeping faults at the present time – unless we consider that some faults with phyllonitic cores are able to deform seismically.

Geological, palaeoseismological and geodetic studies of the Wasatch Fault, Utah also support the notion that faults with phyllonitic cores may be capable of generating large earthquakes. The Wasatch Fault is an intraplate normal fault with a minimum throw of 11 km (Parry & Bruhn 1987). It defines the western limit of the Intermountain Seismic Belt near Salt Lake City and contains a 30 m thick carapace of phyllonite in its footwall (Parry *et al.* 1988). Parry & Bruhn (1986) demonstrated that phyllonite formation took place synchronous with extension at depths $\geq$11 km. A well-defined record of palaeoseismicity has been determined for the past 5600 years based on an analysis of fault morphology and trenching. During this period, the Wasatch Fault experienced 11 scarp-forming paleoearthquakes ($6.8 < M < 7.2$), consistent with a Holocene fault slip rate of 1–2 mm per year (Schwartz & Coppersmith 1984). The last rupture on the Wasatch Fault occurred *c*. 600 years ago. Comparison with a similar, but more recently ruptured, extensional fault in the Basin & Range province – the Lost River Fault, Idaho, which produced the $M = 7.3$ Borah Peak earthquake in 1983 (see Scholz 1990 for a summary) – suggests that the hypocentral depths of the $M \approx 7$ mainshocks and some aftershocks on the Wasatch Fault are likely to have occurred well within the depth range of phyllonite formation constrained by Parry & Bruhn (1986)

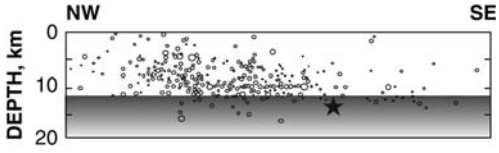

Fig. 9. Section parallel to the Lost River Fault showing schematically the distribution of aftershocks (circles) and mainshock (star) associated with the 1983 Borah Peak earthquake, Idaho. The shaded area represents the region of likely phyllonite generation along comparable Basin and Range normal faults, such as the Wasatch Fault. Adapted from Scholz (1990).

(i.e., $\geq$11 km; Fig. 9). Furthermore, according to Chang *et al.* (2006), the Holocene slip rate on the Wasatch Fault is consistent with the present-day slip rate calculated from the GPS-derived horizontal velocity field. (This calculation assumes that the Wasatch Fault dips $>30^{\circ}$ at depth – a reasonable assumption based on measured fault plane orientations at outcrop and focal mechanisms of large Basin and Range normal fault earthquakes, e.g., Zoback 1983; Doser & Smith 1989.) Speculatively, extrapolating the present-day rate of crustal loading back throughout the Holocene implies that the phyllonite-bearing Wasatch Fault has slipped seismically for at least the past *c*. 5000 years.

Thus, it seems reasonable to suppose that, although many faults with phyllonitic cores creep, some phyllosilicate-rich faults may slip seismically for at least part of their histories (e.g., Holdsworth 2004). These considerations raise three important issues. First, if our argument is valid, there should be widespread geological evidence for seismic slip within the cores of phyllosilicate-rich faults – yet there are few published studies that explicitly identify and describe candidate slip surfaces. Second, it is important to establish how and why seismic slip could occur along faults with phyllonitic cores. Finally, we need to consider the implications of seismic slip for the possible weakening of large-displacement faults with phyllonitic cores.

Geological evidence for seismic slip within phyllonitic fault cores

The Siberia Fault Zone is a 40 km long structure located within the Pacific–Australia plate boundary zone of southern New Zealand. The fault has been exhumed from 8–10 km depth and has accommodated *c*. 3 km dextral slip. It is characterized by a 5–30 m wide damage zone of fractured and kinked schistose country rock that surrounds a 5–40 m thick core. According to White (2001), the fault core consists of foliated cataclasites and pseudotachylytes, which are cross cut by brittle faults and tabular layers of random fabric cataclasite. Petrographic observations show that the cataclastic foliation is defined by anastomosing phyllosilicate seams, strong preferred orientations of microfractures and phyllosilicate grains, alignment of non-equant clasts, chlorite–muscovite–quartz overgrowths on quartzo-feldspathic clasts and by undulating pressure solution seams. These findings are very similar to microstructural observations of phyllonite and foliated cataclastite from the MTL, Japan (Jefferies *et al.* 2006*a*, *b*). A key observation is that clasts of devitrified pseudotachylyte are preserved within foliated cataclasites, whilst intact pseudotachylyte veins appear to be 'interlaced' with the foliated cataclasites (White 2001). These observations led White (2001) to propose that pseudotachylyte generation and shear within the foliated cataclasites were cyclic, i.e. broadly contemporaneous. The important point here is that the presence of pseudotachylyte provides incontrovertible geological evidence for seismic slip (Cowan 1999) synchronous with shearing within a phyllosilicate-rich fault core.

Imber (1998) described foliation-parallel detachments within and along the margins of phyllonitic fault cores associated with the Outer Hebrides Fault Zone (OHFZ), Scotland. The detachments are lined by thin but laterally extensive calcite–albite $\pm$ chlorite veins that are sometimes associated with angular clasts of brecciated phyllonite. It is not possible to correlate footwall and hanging wall structures across detachment surfaces, consistent with significant, but indeterminate, slip along the brittle detachments. In the same area, the phyllonitic fault cores are commonly observed to contain thin but laterally persistent bands of course-grained, angular to rounded calcite-albite-chlorite porphyroclasts. Imber (1998) suggested that the porphyroclasts formed due to brecciation and subsequent macroscopically ductile reworking of the detachment veins. We interpret the detachment surfaces as having formed due to high pore pressures having caused transient embrittlement synchronous with frictional–viscous deformation within the phyllonitic fault cores – an inference that is consistent with the high across-fault sealing capacity of foliated, phyllosilicate-rich fault rocks (Faulkner & Rutter 2001). More speculatively, we suggest that the detachment veins represent seismic slip events that took place during ongoing frictional–viscous shear. Although this interpretation is at odds with the results of most laboratory friction experiments, they are consistent with recent high-strain rotary shear experiments on halite–muscovite aggregates (Niemeijer & Spiers 2006). This research found that, at high strain rates, halite–muscovite gouges showed velocity weakening behaviour accompanied by cataclasis and an increase in porosity. Niemeijer & Spiers (2006)

also showed that microstructurally controlled variations in healing rates mean that fault zone segments that have slipped seismically will rapidly re-strengthen and remain in the unstable, velocity weakening regime, consistent with the idea of repeated slip along detachment surfaces. It is possible that vein emplacement leading to the addition of calcite and albite – minerals that display velocity weakening behaviour in the laboratory – may also have increased the potential for seismic slip within the foliated core of the OHFZ.

Further geological research is required to substantiate these inferences of seismic slip within exhumed phyllosilicate-rich fault cores. According to our analysis, seismicity – hence the presence of reworked pseudotachylytes and/or mineralized detachments and/or breccias – may be commonplace within such cores. However, it is likely that these structures have been largely obscured by the effects of ongoing macroscopically ductile shear or dismembered by later faulting during exhumation, and hence have previously been overlooked. Thus, an important initial step must be to document the range of possible slip surface occurrences, geometries and microstructures within exhumed foliated fault cores. In the absence of pseudotachylyte, it is not possible to demonstrate unequivocally that a brittle fracture surface developed due to seismic slip (Cowan 1999). Nevertheless, detailed field mapping will provide useful comparisons with structures formed at shallower depths in the crust that are generally believed to have formed during seismic slip (e.g., Faulkner *et al.* 2003; Chester *et al.* 2004). A particular issue that needs to be addressed is whether localized slip surfaces in faults with phyllonitic cores are stable, long-lived features – i.e., deeper equivalents of the prominent fracture surfaces described by Chester & Chester (1998) – or more akin to the strain-hardening faults reported by Di Toro & Pennacchioni (2005) and Faulkner *et al.* (2003). A further objective should be to establish the dimensions and offsets of these slip surfaces to determine if they are the products of embrittlement over small portions of the fault surface (cf. Collettini 2002), or indicators of significant localized slip. A related goal should be to quantify the degree of slip partitioning between localized slip and macroscopically ductile frictional–viscous flow, although this is may be difficult to achieve in basement terrains that lack suitable stratigraphic markers.

Controls on seismicity and weakening along faults with phyllonitic cores

The proposal that faults with phyllonitic cores can slip seismically for at least part of their histories requires further consideration. Holdsworth (2004) suggested that such faults might behave as weak structures (i.e., deform by frictional–viscous flow) over long time scales (millions of years), but be intermittently stronger over shorter periods. This idea is consistent with the proposition that the phyllonite-bearing Wasatch Fault may have been characterized by stick–slip behaviour (with $M \approx 7$ earthquakes) throughout the Holocene. Such behaviour requires build-up of sufficient elastic strain energy to drive a large earthquake (consistent with high fault strength; cf. Sibson 1983) and that a fault contains velocity weakening materials to *c*. 15 km depth (e.g., Fig. 9).

Jefferies *et al.* (2006*a*) proposed that a change in fault slip sense (from sinistral to dextral) during Quaternary reactivation of the MTL may have dismembered the previously established crustal-scale network of phyllonitic shear zones (e.g., Fig. 6). Thus, the MTL is currently locked, with the potential for future seismic slip. More generally, any structural reorganization (for example, due to changes in the kinematic boundary conditions or fault slip vector; see below) could lead to dismemberment of an existing interconnected weak layer (IWL). We speculate that a further phase of fluid influx and hydrothermal alteration could take place following the establishment of a new principal slip surface (cf. Chester & Chester 1998). This process could lead to the renewed development of a crustal-scale interconnected weak layer and an eventual return to aseismic creep (Fig. 10a). The timescale over which a switch from seismic to aseismic deformation might take place would depend on how quickly a through-going slip surface was established, the availability of hydrothermal fluids and the metamorphic reaction rates. Nevertheless, it seems reasonable to suppose that such a change could occur within 10^3–10^6 years, which encompasses the period of time over which the Wasatch Fault is likely to have slipped seismically and is consistent with calculated diffusion-controlled reaction rates during the breakdown of K-feldspar to muscovite (a key metamorphic reaction during phyllonite generation) at a geologically reasonable strain rate (O'Hara 2007).

Niemeijer & Spiers (2005) suggested that the complex anastomosing internal structure of many large-displacement faults may lead to stress concentrations around geometric irregularities (e.g., rigid lenses of more intact rock), producing localized brittle failure. They proposed that a mature fault comprises a network of interconnected phyllonitic cores that creep aseismically, with intervening strong lenses and locked portions of varying length scale. Thus, it may be possible to produce earthquakes of varying magnitude and depth down to the base of the traditional 'brittle–ductile' transition (Niemeijer & Spiers 2005). In order to

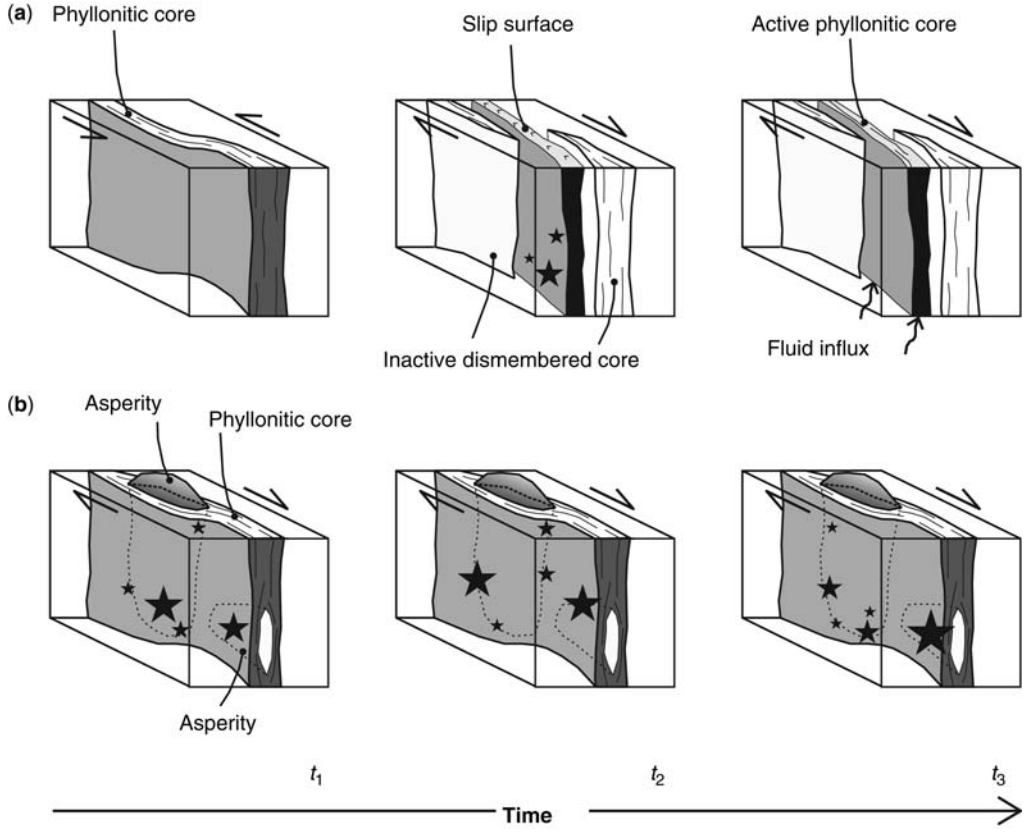

Fig. 10. Schematic diagram illustrating two possible end-member mechanisms for generating seismic slip along faults with phyllonitic cores. Star symbols schematically represent the hypocentres of different sized earthquakes. (**a**) 'IWL dismemberment' mechanism (e.g., Holdsworth 2004; Jefferies *et al.* 2006*a*). At t_1, the phyllonitic core forms a crustal-scale IWL and the fault creeps ($\pm$ small microseismic earthquakes). At t_2, a change fault slip sense (or some other structural reorganization) causes the IWL to be dismembered. A new slip surface is established and the fault slips seismically. At t_3, fluid influx leads to retrogression and phyllonite generation within the fault core. Aseismic creep is re-established. (**b**) 'Asperity rupturing' mechanism (e.g., Niemeijer & Spiers 2005). Asperities and/or jogs on different length scales may become locked giving rise to earthquakes of different sizes. The fault continues to generate earthquakes from t_1 to t_3.

understand how instabilities are able to propagate away from the rigid lenses, it is important to realize that, although phyllonitic fault cores are characterized by a high modal abundance of velocity strengthening phyllosilicates, they also contain layers rich in quartz, albite and calcite (e.g., Imber *et al.* 2001). Thus, rupture fronts initiating within rigid lenses may be able to propagate through phyllosilicate-poor velocity weakening layers within phyllonitic cores (Fig. 10b). As noted previously, Niemeijer & Spiers (2006) have also shown that instabilities in simulated phyllosilicate-bearing fault rocks (halite–muscovite aggregates) can be triggered by local increases in strain rate. Such increases in the rate of deformation could arise due to: (a) irregularities in the fault zone architecture causing the width of the phyllonitic fault core to locally decrease (e.g., Niemeijer & Spiers 2006); (b) increased loading triggered by earthquakes on adjacent faults (e.g., Cowie 1998); and/or (c) spatial migration of activity between different sets of faults within a deforming region (e.g., Jackson 1999).

The mechanisms described above are not mutually exclusive and each could be operative to a greater or lesser extent within any given fault zone. The key point is that these models emphasize the importance of both fault zone geometry and internal structure (e.g., Holdsworth 2004; Wibberley 2007) and long-range elastic interactions between large-displacement faults (e.g., Cowie 1998; Jackson 1999; Walsh *et al.* 2001) in

controlling their slip behaviour. Future studies should aim to document the geological evidence that could discriminate between these possible mechanisms – or indeed highlight other possibilities. Such studies are likely to involve detailed field mapping combined with precise dating of deformation products although, in many cases, it may be difficult to arrive at a unique solution. The first mechanism ('IWL dismemberment'; Fig. 10a) is likely to be characterized by alternating periods of seismic and aseismic slip. In deeply exhumed long-lived faults, such behaviour might be recognized by the presence of multiple generations of cross-cutting phyllonitic fabrics (Fig. 10a). Imber *et al.* (2001) described a possible example of this phenomenon along the southern segment of the Outer Hebrides Fault Zone, in which a switch from sinistral strike–slip to extension was associated with a new phase of phyllonite development. In faults where the second mechanism ('asperity rupturing'; Fig. 10b) is dominant, there may be a close spatial association between localized slip surfaces and geometric irregularities within and along the fault zone (e.g., rigid lenses, bends, etc.). In each case, detailed mapping and microstructural analysis of exhumed fault rocks will also be required to test the hypothesis that slip surfaces propagate along phyllosilicate-poor layers within phyllonitic fault cores.

Finally, it is important to consider the implications for the strength of faults with phyllonitic cores. In the case of the 'IWL dismemberment' mechanism, there are likely to be distinct periods of geological time during which the fault creeps and its strength is controlled by frictional–viscous creep within the phyllonitic core, as predicted by the Utrecht models. In contrast, fault strength during periods of seismic slip may be controlled by frictional–viscous flow, variations in pore pressure and/or the operation of dynamic weakening mechanisms depending on the degree of seismic coupling (see below).

Faults that follow the 'asperity rupturing' mechanism are likely to produce earthquakes of varying sizes throughout their lifetimes. In this case, the operative weakening mechanisms will depend on the degree of seismic coupling. If seismic coupling is low (i.e., the fault moves predominantly by aseismic creep), frictional–viscous flow within the phyllonitic core is likely to be the main control on fault strength. Conversely, if the fault slips seismically, the phyllonitic core will still be weak – as predicted by microphysical models (e.g., Niemeijer & Spiers 2005; Jefferies *et al.* 2006*b*; Figs 2b & 8) – but because creep accommodates a small proportion of the total offset, frictional–viscous flow is unlikely to control the strength or heat production of such a fault. If correct, this analysis suggests that processes other than frictional–viscous flow must bring about weakening of some large-displacement seismogenic faults. These include previously hypothesized mechanisms such as the presence of low-friction clay gouges or talc (e.g., Moore & Rymer 2007), elevated fluid pressures within the fault core and/or dynamic weakening during seismic slip. In such cases, we speculate that the development of phyllonitic cores could be *indirectly* responsible for reducing fault strength by creating conditions that favour the operation of dynamic weakening mechanisms. It is almost certain that hydrothermal fluids will be present within phyllonitic fault cores under mid-crustal conditions. Rapid heating during seismic slip along narrow, foliation-parallel detachment surfaces that are enveloped by low permeability phyllonites may therefore permit dynamic weakening by thermal pressurization (cf. Wibberley & Shimamoto 2005).

Conclusions

1. The initial debate concerned with the weakening of faults in an absolute sense began by focusing on plate boundary structures such as the San Andreas Fault. As the study of fault weakening processes has developed, however, it has become increasingly evident that there is compelling geological and geophysical evidence to suggest that weakening processes are likely to be a general feature of large-displacement faults. The development and long-term persistence of weak intraplate fa ults will probably be a contributory factor that leads to the non-rigid behaviour of many regions of continental lithosphere (e.g., Storti *et al.* 2003).
2. Geological studies of exhumed large-displacement faults suggest that faults exhumed from <5 km depth are characterized by a narrow ultracataclasite core surrounded by a variably fractured damage zone, or by anastomosing gouge-rich strands that enclose blocks of variably fractured country rocks. The former structures are inferred to have velocity-weakening behaviour and to have slipped seismically; the latter are inferred to have velocity-strengthening behaviour and to have deformed by creep punctuated by moderate seismic events. There is little geological evidence to suggest that the presence of low-friction clay gouges causes weakening. The presence of veins attests to the local development of elevated pore pressures in fault cores, but it is unclear from the geological evidence whether this is sufficient to bring about long-term fault weakening.

3. Large-displacement faults exhumed from >5 km depth are characterized by foliated cores comprising phyllonite and/or foliated cataclasite that overprint earlier random fabric cataclasites and brittle fractures. The development of foliated cores is attributed to influx of chemically active fluids into a precursor brittle fault zone. Comparison with microphysical models for quartz-mica phyllonites based on high-strain laboratory experiments suggests that phyllonitic fault cores deform by frictional–viscous flow that is sensitive to the strain rate/temperature in addition to normal stress. These models predict significant (30–70%) weakening of faults that deform by frictional–viscous flow compared with conventional crustal strength profiles based on Byerlee friction and the creep strength of wet quartz.
4. The metamorphic conditions required for phyllonite development are likely to be met within the deeper parts of many (most?) faults that cut continental basement rocks. Comparison with seismological, geodetic and palaeoseismological observations suggest that large-displacement faults with phyllonitic cores may be capable of generating earthquakes. In some cases, there may be periods of time (perhaps 10^3–10^6 years) during which faults with phyllonitic cores slip seismically producing large (at least $M \approx 7$) earthquakes and show a high degree of seismic coupling.
5. Future geological studies should establish the existence and nature of slip surfaces within faults with phyllonitic cores. Key objectives will be to quantify the strain partitioning between macroscopically ductile frictional–viscous flow and seismic slip and to discriminate long-lived slip surfaces from structures that formed during short-lived (single slip?) transient embrittlement events. In addition, new geological studies are needed to test the proposed mechanisms by which seismic slip occurs within phyllonitic fault cores.

We are grateful to D. G. Pearson, T. B. Anderson and R. R. Jones for discussion and to M. Handy and G. Hirth for constructive reviews. C. A. J. Wibberley provided forthright editorial guidance that significantly improved the focus of the manuscript. We thank G. E. Lloyd and E. Condliffe for their expert guidance in using the scanning electron microscope at Leeds University. We also wish to thank Statoil (UK) Ltd for their continuing support of the Reactivation Research Group, including sponsorship of J.I.'s lectureship. S.A.F.S. is supported by a Durham University Doctoral Fellowship, whilst S.P.J. was supported by an NERC Studentship (NER/S/A/2001/06126).

References

ANDERSON, E. M. 1942. *The Dynamics of Faulting and Dyke Formation with Application to Britain*. Oliver & Boyd, Edinburgh.

AXEN, G. J. 1999. Low-angle normal fault earthquakes and triggering. *Geophysical Research Letters*, **26**, 3693–3696.

AXEN, G. J. 2004. Mechanics of low-angle normal faults. *In*: KARNER, G. D., TAYLOR, B., DRISCOLL, N. W. & KOHLSTEDT, D. L. (eds) *Rheology and Deformation of the Lithosphere at Continental Margins*. Columbia University Press, New York, 46–91.

BLANPIED, M. L., MARONE, C. J., LOCKNER, D. A., BYERLEE, J. D. & KING, D. P. 1998. Quantitative measure of the variation in fault rheology due to fluid-rock interactions. *Journal of Geophysical Research*, **103**, 9691–9712.

BOS, B. & SPIERS, C. J. 2000. Effect of phyllosilicates on fluid-assisted healing of gouge-bearing faults. *Earth and Planetary Science Letters*, **184**, 199–210.

BOS, B. & SPIERS, C. J. 2001. Experimental investigation into the microstructural and mechanical evolution of phyllosilicate-bearing fault rock under conditions favouring pressure solution. *Journal of Structural Geology*, **23**, 1187–1202.

BOS, B. & SPIERS, C. J. 2002. Frictional-viscous flow of phyllosilicate-bearing fault rock: microphysical models and implications for crustal strength profiles. *Journal of Geophysical Research*, **107**, doi:10.1029/2001JB000301.

BOS, B., PEACH, C. J. & SPIERS, C. J. 2000*a*. Slip behavior of simulated gouge-bearing faults under conditions favoring pressure solution. *Journal of Geophysical Research*, **105**, 16699–16717.

BOS, B., PEACH, C. J. & SPIERS, C. J. 2000*b*. Frictional–viscous flow of simulated fault gouge caused by the combined effects of phyllosilicates and pressure solution. *Tectonophysics*, **327**, 173–194.

BRAATHEN, A. & OSMUNDSEN, P. T. 2004. Dynamic development of fault rocks in a crustal-scale detachment: An example from western Norway. *Tectonics*, **23**, TC4010, doi:10.1029/2003TC001558.

BRUDY, M., ZOBACK, M. D., FUCHS, K., RUMMEL, F. & BAUMGARTNER, J. 1997. Estimation of the complete stress tensor to 8 km depth in the KTB scientific drill holes: implications for crustal strength. *Journal of Geophysical Research*, **102**, 18453–18475.

BRUHN, D. F., OLGAARD, D. L. & DELL'ANGELO, L. N. 1999. Evidence for enhanced deformation in two-phase rocks: Experiments on the rheology of calcite–anhydrite aggregates. *Journal of Geophysical Research*, **104**, 707–724.

BRUNE, J., HENYEY, T. & ROY, R. 1969. Heat flow, stress, and rate of slip along the San Andreas Fault, California. *Journal of Geophysical Research*, **74**, 3821–3827.

BUTLER, C. A., HOLDSWORTH, R. E. & STRACHAN, R. A. 1995. Evidence for Caledonian sinistral strike–slip motion and associated fault zone weakening, Outer Hebrides Fault Zone, Scotland. *Journal of the Geological Society, London*, **152**, 743–746.

BYERLEE, J. D. 1978. Friction of rocks. *Pure and Applied Geophysics*, **116**, 615–626.

BYERLEE, J. D. 1990. Friction, overpressure, and fault normal compression. *Geophysical Research Letters*, **17**, 2109–2112.

CHANG, W.-L., SMITH, R. B., MEERTENS, C. M. & HARRIS, R. A. 2006. Contemporary deformation of the Wasatch Fault, Utah, from GPS measurements with implications for interseismic fault behavior and earthquake hazard: observations and kinematic analysis. *Journal of Geophysical Research*, **111**, B11405, doi:10.1029/2006JB004326.

CHESTER, F. M. 1995. A rheologic model for wet crust applied to strike–slip faults. *Journal of Geophysical Research*, **100**, 13033–13044.

CHESTER, F. M. & CHESTER, J. S. 1998. Ultracataclasite structure and friction processes of the Punchbowl fault, San Andreas system, California. *Tectonophysics*, **295**, 199–221.

CHESTER, F. M. & HIGGS, N. G. 1992. Multimechanism friction constitutive model for ultrafine quartz gouge at hypocentral conditions. *Journal of Geophysical Research*, **97**, 1859–1870.

CHESTER, F. M. & LOGAN, J. M. 1986. Implications for mechanical properties of brittle faults from observations of the Punchbowl Fault, California. *Pure and Applied Geophysics*, **124**, 79–106.

CHESTER, F. M., FRIEDMAN, M. & LOGAN, J. M. 1985. Foliated cataclasites. *Tectonophysics*, **111**, 139–146.

CHESTER, F. M., EVANS, J. P. & BIEGEL, R. L. 1993. Internal structure and weakening mechanisms of the San Andreas Fault. *Journal of Geophysical Research*, **98**, 771–786.

CHESTER, F. M., CHESTER, J. S., KIRSCHNER, D. L., SCHULZ, S. E. & EVANS, J. P. 2004. Structure of large-displacement, strike-slip fault zones in the brittle continental crust. *In*: KARNER, G. D., TAYLOR, B., DRISCOLL, N. W. & KOHLSTEDT, D. L. (eds) *Rheology and Deformation of the Lithosphere at Continental Margins*. Columbia University Press, New York, 223–260.

COLLETTINI, C. 2002. Hypothesis for the mechanics and seismic behaviour of low-angle normal faults: the example of the Altotiberina fault Northern Apennines. *Annals of Geophysics*, **45**, 683–698.

COLLETTINI, C. & BARCHI, M. R. 2004. A comparison of structural data and seismic images for low-angle normal faults in the Northern Apennines (Central Italy): constraints on activity. *In*: ALSOP, G. I., HOLDSWORTH, R. E., MCCAFFREY, K. J. W. & HAND, M. (eds) *Flow Processes in Faults and Shear Zones*. Geological Society, London, Special Publications, **224**, 95–112.

COLLETTINI, C. & HOLDSWORTH, R. E. 2004. Fault zone weakening and character of slip along low-angle normal faults: insights from the Zuccale fault, Elba, Italy. *Journal of the Geological Society, London*, **161**, 1039–1051.

COLLETTINI, C. & SIBSON, R. H. 2001. Normal fault, normal friction? *Geology*, **29**, 927–930.

COLLETTINI, C., DE PAOLA, N. & GOULTY, N. R. 2006*a*. Switches in the minimum compressive stress direction induced by overpressure beneath a low-permeability fault zone. *Terra Nova*, **18**, 224–231.

COLLETTINI, C., DE PAOLA, N., HOLDSWORTH, R. E. & BARCHI, M. R. 2006*b*. The development and behaviour of low-angle normal faults during Cenozoic asymmetric extension in the Northern Apennines, Italy. *Journal of Structural Geology*, **28**, 333–352.

COWAN, D. S. 1999. Do faults preserve a record of seismic slip? A field geologist's opinion. *Journal of Structural Geology*, **21**, 995–1001.

COWIE, P. A. 1998. A healing-reloading feedback control on the growth rate of seismogenic faults. *Journal of Structural Geology*, **20**, 1075–1087.

DALTON, R. 1999. Go-ahead for San Andreas drilling project. *Nature*, **401**, 5.

DI TORO, G. & PENNACCHIONI, G. 2005. Fault plane processes and mesoscopic structure of a strong-type seismogenic fault in tonalites (Adamello batholith, Southern Alps). *Tectonophysics*, **402**, 55–80.

DI TORO, G., HIROSE, T., NIELSEN, S., PENNACCHIONI, G. & SHIMAMOTO, T. 2006. Natural and experimental evidence of melt lubrication of faults during earthquakes. *Science*, **311**, 647–649.

DOSER, D. I. & SMITH, R. B. 1989. An assessment of source parameters of earthquakes in the cordillera of the western United States. *Bulletin of the Seismological Society of America*, **79**, 1383–1409.

EVANS, J. P. & CHESTER, F. M. 1995. Fluid–rock interaction in faults of the San Andreas system: inferences from San Gabriel fault rock geochemistry and microstructures. *Journal of Geophysical Research*, **100**, 13007–13020.

FAULKNER, D. R. & RUTTER, E. H. 2001. Can the maintenance of overpressured fluids in large strike–slip fault zones explain their apparent weakness? *Geology*, **29**, 503–506.

FAULKNER, D. R., LEWIS, A. C. & RUTTER, E. H. 2003. On the internal structure and mechanics of large strike–slip fault zones: field observations of the Carboneras fault in southeastern Spain. *Tectonophysics*, **367**, 235–251.

FAULKNER, D. R., MITCHELL, T. M., HEALY, D. & HEAP, M. J. 2006. Slip on 'weak' faults by the rotation of regional stress in the fracture damage zone. *Nature*, **444**, 922–925.

FUSSEIS, F., HANDY, M. R. & SCHRANK, C. 2006. Networking of shear zones at the brittle-to-viscous transition (Cap de Creus, NE Spain). *Journal of Structural Geology*, **28**, 1228–1243.

GUERMANI, A. & PENNACCHIONI, G. 1998. Brittle precursors of plastic deformation in a granite: an example from the Mont Blanc massif (Helvetic, western Alps). *Journal of Structural Geology*, **20**, 135–148.

HAN, R., SHIMAMOTO, T., HIROSE, T., REE, J. & ANDO, J. 2006. Physico-chemical changes and dramatic fault weakening induced by thermal decomposition in carbonate fault zones: results from friction tests at seismic slip rates. *Eos Transactions, American Geophysical Union*, **87**, Fall Meeting Supplement, Abstract S33A-0224.

HAN, R., SHIMAMOTO, T., HIROSE, T., REE, J.-H. & ANDO, J.-I. 2007. Ultralow friction of carbonate faults caused by thermal decomposition. *Science*, **316**, 878–881.

HANDY, M. R. 1994. Flow laws for rocks containing two non-linear viscous phases: a phenomenological approach. *Journal of Structural Geology*, **16**, 287–301.

HARDEBECK, J. L. & HAUKSSON, E. 1999. Role of fluids in faulting inferred from stress field signatures. *Science*, **285**, 236–239.

HICKMAN, S. & ZOBACK, M. 2004. Stress orientations and magnitudes in the SAFOD pilot hole. *Geophysical Research Letters*, **31**, L15S12, doi:10.1029/2004GL020043.

HICKMAN, S., ZOBACK, M. & ELLSWORTH, W. 2004. Introduction to special section: Preparing for the San Andreas Fault Observatory at Depth. *Geophysical Research Letters*, **31**, L12S01, doi:10.1029/2004GL020688.

HOLDSWORTH, R. E. 2004. Weak faults – rotten cores. *Science*, **303**, 181–182.

HOLDSWORTH, R. E., STEWART, M., IMBER, J. & STRACHAN, R. A. 2001. The structure and rheological evolution of reactivated continental fault zones: a review and case study. *In*: MILLER, J. A., HOLDSWORTH, R. E., BUICK, I. S. & HAND, M. (eds) *Continental Reactivation and Reworking*. Geological Society, London, Special Publications, **184**, 115–137.

ICHIKAWA, K. 1980. *Geohistory of the Median Tectonic Line of Southwest Japan*. Memoirs of the Geological Survey of Japan, **18**, 187–212.

IMBER, J. 1998. *Deformation and fluid–rock interaction along the reactivated Outer Hebrides Fault Zone, Scotland*. PhD thesis, University of Durham.

IMBER, J., HOLDSWORTH, R. E., BUTLER, C. A. & LLOYD, G. E. 1997. Fault-zone weakening processes along the reactived Outer Hebrides Fault Zone, Scotland. *Journal of the Geological Society, London*, **154**, 105–109.

IMBER, J., HOLDSWORTH, R. E., BUTLER, C. A. & STRACHAN, R. A. 2001. A reappraisal of the Sibson–Scholz fault zone model: the nature of the frictional–viscous ('brittle–ductile') transition along a long-lived, crustal-scale fault, Outer Hebrides, Scotland. *Tectonics*, **20**, 601–624.

JACKSON, J. 1999. Fault death: a perspective from actively deforming regions. *Journal of Structural Geology*, **21**, 1003–1010.

JACKSON, J. A. & WHITE, N. J. 1989. Normal faulting in the upper continental crust: observations from regions of active extension. *Journal of Structural Geology*, **11**, 15–36.

JANECKE, S. U. & EVANS, J. P. 1988. Feldpsar-influenced rock rheologies. *Geology*, **16**, 1064–1067.

JEFFERIES, S. P., HOLDSWORTH, R. E., WIBBERLEY, C. A. J., SHIMAMOTO, T., SPIERS, C. J., NIEMEIJER, A. R. & LLOYD, G. E. 2006*a*. The nature and importance of phyllonite development in crustal-scale fault cores: an example from the Median Tectonic Line, Japan. *Journal of Structural Geology*, **28**, 220–235.

JEFFERIES, S. P., HOLDSWORTH, R. E., SHIMAMOTO, T., TAKAGI, H. & LLOYD, G. E. 2006*b*. The formation and significance of foliated cataclasite and gouge in the cores of crustal-scale faults: examples from the Median Tectonic Line, Japan. *Journal of Geophysical Research*, **111**, B12303, doi:10.1029/2005JB004205.

LACHENBRUCH, A. H. & SASS, J. H. 1980. Heat flow and energetics of the San Andreas Fault Zone. *Journal of Geophysical Research*, **85**, 6185–6222.

LACHENBRUCH, A. H. & SASS, J. H. 1992. Heat flow from Cajon Pass, fault strength, and tectonic implications. *Journal of Geophysical Research*, **97**, 4995–5015.

MANATSCHAL, G. 1999. Fluid- and reaction-assisted low-angle normal faulting: evidence from rift-related brittle fault rocks in the Alps (Err Nappe, eastern Switzerland). *Journal of Structural Geology*, **21**, 777–793.

MARONE, C. 1998. Laboratory-derived friction laws and their application to seismic faulting. *Annual Review of Earth and Planetary Sciences*, **26**, 643–696.

MASSON, R., CHÉRY, J., HATZFELD, D., MARTINOD, J., VERNANT, P., TAVAKOLI, F. & GHAFORY-ASHTIANI, M. 2005. Seismic versus aseismic deformation in Iran inferred from earthquakes and geodetic data. *Geophysical Journal International*, **160**, 217–226.

MELOSH, H. J. 1996. Dynamical weakening of faults by acoustic fluidization. *Nature*, **379**, 601–606.

MOLNAR, P. 1992. Brace–Goetze strength profiles, the partitioning of strike–slip and thrust faulting at zones of oblique convergence, and the stress-heat flow paradox of the San Andreas Fault. *In*: EVANS, B. & WONG, T.-F. (eds) *Fault Mechanics and Transport Properties of Rocks*. Academic Press, London, 435–459.

MOORE, D. E. & RYMER, M. J. 2007. Talc-bearing serpentinite and the creeping section of the San Andreas Fault. *Nature*, **448**, 795–797.

MORA, P. & PLACE, D. 1998. Numerical simulation of earthquake faults with gouge: toward a comprehensive explanation for the heat flow paradox. *Journal of Geophysical Research*, **103**, 21067–21089.

MORROW, C., RADLEY, B. & BYERLEE, J. D. 1992. Frictional strength and the effective pressure law for montmorillonite and illite clays. *In*: EVANS, B. & WONG, T.-F. (eds) *Fault Mechanics and Transport Properties of Rocks*. Academic Press, London, 69–88.

MORROW, C. A., MOORE, D. E. & LOCKNER, D. A. 2000. The effect of mineral bond strength and adsorbed water on fault gouge frictional strength. *Geophysical Research Letters*, **27**, 815–818.

MORROW, C., SOLUM, J., TEMBE, S., LOCKNER, D. & WONG, T.-F. 2007. Using drill cutting separates to estimate the strength of narrow shear zones at SAFOD. *Geophysical Research Letters*, **34**, L11301, doi:10/1029/2007GL029665.

MOUNT, V. S. & SUPPE, J. 1987. State of stress near the San Andreas fault: implications for wrench tectonics. *Geology*, **15**, 1143–1146.

NIEMEIJER, A. R. & SPIERS, C. J. 2005. Influence of phyllosilicates on fault strength in the brittle-ductile transition: insights from rock analogue experiments. *In*: BRUHN, D. & BURLINI, L. (eds) *High Strain Zones: Structure and Physical Properties*. Geological Society, London, Special Publications, **245**, 303–327.

NIEMEIJER, A. R. & SPIERS, C. J. 2006. Velocity dependence of strength and healing behaviour in simulated phyllosilicate-bearing fault gouge. *Tectonophysics*, **427**, 231–253.

O'HARA, K. 2007. Reaction weakening and emplacement of crystalline thrusts: Diffusion control on reaction rate and strain rate. *Journal of Structural Geology*, **29**, 1301–1314.

OHTANI, T., FUJIMOTO, K., ITO, H., TANAKA, H., TOMIDA, N. & HIGUCHI, T. 2000. Fault rocks and past to recent fluid characteristics from the borehole survey of the Nojima fault ruptured in the 1995 Kobe earthquake, southwest Japan. *Journal of Geophysical Research*, **105**, 16161–16171.

OTSUKI, K., MONZAWA, N. & NAGASE, T. 2003. Fluidization and melting of fault gouge during seismic slip: identification in the Nojima fault zone and implications for focal earthquake mechanisms. *Journal of Geophysical Research*, **108**, doi:10.1029/2001JB001711.

PARRY, W. T. & BRUHN, R. L. 1986. Pore fluid and seismogenic characteristics of fault rock at depth on the Wasatch fault, Utah. *Journal of Geophysical Research*, **91**, 730–744.

PARRY, W. T. & BRUHM, R. L. 1987. Fluid inclusion evidence for minimum 11 km vertical offset on the Wasatch fault, Utah. *Geology*, **15**, 67–70.

PARRY, W. T., WILSON, P. N. & BRUHN, R. L. 1988. Pore-fluid chemistry and chemical reactions on the Wasatch normal fault, Utah. *Geochimica et Cosmochimica Acta*, **52**, 2053–2063.

RICE, J. R. 1992. Fault stress states, pore pressure distributions, and the weakness of the San Andreas Fault. *In*: EVANS, B. & WONG, T.-F. (eds) *Fault Mechanics and Transport Properties of Rocks*. Academic Press, London, 475–503.

ROBIN, P.-Y. 1979. Theory of metamorphic segregation and related processes. *Geochimica & Cosmochimica Acta*, **43**, 1587–1600.

RUTTER, E. H., HOLDSWORTH, R. E. & KNIPE, R. J. 2001.The nature and tectonic significance of fault-zone weakening: an introduction. *In*: HOLDSWORTH, R. E., STRACHAN, R. A., MAGLOUGHLIN, J. F. & KNIPE, R. J. (eds) *The Nature and Tectonic Significance of Fault Zone Weakening*. Geological Society, London, Special Publications, **186**, 1–11.

SAFFER, D. M., FRYE, K. M., MARONE, C. & MAIR, K. 2001. Laboratory results indicating complex and potentially unstable frictional behaviour of smectite clay. *Geophysical Research Letters*, **28**, 2297–2300.

SCHLEICHER, A. M., VAN DER PLUIJM, B. A., SOLUM, J. G. & WARR, L. N. 2006. Origin and significance of clay-coated fractures in mudrock fragments of the SAFOD borehole (Parkfield, California). *Geophysical Research Letters*, **33**, L16313, doi:10.1029/2006GL026505.

SCHOLZ, C. H. 1988. The brittle–plastic transition and the depth of seismic faulting. *Geologische Rundschau*, **77**, 319–328.

SCHOLZ, C. H. 1990. *The Mechanics of Earthquakes and Faulting*. Cambridge University Press, Cambridge.

SCHOLZ, C. H. 1998. Earthquakes and friction laws. *Nature*, **391**, 37–42.

SCHOLZ, C. H. 2000. Evidence for a strong San Andreas fault. *Geology*, **28**, 163–166.

SCHOLZ, C. H. & HANKS, T. C. 2004. The strength of the San Andreas Fault: a discussion. *In*: KARNER, G. D., TAYLOR, B., DRISCOLL, N. W. & KOHLSTEDT, D. L. (eds) *Rheology and Deformation of the Lithosphere at Continental Margins*. Columbia University Press, New York, 261–283.

SCHOLZ, C. H., BEAVAN, J. & HANKS, T. C. 1979. Frictional metamorphism, argon depletion, and tectonic stress on the Alpine Fault, New Zealand. *Journal of Geophysical Research*, **84**, 6770–6782.

SCHWARTZ, D. L. & COPPERSMITH, K. J. 1984. Fault behaviour and characteristic earthquakes: examples from the Wasatch and San Andreas fault zones. *Journal of Geophysical Research*, **89**, 5681–5698.

SIBSON, R. H. 1980. Power dissipation and stress levels on faults in the upper crust. *Journal of Geophysical Research*, **85**, 6239–6247.

SIBSON, R. H. 1983. Continental fault structure and the shallow earthquake source. *Journal of the Geological Society, London*, **140**, 741–767.

SOLUM, J. G. & VAN DER PLUIJM, B. A. 2004. Phyllosilicate mineral assemblages of the SAFOD Pilot Hole and comparison with an exhumed segment of the San Andreas Fault System. *Geophysical Research Letters*, **31**, L15S19, doi:10.1029/2004GL019909.

SOLUM, J. G., HICKMAN, S. H., LOCKNER, D. A., MOORE, D. E., VAN DER PLUIJM, B. A., SCHLEICHER, A. M. & EVANS, J. P. 2006. Mineralogical characterization of protolith and fault rocks from the SAFOD Main Hole. *Geophysical Research Letters*, **33**, L21314, doi:10.1029/2006GL027285.

STEWART, M., STRACHAN, R. A. & HOLDSWORTH, R. E. 1999. The structure and early kinematic history of the Great Glen Fault Zone, Scotland. *Tectonics*, **18**, 326–342.

STEWART, M., HOLDSWORTH, R. E. & STRACHAN, R. A. 2000. Deformation processes and weakening mechanisms within the frictional–viscous transition zone of major crustal-scale faults: insights form the Great Glen Fault Zone, Scotland. *Journal of Structural Geology*, **22**, 543–560.

STORTI, F., HOLDSWORTH, R. E. & SALVINI, F. 2003. Intraplate strike-slip deformation belts *In:* STORTI, F., HOLDSWORTH, R. E. & SALVINI, F. (eds) *Intraplate Strike–Slip Deformation Belts*. Geological Society, London, Special Publications, **210**, 1–14.

SUE, C., DELACOU, B., CHAMPAGNAC, J.-D., ALLANIC, C. & BURKHARD, M. 2007. Aseismic deformation in the Alps: GPS vs. seismic strain quantification. *Terra Nova*, **19**, 182–188.

TAKAGI, H. 1986. Implications of mylonitic microstructures for the geotectonic evolution of the Median Tectonic Line, central Japan. *Journal of Structural Geology*, **8**, 3–14.

TANAKA, H., FUJIMOTO, K., OHTANI, T. & ITO, H. 2001. Structural and chemical characterization of shear zones in the freshly activated Nojima fault, Awaji Island, southwest Japan. *Journal of Geophysical Research*, **106**, 8789–8810.

TOURIGNY, G. & TREMBLAY, A. 1997. Origin and incremental evolution of brittle/ductile shear zones in granitic rocks: natural examples from the southern Abitibi Belt, Canada. *Journal of Structural Geology*, **19**, 15–27.

TOWNEND, J. & ZOBACK, M. D. 2000. How faulting keeps the crust strong. *Geology*, **28**, 399–402.

WALSH, J. J., CHILDS, C. *ET AL.* 2001. Geometric controls on the evolution of normal fault systems. *In*: HOLDSWORTH, R. E., STRACHAN, R. A., MAGLOUGHLIN, J. F. & KNIPE, R. J. (eds) *The Nature and Tectonic Significance of Fault Zone Weakening*. Geological Society, London, Special Publications, **186**, 157–170.

WANG, C.-Y. 1984. On the constitution of the San Andreas fault zone in Central California. *Journal of Geophysical Research*, **89**, 5858–5866.

WHEELER, J. 1992. Importance of pressure solution and Coble creep in the deformation of polymineralic rocks. *Journal of Geophysical Research*, **97**, 4579–4586.

WHITE, S. R. 2001. Textural and microstructural evidence for semi-brittle flow in natural fault rocks with varied mica contents. *International Journal of Earth Sciences*, **90**, 14–27.

WIBBERLEY, C. A. J. 2005. Initiation of basement thrust detachments by fault-zone reaction weakening. *In*: BRUHN, D. & BURLINI, L. (eds) *High Strain Zones: Structure and Physical Properties*. Geological Society, London, Special Publications, **245**, 347–372.

WIBBERLEY, C. 2007. Talc at fault. *Nature*, **448**, 756–757.

WIBBERLEY, C. A. J. & SHIMAMOTO, T. 2003. Internal structure and permeability of major-slip fault zones: the Median Tectonic Line in Mie Prefecture, Southwest Japan. *Journal of Structural Geology*, **25**, 59–78.

WIBBERLEY, C. A. J. & SHIMAMOTO, T. 2005. Earthquake slip weakening and asperities explained by thermal pressurization. *Nature*, **436**, 689–692.

WILLIAMS, C. F., GRUBB, F. V. & GALANIS, S. P. JR. 2004. Heat flow in the SAFOD pilot hole and implications for the strength of the San Andreas Fault. *Geophysical Research Letters*, **31**, L15S14, doi:10.1029/2003GL019352.

WILSON, J. E., CHESTER, J. S. & CHESTER, F. M. 2003. Microfracture analysis of fault growth and wear processes, Punchbowl Fault, San Andreas system, California. *Journal of Structural Geology*, **25**, 1855–1873.

WINTSCH, R. P., CHRISTOFFERSON, R. & KRONENBERG, A. K. 1995. Fluid–rock reaction weakening of fault zones. *Journal of Geophysical Research*, **100**, 13021–13032.

ZOBACK, M. D. 2000. Strength of the San Andreas. *Nature*, **405**, 31–32.

ZOBACK, M. D., ZOBACK, M. L. *ET AL*. 1987. New evidence on the state of stress of the San-Andreas Fault System. *Science*, **238**, 1105–1111.

ZOBACK, M., HICKMAN, S. & ELLSWORTH, W. 2006. Structure and properties of the San Andreas fault in central California: Preliminary results from the SAFOD experiment. *Geophysical Research Abstracts*, **8**, 02474.

ZOBACK, M. L. 1983. Structure and Cenozoic tectonism along the Wasatch fault zone, Utah. *In*: MILLER, D. M., TODD, V. R. & HOWARD, K. A. (eds) *Tectonics and Stratigraphy of the Eastern Great Basin*. Geological Society of America Memoirs, **157**, 3–27.

Fault weakening due to CO_2 degassing in the Northern Apennines: short- and long-term processes

C. COLLETTINI[1], C. CARDELLINI[1], G. CHIODINI[2], N. DE PAOLA[1], R. E. HOLDSWORTH[3] & S. A. F. SMITH[3]

[1]*Dipartimento di Scienze della Terra, Università di Perugia, Piazza dell'Università 1, 06100 Perugia, Italy (e-mail: colle@unipg.it)*

[2]*Osservatorio Vesuviano, Istituto Nazionale di Geofisica e Vulcanologia, Napoli, Italy*

[3]*Reactivation Research Group, Department of Earth Sciences, University of Durham, Durham DH1 3LE, UK*

Abstract: The influx of fluids into fault zones can trigger two main types of weakening process that operate over different timescales and facilitate fault movement and earthquake nucleation. Short- and long-term weakening mechanisms along faults require a continuous fluid supply near the base of the brittle crust, a condition satisfied in the extended/extending area of the Northern Apennines of Italy. Here carbon mass balance calculations, coupling aquifer geochemistry to isotopic and hydrological data, define the presence of a large flux (*c*. 12 160 t/day) of deep-seated CO_2 centred in the extended sector of the area. In the currently active extending area, CO_2 fluid overpressures at $\sim$85% of the lithostatic load have been documented in two deep (4–5 km) boreholes. In the long-term, field studies on an exhumed regional low-angle normal fault show that, during the entire fault history, fluids reacted with fine-grained cataclasites in the fault core to produce aggregates of weak, phyllosilicate-rich fault rocks that deform by fluid assisted frictional–viscous creep at sub-Byerlee friction values ($\mu < 0.3$). In the short term, fluids can be stored in structural traps, such as beneath mature faults, and stratigraphical traps such as Triassic evaporites. Both examples preserve evidence for multiple episodes of hydrofracturing induced by short-term cycles of fluid pressure build-up and release. Geochemical data on the regional-scale CO_2 degassing process can therefore be related to field observations on fluid rock interactions to provide new insights into the deformation processes responsible for active seismicity in the Northern Apennines.

The involvement of fluids in faulting has been recognized for over 250 years, particularly in the mining industry (e.g., Von Oppel 1749). Direct evidence of large fluxes of fluids into fault zones comes from oil exploration and from widespread recognition of fault-hosted vein complexes and hydrothermal alteration (e.g., Hulin 1925; Knopf 1929; Cox *et al.* 1986; Boullier & Robert 1992).

Fluid flow into fault zones can trigger two main types of weakening mechanism that operate over different timescales and facilitate fault movement by reducing the shear stress or frictional resistance to slip. In the short term, i.e., during the seismic cycle, which for large earthquakes means timescales of 100 to 10 000 years, crustal fluids can be trapped by low-permeability mature fault zone seals or stratigraphic barriers. The development of fluid overpressures at the base of the fault zone during the interseismic period can help to facilitate fault slip. Once the seal is ruptured by an earthquake, permeability increases and fluids are redistributed from high to low pressure areas. In this model, a fault is considered to act as a valve (Sibson 1981, 1992). The widespread development of crack-seal textures in mineral veins (Ramsay 1980) seems to be consistent with such behaviour, as they suggest repeated cyclic build-ups in fluid pressure, hydrofracture development and fluid pressure release (Secor 1965; Fyfe *et al.* 1978). Similar trends in fluid pressure have been inferred using fluid inclusion studies in the hydrothermally altered footwall rocks of active normal faults (Parry & Bruhn 1990).

Over longer timescales, i.e. during the entire fault history (thousands to millions of years), fluids can react with fine-grained cataclasites in the fault core to produce interconnected and aligned aggregates of phyllosilicate-rich fault rock (e.g., Evans & Chester 1995; Wintsch *et al.* 1995; Wibberley 1999; Holdsworth 2004; Jefferies *et al.* 2006*a*). The phyllosilicate-rich fault rocks are weak (a) due to reaction softening during low-grade alteration and (b) due to the onset of pressure solution. Laboratory experiments, underpinned by theoretical and field observations, have shown that pressure solution-facilitated creep is important in reducing long-term fault strength and in promoting aseismic slip along faults (Rutter & Mainprice

From: WIBBERLEY, C. A. J., KURZ, W., IMBER, J., HOLDSWORTH, R. E. & COLLETTINI, C. (eds) *The Internal Structure of Fault Zones: Implications for Mechanical and Fluid-Flow Properties*. **299**, 175–194.
DOI: 10.1144/SP299.11 0305-8719/08/$15.00

1979; Bos & Spiers; 2002; Collettini & Holdsworth 2004). The frequently observed localization of later fault displacements along the foliated phyllosilicate-rich layers suggests that these processes lead to important fault weakening (Imber *et al.* 2001; Jefferies *et al.* 2006*b*).

All these weakening mechanisms require a continuous fluid supply near to the base of the brittle crust. In this paper, we present new arguments for regional scale fluid involvement during ongoing extension of the Northern Apennine region in Italy based on the integration of new and recently published data. We then use two field examples to illustrate fluid-assisted weakening processes along exhumed normal faults, e.g., the low-angle Zuccale detachment exposed on the isle of Elba, and within the Triassic evaporites in Tuscany, mainland Italy. Finally, we link these observations made at different scales to assess long-term and short-term weakening processes in the extending area of the Northern Apennines.

Regional setting

The Northern Apennines consist of a NE-verging compressional belt formed as a result of the collision between the European continental margin (Sardinia–Corsica block) and the Adriatic microplate (e.g., Alvarez 1972; Reutter *et al.* 1980). The NE migration of active shortening towards the foreland is followed closely by a phase of asymmetric extension in the hinterland, resulting in two spatially and kinematically distinct structural domains in the present day Apennines (e.g., Pauselli *et al.* 2006).

Extension within the brittle upper crust is accommodated by a set of major east-dipping low-angle normal faults (LANF; Barchi *et al.* 1998; Decandia *et al.* 1998) and associated high angle structures (Fig. 1). Extension, now active in the inner zone of the Umbria–Marche Apennines, generates moderate to large earthquakes, $5.0 < M < 7.0$ (Boschi *et al.* 1998), with a regional extension rate of 2.5 mm a^{-1} measured using geodetic techniques (Hunstad *et al.* 2003). In Tuscany, older parts of the extensional system are significantly exhumed due to the combined effects of extension and associated regional uplift. As a result, it is possible to examine extension-related deformation processes at different crustal depths (Collettini *et al.* 2006*a*). In addition, in Tuscany extension has been active for enough time to change the geological and geophysical character of the area: the Moho is shallow (Ponziani *et al.* 1995; Barchi *et al.* 1998), heat flow is high (Mongelli & Zito 1991) and magmatism is widespread (Serri *et al.* 1993).

The extended/extending sector of the Apennines, including most of central and south Italy, is affected by a widespread and vigorous episode of deep-seated CO_2 degassing (Chiodini *et al.* 2004) that seems to have a close association with the regional patterns of seismicity (Collettini & Barchi 2002; Chiodini *et al.* 2004; Miller *et al.* 2004). A similar region where deep-seated CO_2 has been invoked to explain the swarm-like seismicity has been discovered in NW Bohemia at the German–Czech border (Parotidis *et al.* 2003).

Geochemical evidence of fluid involvement during extension

In this section, the evidence for the occurrence of CO_2 degassing processes in the northern Apennines is discussed. The gas–water–rock interaction processes involving the deeply derived gases and shallow fluids are investigated to explain the surface expressions of degassing, to derive a map of the regional CO_2 flux and to quantify the amounts of CO_2 involved in the process.

Recent regional-scale studies have shown that the western regions of Italy are affected by an intense CO_2 degassing process which results at the surface in numerous cold, CO_2-rich gas emissions (Fig. 2a, e.g., Chiodini *et al.* 2000, 2004; Minissale 2004; Rogie *et al.* 2000). The main component of the gas is CO_2, together with lesser amounts of N_2, H_2S, CH_4, H_2, Ar, He and CO (Table 1). The gas flow rates (Table 1) are very high; for example, the biggest gas emissions release amounts of CO_2 similar to diffuse degassing from active volcanoes worldwide (CO_2 fluxes from 6 to 2800 t/day, mean of 430 t/day, Mörner & Etiope 2002).

Because of the relatively high CO_2 solubility in water, the occurrence of gas emissions at the surface depends in some way on the quantitative ratio of groundwater volumes circulating in the sub-surface relative to the amount of gas arriving from depth. The relationship between the injected and dissolved/degassed gasses has been investigated using a gas–water–rock interaction path model (GWRI) that simulates the chemical and isotopic composition of groundwater affected by the input of a CO_2-rich gas phase. The computational details are discussed in Chiodini *et al.* (2000), Cardellini (2003) and Caliro *et al.* (2005). The results (Fig. 2b) show that for low CO_2 input values almost all the CO_2 is dissolved by the groundwater (i.e., fraction of degassed CO_2, $f_{deg} \approx 0$) because the solution degasses the atmospheric gas components dissolved in the groundwater as these are less soluble than the CO_2. As CO_2 input passes a critical threshold value, f_{deg} increases

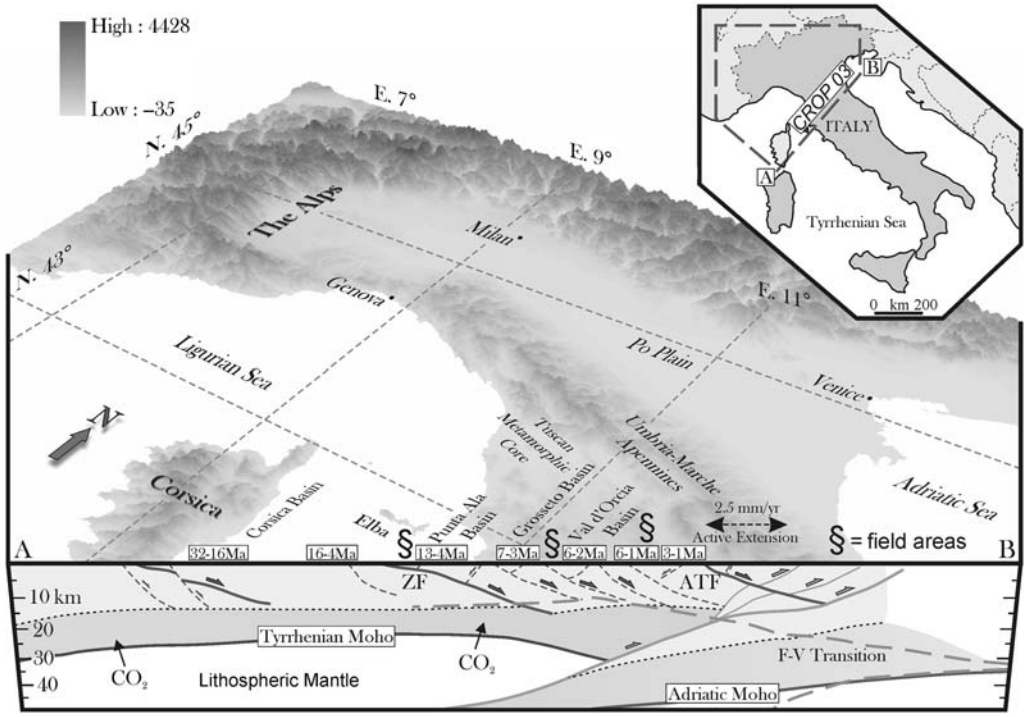

Fig. 1. Block diagram and cross section of the northern Tyrrhenian Sea (Jolivet *et al.* 1998) and the northern Apennines based on the CROP 03 seismic traverse (Pialli *et al.* 1998). Ages of syntectonic basins in white boxes document eastward migration of extension. Suggested location of frictional–viscous transition after Pauselli & Federico (2002). Extension is accommodated by upper-crustal, east-dipping low-angle normal faults and high-angle, west dipping antithetic structures. Extension is active in the Umbria–Marche Apennines. ZF, Zuccale fault; ATF, Altotiberina fault. Ages of extension on Corsica include early core complex formation and late, high-angle faulting (Jolivet *et al.* 1998; Rosenbaum *et al.* 2005).

quickly, indicating that the solution degasses CO_2 as it moves close to saturation point (i.e., $P_{CO_2} \approx 1$ bar). Beyond this point, the curves flatten out at $f_{deg} \approx 1$, since any further input of CO_2 cannot be dissolved and is totally degassed from the groundwater (CO_2 saturation condition).

Because the gas input necessary for the achievement of CO_2 saturation depends also on the amount of water circulating in the aquifers (which is here assumed to be equal to the effective infiltration), the three curves in Figure 2b were derived for the different hydrogeological conditions of the study area: (i) flysch (or Neogene deposits) formations; (ii) volcanic formations; and (iii) carbonate formations, which are assumed to be characterized by mean effective infiltrations of 2, 8 and 20 s^{-1} km^{-2}, respectively (Boni *et al.* 1986; Capelli *et al.* 2005; Di Matteo *et al.* 2006).

The results confirm that gas emissions at the surface are possible (i.e., $f_{deg} > 0.5$) only when the CO_2 influx is higher than ~ 0.5, 2 and 5 $t/day/km^2$ for the flysch, volcanic and carbonate aquifers respectively.

The CO_2 flux threshold value is 10 times higher for the carbonates cropping out in the eastern part of Central Italy, compared with the flysch and volcanic aquifers located in the western sector. Therefore, in the western sector, the rising CO_2 can more easily reach the surface as a free gas phase generating the strong emissions observed at the surface. By contrast, the carbonate aquifers of the eastern sector can dissolve very large amounts of deeply derived CO_2, preventing the formation of gas emissions.

These findings allow a map and an estimation of the deeply derived CO_2 flux to be made for central Italy based on the concentration (C_{ext}) and the isotopic composition ($\delta^{13}C_{ext}$) of the fraction of carbon dissolved in the groundwaters which does not derive from carbonate mineral dissolution (Chiodini *et al.* 2000). Figure 3a shows the C_{ext} and $\delta^{13}C_{ext}$ computed for 88 samples from the larger springs in carbonate regional aquifers of the Apennines and of Tuscany (Chiodini *et al.* 2000; Frondini *et al.* 2007; Fig. 2a). In Figure 3a the samples fall in a hyperbolic domain, highlighted

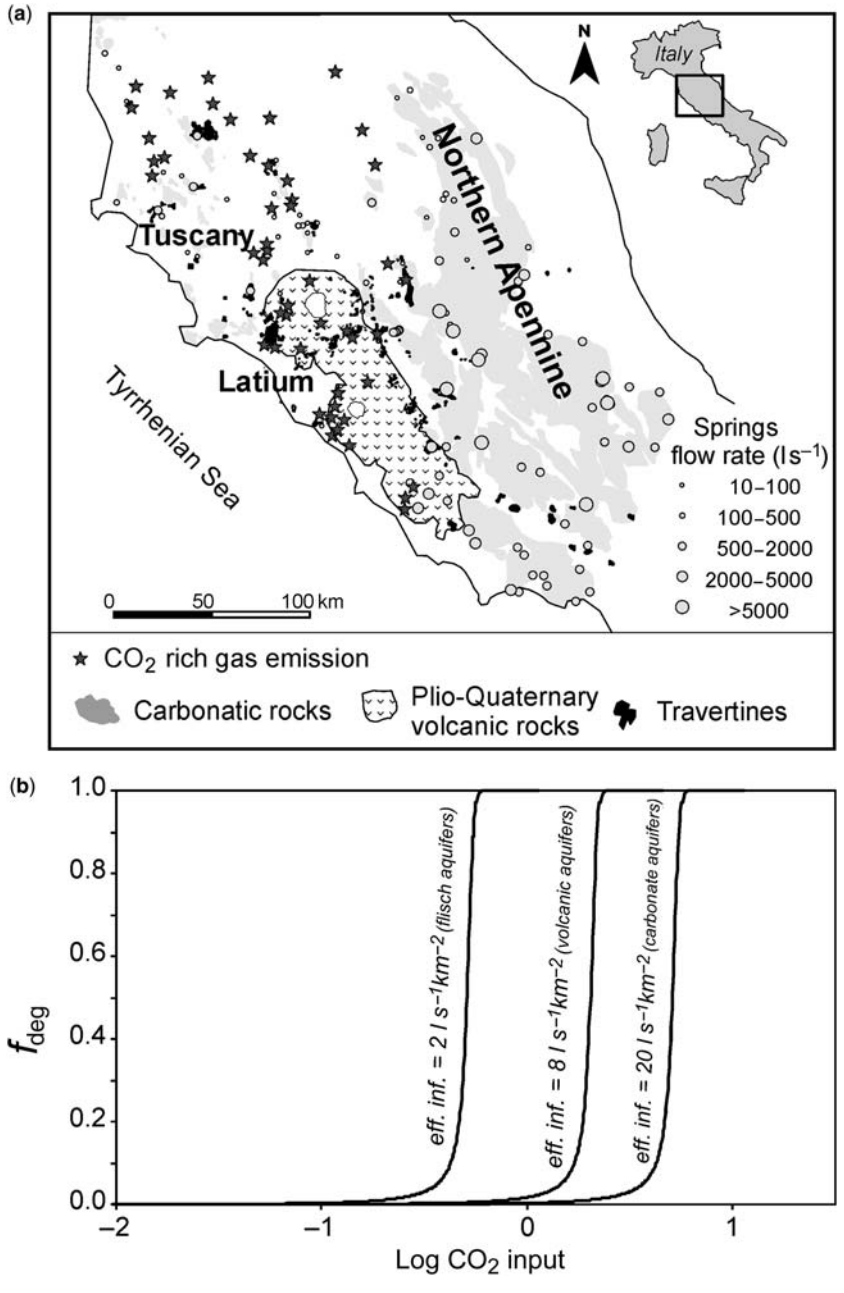

Fig. 2. (**a**) Location map of gas emissions and travertine deposits in central Italy, and of the main springs from carbonate aquifers used to compute the CO_2 flux affecting the region. (**b**) Diagram of the fraction of degassed CO_2 v. the CO_2 input. The ratio between degassed and injected CO_2 (fraction of degassed CO_2, f_{deg}) is compared with the input of CO_2 (CO_2 input, expressed in $t/day/km^2$). The three curves report the theoretical ratios between the input of CO_2 and the degassed CO_2 computed for a variable input of CO_2 in different hydrogeological conditions occurring in central Italy: flysch (and Neogene) formation aquifers, volcanic aquifers and carbonate aquifers.

Table 1. *Chemical and isotopic composition of selected gas emission of central Italy, and measured CO_2 flux*

Sample	Region	CO_2	H_2S	Ar	O_2	N_2	CH_4	H_2	He	CO	$\delta^{13}C$ (‰)	^3He:^4He (R:Ra)	CO_2 flux (t/day)
P.ggio dell'Olivo*	Latium	986 275	1177	10.95	1.99	7658	4853	19.3	3.99	0.083	0.2	0.745	200
Latera Puzzolaie*	Latium	985 938	4748	8.40	0.25	8295	994	9.46	6.12	0.153	1.5	0.442	380
Caldara di Manziana†	Latium	975 441	12 326	2.74	0.35	11 961	225	42.5	0.893	0.253	−2.3	0.081	173
Solfatara di Manziana†	Latium	965 000	9850	138	2280	21 000	12 700	1.00	2.00	0.500	−4.1	n.a.	30
Parco della Mola*	Latium	966 951	1469	12.0	0.53	11 481	20 059	22.5	4.48	0.133	0.1	0.0445	40
Cava dei Selci	Latium	988 000	8950	22.3	4.00	2680	481	0.86	2.27	0.670	0.9	1.54	20
Solforata†	Latium	980 000	10 600	5.4	4.00	9347	109	0.07	9.28	0.530	−3.5	0.95	50
Salcheto‡	Tuscany	970 592	76	7.96	0.69	23 978	5328	6.72	8.75	0.160	−4.8	n.a.	36
Selvena†	Tuscany	885 000	12 500	12.3	0	17 000	80 400	17 000	2.46	9.500	−3.4	0.414	17
Pienza†	Tuscany	942 000	<5	45.0	676	36 700	14 400	2.00	12.0	0	−3.7	0.214	11
Rapolano Cecilia†	Tuscany	963 000	0	7.78	0	32 900	4090	3.37	15.0	0.350	−6.1	0.09	48
Bagni San Filippo*	Tuscany	959 183	1684	7.01	0.38	20 185	18 928	3.24	8.87	0.222	−2.3	n.a.	>160
Umbertide†	Umbria	933 830	664	16.10	1.17	63 080	2352	8.58	47.1	0.164	−3.2	0.035	16
F.sso. Biscina*	Umbria	985 697	46	5.32	24.67	11 528	2675	7.87	14.3	0.571	0.0	n.a.	14
Fersinone*	Umbria	949 313	224	16.15	38.0	49 681	665	4.09	57.4	0.227	n.a.	0.490	n.a.
San Faustino*	Umbria	978 940	523	37.33	154	16 071	4264	0	8.67	1.581	0.6	n.a.	6
Uppiano*	Umbria	837 053	0	212.9	804	115 215	46 331	0	383	0.256	−2.7	n.a.	n.a.

Chemical species are expressed in μmol/mol, ‰ = ‰ v. PDB, $R{:}R_a = (^3He{:}^4He)_{sample}/(^3He{:}^4He)_{air}$.
* Unpublished data from National Research Project: ING-DPC-V5.
† Data from Rogie *et al.* (2000) and references therein.
‡ Data from Frondini *et al.* (2007).

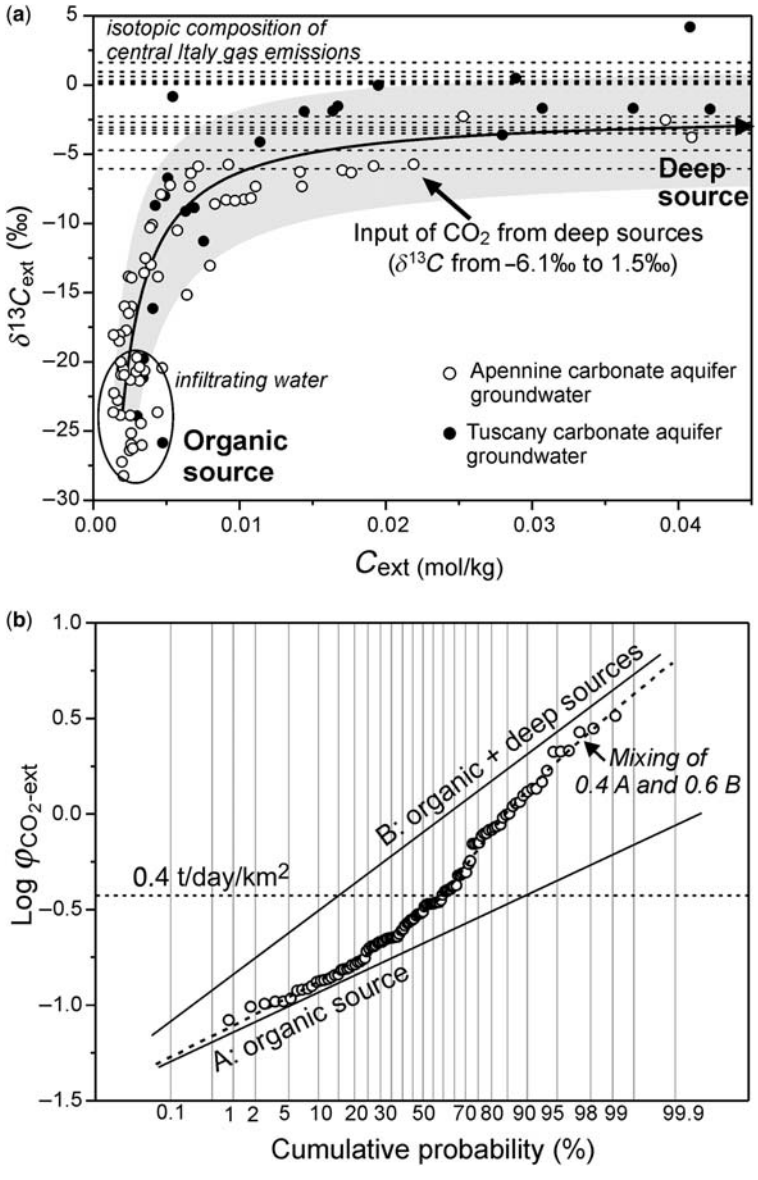

Fig. 3. (**a**) Diagram of $\delta^{13}C_{ext}$‰ v. C_{ext} of groundwater from Apennine and Tuscany carbonate aquifer. The grey area represents the theoretical compositions of infiltrating waters (i.e., where only biological CO_2 is dissolved) to which were added variable amounts of deeply derived CO_2, as computed by GWRI simulations. The isotopic composition of deeply derived CO_2 was considered in the range −6.1‰ to +1.5‰, which corresponds to the isotopic composition of CO_2 released by gas emission in the study area (horizontal, dashed lines). The samples with lower C_{ext} and $\delta^{13}C_{ext}$ (−18‰ to −28‰) are compatible with infiltrating waters, while the samples with a relatively higher C_{ext} and $\delta^{13}C_{ext}$ are compatible with a further input of deeply derived CO_2. (**b**) Logarithmic probability plot of the CO_2 flux ($\varphi_{CO_2\text{-ext}}$) for the groundwater of Apennine and Tuscany carbonate aquifers. The $\varphi_{CO_2\text{-ext}}$ refers to the CO_2 from sources external to the aquifer. The computed values fit a curve with an inflection point. This shape is typical of bimodal distributions caused by the partial overlapping of two log–normal populations. Population A, which comprises 40% of the samples [mean = 0.23 t/day/km^2, computed by Sichel's t-estimator, David (1977) and central 90% confidence interval = 0.21–0.26 t/day/km^2] represents the samples where carbon derives from biological CO_2. Population B (mean = 1.04 t/day/km^2, central 90% confidence interval = 0.86–1.35 t/day/km^2) which includes 60% of the samples, represents the samples where the carbon partially derives from a deep source. The CO_2 flux value of 0.4 t/day/km^2, chosen to discriminate the occurrence of deep CO_2 flux, is highlighted.

by the grey area, that represents the theoretical compositions of infiltrating waters to which are added variable amounts of CO_2 with an isotopic composition in the range typical of the deeply derived CO_2 released in the study area (Table 1).

The flux of CO_2 into the aquifers ($\varphi_{CO_2\text{-ext}}$, $t/day/km^2$) was computed for each spring on the basis of the C_{ext}, of the flow rates of the springs and of the corresponding extension of the hydrogeological basin. The probability distribution of $\varphi_{CO_2\text{-ext}}$ (Fig. 3b) shows the presence of two statistical flux populations that can be partitioned using the method of Sinclair (1974). Population A, with lower values, represents the CO_2 flux connected only to the biogenic CO_2 dissolved by groundwater during surface infiltration. Figure 3b shows that a value of $0.4\ t/day/km^2$ is a reliable upper limit for population A. The highest values of population B represent the addition of deeply derived CO_2.

The calculated values of $\varphi_{CO_2\text{-ext}}$ for each spring were used to draw a map of the CO_2 flux using an algorithm of sequential Gaussian simulation (Deutsch & Journel 1998). The map (Fig. 4a) highlights the presence of a large region where the CO_2 flux is due to deeply derived CO_2 (i.e., CO_2 flux higher than $0.4\ t/day/km^2$) that includes Tuscany, Latium and the western sector of the Umbria–Marche Apennines (Fig. 4a). The presence of this regional degassing structure was previously reported by Chiodini *et al.* (2004) using a probability map. The improved version shown here allows the total flux of external CO_2 affecting the study area to be derived for the entire region (an area of $45\ 512\ km^2$).

The total CO_2 flux results in $22\ 630\ t/day$. This includes both the biogenic and deeply derived CO_2. If we assume a constant flux of biogenic CO_2 over the area, equal to the mean of Population A (Fig. 3b), the total amount of deeply derived CO_2 is estimated to be $12\ 160\ t/day$. Given that the eventual CO_2 degassing from the groundwater is neglected, this value has to be considered a minimum estimation.

Origin and circulation of deep fluids

The origin of the deeply derived CO_2 is still a matter of debate. From petrological and petrographical investigations Gianelli (1985) proposed a metamorphic origin for the CO_2 based on the nature of decarbonation reactions of impure limestones ($T > 200\ ^\circ C$) within the Paleozoic metamorphic basement located at shallow depths (e.g., 4–8 km at Larderello geothermal field). However a shallow crustal metamorphic source for the whole regional CO_2 earth degassing seems to be inconsistent with other evidence. For example, the isotopic compositions of the carbon in the gas emissions (Table 1) and dissolved in the groundwater are not compatible with a CO_2 derivation only from shallow crustal metamorphic reactions involving carbonate formation (e.g., Marini & Chiodini 1994; Chiodini *et al.* 2000). In addition, the CO_2 pressures and temperatures encountered in the geothermal reservoirs of Tuscany and Latium, and in deep wells located in the western sector of the Umbria–Marche Apennines (San Donato and Santo Stefano wells, see location in Fig. 4a), are not compatible with any of the typical thermo-metamorphic reactions involving silicate and carbonate, or with hydrothermal reactions producing CO_2. In general, the CO_2 fugacity (f_{CO_2}) of the deep well fluids is 2–3 orders of magnitude higher than that expected for a hydrothermal–metamorphic derivation within the reservoirs (Fig. 4b). A partial origin for the CO_2 from hydrothermal–metamorphic reactions within the reservoir is thermodynamically possible only in the high temperature geothermal systems like Larderello and Mt Amiata. Therefore, excluding these extreme cases, Figure 4b suggests that the CO_2 is mainly supplied by external and deep sources. In addition, the P_{CO_2} of these systems can be closely correlated with the depth of the reservoirs. Thus the P_{CO_2} values are close to hydrostatic at shallow crustal levels (1–2 km) and approach lithostatic values at greater depths (3–5 km; Fig. 4c). This suggests that the buried reservoirs in central Italy act as traps for CO_2 of external, deep provenance and contain as much gas as possible for their depth (Marini & Chiodini, 1994; Chiodini *et al.* 1995, 1999).

Chiodini *et al.* (2004) have suggested that the CO_2 was derived from mantle rocks overlying the Adriatic subduction zone which were metasomatized by crustal fluids originating from the downgoing slab. This hypothesis is supported by the relatively low $^3He:^4He$ ratios (0.019–1.5 R:Ra) of gas emissions in central Italy (e.g., Table 1), which fall in the same range as the He (0.44–1.73 R:Ra, Martelli *et al.* 2004) recorded from fluid inclusions trapped within olivine and pyroxene phenocrysts associated with mantle-derived basic lavas and pyroclastic rocks from the volcanic districts of central Italy (e.g., Albani and Vulsini in Latium region, Martelli *et al.* 2004).

Geological evidence of fluid involvement during extension

Here we document and analyse field examples of fluid-assisted weakening processes along exposed fault zones in the Apennine region. In particular

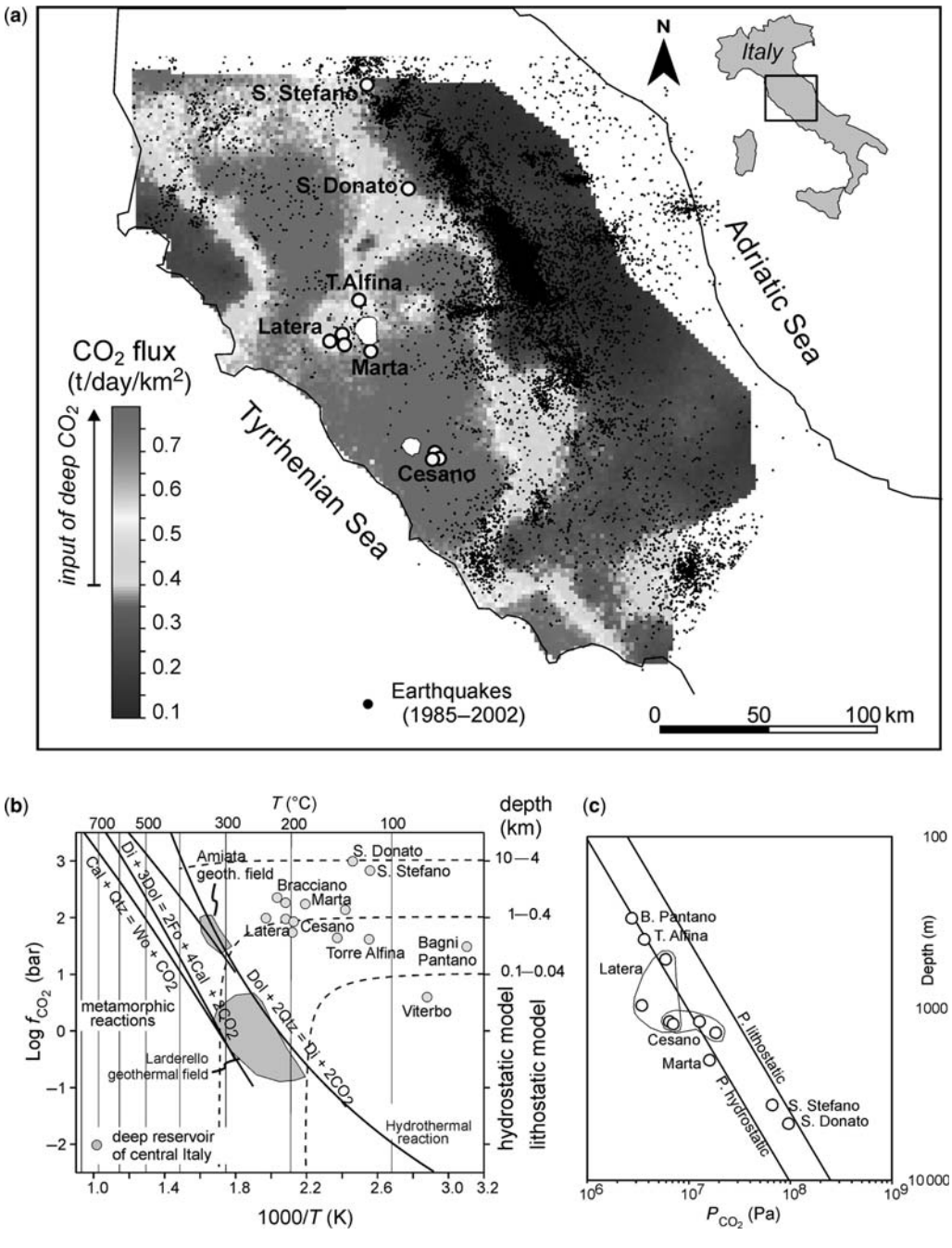

Fig. 4. (**a**) Map of the flux of CO_2. CO_2 fluxes above 0.4 t/day/km^2 are related to the presence of a deep source of CO_2. The map was obtained by a point-wise linear averaging of all 100 realizations of the CO_2 flux distribution performed using an algorithm of sequential Gaussian simulation, in a computational domain of 11 378 squared cells of 4 km^2. The locations of deep wells are also shown. (**b**) Plot of CO_2 fugacity (f_{CO_2}; at pressure and temperature of interest f_{CO_2} can be considered equal to the CO_2 pressure, P_{CO_2}) and temperature measured in geothermal wells of Tuscany and Latium reservoirs and in deep wells located in the Apennines (San Donato and Santo Stefano wells). Values of f_{CO_2} and temperature fixed by relevant metamorphic reactions and by the full equilibrium function of Giggenbach (1988) are also shown. (**c**) Depth v. CO_2 pressure (f_{CO_2}) measured in the same wells.

we focus on the Zuccale LANF cropping out on the isle of Elba and on evaporite-bearing outcrops located in the footwalls of major normal faults in Tuscany. These localities give a direct insight into the mechanics of earthquakes responsible for the Umbria–Marche seismicity during crustal extension. The seismicity in this part of the Apennines is noteworthy in two main ways: (1) an active LANF – the Altotiberina Fault (ATF) – can be shown to exist at depth from the integration of seismic profiles with data recorded during two detailed microseismic surveys (Boncio *et al.* 2000; Collettini & Barchi 2002; Piccinini *et al.* 2003); and (2) the recent seismic sequences which affected the Umbria–Marche Apennines (Colfiorito $M_w = 6.0$, 1997; Gualdo Tadino $M_w = 5.1$, 1998) nucleated at a depth of *c*. 6 km within Triassic evaporites, as shown by the integration of seismic reflection profiles with well-located earthquakes (Barchi 2002; Mirabella & Pucci 2002; Miller *et al.* 2004; Ciaccio *et al.* 2005).

The Zuccale low-angle normal fault

The Zuccale fault (ZF) is a regional fault cropping out on the isle of Elba (Fig. 5a). On a regional scale, it dips on average 15° east and cuts downsection through an earlier thrust stack formed during the late Cretaceous to early Miocene compressional phase (Trevisan *et al.* 1967; Keller & Pialli 1990). Eastward-directed displacement, in the range of 7–8 km (Keller & Coward 1996), occurred along the fault from the middle Miocene to the early Pliocene, and the fault has been exhumed from a depth of 3–6 km. Details of the structural geology of the fault including fault zone architecture, geometry and kinematics are illustrated in Collettini & Holdsworth (2004). These authors used field observations, fault rock distribution and microstructures to assess fluid-assisted weakening mechanisms along the fault zone. One key feature of the Zuccale fault is the development of a pervasively foliated fault core,

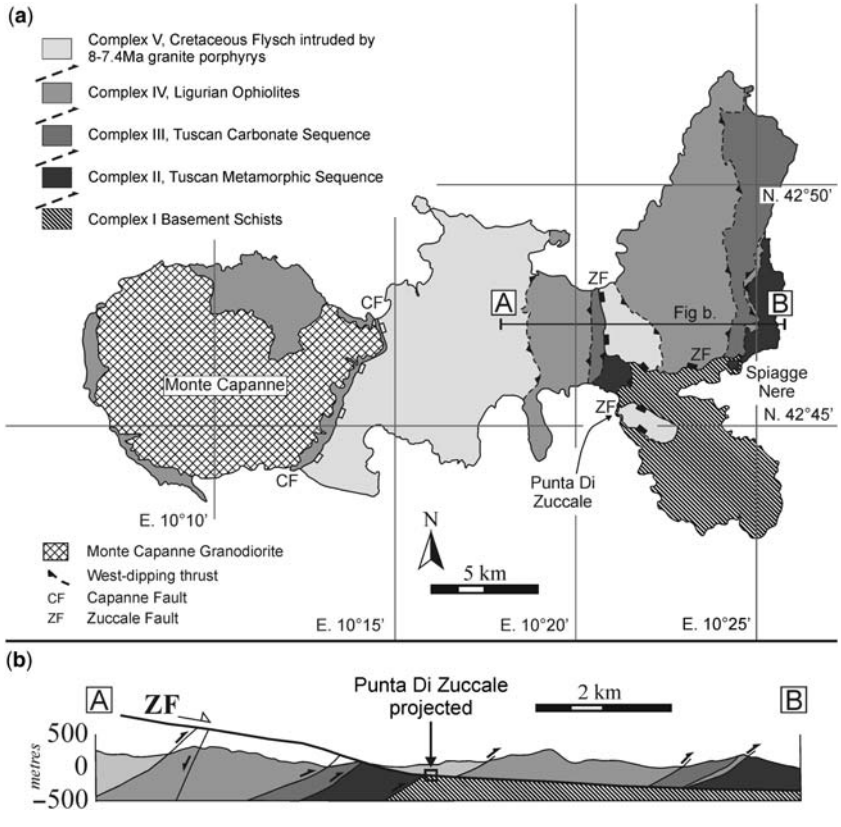

Fig. 5. Geology of Elba (modified after Trevisan *et al.* 1967; Bortolotti *et al.* 2001; Collettini & Holdsworth 2004). (**a**) Schematic geological and structural map of the isle of Elba. The position of two main outcrops, at Punta Di Zuccale and Spiagge Nere, is indicated. Quaternary deposits are white. (**b**) Geological cross-section through central and eastern Elba, modified after Collettini & Holdsworth (2004). The position of the Zuccale fault at depth is constrained using borehole data (Bortolotti *et al.* 2001).

generally 3–8 m thick, sandwiched between footwall and hanging wall blocks in which the normal fault-related deformation is exclusively brittle (Fig. 6). In the hanging wall, brittle normal faults are observed to link directly downwards into the detachment and commonly show dip–slip kinematics with top- to-the-east shear sense. Similarly, small displacement normal faults in the footwall of the main detachment, which may have listric geometries, are observed to control fault zone thickness and the internal distribution of fault rocks within the core of the Zuccale Fault

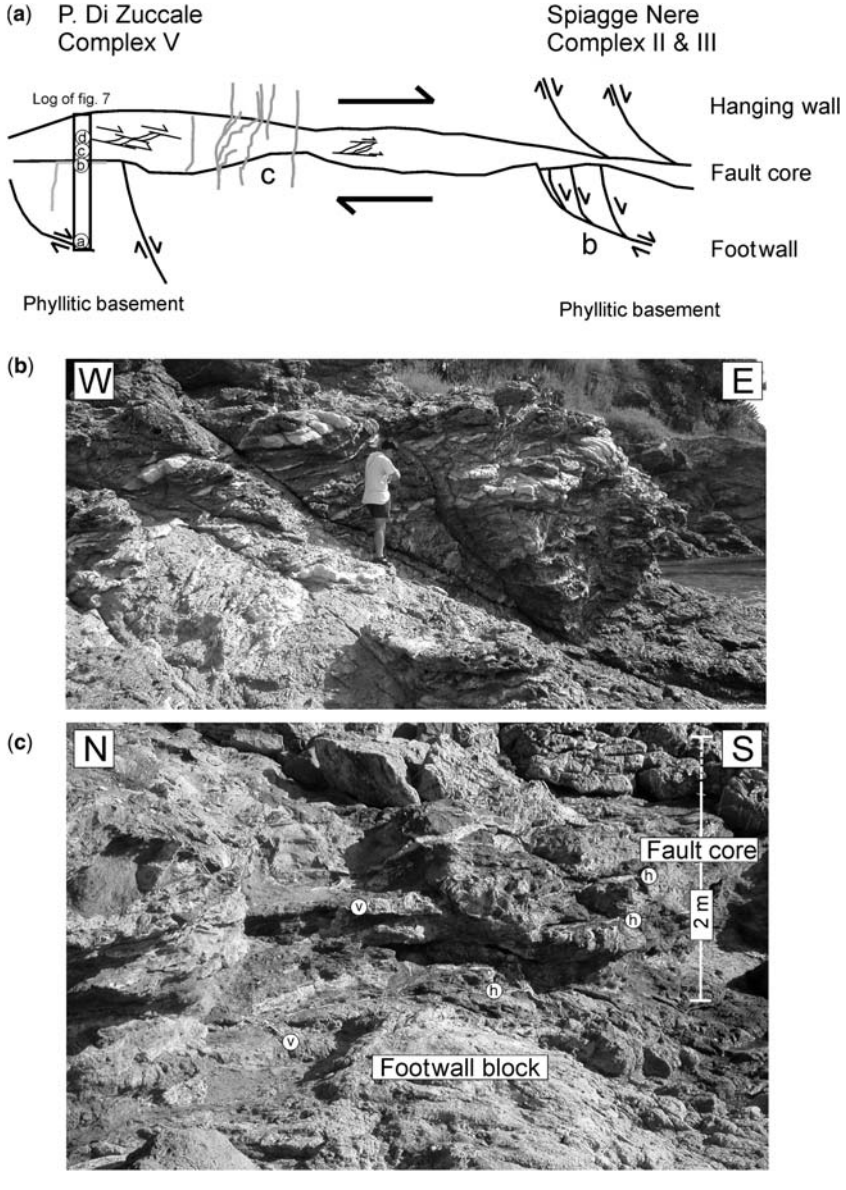

Fig. 6. (**a**) Schematic representation of the Zuccale fault (ZF) architecture linking the Punta di Zuccale and Spiagge Nere outcrops (not to scale, see location in Fig. 5). Location of the structural log reported in Fig. 7. (**b**) Listric normal fault within the basement footwall of the ZF (see location in *a*). (**c**) Down-dip view of the syntectonic hydrofracture system: (h) sub-horizontal veins, (v) vertical veins. Note the thick subhorizontal hydrofracture at the footwall fault core boundary.

(Fig. 6a & b). Footwall structures appear to have been active throughout the history of the Zuccale fault, indicating that high- and low-angle normal faults were active contemporaneously. The fault rock distribution, moving from the low-strain footwall domain towards the high-strain fault core, changes very markedly. Immediately below the detachment we observe a heterogeneous quartz cataclasite set in a carbonate–chlorite–quartz-rich matrix and containing localized brittle faults due to the presence of minor, steeply-dipping normal faults and linking transfer faults (Fig. 7a). At the footwall-to-fault core transition, we observe a collapse of the cataclastic microstructure triggered by reaction softening and the onset of ductile deformation (Fig. 7b). Moving into the high strain regions of the fault core, a highly foliated unit of green serpentinites plus tremolite–talc–chlorite schists (Fig. 7c) occurs and is associated with a heterogeneous unit of chlorite phyllonites (Fig. 7d). In these rocks, the main grain-scale deformation processes are pressure solution and precipitation, which are indicated by the presence of dark dissolution seams and fibrous overgrowth of tremolite, talc and calcite wrapping the carbonate clasts (e.g., Fig. 7d). The observed fault rock textures appear to record a switch in deformation processes from cataclasis to pressure solution-accommodated slip as one moves into the fault core (Collettini & Holdsworth 2004). This switch appears to be triggered by cataclastic grain-size reduction and simultaneous influx of hydrous fluids into the fault zone, together with reaction softening due to the effects of secondary alteration of strong minerals into fine-grained, highly aligned aggregates of weak phyllosilicates.

The fault zone is also characterized by a complex system of carbonate-infilled syntectonic hydrofractures (Fig. 6c) formed during repeated cycles of fluid pressure build up and release (Collettini & Holdsworth 2004). Many of these hydrofractures link directly into footwall normal faults, indicating that footwall structures are able to periodically tap and release fluids. The latest veins preserve good crack-seal textures whilst earlier veins are sheared and reworked into the fault zone. The thick, *c*. 2 cm, sub-horizontal vein located at the footwall block–fault core boundary (Fig. 6c) preserves crack-seal textures and shows vertically oriented calcite fibres, suggesting the local attainment of lithostatic fluid pressures during fault activity (Collettini *et al.* 2006*b*).

The footwall evaporites of Tuscany

In Tuscany, the Triassic evaporites form a thick sequence, up to 2–2.5 km, composed of decimetric- to-decametre scale interbeds of gypsum-anhydrite and dolostone, with minor halite (Fig. 8a & b; Ciarapica & Passeri 1976; Lugli 2001). This unit is interposed between the Permian–Triassic phyllitic basement and the Meso-Cenozoic carbonate multilayer sequences and has been affected by diagenetic processes and post-depositional tectonics. The diagenetic history of the evaporites began during the early Jurassic/late Cretaceous, after about 1 km of burial, when gypsum, originally deposited within shallow water environments, became unstable and was replaced by anhydrite (Murray 1964; Ciarapica & Passeri 1976; Lugli 2001). The evaporites experienced the two main eastward-migrating tectonic phases that affected the Northern Apennines, with extension superimposed on shortening (for details see Pauselli *et al.* 2006). The mechanical behavior of the evaporites in the tectonic evolution of the Northern Apennines is still not fully understood. They are considered to be the relatively ductile décollément zone for the Umbria–Marche thrust and fold belt (e.g., Bally *et al.* 1986). However, the integration of commercial seismic reflection profiles with well-located earthquakes has recently shown that the main seismic sequences of the Umbria region nucleated within the evaporites (e.g., Barchi 2002; Mirabella & Pucci 2002; Ciaccio *et al.* 2005), with the extensional mainshocks triggered by fluid overpressures trapped within this sequence (Miller *et al.* 2004).

In order to determine the deformation processes operating at depth in the seismogenic zone of the Umbria region, we studied exhumed outcrops of Triassic evaporites in Tuscany (see location on Fig. 1). Here the evaporites extensively crop out due to the effects of extension (crustal thinning) and regional uplift. We focused on two large exposures in the Roccastrada and Chianciano quarries, located in the footwalls of large, moderately to steeply dipping normal faults. During the early compressional, syn-orogenic deformation, the evaporites developed a strong foliation resulting from the shearing of an earlier compositional layering (Fig. 8b). This can be observed within the sulfate layers which are characterized by flow structures (e.g., isoclinal folds) and dismembered original sedimentary layers forming a millimetric-to-centimetric-scale transposed foliation (Fig. 8). The dolostone layers are characterized by the intense development of gypsum-filled fractures and appear strongly stretched with variably-sized boudins of dolostone set in a sulfate ground mass (Fig. 8).

The style of deformation in the evaporites during the later, post-orogenic extensional episode is strongly controlled by the pre-existing fabric and lithology. Small displacement faults (up to few metres in throw) develop different fault zone

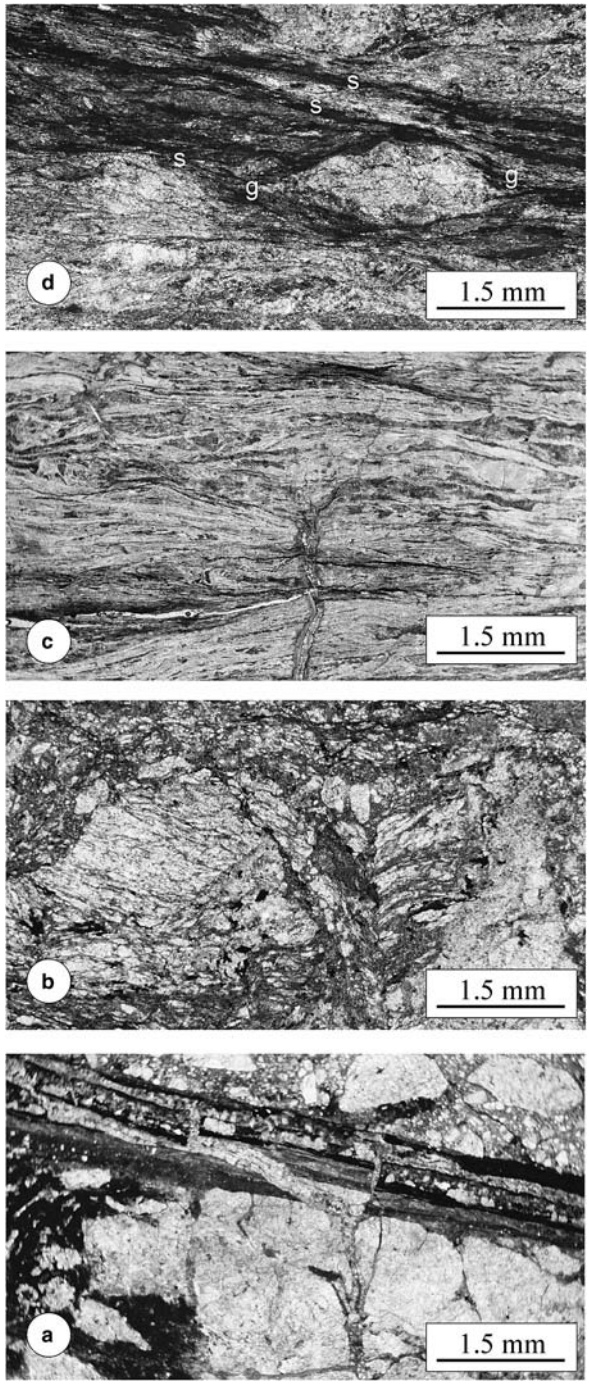

Fig. 7. Microstructural evolution along a transect from the footwall block up into the fault core. (**a**) Quartz-rich cataclasites in a carbonate–chlorite–quartz rich matrix and a brittle fault plane. (**b**) Collapse of the cataclastic load-bearing microstructure at the footwall fault core boundary. (**c**) Foliated unit of green serpentinites plus tremolite–talc–chlorite schists containing a calcite-rich hydrofracture. (**d**) Heterogeneous unit of chlorite phyllonites with dark dissolution seams (s) and fibrous overgrowths of talc and calcite (g).

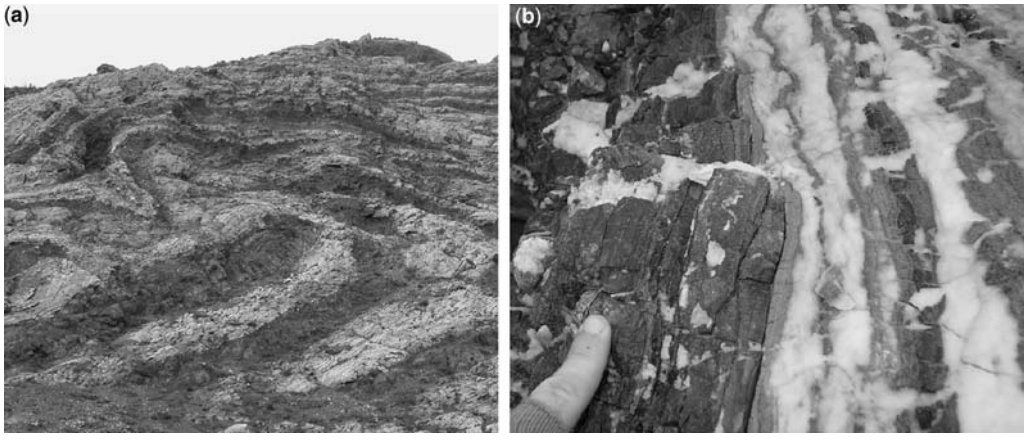

Fig. 8. (**a**) Massive stretched (boudinaged) and folded dolomitic mudstone (dark grey) between foliated and folded gypsum rocks after anhydrites (white). Syn-orogenic deformation of the Triassic evaporites produced a transposed foliation with flow structures within the sulfates and dismembered and stretched original layers within the more competent dolostone. (**b**) Thin stretched and folded dolostone layers intercalated with foliated/laminated gypsum rocks after anhydrites.

architecture as the fault zone cuts different rock types in the protolith. Faults developed within dolostone-rich layers display brittle features with well-defined striated fault planes and associated fault rocks (Fig. 9a & b). Fault zones here are characterized by a fault core with a thin layer of fine grained cataclasite (up to 1 cm) in contact with a relatively thicker, coarse-grained cataclasite with a high to moderate clast/matrix ratio and rounded fragments suggesting that they have originated by frictional attrition of the wall rocks (Fig. 9c). A well-developed damage zone extends for a few metres from the fault core. Small extensional faults preserved within the anhydrite- and gypsum-rich layers cut through the pre-existing fabric developed during the earlier compressional deformation event (Fig. 9d). Here the faults are characterized by a thin fault core and absence of a damage zone. The fault core consists of a dark, fine grained, cataclasite matrix with small dolostone clasts embedded within it (Fig. 9e). Dolostone clasts are observed here to be smeared out into the fault plane (Fig. 9f).

Large displacement faults (>100 m) cut across the entire multilayer stratigraphy with dips in the range of 40–50°. No significant changes in dip have been recorded due to changes in lithology (Fig. 10a). The fault cores, up to 2 m thick, are characterized by a grey fault gouge, dolostone-rich fault breccia and cataclasites, which, in some cases, evolve into foliated cataclasites with S-C fabrics. Damage zones of the major extensional faults are absent to poorly developed when the fault cuts gypsum/anhydrite bearing rocks. On the other hand, damage zones are well developed in thick dolostone layers. In this case, the damage zone structures are mainly controlled by penetrative (up to few metres thick) and intense fault/fracture mesh development (Fig. 10). The fault/fracture mesh is composed of vein-rich normal faults forming dilational jogs, conjugate extensional shear fractures and subvertical hydrofractures with crack-seal texture preserving evidence of multiple episodes of opening (Fig. 10b). Hydrofractures also developed during the earlier compression phase, but those formed by fluid-assisted processes during the post-orogenic extension can be distinguished because: (1) the hydrofractures possess the same strike as the associated normal faults with a majority indicating a vertical σ_1 orientation; (2) the fluid-rich normal faults possess the same orientation and kinematics as the regional extensional structures; and (3) the hydrofractures cut the earlier, syn-orogenic features such as transposed foliation and folds.

Discussion

Fluids in the Northern Apennines

Following slab retreat and roll-back beneath the Apennine chain (e.g., Doglioni *et al.* 1999) extension in the Northern Apennines migrated with time from the Tyrrhenian Sea to the Umbria–Marche Apennines from *c.* 15 Ma to the present day. Extension is accommodated by east-dipping low-angle normal faults and antithetic structures. In the extended/extending region geochemical and isotopic data from CO_2 gas emissions and

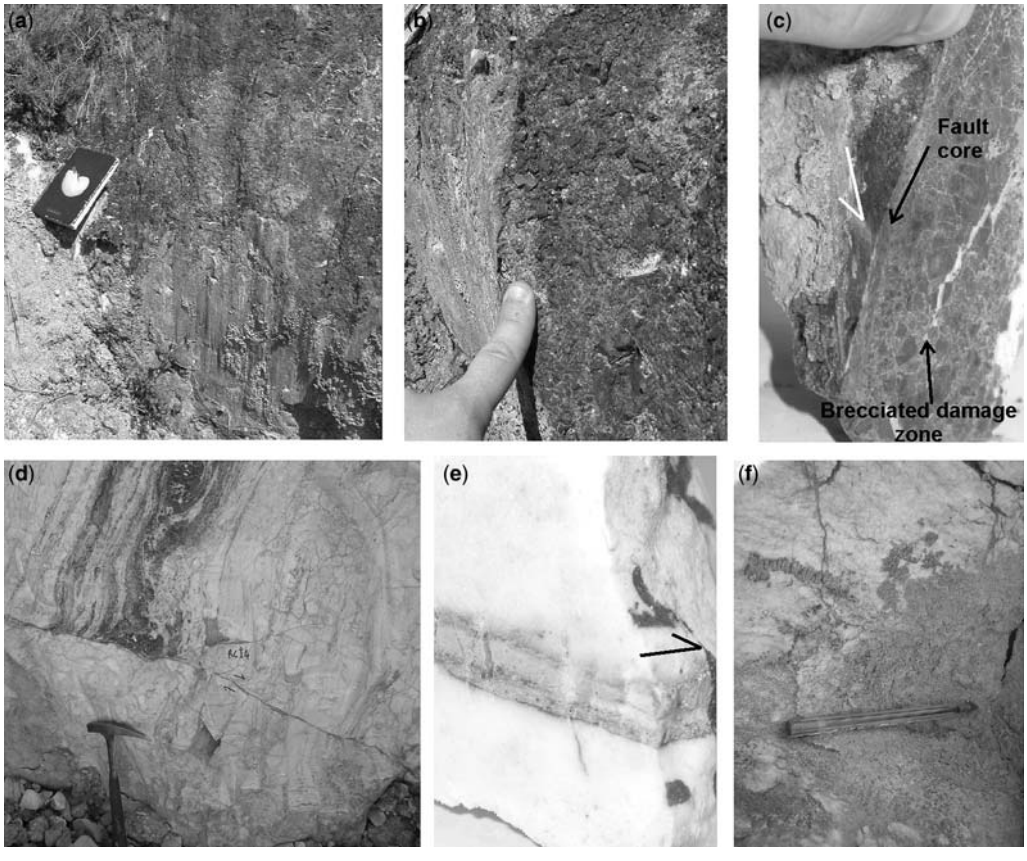

Fig. 9. (**a**) Striated normal fault plane within dolostone rocks. (**b** & **c**) Details of dolostone fault core architecture in the field (b) and saw-cut hand-specimen (c) show a fine-grained cataclasite within the slip zone in contact with a coarse-grained cataclasite. (**d**) Small displacement normal fault within gypsum rocks cutting through the pre-existing fabric (transposed foliation) developed during the syn-orogenic deformation event. (**e**) Saw-cut hand-specimen shows a thin fault zone with small dolostone clasts embedded within a dark and fine-grained cataclasite. (**f**) Dolostone clasts are smeared out into a normal fault plane developed within gypsum rocks.

CO_2 dissolved in groundwaters circulating in the carbonate aquifers suggest that the area is affected by variable but generally large inputs of CO_2 derived from metasomatism of the mantle wedge overlying the Adriatic subducted slab (Chiodini *et al.* 2004).

Assuming that a mantle origin for the CO_2-rich fluid is correct, we suggest a simple conceptual model for fluid circulation within the extended/extending sector of the Northern Apennines (Fig. 11). In the western extended sector (Tuscany and Latium), characterized by a marked upwelling of the mantle, deeply sourced fluids enter the ductile lower crust and infiltrate upwards through interconnected networks of extensional fractures and normal faults. The fluids accumulate in shallow crustal traps and feed the high-CO_2 flux region observed at the surface. In the eastern actively extending sector, we propose that the process of crustal thinning has not yet gone to completion, so that stratigraphic and/or structural seals can trap deeply sourced CO_2-rich fluids to produce fluid overpressures. It is worth noting that the CO_2 flux anomaly at the surface seems to rapidly disappear close to the active extensional front (Figs 4 & 11), where two deep wells, S. Donato and Pieve S. Stefano, encountered CO_2 pressures of about 98 and 67 MPa at depths of 4750 and 3700 m b.s.l., respectively (i.e., *c*. 0.8 of the lithostatic). In addition, this area of high CO_2 fluid overpressure at depth corresponds closely to the area of active extension and seismicity (Fig. 4a), suggesting that a key role is played by trapped fluid pressures in earthquake triggering.

The presence of an intense and widespread deep-seated CO_2 Earth degassing process, produced by

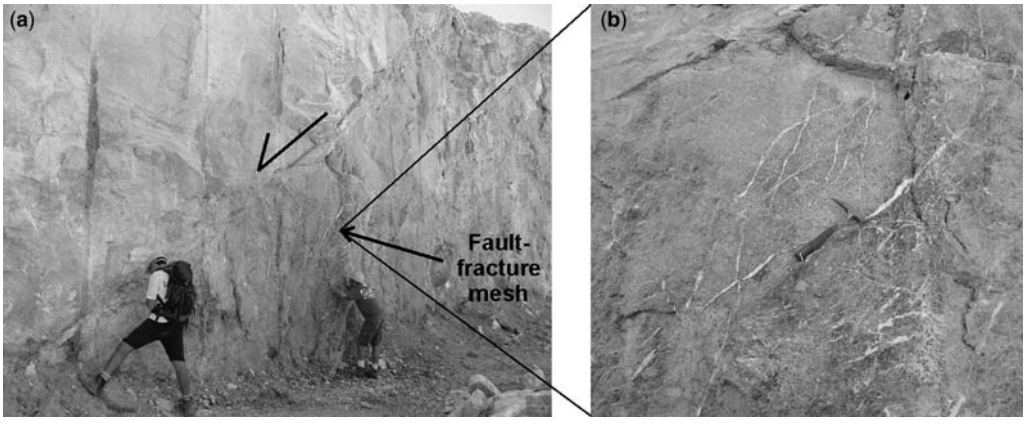

Fig. 10. (**a**) Normal fault cuts across the entire multicompetent stratigraphy. Note that no significant changes in dip have been observed as a function of lithology. Fault-fracture meshes have been observed within dolostone-bearing rocks adjacent to the fault zone. (**b**) Details of the fault-fracture mesh developed within the dolostone-bearing rocks in the footwall of the normal fault. Conjugate shear fractures and hydrofractures are consistent with extensional kinematics of the main fault.

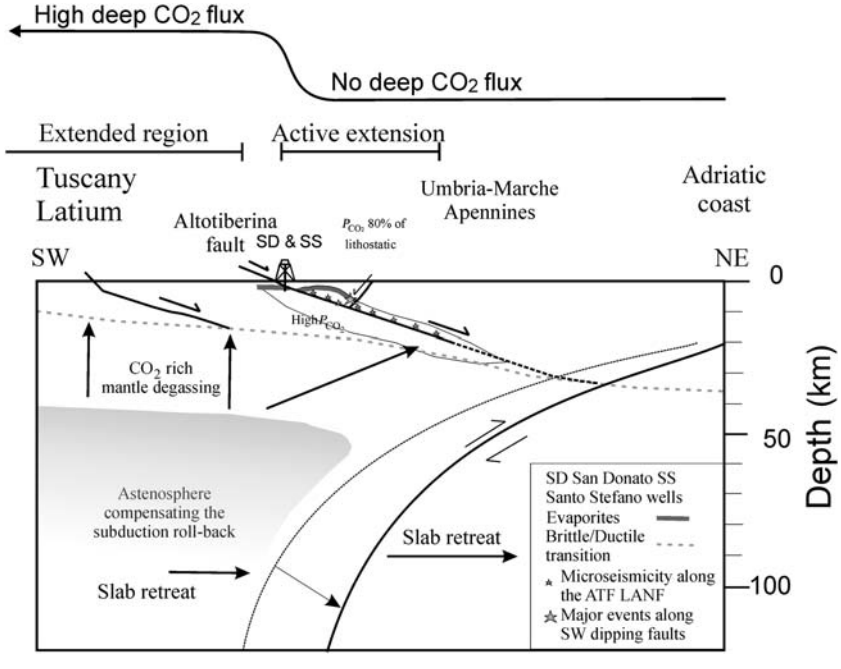

Fig. 11. Comprehensive conceptual model integrating geochemical, geological and geophysical observations for the Northern Apennines. Mantle wedge metasomatized by crustal fluids derived from the subducted Adriatic plate (e.g., Di Stefano *et al.* 1999; Doglioni *et al.* 1999) represents the deep source of CO_2-rich fluids (Chiodini *et al.* 2004). The deeply sourced CO_2 degassing potentially represents a continuous fluid supply rising into the brittle crust that triggers long-term fluid rock interactions. In the extending portion of the Northern Apennines CO_2-rich fluids are trapped by stratigraphical (i.e., the evaporites) and/or structural seals (i.e., mature structures like the Altotiberina fault) and develop fluid overpressures (as documented in the San Donato, SD, and Santo Stefano, SS, wells). Trapped fluid overpressures represent a short-term weakening mechanism that strongly influences the nucleation of microearthquakes along the Altotiberina fault (e.g., Collettini & Barchi 2002; Piccinini *et al.* 2003) and major events, $M > 5.0$, on SW dipping structures (e.g., the Colfiorito 1997 earthquakes, Miller *et al.* 2004).

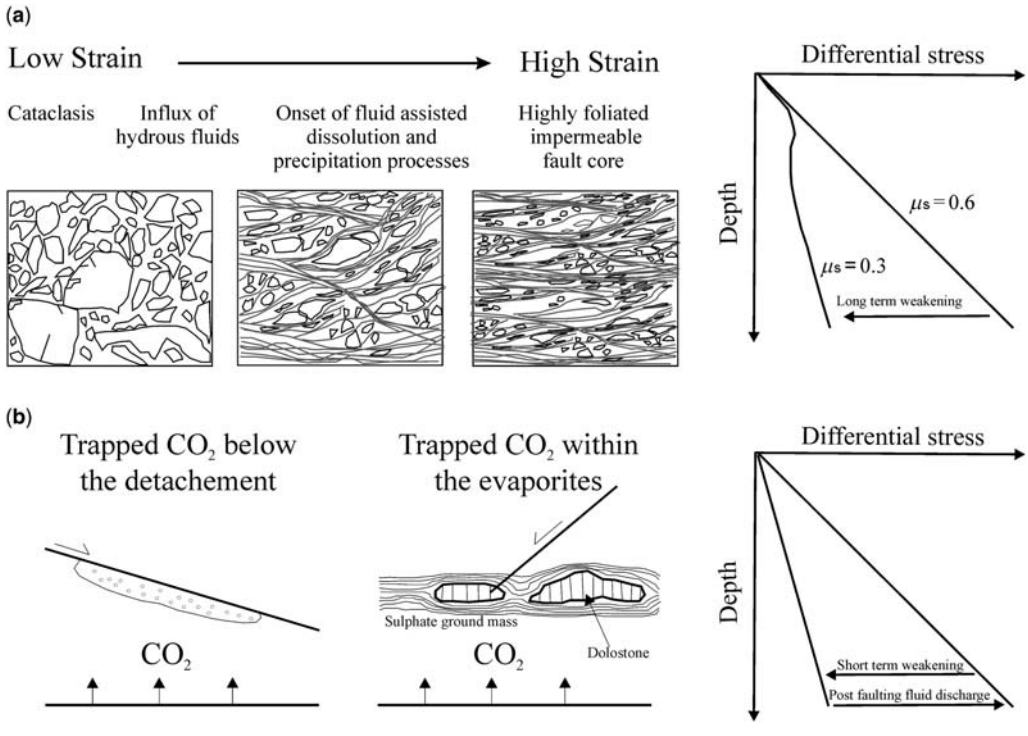

Fig. 12. Long- v. short-term fluid-assisted weakening mechanisms. (**a**) Long-term weakening processes observed along the Zuccale fault suggest that fluid influx into the fault zone triggered reaction softening and the onset of fluid-assisted dissolution and precipitation processes. The fault zone microstructure evolves from a cataclasite to a highly foliated fault rock with an associated decrease in friction coefficient at sub-Byerlee friction values ($\mu < 0.3$). (**b**) Short-term weakening processes observed in the field and documented in deep boreholes suggest that mantle-derived CO_2-rich fluids can be easily trapped by structural and/or stratigraphical seals that promote fluid overpressures. Fluid overpressures produce a short-term weakening since they reduce the differential stress required for faulting. Fluid-assisted ruptures create permeability allowing fluid discharge with associated fluid pressure drop. The field analogue of this process is represented by the hydrofracture systems within the Zuccale and the evaporite-bearing faults (Figs 6c & 10).

the eastward migration of extension following slab retreat, suggests a continuous fluid supply near to the base of the brittle crust. As we explain below, this allows both long- and short-term fluid-assisted weakening processes to occur widely (Fig. 12) and probably provides an explanation for the widespread development of LANF in the Northern Apennines.

Long-term fluid-assisted-weakening processes

From the microstructural evolution of the long-lived Zuccale fault zone we suggest the following model for long-term weakening (Fig. 12a). An initial phase of cataclasis increased fault zone permeability and helped focus fluid flow into the fault zone. Fluid interaction with the fine-grained cataclasites led to alteration, reaction softening and the onset of fluid-assisted dissolution and precipitation processes, such as pressure solution, in the highly deformed fault core (Collettini & Holdsworth 2004). The deformation accommodated by pressure solution and slip along the phyllosilicate-rich foliae would reduce the shear strength of the fault by reducing the coefficient of sliding friction to $\mu_s < 0.3$, allowing fault slip under low values of shear stress (Fig. 12a). Similar weakening mechanisms have been demonstrated in deformation experiments on rock analogues of phyllosilicate-rich fault rocks (Bos & Spiers 2001, 2002), where the switch from cataclastic to pressure-solution accommodated deformation is accompanied by a decrease in friction coefficient.

These weakening processes can be used to explain movements on LANF throughout the

Northern Apennine region and also provide an explanation for the activity of the currently active Altotiberina low-angle normal fault located in the extending area of the Umbria–Marche Apennines (Fig. 11, see Collettini & Holdsworth 2004).

Short-term fluid-assisted weakening processes

The influence of trapped fluid overpressure in promoting earthquake nucleation is well illustrated in the active area of the Umbria–Marche Apennines, where overpressures have been recorded in two deep boreholes (San Donato and Santo Stefano, Figs 4 & 11) within the Triassic evaporites at depth. Significantly, both wells are also located in the footwall block of the Altotiberina extensional detachment (Fig. 11). These data suggest that structural (e.g., large displacement LANF possessing a well-developed fault core) and stratigraphical seals (e.g., the Triassic evaporites) can act as traps for the CO_2-rich fluids and promote the development of fluid overpressures that facilitate fault slip (Fig. 12b).

The short-term structural control on fluid overpressure is well illustrated by the presence of syntectonic hydrofractures in the immediate footwall and intervening fault core of the exhumed Zuccale detachment (Fig. 6c). We interpret the hydrofracture system formed during the ZF activity as indicating high fluid pressures and short-term fluid-assisted weakening processes. In particular the development of the thick, *c*. 2 cm, subhorizontal vein located at the footwall block–fault core boundary testifies to the sealing capacity of the ZF foliated fault core, which was therefore able to trap crustal fluids during their ascent and promote fluid overpressure. Fluid overpressure facilitated brittle processes that transiently increased permeability, favouring fluid release and fluid pressure drop.

Collettini & Barchi (2002) and Collettini & Holdsworth (2004) have used these field observations to explain the microseismicity observed along the Altotiberina fault, suggesting that cyclic build-up in fluid pressure below the fault zone promotes a temporary switch from the pressure-solution-accommodated deformation (the long-term weakening process resulting in aseismic creep) to fluid-assisted brittle faulting, e.g., hydrofractures that can be interpreted as microseismic processes.

The evaporite-bearing outcrops in Tuscany provide an opportunity to investigate lithological controls on fluid overpressure development. Different rheological behaviours are recognized–ductile in the gypsum/anhydrite layers v. brittle/ductile in the dolostones–leading to the development of a syn-orogenic transposed foliation, which enhanced the low-permeability character of the gypsum/anhydrite units. This inherited lithological/structural anisotropy favoured the build-up of fluid overpressures during the post-orogenic extensional phase by trapping CO_2 rich fluids during their ascent (Fig. 12b). Fluid overpressures loaded the evaporites-bearing faults and promoted fluid-assisted slip processes and associated fluid discharge. This process is documented in the field by vein-rich brittle fault zones associated with well-developed damage zones, with networks of subsidiary hydrofractures observed especially in correspondence with thick dolostone layers (Fig. 10). Finally, the inferred fluid-assisted slip behaviour observed in the field is consistent with the recognition of the fluid-driven nucleation of the largest events of the Umbria–Marche area within the Triassic evaporites (e.g., the 1997–1998 $M = 6.0$ Colfiorito seismic sequence; Barchi 2002; Miller *et al.* 2004).

References

ALVAREZ, W. 1972. Rotation of the Corsica-Sardinia microplate. *Nature*, **248**, 309–314.

BALLY, A., BURBI, L., COOPER, C. & GHELARDONI, R. 1986. Balanced sections and seismic reflection profiles across the Central Apennines. *Memorie della Società Geologica Italiana*, **35**, 257–310.

BARCHI, M. R. 2002. Lithological and structural controls on the seismogenesis of the Umbria Region: observations from seismic reflection profiles. *Bollettino della Società Geologica Italiana*, **1**, 855–864.

BARCHI, R. M., MINELLI, G. & PIALLI, G. 1998. The crop 03 profile: a synthesis of results on deep structures of the Northern Apennines. *Memorie della Società Geologica Italiana*, **52**, 383–400.

BONCIO, P., BROZZETTI, F. & LAVECCHIA, G. 2000. Architecture and seismotectonics of a regional low-angle normal fault zone in central Italy. *Tectonics*, **19**, 1038–1055.

BONI, C., BONO, P. & CAPELLI, G. 1986. Schema idrogeologico dell'Italia Centrale. *Memorie della Società Geologica Italiana*, **35**, 991–1012.

BORTOLOTTI, V., FAZZUOLI, M., PANDELI, E., PRINCIPI, G., BABBINI, A. & CORTI, S. 2001. Geology of central and Eastern Elba island, Italy. *Ofioliti*, **26**, 97–150.

BOS, B. & SPIERS, C. J. 2001. Experimental investigation into the microstructural and mechanical evolution of phyllosilicate-bearing fault rock under conditions favouring pressure solution. *Journal of Structural Geology*, **23**, 1187–1202.

BOS, B. & SPIERS, C. J. 2002. Frictional–viscous flow of phyllosilicate-bearing fault rock: microphysical model and implications for crustal strength profiles. *Journal of Geophysical Research*, **107**, B, doi: 10.1029/2001JB000301.

BOSCHI, E., GUIDOBONI, E., FERRARI, G. & VALENSISE, G. 1998. *I terremoti dell'Appennino Umbro-Marchigiano area sud orientale dal 99 a.C.*

al 1984 – A cura dell'Istituto Nazionale di Geofisica e della SGA Storia Geofisica Ambiente, Editrice Compositori, Luglio 1998, 267.

BOULLIER, A. M. & ROBERT, F. 1992. Paleosismic events recorded in Archaean gold-quarts vein networks, Val d'Or, Albitibi, Quebec, Canada. *Journal of Structural Geology*, **14**, 161–179.

CALIRO, S., CHIODINI, G., AVINO, R., CARDELLINI, C. & FRONDINI, F. 2005. Volcanic degassing at Somma-Vesuvio (Italy) inferred by chemical and isotopic signatures of groundwater. *Applied Geochemistry*, **20**, 1060–1076.

CAPELLI, G., MAZZA, R. & GAZZETTI, C. 2005. Strumenti e strategie per la tutela e l'uso compatibile della risorsa idrica nel Lazio. *In:* ZAVATTI, A. (ed.) *Quaderni di Tecniche di Protezione Ambientale*, **78**, Pitagora Editrice, Bologna.

CARDELLINI, C. 2003. *Carbon dioxide diffuse degassing from active volcanoes and non-volcanic areas: methods and applications to southern Italy and Greece*. PhD thesis, Dipartimento di Scienze della Terra, Università di Perugia.

CHIODINI, G., FRONDINI, F. & PONZIANI, F. 1995. Deep structures and carbon dioxide degassing in Central Italy. *Geothermics*, **24**, 81–94.

CHIODINI, G., FRONDINI, F., KERRICK, D. M., ROGIE, J., PARELLO, F., PERUZZI, L. & ZANZARI, A. R. 1999. Quantification of deep CO_2 fluxes from Central Italy. Examples of carbon balance for regional aquifers and of soil diffuse degassing. *Chemical Geology*, **159**, 205–222.

CHIODINI, G., FRONDINI, F., CARDELLINI, C., PARELLO, F. & PERUZZI, L. 2000. Rate of diffuse carbon dioxide Earth degassing estimated from carbon balance of regional aquifers: the case of central Apennine, Italy. *Journal of Geophysical Research – Solid Earth*, **105**, 8423–8434.

CHIODINI, G., CARDELLINI, C., AMATO, A., BOSCHI, E., CALIRO, S., FRONDINI, F. & VENTURA, G. 2004. Carbon dioxide Earth degassing and seismogenesis in central and southern Italy. *Geophysical Research Letters*, **31**, L07615, doi:10.1029/2004GL019480.

CIACCIO, M. G., BARCHI, M. R., CHIARABBA, C., MIRABELLA, F. & STUCCHI, E. 2005. Seismological, geophysical and geological constraints for the Gualdo Tadino fault, Umbria–Marche Apennines (Central Italy). *Tectonophysics*, **406**, 233–247.

CIARAPICA, G. & PASSERI, L. 1976. Deformazione da fluidificazione ed evoluzione diagenetica della formazione evaporitica di Burano. *Bollettino della Società Geologica Italiana*, **95**, 1175–1199.

COLLETTINI, C. & BARCHI, M. R. 2002. A low angle normal fault in the Umbria region (Central Italy): a mechanical model for the related microseismicity. *Tectonophysics*, **359**, 97–115.

COLLETTINI, C. & HOLDSWORTH, R. E. 2004. Fault zone weakening processes along low-angle normal faults: insights from the Zuccale Fault, Isle of Elba, Italy. *Journal of the Geological Society*, **161**, 1039–1051.

COLLETTINI, C., DE PAOLA, N., HOLDSWORTH, R. E. & BARCHI, M. 2006*a*. The development and behaviour of low-angle normal faults during Cenozoic asymmetric extension in the Northern Apennines, Italy. *Journal of Structural Geology*, **28**, 333–352.

COLLETTINI, C., DE PAOLA, N. & GOULTY, N. R. 2006*b*. Switches in the minimum compressive stress direction induced by overpressure beneath a low-permeability fault zone. *Terra Nova*, **18**, 224–231.

COX, S. F., ETHERIDGE, M. A. & WALL, V. J. 1986. The role of fluids in syntectonic mass transport, and localization of metamorphic vein type ore deposits. *Ore Geology Review*, **2**, 65–86.

DAVID, M. 1977. *Geostatistical Ore Reserve Estimation*. Elsevier Scientific, Amsterdam.

DECANDIA, F. A., LAZZAROTTO, A., LIOTTA, D., CERNOBORI, L. & NICOLICH, R. 1998. The CROP 03 traverse: insights on post-collisional evolution of the Northern Apennines. *Memorie della Società Geologica Italiana*, **52**, 413–425.

DEUTSCH, C. V. & JOURNEL, A. G. 1998. *GSLIB: Geostatistical Software Library and User's Guide*, 2nd edition. Oxford, New York, Oxford University Press.

DI MATTEO, L., DRAGONI, W., PIERUCCI, L. & VALIGI, D. 2006. Studio idrogeologico e climatico del bacino del lago di Montedoglio (F. Tevere, Arezzo Italia Centrale). *Giornale di Geologia Applicata*, **3**, 1–7.

DI STEFANO, R., CHIARABBA, C., LUCENTE, F. & AMATO, A. 1999. Crustal and uppermost mantle structure in Italy from the inversion of P-wave arrival times: geodynamic implications. *Geophysical Journal International*, **139**, 483–498.

DOGLIONI, C., HARABAGLIA, P., MERLINI, S., MONGELLI, F., PECCERILLO, A. & PIROMALLO, C. 1999. Orogens and slabs vs. their direction of subduction. *Earth Science Reviews*, **45**, 167–208.

EVANS, J. P. & CHESTER, F. M. 1995. Fluid rock interaction in faults of the San Andreas system: Inferences from San Gabriel fault-rock geochemistry and microstructures. *Journal of Geophysical Research*, **100**, 13007–13020.

FRONDINI, F., CALIRO, S., CARDELLINI, C., CHIODINI, G., MORGANTINI, N. & PARELLO, F. 2007. Carbon dioxide degassing from Tuscany and Northern Latium (Italy). *Global and Planetary Change* doi:10.1016/j.gloplacha.2007.08.009.

FYFE, W. S., PRICE, N. J. & THOMSON, A. B. 1978. *Fluids in the Earth's Crust*. Elsevier, New York.

GIANELLI, G. 1985. On the origin of geothermal CO_2 of metamorphic processes. *Boll. Soc. Geol. It.*, **104**, 575–584.

GIGGENBACH, W. F. 1988. Geothermal solute equilibria. Derivation of Na–K–Mg–Ca geoindicators. *Geochimica et Cosmochima Acta*, **52**, 2749–2765.

HOLDSWORTH, R. E. 2004. Weak faults – rotten cores. *Science*, **303**, 181–182.

HULIN, C. D. 1925. Structural control on ore deposition. *Economic Geology*, **24**, 15–49.

HUNSTAD, I., SELVAGGI, G., D'AGOSTINO, N., ENGLAND, P., CLARKE, P. & PIEROZZI, M. 2003. Geodetic strain in peninsular Italy between 1875

and 2001. *Geophysical Research Letters*, **30**, 1181, doi:10.1029/2002GL016447.

IMBER, J., HOLDSWORTH, R. E., BUTLER, C. A. & STRACHAN, R. A. 2001. A reappraisal of the Sibson-Scholz fault model: the nature of the frictional to viscous (brittle–ductile) transition along a long-lived, crustal-scale fault, Outer Hebrides, Scotland. *Tectonics*, **20**, 601–624.

JEFFERIES, S. P., HOLDSWORTH, R. E., SHIMAMOTO, T., TAKAGI, H., LLOYD, G. E. & SPIERS, C. J. 2006*a*. Origin and mechanical significance of foliated cataclastic rocks in the cores of crustal-scale faults: examples from the Median Tectonic Line, Japan. *Journal of Geophysical Research*, **111**, B12303, doi:10.1029/2005JB004205.

JEFFERIES, S. P., HOLDSWORTH, R. E., WIBBERLEY, C. A. J., SHIMAMOTO, T., SPIERS, C. J., NIEMEIJER, A. R. & LLOYD, G. E. 2006*b*. The nature and importance of phyllonites development in crystal scale fault cores: an example from the Median Tectonic Line, Japan. *Journal of Structural Geology*, **28**, 220–235.

JOLIVET, L., FACCENNA, C. *ET AL*. 1998. Midcrustal shear zones in postorogenic extension: example from the northern Tyyhenian Sea. *Journal of Geophysical Research*, **103**, 12123–12160.

KELLER, J. V. A. & COWARD, M. P. 1996. The structure and evolution of the Northern Tyrrhenian Sea. *Geological Magazine*, **133**, 1–16.

KELLER, J. V. A. & PIALLI, G. 1990. Tectonics of the island of Elba: a reappraisal. *Bollettino Società Geologica Italiana*, **109**, 413–425.

KNOPF, A. 1929. *The Mother Lode System in California*. USGS Professional Papers, **157**.

LUGLI, S. 2001. Timing of post-depositional events in the Burano Formation of the Secchia Valley (Upper Triassic, Northern Apennines), clues from gypsum–anhydrite transitions and carbonate metasomatism. *Sedimentary Geology*, **140**, 107–122.

MARINI, L. & CHIODINI, G. 1994. The role of carbon dioxide in the carbonate–evaporite geothermal systems of Tuscany and Latium (Italy). *Acta Vulcanologia*, **5**, 95–104.

MARTELLI, M., NUCCIO, P. M., STUART, F. M., BURGESS, R., ELLAM, R. M. & ITALIANO, F. 2004. Helium–strontium isotope constraints on mantle evolution beneath the Roman Comagmatic Province, Italy. *Earth and Planetary Science Letters*, **224**, 295–308.

MILLER, S. A., COLLETTINI, C., CHIARALUCE, L., COCCO, M., BARCHI, M. R. & KAUS, B. 2004. Aftershocks driven by a high pressure CO_2 source at depth. *Nature*, **427**, 724–727.

MINISSALE, A. 2004. Origin, transport and discharge of CO_2 in central Italy. *Earth-Science Reviews*, **66**, 89–141.

MIRABELLA, F. & PUCCI, S. 2002. Integration of geological and geophysical data along a section crossing the region of the 1997–98 Umbria–Marche earthquakes (Italy), *Bollettino Società Geologica Italiana*, **1**, 891–900.

MONGELLI, F. & ZITO, G. 1991. Flusso di calore nella regione Toscana. *Studi Geologici Camerti*, **1**, 91–98.

MÖRNER, N. A. & ETIOPE, G. 2002. Carbon degassing from the lithosphere. *Global and Planetary Change*, **33**, 185–203.

MURRAY, R. C. 1964. Origin and diagenesis of gypsum and anhydrites. *Journal of Sedimentary Petrology*, **34**, 512–523.

PARRY, W. T. & BRUHN, R. L. 1990. Fluid pressure transients on seismogenic normal faults. *Tectonophysics*, **179**, 335–344.

PAROTIDIS, M., ROTHERT, E. & SHAPIRO, S. A. 2003. Pore pressure diffusion: a possible triggering mechanism for the earthquake swarms 2000 in Vogtland/NW-Bohemia, Central Europe. *Geophysical Research Letters*, **30**, doi:10.1029/2003GL018110.

PAUSELLI, C. & FEDERICO, C. 2002. The brittle/ductile transition along the Crop03 seismic profile: relationship with the geological features. *Bollettino della Società Geologica Italiana*, **1**, 25–35.

PAUSELLI, C., BARCHI, M. R., FEDERICO, C., MAGNANI, B. M. & MINELLI, G. 2006. The crustal structure of the Northern Apennines (Central Italy): an insight by the CROP03 seismic line. *American Journal of Science*, **306**, 428–450.

PIALLI, G., BARCHI, M. R. & MINELLI, G. 1998. Results of the CROPO3 deep seismic reflection profile. *Memorie della Società Geologica Italiana*, **52**, 657.

PICCININI, D., CATTANEO, M. *ET AL*. 2003. Microseismic study in a low seismicity area of Italy: the Città di Castello 2000–2001 experiment. *Annals of Geophysics*, **46**, 1315–1324.

PONZIANI, F., DE FRANCO, R., MINELLI, G., BIELLA, G., FEDERICO, C. & PIALLI, G. 1995. Crustal shortening and duplication of the Moho in the Northern Apennines: a view from seismic refraction data. *Tectonophysics*, **252**, 391–418.

RAMSAY, J. G. 1980. The crack-seal mechanism of rock deformation. *Nature*, **284**, 135–139.

REUTTER, K. J., GIESE, P. & CLOSS, H. 1980. Lithospheric split in the descending plate: observations from the Northern Apennines. *Tectonophysics*, **64**, T1–T9.

ROGIE, J. D., KERRICK, D. M., CHIODINI, G. & FRONDINI, F. 2000. Flux measurements of nonvolcanic CO_2 emission from some vents in central Italy. *Journal of Geophysical Research – Solid Earth*, **105**, 8435–8445.

ROSENBAUM, G., REGENAUER-LIEB, K. & WEINBERG, R. 2005. Continental extension: From core complexes to rigid block faulting. *Geology*, **33**, 609–612.

RUTTER, H. E. & MAINPRICE, D. H. 1979. On the possibility of slow fault slip controlled by diffusive mass transfer processes. *Gerlands Beitre Geophysics*, **88**, 154–162.

SECOR, D. T. 1965. Role of fluid pressure in jointing. *American Journal of Science*, **263**, 633–646.

SERRI, G., INNOCENTI, F. & MANETTI, P. 1993. Geochemical and petrological evidence of the subduction of delaminated Adriatic continental lithosphere in the genesis of the Neogene-Quaternary magmatism of central Italy. *Tectonophysics*, **223**, 117–147.

SIBSON, R. H. 1981. Fluid flow accompanying faulting: field evidence and models. *In*: SIMPSON, D. W. & RICHARDS, P. G. (eds) *Earthquake Prediction: an*

International Review. Maurice Ewing Series 4, American Geophysical Union, Washington, DC. 593–603.

SIBSON, R. H. 1992. Implications of fault-valve behaviour for rupture nucleation and recurrence. *Tectonophysics*, **211**, 283–293.

SINCLAIR, A. J. 1974. Selection of threshold values in geochemical data using probability graphs. *Journal of Geochemical Exploration*, **3**, 129–149.

TREVISAN, L., MARINELLI, G. *ET AL*. 1967. *Carta Geologica dell'Isola d'Elba.* Scala 1:25.000. Consiglio Nazionale delle Ricerche, Gruppo di Ricerca per la Geologia dell'Appennino centro-settentrionale e della Toscana, Pisa.

VON OPPEL, F. W. 1749. *Anleitung zur Markscheidekunst*, Dresden.

WIBBERLEY, C. A. J. 1999. Are feldspar-to-mica reactionsnecessarily reaction-softening processes in fault zones? *Journal of Structural Geology*, **21**, 1219–1227.

WINTSCH, R. P., CHRISTOFFERSEN, R. & KRONENBERGER, A. K. 1995. Fluid–rock interaction weakening of fault zones. *Journal of Geophysical Research*, **100**, 13021–13032.

Deep-crust strike–slip earthquake faulting in southern Italy aided by high fluid pressure: insights from rheological analysis

PAOLO BONCIO

Geodynamics and Seismogenesis Laboratory, Dipartimento di Scienze della Terra, Università 'G. d'Annunzio', 66013 Chieti, Italy (e-mail: pboncio@unich.it)

Abstract: I present the results of a crustal rheological analysis of the Potenza 1990 and Molise 2002 (southern Italy) deep foci (10–25 km) strike–slip earthquake sequences ($M_{max} = 5.7$) located in the upper half of the middle crust. The analysis consists of geotherms and two-mechanism (brittle frictional v. ductile plastic flow) strength envelopes. Strength envelopes are calculated along a sub-vertical E–W-striking inherited crustal-scale fault zone reactivated under a strike–slip tectonic regime. The effects of high pore-fluid pressure (*Pf*) and strain rate increase due to afterslip processes during the co-seismic and early post-seismic phases are evaluated. The results are compared with the depth-distribution of seismicity. Under long-term strain rates, the rheology predicts a brittle layer in the upper part of the middle crust embedded by two plastic horizons: the base of the carbonates and the Verrucano layer (above) and the lower part of middle crust (below). The best rheological model for the observed seismicity is that considering high *Pf* in the middle crust ($\lambda \geq 0.65$). Brittle faulting aided by high *Pf* in the middle crust is in agreement with the focal depths and magnitudes of the main shocks. The upward and downward widening of the brittle layer in the middle crust, due to the increased strain rate in the co-seismic and early post-seismic phases (afterslip), agrees with the width of the aftershock zones. The weak ductile layer at the base of the carbonates (and possibly within the Verrucano) appears to have an important role in delimiting the seismogenic faulting upwards and probably played a role in defining a seal to fluid up-flow along the fault zone.

On 5 May 1990, a moderate magnitude earthquake ($M = 5.7$) struck the Potenza area in southern Italy (Fig. 1). The kinematics of the main shock was strike–slip; the aftershock sequence was crustal but relatively deep, being mainly located between 15 and 25 km (Azzara *et al.* 1993; Ekstrom 1994). Both the strike–slip kinematics of the main shock and the relatively deep aftershock sequence aroused interest due to the closeness to and striking differences from the adjacent Apennine seismic area (Fig. 1). The seismotectonic features of the Apennine area were synthesized by the deeply studied 1980 Irpinia earthquake, a large ($M = 6.9$) normal-faulting earthquake sequence located in the upper crust at depths shallower than 15 km (Westaway & Jackson 1987; Bernard & Zollo 1989; Pantosti & Valensise 1990; Amato & Selvaggi 1993 and references therein). Recently, the 1990 Potenza earthquake sequence was revised by locating the aftershocks with detailed velocity models, computing the focal mechanisms of several aftershocks, and inverting the focal mechanisms for stress analysis (Boncio *et al.* 2007). The hypocentral locations confirmed the deep crustal source of the earthquake; the focal mechanism analysis constrained the strike–slip nature of the active stress in the focal region (sub-horizontal N142°E-trending $\sigma 1$ and sub-horizontal N232°E-trending $\sigma 3$; Fig. 2).

In October–November 2002, two moderate magnitude earthquakes (31 October, $M = 5.7$ and 1 November, $M = 5.7$) occurred in Molise, *c.* 140 km NNW of Potenza. They are located in the same seismotectonic domain as the 1990 earthquake, just to the east of the Apennine extensional area (Fig. 1). A large number of aftershocks were recorded and accurately located (Chiarabba *et al.* 2005*a*). The Molise earthquake sequence shares with the Potenza both the fault kinematics and the focal depths (depths mainly between 10 and 25 km; Fig. 1b), as well as the particularity of having low stress drop values (Ekstrom 1994; Rovelli *et al.* 2004). In cross section, both sequences are located in the same structural–stratigraphic position (Fig. 3). The main shocks and the main aftershock clusters lie below the bottom of the outer Apulian carbonate platform, the sedimentary cover of the Apulian foreland crust, at the footwall of the easternmost Apennine thrust system. It is generally accepted that the Molise and Potenza earthquakes are due to reactivation with right-lateral strike–slip kinematics of inherited E–W- striking faults located within the Apulian crust (Di Bucci & Mazzoli 2003; Valensise *et al.* 2004). The surface expression of active strike–slip faulting in the Apulian foreland is represented by the E–W right-lateral Mattinata fault in the Gargano promontory (Fig. 1; Tondi *et al.* 2005). What are not yet

From: WIBBERLEY, C. A. J., KURZ, W., IMBER, J., HOLDSWORTH, R. E. & COLLETTINI, C. (eds) *The Internal Structure of Fault Zones: Implications for Mechanical and Fluid-Flow Properties*. **299**, 195–210.
DOI: 10.1144/SP299.12 0305-8719/08/$15.00

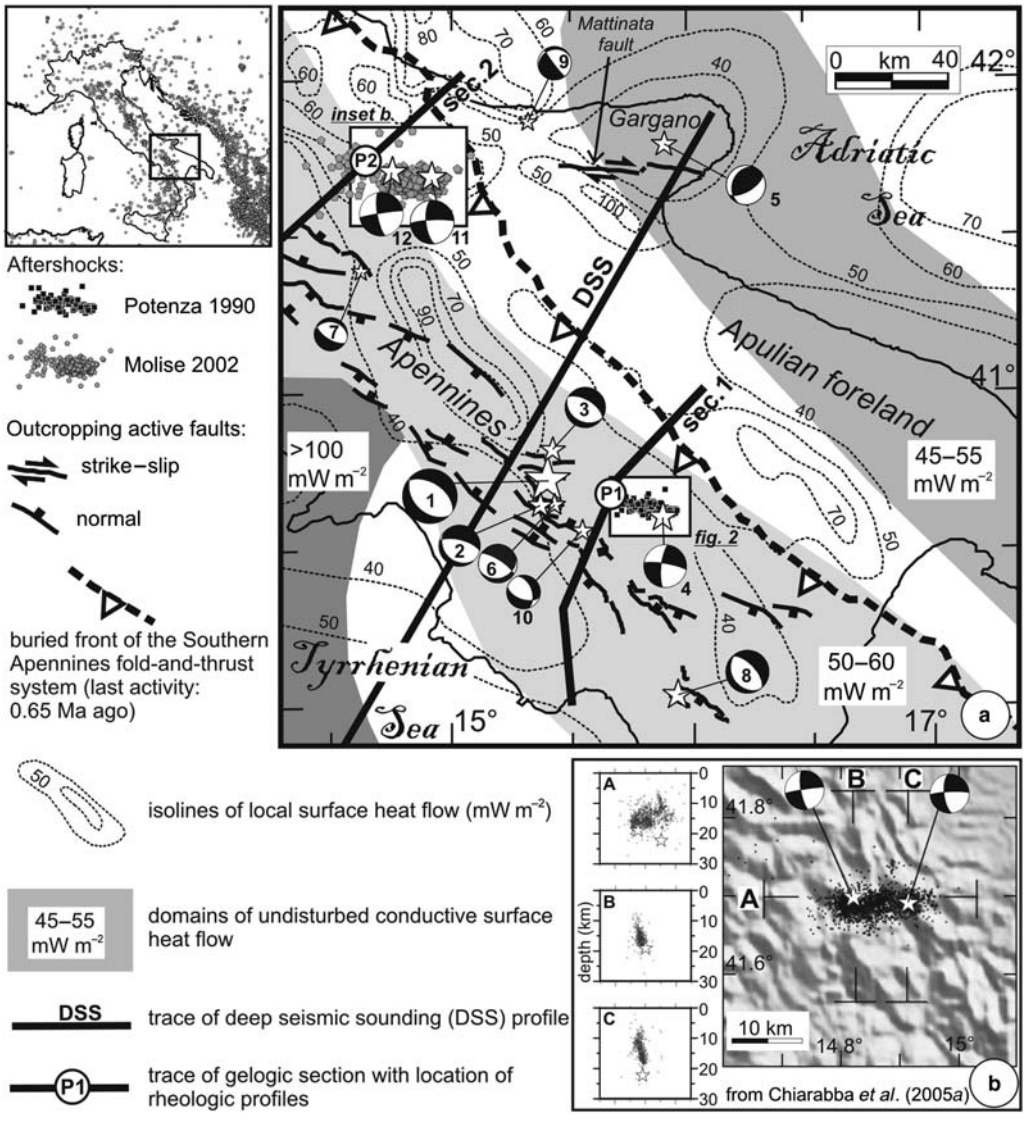

Fig. 1. (**a**) Simplified structural map of southern Italy with location of the analysed Potenza 1990 and Molise 2002 seismic sequences; isolines of local surface heat flow and domains of undisturbed surface heat flow (from Della Vedova *et al.* 2001); trace of geologic/geophysic sections (section1 from Menardi Noguera & Rea 2000; section 2 from Mazzoli *et al.* 2000; DSS from Scarascia *et al.* 1994); focal mechanisms since 1980 for $M > 4.0$ earthquakes (from Harvard-CMT database at www.seismology.harvard.edu and Mednet-RCMT database at http://mednet.rm.ingv.it; no. 4 from Ekstrom 1994; no 6 from Cocco *et al.* 1999). (**b**) Epicentral map and hypocentral sections for the Molise 2002 seismic sequence (from Chiarabba *et al.* 2005*a*). Focal mechanisms: (1) 1980/11/23 M 6.9; (2) 1980/11/25 M 5.4; (3) 1981/01/16 M 5.2; (4) 1990/05/05 M 5.7; (5) 1995/09/30 M 5.2; (6) 1996/04/03 M 4.9; (7) 1997/03/19 M 4.5; (8) 1998/09/09 M 5.6; (9) 2001/07/02 M 4.3; (10) 2002/04/18 M 4.4; (11) 2002/10/31 M 5.7; (12) 2002/11/01 M 5.7.

understood are the rheologic conditions that might justify the occurrence of the observed seismicity at deep crust levels. In this work I analyse the crustal rheology in two sections corresponding to the Potenza and Molise seismic areas. First, I compute the geotherms starting from the regional surface heat flow and incorporate into the thermal regime the likely effect of recent (Late

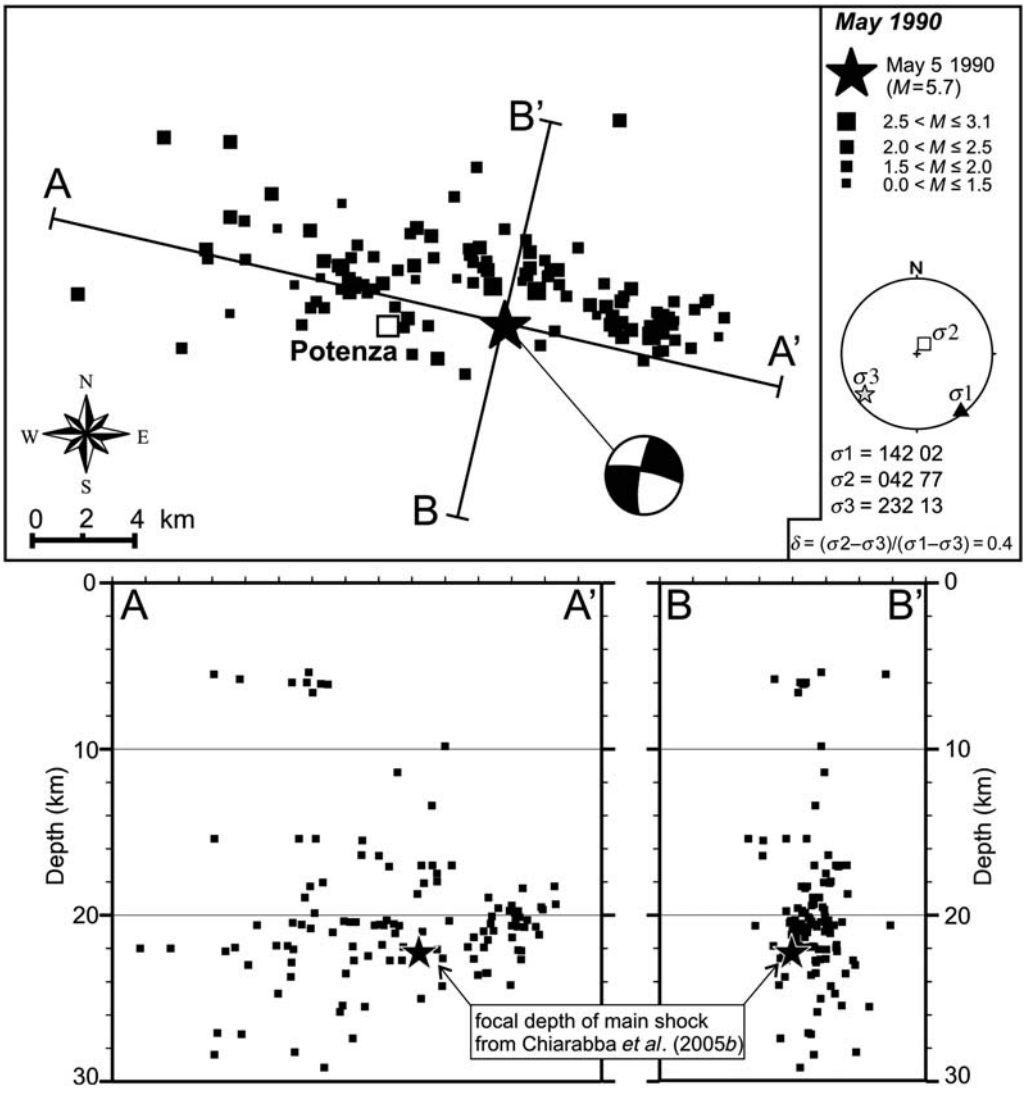

Fig. 2. Epicentral map, hypocentral sections, and stress tensor from inversion of aftershock focal mechanisms of the Potenza 1990 seismic sequence (from Boncio *et al.* 2007).

Pliocene–Middle Pleistocene) thrust faulting and thickening of the sedimentary cover. Then, I calculate the strength and behaviour of the crust using simple two-mechanism (brittle frictional behaviour v. ductile plastic flow) rheologic profiles (e.g., Goetze & Evans 1979; Brace & Kohlstedt 1980; Sibson 1982; Ranalli & Murphy 1987). The rheologic profiles are computed also considering the effects of: (i) high fluid pressure at deep crustal levels; and (ii) strain rate variations due to afterslip processes. The obtained strength envelopes are compared with the depth-distribution of main shocks and aftershocks; the results are discussed, also considering the limitations and unknowns implicit in the two-mechanism rheologic approach. In addition, a possible mechanical model for deep-crust sub-vertical strike–slip faulting is proposed for the southern Apennines of Italy.

Rheological analysis

The rhelogical analysis was carried out for a crustal-scale sub-vertical fault zone inherited from

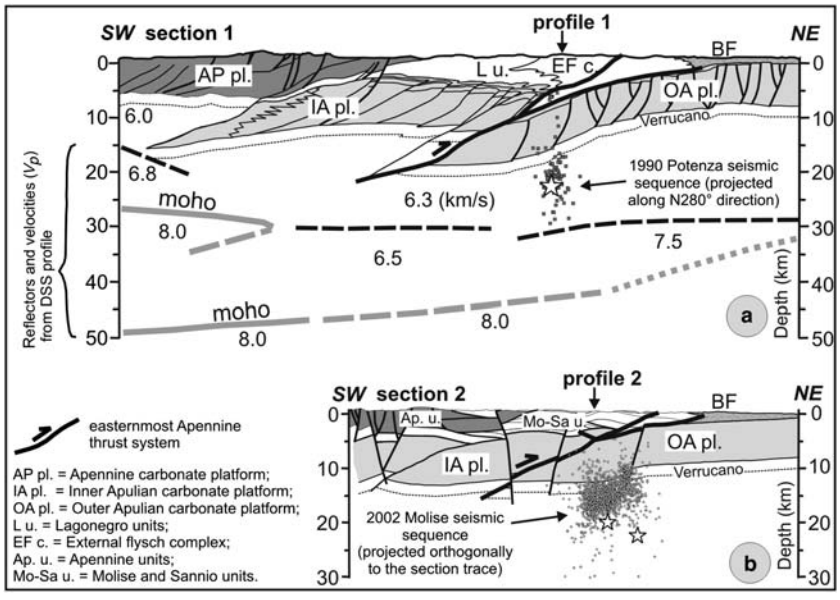

Fig. 3. (**a**) Geologic section (redrawn from Menardi Noguera & Rea 2000) integrated with DSS data (from Scarascia *et al.* 1994) across the Potenza 1990 seismic sequence. (**b**) Geologic section (redrawn from Mazzoli *et al.* 2000) across the Molise 2002 seismic sequence. Location of section traces in Figure 1.

previous tectonic phases and reactivated under the present-day strike–slip tectonic regime. The analysis included: (i) definition of the crustal stratigraphy; (ii) computation of the geotherm; (iii) association with crustal layers of known rheologies; and (iv) computation of strength envelopes.

Crustal stratigraphy

The crustal stratigraphy was defined using two geologic sections constrained by seismic reflection data up to depths corresponding to the bottom of the sedimentary cover. The first, from Menardi Noguera & Rea (2000), crosses the Southern Apennines close to the 1990 Potenza earthquake sequence (Fig. 3a). The second, from Mazzoli *et al.* (2000), crosses the Molise Apennines close to the 2002 Molise earthquake sequence (Fig. 3b). Below the carbonate sedimentary cover, I placed a horizon corresponding to the Verrucano formation, which consists of metamorphosed Permo-Triassic siliciclastic deposits (mainly quartzites and phyllites). The presence of the Verrucano below the carbonates is documented by the Puglia 1 well, which penetrated this formation for about 1000 m (see Mazzoli *et al.* 2000). The thickness of the Verrucano is unconstrained. I assumed a constant thickness of about 2 km on the basis of deep seismic sounding (DSS) data from the central–northern Apennines (Ponziani *et al.* 1995). The upper crust stratigraphy was integrated with information on the deep crustal layers and related *P*-wave velocities (V_p) from the Southern Apennines DSS profile (Scarascia *et al.* 1994). The deep crust reflectors/refractors from the DSS profile are projected onto the section of Figure 3a. At the longitude of the 1990 Potenza earthquake sequence, the bottom of the carbonates is at depths of *c.* 15 km. The middle crust (below the Verrucano layer) is *c.* 14 km thick with an average V_p of 6.3 km s^{-1}; the lower crust is *c.* 12 km thick with high V_p (7.5 km s^{-1}). The Moho is at depths of *c.* 43 km. In the Molise seismic area (Fig. 3b), the bottom of the carbonates is at depths of *c.* 13 km. Below the sedimentary cover I assumed the same stratigraphy and layer thickness as the Potenza area. The reconstructed stratigraphies are illustrated in Figures 4 & 5.

Surface heat flow and geotherms

A map of the surface heat flow in Italy, together with the domains of undisturbed conductive heat flow (that is, the surface heat flow corrected for local and/or shallow non-conductive thermal processes), was proposed by Della Vedova *et al.* (2001; fig. 1a). The Molise area, as well as all the eastern side of the Southern Apennines, lies in a zone of poorly-defined surface heat flow. This zone is located between the stable Apulian foreland, having an average undisturbed surface heat flow of

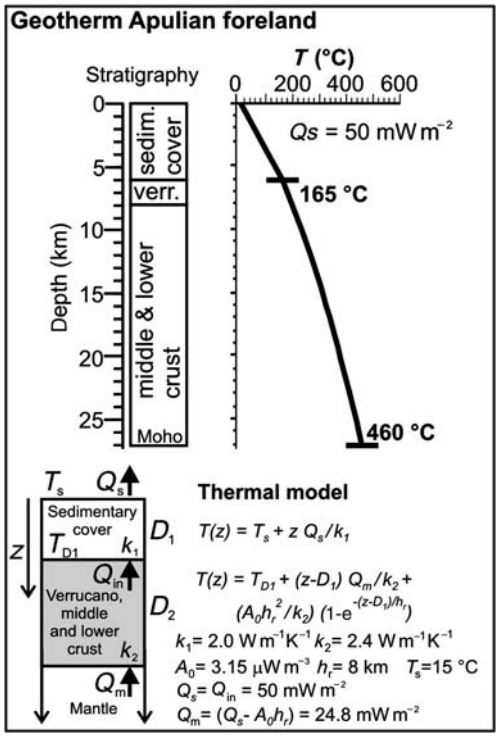

Fig. 4. Stratigraphy and steady-state geotherm for the stable Apulian foreland. The crustal thickness is from the DSS profile; the thickness of the sedimentary cover is from the Puglia 1 well (in Mazzoli *et al.* 2000).

50 mW m^{-2}, and the extensional Apennine area, having an undisturbed surface heat flow ranging from 50 to 60 m-W m^{-2} (Fig. 1a). The highest value (60 m W m^{-2}) is probably associated with the western Apennine area, characterized by a thinned crust and lithosphere (e.g., Scarascia *et al.* 1994), while the lowest value (50 mW m^{-2}) is more representative of the eastern Apennine area, which is presently affected by crustal extension. Also, the Potenza area, which has the same structural–stratigraphic location of the Molise area, should be considered in a zone of poorly defined surface heat flow.

First, I computed the geotherm for the stable Apulian foreland under the assumption of steady-state conditions, starting from the average undisturbed conductive surface heat flow (50 m W-m^{-2}, Fig. 4). The crustal stratigraphy was simplified in two layers corresponding to: (1) the sedimentary cover, with negligible internal heat production; and (2) the Verrucano, middle crust and lower crust, with internal radiogenic heat production decreasing exponentially with depth. The used thermal parameters [thermal conductivity (k); radiogenic heat production at the top of the crystalline crust (A_0), and length-scale for exponential decrease in radiogenic heat production (h_r)] are from Dragoni *et al.* (1996). The thermal conductivities (k) are average values accounting for both the crustal lithology and variations in k with increasing depths and temperatures (Dragoni *et al.* 1996). The thermal model and the resulting geotherm are illustrated in Figure 4; the predicted heat flow incoming at the base of the crust from the mantle (Q_m) is *c.* 25 mW m^{-2}.

The geotherm of the stable Apulian foreland is inappropriate for the Potenza and Molise areas. Actually, the geologic sections show the presence of the frontal Apennine thrust system which produced a considerable thickening of the sedimentary cover (Fig. 3). The thrust is presently inactive; it was active from the Late Pliocene to 0.65 Ma ago (Menardi Noguera & Rea 2000; Patacca & Scandone 2001). The total displacement, measured along the section crossing the Potenza area, is *c.* 16 km (Menardi Noguera & Rea 2000). If we consider the onset of thrusting at 2.58 Ma ago (base of Late Pliocene), the estimated thrust activity is *c.* 1.9 Ma and the average slip rate of *c.* 8.4 mm/a. Considering that in the Potenza and Molise seismic areas the thrust produced thickening of the exclusively conductive part of the crust (carbonate sedimentary cover, with negligible internal heat production), the effect should be of two types: (1) steepening of the conductive temperature profile of the initial steady-state geotherm; and (2) heating due to friction along the thrust. I analysed the thermal effect due to thrusting by using the solution proposed by Molnar *et al.* (1983), which allows for separation of the different contributions to the geotherm due to: (1) incoming heat flow; (2) frictional heating; and (3) radiogenic heating. Molnar *et al.*'s solution was applied only to the sedimentary cover; therefore, the radiogenic heating was not considered. The geotherm of the stable Apulian foreland was considered as the initial (before thrusting) steady-state geotherm with an incoming heat flow at the base of the sediments (Q_{in} in Figs 4 & 5) equal to the presently measured undisturbed surface heat flow in the Apulian foreland ($Q_s = 50$ mW m^{-2}). In the Potenza seismic area, the thrust system consists of two main splays located at depths of about 5 and 7.5 km. I simplified this structural setting by considering only one thrust fault at *c.* 7.5 km depth with average kinematic parameters as previously described (onset of thrusting, 2.58 Ma; thrust activity, 1.9 Ma; slip rate, 8.4mm/a). The shear stress (τ), which enters in the calculation of shear heating, was calculated using Sibson's (1974) formulation for favourably oriented thrust faults at 7.5 km depths under hydrostatic pore-fluid conditions, with the friction coefficient (μ) equal to 0.6 (see also the following section); the obtained value was $\tau \approx 140$ MPa. The same kinematic

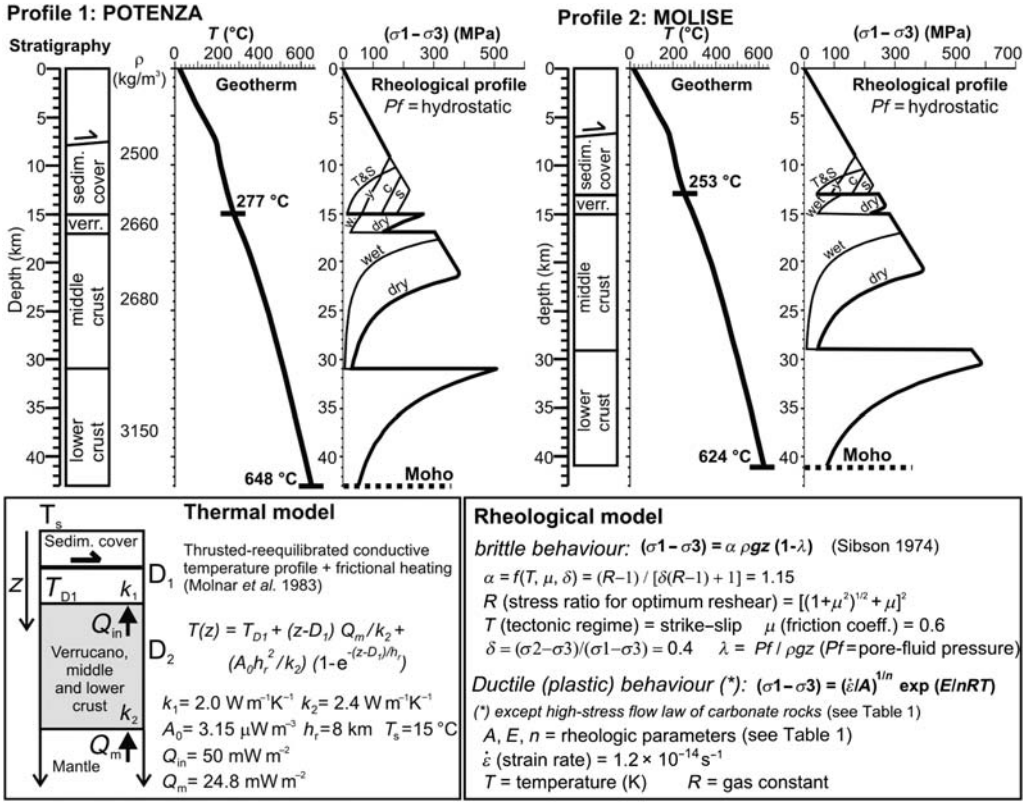

Fig. 5. Stratigraphy, geotherm and rheological profile (under a long-term strain rate and hydrostatic pore-fluid pressure) for the Potenza and Molise seismic areas. The used thermal and rheological models are indicated. Flow strength of carbonates (see Table 1): T&S = limestone from Turcotte & Schubert (2002); y = Yule marble; c = Carrara marble; s = Solnhofen limestone. Location of profiles in Figure 3.

parameters were used for the Molise seismic area; differences arise concerning the depth of the thrust (6.5 km) and the corresponding shear stress ($\tau \approx 120$ MPa). The effect of thrusting on the temperature profile rapidly disappears at depths larger than the base of the sedimentary cover (15 and 13 km in the Potenza and Molise areas, respectively); therefore, I solved the temperature profile for the crystalline crust underlying the sediments with the steady-state equation used for the crystalline Apulian foreland crust, starting from the temperature at the base of sediments (T_{D1}) and using the mantle heat flow obtained for the Apulian area ($Q_m = 24.8$ mW m^{-2}). The obtained geotherms and the thermal model are illustrated in Figure 5.

Strength envelopes

The strength and behaviour (brittle v. ductile) of the crust was estimated by comparing the strength for frictional failure along pre-existing sub-vertical strike–slip faults favourably oriented for reactivation (brittle behaviour; Sibson 1974) with the plastic strength for steady-state flow, most commonly dominated by power-law creep (ductile behaviour; Kirby 1983; Ranalli & Murphy 1987).

The brittle strength, in terms of differential stress (Fig. 5), depends on the rock density (ρ), tectonic regime, friction coefficient (μ), pore-fluid pressure (Pf) and in the case of strike–slip regime, stress ratio [$\delta = (\sigma 2 - \sigma 3)/(\sigma 1 - \sigma 3)$]. The adopted rock densities are reported in Figure 5. The tectonic regime is strike–slip according to focal mechanisms data; the stress ratio (δ) is constrained by the stress inversion of the 1990 aftershock focal mechanisms (Figs 1 & 2). Considering that we are analysing fault zones inherited from previous tectonic phases, I used $\mu = 0.6$, which has been suggested to be more appropriate for long-lived faults (Lockner & Byerlee 1993; Sibson 1998) and, in general, is suitable for seismogenic faults (Sibson & Xie 1998; Collettini & Sibson 2001).

The ductile (plastic) strength, in terms of differential stress (Fig. 5, Table 1), depends on the temperature, strain rate and rheological parameters. The strain rate ($\acute{\varepsilon}$) is in this case the strain rate due to simple shear. It depends on the average slip rate of the fault (v) and the width of the zone within which the strain accumulates (D):

$$\acute{\varepsilon} = v/2D \quad (s^{-1}).$$

There are not direct measurements of v and D for the Potenza and Molise areas. Estimates of the average slip rate for active E–W-striking right-lateral faults in the Apulian foreland are available only for the outcropping Mattinata fault in the Gargano promontory (0.7–0.8 mm/a; Tondi *et al.* 2005). I used a simple shear strain rate homogeneously accumulated within a fault zone of thickness (D) on the order of 10^3 m via use of an average slip rate of 0.75 mm/a. The used fault zone thickness seems a reasonable value for a long-lived fault zone at mid-crustal depths (e.g., Sibson 1983); these are the depths of major interest in the present analysis. The obtained strain rate is *c.* 1.2×10^{-14} (s^{-1}).

The flow laws and rheological parameters used in this work are listed in Table 1. The carbonate sedimentary cover was modelled by comparing different rheologies proposed for carbonate rocks (e.g., Schmid *et al.* 1980 and references therein; Table 1). The different strengths obtained by the different carbonate rheologies can be considered as an estimate of the uncertainty in determining the rheological behaviour of carbonates (Fig. 5). The Verrucano layer, consisting of quartzites and phyllites, was modelled using quartzite rheology. Concerning the middle and lower crust, the literature offers only a limited number of rheological parameters. The most commonly used rheologies are: quartzite, granite and quartz–diorite for middle crust and diabase, felsic granulite, mafic granulite and anorthosite for lower crust (e.g., Ranalli 1995, p. 334). The most appropriate rheologies were chosen by comparing the observed V_p from DSS data (Fig. 3a) with a compilation of V_p for different crustal rocks at different depths and thermal gradients published by Christensen & Mooney (1995). The middle crust shows velocities of 6.3 km s^{-1} which, at the observed depths and temperatures, are between velocities typical of granite–granodiorite ($V_p = 6.1$–6.2 km s^{-1}) and diorite ($V_p = 6.4$–6.5 km s^{-1}) rocks. Therefore, I used quartz-diorite rheology for the middle crust. The lower crust shows high velocities (7.5 km s^{-1}) which are typical of mafic rocks. Therefore, I used mafic granulite rheology for the lower crust. For the Verrucano quartzites and the middle crust, I compared rheological parameters obtained experimentally from both nominally dry (oven dried) and wet (water added) specimens (Table 1) in order to account for possible weakening in flow strength due to the activity of water (hydrolytic weakening). Though hydrolytic weakening is likely in the upper crust where water is commonly present, at middle and lower crustal depths (>10–15 km) the activity of water may be very

Table 1. *Flow law equations and rheological parameters*

Stratigraphy	Rheology	Flow law	A ($MPa^{-n}s^{-1}$)*	n	E (kJ mol^{-1})	σ_0 (MPa)	Reference
Sedimentary cover (carbonates)	Solnhofen limestone R1	(1) $\sigma = \sigma_0\,[\ln(\dot{e}/A) + (E/RT)]$	$10^{-0.12}$ (s^{-1})	—	197	16	1,2
	Yule marble R1		$10^{7.0}$ (s^{-1})	—	238	13.8	2
	Carrara marble R1		$10^{5.8}$ (s^{-1})	—	259	11.4	1,2
	Solnhofen limestone R2		2.5×10^{3}	4.7	298	—	2
	Yule marble R2		2.5×10^{-4}	7.7	256	—	2
	Carrara marble R2		1.3×10^{3}	7.6	418	—	2
	Limestone		4.0×10^{3}	2.1	210	—	3
Verrucano	Quartzite	(2) $\sigma = (\dot{e}/A)^{1/n}$	6.7×10^{-6}	2.4	156	—	4
	Quartzite WET	$\exp(E/\mathrm{n}RT)$	3.2×10^{-4}	2.3	154	—	4
Middle crust	Quartz–diorite		1.3×10^{-3}	2.4	219	—	4
	Quartz–diorite WET		3.2×10^{-2}	2.4	212	—	5
Lower crust	Mafic granulite		1.4×10^{4}	4.2	445	—	4

R1 = high-stress flow regime in carbonates; R2 = high-temperature flow regime in carbonates; σ = stress difference ($\sigma 1 - \sigma 3$); $\dot{e}$ = strain rate (s^{-1}); R = gas constant; T = temperature (K); * = units are MPa^{-n} s^{-1} for equation (2), s^{-1} for equation (1).
References: 1 = Rutter (1974); 2 = Schmid *et al.* (1980); 3 = Turcotte & Schubert (2002, p. 321); 4 = Ranalli (1995, p. 334); 5 = Carter & Tsenn (1987).

small due to dehydration or mixing with other fluids such as CO_2; this suggests that the flow strength could be approximated by that of dry specimens (Ord & Hobbs 1989). In this work, dry and wet rheologies are also compared for the middle crust (depths between 15–17 and 29–31 km) with the results being considered as the upper and lower bounds of the flow strength, respectively.

The strength envelopes were first computed by considering only hydrostatic pore-fluid pressures (*Pf*). Hydrostatic *Pf* has been found from deep boreholes to be a common feature in actively deforming intraplate areas, at least in the upper crust (to depths of as much as 12 km; Zoback & Townend 2001). Hydrostatic *Pf* corresponds to pore-fluid factors ($\lambda = Pf/$lithostatic load) decreasing with depth from 0.4 to 0.36.

The results are illustrated in Figure 5. The carbonates are brittle up to depths ranging from 9 to *c.* 12 km, depending on the carbonate rheology. The deepest portion of the carbonates is expected to flow plastically (ductile). The Verrucano is ductile in the Potenza area independently if we consider dry or wet rheology. In the Molise area, the Verrucano is entirely ductile for wet rheology and ductile in the lower half for dry rheology. The middle crust is brittle in its upper part. The brittle layer is very thin for wet rheology, ranging from 1 km (Potenza) to 2 km (Molise). The thickness of the brittle layer increases if we consider dry rheology, ranging from *c.* 4 km (Potenza) to *c.* 6 km (Molise). The remaining middle and lower crust is mostly ductile below depths of *c.* 21 km.

Comparing rheological profiles with aftershock distribution

The results from the rheological profiles under constant long-term strain rates and hydrostatic *Pf* were compared with the earthquake distribution at depth. The seismicity databases are of good quality. For the Potenza seismic sequence, most of the aftershocks have vertical errors less than 3 km (Boncio *et al.* 2007). For the Molise seismic sequence, I used the database from Chiarabba *et al.* (2005*a*), selected for its hypocentral errors of less than 2 km. The crustal depths of major interest are those corresponding to the middle crust where the seismicity concentrates (Figs 3 & 6).

The middle crust is brittle in its upper part but the comparison with the seismicity is not satisfactory, especially for the Potenza 1990 seismic sequence (Fig. 6a). The maximum thickness (dry rheology) of the long-term, hydrostatic *Pf*, brittle layer in the middle crust is *c.* 4 km (from 17 to *c.* 21 km depths). This thin layer disagrees with both the width of the aftershock zone and the depth of the main shock. Moreover, it seems difficult to reconcile a 4 km-thick brittle layer with the observed magnitude of the main shock ($M = 5.7$). For a $M = 5.7$ earthquake, we expect a rupture area on the order of 50 km^2 (e.g., Wells & Coppersmith 1994). Peruzza & Pace (2002) found an empirical relationship between the width of the seismogenic fault (W) and the maximum possible rupture length for a single rupture episode ($L^{\#}$). According to these relationships, in order to have a $M = 5.7$ earthquake, a minimum W of 5–6 km is needed; this corresponds to a maximum possible $L^{\#}$ of 8–10 km.

The comparison between the rheological profile and the 2002 Molise seismicity is better, even if not fully satisfactory (Fig. 6b). The maximum thickness (dry rheology) of the long-term, hydrostatic *Pf*, brittle layer in the middle crust is *c.* 6 km (from 15 to *c.* 21 km depths) and might justify the observed magnitudes ($M = 5.7$). However, one of the two main shocks is deeper and the aftershock zone is wider than the brittle layer.

Inconsistencies between rheological profiles and depth-distribution of seismicity: lower frictional strength?

Inconsistencies between the rheological profiles and depth-distributions of the seismic sequences, observed especially for the 1990 Potenza seismicity, might be due to a lower frictional strength of the fault at middle crustal depths, a higher plastic flow strength, or both causes. Probably, both causes must be considered.

Assuming that the used rheological approach is correct at least to a first approximation (see also the Discussion section), it is reasonable to expect that the main shocks nucleate well within the brittle layer obtained under long-term strain rates. It requires a lower frictional strength of the fault with consequent widening of the brittle layer.

There are several arguments concerning the strong role played by high *Pf* in reducing the frictional strength of faults. Processes of permeability reduction at elevated depths and temperatures might favour high *Pf*, probably maintained over long times (Nur & Walder 1990). High *Pf* in the fault zone has been shown to be an important parameter in controlling the strength of seismogenic faults worldwide (e.g., Sibson 1990; Rice 1992; Miller 2002) and in the Apennines of Italy (e.g., Miller *et al.* 2004). High *Pf* (supported by observations from deep boreholes) and its possible role in triggering microseismicity on active low-angle normal faults have been highlighted in the upper crust of central Apennines (Collettini & Barchi 2002). A large discharge of fluids of

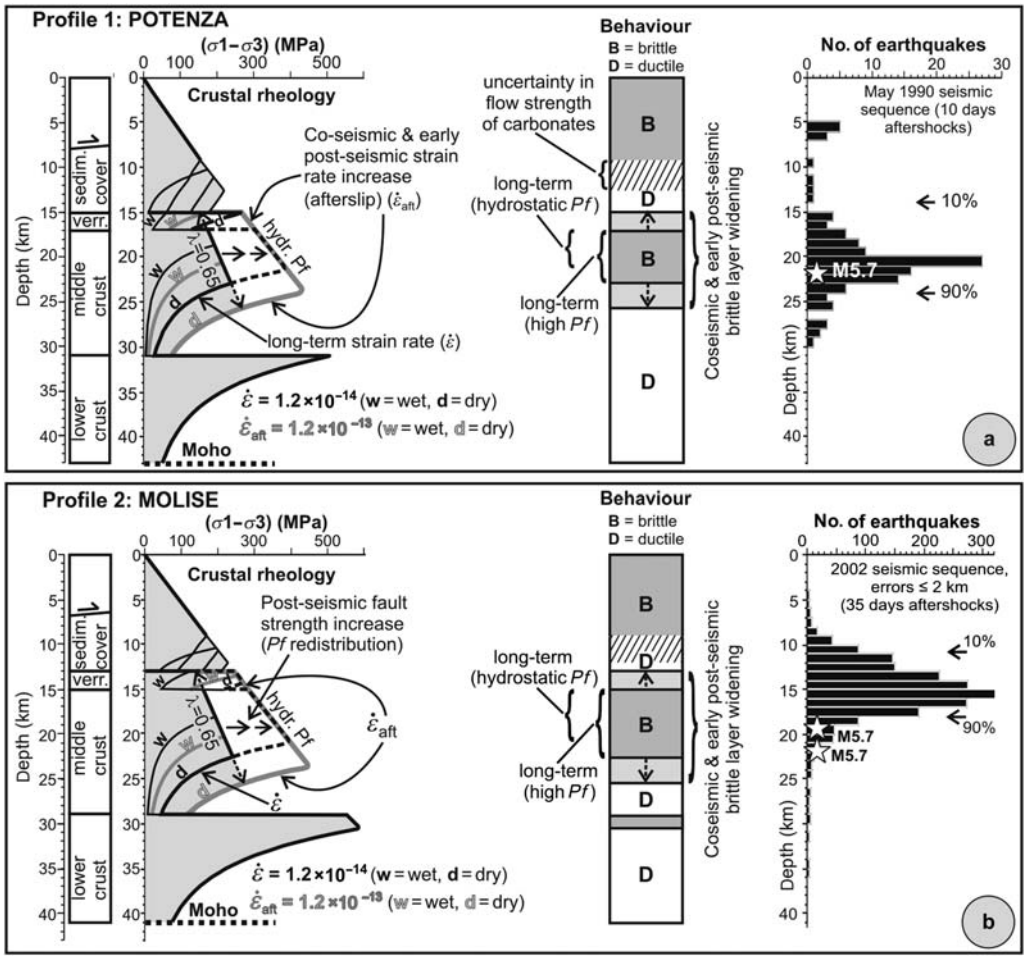

Fig. 6. Comparison between rheological profiles and depth distribution of aftershocks for the Potenza 1990 (**a**) and Molise 2002 (**b**) seismic sequences. Stars indicate main shocks. The effects of high *Pf* in the middle crust ($\lambda = 0.65$) and increased strain rate due to afterslip processes ($\dot{\varepsilon}_{aft}$) are indicated. The predicted crustal behaviour (brittle v. ductile, middle column) is indicated for dry rheology. The long-term brittle behaviour refers to the long-term strain rate ($\dot{\varepsilon}$); the coseismic and early post-seismic brittle layer widening refers to the increased strain rate ($\dot{\varepsilon}_{aft}$). Note that the upper bound of the Molise aftershocks at 9–10 km is mainly due to a geometrical effect related to the one-dimensional representation; the depth of the top of the major aftershock volume ranges from 9–10 to 12–13 km moving from east to west (compare Fig. 3b).

mantle origin (CO_2) has been documented in central-southern Italy (Chiodini *et al.* 2000, 2004); the presence of overpressurized reservoirs of CO_2 trapped within the crust beneath the Apennines and its role in inducing seismicity have been proposed (Chiodini *et al.* 2004).

An interesting observation, possibly having implications in terms of frictional strength of the fault, is that both the Molise and Potenza earthquakes showed relatively low stress drops when compared with other Apennine earthquakes. For the Molise earthquakes, Rovelli *et al.* (2004) found stress drops ranging from 1 to 3 MPa for *M* ranging from 3.0 to 6.0, respectively. A low stress drop, even if not quantitatively constrained, was also found for the Potenza 1990 earthquake (Ekstrom 1994). The observed stress drops are within the range of stress drops observed worldwide (mostly in the range 0.1–10 MPa; Hanks 1977), but towards the lower half of the range. The observed stress drops are lower than those observed for other Apennine earthquakes ($\geq$8 MPa; Rovelli *et al.* 1988, 1991; Cocco *et al.* 1999; Selvaggi *et al.* 2001). Interpretations of fault strength from

source properties such as the stress drop (which is related to the rupture behaviour), must be argued carefully; nevertheless, the observed differences might indicate an average lower frictional strength of the Potenza and Molise faults compared with other seismogenic Apennine faults. In the following, reduced frictional strength of the Potenza and Molise faults due to high *Pf* in the fault zone will be explored.

A higher plastic flow strength of the fault zone, compared with that obtained with long-term strain rates, must also be considered. Earthquake faulting produces a stress increase in both the lower and upper stable-sliding (aseismic) zones embedding the seismogenic fault. This stress increase produces a post-seismic slip known as afterslip (e.g., Marone *et al.* 1991). For the Potenza and Molise seismic areas, the stable-sliding zones should correspond to the layers showing plastic rheology above and below the brittle layer of the middle crust. The afterslip increases the strain rate in these plastic layers. Therefore, the strength for plastic flow is also increased, being strongly dependent on strain rate (e.g., Zhou & He 2004).

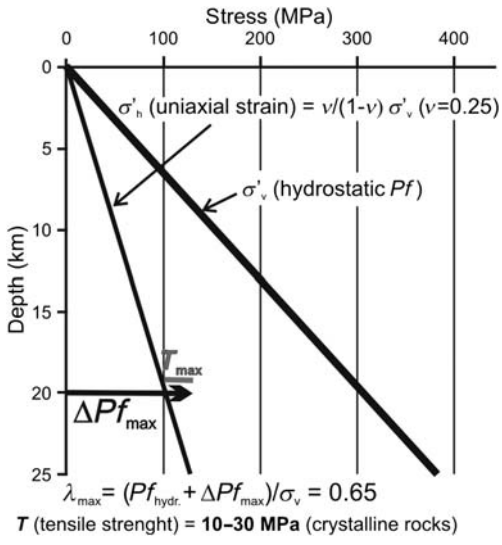

Fig. 7. Maximum sustainable pore-fluid pressure (*Pf*) in terms of pore-fluid factor (λ), estimated for uniaxial-strain state of stress. ν = Poisson's ratio; σ'_v = effective vertical stress for hydrostatic *Pf* ($Pf_{hydr.}$);σ'_h = effective horizontal stress for hydrostatic *Pf*; ΔPf_{max} = maximum possible increase in *Pf* from hydrostatic values. When ΔPf equals σ'_h plus the maximum tensile strength (T_{max} = 30 MPa), vertical hydraulic fractures might form and thereby determine a redistribution of *Pf*.

Exploring the role of high pore-fluid pressure and afterslip processes

There is an upper bound to the maximum possible sustainable *Pf* in the crust, such as the *Pf* able to produce vertical hydraulic extension fractures with consequent *Pf* redistribution. Under horizontal minimum principal stress (σ3), this condition is met for *Pf* equal to the σ3 plus the tensile strength of the rock (e.g., Sibson 2000 and references therein). The tectonic regime controls the maximum possible *Pf*, with highest values (up to lithostatic or supra-lithostatic) expected for thrust-faulting regimes (vertical σ3). Lithostatic *Pf* is unlikely for strike–slip and normal-faulting regimes (horizontal σ3); *Pf* higher than σ3 will produce vertical hydraulic fractures before reaching lithostatic values. The Potenza and Molise seismic areas are affected by strike–slip tectonic regime with horizontal σ3. The maximum sustainable *Pf* is difficult to assess because we do not know the absolute value of σ3. I estimated a probable minimum value of σ3 by calculating the horizontal stress due to the elastic response of the crust to the vertical lithostatic load under uniaxial strain conditions (σ_h in Fig. 7). The corresponding sustainable *Pf* was considered as the obtained σ3 plus the maximum tensile strength of the rock (T_{max} in Fig. 7). For the tensile strength, I used the values of crystalline rocks compiled by Lockner (1995) (10–30 MPa). The obtained value, in terms of pore-fluid factor (λ), is $\lambda = 0.65$ (Fig. 7). This must be considered as a minimum value, because it neglects the possible contribution of horizontal compression along the σ1 direction, which in turn produces an increase of σ3 due to plain strain.

Afterslip is a process which starts with the co-seismic faulting and lasts for several days during the post-seismic phase, decreasing progressively with time towards the long-term slip rates. In Figure 8, a typical afterslip curve (from Marone *et al.* 1991), together with the effect in terms of shear strain rate variations, is shown. The increase of strain rate, compared with the long term, is of one order of magnitude and is even more in the first days after the co-seismic phase. The afterslip effect on the rheology of the plastic layers embedding the seismogenic faults of the Potenza and Molise seismic areas (i.e., the Verrucano layer above and the ductile middle crust below) was estimated by increasing the long-term strain rate by one order of magnitude (from 1.2×10^{-14} s^{-1} to 1.2×10^{-13} s^{-1}).

The effects of high *Pf* and increased strain rate due to afterslip can probably be considered together only for the co-seismic and early post-seismic phases. In fact, co-seismic faulting might trigger a mechanism of *Pf* redistribution towards hydrostatic conditions during the post-seismic phase. Contemporaneously, the strain rate will decrease

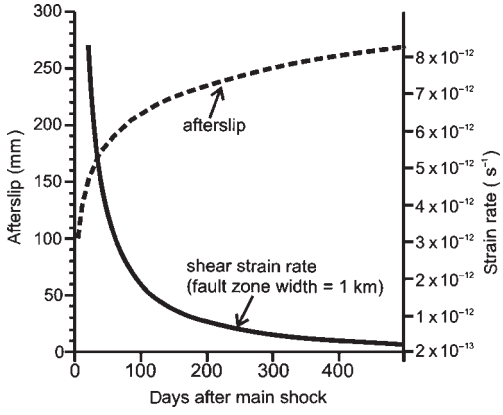

Fig. 8. Typical afterslip curve (from Marone *et al.* 1991 for the 1966 Parkfield earthquake at Parkfield City site) and associated strain rate variations. Strain rate was calculated as simple shear strain rate in a 1 km-wide fault zone.

towards the long-term values. The combined effects of high *Pf* and increased strain rate during the co-seismic and early post-seismic phases are illustrated in Figure 6. It seems reasonable that the combined effects on fault rheology can be compared with the time-duration of the aftershock activity, which covers the early post-seismic phase.

In the middle crust of the Potenza and Molise seismic areas (Fig. 6), high *Pf* ($\lambda = 0.65$) increases the maximum width of the brittle layer (dry rheology) by *c.* 2 km from *c.* 4 to *c.* 6 km in the Potenza area (Fig. 6a); from *c.* 6 to *c.* 8 km in the Molise area (Fig. 6b). The increased strain rate due to afterslip also produces a widening of the brittle layer which may occur both immediately above and below. Above, the Verrucano quartzites which are expected to flow plastically under long-term strain rates, become mostly brittle in the co-seismic and early post-seismic phases if dry rheology applies. The Verrucano remains mostly ductile if wet rheology applies. At the same time, the brittle–ductile transition within the middle crust for dry rheology deepens by 2–3 km. In the rheological model of Figure 6, the increase in strain rate was not extended upwards within the carbonates. Nevertheless, an increase in strain rate at the base of the carbonates does not change the fault zone rheology in the Potenza area where carbonates show low plastic strength due to high temperatures. In the Molise area, a propagation of the increased strain rate within the sediments may produce a transition from ductile to brittle behaviour.

The comparison between the depth-distribution of seismicity and the 'modified' strength envelope is much more satisfactory, if we consider dry rheology. In the Potenza area, the long-term (high *Pf*) brittle layer in the middle crust includes the focal depth of the main shock (Fig. 6a). The width of the brittle layer is *c.* 6 km, in agreement with the minimum value required for an $M = 5.7$ earthquake according to empirical relationships (5–6 km; Peruzza & Pace 2002). The thickened brittle layer due to afterslip processes includes most of the aftershocks. It is interesting to observe the striking correspondence between the upper bound of the major aftershock volume, at *c.* 15 km in the depth-histogram of Figure 6a, and the ductile layer at the base of the carbonate sedimentary cover. This reinforces the idea of an upper rheological boundary to seismogenic faulting represented by the deepest part of the carbonates, also during the co-seismic and early post-seismic phases. In the Molise area, the long-term (high *Pf*) brittle layer in the middle crust includes the focal depths of the main shocks (Fig. 6b). The width of the brittle layer is *c.* 8 km, compatible with $M = 5.7$ earthquakes. The thickened brittle layer due to afterslip processes includes most of the aftershocks. The upper bound of the major aftershock volume, at 9–10 km in the depth-histogram of Figure 6b lies within the sedimentary cover. This is mainly due to a geometrical effect related to the one-dimensional representation. Actually, the view in cross section (Fig. 3b) shows a westward deepening of the top of the aftershock volume, miming the westward deepening of the bottom of the Apulian carbonates. The major aftershock volume is mostly within the middle crust and within the Verrucano; only a few aftershocks are within the carbonate sedimentary cover. Therefore, also in the Molise area, there is suggestion that the deepest part of the carbonates is an upper rheological boundary to seismogenic faulting.

Discussion and conclusions

The rheological profiles used here are affected by a number of uncertainties including inherent assumptions of the method (e.g., constant strain rate), uncertainties on temperatures and uncertainties on rheological parameters (see Fernàndez & Ranalli 1997 for a discussion). A source of uncertainty is the applicability to large depths of the brittle strength predicted by the frictional failure law along pre-existing faults (also known as 'Byerlee's law'; Byerlee 1978), as well as the role of semi-brittle deformation in the transition zone to the ductile plastic flow (e.g., Kirby 1983; Carter & Tsenn 1987; Ord & Hobbs 1989; Kohlsted *et al.* 1995; Chester 1995; Scholz 2002, section 3.4). On the other hand, stress measurements and

experiments of fluid-induced seismicity in deep boreholes suggest that the Byerlee's law can be applied to great crustal depths with temperatures approaching the brittle–ductile transition (Zoback & Harjes 1997). Certainly, the brittle–ductile transition is a broad kilometre-scale transition zone and is not as sharp as the two-mechanism rheological model predicts. Therefore, strength envelopes provide only a first-order estimate of the strength and behaviour of the crust.

In addition, the computation of strength envelopes follows a static approach, while earthquakes are due to dynamic instabilities (Tse & Rice 1986; see also Scholz 1998 for a review). Strength envelopes cannot constrain the conditions for velocity-weakening unstable (seismogenic) faulting or velocity-strengthening stable-sliding (aseismic) faulting. Nevertheless, the frictional stability transition from velocity-weakening to velocity-strengthening occurring at high temperatures in the crust, such as that at the bottom of the seismogenic zone (lower stability transition), is controlled by the onset of intra-crystalline plasticity of the most ductile component. Therefore, a first-order convergence between the lower stability transition and the brittle–ductile transition from rheologic profiles can be reasonably expected. In the middle crust of the studied areas, a convergence is expected, if the lower stability transition is controlled mainly by the onset of plasticity of feldspars, which are the likely stress-supporting (strength-controlling) components of the Potenza–Molise middle crustal rocks, as inferred from seismic velocities (V_p between granodiorite and diorite).

In this work, first-order correspondence between strength envelopes and seismicity distribution is observed, especially if we consider dry rheology for the middle crust. Seismicity is unambiguously located in the upper part of the middle crust, just below the bottom of the sedimentary cover (Fig. 3). In more detail, the aftershocks concentrate mostly below the Verrucano layer. This is evident for the Potenza 1990 aftershocks. The relationships between the Verrucano and aftershock concentrations are less evident for the Molise sequence; nevertheless, the largest concentration of seismicity is certainly located below the Verrucano, also in the Molise area.

The strength envelopes predict a ductile behaviour of the lower part of the sedimentary cover due to the high-temperature low plastic flow strength of carbonates. The Verrucano layer is stronger than carbonates but is still mostly ductile due to the high-temperature low plastic flow strength of quartzites. The middle crust is stronger and is brittle in its upper portion, independently of the adopted friction parameters and *Pf*. Keeping in mind the limits of the approach, the aforementioned observations are sufficient to find the first-order correspondence between predicted rheology and seismicity.

The correspondence is striking if we modify the strength envelopes by introducing high *Pf* in the middle crust and a strain rate increase just above and below the seismogenic fault during the co-seismic and early post-seismic phases. Both modifications are justified by observations and therefore can be considered improvements of the model:

- High *Pf* is justified by the observed large degassing of CO_2 from the mantle with possible overpressurized reservoirs beneath the Apennines (Chiodini *et al.* 2004). The presence of abundant CO_2 within the crust might also justify why dry rheology for the middle crust provides better results than wet rheology. CO_2 may mix with water, reducing the activity of water in terms of hydrolytic weakening and determining an average flow strength that can be better approximated by experimental data on dry, rather than water-added, specimens.
- A lower frictional strength, possibly due to high *Pf*, is also inferred from the observation that both the Potenza and Molise main shocks showed stress drops lower than other Apennine earthquakes.
- The increased strain rate in the co-seismic and early post-seismic phases is motivated by the observation that we are analysing aftershock sequences which are related to short-term, relatively large displacement episodes. We are not analysing continuous back-ground seismicity probably associated with constant long-term tectonic processes. Large displacement episodes produce afterslip and strain rate increase in the plastic regions embedding the seismogenic fault. Aftershocks are post-seismic phenomena and are not necessarily located only within the fault portion ruptured by the main shock. Earthquake case studies show that aftershocks often concentrate beyond the rupture in zones of increased stress due to the co-seismic rupture (see Scholz 2002 for a review). Therefore, the comparison between crustal rheology and aftershock distribution is feasible if the rheology accounts for fault strength variations during the co-seismic and post-seismic phases.

The adopted values, in order to account for high *Pf* and increased strain rate ($\acute{\varepsilon}$), are $\lambda = 0.65$ and $\acute{\varepsilon} = 1.2 \times 10^{-13}\,\mathrm{s}^{-1}$ (one order of magnitude larger than the long-term strain rate). The used *Pf* is probably a lower estimate of the maximum sustainable *Pf* in a crust stressed by strike–slip tectonics (Fig. 7). In fact, in the central Apennines affected by extensional tectonics (where the

maximum sustainable *Pf* should be less than that expected for a strike–slip regime) fluid overpressures with λ up to 0.8 have been found (Collettini & Barchi 2002; Collettini *et al.* 2006). Also, the adopted increase in strain rate is probably a lower estimate (Fig. 8).

Although the adopted values are considered reasonable, the first-order overall effect of the 'model-improvement' is probably more important than the exact values to be used. The width of the brittle layer in the upper part of the middle crust, under high *Pf* and long-term strain rates, is consistent with the focal depths and magnitudes of the main shocks. The brittle layer widening during the co-seismic and early post-seismic phases due to the increased strain rate explain the width of the aftershock zone. Moreover, the increased strain rate does not significantly modify the rheologic control to the seismogenic faulting played by the ductile lower part of the carbonates (especially for the Potenza 1990 seismic sequence) and the ductile lower part of the middle crust. Obviously, I do not expect a perfect matching between the widened brittle layer and the width of the aftershock zone, or a higher concentration of aftershocks in the zone where the brittle layer widens. Brittle behaviour is viewed as a necessary but not sufficient condition for aftershock occurrence. We can have brittle behaviour but not aftershocks, for example because the afterslip does not propagate very far from the rupture. What is expected is that aftershocks lie mostly within the obtained brittle layer. The results are satisfactory from this point of view (compare Figs 3 & 6).

The results obtained in this work suggest that rheologic analysis might provide useful information on the first-order strength and likely seismogenic behaviour of the crust, provided that the rheological parameters can be constrained by geological–geophysical information.

Seismotectonic implications

Concerning the Potenza and Molise areas, rheological analysis and comparison with the seismic sequences give insights on a possible mechanical model for active crustal faulting within the Apulian crust. The model, illustrated in Figure 9, was built for the Potenza seismic area but can be exported also in the Molise area. To the east, the model was ideally extended to the Apulian foreland, where the only observable east–west-striking right-lateral active seismogenic fault of the Apulian crust crops out (the Mattinata fault in the Gargano promontory; Fig. 1). The crustal thickness of the Apulian foreland is constrained by the DSS profile (see location in Fig. 1), while the thickness of the brittle layer is constrained by a rheological profile built using the geotherm of Figure 4 (stable Apulian crust) and the same kinematic and

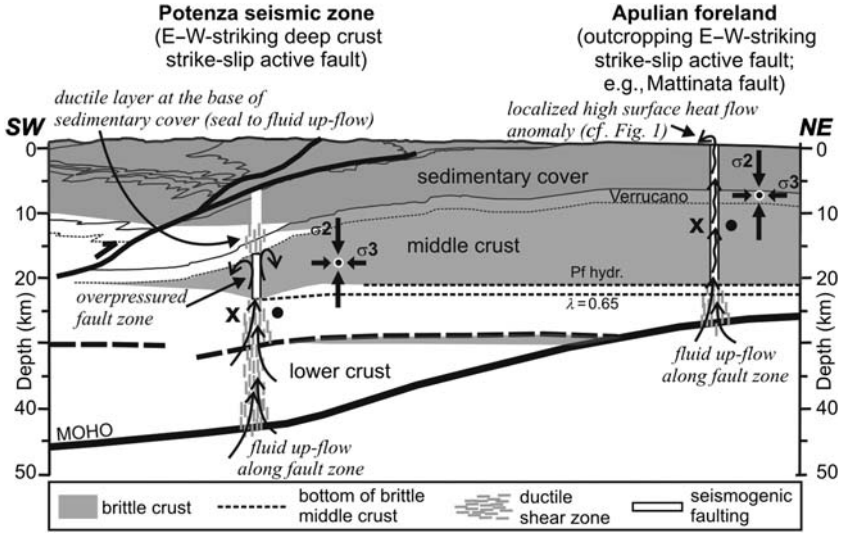

Fig. 9. Speculative model for active strike–slip faulting in the Potenza 1990 seismic area ideally extended to the east, up to the Apulian foreland. The western part of the model is applicable also to the Molise 2002 seismic area and in general to the western Apulian crust at the footwall of the eastern Apennine thrust system. The eastern part of the model is applicable to the Gargano promontory where an active E–W strike–slip fault crops out (Mattinata fault, see Fig. 1). The thickness of the brittle layer in the Apulian foreland was computed using the geotherm of the Apulian foreland (Fig. 4) and the same kinematic and rheologic parameters as the Potenza–Molise areas.

rheological parameters used for the Potenza and Molise fault zones.

In general, the western part of the model (Potenza seismic zone) is applicable to the Apulian crust at the footwall of the eastern Apennine thrust system, where the bottom of the carbonates is underthrusted to depths larger than *c.* 12 km. Below these depths, the carbonates are expected to flow plastically and represent a weak rheological layer. The model considers sub-vertical ancient east–west-striking fault zones of crustal (or possibly litospheric) scale inherited from previous tectonic phases, dislocated by the Apennine thrust, and reactivated under the present-day strike–slip tectonic regime. Fluids of mantle (e.g., CO_2) and deep crust origin are inferred to accumulate in the fault zones. In the Potenza seismic zone, the weak ductile layer at the base of carbonates (and possibly within the Verrucano) might represent a seal to fluid up-flow along the fault zone, favouring high *Pf* accumulation in the middle crust. Deep crust strike–slip seismicity of the Potenza and Molise areas can therefore be related to brittle faulting in the upper part of the middle crust, aided by high *Pf*. The width of the brittle seismogenic layer is variable; it depends on the amount of displacement along the Apennine thrust and on the relative position of the inherited fault zone at the footwall of the thrust. Across the Potenza seismic zone, the width of the brittle layer varies, increasing as we move from west to east. In this view, the occurrence of deep crust strike–slip events in the western Apulian crust (and possibly the maximum magnitude, if it is constrained by the width of the brittle layer) is strongly dependent on the local structural geology, the long-term rate of strain accumulation, and the rather unpredictable rate of fluid accumulation in the fault zone.

The absence of weak ductile layers sandwiched within the brittle upper part of the crust in the eastern Apulian foreland (eastern part of the model of Fig. 9), might be a less favourable condition for trapping overpressured fluids in the middle crust. Fluids of deep origin might reach the surface more easily along the brittle fault zone, producing localized anomalies of high surface heat flow such as that pointed out by Della Vedova *et al.* (2001) close to the outcropping active Mattinata strike–slip fault (heat flow up to 100 mW m^{-2}, Fig. 1). Contrary to the Potenza seismic zone, there are no particular rheological restrictions to the maximum width of the brittle layer (and possibly to the maximum width of the seismogenic faulting) in the Apulian foreland. The brittle layer extends with continuity from the surface to depths corresponding to the onset of ductile plastic flow in the middle crust (*c.* 21 km). Therefore, if a relationship exists between the maximum width of the seismogenic layer and the maximum earthquake rupture length (e.g., Peruzza & Pace 2002), there are no particular restrictions to the maximum expected magnitude except those imposed by the along-strike segmentation of the active fault.

I am grateful to G. Selvaggi (INGV, Rome), who kindly provided the hypocentral parameters of the Molise 2002 aftershocks. I am also grateful to C. Collettini, S. A. Miller and S. Barba for their helpful review of the paper, although I remain responsible for the views expressed here. This work was funded by the Italian Dipartimento della Protezione Civile in the frame of the 2004–2006 agreement with Istituto Nazionale di Geofisica e Vulcanologia (INGV) – Seismological Projects, Project S2, Research Unit S2/2.10 (resp. G. Lavecchia).

References

AMATO, A. & SELVAGGI, G. 1993. Aftershock location and P-velocity structure in the epicentral region of the 1980 Irpinia earthquake. *Annali di Geofisica*, **36**, 3–15.

AZZARA, R., BASILI, A., BERANZOLI, L., CHIARABBA, C., DI GIOVAMBATTISTA, R. & SELVAGGI, G. 1993. The seismic sequence of Potenza (May 1990). *Annali di Geofisica*, **36**, 237–243.

BERNARD, P. & ZOLLO, A. 1989. The Irpinia (Italy) 1980 earthquake: detailed analysis of a complex normal faulting. *Journal of Geophysical Research*, **94**, 1631–1647.

BONCIO, P., MANCINI, T., LAVECCHIA, G. & SELVAGGI, G. 2007. Seismotectonics of strike-slip earthquakes within the deep crust of southern Italy: geometry, kinematics, stress field and crustal rheology of the Potenza 1990–1991 seismic sequences (Mmax 5.7). *Tectonophysics*, **445**, 281–300.

BRACE, W. F. & KOHLSTEDT, D. L. 1980. Limits on lithospheric stress imposed by laboratory experiments. *Journal of Geophysical Research*, **85**, 6248–6252.

BYERLEE, J. D. 1978. Friction of rocks. *Pure and Applied Geophysics*, **116**, 615–626.

CARTER, N. L. & TSENN, M. C. 1987. Flow properties of continental lithosphere. *Tectonophysics*, **136**, 27–63.

CHESTER, F. M. 1995. A rheologic model for wet crust applied to strike–slip faults. *Journal of Geophysical Research*, **100**, 13 033–13 044.

CHIARABBA, C., DE GORI, P. *ET AL.* 2005*a*. Mainshocks and aftershocks of the 2002 Molise seismic sequence, southern Italy. *Journal of Seismology*, **9**, 487–494.

CHIARABBA, C., JOVANE, L. & DI STEFANO, R. 2005*b*. A new view of Italian seismicity using 20 years of instrumental recordings. *Tectonophysics*, **395**, 251–268.

CHIODINI, G., CARDELLINI, C., AMATO, A., BOSCHI, E., CALIRO, S., FRONDINI, F. & VENTURA, G. 2004. Carbon dioxide Earth degassing and seismogenesis in central and southern Italy. *Geophysical Research Letters*, **31**, doi:10.1029/2004GL019480.

CHIODINI, G., FRONDINI, F., CARDELLINI, C., PARELLO, F. & PERUZZI, L. 2000. Rate of diffuse carbon dioxide

Earth degassing estimated from carbon balance of regional aquifers: the case of central Apennines, Italy. *Journal of Geophysical Research*, **105**, 8423–8434.

CHRISTENSEN, N. I. & MOONEY, W. D. 1995. Seismic velocity structure and composition of the continental crust: a global view. *Journal of Geophysical Research*, **100**, 9761–9788.

COCCO, M., CHIARABBA, C. *ET AL*. 1999. The April 1996 Irpinia seismic sequence: evidence for fault interaction. *Journal of Seismology*, **3**, 105–117.

COLLETTINI, C. & BARCHI, M. R. 2002. A low-angle normal fault in the Umbria region (Central Italy): a mechanical model for the related microseismicity. *Tectonophysics*, **359**, 97–115.

COLLETTINI, C. & SIBSON, R. H. 2001. Normal faults, normal friction? *Geology*, **29**, 927–930.

COLLETTINI, C., DE PAOLA, N., HOLDSWORTH, R. E. & BARCHI, M. R. 2006. The development and behaviour of low-angle normal faults durino Cenozoic asymmetric extension in the Northern Apennines, Italy. *Journal of Structural Geology*, **28**, 333–352.

DELLA VEDOVA, B., BELLANI, S., PELLIS, G. & SQUARCI, P. 2001. Deep temperatures and surface heat flow distribution. *In*: VAI, G. B. & MARTINI, I. P. (eds) *Anatomy of an Orogen: the Apennines and Adjacent Mediterranean Basins*. Kluwer Academic, Dordrecht, 65–76.

DI BUCCI, D. & MAZZOLI, S. 2003. The October–November 2002 Molise seismic sequence (southern Italy): an expression of Adria intraplate deformation. *Journal of the Geological Society, London*, **160**, 503–506.

DRAGONI, M., DOGLIONI, C., MONGELLI, F. & ZITO, G. 1996. Evaluation of stress in two geodynamically different areas; stable foreland and extensional backarc. *Pure and Applied Geophysics*, **146**, 319–341.

EKSTROM, G. 1994. Telesismic analysis of the 1990 and 1991 earthquakes near Potenza. *Annali di Geofisica*, **37**, 1591–1599.

FERNÀNDEZ, M. & RANALLI, G. 1997. The role of rheology in extensional basin formation modelling. *Tectonophysics*, **282**, 129–145.

GOETZE, C. & EVANS, B. 1979. Stress and temperature in the bending lithosphere as constrained by experimental rock mechanics. *Geophysics Journal of the Royal Astronomy Society*, **59**, 463–478.

HANKS, T. C. 1977. Earthquake stress drops, ambient tectonic stresses and stresses that drive plate motion. *Pure and Applied Geophysics*, **115**, 441–458.

KIRBY, S. H. 1983. Rheology of the lithosphere. *Reviews of Geophysics and Space Physics*, **21**, 1458–1487.

KOHLSTEDT, D. L., EVANS, B. & MACKWELL, S. J. 1995. Strength of the lithosphere: constraints imposed by laboratory experiments. *Journal of Geophysical Research*, **100**, 17 587–17 602.

LOCKNER, D. A. 1995. Rock failure. *In*: *Rock Physics and Phase Relations: a Handbook of Physical Constants*. AGU Reference Shelf 3, 127–147.

LOCKNER, D. A. & BYERLEE, J. 1993. How geometrical constraints contribute to the weakeness of mature faults. *Nature*, **363**, 250–252.

MARONE, C., SCHOLZ, C. H. & BILHAM, R. 1991. On the mechanics of earthquake afterslip. *Journal of Geophysical Research*, **96**, 8441–8452.

MAZZOLI, S., CORRADO, S. *ET AL*. 2000. Time and space variability of 'thin-skinned' and 'thick-skinned' thrust tectonics in the Apennines (Italy). *Rendiconti Lincei, Scienze Fisiche e Naturali, 9 Series*, **11**, 5–39.

MENARDI NOGUERA, A. & REA, G. 2000. Deep structure of the Campanian–Lucanian arc (Southern Apennine, Italy). *Tectonophysics*, **324**, 239–265.

MILLER, S. A. 2002. Earthquake scaling and the strength of seismogenic faults. *Geophysical Research Letters*, **29**, doi:10.1029/2001GL014181.

MILLER, S. A., COLLETTINI, C., CHIARALUCE, L., COCCO, M., BARCHI, M. & KAUS, B. J. P. 2004. Aftershocks driven by a high-pressure CO_2 source at depth. *Nature*, **427**, 724–727.

MOLNAR, P., CHEN, W. P. & PADOVANI, E. 1983. Calculated temperatures in overthrust terrains and possible combinations of heat sources responsible for the tertiary granites in the greater Himalaya. *Journal of Geophysical Research*, **88**, 6415–6429.

NUR, A. & WALDER, J. 1990. Time-dependent hydraulics of the heart's crust. *In*: BREDEHOEFT, J. D. & NORTON, D. L. (eds) *The Role of Fluids in Crustal Processes*. National Academy Press, Washington, DC, 113–127.

ORD, A. & HOBBS, B. E. 1989. The strength of the continental crust, detachment zones and the development of plastic instabilities. *Tectonophysics*, **158**, 269–289.

PANTOSTI, D. & VALENSISE, G. 1990. Faulting mechanism and complexity of the 23 November, 1980, Campania–Lucania earthquake inferred form surface observations. *Journal of Geophysical Research*, **95**, 15319–15341.

PATACCA, E. & SCANDONE, P. 2001. Late thrust propagation and sedimentary response in the thrust–belt–foredeep system of the Southern Apennines (Pliocene-Pleistocene). *In*: VAI, G. B. & MARTINI, I. P. (eds) *Anatomy of an Orogen: the Apennines and Adjacent Mediterranean Basins*. Kluwer Academic, Dordrecht, 401–440.

PERUZZA, L. & PACE, B. 2002. Sensitivity analysis for seismic source characteristics to probabilistic seismic hazard assessment in central Apennines (Abruzzo area). *Bollettino di Geofisica Teorica ed Applicata*, **43**, 79–100.

PONZIANI, F., DE FRANCO, R., MINELLI, G., BIELLA, G., FEDERICO, C. & PIALLI,G. 1995. Crustal shortening and duplication of the Moho in the Northern Apennines; a view from seismic refraction data. *Tectonophysics*, **252**, 391–418.

RANALLI, G. 1995. *Rheology of the Earth*, 2nd edn. Chapman & Hall, London.

RANALLI, G. & MURPHY, D. C. 1987. Rheological stratification of the lithosphere. *Tectonophysics*, **132**, 281–295.

RICE, J. R. 1992. Fault stress states, pore pressure distributions, and the weakness of the San Andreas fault. *In*: EVANS, B. & WONG, T. F. (eds) *Fault Mechanics and Transport Properties of Rock*. Academic Press, London, 475–503.

ROVELLI, A., BONAMASSA, O., COCCO, M., DI BONA, M. & MAZZA, S. 1988. Scaling laws and spectral parameters of the ground motion in active extensional

areas in Italy. *Bulletin of the Seismology Society of America*, **78**, 530–560.

ROVELLI, A., CALDERONI, G., VALENSISE, G. & MILANA, G. 2004. Evidence for low stress drop during the October–November 2002 earthquakes in Molise, central–southern Italy, 23rd *G.N.G.T.S. National Conference*, Rome, 14–16 December 2004, extended abstract CD-ROM.

ROVELLI, A., COCCO, M., CONSOLE, R., ALESSANDRINI, B. & MAZZA, S. 1991. Ground motion waveforms and source spectral scaling from close-distance accelerograms in a compressional regime area (Friuli, Northeastern Italy). *Bulletin of the Seismology Society America*, **81**, 57–80.

RUTTER, E. H. 1974. The influence of temperature, strain rate and interstitial water in the experimental deformation of calcite rocks. *Tectonophysics*, **22**, 311–334.

SCARASCIA, S., LOZEJ, A. & CASSINIS, R. 1994. Crustal structures of the Ligurian, Tyrrhenian and Ionian seas and adjacent onshore areas interpreted from wide-angle seismic profiles. *Boll. Geofis. Teor. Appl.*, **36**, 5–19.

SCHMID, S., PATERSON, M. S. & BOLAND, J. N. 1980. High temperature flow and dynamic recrystallization in Carrara marble. *Tectonophysics*, **65**, 245–280.

SCHOLZ, C. H. 1998. Earthquakes and friction laws. *Nature* **391**, 37–42.

SCHOLZ, C. H. 2002. *The Mechanics of Earthquakes and Faulting* 2nd edn. Cambridge University Press, Cambridge.

SELVAGGI, G., FERULANO, F. *ET AL*. 2001. The M_w 5.4 Reggio Emilia 1996 earthquake: active compressional tectonics in the Po Plain, Italy. *Geophysics Journal International*. **144**, 1–13.

SIBSON, R. H. 1974. Frictional constraints on thrust, wrench and normal faults. *Nature*, **249**, 542–544.

SIBSON, R. H. 1982. Fault zone models, heat flow, and the depth distribution of earthquakes in the continental crust of the United States. *Bulletin of the Seismology Society of America*, **72**, 151–163.

SIBSON, R. H. 1983. Continental fault structure and the shallow earthquake source. *Journal of the Geological Society London*, **140**, 741–767.

SIBSON, R. H. 1990. Rupture nucleation on unfavorably oriented faults. *Bulletin of the Seismology Society of America*, **80**, 1580–1604.

SIBSON, R. H. 1998. Brittle failure mode plots for compressional and extensional tectonic regimes. *Journal of Structural Geology*, **20**, 655–660.

SIBSON, R. H. 2000. Tectonic controls on maximum sustainable overpressure: fluid redistribution from stress transitions. *Journal of Geochemical Exploration*, **69–70**, 471–475.

SIBSON, R. H. & XIE, G. 1998. Dip range for intracontinental reverse fault ruptures: truth not stranger than friction?. *Bulletin of the Seismology Society of America*, **88**, 1014–1022.

TONDI, E., PICCARDI, L., CACON, S., KONTNY, B. & CELLO, G. 2005. Structural and time constraints for dextral shear along the seismogenic Mattinata Fault (Gargano, southern Italy). *Journal of Geodynamics*, **40**, 134–152.

TSE, S. T. & RICE, J. R. 1986. Crustal earthquake instability in relation to the depth variation of frictional slip properties. *Journal of Geophysical Research*, **91**, 9452–9472.

TURCOTTE, D. L. & SCHUBERT, G. 2002. *Geodynamics*, 2nd edn. Cambridge University Press, Cambridge.

VALENSISE, G., PANTOSTI, D. & BASILI, R. 2004. Seismology and tectonic setting of the 2002 Molise, Italy, earthquake. *Earthquake Spectra*, **20**, S23–S37.

WELLS, D. L. & COPPERSMITH, K. J. 1994. New empirical relationships among magnitude, rupture length, rupture width, rupture area, and surface displacement. *Bulletin of the Seismology Society of America*, **84**, 974–1002.

WESTAWAY, R. & JACKSON, J. 1987. The earthquake of 1980 November 23 in Campania–Basilicata (southern Italy). *Geophysics Journal of the Royal Astronomy Society*, **90**, 375–443.

ZHOU, Y. & HE, C. 2004. Temporal evolution of focal depths of aftershock sequence following Lijiang Ms7.1 earthquake and the implication for rheological property of the middle crust. *The 3rd International Conference on Continental Earthquakes*, Beijing, Abstracts, 128.

ZOBACK, M. D. & HARJES, H- P. 1997. Injection-induced earthquakes and crustal stress at 9 km depth at the KTB deep drilling site, Germany. *Journal of Geophysics Research*, **102**, 18 477–18 491.

ZOBACK, M. D. & TOWNEND, J. 2001. Implications of hydrostatic pore pressures and high crustal strength for the deformation of intraplate lithosphere. *Tectonophysics*, **336**, 19–30.

Deformation partitioning within a sinistral transpression zone along the southwestern margin of the Tauern Window (eastern Alps)

ANDREAS WÖLFLER[1], ROBERT RABITSCH[2], HARALD FRITZ[3], HEIKO GAICH[2], WALTER KURZ[3] & ANGELIKA REITER[3]

[1]*University of Tübingen, Institute of Geosciences, Tübingen, Germany (e-mail: andreas.woelfler@uni-tuebingen.de)*

[2]*Graz University of Technology, Institute of Applied Geosciences, Graz, Austria*

[3]*University of Graz, Institute of Earth Sciences, Graz, Austria*

Abstract: This study is concerned with a newly recognized structure at the southwestern border of the Tauern Window and the neighbouring Austroalpine basement rocks, the Lappach Structure. Structural and isotopic investigations show that this structure is the result of sinistral transpression and backthrusting along the Austroalpine–Penninic contact. Deformation partitioning and differential exhumation of crustal wedges is documented by a succession of ductile and brittle deformation stages. Two stages are distinguished: (1) up-doming of Penninic units and associated advective heat transfer caused a strong temperature variation with the highest temperatures in central portions of the Tauern Window. Coeval transpression with distributed sinistral shear formed high-temperature, partly annealed fabrics in central portions and lower-temperature fabrics with strong crystallographic preferred orientation of quartz along the Tauern Window margin. Southward decrease of temperatures was matched by increases in stress and deformation intensity. (2) Progressive cooling was accompanied by shear localization, deformation partitioning and fluid infiltration. Overall sinistral shear resolved in a discrete strike slip–fault and south vergent folds with associated thrusts defining a backthrust zone along the southern Tauern margin. Southwards extrusion disturbed previously established palaeo-isograde and juxtaposed rocks from greater depths against lower-grade metamorphic units. Fluids penetrated faults, reduced shear strength and contributed to shear localization.

The southern margin of the Tauern Window represents one of the areas where a former plate boundary is exposed in the eastern Alps. It shows a complex structural and metamorphic evolution. After the subduction of both oceanic and continental Penninic domains beneath the Austroalpine upper plate, major exhumation-related displacement was localized along this margin by the formation of a shear belt between the southern part of the Tauern Window and the Periadriatic Fault (Fig. 1) (Ratschbacher *et al.* 1991; Kurz & Neubauer 1996; Lammerer & Weger 1998; Frisch *et al.* 2000). Relevant tectonic features within this domain include exhumation of Penninic units within the Tauern Window, transcurrent shear and vertical motion within the Austroalpine south to the Tauern Window, and intrusion of a chain of granitoides along this shear belt. In the central eastern Alps, models of slab break-off subsequent to underplating (Davis & von Blanckenburg 1995; von Blanckenburg & Davis 1996) and backthrusting of previously buried units along the Periadriatic Fault (Schmid *et al.* 1996; Castellarin *et al.* 2006; Kummerow *et al.* 2006; Lüschen *et al.* 2006; Millahn *et al.* 2006) have been proposed to explain this scenario. In contrast to the Swiss central Alps, the Penninic units are not directly in contact with the Southalpine units along the Periadriatic Fault in the Eastern Alps (Fig. 1). Instead, a sliver of Austroalpine units is squeezed in between the Tauern Window and the Periadriatic Fault, being strongly deformed during the Oligocene and showing heterogenous pre-Alpine and Alpine metamorphic overprint (Borsi *et al.* 1980). Alpine metamorphic overprint decreases from north to south within this wedge, suggesting different vertical displacement of distinct blocks (i.e., exhumation) separated by major faults (Borsi *et al.* 1973, 1978; Schulz 1994, 1997; Mancktelow *et al.* 2001; e.g., Defreggen–Antholz–Vals Fault; Fig. 2). Within the Tauern Window, mapped metamorphic isograde display a modal shape crossing lithological and tectonic boundaries with highest metamorphism in the central parts (Selverstone 1985). This opens questions about time relations between metamorphism and tectonics in the Tauern Window in relation to Austroalpine units, and on the structural evolution and architecture of this shear belt.

From: WIBBERLEY, C. A. J., KURZ, W., IMBER, J., HOLDSWORTH, R. E. & COLLETTINI, C. (eds) *The Internal Structure of Fault Zones: Implications for Mechanical and Fluid-Flow Properties*. **299**, 211–230.
DOI: 10.1144/SP299.13 0305-8719/08/$15.00

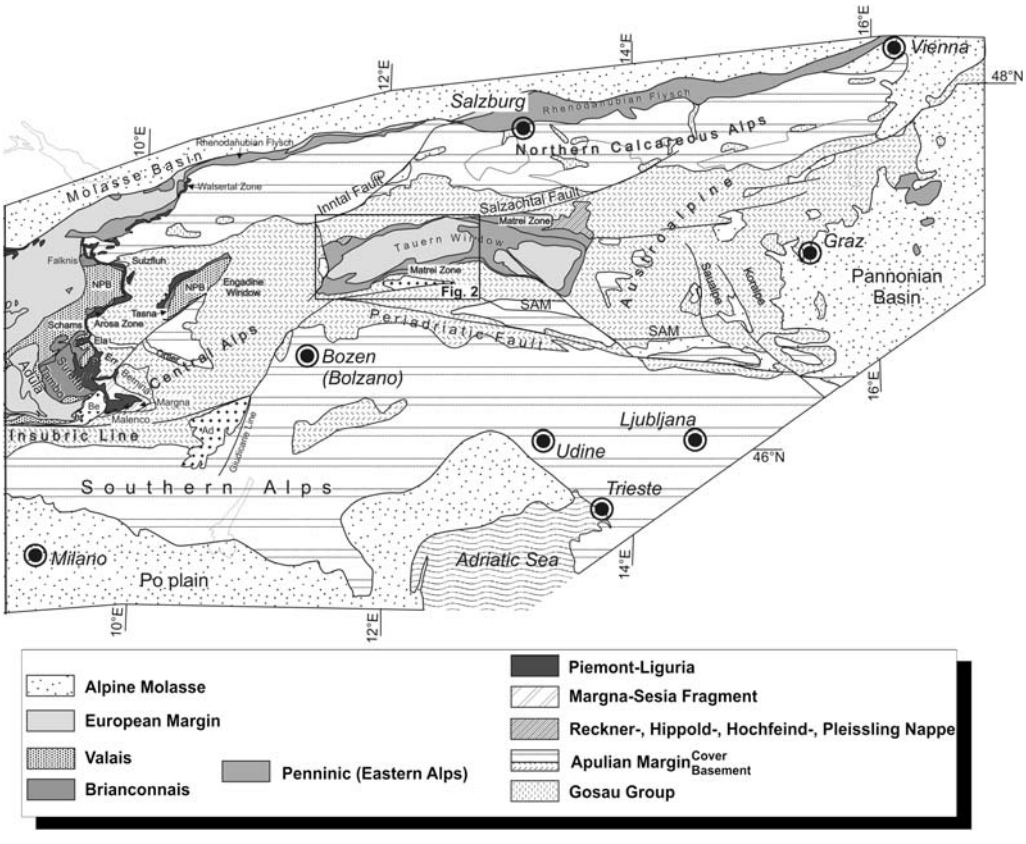

Fig. 1. Tectonic sketch map of the Eastern Alps showing the distribution of major structural units and their palaeographic origin (Ad, Adamello Pluton; Av, Avers Bündnerschiefer; Be, Bergell Pluton; NPB, North-Penninic Bündnerschiefer; P, Platta Nappe; S, Schober Group; Sieg, Sieggraben Unit; T, Texel Group). U-Ju, Upper Juvavic Nappes; SAM, Southern limit of Alpine Metamorphism (modified after Kurz & Froitzheim 2002).

To resolve this problem we focus on the structural and metamorphic evolution along the Tauern Window's southern margin. Possible gradients in thermal evolution, structural style, kinematics of successive events and differential stresses are elaborated along a section extending from the Austroalpine unit to the central Tauern Window.

Geological setting of the Tauern Window

The Alps (Fig. 1) are the result of the still ongoing convergence between Africa and Europe. Plate tectonic units involved in the Alpine orogen are the European continent, which is represented by the Helvetic Nappes, the External Massifs and part of the Penninic Nappes, two partly oceanic basins in the Penninic realm (Valais and Piemont-Liguria) and the Apulian (Adriatic) microcontinent including the Austroalpine and South Alpine units. The Valais and Piemont–Ligura basins probably merge into one single Penninic ocean in the Eastern Alps (e.g., Kurz 2006).

In the eastern Alps the tectonic units that originate from the Penninic domains are widely buried by the Austroalpine nappe complex. These Penninic units are only exposed within several tectonic windows exposed along the strike of the orogen. The Tauern Window represents the largest exposed section of Penninic units in the eastern Alps (Fig. 1). It constitutes an exhumed section of the Penninic nappe stack that developed in a collision zone subsequent to closure of the Penninic ocean in the Late Cretaceous and Paleogene. From base to top, the Penninic nappe stack includes (Kurz *et al.* 1998*b*, 2001*b*, *c* and references therein):

(1) The Venediger Nappe and the Wolfendorn Nappe comprise a pre-Variscan basement (e.g., Cliff 1981; Vavra & Frisch 1989; Frisch *et al.* 1993; Kebede *et al.* 2005) intruded

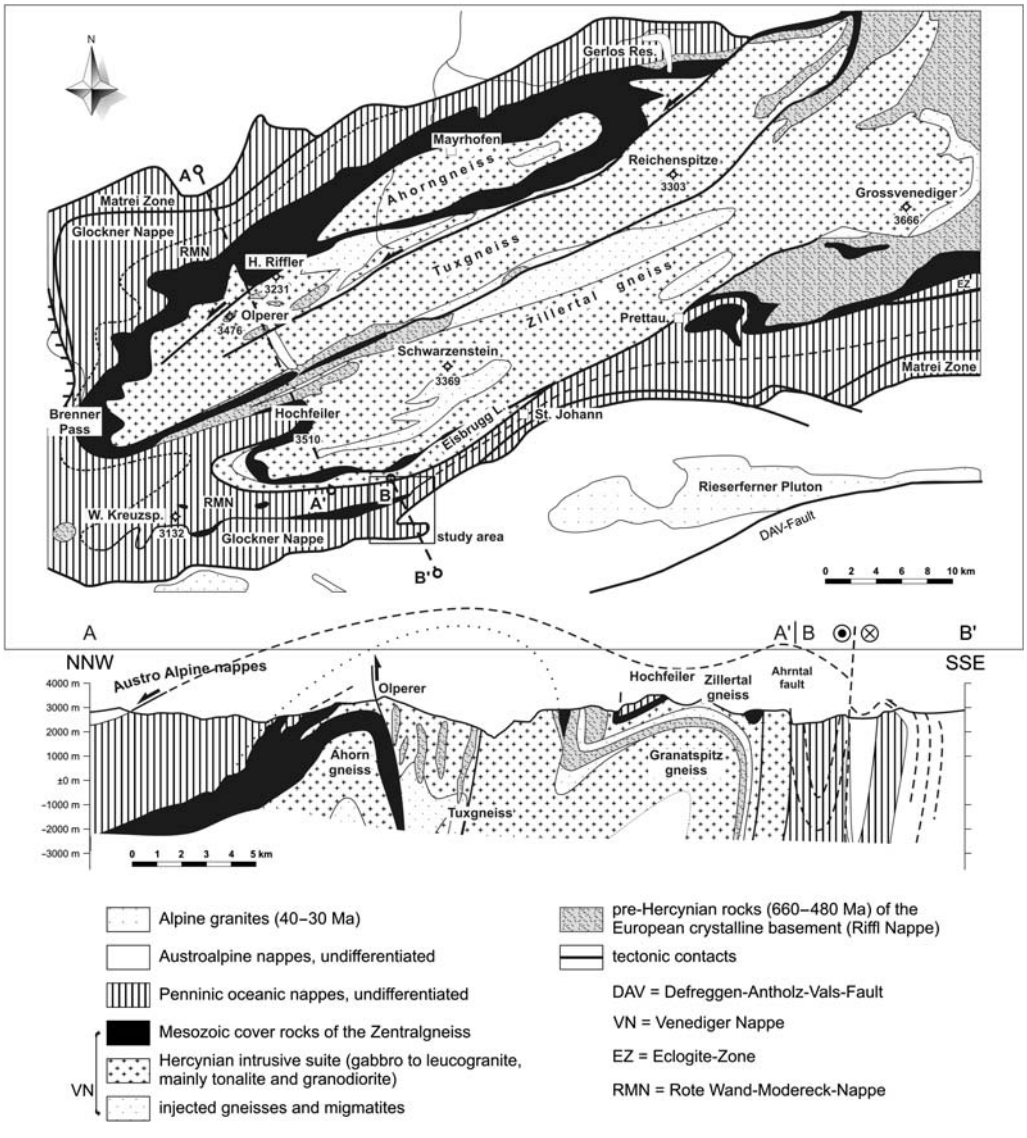

Fig. 2. (**a**) Geological map of the Western Tauern Window (modified after Lammerer & Weger 1998). The study area with the prominent 'Lappach structure' is shown in a box; (**b**) geological cross section through the western Tauern Window.

by Variscan granitoides (the 'Zentralgneis') with a cover sequence of Jurassic metacarbonates ('Hochstegen Marble Formation') and Cretaceous metapelites and metapsammites (Thiele 1970, 1974) ('Kaserer Group', with sedimentation up to Eocene; Frisch 1975, 1980, 1984; Lammerer 1988). The Wolfendorn Nappe is mainly a duplex of the Hochstegen Marble Formation and the Kaserer Group cover sequences, underlain by thin slices of former continental basement. The nature of the tectonic contact between the Venediger Nappe and the Riffl Nappe above (Fig. 2) is discussed controversially. It is interpreted as being related to the Variscan orogeny by Frisch (1977, 1980).

(2) The Storz Nappe comprises polymetamorphic basement rocks covered by metapelites and graphitic quartzites of the Murtörl Group, which was assumed to be of either late Paleozoic or, more likely, Cretaceous age.

(3) The Eclogite Zone is restricted to the central southern Tauern Window and is characterized by a Mesozoic volcano-sedimentary sequence of a distal continental slope that has experienced high-pressure metamorphism. The Eclogite Zone is tectonically positioned above the Venediger Nappe and is overlain by the Rote Wand–Modereck Nappe (Fig. 2). Where the Eclogite Zone is absent, however, the Rote Wand–Modereck Nappe is thrust directly onto the Venediger Nappe (Fig. 2a).

(4) The Rote Wand–Modereck Nappe is formed from basement rocks of the Rote Wand–Modereck Lamella, that is covered by Permian to Triassic quartzites, Triassic metacarbonates, Jurassic breccias, calcareous micaschists and metatuffs as well as Cretaceous metapelites and metapsammites.

(5) The Glockner Nappe comprises an oceanic basement made up of an incomplete ophiolitic sequence of serpentinites, ultramafic rocks, MORB-type metabasites (greenschists and amphibolites) of supposed Jurassic to Cretaceous age (Bickle & Pearce 1975; Höck & Miller 1980), covered or intercalated with a sequence of quartzites, micaceous calcitic marbles and calcareous schists ('Bündner Schiefer'). It is very important to note that the base of the Glockner Nappe is made up of former oceanic mantle lithosphere, while the cover sequences of all other nappes within the Tauern Window are underlain by continental basement. The separation of the Glockner Nappe from the Rote Wand–Modereck Nappe below is only possible where serpentinites and other remnants of former oceanic lithosphere occur within the metasediments.

(6) The Matrei Zone is interpreted to represent an accretionary wedge that is characterized by metamorphic flysch sediments (mainly calcareous and carbonate-free micaschists), breccias and olistolites, of Austroalpine and Penninic derivation (Frisch & Raab 1987).

Along its northern and southern margins, the Tauern Window is bordered by sinistral strike–slip faults, linked with several major dextral faults (Ratschbacher *et al.* 1991; Kurz *et al.* 1994; Wang & Neubauer 1998). Along its western and eastern margins it is bordered by low-angle normal faults (Selverstone 1988; Behrmann 1988, 1990, Genser & Neubauer 1989; Figs 1 & 2). The arrangement of these major faults was interpreted in terms of a pull-apart structure that triggered unroofing and subsequent exhumation of underplated Penninic lithosphere in the area of the Tauern Window (Genser & Neubauer 1989).

Generally, three major phases of deformation (D_1, D_2, D_3) are distinguished within the Penninic units of the Tauern Window (Bickle & Hawkesworth 1978; Droop 1981; Lammerer 1988; Behrmann 1990; Kurz & Neubauer 2006; Kurz *et al.* 1998*a*, *b*, 2000, 2001*b*, *c*). D_1 is related to the top-N emplacement of nappes, accompanied by the development of a foliation (S_1), and a north-trending stretching lineation (L_1). Distinct parts, in particular the Eclogite Zone and the southern parts of the Rote Wand–Modereck Nappe and the Glockner Nappe (Kurz and Froitzheim 2002; Kurz 2005), were affected by high-pressure (eclogite facies) metamorphism (M_{a1}) previous to their emplacement. D_2 is characterized by the development of a foliation S_2, and a W- to NW-trending stretching lineation L_2, being related to the emplacement of the Penninic nappe stack onto the European foreland (Kurz *et al.* 1998a). In particular, the western and southeastern parts of the Tauern Window have been pervasively affected by D_2; within the central part of the Tauern Window, D_1 fabrics are preserved. A phase of lower amphibolite to greenschist facies metamorphism (M_{a2}) (Tauern Crystallization), which was related to the thermal equilibration subsequent to the subduction of the Penninic units and collision with the Austroalpine unit, is documented subsequent to D_1. Locally, D_2 was contemporaneous with this metamorphic phase. Generally, the metamorphic grade decreases from the central parts (amphibolite facies) to the margins (greenschist facies) (Höck 1980; Droop 1985). D_3 is related to the formation of the dome structure of the Tauern Window. This D_3 phase is characterized by the interference of multiple structures, and by deformation partitioning and shear localization along the dome margins (Behrmann & Frisch 1990; Kurz & Neubauer 1996), accompanied by the development of a foliation S_3 and a subhorizontal west–east trending stretching lineation L_3. The exhumation history of the Penninic units is constrained by petrological and geochronological (Cliff *et al.* 1985; Droop 1985; Selverstone 1985, 1988, 1993; Christensen *et al.* 1994; Liu *et al.* 2001) and by structural data (Behrmann 1988; Genser & Neubauer 1989; Kurz & Neubauer 1996; Selverstone 1988).

Study area: southwestern Tauern Window and ajacent units

The western Tauern Window exposes the distinct 'Zentralgneis' domes separated by synforms containing pre-intrusive units (Fig. 2). These are covered by the Hochstegen Group (marble,

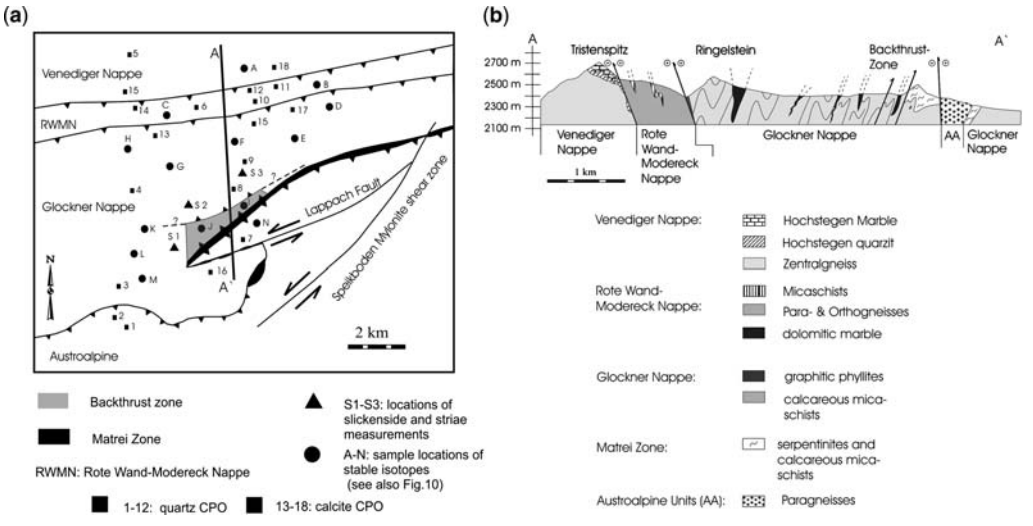

Fig. 3. (**a**) Simplified map of the study are with sample locations for isotope data, representative quartz- and calcite CPO shown in Fig. 8. (**b**) Structural cross section of the study area.

quartzite) and by the Kaserer Group, altogether forming the Venediger Nappe (Fig. 3). The Rote Wand–Modereck Nappe is defined by the basal Eisbrugg orthogneiss lamella (Lammerer *et al.* 1981) and by Permian to Triassic quartzites, meta-carbonates and schists. Calcareous micaschists, graphitic phyllites and meta-basaltic rocks of the Glockner Nappe overlie these units. The base of the Glockner Nappe contains slices of serpentinites, dolomites and local quartzites. The Penninic–Austroalpine boundary is marked by the stripe of the Matrei Zone that may be traced all along the Tauern Window south margin until it terminates in the study area at Lappach (Fig. 3). The Matrei Zone contains tectonically intercalated elements from the Glockner Nappe (serpentinites) and sediments probably derived from the Austroalpine (quartzite, metacarbonate, shale).

Southerly adjacent rocks from the Austroalpine plate contain paragneisses and amphibolites intruded by Ordovician orthogneisses (Borsi *et al.* 1973, Hammerschmidt 1981). In the study area all units trend west–east with lower tectonic units exposed in the north and higher tectonic units in the south (Fig. 3a, b).

In the study area (southwestern Tauern Window), the penetrative foliation is generally parallel to the tectonic boundaries separating Penninic nappes (Glockner Nappe, Rote Wand–Modereck Nappe, Venediger Nappe) and to the Penninic–Austroalpine boundary. The west–east trending foliation is generally sub-vertical, in parts steeply dipping to the north, the sub-horizontal stretching lineation trends west–east. The foliation, especially in the southern Glockner Nappe, is refolded along west–east trending fold axes associated with a steeply north dipping crenulation cleavage. This folding event refolds the Penninic–Austroalpine thrust contact arising in a unique map scale fold structure at the Tauern Window south margin, the Lappach structure (Fig. 3). Later semi-brittle shear zones and faults transect both the Austroalpine and the Penninic units. These include both, sinistral shear zones (Lappach Fault, Speikboden shear zone, dated *c*. 20 Ma: Müller *et al.* 2001) and north-dipping thrust faults with north-side-up displacement. Semi-brittle shear zones are highly fluid infiltrated as indicated by intense veining and precipitation of newly formed carbonate and quartz. We defined the zone of intense refolding and top south thrusting as backthrust zone (Fig. 3).

Metamorphic conditions are highly variable within the study area and reflect various increments of final Alpine collision. The Austroalpine block to the south of the Tauern Window shows decreasing Alpine metamorphic conditions from 400 to 450 °C in the north (Tauern Window margin) to temperatures below 300 °C in the south (Borsi *et al.* 1978). Boundaries between domains of distinct metamorphic conditions are represented by Oligocene to Miocene shear zones (Stöckhert 1984), namely the Defreggen–Antholz–Vals Fault (Fig. 2) and the Periadriatic Fault (Fig. 1). Thus, the metamorphic imprint is considered to be of pre- to syn-Oligocene age. North of the Defreggen–Antholz–Vals Fault cooling ages of white mica (Rb–Sr and K–Ar systems), which record cooling between *c*. 500 and 400 °C, cluster between 30 and

60 Ma (Borsi *et al.*, 1973, 1978; Satir 1976; Satir & Morteani 1982; von Blanckenburg & Davis 1995; Most 2003), whereas south of the Defreggen–Antholz–Vals Fault Variscan cooling ages are still preserved. These data document pronounced exhumation of domains to the north of the Defreggen–Antholz–Vals Fault.

Within the Tauern Window a metamorphic temperature peak, known as Tauern Metamorphic Event ('Tauern Crystallization') is dated around 30 Ma (Spear & Franz 1986; Dachs 1990; Kurz *et al.* 1999; Dachs & Proyer 2002; Glodny *et al.* 2005; Kebede *et al.* 2005). Cooling ages of the white mica system (Rb/Sr and K/Ar) range between 30 and 15 Ma (Stöckhert 1984). Palaeo-thermal isograds, mapped using oxygen isotope thermometry (Friedrichsen & Morteani 1979; Grundmann & Morteani 1985), show conditions of *c*. 400–500 °C along the Tauern Window's southern margin and steady temperature increase up to 650 °C in central portions of the Tauern Window. All these data support a north-side-up motion of blocks between faults dated *c*. 30 and 12 Ma (e.g., Periadriatic Fault, Defreggen–Antholz–Vals Fault, Tauern window margin and associated faults; Mancktelow *et al.* 2001; Müller *et al*. 2001).

Methods

Our approach intends to work out gradients in structural and metamorphic evolution along a section across a major shear zone by the combination of several techniques. The study of microstructures of quartz and calcite is aimed to document possible changes in deformation mechanisms that are known to be sensitive to temperature (Stipp *et al.* 2002) and strain rate (Hirth & Tullis 1992; Hirth *et al.* 2001). With studies upon these two minerals a wide range of syntectonic temperatures (200–700 °C) is covered. In addition, crystallographic preferred orientations (CPOs) provide information on intracrystalline gliding systems, being sensitive to temperature and strain rate as well, e.g., Tullis *et al.* (1973), Blacic (1975), Behrmann (1985), Price (1985), Platt & Behrmann (1986), Schmid & Casey (1986), Law (1987), Law *et al.* (1990) for quartz, Schmid *et al.* (1980, 1987), Wenk (1985), Wenk *et al.* (1987), Borradaille & McArthur (1990), and Burkhard (1993) for calcite. For quartz we followed the systematics given by Passchier & Trouw (1996) and Stipp *et al.* (2002); these are summarized in Figure 4. Accordingly, below *c*. 300 °C cataclasis and pressure solution are dominant. Between *c*. 300 and 400 °C bulging mechanisms (BG) are active followed by subgrain rotation mechanisms (SGR *c.* 400–500 °C). Grain boundary migration mechanisms (GBM *c*. 500–600 °C) are subdivided into a lower-temperature regime with bimodal amoeboid grains and a higher-temperature regime with unimodal polygonal grains. Above 600–650 °C, disc and chessboard quartz patterns are formed, and the increase in grain boundary area reduction (GBAR) mechanisms straightens grain boundaries (Hippert *et al.* 2001).

Deformation geometry and shear sense are deduced from CPOs following the methods described, for example, by Simpson & Schmid (1983), Ramsey & Huber (1983) and Bell & Johnson (1992). The CPOs described in this study where measured with the standard universal stage method.

Generally, calcite fabrics mainly reflect the final phases of crustal deformation under decreasing temperatures (e.g., Burkhard 1993). Therefore, palaeostress estimation using twinning fabrics of

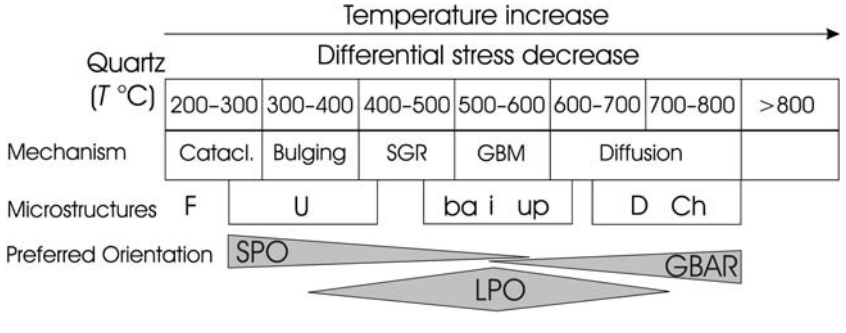

Fig. 4. Microstructures and rheological behaviour of quartz (modified after Fritz *et al.* 2005). F, fluid; U, undulatory extinction; ba, bimodal amoeboid; i, interlobate; up, unimodal polygonal; D, disc-shaped; Ch, chessboard pattern; SPO, shape preferred orientation; LPO, lattice preferred orientation; GBAR, grain boundary area reduction.

calcite was used to constrain the conditions during late-stage tectonic overprint. Since Turner (1953) it is known that the incidence of twin lamellae in calcite grains of marbles and limestones can be used to determine the magnitude of principal stresses that caused the deformation. By means of twin density per millimetre within calcite grains, it is possible to calculate differential stress that produced twinning (Rowe & Rutter 1990). These authors showed that the number of twins per millimetre is independent of grain size. The orientation of the maximum principal stress σ_1, from calcite twins and *c*-axes was evaluated using the method described by Dietrich & Song (1984). Slickenside and striae data for Paleostress orientation analyses were collected following the methods proposed by Angelier & Mechler (1977) and Angelier (1979), using a computer program developed by Wallbrecher & Unzog (2003).

The structural study is linked with stable isotope thermometry to constrain temperature conditions and possibly fluid mobility during deformation. Here, the uniform lithologies with calcareous micaschists hamper application of conventional thermobarometry. Therefore we expand previous studies on oxygen and carbon isotopes by Friedrichsen *et al.* (1973), Hoernes & Friedrichsen (1974), Schoell *et al.* (1975), Hoernes & Friedrichsen (1978), Friedrichsen & Morteani (1979) and Satir & Friedrichsen (1986). These authors attained *c*. 630 °C for the central Tauern Window and 400 °C for the margins of the Tauern Window. Rock samples with very similar bulk compositions containing approximately 60–80% calcite and 5–20% quartz and white mica were taken along a north–south profile (Fig. 3).

Mineral concentrates of muscovite and quartz were separated using conventional separation techniques including crushing, sieving, magnetic separating and finally hand-picking. X-ray runs and checking by optical microscopy were performed to guarantee 99% purification of concentrates. Calcite has been recognized as the sole carbonatic phase and has been measured as 'whole-rock concentrate'. This is justified because oxygen and carbon isotope extraction from calcite by reaction with 100% phosphoric acid (H_3PO_4) at 75 °C reaction temperature has no effect on isotope composition of silica phases.

Oxygen and carbon isotope ratios were measured in the isotope lab with a 'Delta-Plus' mass spectrometer equipped with a dual inlet system at the Institute of Earth Sciences, University of Graz. Isotope extraction of silicate was performed using an online laser fluorination system with BrF_5 as reactant (Sharp 1990). Isotope extraction from calcite was performed using the commercial 'Kiel II' system. From each individual mineral concentrate at least two aliquot grain fractions have been analysed (analytical errors of ± 0.2 δ‰ were allowed) and calibrated against NBS28 (quartz), NBS30 (biotite) and NBS18 (calcite) standards (IAEA). Data are displayed as $\delta^{18}O$ with respect to SMOW. From individual mineral pairs (quartz/muscovite, quartz/calcite, calcite/muscovite) the Δ-values (differences of δ values of relevant mineral pairs *x, y*) translate into apparent temperatures when fractionation coefficients are known (e.g., Cole & Ohmoto 1986).

$$\Delta_{(x-y)} \approx \frac{A \cdot 10^6}{T^2} + \frac{B \cdot 10^3}{T} + C.$$

For quartz/muscovite pairs we took the fractionation coefficients $A = 1.22$; $C = 0.11$ calibrated by O'Neil & Taylor (1969), and for quartz/calcite pairs ($A = 0.87$; $C = 0$) the calibration of Sharp & Kirschner (1994). This is justified because these fractionation coefficients have been calibrated for similar temperature regimes to the ones expected in the study area. For consistency calcite/muscovite fractionation coefficients ($A = 0.35$; $C = 0.11$) have been derived from the above-mentioned data sets.

Microstructures

We describe all data along a N–S section from the Venediger Nappe to the Austroalpine. A general scheme for the temperature- and differential-stress-dependent evolution of quartz microstructures is shown in Figure 4. A summary of all observed quartz microstructures in the study area is displayed in Figure 5.

Quartz

In the northern part of the study area polygonal quartz grains with highly mobile grain boundaries as result of grain boundary migration dominate the fabric. To a lesser extend subgrain rotation (SGR) as well as straight and high angle crystallographic grain boundaries as result of diffusion mechanism can be observed. Straight grain boundaries and partly 120° triple junctions point to a certain amount of grain boundary area reduction (Fig. 6a & b). These features suggest syntectonic temperatures exceeding 550 °C followed by static annealing, which is also documented by white mica overgrowing the penetrative foliation. In this area the quartz fabrics document that a main part of the deformation happened either at peak conditions, or subsequently at amphibolite facies metamorphic overprint. SGR and GBM are the main deformation mechanisms.

Quartz (*T* °C) — Temperature increase / Differential stress decrease

	200–300	300–400	400–500	500–600	600–700	700–800	>800	Recovery
	Cataclasis and Pressure solution	Bulging	SGR	GBM	Diffusion			
	Fluid F	Undulatory extinction U		(1) (2) (3)	Disc quartz D chessboard pattern Ch			T-Temperature > D-Deformation
1)AAU	XXX	XX						
2)GN	XXX	XX	XX					
3)RWMN		X	XXX	XXX (1) (2)	X			
4)VN			X	XXX (3)	XX			XX

AAU: Austroalpine Unit — RWMN: Rote Wand - Modereck Nappe — 1) bimodal amoeboid (ba) — 3) unimodal polygonal (up)
GN: Glockner Nappe — VD: Venediger Nappe — 2) interlobate
X - XXX: occurence and frequency of the observed deformation mechanism

Fig. 5. The variation of quartz microstructures along a north–south profile in the study area.

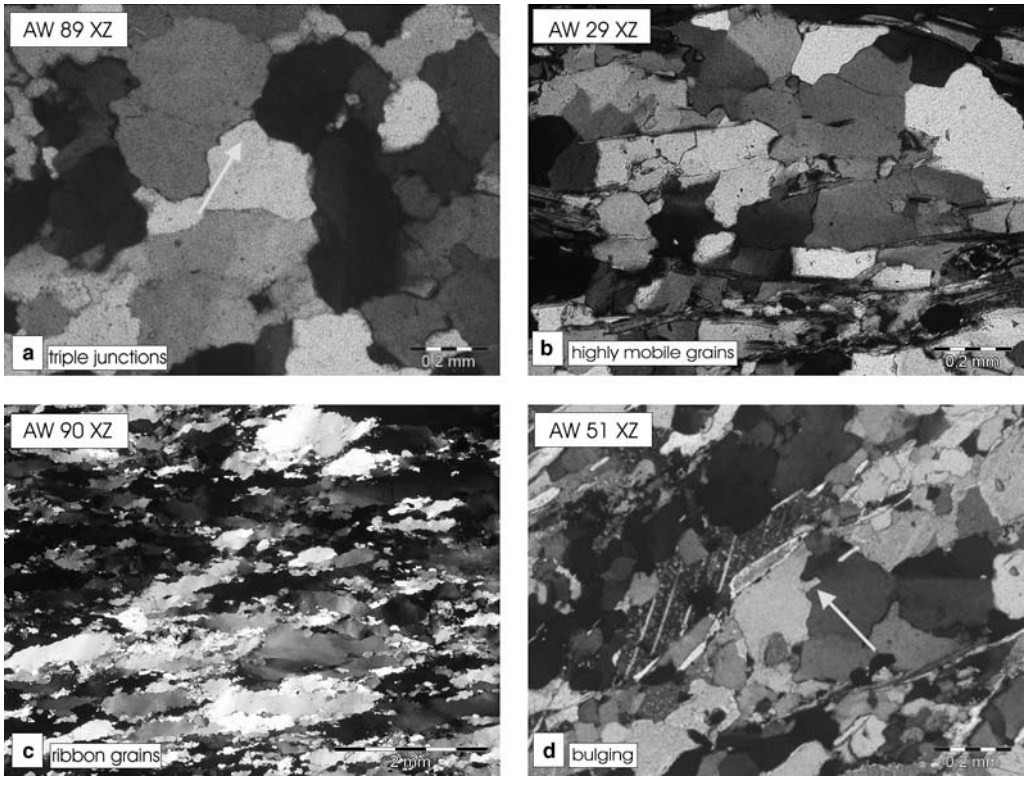

Fig. 6. Characteristic quartz microstructures of the study area. From north to south: (**a**) grains with mobile boundaries, partly forming triple junctions (arrow) from the Venediger Nappe of the study area. (**b**) Highly mobile quartz grains (GBM). (**c**) Strongly elongated grains with the formation of small subgrains and recrystallised grains (bulging) from the Glockner Nappe. (**d**) Bulging (arrow) and subgrain rotation are the main deformation mechanisms within the Glockner Nappe.

In the southern part quartz grains are highly elongated (Fig. 6c), forming shape oriented grains ($R_f > 10$, where R_f is the elliptic ratio of objects). These grains are characterized by undulatory extinction, the formation of small subgrains, deformation lamellae and deformation bands, and by sutured, lobate and bulged grain boundaries. The subgrains show undulatory extinction too. The deformation mechanism is dominated by bulging and SGR. Generally, the elongated grains are arranged subparallel to the penetrative foliation. In places, the elongated grains show a shape-preferred orientation oblique to the foliation documenting a top-to-the WSW simple shear component. Single dynamically recrystallized grains (grain size *c*. 0.05–0.1 mm) developed preferrently along the grain boundaries. A dramatic decrease of the grain size is documented due to secondary grain size reduction. Under decreasing temperatures, the plastic deformation of quartz grains ceased. Along the shear zones confining the Tauern Window a continuous transition from plastic to brittle fabrics including the development of cataclasites within quartz- and feldspar-rich rocks is documented. Quartz grains are affected by extensional cracks, which are filled mainly with calcite. Generally, the extensional cracks are oriented oblique to the penetrative foliation, indicating a simple shear component within the strike-slip faults. Bulging (Fig. 6d) and subgrain rotation dominate the processes of dynamic recrystallization.

Calcite

Two types of calcite microstructures can be distinguished in the study area. In the northern part (Fig. 7a), in addition to twinning mechanisms highly mobile grain boundaries are documented. Sometimes the grain boundaries meet in triple junctions. Grain size is variable and strongly depends on the presence of additional mineral phases, especially white mica and graphite that influence the size of recrystallized grains. Generally the grain size increases from S to N and reaches 1.5 mm, according to the general trend of increasing

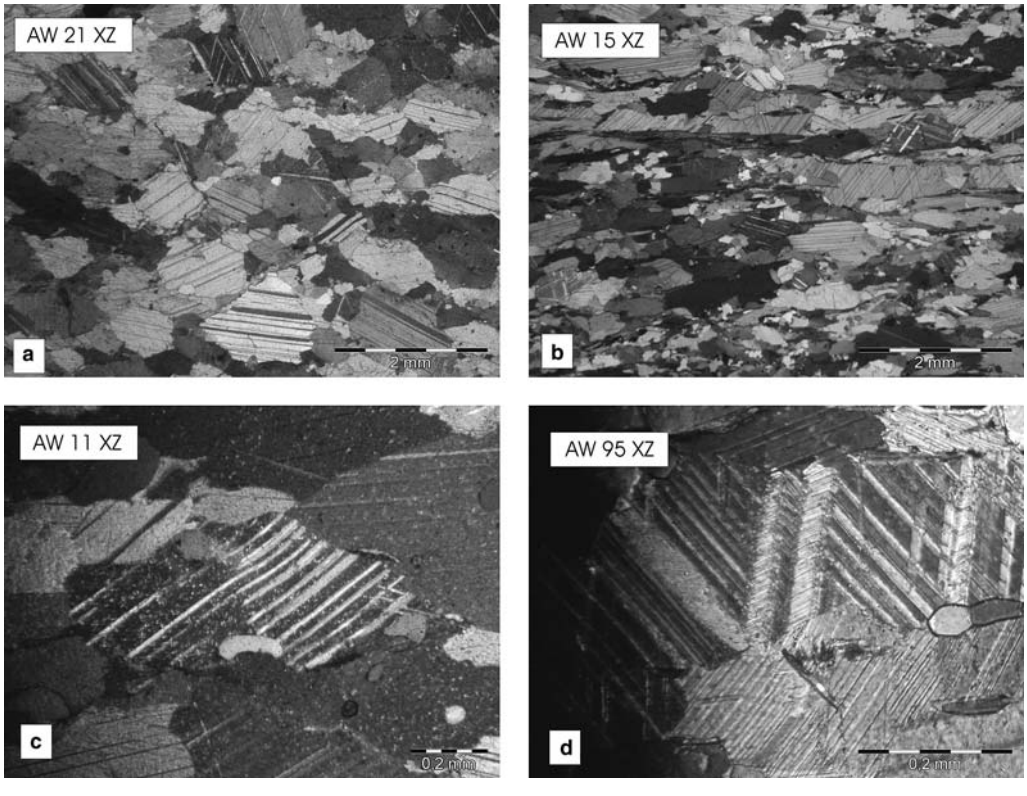

Fig. 7. Calcite microstructures. (**a**) Slightly elongated, twinned calcite grains from the Venediger Nappe with irregular, mobile grain boundaries. (**b**) Elongated calcite grains are typically for the southern part of the Glockner nappe. (**c**) Curved twins (Venediger Nappe), which are comparable to type 3 after Burkhard (1993). (**d**) Twin-formation within twins (Rote Wand–Modereck Nappe).

metamorphic grade. In the southern part calcite grains show either straight or slightly sutured boundaries. The grains are strongly elongated (R_f *c*. 5–8), and form a shape-preferred orientation either parallel or oblique to the S_2 foliation plane (Fig. 7b). In single domains the grains define a plane of mean elongation, which is slightly inclined (10–15°) to the mesoscopic foliation. However, the elongation of calcite grains is stronger near the margins of the Tauern Window (R_f 5–8; Fig. 7b) than within the northern part (R_f 1–3; Fig. 7a). By contrast to the northern portion, calcite microfabrics from the south are dominated by twinning. In order to build twin lamellae in calcite, differential stresses play an important role (Ferril 1991; Burkhard 1993). In addition the shapes of e-twin lamellae have been found to be temperature sensitive (Burkhard 1993).

The calcite grains show multiple sets of twins; however one set of e-twins, generally oriented subparallel to the S_2 foliation plane, dominates, especially along the margin of the Tauern Window. Most calcite twins show moderately thick-to-thick twins and straight lamellae, similar to the geometric types I and II described by Burkhard (1993). In general, twin widths are larger near the margins of the Tauern Window and decrease towards the northern part, from 0.2 to 0.1 mm. The grains in the northern part of the study area sometimes show curved twins and twins in twins, as a feature of polyphase twinning (Fig. 7c & d). Thus they can be compared with the types III and IV after Burkhard (1993).

Both quartz and calcite fabric display qualitatively increase of syntectonic temperature conditions towards North.

Crystallographic preferred orientation

Quartz

In the whole area (Figs 3 & 8) the quartz *c*-axes [001] are mainly characterized by single girdle distributions (Fig. 8). Remnants of asymmetric type I cross girdles occur especially in the north, with a trailing edge that is weakly developed. (Fig. 8, pole figures 5, 6, 9 & 10). In the northern part one cluster is often located within the *Y*-axis of the finite strain ellipsoid, and two clusters may be located between the *Y*- and *Z*-axes (Fig. 8, pole figures 11 & 12). One maximum can be observed around *Y* and a well-developed small circle is documented oblique to *Z*. However, towards the east the maximum around *Y* is more strongly pronounced, and only weakly pronounced remnants of former cross girdles have been observed. This seems to indicate a transitional fabric from type I cross girdles to single girdles and maxima around *Y* from the west to the east (Kurz *et al.* 2000, 2001*a*).

In the southern part of the study area quartz crystallographic preferred orientation (CPO) patterns show mainly maxima or small circle distribution around *Z* (Fig. 8, pole figures 1–4, 7 & 8). The asymmetry of the *c*-axes distributions indicates a top-WSW simple shear component. Generally, the degree of preferred orientation increases from north to south.

Calcite

Two types calcite CPOs can be distinguished in the entire study area. Following the systematics of Wenk *et al.* (1987), high-temperature *c*-axis distributions are restricted to the northern part of the study area, and low-temperature distributions can be found in the north and in the south of the study area (Fig. 8). The high-temperature fabrics generally show two maxima near *Z* with the tendency to be distributed along single girdles near the *Y*–*Z* plane of the finite strain ellipsoid. One maximum is centred near the *Z*-axis, two maxima are situated between the *Y*- and *Z*-axes of the finite strain ellipsoid (Fig. 8, pole figures 14 & 15). Generally the asymmetry ranges between 0 and 5°, which implies a higher pure shear component in the northern study area (Fig. 8, pole figures 13, 14, 15 & 18).

Calcite *c*-axes [001] from shear zones that are bordering the Tauern Window are characterized by clusters close to the *Z*–axis of the finite strain ellipsoid (Fig. 8, pole figures 13 & 16). Only in distinct domains are they asymmetrically arranged; however, the fabric asymmetry reaches 5° at maximum and documents a top-W sense of shear (Fig. 7c, pole figure 16).

In general, high-temperature CPOs are result of twinning and dynamic recrystallization (Fig. 7a), whereas low-temperature CPOs are the result of twinning (Fig. 7b–d).

Stress orientation from calcite twins

Movement on calcite twins can take place in only one direction (Passchier & Trouw 1996). Therefore the orientation of twins and crystallographic *c*-axes can give an impression of the orientation of principal shortening and extension directions. This orientation of the maximum principal axes σ_1, from calcite *c*-axes and twins, reflects the final increment of deformation within pure calcite samples (Dietrich & Song 1984). For this method only straight twins can be used, which restricts

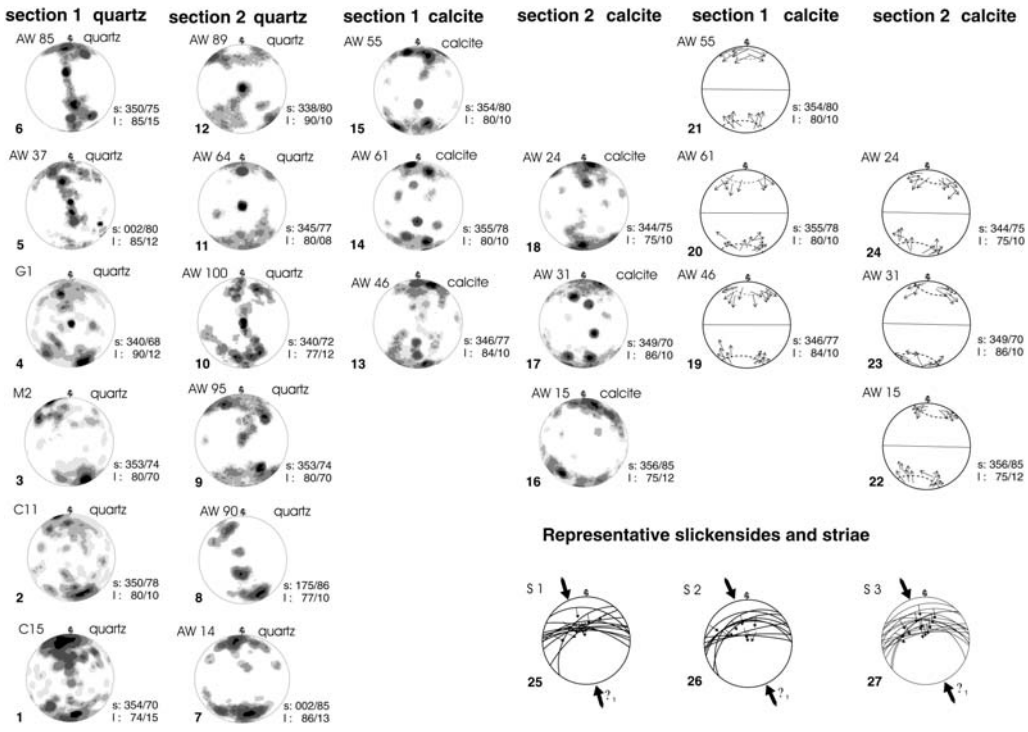

Fig. 8. Representative quartz and calcite CPOs along the southwestern margin of the Tauern Window, and the orientation of maximum principal stress from the orientation of e-twins and *c*-axes (pole figures 19–24; these pole figures correspond to the sample locations 13–18 for the calcite CPOs). S1–S3 show slickenside and striae, documenting brittle reverse faulting (all pole figures in lower hemisphere projection). For sample location see Figure 3a.

use of the method to low-temperature deformation. Thus we can observe NNE–SSW orientation of σ_1 during twinning (Fig. 8, pole figures 19–24).

Mesoscale structures

The tectonic structure of the study area is characterized by upright folds folding the penetrative foliation. The subhorizontal fold axis trends east–west (Fig. 3). Along the southern margin of the Tauern Window these folds are south-vergent and associated with an axial planar crenulation cleavage defined by reoriented mica. These south-vergent fold structures have been recognized by earlier authors (e.g., Lammerer 1988), but they have not been discussed in detail. A prominent sinstral shear deformation evolved especially along the southern margin of the Tauern window with a stretching lineation plunging gently 5–15° to the east. During progressive cooling, ductile to brittle fabrics evolved with north-side-up reverse faults that developed especially along limbs of south-vergent folds. The orientation of principal stress axes deduced from slickensides and striae of the reverse faults is shown in Fig. 8 (pole figures 25–27). These point to a subhorizontal NNW–SSE orientation of the principal stress σ_1. Thus, we conclude that late-stage exhumation and cooling resulted from combined left lateral shear, south-vergent folding and associated top south faulting juxtaposing Tauern window units against Austroalpine units.

Differential stress

By means of high-temperature deformation experiments on calcite rocks Rowe & Rutter (1990) have established empirical relationships between differential stress and twinning incidence. These authors show that a reasonable linear variation of stress (σ) with log twin density (D) is given by:

$$\sigma = -52.0 + 171.1 \log D.$$

The standard error value on stress determinations by the twin density method is about 43 MPa, at any stress level. Although this method has a high standard error we can observe a clear trend within the study area. The values range from 111 MPa in the northern part to 210 MPa to the south of the investigated profile (Fig. 9). This observation means an increase of differential stress and twin density per millimetre to the margin of the Tauern Window, which is bordered by strike–slip faults (Figs 2 & 3).

Isotope thermometry

Firstly we consider a hypothetical oxygen isotope variation within the three-phase system quartz–muscovite–calcite that is cooling from 600 °C downwards. We used the 'fast-grain-boundary' model (Eiler *et al.* 1994) with input parameters representative for rocks and conditions of the Glockner Nappe. Our program input includes a bulk volumetric rock composition with 65% calcite, 20% quartz and 15% white mica and the calculated bulk isotope composition of 19.95 ‰ as starting conditions before onset of cooling. A constant cooling rate from 600 to 200 °C within the last 30 Ma was assumed and the specific mineral geometries were implemented. We used diffusion coefficients published by Cole & Ohmoto (1986) and fractionation coefficients mentioned above. Use of the model allows estimation of cooling rates, which is beyond the scope of the paper. Instead we compare real and synthetic $\delta^{18}O$ data to better constrain plausibility of applied thermometers.

Model results (Fig. 10) show that the $\delta^{18}O$ trend of calcite shows minor variation with time because the system is largely calcite buffered (65%). Quartz with a tendency to accumulate heavy oxygen shows an increase of $\delta^{18}O$ with time, whereas $\delta^{18}O$ in muscovite decreases. In case of isotope equilibrium of all phases the three Δ-values (quartz–muscovite, quartz–calcite and muscovite–calcite) would translate into coherent apparent temperatures. In Figure 10 we draw a hypothetical scenario of disequilibrium where, at 15 Ma, past onset of cooling the calcite trend is modified. Infiltration of isotopically light, carbon-rich meteoric fluid and precipitation of young calcite would lower the $\delta^{18}O$ (calcite) values within a specific infiltration zone. As a result $\Delta^{18}O$ (muscovite/calcite) would decrease and $\Delta^{18}O$ (quartz–calcite) would increase and give meaningless apparent temperatures. However, $\Delta^{18}O$ values of the quartz/muscovite pairs are not influenced, still giving geologically meaningful temperatures.

This is considered as a realistic scenario for the Glockner Nappe. Individual samples show minor variation in $\Delta^{18}O$ of quartz–muscovite pairs but a very spiky pattern of $\Delta^{18}O$ quartz–calcite and muscovite–calcite pairs (Fig. 10a). Low $\Delta^{18}O$ (quartz–calcite) values correspond to high $\Delta^{18}O$ (muscovite–calcite) and vice versa, suggesting disequilibrium between silicates and calcite due to localized fluid infiltration. This is independently documented from studies on thin sections and cathodo-luminiscence images, where secondary calcite has been found along young shear zones and tension gashes.

From the three available thermometers only the quartz–mica one is considered reliable to document regional metamorphic conditions. In addition, sufficient isotope fractionation occurs even at relatively high temperatures to guarantee relatively small errors. All thermometers that involve calcite document variation in fluid species rather than regional metamorphic conditions and give, at least for the Glockner Nappe where secondary calcite is observed, meaningless apparent temperatures.

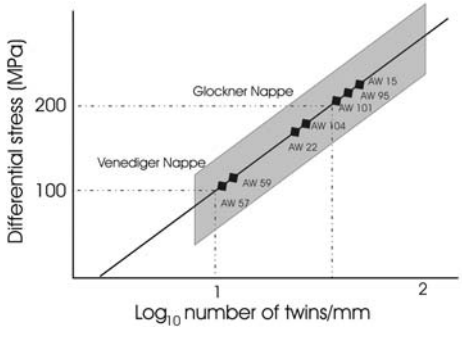

	Sample code	Twins/mm	σ (MPa)
VN	AW 57	9	111
VN	AW 59	11	129
RWMN	AW 22	21	175
RWMN	AW 104	25	187
GN	AW 101	31	204
GN	AW 95	34	210
GN	AW 15	30	200

Fig. 9. Plot of differential stress against log number of twins per mm. The trend line is defined by $\sigma = -52 + 171.1 \log D$, where D is the number of twins per millimetre. The grey box indicates the standard error of 43 MPa. For further explanations see text and Rowe & Rutter (1990). VN, Venediger Nappe; RWMN, Rote Wand–Modereck Nappe; GN, Glockner Nappe.

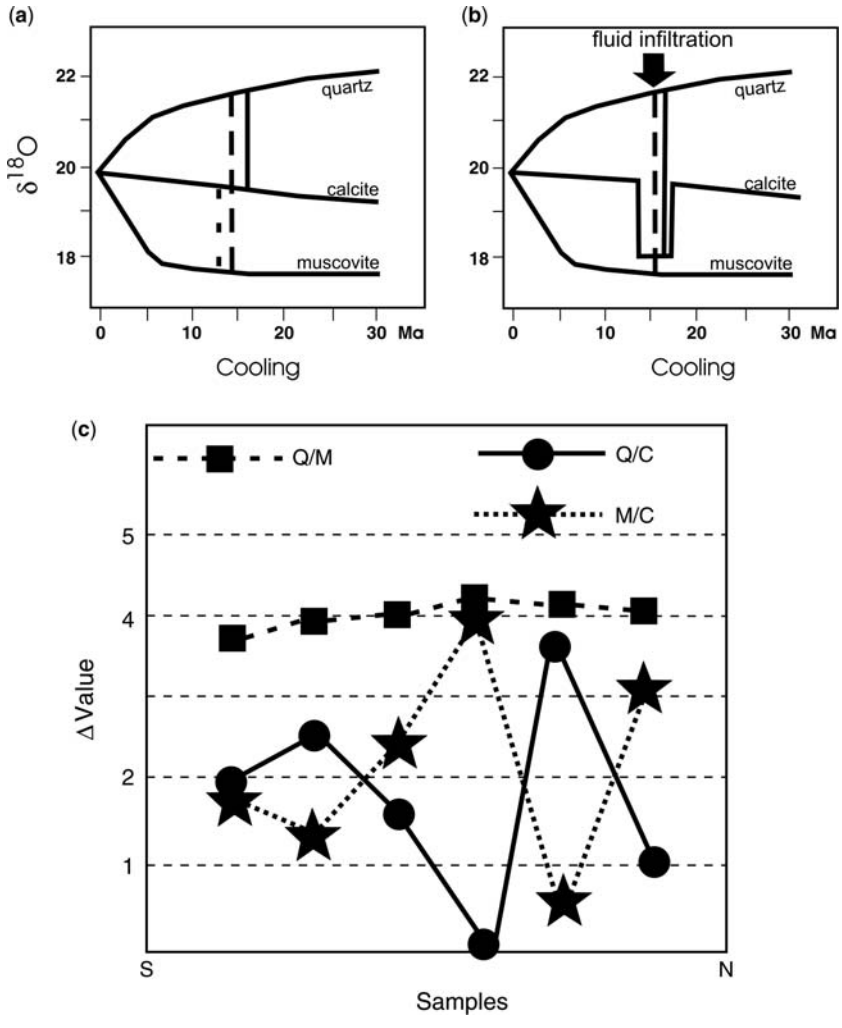

Fig. 10. (**a**) $\delta^{18}O$ time variations of quartz, calcite and muscovite; (**b**) infiltration of carbon-rich fluids will lead to lower $\delta^{18}O$ values of calcite; (**c**) $\Delta^{18}O$ values of mineral pairs. Abbreviations: A–N indicate the sample localities on Figure 3a.

Temperatures derived from quartz–muscovite pairs are plotted along a north–south profile crossing all major tectonic boundaries in the study area (Fig. 11). Temperatures derived from the quartz–calcite and muscovite–calcite thermometers are summary boxes with the intention to document the range of apparent temperatures in individual tectonic units. Consistent with previously published data (Grundmann & Morteani 1985; von Blanckenburg *et al.* 1989; Christensen *et al.* 1994) an increase in metamorphic conditions towards central portions of the Tauern Window is also seen in our quartz–muscovite data. We obtained *c*. 380 °C from the Glockner Nappe, around 480 °C from the Rote Wand Nappe and *c*. 540 °C from the base of the Venediger Nappe. Within the Rote Wand and Venediger Nappes the quartz–calcite and muscovite–calcite thermometers correspond well with data derived from the quartz–muscovite thermometer, suggesting minor fluid infiltration within those units. However, there is a zone of elevated temperatures at the southern margin of the Tauern Window, where we obtained 530–540 °C. These temperatures are unusually high and do not agree with published data (e.g., Grundmann & Morteani 1985; von Blanckenburg *et al.* 1989; Christensen *et al.* 1994).

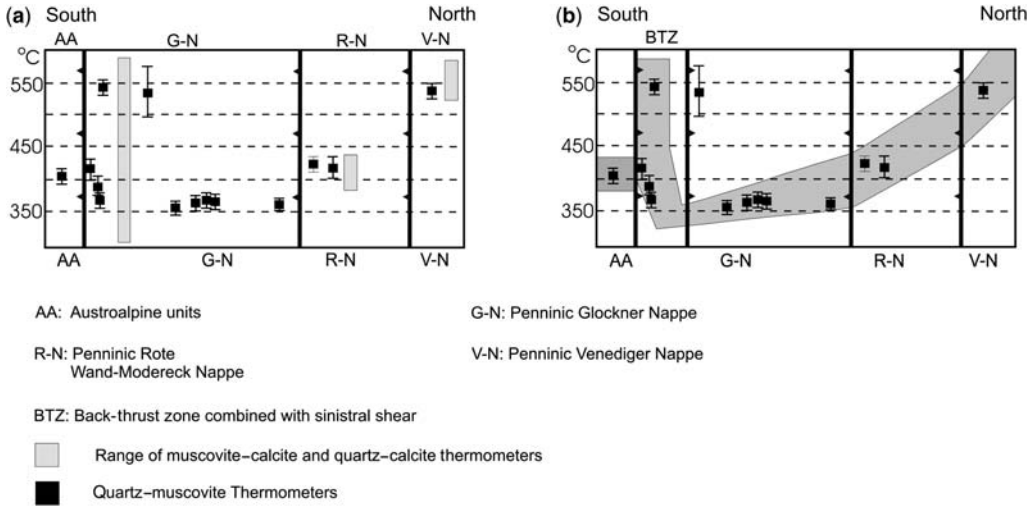

Fig. 11. (**a**) Temperatures gained from quartz/muscovite pairs along a south–north profile; quartz–calcite and muscovite–calcite are displayed in summary boxes (for detailed descriptions see text). (**b**) Temperatures from quartz–muscovite pairs show a zone of elevated temperatures at the southern margin of the Tauern Window. Sample N is derived from the same structural level further east and projected into the profile. For sample location see Figure 3a.

Summary and discussion

This study provides insight into the evolution of a major crustal shear belt that evolved along the former plate boundary between the Penninic lower plate and the Austroalpine upper plate. It documents structures related to exhumation of previously buried Penninic units and associated variations in temperature, stress and fluid infiltration as well as changing mechanical properties.

High-temperature and partly well-equilibrated microstructures and high-temperature CPO dominate the northern study area. Quartz *c*-axis patterns showing maxima in the *Y*-axis are restricted to the Venediger Nappe and the Rote Wand–Modereck Nappe in the north. This can be explained by the dominance of prism glide and is typical for high-grade metamorphic conditions (e.g., Schmid & Casey 1986). The kinematics derived from the external asymmetry shows sinistral strike–slip with a variable component of coaxial flow. Grain boundary area reduction was active, but temperatures of metamorphism were not high enough to erase the preferred orientation of the crystallographic axes. Therefore, we assume that the CPO were preserved or strengthened during subsequent thermal equilibration and static recrystallization (e.g., Schmid & Casey 1986).

Towards the south, decreasing temperature conditions are inferred from transition of rhomb slip to basal slip glide systems in quartz. Along the confining strike–slip faults bordering the Tauern Window, quartz grains are highly elongated, and show fabrics typical for low temperature dislocation creep. This agrees with quartz *c*-axes pattern maxima around *Z* interpreted as resulting from dominant basal glide. Continued deformation at decreasing temperatures is evident from transition to brittle deformation along localized very-low-grade shear zones and faults at the border of the Tauern Window. The kinematics of the ductile fabrics is sinistral, and brittle reverse faults display north-side-up kinematics.

Equilibrated calcite microstructures and symmetric CPOs seem to indicate a dominating flattening component in the northern part. High-temperature fabrics are restricted to the internal parts of the Venediger Nappe. However, calcite LPO textures are largely sensitive to temperatures below *c*. 350 °C (Wenk *et al.* 1987). Thus these textures may reflect a late-stage deformation increment that evolved during cooling of rocks. Low-temperature calcite forms the base of the Rote Wand–Modereck Nappe southwards. These CPOs show stronger asymmetry than those from the Venediger Nappe and are considered as a hint that high-temperature fabrics have been overprinted by subsequent sinistral shear. Temperature decrease from north to south is also supported from calcite twin geometries. Twinning is less evolved in the northern part; curved twins and bulged grain boundaries indicate that plasticity was an important

deformation mechanism. Most twins are thick (0.1–0.3 mm) and curved, and locally show twins in twins (polyphase twining), similar to type III after Burkhard (1993). Such fabrics are typical for synmetamorphic intracrystalline deformation (r- and f-glide). Approaching the margin of the Tauern Window, calcite microstructures are characterized by strong elongation and multiple twinning showing high finite strain at lower temperatures.

By means of twin density per millimetre within calcite grains, we can show an increase of differential stress from north (*c.* 100 MPa) to south (*c.* 200 MPa). Palaeostress orientations derived from the calcite twin geometry show roughly north–south maximum stress axes (Fig. 8) related to late stage deformation.

Summarizing trends from the structural data we conclude that:

(1) syndeformative temperatures generally decrease from north to south;
(2) static annealing is limited to the northernmost part;
(3) the non-coaxial component of flow increases from north to south;
(4) the differential stresses increase from north to south;
(5) the overall kinematics during ductile flow was sinistral strike–slip;
(6) late-stage deformation increments as deduced from calcite twins show north–south compressive stresses;
(7) localized brittle faults are limited to the Tauern Window border and show north-side-up reverse faulting.

Temperatures gained from isotopic equilibrium between muscovite–quartz pairs are in close coincidence with previous published data (Grundmann & Morteani 1985; von Blanckenburg *et al.* 1989; Christensen *et al.* 1994), documenting an increase in metamorphic conditions towards central portions of the Tauern Window. We obtained *c.* 550 °C for the Venediger Nappe, decreasing to *c.* 350 °C to the southern Glockner Nappe, which is in agreement with qualitative estimates from deformation mechanism and LPO patterns. However, there is a zone of elevated temperatures at the southern part of the Tauern Window where temperatures suddenly increase up to 550 °C. This zone corresponds with location of the fluid infiltrated low reverse faults where slivers of serpentinites bodies were exhumed (Fig. 12). This zone is also defined by isotopic disequilibrium inferred from calcite–muscovite and calcite–quartz pairs, suggesting enhanced infiltration of carbon-rich fluids. It is worth mentioning that the zone of brittle shearing and fluid infiltration are localized at the contact with mechanically strong serpentinites that were exhumed along this southern back thrust zone.

Our data document a succession of ductile and brittle deformation stages relevant for exhumation of the Tauern Window. Subsequent to thrusting of

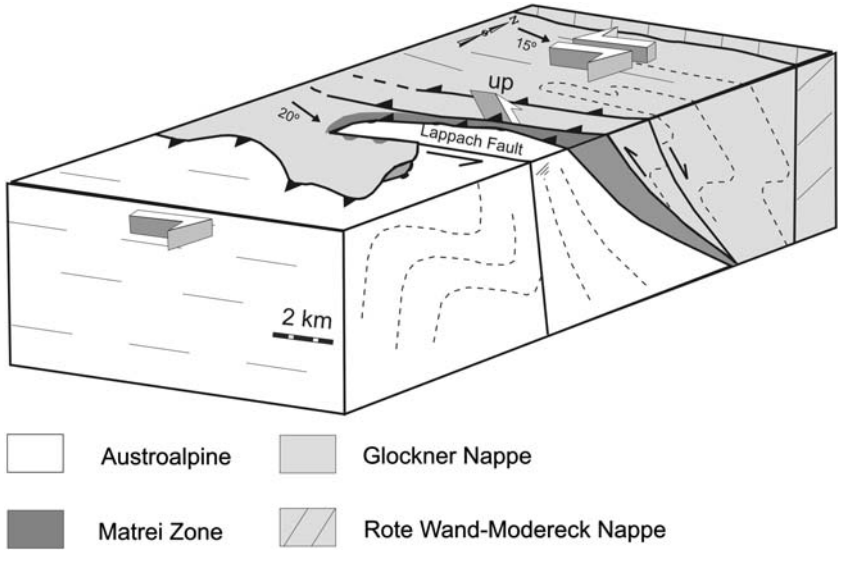

Fig. 12. Block diagram, showing the proposed model for left-lateral shear and oblique back-thrusting along the southwestern margin of the Tauern Window, resulting in the formation of the Lappach structure.

Austroalpine Nappes onto Penninic units and interal nappe stacking within the Tauern Window, the previously buried Penninic units were exhumed. Along the southern margin of the Tauern window and the adjacent Austroalpine, this period is characterized by a pronounced left lateral shear component. The sinistral DAV, numerous associated shear zones and a chain of syntectonic plutons evolved (Müller *et al.* 2001; Krenn *et al.* 2003; Rosenberg 2004). Within the southern part of the Tauern window left lateral shear is documented from our CPO patterns. Coeval advective heat transfer during early stages of exhumation caused the temperature variation within the Tauern window (Tauern metamorphic event) and the north–south temperature gradient as obtained from our data. Left lateral shear was largely coeval with metamorphism; static fabrics are only recorded from the northernmost portion where temperatures exceeded *c.* 550 °C. This stage may have been triggered by slab break-off (von Blanckenburg & Davis 1996). Late-stage rotation of the maximum principle stress σ_1 from NE to N goes along with further shortening by motion of the southalpine indenter. Especially in western sectors of the Tauern south margin where amount of shortening is highest southwards back-thrusting occurred (Fig. 12). Fault plane solution data sensitive to lowest temperatures document this latest increment. Brittle, highly fluid infiltrated zones evolved and northward-up reverse faulting displaced previously frozen metamorphic isograde. The jump in metamorphic grade between the juxtaposed rocks of the Glockner Nappe (540 °C) and the rocks of the Matrei Zone (400 °C) indicates approximately 5 km vertical displacement, assuming a geothermic gradient of 30 °C km^{-1}.

The complex geometry of the study area, i.e., the Lappach Fold structure, is the result of combined sinistral shear and back-thrusting, i.e., partitioning of transpressional deformation during the indentation of the Austroalpine crustal wedge (Fig. 12). Oblique shortening resulted in development of discrete shear zones and heterogeneous deformation along the boundaries of the upbending dome. This contrasts the internal high-grade domains of the Tauern window where distributed shear and homogenous deformation are observed. Thus, shear localization and displacement partitioning seem to be temperature-dependent, and consequently rheology-dependent. Discrete faults develop preferrently at low-temperature conditions and along domains of strong competence contrast. Partitioning of transpressional deformation can occur when stress is applied oblique to pre-existing zones of weakness (Jones & Tanner 1995). Zones of weakness include lithological contacts and rheological heterogeneities. The most pronounced rheology contrast occurs along the serpentinites of the Matrei zone that represent strong rigid bodies next to the metasediments of the Glockner Nappe where the vertical component of flow is highest. Here partitioned deformation released in a vertical component of flow, and associated faults enabled penetration of fluid phases. Fluids contribute themselves in reducing rock strength and a positive feedback cycle is installed.

A simple schematic model for the structural evolution of these shear zones is given in Figure 12. The formation of the Lappach structure results from south-vergent folding and faulting in connection with a synthetic sinistral Riedel shear of the Speikboden mylonite zone (Mancktelow *et al.* 2001) in the east of our study area. The Speikboden mylonite zone itself is discussed as a part of the Defreggen–Antholz–Vals Fault system, and acts as an antithetic Riedel to the Periadriatic Fault (Mancktelow *et al.* 2001).

Conclusions

Deformation partitioning is considered to be responsible for the formation of a transpressive wrench corridor (Lappach Structure) at the southwestern Penninic–Austroalpine border. Ductile folding and backfolding of Penninic units is related to nappe stacking and subsequent doming of the Tauern Window. This was coeval with oblique lateral displacement that continued during decreasing temperatures. Different rheological behaviour between the lithological units of the Matrei Zone and metasediments of the Glockner Nappe plays an important role in fault propagation. Therefore, deformation was continuously transferred into rheologically weak lithologies, especially carbonates. Associated fluid phases caused further reduction of rock strength. This resulted in strain localization with higher differential stress and higher finite strain within the shear zones. Furthermore a continuous transition of well-equilibrated microstructures from the inner parts of the Tauern Window to highly elongated fabrics to its margin documents an increase of deformation towards the Lappach Structure. However, there is a zone of elevated temperatures at the southern border of the Tauern Window. This zone is interpreted as a result of backthrusting of amphibolite facies rocks of the Glockner Nappe onto greenschist facies rocks of the Matrei Zone.

We appreciate discussions on the manuscript with C. Dekant and M. Daniší́k. Furthermore we gratefully acknowledge very careful reviews by F. Neubauer and N. Froitzheim.

References

ANGELIER, J. 1979. Determination of the mean principal direction of stresses for a given fault population. *Tectonophysics*, **56**, T17–T26.

ANGELIER, J. & MECHLER, P. 1977. Sur une methode graphique de rechereche des contraintes principles egalement utilisable en tectonique et en seismologie: la methode des diedre droits. *Bulletin de la Societe Geologique de France*, **19**, 1309–1318.

BEHRMANN, J. H. 1985. Crystal plasticity and super plasticity in quartzite: a natural example. *Tectonophysics*, **115**, 101–129.

BEHRMANN, J. H. 1988. Crustal-scale extension in a convergent orogen: the Sterzing–Steinach mylonite zone in the Eastern Alps. *Geodinamica Acta*, **2**, 63–73.

BEHRMANN, J. H. 1990. Zur Kinematik der Kontinentkollision in den Ostalpen. *Geotektonische Forschung*, **76**, 1–180.

BEHRMANN, J. H. & FRISCH, W. 1990. Sinistral ductile shearing associated with metamorphic decompression in the Tauern Window, Eastern Alps. *Jahrbuch der Geologischen Bundesanstalt*, **133**, 135–146.

BELL, T. H. & JOHNSON, S. E. 1992. Shear sense: a new approach that resolves conflicts between criteria in metamorphic rocks. *Journal of Metamorphic Geology*, **10**, 99–124.

BICKLE, M. J. & HAWKESWORTH, C. J. 1978. Deformation phases and the tectonic history of the Eastern Alps. *Geological Society of America Bulletin*, **89**, 293–306.

BICKLE, M. J. & PEARCE, J. A. 1975. Oceanic mafic rocks in the eastern Alps. *Contributions to Mineralogy and Petrology*, **49**, 177–189.

BLAGIC, J. D. 1975. Plastic deformation mechanisms in quartz: the effect of water. *Tectonophysics*, **27**, 271–294.

BORRADAILLE, G. J. & MCARTHUR, J. 1990. Experimental calcite fabrics in a synthetic weaker aggregate by coaxial and non-coaxial deformation. *Journal of Structural Geology*, **12**, 351–363.

BORSI, S., DEL MORO, A., SASSI, F. P. & ZIRPOLI, G. 1973. Metamorphic evolution of the Austridic rocks to the south of the Tauern Window (Eastern Alps). Radiometric and geologic data. *Memorie della Societá Geologica Italiana*, **12**, 549–571.

BORSI, S., DEL MORO, A., SASSI, F. P., ZANFERRARI, A. & ZIRPOLI, G. 1978. *New Geopetrologic and Radiometric Data on the Alpine History of the Austridic Continental Margin South of the Tauern Window.* Memorie di Szienze Geologiche, **32**.

BORSI, S., DEL MORO, A., SASSI, F. P., VISONA, D. & ZIRPOLI, G. 1980. On the existence of Hercynian aplites and pegmatites in the lower Autina Valley (Ahrntal, Austrides, Eastern Alps). *Neues Jahrbuch für Mineralogie. Monatshefte*, **11**, 501–514.

BURKHARD, M. 1993. Calcite twins, their geometry, appearance and significance as stress–strain markers and indicators of tectonic regime: a review. *Journal of Structural Geology*, **15**, 351–368.

CASTELLARIN, A., NICOLICH, R., FANTONI, R., CANTELLI, L., SELLA, M. & SELLI, L. 2006. Structure of the lithosphere beneath the Eastern Alps (southern sector of the TRANSALP transect). *Tectonophysics*, **414**, 259–282.

CHRISTENSEN, J. N., SELVERSTONE, J., ROSENFELD, J. L. & DEPAOLO, D. J. 1994. Correlation by Rb-Sr geochronology of garnet growth histories from different structural levels within the Tauern Window, Eastern Alps. *Contributions to Mineralogy and Petrology*, **118**, 1–112.

CLIFF, R. A. 1981. Pre-Alpine history of the Penninic zone in the Tauern Window, Austria: U–Pb and Rb–Sr geochronology. *Contributions to Mineralogy and Petrology*, **77**, 262–266.

CLIFF, R. A., DROOP, G. T. R. & REX, D. C. 1985. Alpine metamorphism in the south-east Tauern Window, Austria: II, heating, cooling and uplift rates. *Journal of Metamorphic Geology*, **3**, 403–415.

COLE, D. R. & OHMOTO, H. 1986. Kinetics of isotope exchange at elevated temperatures and pressures. *In*: VALLEY, J. W., TAYLOR, H. P., JR & O'NEIL, J. R. (eds) *Stable Isotopes in High Temperature Geological Processes.* Reviews in Mineralogy and Geochemistry, **16**, 41–90.

DACHS, E. 1990. Geothermobarometry in metasediments of the southern Grossvenediger area (Tauern Window, Austria). *Journal of Metamorphic Geology*, **8**, 217–230.

DACHS, E. & PROYER, A. 2002. Constraints on the duration of high-pressure metamorphism in the Tauern Window from diffusion modelling of discontinuous growth zones in eclogite garnet. *Journal of Metamorphic Geology*, **20**, 769–780.

DAVIS, J. H. & VON BLANCKENBURG, F. 1995. Slab breakoff; a model of lithosphere detachment and its test in the magmatism and deformation of collisional orogens. *Earth and Planetary Science Letters*, **129**, 85–102.

DIETRICH, D. & SONG, H. 1984. Calcite fabrics in a natural shear environment, the Helvetic nappes of western Switzerland. *Journal of Structural Geology*, **6**, 19–32.

DROOP, G. T. R. 1981. Alpine metamorphism of pelitic schists in the south-east Tauern Window, Austria. *Schweizer Mineralogische Petrologische Mitteilungen*, **61**, 237–273.

DROOP, G. T. R. 1985. Alpine metamorphism in the south-east Tauern Window, Austria: P-T variations in space and time. *Journal of Metamorphic Geology*, **3**, 371–402.

EILER, J. M., BAUMGARTNER, L. P. & VALLEY, J. W. 1994. Fast Grain Boundary: a Fortran-77 program for calculating the effects of retrograde interdiffusion of stable isotopes. *Computers & Geosciences*, **20**, 1415–1434.

FERRIL, D. A. 1991. Calcite twin width and intensities as metamorphic indicators in natural low-temperature deformation of limestone. *Journal of Structural Geology*, **13**, 667–675.

FRIEDRICHSEN, H. & MORTEANI, G. 1979. Oxygen and hydrogen isotope studies on minerals from Alpine fissures and their gneissic host rocks, Western Tauern Window (Austria). *Contributions to Mineralogy and Geology*, **70**, 149–152.

FRIEDRICHSEN, H., MÜLLER, G. & STAHL, W. 1973. Sauerstoff-isotopenuntersuchungen an Mineralen

eines Metamorphen Profils der Hohen Tauern, Österreich. *Contributions to Mineralogy and Petrology*, **40**, 159–168.

FRISCH, W. 1975. Ein Typ-Profil duch die Schieferhülle des Tauernfensters: Das Profil am Wolfendorn (westlicher Tuxer Hauptkamm, Tirol. *Verhandlungen der Geologischen Bundesanstalt*, **2–3**, 201–221.

FRISCH, W. 1977. Der alpidische Internbau der Venedigerdecke im westlichen Tauernfenster (Ostalpen). *Neues Jahrbuch für Geologie und Paläontologie, Monatshefte*, 675–696.

FRISCH, W. 1980. Tectonics of the western Tauern window. *Mitteilungen der Österreichischen Geologischen Gesellschaft*, **71/72**, 65–71.

FRISCH, W. 1984. Metamorphic history and geochemistry of a lowgrade amphibolite in the Kaserer Formation (Marginal Bündner Schiefer of the western Tauern Window, eastern Alps). *Schweizer Mineralogische und Petrographische Mitteilungen*, **64**, 193–214.

FRISCH, W. & RAAB, D. 1987. Early Paleozoic back-arc and island-arc settings in Greenstone sequences of the Central Tauern Window (Eastern Alps). *Jahrbuch der Geologischen Bundesanstalt*, **129**, 545–566.

FRISCH, W., DUNKL, I. & KUHLEMANN, J. 2000. Post-collisional orogen-parallel large-scale extension in the Eastern Alps. *Tectonophysics*, **327**, 239–265.

FRISCH, W., VAVRA, G. & WINKLER, M. 1993. Evolution of the Penninic basement of the eastern Alps. *In*: RAUMER, J. F. & VON NEUBAUER, F. (eds) *Pre-Mesozoic Geology in the Alps.* Springer, Berlin, 349–360.

FRITZ, H., TENCZER, V., HAUZENBERGER, C. A., WALLBRECHER, E., HOINKES, G., MUHONGO, S. & MOGESSIE, A. 2005. Central Tanzanian tectonic map: a step forward to decipher Proterocoic structural events in the East African Orogen. *Tectonics*, **24**, pTC6013.

GENSER, J. & NEUBAUER, F. 1989. Low angle normal faults at the eastern margin of the Tauern Window (Eastern Alps). *Mitteilungen der Österreichischen Geologischen Gesellschaft*, **81**, 233–243.

GLODNY, J., RING, U., KÜHN, A., GLEISSNER, P. & FRANZ, G. 2005. Crystallization and very rapid exhumation of the youngest Alpine eclogites (Tauern Window, Eastern Alps) from Rb/Sr mineral assemblage analysis. *Contributions to Mineralogy and Petrology*, **149**, 699–712.

GRUNDMANN, G. & MORTEANI, G. 1985. The young uplift and thermal history of the Central Eastern Alps (Austria/Italy), evidence from apatite fission track ages. *Jahrbuch der Geologischen Bundesanst (Wien)*, **128**, 197–216.

HAMMERSCHMIDT, K. 1981. Isotopengeologische Untersuchungen am Augengneis vom Typ Campo Tures bei Rein in Taufers, Südtirol. *Memoir of the Institute of Geology & Mineralogy, University of Padova*, **34**, 273–300.

HIPPERT, J. A., ROCHA, C., LANA, M., EGYDIO, S. & TAKESHITA, T. 2001. Quartz plastic segretation and ribbon development in high-grade striped gneisses. *Journal of Structural Geology*, **14**, 145–159.

HIRTH, G. & TULLIS, J. 1992. Dislocation creep regimes in quartz aggregates. *Journal of Structural Geology*, **14**, 145–159.

HIRTH, G., TEYSSIER, C. & DUNLAP, W. J. 2001. An evaluation of quartzite flow laws based on comparisons between experimentally and naturally deformed rocks. *International Journal of Earth Sciences*, **90**, 77–87.

HÖCK, V. 1980. Distribution maps of minerals of the Alpine metamorphism in the penninic Tauern Window. Austria. *Mitteilungen der Österreichischen Geologischen Gesellschaft*, **71/72**, 119–127.

HÖCK, V. & MILLER, C. 1980. Chemistry of mesozoic metabisites in the middle and eastern part of the Hohe Tauern. *Mitteilungen der Österreichischen Geologischen Gesellschaft*, **71/72**, 81–88.

HOERNES, S. & FRIEDRICHSEN, H. 1974. Oxygen isotope studies on metamorphic rocks of the Western Hohe Tauern area (Austria). *Schweizerische Mineralogische und Petrographische Mitteilungen*, **54**, 769–788.

HOERNES, S. & FRIEDRICHSEN, H. 1978. Oxygen and hydrogen study of the polymetamorphic area of the Northern Ötztal-Stubai Alps (Tyrol). *Contributions to Mineralogy and Petrology*, **67**, 305–315.

JONES, R. & TANNER, P. W. 1995. Strain partitioning in transpression zones. *Journal of Structural Geology*, **17**, 793–802.

KEBEDE, T., KLÖTZLI, U., KOSLER, J. & TORBJÖRN, S. 2005. Understanding the pre-Variscan and Variscan basement components of the central Tauern Window, Eastern Alps (Austria): constraints from single zircon U-Pb geochronology. *International Journal of Earth Sciences*, **94**, 336–353.

KRENN, K., FRITZ, H., BIERMEIER, CH. & SCHOLGER, R. 2003. The Oligocene Rensen Pluton (Eastern Alps, South Tyrol): magma emplacement and structures during plate convergence. *Mitteilungen der Österreichischen Geologischen Gesellschaft*, **94**, 9–26.

KUMMEROW, J. & KIND, R. & TRANSALP Working Group. 2006. Shear wave splitting in the Eastern Alps observed at the TRANSALP network. *Tectonophysics*, **414**, 117–127.

KURZ, W. 2005. Constriction during exhumation; evidence from eclogite microstructures. *Geology*, **33**, 37–40.

KURZ, W. 2006. Penninic Paleogeography from the Western toward the Eastern Alps – still open questions? *International Geology Review*, **48**, 996–1022.

KURZ, W. & FROITZHEIM, N. 2002. The exhumation of eclogite-facies metamorphic rocks; a review of models confronted with examples from the Alps. *International Geology Review*, **44**, 702–743.

KURZ, W. & NEUBAUER, F. 1996. Deformation partitioning and shear localization during the updoming of the Sonnblick area in the Tauern Window (Eastern Alps). *Journal of Structural Geology*, **18**, 1327–1343.

KURZ, W., NEUBAUER, F., GENSER, H. & HORNER, H. 1994. Sequence of Tertiary brittle deformations in the eastern Tauern Window (eastern Alps). *Mitteilungen der Österreichischen Geologischen Gesellschaft*, **86**, 153–164.

KURZ, W., NEUBAUER, F. & DACHS, E. 1998*a*. Eclogite meso- and microfabrics: implications for the burial and exhumation history of eclogites in the Tauern Window

(Eastern Alps) from P-T-d paths. *Tectonophysics*, **285**, 183–209.

KURZ, W., NEUBAUER, F., GENSER, J. & DACHS, E. 1998*b*. Alpine geodynamic evolution of passive and active continental margin sequences in the Tauern Window (Eastern Alps, Austria, Italy): a review. *Geologische Runschau*, **87**, 225–242.

KURZ, W., NEUBAUER, F. & UNZOG, W. 1999. Evolution of Alpine Eclogites in the Eastern Alps: implications for Alpine Geodynamics. *Physics, Chemistry and Earth Sciences (A)*, **24**, 667–674.

KURZ, W., NEUBAUER, F., UNZOG, W., GENSER, J. & WANG, X. 2000. Quartz, Dolomite and Calcite Microstructures and Textures within the Tauern Window (Eastern Alps). *Jahrbuch der Geologischen Bundesanstalt*, **142**, 33–71.

KURZ, W., NEUBAUER, F., UNZOG, W. & GENSER, J. 2001*a*. Evolution of quartz microstructures and textures during polyphase deformation within the Tauern Window (Eastern Alps). *International Journal of Earth Sciences*, **90**, 361–378.

KURZ, W., FRITZ, H., PILLER, W. E., NEUBAUER, F. & GENSER, J. 2001*b*. Overview of the Paleogene of the Eastern Alps. *In*: PILLER, W. E. & RASSER, M. (eds) *Paleogene of the Eastern Alps.* Schriftenreihe der Erdwissenschaftlichen Kommissionen, **14**, 11–56.

KURZ, W., NEUBAUER, F., GENSER, J., UNZOG, W. & DACHS, E. 2001*c*. Tectonic evolution of Penninic Units in the Tauern Window during the Paleogene; constraints from structural and metamorphic geology. *In*: PILLER, W. E. & RASSER, M. (eds) *Paleogene of the Eastern Alps.* Schriftenreihe der Erdwissenschaftlichen Kommissionen, **14**, 347–375.

LAMMERER, B. 1988. Thrust-regime and transpression-regime tectonics in the Tauern Window (Eastern Alps). *Geologische Rundschau*, **77**, 143–156.

LAMMERER, B. & WEGER, M. 1998. Footwall uplift in an orogenic wedge: the Tauern Window in the Eastern Alps of Europe. *Tectonophysics*, **285**, 213–230.

LAMMERER, B., SCHMIDT, K. & STADLER, R. 1981. Zur Stratigraphie und Genese der Penninischen Gesteine des südwestlichen Tauernfensters. *Neues Jahrbuch für Geologie und Paläontologie, Monatshefte*, 678–696.

LAW, R. D. 1987. Heterogeneous deformation and quartz crystallographic fabric transitions: natural examples from the Stack of Glencoul, northern Assynt. *Journal of Structural Geology*, **9**, 819–833.

LAW, R. D., SCHMID, S. M. & WHEELER, J. 1990. Simple shear deformation and quartz crystallographic fabrics: a possible natural example from the Torridon area of NW Scotland. *Journal of Structural Geology*, **12**, 29–45.

LÜSCHEN, E., BORRINI, D., GEBRANDE, H., LAMMERER, B., MILLAHN, K., NEUBAUER, F. & NICOLICH, R. & TRANSALP Working Group. 2006. TRANSALP-deep crustal Vibroseis and explosive seismic profiling in the Eastern Alps. *Tectonophysics*, **414**, 9–39.

MANCKTELOW, N. S., STÖCKLI, D. F., GROLLIMUND, B., MÜLLER, W., FÜGENSCHUH, B., VIOLA, G., SEWARD, D. & VILLA, I. M. 2001. The DAV and Periadriatic fault systems in the Eastern Alps south of the Tauern Window. *International Journal of Earth Sciences*, **90**, 593–622.

MILLAHN, K., LÜSCHEN, E. & GEBRANDE, H. & TRANSALP Working Group. 2006. TRANSALP-cross-line recording during the seismic reflection transect in the Eastern Alps. *Tectonophysics*, **414**, 39–51.

MOST, P. 2003. Late Alpine cooling histories of tectonic blocks along the central part of the TRANSALP-traverse (Inntal-Gardertal): constraints from geochronology. *Tübinger Geowissenschaftliche Arbeiten, Reihe A*, **67**, 1–97.

MÜLLER, W., PROSSER, G., MANCKTELOW, N. S., VILLA, J. M., KELLEY, S. P., VIOLA, G. & OBERLI, F. 2001. Geochronological constraints on the evolution of the Periadriatic Fault System (Alps). *International Journal of Earth Sciences*, **90**, 623–653.

O'NEIL, J. R. & TAYLOR, H.-P., JR. 1969. Oxygen isotope equilibrium between muscovite and water. *Journal of Geophysical Research*, **74**, 6012–6022.

PASSCHIER, C. W. & TROUW, R. A. J. 1996. *Microtectonics*. Springer, Berlin.

PLATT, J. P. & BEHRMANN, J. H. 1986. Structures and fabrics in crustal scale shear zone, Betic Cordillera, SE Spain. *Journal of Structural Geology*, **8**, 15–33.

PRICE, G. P. 1985. Preferred orientations in quarzites. *In*: WENK, H. R. (ed.) *Preferred Orientations in Deformed Metals and Rocks*. Academic Press, London, 385–405.

RAMSAY, J. G. & HUBER, M. I. 1983. *The Techniques of Modern Structural Geology – 1: Strain Analysis.* Academic Press, London.

RATSCHBACHER, L., FRISCH, W., LINZER, G. & MERLE, O. 1991. Lateral extrusion in the eastern Alps, part 2: structural analysis. *Tectonics*, **10**, 257–271.

ROSENBERG, C. L. 2004. Shear zones and magma ascent: a model based on a review of the Tertiary magmatism in the Alps. *Tectonics*, **23**, doi:10.1029/2003TC001526.

ROWE, K. J. & RUTTER, E. H. 1990. Paleostress estimation using calcite twinning: experimental calibration and application to nature. *Journal of Structural Geology*, **12**, 1–17.

SATIR, M. 1976. Rb-Sr- und K-Ar-Altersbestimmungen an Gesteinen und Mineralien des suedlichen Oetztalkristallins und der westlichen Hohen Tauern. *Geologische Rundschau*, **65**, 394–410.

SATIR, M. & FRIEDRICHSEN, H. 1986. Geochronological and stable investigations on polymetamorpic rocks from Eastern Alps (Western Tauern Window, Austria). *Neues Jahrbuch fuer Mineralogie. Abhandlungen*, **154**, 313–334.

SATIR, M. & MORTEANI, G. 1982. Petrological study and radiometric age determination of the migmatites in the Penninic rocks of the Zillertaler Alpen (Tyrol/Austria). *Tschermaks Mineralogische und Petrographische Mitteilungen*, **30**, 59–75.

SCHMID, S. M. & CASEY, M. 1986. Complete fabric analysis of some commonly observed quartz c-axis patterns. *In*: HOBBS, B. E. & HEARD, H. C. (eds) *Mineral and Rock Deformation: Laboratory Studies, The Paterson Volume.* American Geophysical Union, Geophysical Monographs, **36**, 263–286.

SCHMID, S. M., PANOZZO, R. & BAUER, S. 1987. Simple shear experiments on calcite rocks: rheology and microfabric. *Journal of Structural Geology*, **9**, 747–778.

SCHMID, S. M., PATERSON, M. S. & BOLAND, J. N. 1980. High temperature flow and dynamic recrystallisation in Carrara Marble. *Tectonophysics*, **65**, 245–280.

SCHMID, S. M., PFIFFNER, O. A., FROITZHEIM, N., SCHOENBORN, G. & KISSLING, E. 1996. Geophysical–geological transect and tectonic evolution of the Swiss–Italian Alps. *Tectonics*, **15**, 1036–1064.

SCHOELL, M., MORTEANI, G. & HÖRMANN, P. K. 1975. $^{18}O/^{16}O$ and $^{13}C/^{12}C$ ratios of carbonates from gneisses, serpentinites and marbels of the Zillertaler Alpen, Western Tauern area (Austria). *Neues Jahrbuch für Mineralogie. Monatshefte*, **10**, 444–459.

SCHULZ, B. 1994. Microstructural evolution of metapelites from the Austroalpine basement north of Staller Sattel during pre-Alpine and Alpine deformation and metamorphism (Eastern Tyrol, Austria). *Jahrbuch der Geologischen Bundesanstalt*, **137**, 197–212.

SCHULZ, B. 1997. Pre-Alpine tectonometamorphic evolution in the Austroalpine basement to the south of the central Tauern Window. *Schweizerische Mineralogische und Petrographische Mitteilungen*, **77**, 229–239.

SELVERSTONE, J. 1985. Petrologic constraints on imbrication, metamorphism, and uplift in the SW Tauern Window, Eastern Alps. *Tectonics*, **4**, 687–704.

SELVERSTONE, J. 1988. Evidence for east-west crustal extension in the Eastern Alps: Implications for unroofing of the Tauern Window. *Tectonics*, **7**, 87–105.

SHARP, Z. D. 1990. *In situ* microbe techniques for stable isotope analysis. *Chemical Geology*, **101**, 3–19.

SHARP, Z. D. & KIRSCHNER, D. L. 1994. Quartz–calcite oxygen isotope thermometry: a calibration based on natural isotopic variations. *Geochimica et Cosmochimica Acta*, **58**, 4491–4501.

SIMPSON, C. & SCHMID, S. M. 1983. An evaluation of criteria to deduce the sense of movements in sheared rocks. *Geological Society of America, Bulletin*, **94**, 1281–1288.

SPEAR, F. S. & FRANZ, G. 1986. P-T evolution of metasediments from the Eclogite Zone, south central Tauern Window, Austria. *Lithos*, 219–234.

STIPP, M., STÜNITZ, H., HEILBRONNER, R. & SCHMID, S. M. 2002. The eastern Tonale fault zone: a laboratory for crystal plastic deformation of quartz over a temperature range from 250 to 700 °C. *Journal of Structural Geology*, **24**, 1861–1884 .

STÖCKHERT, B. 1984. K-Ar determinations on muscovites and phengites from deformed pegmatites, and the minimum age of the old alpine deformation in the Austridic Basement to the south of the western Tauern Window (Ahrn valley, Southern Tyrol, Eastern Alps). *Neues Jahrbuch Mineralogische. Abhandlungen*, **150**, 103–120.

THIELE, O. 1970. Zur Stratigraphie und Tektonik der Schieferhülle der westlilchen Hohen Tauern (Zwischenbericht und Diskussion über Arbeiten auf Blatt Lanersbach, Tirol). *Verhandlungen der Geologischen Bundesanstalt*, **2**, 230–244.

THIELE, O. 1974. Tektonische Gliederung der Tauernschieferhülle zwischen Krimml und Mayrhofen. *Jahrbuch der Geologischen Bundesanstalt*, **117**, 55–74.

TULLIS, J., CHRISTIE, M. & GRIGGS, D. T. 1973. Microstructures and preferred orientations of experimentally deformed quartzites. *Geological Society of America, Bulletin*, **84**, 297–314.

TURNER, F. J. 1953. Nature and dynamic interpretation of deformation in calcite of three marbles. *American Journal of Science*, **251**, 276–298.

VAVRA, G. & FRISCH, W. 1989. Pre-variscan back-arc and island-arc magmatism in the Tauern Window (Eastern Alps). *Tectonophysics*, **169**, 271–280.

VON BLANCKENBURG, F. & DAVIS, J. H. 1995. Slab breakoff; a model for syncollisional magmatism and tectonics in the Alps. *Tectonics*, **14**, 120–131.

VON BLANCKENBURG, F. & DAVIS, J. H. 1996. Feasibility of double slab breakoff (Cretaceous and Tertiary) during the Alpine convergence. *Eclogae geologica Helvetica*, **89**, 111–127.

VON BLANCKENBURG, F., VILLA, I. M., BAUR, H., MORTEANI, G. & STEIGER, R. H. 1989. Time calibration of PT-path from the Western Tauern Window, Eastern Alps: the problem of closure temperatures. *Contributions to Mineralogy and Petrology*, **101**, 1–11.

WALLBRECHER, E. & Unzog W. 2003. *GEFÜGE 7: Ein Programmpaket zur Behandlung von Richtungsdaten*. University of Graz, Institute of Earth Sciences, Graz.

WANG, X. & NEUBAUER, F. 1998. Orogen parallel strike-slip faults bordering metamorphic core complexes; the Salzach–Enns fault zone in the Eastern Alps, Austria. *Journal of Structural Geology*, **20**, 799–818.

WENK, H.-R. 1985. *In*: WENK, H. R. (ed.) *Preferred Orientation in Deformed Metals and Rocks: An Introduction to Modern Texture Analysis.* Academic Press, London, 361–383.

WENK, H.-R., TAKESHITA, T., BECHLER, E., ERSINKE, B. G. & MATTHIES, S. 1987. Pure shear and simple shear calcite textures. Comparison of experimental, theoretical and natural data. *Journal of Structural Geology*, **12**, 731–745.

How can we improve estimates of bulk fault zone hydraulic properties?

REBECCA J. LUNN[1], ZOE K. SHIPTON[2] & AILEEN M. BRIGHT[3]

[1]*Department of Civil Engineering, University of Strathclyde, Glasgow G4 0NG, UK (e-mail: rebecca.lunn@strath.ac.uk)*

[2]*Department of Geological and Earth Sciences, University of Glasgow, Glasgow G12 8QQ, UK*

[3]*Department of Geology, Trinity College, Dublin, Dublin 2, Ireland*

Abstract: The fluid flow properties of faults are highly variable and spatially heterogeneous. We use numerical simulation of flow through field maps of detailed fault zone architecture to demonstrate that flow across the fault zone is controlled by connected high-permeability pathways, which are highly tortuous in mapped fault outcrops. Such small-scale, geometrically complex, fault zone architectural features can never be resolved for *subsurface* faults. Consequently, the key to prediction of subsurface bulk fault zone hydraulic properties is a statistical characterisation of the likelihood and frequency of such connected pathways. We demonstrate for a single architectural feature, the fault core, that thickness variation along strike can be well described by a spatially correlated random field with a spherical covariance structure. These data are from a single site in a specific lithology. To enable such statistics to be used to make predictions at other sites, a large number of similar datasets must be pooled. This will enable us to relate such spatial statistics to gross properties such as host rock lithology and fault throw, which are measurable for subsurface faults.

The bulk hydraulic behaviour of fault zones is difficult to predict, since faults frequently contain complex spatially varying patterns both of low- and high-permeability structures (Antonellini & Aydin 1995; Foxford *et al*. 1998; Knipe *et al.* 1998; Shipton & Cowie 2001; Jones & Hillis 2003). Faults can be barriers to flow, conduits, or combinations of the two, and their hydraulic properties vary considerably over both space and time (Hooper 1991; Fairley & Hinds 2004; do Nascimento *et al.* 2005). Fault zones can be defined by distinct architectural components: the majority of strain occurs within the fault core; strain is often further localized onto principal slip zone(s); the fault core is generally surrounded by a damage zone (Caine *et al.* 1996; Evans *et al.* 1997). Fluid flow through a fault zone is influenced by cross-fault juxtaposition of different lithologies, fault zone architecture and the intrinsic hydraulic properties of these fault zone architectural components. The hydraulic properties of the fault zone components vary considerably depending on the host lithology being deformed, the conditions of deformation, and the timing and chemistry of the fluid flow. For instance the damage zone in high-porosity rocks tends to be dominated by low-porosity deformation bands, whereas the damage zone in low-porosity rock tends to be dominated by open fractures (e.g., Johansen *et al.* 2005). Different fault rocks can be produced in the same host rock depending on the deformation mechanism active under different conditions (e.g., Knipe & Lloyd 1994; Bolton *et al.* 1998).

In this paper, we emphasize the importance of characterising *micro*, as opposed to *average*, fault hydraulic properties. Downey (1984) describes the influence of small-scale heterogeneity with reference to top seal in oil and gas reservoirs: 'the measured values from a random core sample, unfortunately, have little relevance to the problem of determining the weakest link point of the seal. Just as little comfort can be taken from a guarantee that your parachute will (on the average) open, explorationists are not really interested in the average properties of an enclosing sealing surface'. This discussion is equally applicable to the hydraulic properties of faults in general, where a small number of high-permeability pathways may control fluid flow (Evans *et al.* 2005). Further, the resolution limits on subsurface data mean that such pathways are unidentifiable.

In practice, the only data that are available to make predictions of fault flow in the subsurface are the fault throw distribution and the host rock properties. In the oil and gas industry these data come from three-dimensional seismic data and core or well-log data. Additional data such as pore pressure distribution and hydrocarbon column

From: WIBBERLEY, C. A. J., KURZ, W., IMBER, J., HOLDSWORTH, R. E. & COLLETTINI, C. (eds) *The Internal Structure of Fault Zones: Implications for Mechanical and Fluid-Flow Properties*. **299**, 231–237.
DOI: 10.1144/SP299.14 0305-8719/08/$15.00

height give information on the fault properties (e.g., Bretan *et al.* 2003). There are currently no foreseeable technological advances that will substantially increase the resolution of these data. Throw and host rock property data are already used in algorithms for predicting the percentage clay in the fault gouge, which can be related to fault seal potential (see review in Clarke *et al.* 2005; Manzocchi *et al.* 1998, 1999). These fault seal algorithms are successful at predicting the maximum across-fault pressure difference for a given clay-rich fault seal, but do not predict pressure differences below this bound (Bretan *et al.* 2003). These algorithms have been used as a guide to defining differences in permeability within and between faults (Harris *et al.* 2002). However, the percentage clay in the fault gouge is only one factor that controls permeability (Eichhubl *et al.* 2005) and these algorithms do not capture the architectural heterogeneity that we demonstrate to be a controlling factor on flow. Furthermore, algorithms relating throw to host rock properties do not yet exist for sand–sand juxtapositions, or for flow through open-mode fracture-dominated fault systems, which are of increasing importance for oil and gas production, waste disposal and gas storage.

In this paper we use simulations of flow through the detailed damage zone architecture of the Big Hole fault to demonstrate the influence of small scale structural controls on fluid flow. We show that, in the case of tight, impermeable slip surfaces flow is concentrated through sections where the fault core is thin, whereas in the case of open slip surfaces flow is within tortuous connected pathways linking the host rock and the open slip surfaces. This small-scale architectural data is never likely to be available at depth. However, we propose that a way forward for improving estimates of fault permeability is by statistical characterization of the likelihood and frequency of connected permeable pathways using field architectural data. As an example, we take fault core thickness data from outcrop maps of a well-exposed fault and show that they are well described by a spatially correlated random field with a spherical covariance structure. To use these statistics to estimate spatially varying core thickness for a particular fault at depth requires collection of a sufficiently large database of fault architectures. This can only be achieved through pooling data from many field areas. This pooling would require classification of faults by large-scale parameters such as lithology, length and stress history where known, in addition to inputting data on small-scale architectural features. Data could then be combined to perform multivariate statistical analyses and to determine which large-scale properties significantly influence small-scale flow pathways and hence permeability. Ultimately, distributions of up-scaled fault permeabilities (including spatially variable statistics) could be calculated for inclusion into industry flow simulations. As the size of the database increases, so the level of uncertainty in permeability predictions will reduce.

The Big Hole fault zone: a small number of pathways can control fluid flow

The following simulations demonstrate the influence of fault architecture on fluid flow predictions for the Big Hole fault in central Utah (Fig. 1), which has exceptional along-strike exposures of fault zone structures. The fault is 4.1 km long, with a maximum throw of 29 m (Shipton & Cowie 2001; Shipton *et al.* 2002, 2005). The fault cuts Jurassic Navajo Sandstone, a medium-grained aeolian arenite with an average porosity of 20%. The fault core of the Big Hole fault consists of a zone of intense grain crushing, pressure solution and cementation (Shipton *et al.* 2005; Bright 2006), which is always associated with thin (<1 mm aperture), highly polished, slip surfaces (the name commonly used for the principal slip zone of a deformation-band dominated fault). The surrounding damage zone comprises deformation band clusters with occasional subsidiary slip surfaces.

To simulate fluid flow through the Big Hole fault we have used the well-established groundwater code, MODLFOW and its particle-tracking model, MODPATH (McDonald & Harbaugh 2003). These have been applied via the graphical interface Groundwater Vistas v4.0 (Environmental Simulations International 2005). The modelled regions were selected as being representative of the fault's architectural complexity; it comprises host rock, fault core, slip surfaces and deformation bands with varying thicknesses and geometries. The

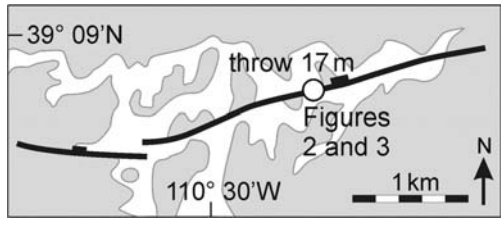

Fig. 1. Map of the Big Hole fault, central Utah. The outcrop of the Navajo Sandstone is indicated in white, overlying rocks are in grey. The locations of Figures 2 and 3 are marked with the throw values calculated from the vertical offset of the top of the Navajo Sandstone (after Shipton & Cowie 2001).

fault core permeability structure and damage zone architecture in the footwall only are represented explicitly on a cell-by-cell basis and permeability values are assigned to each architectural component.

The intrinsic permeabilities of the individual fault architectural components in the Navajo Sandstone are taken from probe permeameter data (Shipton *et al.* 2002). Measured values of permeability are 200–600 mD for the host rock, 0.1–0.4 mD for the deformation bands and 0.007–0.1 mD for the fault core. In the case of the slip surfaces, measurements from Shipton *et al.* (2002) and Antonellini & Aydin (1994) range over 7 orders of magnitude from 0.1 to 10^6 mD. The wide range in slip surface permeability is supported by observations from five boreholes drilled through the fault zone (Shipton *et al.* 2002, 2005). Two of the boreholes showed a tight slip surface contained within a highly indurated fault core, whereas the other three boreholes showed open fractures along the slip surface with associated fluid ingress (Shipton *et al.* 2005). This uncertainty inherent in characterizing whether slip-surfaces are open or closed is investigated using two values for slip surface permeability: 1000 mD to represent the case of open mode fractures where the permeability is greater than that of the host rock; and 0.1 mD for the case of tight slip surfaces where the slip surface permeability is less than that of the deformation bands.

The modelled region is a 4×2.5 m plan-view section through the fault core and footwall damage zone (Fig. 2a & b). Flow through the hanging wall is not simulated. To simulate two-dimensional cross-fault flow, fixed heads are assigned to the top and bottom boundaries, with the left and right hand boundaries being no-flow. Figure 2a shows predicted velocity vectors for flow across the fault in the case of tight slip surfaces (0.1 mD). The length of the vector is proportional to the velocity. In this simulation, velocity vectors converge at the location where the fault core thickness is zero. Hence, the flow rate across the fault is governed by the number of deformation bands that must be crossed to reach this location and the size of this region of zero core thickness. In contrast, for the simulation with open slip surfaces (1000 mD), velocity vectors converge within the slip surfaces that cut across the fault core (Fig. 2b). The length scale for the velocity vectors in Figure 2b is two orders of magnitude greater than for those in Figure 2a, demonstrating that the flow rate is substantially reduced in the case where the slip surfaces are tight. For the open slip surfaces (Fig. 2b) the fluid travels for up to a metre along slip surfaces that run parallel to the core, before cutting across it.

It is important to note that, in Figure 2b, not all of the slip surfaces act as conduits; only those slip surfaces connected to host-rock pathways show focussing of flow. Thus, in the case of open mode fractures, the rate of fault leakage is not primarily governed by the fault core thickness (in contrast to the simulations with tight slip surfaces), or even by the density of deformation bands, but by the fault zone architectural structure: the velocity vectors cross as few deformation bands as possible, following pathways within the host rock and the connecting slip surfaces. If connected pathways exist through the host rock and slip surfaces, no matter how tortuous, it is the frequency of these pathways that will control fault flow. In all of the examples it is this connected nature of highly tortuous high-permeability pathways that governs the bulk hydraulic properties of the fault zone.

Statistical characterization of fault architectural components

To improve estimates of fault permeability in the subsurface, we require a way to combine lithological information and large-scale measurable properties, such as fault throw, with detailed field studies of fault zones and laboratory permeability data. To date, field and laboratory studies have been used to estimate bulk up-scaled permeability values for individual sites using two different approaches. The first assumes that cross-fault flow paths cut each architectural feature at 90° and that each feature is continuous along strike. Bulk cross-fault permeability is then calculated as a simple harmonic mean dependent on the thickness, density and permeability of the individual architectural components (i.e., a parallel plate model; e.g., Rawling *et al.* 2001; Shipton *et al.* 2002). In the second, fluid flow is simulated through detailed maps of fault architectural structure (as in the simulations presented here) and the resulting flow predictions are used to calculate an equivalent permeability tensor (Flodin *et al.* 2001; Jourde *et al.* 2002).

Both of the above methods for estimating up-scaled fault permeability from field observations use a deterministic approach based on data from individual sites. Yet such detailed architectural data are never available for faults at depth. So, what information on fault architecture could we collect to improve estimates of fault-related fluid flow? Can we create large field-based databases for individual lithologies to make statistically based predictions of fault hydraulic behaviour? To statistically characterize spatial permeability variations in faults requires a number of steps. First, we need to determine the architectural components

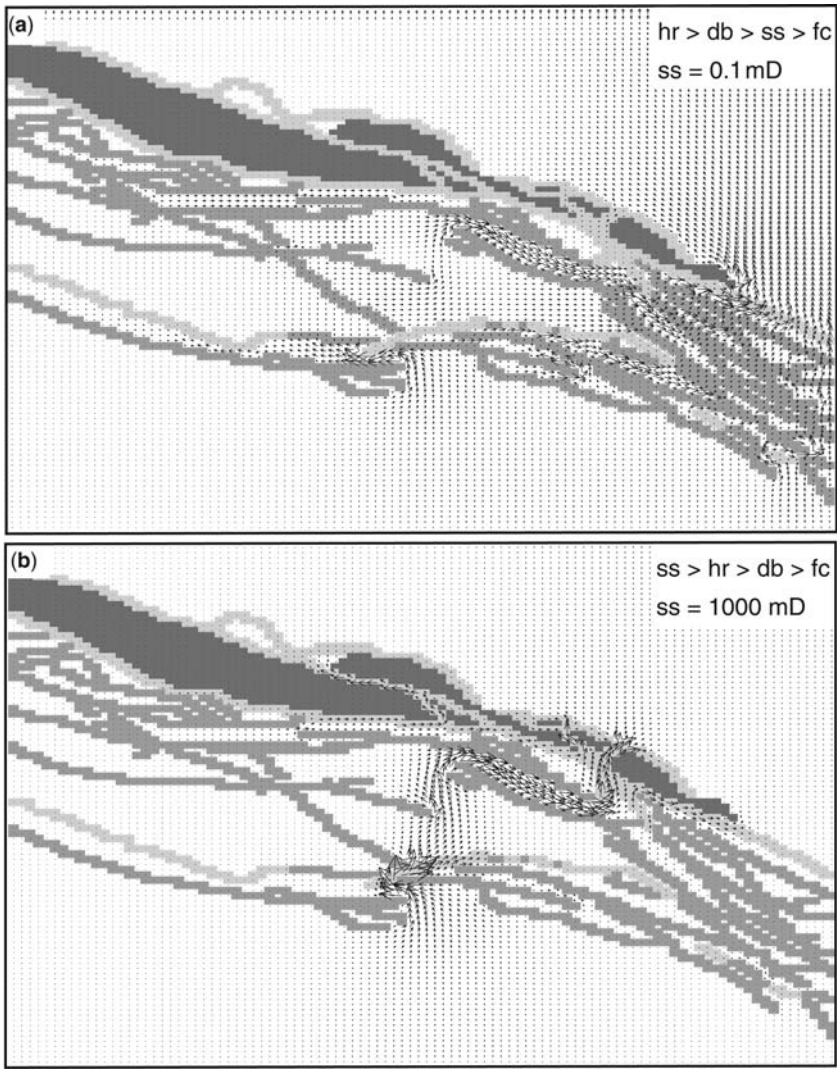

Fig. 2. Flow simulations through the fault damage zone maps of Shipton and Cowie (2001). Permeability data have been assigned to each architectural component based on data in Antonellini and Aydin (1994) and Shipton *et al.* (2002). The host rock (hr) is assigned a fixed permeability of 600 mD (white), the deformation bands (db) 0.4 mD (mid-grey), and the fault core (fc) 0.007 mD (dark grey). Slip surfaces (ss) are either open (1000 mD) or closed (0.1 mD; pale grey). Map view of a 4 × 2.5 m section of the Big Hole fault at a location with 17 m total throw has simulations for (**a**) open slip surfaces and (**b**) closed slip surfaces.

that dominate fluid flow in a particular lithology. Second, we need to identify the large-scale physical controls on these features, so that these effects can be removed from any statistical analysis to characterize their spatial distribution. Third, we need to characterize the spatial statistics of these features in terms of, for example, their mean value and spatial covariance structure (Kitanidis 1997). Finally we need to relate the statistics on architectural features to a statistically based estimate of bulk permeability values.

If we take as an example faults at sand-on-sand contacts as investigated here, we have already shown that, for the case of tight slip-surfaces, fluid flow is primarily controlled by patches with no fault core. Hence, key to estimating fault permeability in this case is to characterize the spatial variability of fault core thickness. Figure 3a shows

fault core thickness plotted against along-strike distance for a 20 m-long section of the Big Hole fault at the same location as the flow simulations in Figure 2a & b. Short periodic sections of thick and thin core can clearly be identified. The spatial variation in core thickness is very well characterized by a spatially correlated field with a spherical covariance structure (Fig. 3b). The *x*-axis on Figure 3b is the distance between each pair of points, called the *lag*. The *y*-axis is the mean of the square differences in core thickness between all pairs of points that are a given distance apart, called the variogram function (and equal to 1 − the covariance; Kitanidis 1997). The data points on Figure 3b are the values of the variogram function (called the experimental variogram) calculated from the data in Figure 3a. Also shown on Figure 3b is the best-fit statistical distribution to the data (the theoretical variogram), which has a variance of 32 and a range of 1.45 m. In terms of the observation data, the variance describes the variability in the core thickness and the range describes the length scale of variation in fault core thickness (Kitanidis 1997). Figure 3 demonstrates that fault architectural properties can, as suggested earlier, be characterized using spatial statistics, and that, in this case, core thickness is well described by a spherical covariance function. This covariance function could be used to predict the likelihood, length and frequency of patches of zero core thickness along strike of the Big Hole fault. Finally, we need to relate these patches of zero core thickness to bulk permeability estimates. At locations with zero fault core, across-fault fluid flow is governed only by the number of deformation bands crossed and the number and length of patches with no core material. Permeability estimates could be made either (1) by assuming a parallel plate model for flow at these locations (e.g., Rawling *et al.* 2001; Shipton *et al.* 2002) in combination with a distribution describing the likelihood of a given number of fault-parallel deformation bands – this would give you a likelihood distribution for permeability these patches, or (2) by using a more complex Monte-Carlo simulation methodology whereby for each of a number of detailed stochastically generated fault architectures, two-dimensional fluid flow simulations are up-scaled to give bulk permeability estimates in the manner of Flodin *et al.* (2001) and Jourde *et al.* (2002).

For such statistical estimates of bulk fault permeability to be reliably used for prediction of flow through an unexposed fault, we need to account for any systematic behaviour associated with variables other than the host rock lithology. Say, for example, there is a relationship between the offset and the mean core thickness; this relationship must be determined and incorporated into the statistical model before making predictions at another location. Figure 4 shows core thickness measured along-strike for a fault in Entrada sandstone, Goblin Valley, USA. Fault offset at this location varies from 5 m at the start of the exposure (0 m on the *x*-axis on Fig. 4) to 20 m at the end of the exposed section (80 m on the *x*-axis on Fig. 4). The figure shows a clear trend in the underlying mean core thickness, which is rising with increasing offset. Superimposed on this trend,

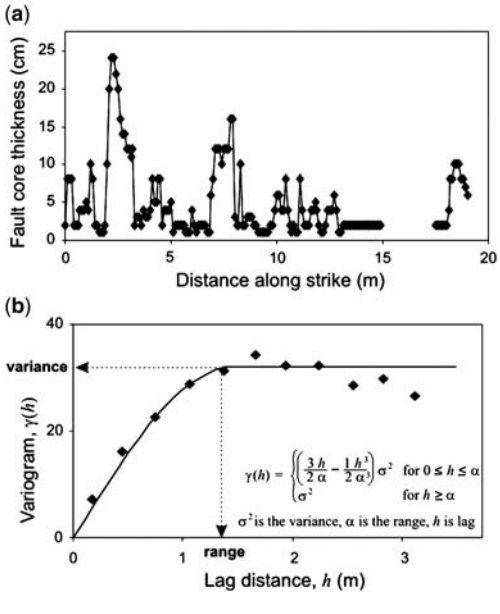

Fig. 3. (**a**) Variation of fault core thickness along strike for the location on the Big Hole fault with 17 m total throw. (**b**) Experimental and theoretical variogram derived from the data shown in (a). The fitted variogram is for a spherical covariance distribution with a range of 32 and a variance of 1.45.

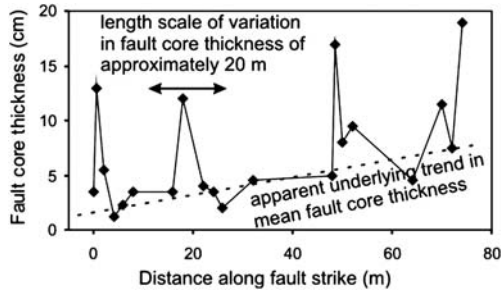

Fig. 4. Variation of fault core thickness along strike for a fault in Goblin Valley, Utah. This fault is one segment of a linked fault system over 220 m long with a maximum throw of 1 m. After Bright (2006, fig. 4.7b).

however, is a spatial covariance structure, such as that in Figure 3, which results in repeated 'patches' of thick and thin core along strike.

The simulations and examples discussed above are confined to a scenario of characterizing across-fault fluid flow. However, the proposed approach of deriving statistically based permeability estimates from multiple field sites is equally valid for along-fault flow. Clearly, the governing fault architectural features in the latter case are likely to be different.

Figure 4 underlines the requirement for a multivariate approach to characterizing fault architecture, and hence to predicting fault permeability. This implies that a *very large* database of fault architecture is needed to accurately characterize fault permeability distributions. This can only be achieved by pooling a large number of field datasets. This would require an international consensus on the recording of the gross parameters (e.g., lithology, offset, stress history) and the architectural detail at each site. Trends relating to gross parameters, as well as small scale variability such as that described in Figures 3 & 4, could be identified from these pooled datasets. As the number of pooled datasets increases, the risk due to uncertainty in each parameter will continue to be reduced. Thus, an international database of fault architectures is required that will lead to improved estimates of fault permeability for input into fluid flow models.

Conclusions

Fault architecture is heterogeneous in single fault zones and between different faults cutting the same host rock. This makes deterministic prediction of fault permeability unreliable. Current practice attempts to find correlations between measurable parameters such as throw and host rock property data to deterministically estimate fault zone petrophysical properties. This severely underestimates the complexity of real fault zones and the variability in fault zone properties. Using simulations of flow through a well-characterized fault zone, we show here that micro-scale architectural properties are critical to hydraulic behaviour. We present data on fault core thickness to show that individual architectural properties can be well described by spatial statistics at a given location, but that systematic relationships to gross parameters such as fault throw must be determined to apply these statistics to prediction on unexposed faults. These results suggest that, rather than looking at individual sites, field analogue data could be employed to much greater effect if statistics to characterize such properties were derived from multiple sites. The pooling of fault architectural data from a large number of field sites, along with the recording of gross parameters such as throw and lithology at each site, will allow for multivariate statistics to be derived and lead to improved estimates of fault permeability at depth.

G. Dudgeon and S. Loiseau ran early versions of the models. We thank T. Manzocchi and the participants of the 2005 GSA short course on Reservoir-Scale Normal Faults in Central Utah for useful discussions. Thanks to J. Fairley and H. Sheldon for constructive reviews.

References

ANTONELLINI, M. A. & AYDIN, A. 1994. Effect of faulting on fluid flow in porous sandstones: petrophysical properties. *American Association of Petroleum Geologists Bulletin*, **78**, 355–377.

ANTONELLINI, M. A. & AYDIN, A. 1995. Effect of faulting on fluid flow in porous sandstones: geometry and spatial distribution. *American Association of Petroleum Geologists Bulletin*, **79**, 642–671.

BOLTON, A. J., MALTMAN, A. J. & CLENNELL, M. B. 1998. The importance of overpressure timing and permeability evolution in fine-grained sediments undergoing shear. *Journal of Structural Geology*, **20**, 1013–1022.

BRETAN, P., YIELDING, G. & JONES, H. 2003. Using calibrated shale gouge ratio to estimate hydrocarbon column heights. *American Association of Petroleum Geologists Bulletin*, **87**, 397–413.

BRIGHT, A. M. 2006. *Deformation band fault core: character, evolution and influence on bulk fluid flow*. PhD thesis, Trinity College, Dublin.

CAINE, J. S., EVANS, J. P. & FORSTER, C. B. 1996. Fault zone architecture and permeability structure. *Geology*, **24**, 1025–1028.

CLARKE, S. M., BURLEY, S. D. & WILLIAMS, G. D. 2005. A three-dimensional approach to fault seal analysis: fault-block juxtaposition & argillaceous smear modeling. *Basin Research*, **17**, 269–288.

DO NASCIMENTO, A. F., LUNN, R. J. & COWIE, P. A. 2005. Numerical modelling of pore-pressure diffusion in a reservoir-induced seismicity site in NE Brazil. *Geophysics Journal International*, **160**, 249–262.

DOWNEY, M. W. 1984. Evaluating seals for hydrocarbon accumulations. *Bulletin of the American Association of Petroleum Geologists*, **68**, 1752–1763.

EICHHUBL, P., D'ONFRO, P., AYDIN, A., WATERS, J. & MCCARTY, D. K. 2005. Structure, petrophysics, and diagenesis of shale entrained along a normal fault at Black Diamond Mines, California – Implications for fault seal. *AAPG Bulletin*, **89**, 1113–1137.

Environmental Simulations International. 2005. www.groundwatermodels.com.

EVANS, J. P., FORSTER, C. B. & GODDARD, J. V. 1997. Permeabilities of fault-related rocks and implications for fault-zone hydraulic structure. *Journal of Structural Geology*, **19**, 1393–1404.

EVANS, K. F., GENTER, J. & SAUSSE, J. 2005. Permeability creation and damage due to massive fluid

injections into granite at 3.5 km at Soultz: 1. Borehole observations. *Journal of Geophysical Research*, **110**, B04203.

FAIRLEY, J. P. & HINDS, J. J. 2004. Field observation of fluid circulation patterns in a normal fault system. *Geophysical Research Letters*, **31**, 1–4.

FLODIN, E. A., AYDIN, A., DURLOFSKY, L. J. & YETEN, B. 2001. Representation of fault zone permeability in reservoir flow models. *Society of Petroleum Engineers Annual Technical Conference and Exhibition*, New Orleans, LA, Paper 71671, 27–30.

FOXFORD, K. A., WALSH, J. J., WATTERSON, J., GARDEN, I. R., GUSCOTT, S. C. & BURLEY, S. D. 1998. Structure and content of the Moab Fault Zone, Utah, U.S.A., and its implications for fault seal prediction. *In*: *Faulting, Fault Sealing and Fluid Flow in Hydrocarbon Reservoirs*. Geological Society of London, Special Publications, **147**, 87–103.

HARRIS, D., YIELDING, G., LEVINE, P., MAXWELL, G., ROSE, P. T. & NELL, P. 2002. Using shale gouge ratio (SGR) to model faults as transmissibility barriers in reservoirs: an example from the Strathspey Field, North Sea. *Petroleum Geoscience*, **8**, 167–176.

HOOPER, E. C. D. 1991. Fluid migration along growth faults in compacting sediments. *Journal of Petroleum Geology*, **14**, 161–180.

JOHANSEN, T. E. S., FOSSEN, H. & KLUGE, R. 2005. The impact of syn-faulting porosity reduction on damage zone architecture in porous sandstone: an outcrop example from the Moab Fault, Utah. *Journal of Structural Geology*, **27**, 1469–1485.

JONES, R. M. & HILLIS, R. R. 2003. An integrated, quantitative approach to assessing fault-seal risk. *American Association of Petroleum Geologists Bulletin*, **87**, 507–524.

JOURDE, H., FLODIN, E. A., AYDIN, A., DURLOFSKY, L. J. & WEN, X. H. 2002. Computing permeability of fault zones in eolian sandstone from outcrop measurements. *AAPG Bulletin*, **86**, 1187–1200.

KITANIDIS, P. K. 1997. *Introduction to Geostatistics*. Cambridge University Press, Cambridge, 249.

KNIPE, R. J. & LLOYD, G. E. 1994. Microstructural analysis of faulting in quartzite, Assynt, NW Scotland: Implications for fault zone evolution. *Pure and Applied Geophysics*, **143**, 229–254.

KNIPE, R. J., JONES, G. & FISHER, Q. J. 1998. Faulting, fault sealing and fluid flow in hydrocarbon reservoirs: and introduction. *In*: JONES, G., FISHER, Q. J. & KNIPE, R. J. (eds) *Faulting, Fault Sealing and Fluid Flow in Hydrocarbon Reservoirs*. Geological Society, London, Special Publications, **147**, vii–xxi.

MANZOCCHI, T., RINGROSE, P. S. & UNDERHILL, J. R. 1998. Flow through fault systems in high-porosity sandstones. *In*: COWARD, M. P., DALTABAN, T. S. & JOHNSON, H. (eds) *Structural Geology in Reservoir Characterisation*. Geological Society, London, Special Publications, **127**, 65–82.

MANZOCCHI, T., WALSH, J. J., NELL, P. A. R. & YIELDING, G. 1999. Fault transmissibility multipliers for flow simulation models. *Petroleum Geoscience*, **5**, 53–63.

MCDONALD, M. G. & HARBAUGH, A. W. 2003. The history of MODFLOW. *Groundwater*, **41**, 280–283.

RAWLING, G. C., GOODWIN, L. B. & WILSON, J. L. 2001. Internal architecture, permeability structure, and hydrologic significance of contrasting fault-zone types. *Geology*, **29**, 43–46.

SHIPTON, Z. K. & COWIE, P. A. 2001. Analysis of three-dimensional damage zone development over a micron to km scale range in the high-porosity Navajo sandstone, Utah. *Journal of Structural Geology*, **23**, 1825–1844.

SHIPTON, Z. K., EVANS, J. P., ROBESON, K., FORSTER, C. B. & SNELGROVE, S. 2002. Structural heterogeneity and permeability in faulted eolian sandstone: implications for subsurface modelling of faults. *American Association of Petroleum Geologists Bulletin*, **86**, 863–883.

SHIPTON, Z. K., EVANS, J. P. & THOMPSON, L. B. 2005. The geometry and thickness of deformation band fault core, and its influence on sealing characteristics of deformation band fault zones. *In*: SORKHABI, R. & TUSUJI, Y. (eds) *Faults, Fluid Flow and Petroleum Traps*. American Association of Petroleum Geologists Memoirs, **85**, 181–195.

Fault-related dilation, permeability enhancement, fluid flow and mineral precipitation patterns: numerical models

Y. ZHANG[1,3], P. M. SCHAUBS[1], C. ZHAO[1], A. ORD[1], B. E. HOBBS[1] & A. C. BARNICOAT[2]

[1]*Predictive Mineral Discovery Cooperative Research Centre, CSIRO Exploration & Mining, PO Box 1130, Bentley, WA 6102, Australia (e-mail: Yanhua.Zhang@csiro.au)*

[2]*Predictive Mineral Discovery Cooperative Research Centre, Geoscience Australia, GPO Box 378, Canberra 2601, Australia*

[3]*CAS Guangzhou Institute of Geochemistry, Guangzhou 510640, China*

Abstract: Fault-related host rock deformation and dilation control fluid flow and mineralization in many world-class mineral deposits. This numerical modelling study explores the interactions between deformation, faulting, dilation, fluid flow and chemical processes, which are suggested to result in this control, with special attention to fault dilatant jog structures. Our two-dimensional numerical models focus on faulting-related deformation, dilation and permeability enhancement, fluid flow patterns and fluid focusing/mixing locations, while three-dimensional models examine several different cases of fault underlap and overlap. The results show that fault-dilation and faulting-induced permeability enhancement, which are closely associated with tensile failure, represent important ways to generate fluid flow conduits for more effective fluid flow and mixing. Dilation during strike–slip faulting is localized near fault tips (wing crack locations) and jog sites, where fluids are strongly focused and mixed. These locations are the tensile domains of the strike–slip regime. In overlapping-fault (dilatant jog) cases, the magnitude of dilation and the extent of the dilatant region are closely related to the extent of fault overlap. These results provide insight into the transport of fluids through low-permeability rocks with isolated, but more permeable, faults. Gold and quartz precipitation patterns as a result of the coupling of chemical reactions to deformation induced fluid flow velocities are also computed. The rates of precipitation depend on structural and fluid flow conditions and on the geometrical relation between local fluid velocity and chemical concentration gradients generated by mixing. Maximum precipitation rates for gold occur in the dilation zones and in faults where high fluid flow rates, sufficient fluid mixing and high concentration gradients of critical chemical species are all present, while the quartz precipitation rate is predominantly controlled, in this isothermal situation, by the rate of fluid flow across concentration gradients in the aqueous silica concentration.

Brittle fracturing is ubiquitous in the upper crust, and represents a set of common features associated with many structurally controlled ore deposits. This is commonly expressed by high-grade mineralization controlled by faults and the associated fractures, veins and zones of rock brecciation. Examples of such structural control on mineralization can be found in many ore deposits in the world (e.g., Nguyen *et al.* 1998; Cox 1999; Schaubs & Wilson 2002; Cox & Ruming 2004; Ferrari & Choudhuri 2004; Jolley *et al.* 2004; Zhang *et al.* 2007). A key process of such structural control is the development of regions of voids (dilation) in faulted rocks. During faulting, faults may experience large displacements, resulting in severe damage zones, dilatant sites and permeability enhancement. As such, faults are generally recognized as one type of structure having enormous capacity to create efficient fluid pathways in the crust (e.g., Sibson *et al.* 1975; Knipe 1993; Sibson 1994), which is otherwise relatively impermeable.

The features of damage and dilation zones around a single or multiple faults have been described in several previous studies based on field observations (Rispoli 1981; Sibson 1986; Curewitz & Karson 1997; Lee & Wiltschko 2000; Kim *et al.* 2004; d'Alessio & Martel 2004). These authors noted that faulting-related active damage and dilatancy develop predominately at fault tips. This can be summarized as wing-crack-type damage at the tip of a single fault or dilatant jog-type damage at overlapping and interacting fault tips; significant dilatancy can also develop along the dilatant segments of curved faults (e.g., Nguyen *et al.* 1998). Fracturing damage may also develop at contractional fault jogs. At these damage sites, host rocks commonly show extensive development of breccias and fractures (e.g., Rispoli 1981; Sibson 1986; Kim *et al.* 2004). Rock

From: WIBBERLEY, C. A. J., KURZ, W., IMBER, J., HOLDSWORTH, R. E. & COLLETTINI, C. (eds) *The Internal Structure of Fault Zones: Implications for Mechanical and Fluid-Flow Properties*. **299**, 239–255.
DOI: 10.1144/SP299.15 0305-8719/08/$15.00

permeability at these sites must also be significantly enhanced, providing favourable sites for fluid flow and focusing, as evidenced by the extensive observations of veins or mineralized breccias and veins along wing cracks and dilatant jogs (e.g., Rispoli 1981; Cox 1999; Nguyen *et al.* 1998; Lee & Wiltschko 2000; Cox & Ruming 2004). Lee and Wiltschko (2000) further showed that the opening of fractures in dilatant jogs can be sequential, leading to the development of multi-event overprinting veins with individual veins normal to local extension directions. Shipton & Cowie (2001, 2003) noted that faults in high-porosity sandstone show progressive fracture propagation (a series of slip and rupture) and have a broad damage core surrounding the entire fault length.

There have been numerous numerical and experimental modelling studies on displacement and stress patterns associated with strike–slip faulting under various boundary conditions (e.g., Chinnery 1963; Wang *et al.* 1987; Willemse & Pollard 2000; Joussineau *et al.* 2001). Several previous studies focused on fault jogs (Connolly & Gosgrove 1999*a*, *b*; Bürgmann & Pollard 1994; Nečmok *et al.* 2002). Bürgmann & Pollard (1994) numerically simulated the stress distribution around fault terminations and extensional step echelon arrays (dilatant jog), using a boundary element method. Nečmok *et al.* (2002) also numerically simulated the patterns of faulting-related stresses but for a contractional jog bounded by strike–slip faults, using a finite element method. The stress patterns derived from both studies agree well with their field structural observations; however, both models assumed isotropic elastic rheology without consideration of rock failure under high stresses. Such models may lead to overestimation of stress magnitudes when involving large fault slip and cannot predict the development of plastic dilation in faulted regions. Using photoelastic analogue modelling experiments, Connolly & Cosgrove (1999*a*, *b*) investigated the patterns of mean and differential stresses and stress trajectories around dilatant fault jogs. They also calculated the formation of fracture sets based on principal stress orientations, and inferred fluid flow patterns based on mean stress patterns. Their results showed that fluids can flow into a dilatant fault jog in overlapping jog situations or out of a dilatant jog in underlapping and neutral jog situations, representing important contributions to our knowledge of the mechanical and hydrological behaviours of dilatant jogs. The assumption of a straightforward relationship between mean stresses and fluid flow means that the fluid flow patterns inferred from the experiments do not reflect full deformation and fluid flow coupling, particularly through time, and as such require further scrutiny. It also needs to be emphasized that the majority of the studies noted above utilized isotropic elasticity for the constitutive behaviour.

To advance our understanding of the interactions between faulting, host rock deformation, permeability enhancement and fluid flow, this paper presents a set of coupled deformation-fluid flow numerical models (2D and 3D) and fluid flow–chemical reaction models (2D) for the single fault and multiple fault (dilatant jog) cases. The current work has employed an elastic–plastic constitutive law and considered full interaction between mechanical deformation and fluid flow. The questions to be explored here include: (1) what are the patterns of dilatancy and permeability enhancement as a result of faulting? (2) How are fluids transported through low permeability rocks containing isolated, but more permeable faults? (3) Where and why are fluids most likely to focus and mix? (4) What would be the corresponding mineral precipitation patterns? The chemical reaction models presented in this study assume simplified fluid–fluid reaction scenarios during the coupled processes. This analysis allows the prediction of mineral precipitation patterns (in this case, gold and quartz) in unreactive host rocks.

Methods

Model description

This study presents a combination of 2D and 3D simple conceptual models to explore several faulting and fluid flow cases. Two 2D models have been constructed, simulating a 4×5 km plan (horizontal) view domain containing a single fault (Fig. 1a) or two faults (Fig. 1b), respectively. The 2D models were loaded in compression as illustrated in Figure 1, aiming to initialize strike–slip along the fault and create a dilatant jog scenario in the two fault cases. The top and bottom boundaries of the model were loaded by a compressive stress of 90 MPa, and a confining stress of 10 MPa was applied to the left and right boundaries. A homogeneous initial fluid pore pressure of 1 MPa was applied to the models. In the model with one fault (Fig. 1a), an impermeable fluid flow boundary condition (i.e., closed box) was assumed. In the models with two faults (Fig. 1b), fluid sources represented by a volume rate of flow per unit volume (0.5×10^{-7}) were applied to the top and bottom boundaries of the models in order to explore how these two fluids are transported through the host-rock towards isolated faults.

Three-dimensional models, $3.2 \times 3.5 \times 1$ km in size (Fig. 1c), were used to explore dilation and fluid flow patterns in a 3D space. The models aim to determine the effects of different fault overlap (O)

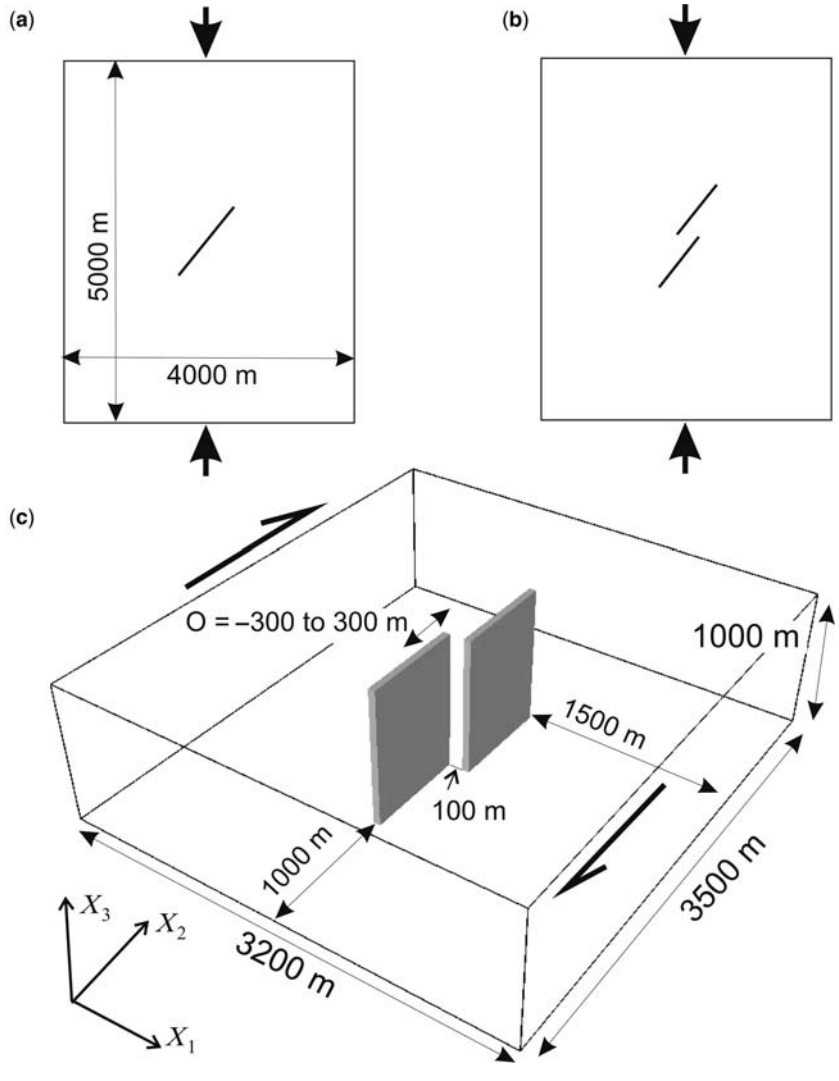

Fig. 1. Geometries of the models. (**a**) One-fault 2D model. (**b**) Two-fault 2D model; 2D models lie in a horizontal plane. (**c**) Two-fault 3D model. The arrows indicate the direction of the compressive loading stress (2D models) or shearing direction (3D model). In (c), O denotes the length of fault overlap where a positive O means a positive overlap and a negative O means underlap or negative overlap.

ranging from overlap (positive O) to underlap (negative O). These 3D models bear similarities to the approach of Connolly and Cosgrove's (1999*a*, *b*) analogue experimental work. The 3D models are deformed in a dextral strike–slip manner in a direction parallel to the faults (Fig. 1c). An initial velocity is applied as a gradient across the model perpendicular to the X_1 axis. The left and right boundaries (parallel to the $X_2 - X_3$ plane) continue to have this initial velocity as the model is deformed, while the internal portions of the model are allowed to move in any direction. The bottom boundary is fixed only in the X_3 direction and is free to move within the $X_1 - X_2$ plane. The front and back boundaries (parallel to the $X_1 - X_3$ plane) are constrained by a stress boundary condition where a normal stress is applied consistent with a change in depth. The top of the model is simulated to be at a depth of 5 km and therefore a stress boundary condition based on this depth and an assumed overburden density of 2500 kg m^{-3} is also applied here. The initial pore-pressure is consistent with a pore-fluid factor of 0.5, where hydrostatic is 0 and lithostatic is 1. The 3D

models are run as closed systems where the boundaries are impermeable but pore pressure is allowed to change. No external fluid sources or fluxes are applied to the model.

The current 2D and 3D models have only considered a straight fault geometry that represents the simplest of fault geometry scenarios. In nature, faults can have more complex geometries (e.g., anatomizing surfaces) and hence more complex mechanical and fluid behaviours. Note also that faults in the models (Fig. 1) have a thickness of about 30 m (2D) and 50 m (3D).

Finally, two chemical reaction models evaluating gold and quartz precipitation rates were constructed, which used the geometry and fluid flow field output from the one-fault and two-fault 2D mechanical and fluid flow models above (Fig. 1a & b).

Deformation and fluid flow modelling methodologies

Numerical codes. Coupled deformation–fluid flow modelling has been carried out using the finite difference codes, FLAC2D and FLAC3D (Fast Lagrangian Analysis of Continua), where the discretized equations are solved by a dynamic relaxation scheme (Cundall & Board 1988; Itasca 1998, 2003). The accuracy of the approximation methodologies of the codes is similar to that of finite element methods; however, the FLAC codes incorporate an efficient strategy for handling volumetric constraints and the relaxation technique is robust and stable in connection with localization modelling (Cundall & Board 1988). The codes are capable of simulating the interactions between deformation and fluid flow in porous media and have been used successfully in the simulation of a series of geological problems, such as shear zones (Hobbs & Ord 1989; Ord 1991), deformation and fluid flow (Strayer *et al.* 2001; Sorjonen-Ward *et al.* 2002) and thrusting (Erickson *et al.* 2001).

Mechanical constitutive law. The rocks in the current models are modelled as Mohr–Coulomb isotropic elastic–plastic materials (Jaeger & Cook 1979, p. 228; Vermeer & de Borst 1984; Ord 1991), the constitutive parameters of which (Table 1) include shear (G) and bulk (K) elastic moduli, cohesion (C), tensile strength (T), friction angle (ϕ) and dilation angle (ψ). Such a material under loading deforms initially in an elastic manner up to a yield point (i.e., before the maximum shear stress reaches a threshold magnitude), after which it deforms in a plastic manner. The yield function, f, is defined by:

$$f = \tau^* + \sigma^* \sin\phi - \cos\phi \qquad (1)$$

Table 1. *Initial material properties*

Model unit	Density (kg m^{-3})	Bulk modulus (Pa)	Shear modulus (Pa)	Cohesion (Pa)	Tensile strength (Pa)	Permeability (m^2)	Porosity	Friction angle (deg)	Dilation angle (deg)
Bulk material	2500	4.7×10^{10}	2.8×10^{10}	2×10^{7}	2×10^{6}	2.0×10^{-14}	0.3	30	2
Fault	2500	4.7×10^{10}	2.8×10^{10}	2×10^{7}	2×10^{6}	2.0×10^{-13}	0.3	30	2
Foliation within faults		4.7×10^{10}	2.8×10^{10}	5×10^{6}	2×10^{6}			5	

and the plastic potential function, g, is defined by:

$$g = \tau^* + \sigma^* \sin\psi - \cos\psi \quad (2)$$

where τ^* and σ^* are the maximum shear stress and the mean stress, respectively. The plastic strain-rate, $\dot{\varepsilon}_{ij}$, is given by the flow rule (Malvern 1969; Ord *et al.* 2004):

$$\dot{\varepsilon}_{ij} = \lambda \frac{\partial g}{\partial \sigma_{ij}} \quad (3)$$

where λ is a constant and σ_{ij} is the stress tensor.

To simulate faults, a penetrative foliation (parallel to and within the faults) was incorporated into the narrow zones of the models representing faults (Fig. 1). Sliding along the foliation within faults is also governed by the Mohr–Coulomb failure criterion, equation (1). Using smaller cohesion and friction angle for the foliation (Table 1), the faults are in effect simulated as weak zones, and deform more easily than the surrounding matrix. The full mechanical properties of the models are summarized in Table 1. A compressive stress is assumed negative, so that tension is positive, and a volume increase or dilation is positive. This represents the engineering stress-sign convention (adopted in FLAC2D and FLAC3D), opposite to the common convention in structural geology.

An important modelling output parameter in the present model is dilatancy or positive volume change that occurs with shear distortion of a material. The dilatant potential of the Mohr–Coulomb material for plastic deformation is characterized by the dilation angle, ψ. This angle can be specified in the Mohr–Coulomb plasticity model (see Vermeer & de Borst 1984) and can also be found from a plot of volumetric strain v. axial strain or shear strain determined for triaxial tests or shear box tests (e.g., Edmond & Paterson 1972; Ord 1991).

Fluid flow law. Fluid flow in the current models is governed by Darcy's law (Mandl 1988; Itasca 1998), defined for an anisotropic porous medium as:

$$V_i = -k_{ij} \frac{\partial}{\partial x_j}(P + \rho_w g x_i) \quad (4)$$

where V_i is the specific discharge (or flow) velocity, P is the fluid pressure, k_{ij} is the permeability tensor and x_j reflects the positions of a material point (see Fig. 1c), g is gravity and ρ_w is fluid density. Therefore, fluid flow velocities are primarily a function of gradients in fluid pore pressures, and variations in permeability. The hydrological parameters of the models include permeability and porosity (Table 1).

Deformation-fluid flow coupling. Two main aspects of mechanical–fluid flow interaction are maintained during the current modelling: (1) changes in pore pressure cause changes in effective stress, which affect the response of the solid (e.g., a reduction in effective stress may induce plastic yield); and (2) the fluid in the model, which is represented as a compressible fluid with bulk modulus of 2×10^8 Pa (2D models) and 2×10^9 Pa (3D models), reacts to mechanical volume changes by a change in pore pressure (volume increase or dilation leads to a pore pressure decrease).

To explore permeability change during the faulting process, a numerical algorithm has been implemented to enable permeability to increase from 2×10^{-14} and 2×10^{-13} m^2 (Table 1) to 1×10^{-12} m^2 once the host rock and fault materials fail in tension. Tensile failure occurs when the following condition is met:

$$P - \sigma_{\min} = T \quad (5)$$

where $\sigma_{\min}$ is the minimum principal stress (compressive stress denotes negative), P is pore pressure and T is tensile strength.

Chemical reaction modelling methodologies

Chemical reaction–transport modelling has been carried out using a finite element code (FIDAP, Fluid Dynamics International 1997) based on the fluid flow field resulting from the deformation–fluid flow modelling. FIDAP is a robust numerical solver, which deals with reactive transport problems in undeformable porous rocks. A general interface (Zhao *et al.* 1999) has been used to import the fluid flow field computed from FLAC2D into FIDAP. This is a partial coupling between the chemical transport modelling and the deformation – fluid flow modelling, where the results of the FLAC models were used as boundary conditions for the subsequent chemical analysis using FIDAP. It should be pointed out that, although FIDAP can be used to simulate heat transfer processes, we have assumed an isothermal geochemical system here to save computation time. The chemical modelling algorithm simulates the mixing of a reduced hydrous fluid (CH_4-bearing) with an oxidized hydrous fluid (CO_2-bearing), and computes the related gold mineralization and quartz precipitation.

We have used the dynamic mineralization theory for permeable reactive rocks (Phillips 1991; Zhao *et al.* 2002) to compute the gold and quartz precipitation pattern in our numerical models. The dynamic mineralization theory states that, if the dispersion process plays a relatively minor role in the control of mineral precipitation,

the precipitation rate of a mineral in permeable reactive rocks is the scalar product of the fluid velocity flowing through the rock with the gradient of the equilibrium concentration of the chemical species. We assume that the precipitation and dissolution of gold in the chemical reaction models are largely controlled by the following chemical reaction:

$$8Au + 16H_2S(aq.) + H_2CO_3 \Leftrightarrow 8Au(HS)_2^- + 8H^+ + 3H_2O + CH_4(aq.). \quad (6)$$

Under the control of this chemical reaction, we need not only consider the fluid mixing between CO_2 and CH_4, but the advection and dispersion of other chemical species such as H_2S and H_2CO_3 in the geochemical system as well.

Since the equilibrium concentration of a mineral is dependent on temperature, pressure and the concentrations of other species, the mineral precipitation rate of the mineral can be expressed in the following form:

$$PR_q = -u \cdot \nabla C_q^e = -\left[\frac{\partial C_q^e}{\partial T}(u_j T_j) + \frac{\partial C_q^e}{\partial p}(u_j p_j) + \sum_{r=1}^{n} \frac{\partial C_q^e}{\partial C_r}(u_j C_{r,j})\right] \quad (7)$$

where PR_q is the precipitation rate of mineral associated with the species q; u_j are the Darcy velocity components in the x_j directions; C_q^e is the equilibrium concentration of the species q; T and p are temperature and pressure respectively; C_r is the equilibrium concentration of species r; and n is the total number of relevant species to determine the equilibrium concentration of species q in the chemical reaction.

Using the chemical reaction expressed in equation (6), the equilibrium concentration of the gold species can be expressed as

$$C_{Au(HS)_2^-}^e = \frac{(C_{H_2S})^{16} C_{H_2CO_3}}{K_{Au}(C_{H^+})^8 C_{CH_4}} \quad (8)$$

where $C_{Au(HS)_2^-}^e$ is the equilibrium concentrations of the aqueous gold species; K_{Au} is the chemical equilibrium reaction constant for the chemical reaction expressed by equation (6); C_{H^+} and C_{H_2S} are the concentrations of H^+ and H_2S; and C_{CH_4} and $C_{H_2CO_3}$ are the concentrations of CH_4 and H_2CO_3 in the geochemical system. Note that the equilibrium constant for the chemical reaction is dependent on both temperature and pressure. The value of the equilibrium constant can be determined from the relevant thermodynamic database (Wolery 1979).

The above equation clearly indicates that, in the isothermal case considered in this paper, the equilibrium concentration of the gold is controlled by the distributions of the concentrations of H^+, H_2S, CH_4 and H_2CO_3 in the computational model as well as by pressure. Note that the concentration of H_2CO_3 is directly dependent on that of CO_2 in the considered geochemical system. For these reasons, the gold precipitation pattern is controlled by the concentration distributions of H^+, H_2S, CH_4 and H_2CO_3 in the computational model. The equilibrium concentration of silica is strongly dependent on temperature but slightly dependent on pressure. However, in the isothermal situation modelled here, the quartz precipitation pattern is controlled by the scalar product of the fluid velocity and the pressure gradient as quartz solubility is otherwise a function only of H_2O.

The geometry (mesh) and fluid flow field inputs to FIDAP for the chemical reaction models were taken from the results of the two FLAC2D models (Fig. 1a, b) with one and two faults, respectively. The reduced fluid and the oxidized fluid were injected from the bottom and top boundaries of the model respectively. Hydrogen sulfide (H_2S) was also injected from the bottom boundary. Both fluids were assumed to be saturated with gold. The concentrations of the mineral-bearing fluids can vary several orders of magnitude in real geochemical systems (Barnes 1979). In the current simple generic model, the maximum concentrations specified were: (1) 0.1 kmol m^{-3} for CH_4; (2) 0.01 kmol m^{-3} for H_2S; and (3) 1 kmol m^{-3} for CO_2. The specific concentration boundary conditions concerning the concentrations of the major chemical components are listed in Table 2.

Fluid flow and fluid mixing in the models create chemical gradients leading to favourable environments for gold mineralization where fluid flow vectors cross these gradients at a high angle.

Table 2. *Boundary conditions of the related concentrations*

Reactive fluids	CH_4 (kmol m^{-3})	CO_2 (kmol m^{-3})	H_2 (kmol m^{-3})	H_2S (kmol m^{-3})	Cl^- (kmol m^{-3})
Top	0.001	1.0	1×10^{-5}	0.001	0.1
Bottom	0.1	0.5	0.001	0.01	1.0

A dispersion coefficient of $2 \times 10^{-6}\,m^2\,s^{-3}$ is adopted in the model. An isothermal condition of 300 °C has been adopted throughout modelling. The adoption of such a temperature does not necessarily mean that the model simulates the deep levels of crust (e.g., *c*. 10 km, if assuming 30 °C km^{-1}), as temperatures of 300 °C have been observed at the shallow levels in the crust as a consequence of hydrothermal fluid flow. Since the chemical reactions involved here are not particularly sensitive to the ambient rock pressure, this variable has not been included.

Results

Stress distribution

Stresses appear to be asymmetric with respect to the orientation of the fault. The highest differential stresses are localized near and away from fault tips but only on one side of the fault tips (Fig. 2a). The other side of the fault exhibits lower but still quite high differential stresses. There is a low differential stress region (stress shadow) asymmetrically around the central fault segment. The principal stresses reflect similar patterns (Fig. 2b), with the highest maximum principal stress coinciding with the highest differential stress. The asymmetrical stress pattern and stress concentrations are similar to the patterns indicated by the experiments of Joussineau *et al.* (2001), which involved similar loading boundary conditions. For the model with two faults (Fig. 2d & e), the highest differential stress and maximum principal stresses localize at one side of fault tips reflecting the displacement on the faults. The low differential stress/stress shadow region now encloses both faults, and in particular, the overlapping area of the two faults (dilatant jog) displays the lowest differential stresses and principal stresses.

Deformation patterns

The rock failure patterns for the single fault and two fault models are illustrated in Figure 2c & 2f, respectively. In the single fault model, zones of active shear and tensile failure are developed near the fault tip, at the side where lowest minimum principal stresses (σ_3) and relatively high differential stresses (not the highest) occur. The zones of tensile failure display an en echelon array of zones normal to σ_3 orientations. This highlights the tensile domain at one side (shearing away side) near the fault tip and reflects the potential locations for wing crack development (e.g., Rispoli 1981; Dyskin *et al.* 1999; Cox *et al.* 2001; Kim *et al.* 2004). Such asymmetric failure patterns near fault tips are similar to the tensile fracture patterns predicted by the uniaxial compression experiments of Wang *et al.* (1987), which involved a single pre-existing fracture in a marble sample and similar loading boundary conditions. We note that there are several areas that failed in the past but have now unloaded and are currently elastic [determined by the Mohr–Coulomb yield criteria; see equation (1)] in a direction approximately conjugate with the failure zones near the fault tips (Fig. 2c). They reflect the location of earlier plastic failure, which did not develop further due to the predominance of faulting and associated deformation, elsewhere in the model.

The failure pattern of the two fault model is similar (Fig. 2f). In addition to the array of tensile failure zones near non-overlapping fault tips, a major tensile failure zone or tensile domain occurs in the dilatant jog near the overlapping fault tips, the locations with the lowest minimum principal stresses. Note that the failure zones described here only represent failures patterns in the plastic deformation domain under the Mohr–Coulomb elastic–plastic constitutive laws. They do not necessarily mean that brittle fractures will form or that faults will propagate.

Dilation patterns

Dilation (volume increase) develops as a result of displacement along the faults. In the 2D model with a single fault (Fig. 3a), this is expressed as the development of an en echelon array of dilation zones, analogous to wing cracks (e.g., Rispoli 1981; Kim *et al.* 2004), at each tip of the fault. More importantly, the location and orientations of these dilation zones coincides with those of tensile failure zones (Fig. 2c) and are confined to the tensile region at one side (shearing away side) of the sliding fault where σ_3 is lowest in the model. Results from these models show that the development of a dilatant structure around a sliding fault is predominantly controlled by tensile failure.

In the 2D model with two adjacent faults (Fig. 3b), dilation zones arrays only develop at the non-interacting ends of the faults, coinciding with tensile failure zones (Fig. 2f). At the overlapping and interacting ends, a major dilation site develops, instead of dilation zone arrays. This represents the formation of a dilatant jog, the location of which also coincides with the site of lowest σ_3 (Fig. 2e) and tensile failure (Fig. 2f). Note that the two highest dilation zones within the dilation jog adjoin the relevant ends of the two faults and their orientations show high angles to the shearing direction. Such dilation patterns are analogous with some observed dilatant jog vein structures (e.g., Lee & Wiltschko 2000).

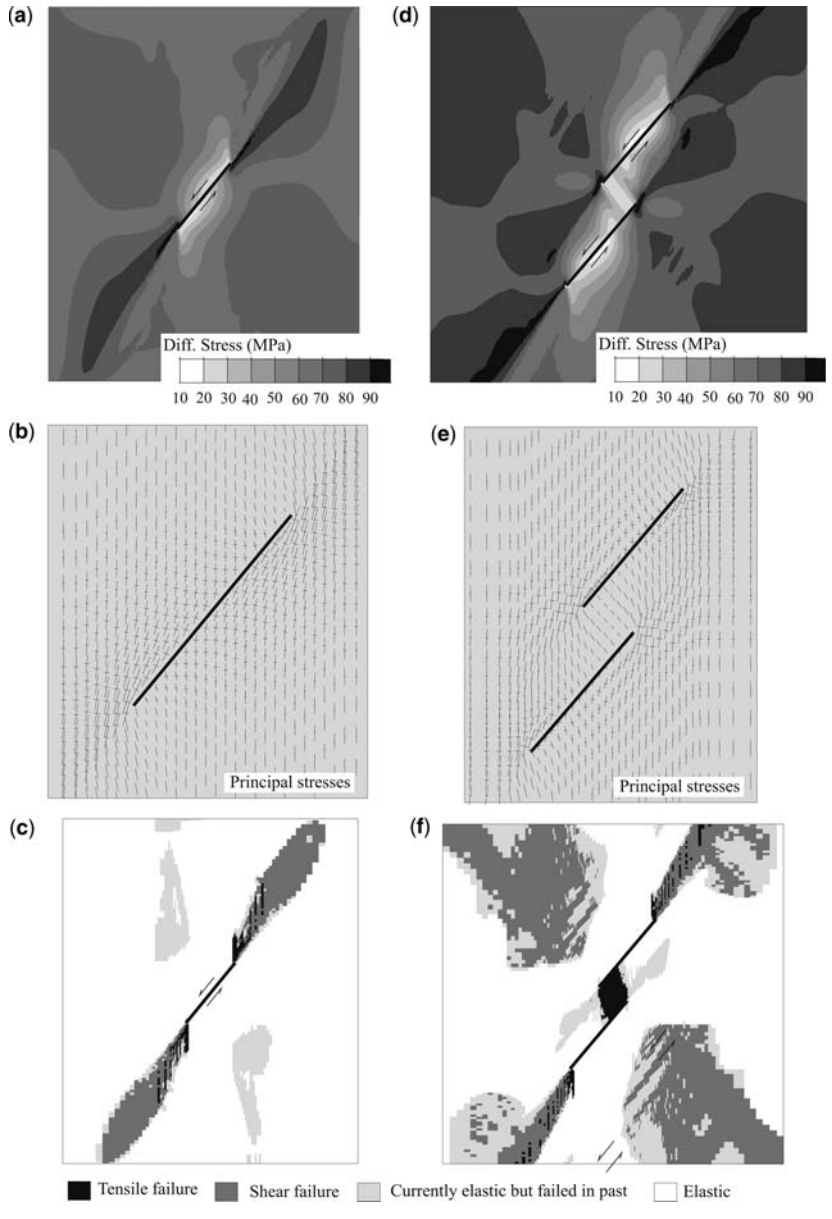

Fig. 2. Results of 2D models. (**a**), (**b**) and (**c**) Differential stresses, principal stresses and mechanical failure patterns for the model with one fault, respectively. (**d**), (**e**) and (**f**) Differential stresses, principal stresses and mechanical failure patterns for the model with two faults. Only central parts of the whole models are plotted. In (b) and (e), the length of the bars is proportional to the magnitude of the stress.

Three-dimensional models may be used to explore more general states of stresses than plane strain or plane stress. In addition, 3D models are designed to explore different fault overlap situations under relatively large displacement conditions. The plan-view dilation patterns of three 3D models with no initial overlap, 300 m overlap and 300 m underlap (negative overlap) are plotted in Figure 4a–c, respectively, and the relationship between dilation and fault overlap is illustrated in Figure 5. The results are generally consistent with the results of the 2D model. Regions of dilation

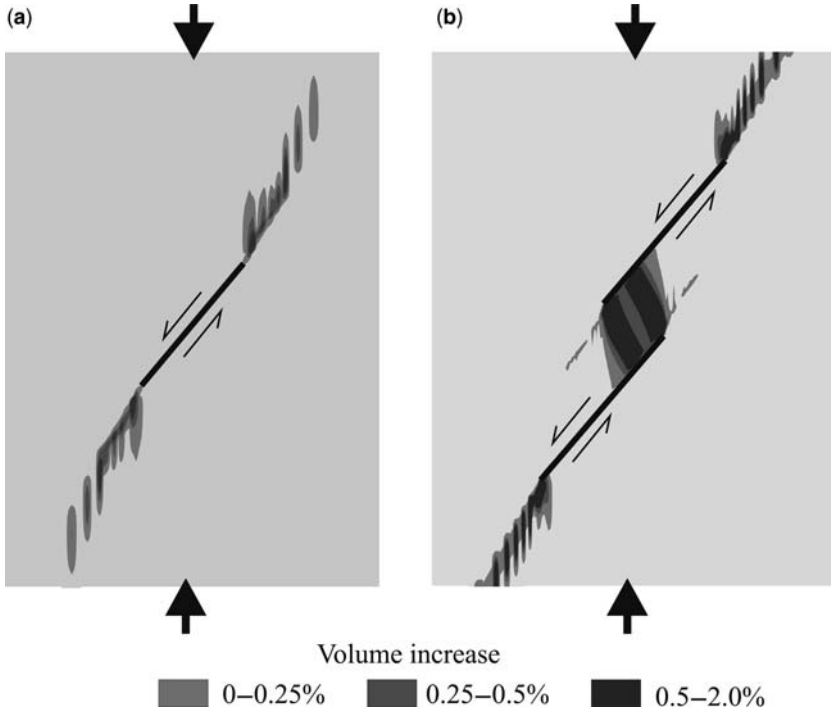

Fig. 3. Dilation (volume increase) patterns for (**a**) one-fault model and (**b**) two-fault model.

localize within the dilatant jog and also on the outward side of the non-interacting ends of the faults. In addition, the result shows that the maximum dilation and total area of the dilation region at the jog site are controlled by fault overlap conditions. The greatest amount of dilation occurs in the model with no fault overlap. In both the models with underlapping and overlapping fault tips, the maximum value of dilation decreases with increasing under- and overlap. In the models where the fault overlap is neutral or negative, the area of maximum dilation occurs in the area where the two faults interact. In models with positive overlap of 100 and 200 m, the region of maximum dilation also occurs where the faults interact; however when the amount of overlap is increased to 300 m (Fig. 4c), the area of maximum dilation occurs at the non-interacting tips of the faults. This is because greater overlap leads to a more diffuse dilatant region with a larger volume at the jog location.

Permeability enhancement and fluid flow patterns in 2D models

The incorporation of permeability enhancement with tensile failure in the present 2D models is a simple way to model the development of new high permeability structures during faulting movement and deformation. Figure 6 shows the locations of the new high permeability structures and Darcy fluid flow velocities. These new high-permeability structures coincide entirely with tensile failure zones (Fig. 2c & f), and predominantly with dilatant structures (Fig. 3a & b).

The emergence of these higher permeability structures enhances fluid flow connectivity in the rock medium (Fig. 6), particularly in the two-fault model where high permeability areas became connected, forming a more efficient fluid transport network. While fluids are still channelled along the pre-existing faults, the fluids are focused into the major dilation zones at fault tips and the dilatant jog site (Fig. 6b & d). Within these dilation zones, fluid flow velocities are much greater than in other parts of the models. As noted earlier, fluid sources (equivalent to high pore pressure conditions) are applied to the top and bottom boundary of the 2D model with two faults. The flow patterns show that these external fluids get transported into the major dilation zone at the jog site through new higher-permeability zones near the top and bottom boundaries (Fig. 6c & d); these higher-permeability zones (dilation is negligible there) only act as fluid transport conduits, rather than fluid focusing/mixing

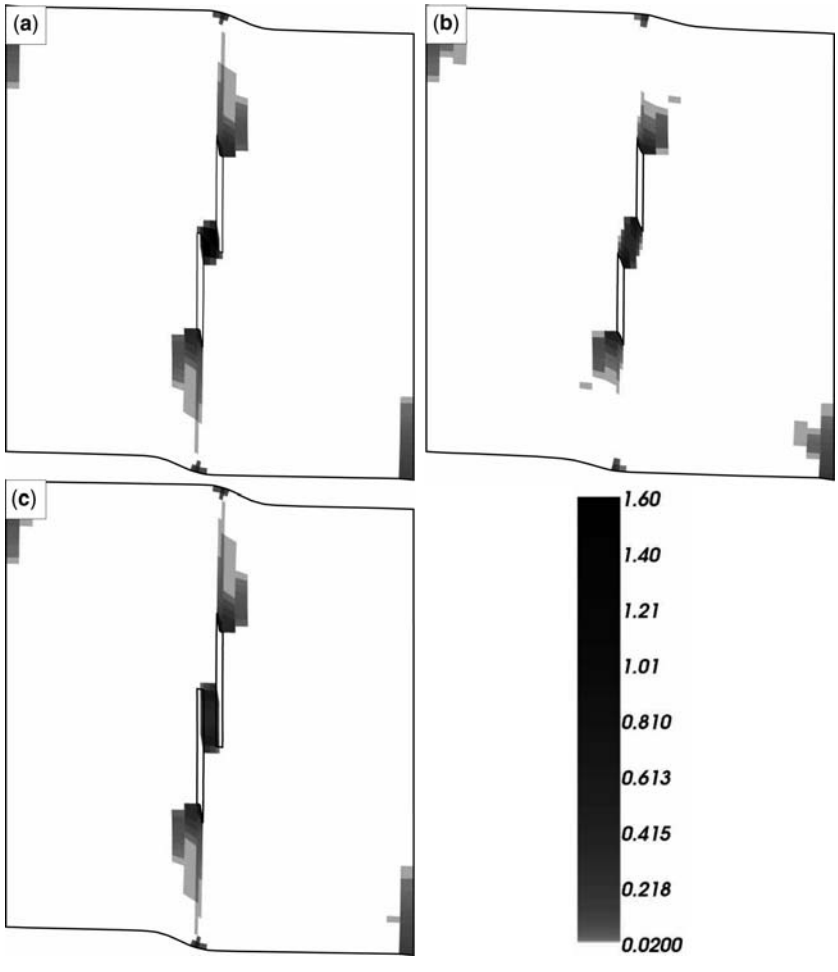

Fig. 4. Plots of volumetric strains on the plan-view plane of 3D models (X_3 is out of plane and positive values indicate dilation). (**a**), (**b**) and (**c**) are for the models with fault overlaps of 0, −300 (negative overlap or under-lap) and 300 m, respectively. White areas represent very low values of either positive or negative volume strain (contraction).

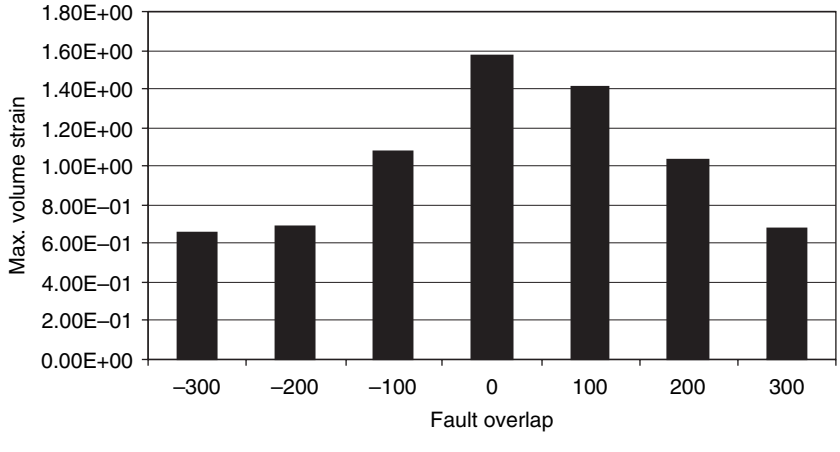

Fig. 5. Histogram showing variations of the maximum volumetric strain in a model with fault overlap for 3D models. The maximum volumetric strain is the maximum volumetric strain value at a single location (numerical mesh element).

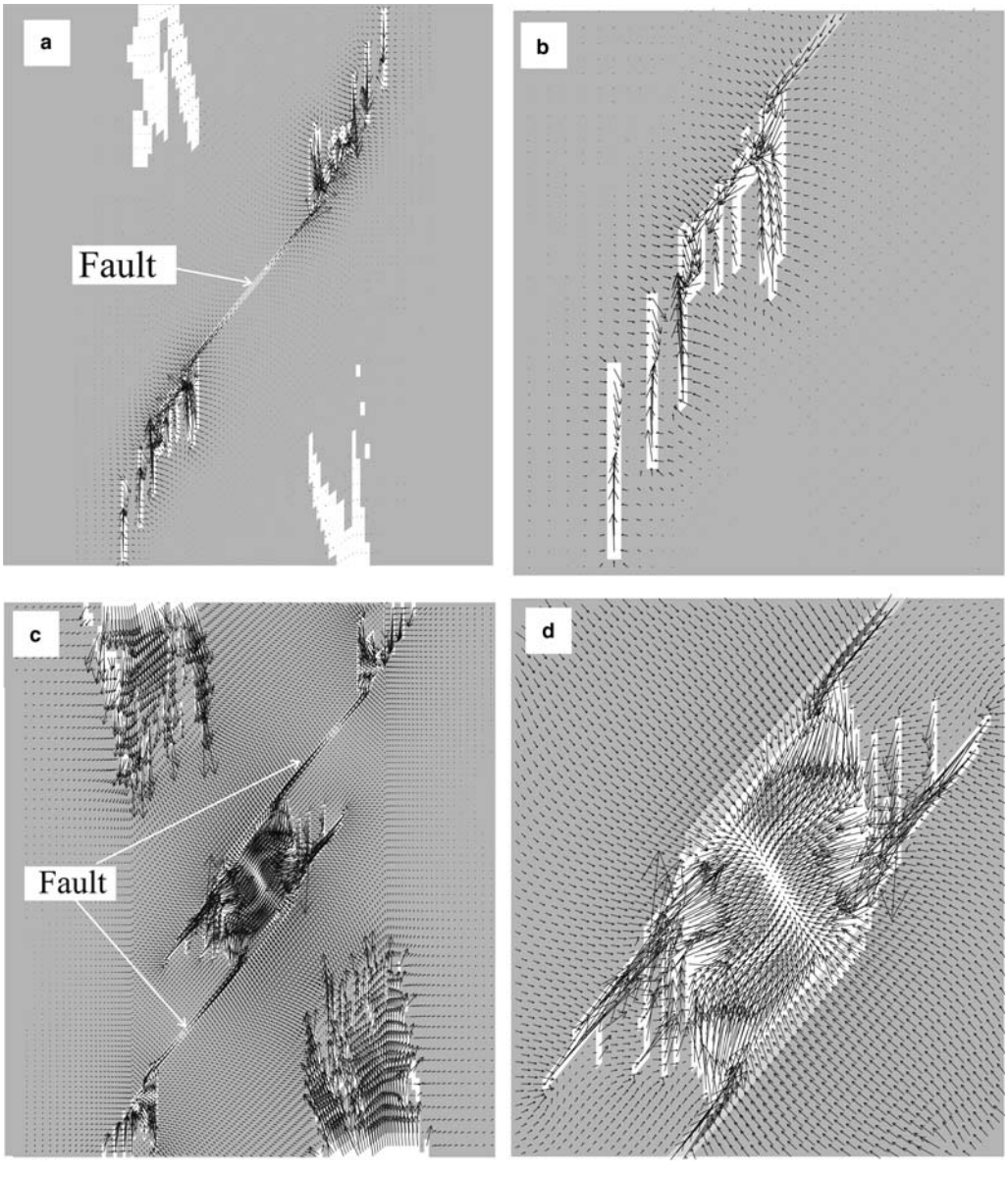

Fig. 6. Instantaneous Darcy fluid flow vectors; the white zones shows the locations of high-permeability structures (5×10^{-12} m^2) developed as a result of faulting. (**a**) The model with an isolated single fault; (**b**) portion of the single-fault model near the lower end of the fault; (**c**) the model with two isolated faults; and (**d**) central portion of the two fault model. The maximum instantaneous flow velocity is 1.5×10^{-6} and 0.9×10^{-6} m s^{-1} for the single- and two-fault models, respectively.

sites. Significant mixing occurs in the major dilation zones both at the fault tips and in the overlap zone as fluids from the top and bottom of the model meet.

Fluid flow vectors in 3D models

The Darcy fluid flow velocities for three 3D models on a horizontal plane are plotted in Figure 7. We have not included a coupling between deformation and deformation-enhanced permeability in the 3D models so the permeability in the 3D models remains constant as deformation takes place; however, fluid flow is still controlled by regions of dilation and contraction. Fluid flow is greatest in the area where the two faults interact in all models. Fluid flow at the non-interacting tips is

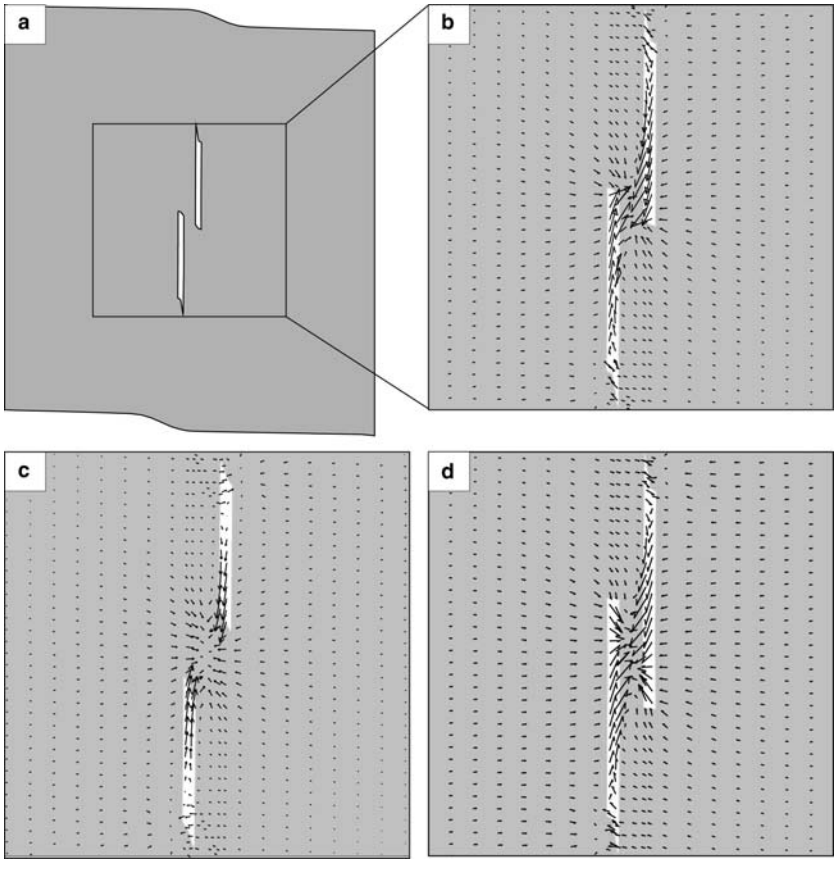

Fig. 7. Instantaneous Darcy fluid flow vectors for 3D models (plotted on a plan-view plane). (**a**) Plan-view geometry of the models after deformation. (**b**), (**c**) and (**d**) are for the model with fault overlaps (O) of 0, −300 and 300 m, respectively. The maximum fluid flow rates for the three models are 2.633×10^{-9}, 1.917×10^{-9} and 1.7×10^{-9} m s^{-1}, respectively.

also enhanced relative to the surrounding matrix. In models with positive overlap, fluid flows out of the sides of the faults towards the area of dilation in between the two faults. In models with negative overlap fluid flows out at the tips of the faults and into the region of dilation. This is consistent with the results of the 2D models above.

Gold and quartz precipitation patterns

Chemical reaction–transport modelling allows us to predict the concentration gradients of relevant chemical species and the precipitation rates of various minerals. In order to ensure the accuracy of numerical computation, several attempts have been made to verify the numerical methods used for solving this kind of mineralization problem in hydrothermal systems (e.g., Zhao *et al.* 2000*a*). As mentioned previously, the fluid flow fields from the FLAC2D models with a single fault and two faults (see Fig. 6) were used in the present chemical reaction FIDAP models.

Figure 8a–d illustrates the equilibrium precipitation patterns of gold and quartz for the single and two fault models, respectively, based on the assumption that isothermal fluid mixing alone is responsible for changes in solubility. Note that the maximum gold precipitation rates (Fig. 8a & b) occur in dilation zones and along some segments of the faults. Gold precipitation rates here are jointly determined by: (1) structural locations (dilation zones and faults) which favour high fluid flow rates (see Fig. 6); (2) favourable geometry which promotes the possibility and efficiency of mixing of two different fluids (see Fig. 6b & d); (3) gradients of pH and concentration gradients of H_2S, as indicated by equation (6). Maximum gold precipitation is only possible when all these conditions are favourable. The patchy distribution of gold precipitation arises from the rapid variations

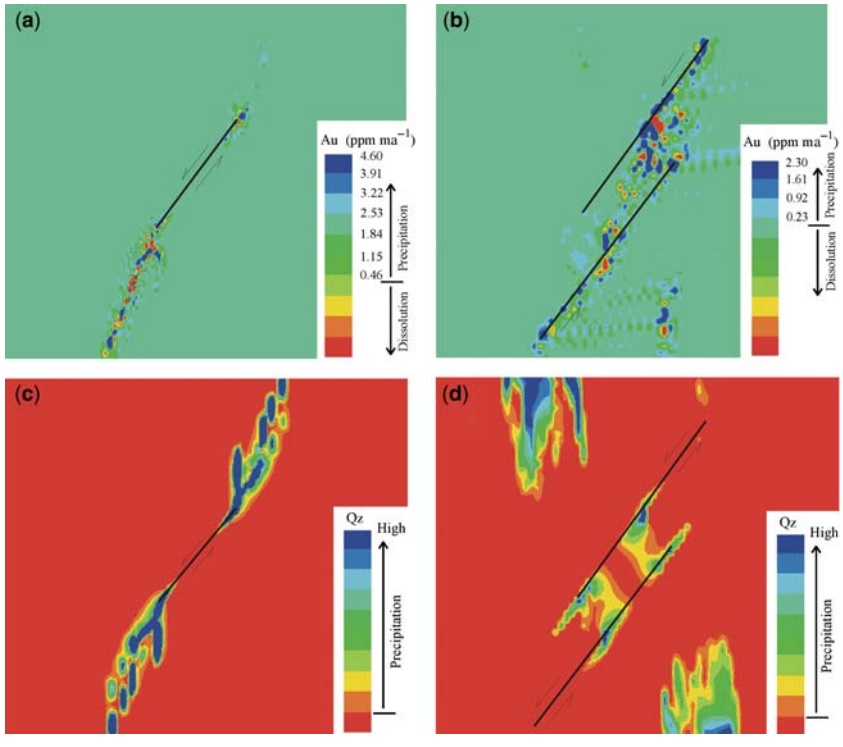

Fig. 8. (**a**) and (**b**) Precipitation rates of gold for the models with a single fault and two faults (ppm per million years by weight), respectively. (**c**) and (**d**) Precipitation rates of quartz for the models with a single fault and two faults, respectively. Only the central portions of the models (see Figs 1 & 6) are plotted.

in fluid flow vectors relative to local gradients in chemistry. Based on the gold precipitation rates predicted by the current model, a gold deposit with a grade of about 3.5 g t^{-1} could be formed in 1.5 million years.

It is noted that gold precipitation and dissolution patterns show clear asymmetry with respect to faults in the models. Precipitation and dissolution rates are greater at one end of the fault than at the other end (see Fig. 8a & b). This is due to the fact that the chemical reaction considered for gold precipitation and dissolution in this investigation is of high-order nonlinear nature, as can be clearly seen from both equations (6) and (8). For a high-order nonlinear chemical reaction system, asymmetric reaction patterns, known as dissipative structures, can be produced, if the chemical instability takes place within the system (Zhao *et al.* 2000*b*). However the essential reason for the asymmetry lies in the asymmetrical chemical boundary conditions described in Table 2 with fluids of different chemical compositions injected at the top and bottom of the model. This results in asymmetrical chemical gradients that impact especially on the sites for precipitation of gold.

Quartz precipitation patterns (Fig. 8c & d) seem to be more closely controlled by fluid flow rates and do not require the fluid mixing condition. Note that under isothermal conditions, quartz precipitation is mainly controlled by the scalar product of the flow velocity and fluid pressure gradient, as demonstrated by the dynamic mineralization theory in permeable reactive rocks (Phillips 1991; Zhao *et al.* 2002). For this reason, high precipitation occurs wherever fluid flow rates are high (see Fig. 6), implying that the fluid pressure gradient is also large in the considered system. For example, in the high fluid flux zone (fluid flow conduits without mixing) near the top and bottom boundaries of the two fault model, quartz precipitation rates are quite high, but in contrast, Au precipitation there is relatively low (top-boundary zone in particular, which is more remote from the H_2S source at the bottom boundary).

Discussions

Styles of host rock damage surrounding faults can be very diverse, depending upon fault history and tectonic setting. For a single event, damage will

most likely be concentrated at fault tips (wing crack-type failure) for a single fault case or at dilatant jog sites (dilatant veins) for multiple fault cases, rather than at the central segment of faults where the maximum displacement occurs. Similar patterns have been observed extensively in field examples (e.g., Rispoli 1981; Lee & Wiltschko 2000; Kim *et al.* 2004) and been predicted by the current models. Mechanically, these locations are tensile sites with relatively high σ_1 and low σ_3 (high tensile stresses) that promote tensile failure, whereas fault central segments are associated with a stress shadow that is characterized by relatively low σ_1, but higher σ_3 (see Fig. 2).

It has also been observed that damage zones develop along entire fault lengths with maximum damage located at the central part of a fault (e.g., Shipton & Cowie 2001, 2003). This case seems to be mainly due to fault propagation as a result of multiple individual slip events. The earliest slip phase occurred at the central part of the fault, and as the fault propagated, the damage zone also developed and was enhanced.

The current models assume high permeability for the faults and simulate permeability enhancement as a result of tensile failure. This is a rather simple approach to modelling fault permeability enhancement, although it is consistent with the general expectations that faults during reactivation phase are more permeable in many cases (e.g., Sorjonen-Ward *et al.* 2002; Yang *et al.* 2004), and tensile fracture/brecciation enhance rock permeability and are favourable for mineralization (e.g., Zhang *et al.* 2007). Rock permeability development during deformation and faulting can be very complex. Zhang *et al.* (1999) and Zhang and Cox (2000) showed that the permeability variations of deforming mud and rocks can be both positive and negative, depending on the deformation stage and mineralogical composition. Permeability can increase significantly during the post-compaction deformation (shearing) phase (quartzo-feldspathic gouges), but can also decrease in strongly sheared mature fault gouge materials. Shipton *et al.* (2002) also showed that fault zones with tightly packed deformation bands and highly crushed rock can have permeability reduction in comparison with the host rock, a high porosity sandstone. Similarly, Fisher *et al.* (2003) and Sheldon *et al.* (2006) demonstrated that fault deformation in high porosity sediments leads to permeability reduction and act as barriers to fluid flow. However, these results are probably not applicable to low porosity rocks. For example, Zoback and Byerlee (1975) showed that the deformation of Westerly granite results in permeability increase. Sheldon *et al.* (2006) also showed that the fault deformation in low porosity materials leads to permeability enhancement. Further work is required to consider complex fault deformation history and fault–host rock characteristics.

The general fluid flow patterns of the current models are characterized by fluid focusing and mixing into dilation zones at fault tips or dilatant jog sites (Figs 6 & 7). This illustrates the processes by which fluids can be attracted into dilatant sites from surrounding rocks or from relatively remote fluid sources, and also represents one of the mechanisms for fluids to migrate efficiently through relatively impermeable rocks. The current fluid flow results for dilatant jog cases are generally consistent with those of Connolly and Cosgrove (1999*a*, *b*), which were entirely based on mean elastic stress patterns. However, there is one difference. The current results suggest fluids are always focused into dilatant jog sites in all of positive-overlap, neutral-overlap and under-overlap situations (see Figs 6 & 7), while the results of Connolly and Cosgrove suggest that fluids migrate out of dilatant jog locations in the neutral- and under-overlap cases. We need to understand this difference in future through further modelling work aided by careful analyses of field vein structures. One field example of Kim *et al.* (2004, Fig. 5b), where extensive fractures and damage formed between two underlap, dilatant jog-type faults, seems to support the current results, that is, dilation still occurs in underlap jog situation and still attracts fluids.

The current 2D and 3D models are at the scales of several thousand metres. We have already described the consistency of the current results with those from the experiments of Wang *et al.* (1987), Connolly and Cosgrave (1999*a*, *b*) and Joussineau *et al.* (2001), all at the scale of centimetres. Stress distribution, rock failure and dilation patterns around a fault should not depend on scale, and tensile failure/fracture and dilation should always develop at the tips of sliding faults with a variety of lengths (see Rispoli 1981; Kim *et al.* 2004). One condition might be that the host rock is relatively homogenous with respect to the discrete fault, which suggests that the mechanical effect of fault sliding dominates over any mechanical effects of textural anisotropy of the host rocks.

Conclusions

Our models have simulated the patterns of deformation, dilation, permeability enhancement, fluid flow and mineral precipitation associated with faulting for simple single fault and two fault cases and adopting a simplified method of reaction transport modelling. The results show that faulting-dilation and faulting-induced host rock permeability enhancement represent important ways to generate

fluid flow conduits for more effective fluid flow and mixing. This is achieved by the development of dilation zones and the generation of higher permeability structures, both of which are closely associated with tensile failure and fracturing. Generation of high dilation during strike–slip faulting is predominantly localized near fault tips (wing crack locations) and dilatant jog sites, which are the tensile domains of the strike–slip regime. When faults overlap, the magnitude of dilation and the extent of the dilatant region are closely related to the extent of fault overlap. These dilatant regions are important sites for fluid focusing and mixing.

Permeability enhancement during deformation allows fluids to be transported through otherwise relatively impermeable rocks, and to focus/mix in structurally favourable locations (dilation zones or pre-existing faults), creating ideal sites for fluid mixing and hence chemical reaction and mineral precipitation. Mineral precipitation rates depend critically on structural and fluid flow conditions and on the geometrical relation between local fluid velocity and chemical concentration gradients generated by mixing. This results in highly variable spatial mineralization sites – a situation common in nature. Maximum precipitation rates for gold are only possible in the dilation zones and faults where high fluid flow rates across gradients in the aqueous silica concentration, sufficient fluid mixing and high concentration gradients of critical chemical species are all present, while quartz precipitation rate is predominantly controlled by fluid flow rates.

A. Billi and P. Connolly are thanked for their constructive reviews and comments, and Walter Kurz is thanked for his editorial help. We would like to thank the Predictive Mineral Discovery Cooperative Research Centre for financial support. The Australian Geodynamics Cooperative Research Centre is acknowledged for the FIDAP license. Y. Zhang acknowledges research support by the CAS/SAFEA International Partnership Program for Creative Research Teams. A.C. Barnicoat publishes with permission of the CEO, Geoscience Australia.

References

BARNES, H. L. 1979. *Geochemistry of Hydrothermal Ore Deposits*. Wiley, New York.

BÜRGMANN, R. & POLLARD, D. D. 1994. Strain accommodation about strike–slip fault discontinuities in granitic rock under brittle-to-ductile conditions. *Journal of Structural Geology*, **16**, 1655–1674.

CHINNERY, M. A. 1963. The stress changes that accompany strike–slip faulting. *Bulletin of the Seismological Society of America*, **53**, 921–932.

CONNOLLY, P. & COSGROVE, J. 1999*a*. Prediction of static and dynamic fluid pathways within and around dilational jogs. *In*: MCCAFFREY, K. J. W., LONERGAN, L. & WILKINSON, J. J. (eds) *Fractures, Fluid Flow and Mineralization*. Geological Society, London, Special Publications, **155**, 105–121.

CONNOLLY, P. & COSGROVE, J. 1999*b*. Prediction of fracture-induced permeability and fluid flow in the crust using experimental stress data. *AAPG Bulletin*, **83**, 757–777.

COX, S. F. 1999. Deformational controls on the dynamics of fluid flow in mesothermal gold systems. *In*: MCCAFFREY, K. J. W., LONERGAN, L. & WILKINSON, J. J. (eds) *Fractures, Fluid Flow and Mineralization*. Geological Society, London, Special Publications, **155**, 123–139.

COX, S. F. & RUMING, K. 2004. The St Ives mesothermal gold system, Western Australia – a case of golden aftershocks? *Journal of Structural Geology*, **26**, 1109–1125.

COX, S. F., KNACKSTEDT, M. A. & BRAUN, J. 2001. Principles of structural control on permeability and fluid flow in hydrothermal systems. *Reviews in Economic Geology* **14**, 1–24.

CUNDALL, P. A. & BOARD, M. 1988. A microcomputer program for modelling large-strain plasticity problems. *In*: SWOBODA, C. (ed.) *Numerical Methods in Geomechanics, Proceedings of the Sixth International Conference on Numerical Methods in Geomechanics*. Balkema, Rotterdam, 2101–2108.

CUREWITZ, D. & KARSON, J. A. 1997. Structural settings of hydrothermal outflow: fracture permeability maintained by fault propagation and interaction. *Journal of Volcanology & Geothermal Research*, **79**, 149–168.

D'ALESSIO, M. A. & MARTEL, S. J. 2004. Fault terminations and barriers to fault growth. *Journal of Structural Geology*, **26**, 1885–1896.

DYSKIN, A. V., GERMANOVICK, L. N. & USTINOV, K. B. 1999. A 3-D model of wing crack growth and interaction. *Engineering Fracture Mechanics*, **63**, 81–110.

EDMOND, J. M. & PATERSON, M. S. 1972. Volume changes during the deformation of rocks at high pressures. *International Journal of Rock Mechanics and Mining Sciences*, **9**, 161–182.

ERICKSON, S. G., STRAYER, L. M. & SUPPE, J. 2001. Initiation and reactivation of faults during movement over a thrust-fault ramp: numerical mechanical models. *Journal of Structural Geology*, **23**, 11–23.

FERRARI, M. A. D. & CHOUDHURI, A. 2004. Structural controls on gold mineralisation and the nature of related fluids of the Paiol gold deposit, Almas Greenstone Belt, Brazil. *Ore Geology Reviews*, **24**, 173–197.

FISHER, Q. J., CASEY, M., HARRIS, S. D. & KNIPE, R. J. 2003. Fluid flow properties of faults in sandstone: the importance of temperature history. *Geology*, **31**, 965–968.

FLUID DYNAMICS INTERNATIONAL. 1997. *Fluid Dynamics Analysis Package: FIDAP*. Fluid Dynamics International, Evanston, IL.

HOBBS, B. E. & ORD, A. 1989. Numerical simulation of shear band formation in a frictional–dilatant material. *Ingenieur-Archiv*, **59**, 209–220.

ITASCA. 1998. *FLAC2D: Fast Lagrangian Analysis of Continua, User Manual, Version 3.4*. Itasca Consulting Group, Minneapolis, MN.

ITASCA. 2003. *FLAC3D: Fast Lagrangian Analysis of Continua in 3 Dimensions, User Manual, Version 2.1*. Itasca Consulting Group, Minneapolis, MN.

JAEGER, J. C. & COOK, N. G. W. 1979. *Fundamentals of Rock Mechanics*, 3rd edn. Chapman and Hall, London.

JOLLEY, S. J., FREEMAN, S. R. *ET AL*. 2004. Structural controls on Witwatersrand gold mineralisation. *Journal of Structural Geology*, **26**, 1067–1086.

JOUSSINEAU, G. de, BOUISSOU, S., PETIT, J. P. & BARQUINS, M. 2001. Experimental analysis of slip distribution along a fault segment under strike–slip and stable sliding conditions. *Tectonophysics*, **337**, 85–98.

KIM, Y. S., PEACOCK, D. C. P. & SANDERSON, D. J. 2004. Fault damage zones. *Journal of Structural Geology*, **26**, 503–517.

KNIPE, R. J. 1993. The influence of fault zone processes and diagenesis on fluid flow. *In*: HORBURY, A. D. & ROBINSON, A. G. (eds) *Diagenesis and Basin Development*. American Association of Petroleum Geologists (AAPG) Studies in Geology, Tulsa, OK, **36**, 135–154.

LEE, Y. J. & WILTSCHKO, D. V. 2000. Fault controlled sequential vein dilation: competition between slip and precipitation rates in the Austin Chalk, Texas. *Journal of Structural Geology*, **22**, 1247–1260.

MALVERN, L. E. 1969. *Introduction to the Mechanics of a Continuous Medium*. Prentice-Hall, Englewood Cliffs, NJ.

MANDL, G. 1988. *Mechanics of Tectonic Faulting*. Elsevier, Amsterdam.

NEČMOK, M., ANDREAS, H., GAYER, R. A., VANDYCKE, S. & HATHAWAY, T. M. 2002. Strike–slip fault bridge fluid pumping mechanism: sisights from field-based palaeostress analysis and numerical modelling. *Journal of Structural Geology*, **24**, 1885–1901.

NGUYEN, P., COX, S. F., HARRIS, L. B. & POWELL, C. M. 1998. Fault-value behaviour in optimally oriented shear zones: an example at the Revenge gold mine, Kambalda, Western Australia. *Journal of Structural Geology*, **20**, 1625–1640.

ORD, A. 1991. Deformation of rock: a pressure-sensitive, dilatant material. *Pure and Applied Geophysics*, **137**, 337–366.

ORD, A., HOBBS, B. E. & REGENAUER-LIEB, K. 2004. A smeared seismicity constitutive model. *Earth, Planets, Space*, **56**, 1121–1133.

PHILLIPS, O. M. 1991. *Flow and Reactions in Permeable Rocks*. Cambridge University Press, Cambridge.

RISPOLI, R. 1981. Stress fields about strike–slip faults inferred from stylolites and tension gashes. *Tectonophysics*, **75**, T29–T36.

SCHAUBS, P. M. & WILSON, C. J. L. 2002. The relative roles of folding and faulting in controlling gold mineralization along the Deborah anticline, Bendigo, Victoria, Australia. *Economic Geology*, **97**, 351–370.

SHELDON, H. A., BARNICOAT, A. & ORD, A. 2006. Numerical modelling of faulting and fluid flow in porous rocks: an approach based on critical state soil mechanics. *Journal of Structural Geology*, **28**, 1468–1482.

SHIPTON, Z. K. & COWIE, P. A. 2001. Damage zone and slip-surface evolution over μm to km scales in high-porosity Navajo sandstone, Utah. *Journal Structural Geology*, **23**, 1825–1844.

SHIPTON, Z. K. & COWIE, P. A. 2003. A conceptual model for the origin of fault damage zone structures in high-porosity sandstone. *Journal of Structural Geology*, **25**, 333–344.

SHIPTON, Z. K., EVANS, J. P., ROBESON, K. R., FORSTER, C. B. & SNELGROVE, S. S. 2002. Sturctural heterogeneity and permeability in faulted eolian sandstone: implications for subsurface modelling of faults. *AAPG Bulletin*, **86**, 863–883.

SIBSON, R. H. 1986. Brecciation processes in fault zones: inferences from earthquake rupturing. *PAGEOPH*, **124**, 159–175.

SIBSON, R. H. 1994. Crustal stress, faulting and fluid flow. *In*: PARNELL, J. (ed.) *Geofluids: Origin, Migration and Evolution of Fluids in Sedimentary Basins*. Geological Society, London, Special Publications, **78**, 69–84.

SIBSON, R. H., MOORE, J. & RANKIN, A. H. 1975. Seismic pumping – a hydrothermal fluid transport mechanism. *Journal of the Geological Society of London*, **131**, 653–659.

SORJONEN-WARD, P., ZHANG, Y. & ZHAO, C. 2002. Numerical modeling of orogenic processes and gold mineralization in the southeastern part of the Yilgarn craton, Western Australia. *Australian Journal of Earth Sciences*, **49**, 1011–1039.

STRAYER, L. M., HUDLESTON, P. J. & LORIG, L. J. 2001. A numerical models of deformation and fluid-flow in an evolving thrust wedge. *Tectonophysics*, **335**, 121–145.

VERMEER, P. A. & DE BORST, R. 1984. Non-associated plasticity for soils, concrete and rock. *Heron*, **29**, 1–64.

WANG, R., ZHAO, Y., CHEN, Y., YAN, H., YIN, Y. Q., YAO, C. Y. & ZHANG, H. 1987. Experiment and finite element simulation of X-type shear fractures from a crack in marble. *Tectonophysics*, **144**, 141–150.

WILLEMSE, E. J. M. & POLLARD, D. 2000. Normal fault growth: evolution of tipline shapes and slp distribution. *In*: LEHNER, F. K. & URAI, J. L. (eds) *Aspects of Tectonic Faulting*. Springer, Berlin.

WOLERY, T. J. 1979. *Calculation of Chemical Equilibria Between Aqueous Solution and Minerals: The EQ3/6 Software Package, UCR-52658*. Lawrence Livermore Laboratory, Livermore, CA.

YANG, J., LARGE, R. & BULL, S. 2004. Factors controlling free thermal convection in faults in sedimentary basins: implications for the formation of zinc-lead mineral deposits. *Geofluids*, **4**, 1–11.

ZHANG, S. & COX, S. F. 2000. Enhancement of fluid permeability during shear deformation of a synthetic mud. *Journal of Structural Geology*, **22**, 795–806.

ZHANG, S., TULLIS, T. E. & SCRUGGS, V. J. 1999. Permeability anisotropy and pressure dependence of permeability in experimentally sheared gouge materials. *Journal of Structural Geology*, **21**, 1385–1393.

ZHANG, Y., LIN, G., WANG, Y. J., ROBERTS, P. A. & ORD, A. 2007. Numerical modelling of deformation and fluid flow in the Shui-Kou-Shan mineralisation district, Hunan Province, South China. *Ore Geology Reviews*, **31**, 261–278.

ZHAO, C., HOBBS, B. E., MÜHLHAUS, H. B. & ORD, A. 1999. A consistent point-searching algorithm for

solution interpolation in unstructured meshes consisting of 4-node bilinear quadrilateral elements. *International Journal for Numerical Methods in Engineering*, **45**, 1509–1526.

ZHAO, C., HOBBS, B. E., MUHLHAUS, H. B., ORD, A. & LIN, G., 2000*a*. Numerical modelling of double diffusion driven reactive flow transport in deformable fluid-saturated porous media with particular consideration of temperature-dependent chemical reaction rates. *International Journal for CAE and Software: Engineering Computations*, **17**, 367–385.

ZHAO, C., HOBBS, B. E., MUHLHAUS, H. B. & ORD, A. 2000*b*. Finite element modelling of dissipative structures for nonequalilibrium chemical reactions in fluid-saturated porous media. *Computer Methods in Applied Mechanics and Engineering*, **184**, 1–14.

ZHAO, C., LIN, G., HOBBS, B. E., WANG, Y., MUHLHAUS, H. B. & ORD, A. 2002. Finite element modelling of reactive fluids mixing and mineralization in pore-fluid saturated hydrothermal/sedimentary basins. *International Journal for CAE and Software: Engineering Computations*, **19**, 364–387.

ZOBACK, M. D. & BYERLEE, J. D. 1975. The effect of microcrack dilatancy on the permeability of Westerly granite. *Journal of Geophysical Research*, **80**, 752–755.

Fault and fluid interaction in a rifted margin: integrated study of calcite-sealed fault-related structures (southern Corinth margin)

A. BENEDICTO[1], V. PLAGNES[2], P. VERGÉLY[1], N. FLOTTÉ[1] & R. A. SCHULTZ[3]

[1]*Dynamics of Fault Systems Group, UMR-7072 Tectonique, Université Paris Sud XI, 91405 Orsay, France (e-mail: Antonio.Benedicto-Esteban@u-psud.fr)*

[2]*UMR-7619 Sisyphe, Université Paris VI, 75252 Paris, France*

[3]*Department of Geological Sciences and Engineering, University of Nevada, Reno, NV, USA*

Abstract: This work integrates microstructural, petrologic, microthermometric and geochemical analysis of calcite-sealed fault-related structures of the major faults of the southern margin of the Corinth rift (Greece). It draws attention to the main deformational processes and fault–fluid interaction in fault zones along the whole margin. Data analysed come from the compact breccia located immediately adjacent to major fault planes. Samples were collected at different positions alongside different faults juxtaposing synrift continental deposits (hanging wall) against the prerift Pindus limestones (footwall). This implies hectometric fault displacements and that the fault zones have recorded a relatively long evolution of deformation. Our study identifies four main deformation features common to all studied faults: calcite cemented breccia, extensional veins, shear veins and fault slip surfaces. The integrated data analysis shows that deformation structures and fault rocks that coexist in the same outcrop formed at different depths and times. During inferred upward fault propagation, the style of deformation evolved from distributed (brecciation) to localized (slip surfaces) and from a closed system with fluid–rock equilibrium during brecciation to a more open one with limited influx of meteoric water during extensional and shear fracturing. This implies relative uplift of the footwall during fault propagation and fault interaction with different water aquifers as the fault propagates upwards. The results demonstrate similar fault evolution and fault–fluid interaction through the entire rifted margin and during the whole rifting period.

The south side of the Gulf of Corinth (Greece) is a much studied area because it is one of the most seismically active areas in the Euro-Mediterranean region (see Bernard *et al.* 2006 and references therein), and it has been selected for drilling and *in situ* monitoring of an active fault (Corinth Rift Laboratory, Cornet *et al.* 2004). Currently stress, strain, chemistry of the aquifer, pore pressure, fluid flow in some aquifers and tide are being continuously monitored and recorded (Henry & Moretti 2006). One of the aims of such a drilling and monitoring project (e.g., the Nojima Fault Drilling, Lin *et al.* 2003) is to investigate fault–fluid interactions during fault activity. Understanding of fault–fluid interactions is essential to understanding fault mechanics and coseismic and interseismic faulting processes. One method to study long-lived fault–fluid interactions is by studying syntectonic mineralization within outcropping ancient fault zones (Labaume *et al.* 1991; Bradbury & Woodwell 1987; Muchez *et al.* 1995). Combined micro-structural, petrologic, microthermometric and geochemical analysis of synkinematic fault and fracture-related calcites permit the evaluation of fluid sources and flow pathways (e.g., Travé *et al.* 1998; Boles & Grivetti 2000; Cello *et al.* 2001; Pili *et al.* 2003), associated deformation mechanisms and fluid-driven mass transfers in fault zones (e.g., Travé *et al.* 1998; Sibson 2000; Labaume *et al.* 2004*a*; Micarelli *et al.*, 2005).

The exposed southern margin of the active Corinth continental rift (northern Peloponnesus) has experienced intensive uplift since rifting started (e.g., Collier *et al.* 1992; Sorel 2000; Leeder *et al.* 2003). Uplift has led to the exhumation and exposition of numerous ancient to active normal faults (Fig. 2). In a similar way to faults described in other areas of the Aegean region (Vita-Finzi & King 1985; Stewart & Hancock 1988, 1990), fault zones in the Northern-Peloponnesus area are characterized by several layers of tectonic breccia rocks and master fault slip surfaces. Breccia fault rocks and fault-related fractures are calcite-sealed, attesting to the presence of palaeofluids during deformation.

Here we combine a micro-structural and petrologic analysis (conventional, C, and cathodoluminescence, CL, microscopy) of breccia fault rocks and major fault planes with a microthermometric (fluid inclusion) and geochemical (stable isotope)

From: WIBBERLEY, C. A. J., KURZ, W., IMBER, J., HOLDSWORTH, R. E. & COLLETTINI, C. (eds) *The Internal Structure of Fault Zones: Implications for Mechanical and Fluid-Flow Properties*. **299**, 257–275.
DOI: 10.1144/SP299.16 0305-8719/08/$15.00

analysis of fault-related syn-kinematic calcite cements collected along the entire southern Corinth rifted margin. The aim is to investigate common patterns of fault and palaeofluid features during spatial–temporal fault evolution at the scale of a rifted margin. An analogous study carried out in the same region but only for a unique outcrop of secondary faults related to a major structure is that of Labaume *et al.* (2004*a*), which presents complementary results.

Geological setting

The Corinth rift is an active N110° striking asymmetric structure belonging to a system of horsts and grabens which extend from the North Anatolian fault termination in the Aegean Sea to the Kephalonia transform fault in the Ionian Sea (Fig. 1). It cuts obliquely through the Cenozoic N160° thrust belt of the external Hellenides which controls the structure of the Triassic to Oligocene prerift basement (Aubouin & Dercourt 1962; Dercourt 1964).

Different rifting models have been proposed in the last several years and these are still debated. Westaway (2002) proposed that the overall form of the Gulf of Corinth is the result of flow of plastic lower continental crust from beneath its subsiding depocentre to beneath its uplifting surroundings. Other authors propose that the rift may be controlled by a major low-angle north-dipping detachment (Sorel 2000; Exadaktylos *et al.* 2003; Flotté 2003), initiated 1.7–1.5 Ma ago (Sorel 2000; Flotté 2003). Numerical modelling by Le Pourhiet (2004) and Le Pourhiet *et al.* (2004), and field analysis by Bally (2005) suggest a deeper detachment related to the presence under the Gulf of Corinth of the inherited Phyllades metamorphic thrust sheet. Additionally, some authors have suggested that some faults such as the Eliki and Aegion faults could have formed during the uplift of the Peloponnese as an 'external' phenomenon superimposed on the opening of the Gulf of Corinth (Moretti *et al.* 2003).

Whatever rifting model is assumed (which is not essential to this paper), the fact is that a great number of normal faults crop out in the southern margin of the Gulf of Corinth (northern Peloponnesus; Fig. 2). They are responsible for south-dipping block tilting and syntectonic half-graben basin formation (Brooks & Ferentinos 1984; Ferentinos *et al.* 1985; Flotté & Sorel 2001; Exadaktylos *et al.* 2003; Sachpazi *et al.* 2003). Since initiation of rifting, normal fault activity has, in a general way, progressively migrated to the north (Seger & Alexander 1993; Sorel 2000; Goldsworthy & Jackson 2001; Flotté 2003; even if locally some faults can be 'out of sequence', see for example Causse

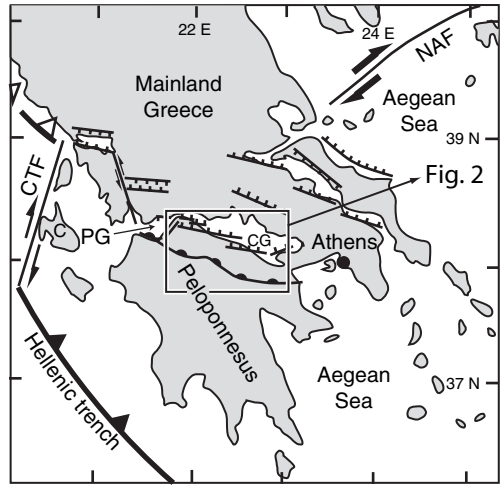

Fig. 1. Location of the Gulf of Corinth (CG) rift in the plate tectonic context. The studied area (southern margin of the rift) is squared. NAF, North Anatolian Fault; CTF, Cephalonian Transfer Fault; PG, Gulf of Patras.

et al. 2004), forming several major extensional fault systems that may be differentiated according to their relative chronostratigraphy of basin-fills (Flotté 2003). Fault activity today is located close to the present day coastline and offshore of the Gulf of Corinth (Lyon-Caen *et al.* 2004; Pi alparin *et al.* 2004).

Major extensional fault systems in the northern Peloponnesus are 20–50 km long (Fig. 2) and are orthogonal to the N10°E direction of extension measured on fault planes from striation and grooves (Flotté & Sorel 2001). Faults cross-cut the Triassic to Oligocene marine rocks forming the prerift basement, and the continental to marine Quaternary deposits associated with the rifting period. The prerift terrains are classically divided into several zones that correspond to the palaeogeographic pre-orogenic and foreland basin of the Hellenides (Dercourt 1964; Aubouin & Dercourt 1962). In the Northern Peloponnesus, three of those units are well represented (Sébrier 1977; De Wever 1975): the Phyllades or Zaroukla zone, composed of metamorphic rocks; the Gavrovo–Tripolitsa zone mainly made up of neritic and platform limestones; and the Pindus–Olonos zone, constituted by radiolarites, deep-basin limestones and flysch deposits (De Wever 1975; Dufaure 1977; Fig. 3). Those palaeogeographic domains were deformed during Hellenides folding and thrusting: the Zaroukla unit is overthrusted by the Gavrovo–Tripolitsa neritic domain which is, in turn, overthrusted by the Pindus–Olonos pelagic domain over more than 100 km (De Wever 1975).

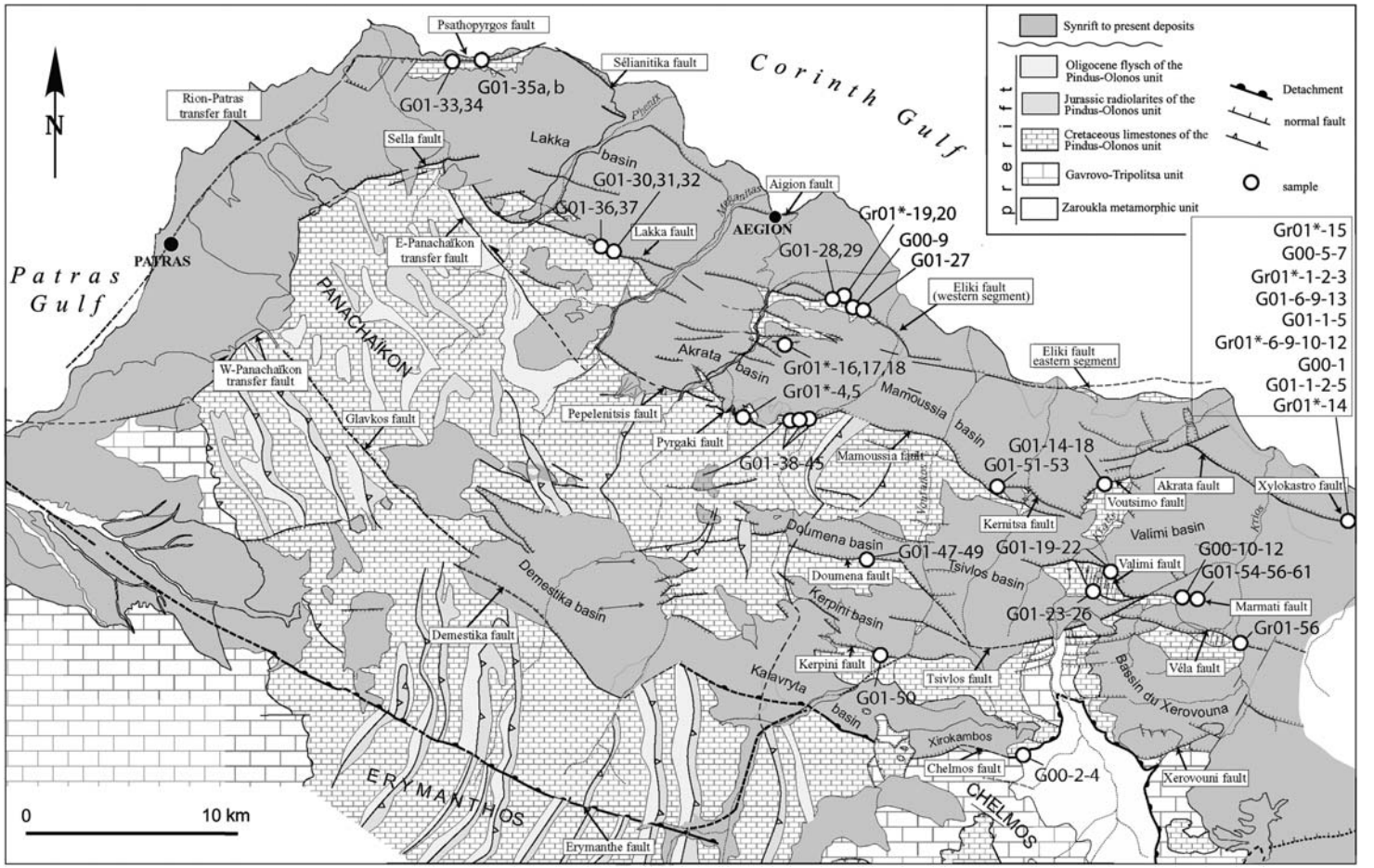

Fig. 2. Tectonic map with sample locations (modified after Flotté 2003).

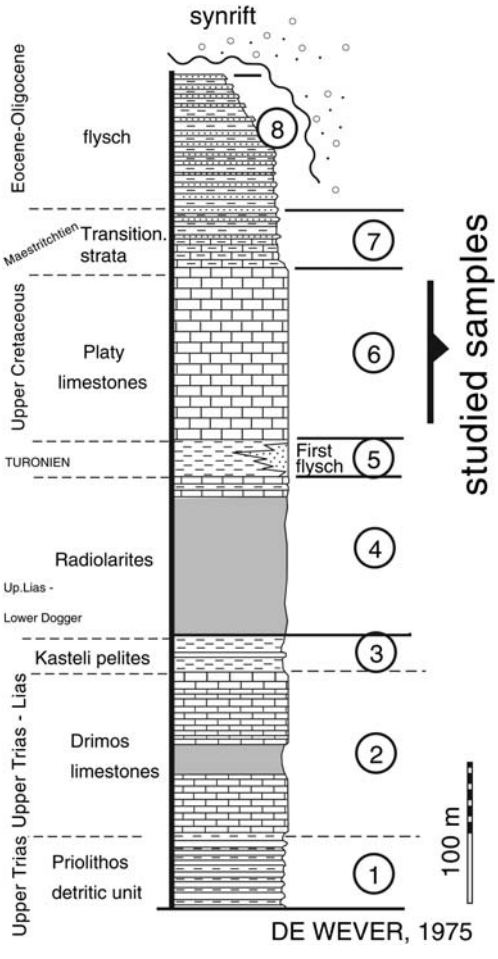

Fig. 3. Stratigraphy of the Pindus–Olonos unit described in the northern Peloponnesus by De Wever (1975). This stratigraphic series mainly forms the outcropping footwall of the studied faults. All samples come from the Upper Cretaceous Platy Limestones formation (numbered 6).

The prerift basement mainly outcrops in the footwalls of normal faults where, except in the footwall of the detachment fault, it is mainly dominated by micritic platy limestones of the Pindus–Olonos unit.

Rifting started in a continental setting and evolved to a marine one. Synrift basin-fill deposits are formed by continental marls, sands and conglomerates, and detritic marine rocks (Ori 1989; Dufaure 1975). Close to the coast, they are generally formed by coarse-grained Gilbert-type fan-deltas (Collier 1990; Seger & Alexander 1993; Dart *et al.* 1994; Malartre *et al.* 2004).

Fault zone data

The fault zones in the prerift carbonate rocks of the Aegean region were first described by Vita-Finzi & King (1985), Stewart & Hancock (1988) and Stewart & Hancock (1990), based on examples of faults located in the Gulf of Alkonides (east of the Gulf of Corinth) and in the Izmir region (Turkey). Following these authors, fault zones are characterized by (see fig. 7 in Stewart & Hancock 1988): (1) a shatter zone of dense fractures disturbing bedding of the footwall; (2) one (or several) zone-parallel layer(s) of incohesive breccia overlain by a compact breccia formed by clast supported elements in a matrix of clast fragments and secondary calcite cement (or 'stylobreccia' when highly deformation occurs); and (3) a slip surface. Breccia layers may be recurrent between several slip planes in larger fault zones.

Studies carried on the northern Peloponnesus (Flotté 2003; Micarelli *et al.* 2003; Daniel *et al.* 2004; Labaume *et al.* 2004*a*; Benedicto *et al.* 2004) also show the major occurrence of alternating cataclastic and/or breccia sheets and fault planes. Micarelli *et al.* (2003) describe the Pyrgaki, Eliki and Aegion faults (Fig. 2) as formed by a fault damage zone composed of several main and secondary fault planes with which are associated fault cores of variable thickness mainly formed by cemented breccia, cohesive cataclasite and/or incohesive gouge, with random or locally foliated fabrics (foliated cataclasites). Clay shearing (Daniel *et al.* 2004; Benedicto *et al.* 2004) and calcite-cemented fractures (Labaume *et al.* 2004*a*) are also representative features.

The common structure of major outcropping faults observed in the northern Peloponnesus may be characterized by a deformed footwall mainly composed of micritic platy limestones of the Pindus–Olonos unit (Pindus Limestones), a fault-parallel zone in which the limestones are partially fractured (shatter zone of Stewart & Hancock 1990) and a zone of compact calcite cemented breccia underlain major, well-exposed, huge slip planes of pure normal motion (Fig. 4). This brecciated fault core constitutes a zone of variable thickness with abundant secondary slip planes locally containing 'pull-apart' synkinematic striated calcite structures (Fig. 5). Locally, non-cohesive breccias (not calcite cemented) may also be present. Further detailed description of several fault zones may be found in Micarelli *et al.* (2003), Daniel *et al.* (2004), Labaume *et al.* (2004*a*) and Benedicto *et al.* (2004).

Data analysed in this paper correspond to the compact breccia immediately located beneath major fault slip surfaces (i.e., compact breccia of Stewart & Hancock 1988 and fault core of Micarelli

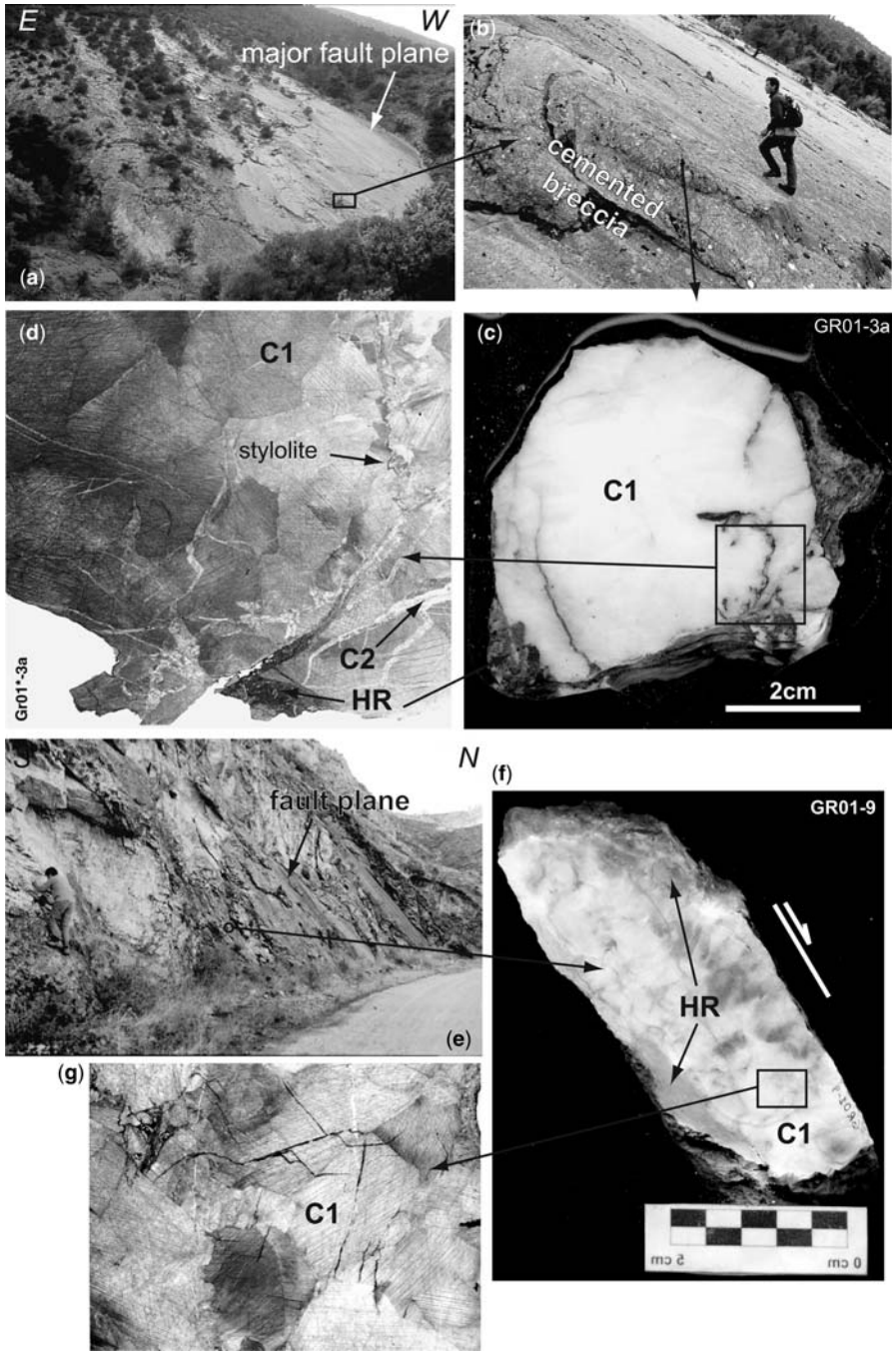

Fig. 4. The Xylokastro fault. (**a**) View of the major fault plane. (**b**) Detail of the cemented breccia underlying the major fault plane. (**c**) Cut sample GR01-3a. (**d**) Thin section viewed under conventional optical microscopy. (**e**) View of the upper part of the Xylokastro fault. (**f**) Cut sample GR01–9. (**g**) Thin section viewed under optical microscopy. C1, calcite cement type 1; C2, calcite cement type 2; HR = host limestone fragment.

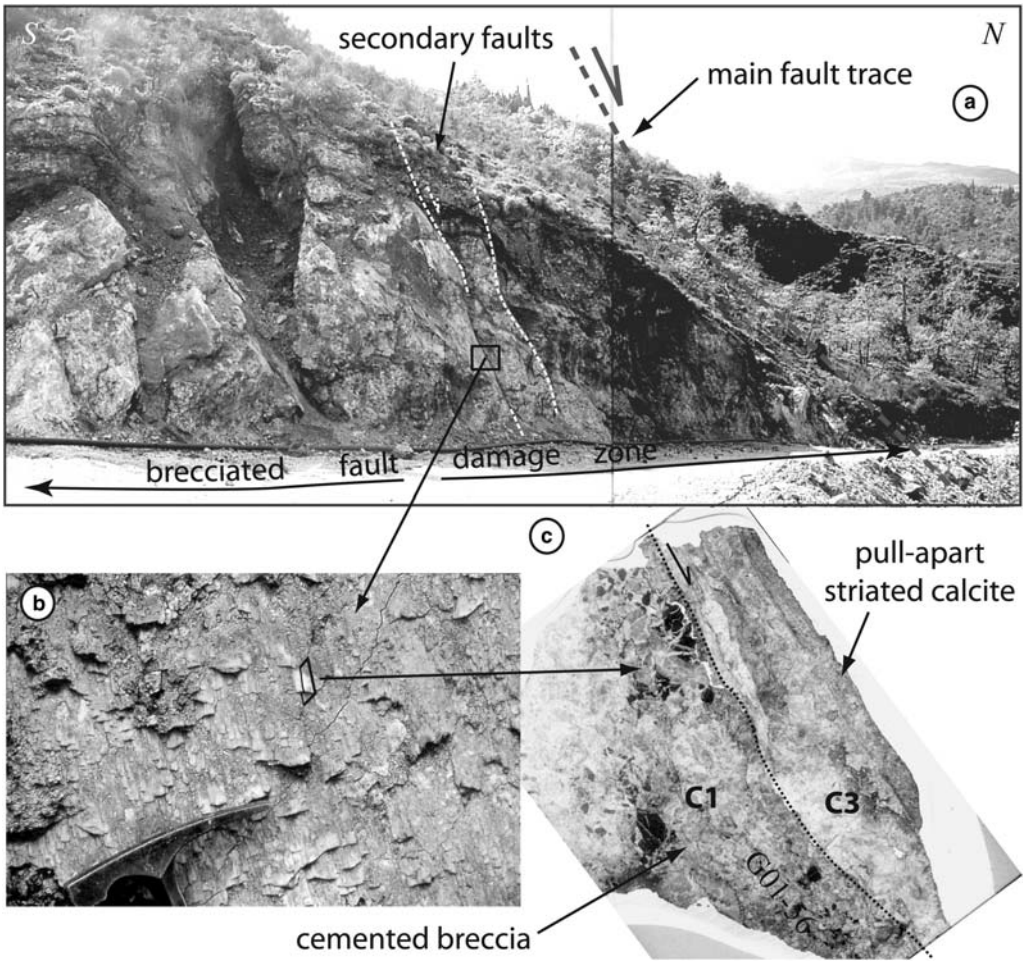

Fig. 5. The Vela fault. (**a**) Picture showing the brecciated damage fault zone cut through by secondary faults. (**b**) Detail of a secondary fault plane with 'pull-apart' syn-kinematic striated calcite. (**c**) Thin section of the sample G01–56.

et al. 2003). Samples were collected at different positions alongside (vertical and horizontal) different faults (Fig. 2). From time to time, slip surfaces are locally sealed by a post-kinematic (karst-type) calcite. For comparison with synkinematic calcites, we also analysed this post-kinematic type. All samples discussed in this paper come from fault zones juxtaposing synrift continental detritic deposits of the hanging wall (presently partially eroded) to the prerift Pindus limestones of the footwall. This implies hectometre fault displacements and that the fault zones analysed have recorded a long fault evolution.

A conventional microstructural and petrologic analysis coupled with a cathodoluminescence analysis was carried out on more than 30 thin sections from 93 samples collected on different faults (Fig. 2). Geochemical analysis for stable isotopes ($\delta^{18}O$ and $\delta^{13}C$) was performed on 31 samples and fluid inclusions for thermometric analysis were investigated in 10 samples.

Microstructural and petrologic analysis

Extensional deformation recorded in the compact breccia is consistently marked by: (i) calcite-cemented breccia (Fig. 6b); (ii) extensional calcite-sealed veins (Fig. 6b); (iii) shear calcite-sealed veins (Fig. 6b); and (iv) stylolites (Fig. 4d). Although stylolite features are abundant and can accommodate large amounts of extensional deformation (Labaume *et al.* 2004*b*; Benedicto *et al.* 2004), here we only focus on the synkinematic

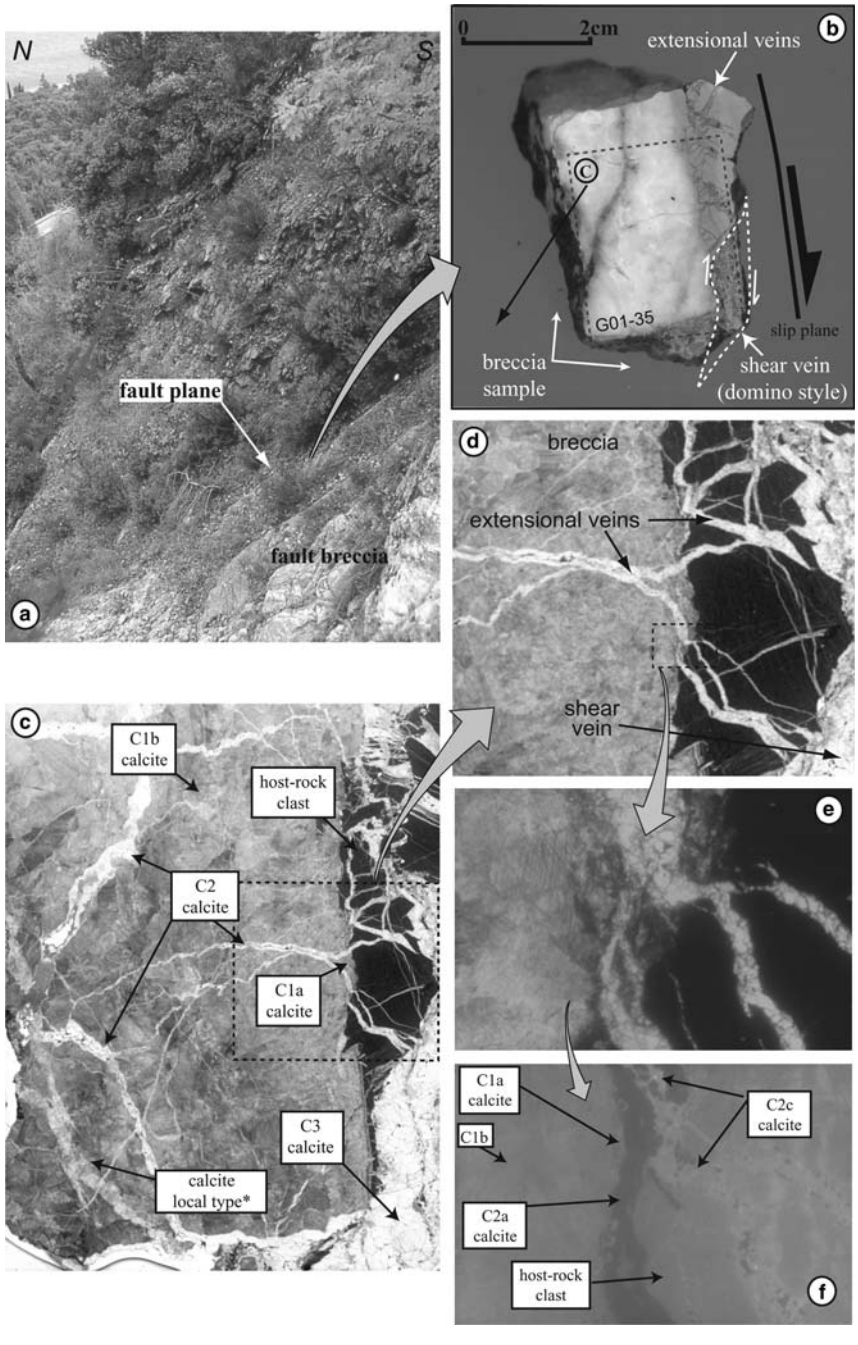

Fig. 6. (**a**) The Psatopyrgos fault. (**b**) Cut sample G01–35. (**c**) & (**d**) Thin section viewed under optical microscopy. Calcite cement types are indicated. (**e**) & (**f**) Zoom on thin section viewed under cathodoluminescence microscopy.

calcite-sealed structures which appear better organized, show clearer cross-cutting relationships and contain information about palaeofluids involved during deformation. This also avoids misinterpretation of stylolites that could be associated with the inherited compressional deformation (Daniel *et al.* 2004). We synthesize the dominant and common deformation and calcite cementation features repeatedly observed along the studied faults and illustrate them with the most characteristic samples.

The microscopy analysis (both optical and cathodoluminescence) reveals: (a) two types of calcite breccia cements; (b) one dominant random network of extensional calcite veins; and (c) one type of shear calcite veins.

Calcite breccia cements (C1)

The host-micrite limestone clasts involved within the breccia are cemented by a rim, very often imperceptible, of micro-sparitic calcite immediately surrounding the clasts, separated from the host-limestone clasts by a vague boundary (C1a in Fig. 6b). When the clasts are slightly disaggregated, this cement may completely fill up the spaces between them (Fig. 7c & d, depicted in light grey). When the clasts are strongly disaggregated, this cement type passes rapidly, but progressively, to sparitic calcite cement with large crystals, anhedral–subhedral, highly twinned and fractured (C1b in Figs 6c & 7d). CL microscopy shows that both types of cements have the same red-orange luminescence as the host-limestone (Figs 6e & 7g). The location of the micro-sparitic cement adjacent to the host-limestone clasts, and its indistinct boundary, suggest that this cement precedes formation of the sparitic one (i.e., associated with early stages of brecciation and cementation). The cementation process seems to be continuous (progressive transition) from the micro-sparitic (C1a) to the sparitic calcite (C1b).

Extensional calcite veins (C2)

Host-limestone clasts and calcite breccia cements are cross-cut by a random network of irregular, thin veins filled by sparitic calcite (Fig. 6b), with small crystals, anhedral–subhedral, few or not twinned and/or fractured (C2 in Figs 6c & 7e). Often, small, darker, twinned calcite crystals can be observed at the centre of the veins (Fig. 7c).

This type of vein is characterized in cathodolum inescence microscopy by a dark red or weakly luminescent calcite (C2a in Figs 6f & 7g), with sometimes a darker central rim (C2b in Fig. 6f) and, occasionally, bright orange luminescent calcite disseminated more or less along the centre of the veins (C2c in Figs 6f & 7g). The spatial relationship between the few luminescent and the bright orange luminescent calcite is not clear. Sometimes the bright orange calcite appears disseminated within the weakly luminescent calcite in the same vein (Fig. 6f); other times it appears mostly filling up the major part of the vein with very few observable patches of the weakly luminescent calcite (Fig. 7g). In all the cases, boundaries between both calcite types are misty. These extensional calcite veins cross-cut and postdate C1 calcite cements.

Shear calcite veins (C3)

Shear calcite veins are present as variably sized, localized, white calcite in domino or 'pull-apart' style structures, located very close to major fault planes (C3 in Figs 6b & 8a) or appear as 'pull-apart' striated calcite on secondary fault planes (Fig. 5b & c). They are composed of three types of calcite crystals: a sometimes visible outer (border) more or less continuous rim of anhedral–subhedral small crystals, a predominant inner zone of large euhedral–subhedral, elongate, twinned calcite crystals arranged orthogonal to the veins boundaries, and a central zone of smaller subhedral crystals (Fig. 8b & c).

This calcite type has the same red-orange luminescence, darker than the C1 cements, but brighter than the C2 calcite type. Sometimes, very thin zones of brighter luminescence may be observed between the elongate crystals (which may be due to recrystallization; Fig. 8e).

In the studied samples, shear calcite veins cross-cut the host-limestone clasts and the C1 cements (Figs 6b & 8b), often underlined by stylolites (Fig. 8b). They also cross-cut the C2 extensional calcite veins, indicating a younger chronology (Fig. 6b), so we call this calcite type C3.

Post-kinematic calcite (Cp)

Clearly younger than all the syn-kinematic calcites described above is crystalline, laminate post-kinematic calcite which may be found locally draping fault slip surfaces (e.g., sample G00-1, from the Xylokastro fault, see description in Flotté *et al.* 2001). We call this calcite type Cp. This calcite type has a special interest for the interpretation of the stable isotopes.

Figure 9 depicts schematically the described microstructures, their petrologic characteristics and their cross-cutting relationships.

Stable isotopes

$\delta^{18}O$ and $\delta^{13}C$ isotope analysis allows characterization of the isotopic signature of fault-related calcites and discussion of the origin of the fluid from which those calcites formed (e.g., Travé *et al.* 1998; Boles & Grivetti 2000; Pili *et al.* 2003).

The three types of synkinematic calcites (C1, C2 and C3) were analysed (via micro-sampling by using a dental drill), plus the host-limestone and the post-kinematic calcite (Cp). Thirty-one from 93 collected samples were analysed for both C and O isotope ratios using a VG Optima mass

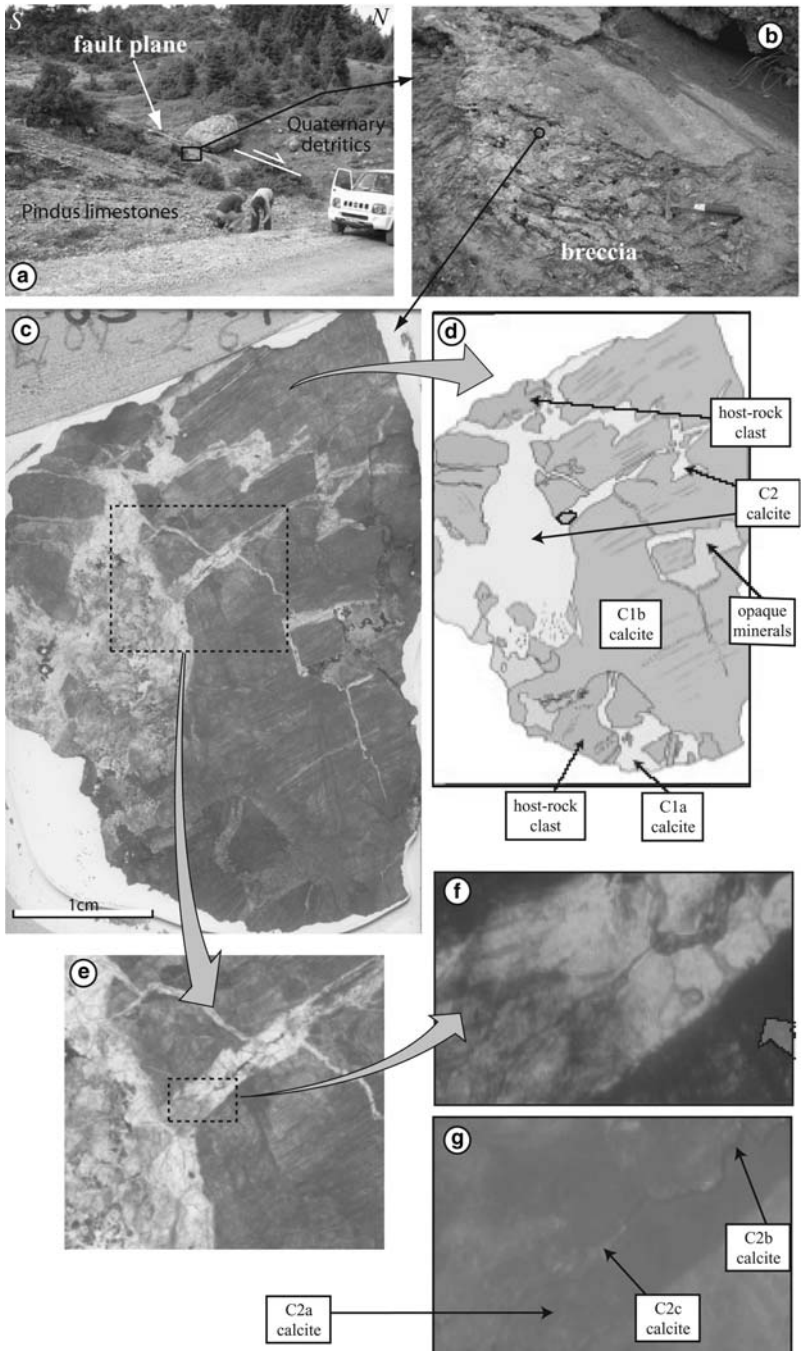

Fig. 7. (**a**) & (**b**) The Valimi fault and the brecciated fault core. (**c**) Thin section of sample G01-26 viewed under optical microscopy. (**d**) Synthetic sketch showing different calcite types. (**e**) Zoom on thin section. (**f**) & (**g**) Zoom on thin section viewed under the cathodoluminescence microscopy.

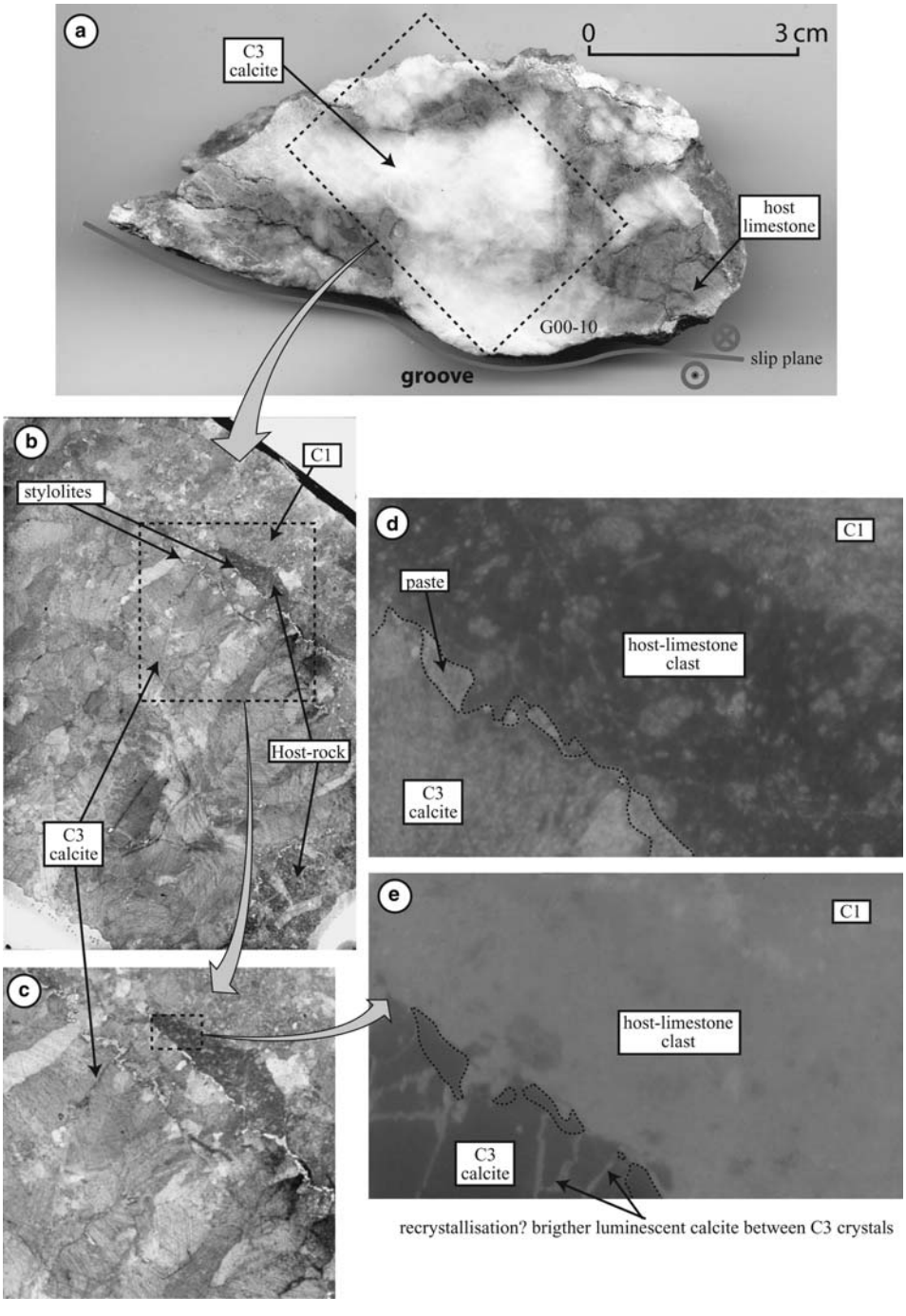

Fig. 8. (**a**) Cut sample G00-10 (from the Valimi fault). (**b**) Thin section viewed under optical microscopy. (**c**) Calcite cement types are indicated. (**d**) & (**e**) Zoom on thin section viewed under cathodoluminescence microscopy.

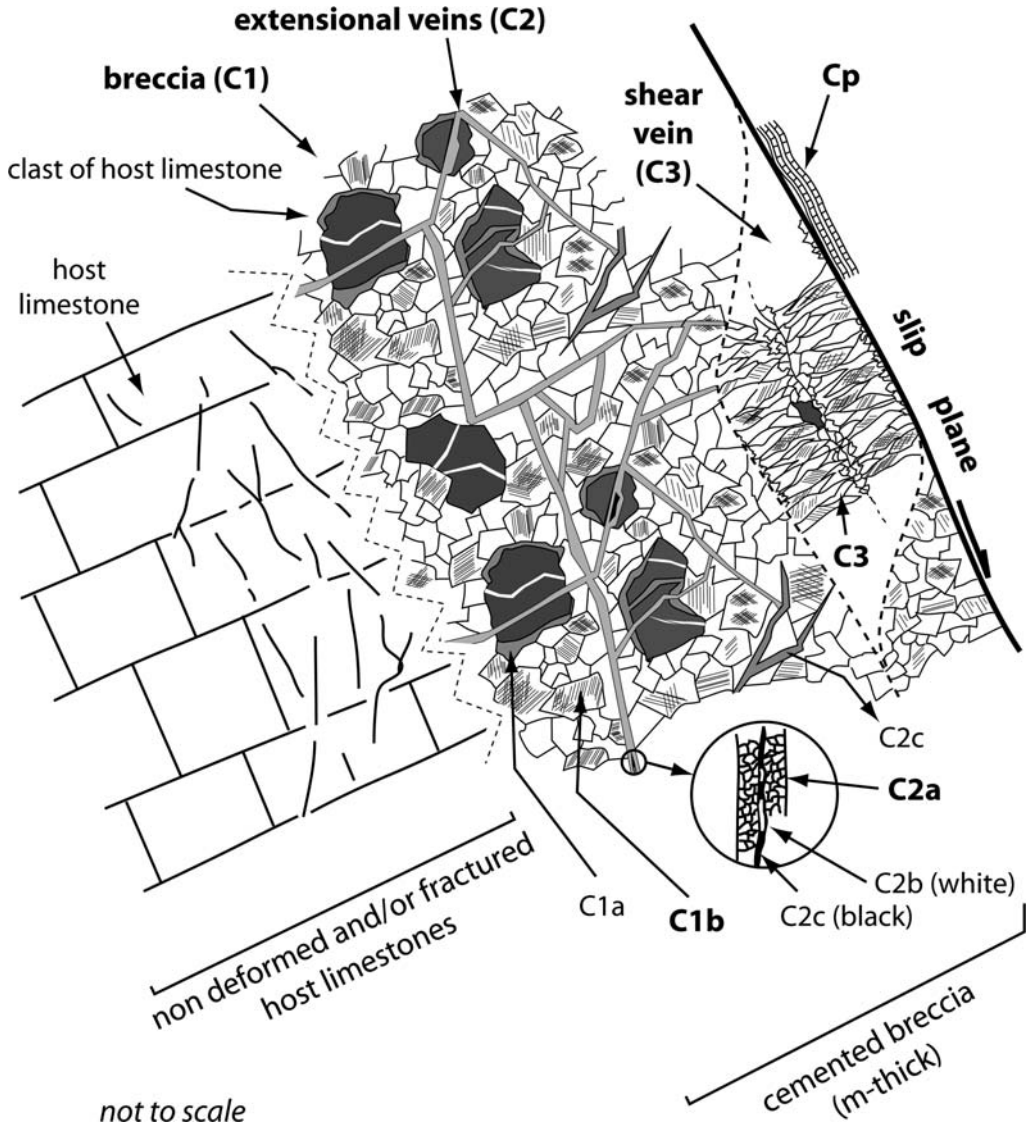

Fig. 9. Synthetic sketch showing the main microstructural and petrological patterns of the fault related calcite sealed structures (breccia with C1 cements, extensional veins with C2 cements, shear veins with C3 cement, and the main slip plane). The sketch shows their cross-cutting relationships.

spectrometer (at the LSCE[3]) after orthophosphoric acid reaction at 90 °C. The data v. PDB (PD Belemnite) have an analytical error of 0.04 and 0.06‰, respectively, for C and O.

Although usable data obtained are reduced in number (25 samples from 31, Fig. 10), values are consistent with microstructural and petrological data and demonstrate that each calcite type is different. Figure 10 shows data plotted in a $\delta^{18}O$ v. $\delta^{13}C$ graph. Although in this paper we mainly focus on the meaning of $\delta^{18}O$ values, the combined plot of $\delta^{18}O$ and $\delta^{13}C$ isotopes allows us to better distinguish the different fields in which the data group. The $\delta^{18}O$ values of the bulk-rock range from -2.1 to -3.1‰ PDB, a range which also corresponds to values of the C1 calcite type (-1.1 to -5.1‰ PDB). The C2 calcite type presents values ranging from -11 to -12 ‰ PDB, the C3

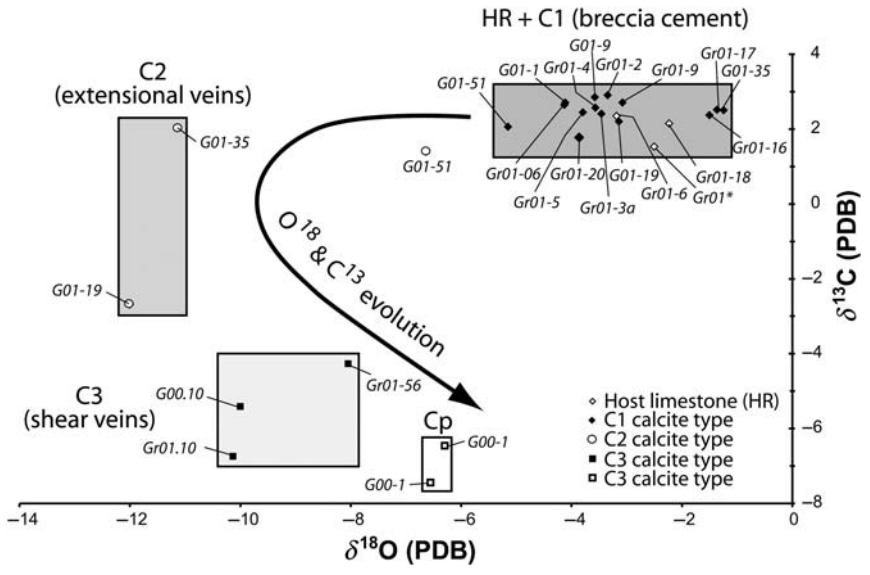

Fig. 10. Plot of values of $\delta^{18}O$ v. $\delta^{13}C$ (calcite in ‰ PDB). The graph shows the characteristic signature of each type of calcite C1, C2, C3, Cp and the host limestone. The syn-kinematic calcite signature evolves from equilibrated with the host limestones for the C1 (breccia cement) towards values of $\delta^{18}O$ in disequilibrium with the host-rock (C2, extensional and C3, shear veins) and progressively closer to that of the post-kinematic karstic-type calcites (Cp).

calcite type has values from −8.5 to −10.1‰ PDB, and the Cp post-kinematic calcite shows values around −6.3‰ PDB. The synkinematic calcite signature evolves from equilibrated with the host limestones for the C1 towards values in $\delta^{18}O$ in disequilibrium with the host-rock and progressively closer to that of the post-kinematic karstic-type calcite (Cp).

Thermometry data

Fluid inclusions were analysed (Université Paris VI-UMR Sisyphe and XI-UMR Orsayterre) in order to estimate palaeo-temperatures of calcite precipitation. Fluid inclusions are rare in the fault-related calcites of the southern margin of the Corinth rift and are difficult to analyse, allowing only a qualitative, but nevertheless helpful, interpretation.

In the C1 calcite cement type (breccia cement), most fluid inclusions are single phase and water filled, suggesting formation (or recrystallisation) at temperatures lower than 60 °C (Roedder 1984; Goldstein & Reynolds 1994). Mono-phase fluid inclusions display homogeneous freezing temperatures (T_{fg}) around −12 °C (Fig. 11). This indicates salinities of NaCl wt% equivalent ≈16 (Bodnar 1993), suggesting relatively 'salty' water (Fig. 11). A few biphasic inclusions were also found within the C1 calcite type. These inclusions systematically disappeared very soon when heating over 40 °C, without coming back upon cooling, indicating a meta-stable state. A confident two-phase inclusion identification comes from the Vela fault (sample G01-56 indicated with a start in Fig. 11). It displays a homogenization temperature (T_h) of 56 °C and a freezing temperature of −12 °C. This freezing temperature, which is exactly the same as that of the one-phase fluid inclusions, indicates a similar formation temperature for the observed one-phase inclusions. Biphasic inclusions have also been observed in samples from the Pyrgaki fault (L. Micarelli, pers. com).

In the C2 calcite type (extensional veins) only one-phase fluid inclusions were found. This fact and the lack of two-phase inclusions suggest formation temperatures lower than 50 °C. Single-phase, water-filled inclusions display homogeneous freezing temperatures around −2 °C (Fig. 11), indicating salinities of NaCl% wt equivalent <4 (Bodnar 1993), lower than that of the two-phase fluid inclusions in C1.

In C3 calcite type (shear veins) very few and localized one-phase inclusions were observed. The lack of fluid inclusions can be attributed to a very low formation temperature or to fluid leakage due to twinning and fracturing during shearing. This latter phenomenon could also explain the poor set of two-phase fluid inclusions 'conserved' in the

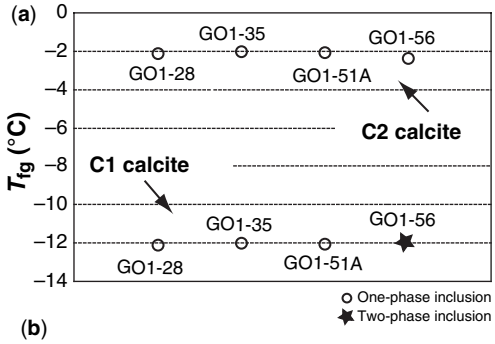

(b)

Sample	C1 calcite T_{fg} (°C)	C2 calcite T_{fg} (°C)
GO1-28	–12.2	–2.2
GO1-35	–12.1	–2.1
GO1-51A	–12.1	–2.1
GO1-56	–12.0	–2.4
	–12.1	–2.2
Salinity (equiv. NaCl%)	16.05	3.71

Fig. 11. Graph and table showing data from fluid inclusions analysis. Note the homogeneous freezing temperature (T_{fg}) of one- and two-phase inclusions observed in the C1 calcite type, and those of the one-phase inclusions observed in the C2 calcite type.

C1 calcite type. Note that C1 and C3 calcites are twinned, while the C2 type is rarely twinned.

Thermometry data suggest that cement calcite type C1 could crystallize at temperatures around/or over 50 °C, corresponding to the minimum temperature required for the genesis of two-phase inclusions in calcite (Roedder 1984; Goldstein & Reynolds 1994). Assuming a normal geothermal gradient of 30 °C km^{-1} and an average surface temperature of 15 °C, this calcite type could form at 1000–1200 m depth. C2 and C3 calcite types should precipitate at shallower depth where temperatures are lower than 50 °C.

Integrated data interpretation

The microstructural and petrologic analysis reveals three types of syn-kinematic calcites (Table 1): breccia cements (C1), calcite-filling extensional veins (C2) and calcite-filling shear veins (C3). Their chronology is determined by cross-cutting relationships. C1 cements are the first generation of calcite. C1 cements are cross-cut by the C2 extensional veins filled by a second generation of calcite. The shear veins filled by the C3 calcite cross-cut C1 and C2, thus post-dating them. C3 constitutes a third generation of calcite. This C3 calcite also forms the 'pull-apart' synkinematic striated structures of secondary faults that cross-cut the compact breccia. All these calcite-filled structures are cross-cut by the large slip surfaces that form the major fault scarps. Fault slip surfaces can in turn be draped by the post-kinematic Gp calcite which constitutes a fourth generation of calcite.

Cathodoluminescence microscopy also suggests that the three generations of calcite are different (Table 1), which is probably related to three main different types of fluids interacting with the faults (at least related to the Fe and Mn composition). We neglect the nuances of C2b and C2c because they appear in very small amounts inside the major C2a type, and are also difficult to analyse and to interpret unambiguously. In a noteworthy way, the C1 (breccia cement) has the same red-orange luminescence as the host-limestone, suggesting fluid probably in chemical equilibrium with the latter. The younger C2 and C3 have different luminescence than the host limestone, suggesting fluid in chemical disequilibrium. Differences of CL between C2 and C3 also indicate different fluid composition for each generation.

$\delta^{18}O$ and $\delta^{13}C$ isotope values (Fig. 10 and Table 1) indicate origins from different fluid (water) types for each generation of calcite: the HR and the C1 show similar values of $\delta^{18}O$ and $\delta^{13}C$. The $\delta^{18}O$ values of the HR are lower than reported for the Cretaceous rocks of marine origin (Pirrie & Marshall 1990), suggesting diagenetic

Table 1. *Synthesis of the calcite types and generations, cathodoluminescence and $\delta^{18}O$ data*

Calcite type		CL	Fluid Inclusions	$\delta^{18}O$(‰ v. PDB)
Host-rock in breccia	HR		—	between −2.1 and −3.1
Cements (generation 1)	C1a	Red-orange	Biphasic, $T > 50$ °C	between −1.1 and −5.1
	C1b			
Extensional veins (generation 2)	C2a	Dark-red	Monophasic, $T < 50$ °C	between −11 and −12
	C2b	Dark	—	—
	C2c	Bright orange	—	—
Shear veins (generation 3)	C3	Red-orange	Monophasic, $T < 50$ °C?	between −8.5 and −10.1
Post-kinematic (generation 4)	Gp		No	around −6.3

alteration of the carbonates in shallow meteoric and/or burial conditions (Travé *et al.* 1998). The salinity of two-phase fluid inclusions within C1 is quite elevated (NaCl% wt equivalent = 16), perhaps implying a marine water origin influenced by evaporation. In fact, this value of salinity is higher than that of marine water. Nevertheless, a strong meteoric water influence is suggested by the low Sr content (1200 ppm, see Labaume *et al.* 2004*b*), and the clearly positive values of $\delta^{13}C$ that are characteristic of meteoric water. A meteoric water influence may additionally be inferred from the observation that the Pindus limestones were exhumed and exposed to a near-surface environment during the Cerozoic Hellenides orogeny, which structured the prerift basement (Dercourt 1964; Aubouin & Dercourt 1962). Moreover, for a similar fluid, the O isotope values can shift to higher values when the water–rock ratio decreases (Craig *et al.* 1956) in contexts of impermeable rocks or sedimentary rocks where fluid flooding is restricted, as may be the case for the Pindus limestones. The origin of the fluid of C1 calcite remains uncertain. Nevertheless, the fact is that $\delta^{13}C$ values (Fig. 10) confirm water in equilibrium with the hosting limestone, consistent with the independent cathodoluminescence data. This indicates a closed hydrological and chemical system during fault-related breccia sealing. Metastable two-phase fluid inclusions indicate breccia cementation (inferred as breccia formation) at a maximum temperature of 55 °C, most probably between 40 and 55 °C.

Figure 12 shows the plot of $\delta^{18}O$-calcite values (in PDB) v. $\delta^{18}O$-fluid (values in SMOW) as a function of the temperature fields diagram [$T = f(\delta^{18}O_{fluid})$]. Groundwater data come from Pizzino *et al.* (2004). Values range between −6 and −9.4‰ SMOW. Isotopic data of meteoric water comes from the GNIP website for Athens (www-naweb.iaea.org/napc/ih/GNIP/IHS_GNIP.html). In order to correct for the influence of the different altitude between the recharge zone in Athens (near sea-level) and in the northern Peloponnesus (*c.* 2000 m), a *c.* 2000 m elevation correction was applied. The extrapolated value to the northern Peloponnesus $\delta^{18}O$ of meteoric recharge then ranges from −5 to −10‰ SMOW.

In the C2 (calcite in extensional veins), the lack of two-phase fluid inclusions indicates that calcite precipitated at temperatures lower than those established for the C1, namely lower than 40 °C (Fig. 12). Taking into account this range of temperature, the $\delta^{18}O$ isotope values (Fig. 10) indicate fluid provenance from meteoric water (Fig. 12). This is consistent with the $\delta^{13}C$ values (Fig. 10), indicating water in disequilibrium with the host limestone during extensional fracturing and sealing. The probable meteoric origin of C2 calcite can also explain the lower salinity of the one-phase fluid inclusions (NaCl wt% equivalent = 4). Nevertheless, this salinity remains quite elevated, suggesting

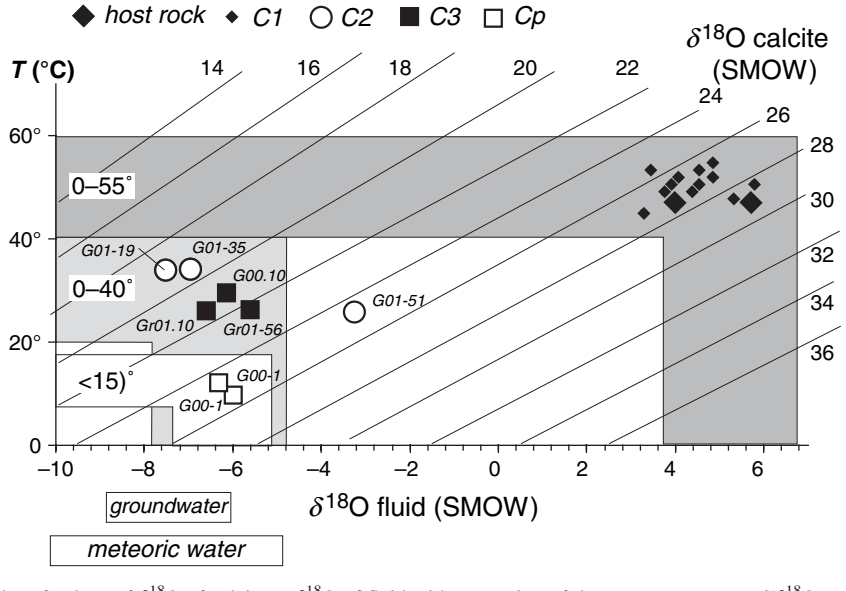

Fig. 12. Plot of values of $\delta^{18}O$ of calcite v. $\delta^{18}O$ of fluid with correction of the temperature, $T = f(\delta^{18}O_{fluid})$. The O isotope composition is interpreted by using the crystallization temperatures estimated from fluid inclusions and the isotopic fractionation coefficients of Kim & O'Neil (1997).

either significant evaporation or mixing with a more saline fluid from previous episodes (e.g., remaining C1-type fluid).

An equivalent result is found for C3 (calcite-filling shear fractures) that does not host fluid inclusions and displays values of δ^{18}O-fluid (Fig. 12), also indicating formation from meteoric water. As C3 always post-dates (cross-cuts) C2, we infer similar or lower temperatures during this calcite precipitation, probably under 30 °C. Different CL colour than C2 could suggest little variation in the composition of water. We infer that C4 (Cp) formed under near-surface conditions, at temperatures around 10–15 °C, recording the more recent palaeowater characteristics of δ^{18}O, very close to those of rain water (Fig. 12).

Concerning the ^{13}C isotopic compositions, Figure 10 shows that the C1 and the HR present a homogeneous carbon isotopic composition, clearly indicating that the fluid was equilibrated with the host limestone (Morse & Mackenzie 1990; Clark & Fritz 1997). By contrast, C2 veins exhibit more heterogeneous δ^{13}C, and C3 and C4 present clearly negative values, indicating an increasing disequilibrium with the host rock.

Faulting and fluid–rock interaction in the fault zone

Labaume *et al.* (2004*a*) studied a secondary fault set related to the Pyrgaki fault (see location in Fig. 2) and located some tens of metres north of the major fault plane, at the Taxarchion outcrop (Labaume *et al.* 2004*a*, *b*; Benedicto *et al.* 2004). They propose a model of fault zone development related to the upward propagation of a normal fault tip, derived from the model proposed by Stewart & Hancock (1988, 1990). They suggest that the central part of the fault develops with a tendency of deformation concentration from distributed stylolites and veins at the fault tip through disconnected then connected slip surfaces, attrition breccia and eventually formation of a large-scale discrete slip surface within the breccia. Our integrated microstructural, petrologic, palaeothermal and isotopic study of major faults through the entire margin supports this model and additionally suggests that deformational mechanisms organize spatially and temporally during upward fault propagation.

The first deformation mechanism occurring in the studied fault zones was random brecciation, sealed by the C1 cement. This occurred in a more or less wide zone of distributed deformation and, as suggested by fluid inclusions, at a temperature around 55 °C, that is, equivalent to a depth of around 1300 m. The cathodoluminescence and the isotopic signature of calcite cements show that this deformation occurred in a closed system with the fluid and the host rock in equilibrium. Accordingly, brecciation occurred at a minimum depth beyond the influence of the meteoric flooding water. This implies that during brecciation any external fluid flowed through the breccia corridor. This distributed deformation may be related to hydraulic extension fractures developed under a hydrostatic regime before the development of the through-going fault (Sibson 2000). Brecciation most probably occurred ahead of (above) the fault tip and breccia corridors (in the sense of Labaume *et al.*, 2004*a*) served as the initiation sites for the propagating fault through kink folding of the carbonate sequence above the fault (e.g., Johnson & Fletcher 1994).

As the C1 cement seals the breccia everywhere along the fault, it represents a potentially large volume of saturated fluid that could interact with the fault. Although the precipitation of calcite is very sensitive to the fluid saturation, the chemical fluid composition, the flow velocity, the fluid pressure and the fluid–rock ratio, Morse & Mackenzie (1993) and Lee *et al.* (1996) showed by experimental modelling that an extremely large volume of supersaturated water (i.e., 20 000 l) is required to pass through a vein (i.e., 2 mm wide, 10 cm high and 100 cm long) in order to eventually fill it with calcite. As the fault breccia is in general wider than several metres and is present all along (vertical and lateral) the fault zones, enormous quantities of flooding water would be necessary to seal it with calcite, the water coming from deeper, shallower or lateral areas. In such a case, rather than a homogeneous cement, as the C1 is, different types of calcite cements should be found, with different cathodoluminescent and geochemical signatures, in disequilibrium with the host limestone in which calcite crystallizes. This suggests that the water was rather stable in an aquifer at a given depth, and that fault–fluid interaction occurred when the fault propagated through this aquifer. Mass transfer from the host rock to the fault breccia most probably occurred by local dissolution and diffusion during micro-fracturing (see Renard *et al.* 2000) without significant water drainage (flooding) through or along the fault zone.

The second type of deformation is the small, discrete extensional fracturing that overprints the breccia and is sealed by the C2 calcite. Thermometric data indicate that this deformation pattern formed in a shallower zone than the breccia. Cathodoluminescence and isotopic signatures indicate that it occurred under the influence of meteoric water flooding (corresponding to an open system). Note that the extensional veins overprint the calcite-sealed breccia but they never contain the C1

cement; in contrast, the breccia is never cemented by the C2 calcite type. This attests to diachronous timing and/or spatial location of both deformational processes: brecciation should occur deeper than extensional fracturing. Shallower conditions during extensional fracturing must then be related not to the upward propagation of the fault tip itself but to the uplift of the whole fault zone (or footwall fault zone). Uplift may be explained by regional exhumation (i.e., Collier *et al.* 1992; Roberts & Stewart 1994; Dia *et al.* 1997; Sorel 2000; Leeder *et al.* 2003) and/or denudation of the overhead prerift and synrift series. Uplift of the fault zone of several hundred metres is then accompanied by a significant change of the mode of deformation from distributed (brecciation) to more localized extensional fracturing as suggested by Labaume *et al.* (2004*a*, *b*). This strain localization could be induced during footwall exposure by both cooler conditions and a decreasing vertical overburden stress σ_1 and a decreasing stress ratio σ_1'/σ_3' as the erosion cuts the top of the footwall and the hanging wall moves down.

The facts that (i) the C1 and C2 cements are not mixed either within the breccia or within the extensional veins, and that (ii) the C1 cement formed in a closed system (inferred at depth), emphasize that both deformational processes actually observed together in the same location must happened sequentially. Effectively, in shallower conditions where (and when) discrete extensional fracturing occurs, brecciation does not, and conversely, at depth, where brecciation occurs, discrete extensional fracturing does not.

As strain localizes along what is now the weakened fault zone, discrete shear surfaces, veins and calcite-filled 'pull-aparts' develop, overprinting and cross-cutting the breccia and the extensional veins formed previously. As deformation increases, shear structures such as the 'pull-aparts' progressively connect by short slip planes (secondary faults). This stage of deformation is equivalent to formation of a zone of gouge within which shear strains begin to localize (e.g., Bartlett *et al.* 1981; Mair & Marone 1999). Note again that the cathodoluminescent and isotopic signatures of the C3 (shear fractures cement) differ from those of the C1 and C2, and they never appear mixed in the same microstructure. Stable isotopes of C3 cement indicate a fluid closer to the signature of post-tectonic calcites (Cp) or present groundwater (see Figs 10 & 12). This suggests again diachronous timing of development related to the C1 and C2. This 'third' stage of deformation is confirmed by cross-cutting relationships between breccia, extensional and shear veins.

During upward fault propagation and progressive uplift, the fault reached and propagated through successively more shallow aquifers, trapping palaeowater present in each aquifer into the extensional (C2) and shear (C3) fractures. Note that extensional fractures are homogeneously distributed through the breccia but they are few, dense and very thin; shear veins are relatively thin and localized. Compared with the quantity of fluid necessary to form the abundant breccia cement, the relative volume of water interacting to seal extensional and shear fractures had to have been relatively small. Even in the case in which water could flow through or along the fault zone, this should represent only modest quantities.

The final stage in the faulting process is represented by the growth and emergence of the propagating fault formed by link-up of the smaller shearing fractures and short slip surfaces discussed in stage 3. At this stage, fault motion is mainly concentrated along these rough fault surfaces that progressively become the large fault escarpments outcropping at the present day. From this moment, strain and deformation are entirely concentrated along the major fault plane and displacement can increase while inducing little deformation in the surrounding areas. This could explain why the C3 calcite in the shear fractures is twinned while the C2 calcite is not.

Conclusions

This work integrates microstructural, petrologic, microthermometric and geochemical studies of calcite-sealed fault-related structures of major faults of the offshore southern margin of the Corinth rift. Results show the homogeneity through the entire margin and during the rifting period of (i) main deformational processes and fault zone evolution, and (ii) fluid–rock interaction in fault zones. It points out four main deformation patterns common to all studied faults in which large slip (fault) surfaces and related cohesive breccias are present. These are: calcite-cemented breccia, extensional veins, shear veins and fault slip surfaces. Cross-cutting relationships indicate that the breccia formed first, the extensional veins second, the shear veins third and the slip planes fourth. It occurred in progressively shallower conditions during upward fault propagation and regional uplift.

Fault zones started to develop by forming random brecciation corridors (hydraulic extension fractures). This stage represents one of distributed deformation. Calcite breccia cements, chemically equilibrated with the host limestones, indicate that at this state deformation occurred in a closed fluid–rock system. During footwall uplift and unloading by regional exhumation and/or erosion, cooler conditions, plus a decreasing vertical σ_1

and stress ratio σ_1'/σ_3' as the top of the footwall is denuded and the hanging wall moves downwards, strain localization was induced and deformation concentrated on extensional veins and shear veins respectively. Calcite cements of extensional and shear veins, in respectively higher disequilibrium with the host limestones, indicate that at this state deformation occurred in an open fluid–rock system. Link-up of shear veins led to the formation of the emergent fault slip surfaces which rapidly concentrated all the subsequent deformation.

In this faulting model, fault-related structures and rocks evolved from a closed system with fluid–rock equilibrium at depth to a more open system with limited influx of meteoric water in shallower conditions.

We especially thank D. Blamard (LSCE-Gif Sur Yvette) for the isotopes analysis and his help for data interpretation, M. Bussolotto (UPXI), J. Thibieroz (UPVI) and M. Pagel (UPXI) for their help with fluid inclusions analysis and interpretation, and J. P. Bilotte (UPXI) for making the thin sections. Thanks to A. McCaig and C. Wibberley whose comments helped to improve the manuscript.

References

AUBOIN, J. & DERCOURT, J. 1962. Zone préapulienne, zone ionienne et zone du Gavrovo en Péloponnèse occidental. *Bulletin de la Société Géologique, France*, **7**, 785–794.

BALLY, V. 2005. *Le mécanisme d'ouverture du rift de Corinthe, localisation d'un détachement et rôle de la Nappe des Phyllades.* Rapport Master II, Université de Paris VI, inédit.

BARTLETT, W. L., FRIEDMAN, M. & LOGAN, J. M. 1981. Experimental folding and faulting rocks under confining pressure, part IX. Wrench faults in limestone layers. *Tectonophysics* **79**, 255–277.

BENEDICTO, A., LABAUME, P., MICARELLI, L. & CARRIO, E. 2004. Deformation mechanisms in extensional fault propagation folding involving carbonate rocks: the Pyrgaki fault, Corinth rift (Greece). *In*: *Réunion des Sciences de la Terre, Poster Proceeding*. Société Geologique de France, Strasbourg.

BERNARD, P., LYON-CAEN, H. *ET AL*. 2006. Seismicity, deformation and seismic hazar in the western rift of Corinth: new insights from the Corinth Rift Laboratory (CRL). *Tectonophysics*, **426**, 7–30.

BODNAR, R. J. 1993. Revised equation and table for determining the freezing point depression of H2O-NaCl solution. *Geochimica et Cosmochimica Acta*, **57**, 683–684.

BOLES, J. R. & GRIVETTI, M. 2000. Calcite cementation along the Refugio/Carneros fault, Coastal California: a link between deformation, fluid movement and fluid–rock interaction at a basin margin. *Journal of Geochemical Exploration*, **69–70**, 313–316.

BRADBURY, H. J. & WOODWELL, G. R. 1987. Ancient fluid flow within foreland terrains. *In*: GOFF, J. C. & WILLIAMS, B. P. J. (eds) *Fluid Flow in Sedimentary Basins and Aquifers.* Geological Society of London. Special Publications, **34**, 87–102.

BROOKS, M. & FERENTINOS, G. 1984. Tectonics and sedimentation in the Gulf of Corinth and the Zakynthos and Kefallinia Channels, western Greece. *Tectonophysics*, **101**, 25–54.

CAUSSE, C., MORETTI, I., ESCHARD, R., MICARELLI, L., GHALEB, B. & FRANK, N. 2004. Kinematics of the Corinth Gulf inferred from calcite dating and syntectonic sedimentary characteristics. *Comptes Rendus Geoscience*, **336**, 281–290.

CELLO, G., INVERNIZZI, C., MAZZOLI, S. & TONDI, E. 2001. Fault properties and fluid flow patterns from Quaternary faults in the Apenines, Italy. *Tectonophysics*, **336**, 63–78.

CLARK, I. & FRITZ, P. 1997. *Environmental Isotopes in Hydrogeology*. CRC Press, Boca Raton, FL.

CRAIG, H., BOATO, G. & WHITE, D. E. 1956. *Isotopic Geochemistry of Thermal Waters.* US National Academy of Sciences and National Research Council, Pubications, **400**, 29–38.

COLLIER, R. E. L. 1990. Eustatic and tectonic controls upon Quaternary coastal sedimentation in the Corinth Basin, Greece, *Journal of Geological Society of London*, **147**, 301–314.

COLLIER, R. E. L., LEEDER, M. R., ROWE, P. J. & ATKINSON, T. C. 1992. Rates of tectonic uplift in the Corinth and Megara basins, central Greece. *Tectonics*, **11**, 1159–1167.

CORNET, F. H., DOAN, L. M., MORETTI, I. & BORM, G. 2004. Drilling through the active Aigion Fault: the AIG10 well observatory. *Comptes Rendus Geoscience*, **336**, 395–406.

DANIEL, J. M., MORETTI, I., MICARELLI, L., ESSAUTIER CHUYNE, S. & DELLE PIANE, C. 2004. Macroscopic structural analysis of AIG10 well (Gulf of Corinth, Greece). *Comptes Rendus Geoscience*, **336**, 435–444.

DART, C. J., COLLIER, R. E. L., GAWTHORPE, R. L., KELLER, J. V. A. & NICHOLS, G. 1994. Sequence stratigraphy of (?)Pliocene–Quaternary synrift, Gilbert-type fan deltas, northern Peloponnesus, Greece. *Marine and Petroleum Geology*, **11**, 545–560.

DERCOURT, J. 1964. *Contribution à l'étude géologique d'un secteur du Péloponnèse septentrional.* Thèse d'état, Université de Paris, *Annales Géologiques des Pays Helléniques*, **15**.

DE WEVER, P. 1975. *Etude géologique des séries apparaissant en fenêtre sous l'allochtone pindique (série de Tripolitza et série epimétamorphique de Zaroukla), Péloponnèse septentrional, Grèce.* Thèse 3ème cycle, Université de Lille, France, inédite.

DIA, A. N., COHEN, A. S., O'NIONS, R. K. & JACKSON, J. A. 1997. Rates of uplift investigated through 230Th dating in the Gulf of Corinth (Greece). *Chemical Geology*, **138**, 171–184.

DUFAURE, J. J. 1975. *Le relief du Péloponnèse.* Thèse d'état, Université Paris IV, France, inédite.

DUFAURE, J. J. 1977. *Carte géologique du Péloponnèse à 1/200.000*. CNRS-Institut de Géographie, Paris.

EXADAKTYLOS, G. E., VARDOULAKIS, I., STAVROPOULOU, M. C. & TSOMBOS, P. 2003. Analogue and numerical modelling of normal fault patterns produced due to slip along a detachment zone. *Tectonophysics*, **376**, 117–134.

FERENTINOS, G., BROOKS, M. & DOUTSOS, T. 1985. Quaternary tectonics in the Gulf of Patras, western Greece. *Journal of Structural Geology*, **7**, 713–717.

FLOTTÉ, N. 2003. *Caractérisation structurale et cinématique d'un rift sur détachement: le rift de Corinthe-Patras, Grèce*. Thèse de doctorat, Université Paris XI Orsay, France, Inédite.

FLOTTÉ, N. & SOREL, D. 2001. Structural cross-sections through the Corinth-Patras detachment fault-system in the northern Peloponnesus, Aegean Arc, Greece, *In*: *9th International Congress, XXXIV/1*, Athens, Greece. Bulletins of the Geological Society of Greece, Athens, 235–241.

FLOTTÉ, N., PLAGNES, V., SOREL, D. & BENEDICTO, A. 2001. Attempt to date Pleistocene normal faults of the Corinth-Patras Rift (Greece) by U/Th method, and tectonic implications. *Geophysical Research Letters*, **28**, 3769–3772.

GIURGEA, V., TRETTENMAIER, D., PIZZINO, L., UNKEL, I., HÖTZL, H., FÖSTER, A. & QUATTROCCHI, F. 2004. Preliminary hydrogeological interpretation of the Aegion area from the AIG10 borehole data. *Comptes Rendus Geoscience*, **336**, 467–475.

GOLDSTEIN, R. H. & REYNOLDS, T. J. 1994. *Systematic of Fluid Inclusions in Diagenetic Minerals.* Society of Economic Paleontologists and Mineralogists, Tulsa, Short Course **31**.

GOLDSWORTHY, M. & JACKSON, J. 2001. Migration of activity within normal fault systems: examples from the Quaternary of mainland Greece. *Journal of Structural Geology*, **23**, 489–506.

HENRY, P. & MORETTI, I. 2006. The understanding of fault activity from natural laboratories. *Tectonophysics*, **426**, 1–5.

JOHNSON, A. M. & FLETCHER, R. C. 1994. *Folding of Viscous Layers – Mechanical Analysis and Interpretation of Structures in Deformed Rock*. Columbia University Press, New York.

KIM, S. T. & O'NEIL, J. R. 1997. Equilibrium and nonequilibrium oxygen isotope effects in synthetic carbonates. *Geochimica Cosmochimica Acta*, **61**, 3461–3475.

LABAUME, P., BETTY, C. & LAURENT, P. 1991. Syndiagenetic evolution of shear structures in superficial nappes: an example from the Northern Apennines (NW Italy). *Journal of Structural Geology*, **13**, 385–398.

LABAUME, P., CARRIO-SCHAFFHAUSER, E., GAMOND, J. F. & RENARD, F. 2004*a*. Deformation mechanisms and fluid-driven mass transfers in the recent fault zones of the Corinth Rift (Greece). *Comptes Rendus Geoscience*, **336**, 375–383.

LABAUME, P., CARRIO-SCHAFFHAUSER, E. & TRAVÉ, A. 2004*b*. Fluid-driven mass transfer in recent normal fault zones of the Corinth Rift (Greece). Constraints from microstructural and geochemical analysis of calcite cements. *In*: *Réunion des Sciences de la Terre, Poster Proceeding*. Société Géologique de France, Strasbourg.

LEE, Y. L., MORSE, J. W. & WILTSCHKO, D. V. 1996. An experimentally verified model for calcite precipitation in veins. *Chemical Geology*, **130**, 203–215.

LEEDER, M. R., MCNEILL, L., COLLIER, R. E. L., PORTMAN, C., ROWE, P., ANDREWS, J. & GAWTHORPE, R. L. 2003. Corinth Rift margin uplift: new evidence from Late Quaternary marine shorelines. *Geophysical Research Letters*, **30**, 1611.

LE POURHIET, L. 2004. *Modélisation thermo-mécanique de l'extension continentale: développements théoriques et application au Golfe de Corinthe (Grèce).* Thèse de Doctorat, Université de Paris VI, inédite.

LE POURHIET, L., EVGENII, B. & MORETTI, I. 2004. Rifting through a stack of inhomegeneous thrusts (the dipping pie concept). *Tectonics*. **23**, TC4005.

LIN, A., TANAKA, N., UDA, S. & SATISH-KUMAR, M. 2003. Repeated coseismic infiltration of meteoric and seawater into deep fault zones: a case study of the Nojima fault zone, Japan. *Chemical Geology*, **202**, 139–153.

LYON-CAEN, H., PAPADIMITRIOU, P., DESCHAMPS, A., BERNARD, P., MAKROPOULOS, K., PACCHIANI, F. F. & PATAU, G. 2004. First results of the CRLN seismic network in the western Corinth Rift: evidence for old-fault reactivation. *Comptes Rendus Geoscience*, **336**, 343–351.

MAIR, K. & MARONE, C. 1999. Friction of simulated fault gouge for a wide range of velocities and normal stresses. *Journal of Geophyical Research*, **104**, 28 899–28 914.

MALARTRE, F., FORD, M. & WILLIAMS, E. A. 2004. Preliminary biostratigraphy and 3D geometry of the Vouraikos Gilbert-type fan delta, Gulf of Corinth, Greece. *Comptes Rendus Geoscience*, **336**, 269–280.

MICARELLI, L., MORETTI, I. & DANIEL, J. M. 2003. Structural properties of rift-related normal faults: the case study of the Gulf of Corinth, Greece. *Journal of Geodynamics*, **36**, 275–303.

MICARELLI, L., BENEDICTO, A., INVERNIZZI, C., SAINT-BEZAR, B., MICHELOT, J. L. & VERGÉLY, P. 2005. Influence of P/T conditions on the style of normal fault initiation and growth in limestones from the SE-Basin, France. *Journal of Structural Geology*, **27**, 1577–1598.

MORETTI, I., SAKELLARIOU, D., LYKOUSIS, V. & MICARELLI, L. 2003. The Gulf of Corinth: an active half graben? *Journal of Geodynamics*, **36**, 323–340.

MORSE, J. W. & MACKENZIE, F. T. 1993. Geochemistry of sedimentary carbonates: developments in sedimentology. *Geochimica et Cosmochimica Acta*, **57**, 2919–2920.

MUCHEZ, P., SLOBODNIK, M., VIAENE, W. A. & KEPENS, E. 1995. Geochemical constraints on the origin and migration of paleofluids in the northern margin of the Variscan foreland, southern Belgium. *Sedimentary Geology*, **96**, 191–200.

ORI, G. G. 1989. Geologic history of the extensional basin of the Gulf of Corinth (Miocene–Pleistocene), Greece. *Geology*, **17**, 918–921.

PI ALPARIN, J. M., MARTHELOT, J. M., GALVÉ, A., SACHPAZI, M., TAYLOR, B., LAIGLE, M. & HIRN, A. 2004. Seismic refraction imaging of the southern Corinth Rift shoulder at Derveni. *Comptes Rendus Geoscience*, **336**, 251–257.

PILI, E., POITRASSON, F. & GRATIER, J. P. 2003. Carbon–oxygen isotope and trace element constraints on how fluids percolate faulted limestones from the San Andreas Fault System: partitioning of fluid sources and pathways. *Chemical Geology*, **190**, 231–250.

PIRRIE, D. & MARSHALL, J. D. 1990. High-paleolatitude Late Cretaceous paleotemperatures: new data from James Ross Island, Antarctica. *Geology*, **18**, 31–34.

PIZZINO, L., QUATTROCCHI, F., CINTI, D. & GALLI, G. 2004. Fluid geochemistry along the Eliki and Aigion seismogenic segments (Gulf of Corinth, Greece). *Comptes Rendus Geosciences*, **336**, 367–374.

RENARD, F., GRATIER, J. P. & JAMTVEIT, B. 2000. Kinetics of crack-sealing, intergranular pressure solution, and compaction around active faults. *Journal of Structural Geology*, **22**, 1395–1407.

ROBERTS, G. & STEWART, I. 1994. Uplift, deformation and fluid involvement within an active normal fault zone in the Gulf of Corinth, Greece. *Journal of the Geological Society of London*, **151**, 531–541.

ROEDDER, E. 1984. *Fluid Inclusions*. Mineralogical Society of America.

SACHPAZI, M., CLÉMENT, C., LAIGLE, M., HIRN, A. & ROUSSOS, N. 2003. Rift structure, evolution, and earthquakes in the Gulf of Corinth, from reflection seismic images. *Earth and Planetary Science Letters*, **216**, 243–257.

SÉBRIER, M. 1977. *Tectonique récente d'une transversale à l'arc égéen. Le golfe de Corinthe et ses régions périphériques.* Thèse de 3ème cycle, Université Paris XI, Orsay, inédite.

SEGER, M. & ALEXANDER, J. 1993. Distribution of Plio-Pleistocene and modern coarse-grained deltas south of the Gulf of Corinth, Greece. *In*: FROSTICK, L. E. & STEEL, R. J. (eds) *Tectonic Controls and Signatures in Sedimentary Successions*. Association of Sedimentologists, Special Publications, **20**, 37–48.

SIBSON, R. H. 2000. Fluid involvement in normal faulting. *Journal of Geodynamics*, **29**, 469–499.

SOREL, D. 2000. A Pleistocene and still-active detachment fault and origin of the Corinth-Patras Rift, Greece. *Geology*, **28**, 83–86.

STEWART, I. & HANCOCK, P. L. 1988. Normal fault zone evolution and fault scarp degradation in the Aegean region. *Basin Research*, **1**, 139–153.

STEWART, I. S. & HANCOCK, P. L. 1990. Brecciation and fracturing within neotectonic normal fault zones in the Aegean region. *In*: KNIPE, R. J. & RUTTER, E. H. (eds) *Deformation Mechanisms, Rheology and Tectonics.* Geological Society, Special Publications, **54**, 105–112.

TRAVÉ, A., CALVET, F., SOLER, A. & LABAUME, P. 1998. Fracturing and fluid migration during Paleogene ompression and Neogene extension in the Catalan coastal ranges, Spain. *Sedimentology*, **45**, 1063–1082.

VITA-FINZI, C. & KING, G. C. P. 1985. The seismicity, geomorphology and structural evolution of the Corinth area of Greece. *Philosophical Transactions of the Royal Society of London*, **314**, 379–407.

WESTAWAY, R. 2002. The Quaternary evolution of the Gulf of Corinth, Central Greece: coupling between surface processes and flow in the lower continental crust. *Tectonophysics*, **348**, 269–318.

Fluid flow properties of basin-bounding normal faults in platform carbonates, Fucino Basin, central Italy

FABRIZIO AGOSTA[1,2]

[1]*Department of Geological and Environmental Sciences, Stanford University, Stanford, CA, USA (e-mail: fabrizio_agosta@hotmail.com)*

[2]*Present address: Dipartimento di Scienze della Terra, Università di Camerino, Camerino, Italy via Gentile III da Varano, 62032 Camerino (MC), Italy*

Abstract: Both structural and petrophysical (porosity, ϕ, and permeability, k) data show that the basin-bounding normal faults of the Fucino Basin, central Italy, have a combined barrier–conduit effect on fluid flow. The deformed carbonates comprise fault cores of both matrix- and cement-supported fault rocks (low ϕ and k) and major slip surfaces, and damage zones of fragmented and pulverized carbonates (high ϕ and k) and small faults. The host rocks are Mesozoic, platform-related boundstones with low ϕ ($<1\%$) and low k ($<1 \times 10^{-4}$ mD). The results of ultrasonic analysis suggest that the fragmented carbonates contain pores with a high aspect ratio, whereas the fault rocks have pores with a low aspect ratio and some moldic porosity. These two separate fluid units are modelled as an elastic cracked medium (fragmented carbonates), and as a granular medium (fault core). By using well-known correlations, their permeability is then computed from known values of ϕ, pore radii and elastic moduli.

Fault zones include an inner part of highly deformed fault rocks and major slip surfaces, the fault core, flanked by less deformed rocks of the damage zone. The fault rocks form due to comminution, dissolution/precipitation, mechanical and chemical processes that destroy the original host rock fabric (Sibson 1977; Chester & Logan 1986; Cello 2000). Conversely, the rocks of the damage zone, although are crosscut by numerous fractures and small faults, preserve their original fabric (Cowie & Scholz 1992). Both fault core and damage zone are sandwiched between host rocks characterized by a background value of deformation intensity. Both thickness and lateral variability of fault zones are related to the length, amount of slip, internal geometry and structural complexities of the individual fault segments (Scholz 1990; Antonellini & Aydin 1995; Shipton & Cowie 2001; Kim *et al.* 2004; Myers & Aydin 2004; De Jossineau & Aydin 2007).

In order to build up predictive models of fluid pathways in faulted and fractured reservoirs, a good understanding of their deformation mechanisms, petrophysical and mechanical properties is crucial (Caine *et al.* 1996; Aydin 2000). However, the models of fault permeability proposed for clastic and crystalline rocks (Scholz 1990; Bruhn *et al.* 1994; Antonellini & Aydin 1994; Caine & Forster 1999; Rawling *et al.* 2001; Flodin *et al.* 2005) are not applicable to carbonate rocks because of their peculiar deformation mechanisms (Alvarez *et al.* 1978; Marshak *et al.* 1982; Peacock & Sanderson 1995; Kelly *et al.* 1998; Salvini *et al.* 1999) and pore structures (Wang 1997; Lucia 1999). For this reason, recent work has focused on the characterization of the faulting processes in carbonate rocks (Willemse *et al.* 1997; Graham *et al.* 2003; Tondi *et al.* 2006; Agosta & Aydin 2006; Antonellini *et al.* 2007), and on the petrophysical properties of carbonate fault rocks (Agosta *et al.* 2007). To contribute to this current effort, this manuscript summarizes the main results of field and laboratory analyses of basin-bounding normal fault zones that formed in massive, Mesozoic platform carbonates.

The fieldwork was carried out in the Fucino Basin, central Italy, to document individual fault segments that form two normal fault zones, and the relay ramp area they bound. Attention was paid to characterizing the structural domains present in the Venere fault footwall, which is exposed in several quarries, and its internal architecture. The laboratory study aimed to assess the petrophysical properties (porosity, permeability), pore structure and capillary pressure of samples collected from the two normal fault zones. The results of field and laboratory analyses are discussed in terms of fluid flow properties of the normal fault zones. Based on the petrophysical and ultrasonic data, the fault cores are thought to form barriers to cross-fault fluid flow, which are modelled as granular media. Transient pathways for along-fault fluid flow may form in the fault core during seismic faulting due to dilation and opening of

From: WIBBERLEY, C. A. J., KURZ, W., IMBER, J., HOLDSWORTH, R. E. & COLLETTINI, C. (eds) *The Internal Structure of Fault Zones: Implications for Mechanical and Fluid-Flow Properties*. **299**, 277–291.
DOI: 10.1144/SP299.17 0305-8719/08/$15.00

cracks. In contrast, the carbonate damage zones are envisioned as fluid conduits modelled as elastic cracked media. The permeability of these two units is then computed using measured values of porosity, pore radii and elastic moduli and the Kozeny–Carmen (granular medium) and Budiansky-O'Connell correlations (elastic cracked medium).

Geological setting

The study area is located on the eastern side of the Fucino Basin, central Italy, within the Lazio-Abruzzi tectonic unit (Fig. 1). There, the imbricate edifice of central Apennines comprises primarily east-verging thrust sheets that formed during Late Miocene–Pliocene thrust tectonics (Bigi *et al.* 1992). Since the Late Pliocene–Early Pleistocene, this edifice has been crosscut and downfaulted by, mainly, NW-striking and SW-dipping normal faults, which were active while the entire area was uplifted and exhumed. The uplift rates calculated for the Maiella Mountain, about 50 km to the east of the Fucino Basin, range between 1.4 and 3.0 mm/year (Ghisetti & Vezzani 1999).

The Fucino is a rhomb-shaped basin, about 30 km wide, filled with Late Pliocene–Holocene fluvio-lacustrine sediments (Bosi *et al.* 1995). This basin, characterized by a half-graben geometry (Cavinato *et al.* 2002), is bounded by two major normal fault zones: the Celano–Pescina–Parasano (CPP) to the northeast and the Venere–Sperone (VS) to the southeast (Fig. 1). Both CPP and VS fault zones juxtapose Quaternary continental sediments of the hanging walls against deformed platform carbonates.

The platform carbonates consist of Upper Jurassic–Lower Cretaceous boundstones with less than 1% of porosity, and less than 1×10^{-4} mD of permeability (Agosta *et al.* 2007). These rocks, about 1200 m thick, are overlain by hundreds of metres thick Miocene carbonate grainstones, Messinian flysch and Lower Pliocene calcilutites (Vezzani & Ghisetti 1998). The structural grain of the Mesozoic boundstones includes several sets of pressure solution seams joints/veins, sheared pressure solution seams, and sheared joints/veins which formed, prior to normal faulting, during burial diagenesis and Late Miocene–Pliocene thrust tectonics (Agosta & Aydin 2006).

Methodology

In the field, the geological map of the relay ramp area bounded by the CPP and VS fault zones was made at a scale of 1:10 000 from topographic and ortho-rectified aerial photographs (Fig. 2). The internal fault strands and structural elements of the Venere fault were similarly mapped at 1:2000 and 1:5000 scales. The detailed analysis of the modes, distribution, crosscutting and abutting relationships of the structural elements present in the Venere fault footwall was carried on using ground photo mosaics, string line mapping and by taping acetate sheets to the outcrops.

The laboratory work was performed on four hand specimens of fractured host rocks collected

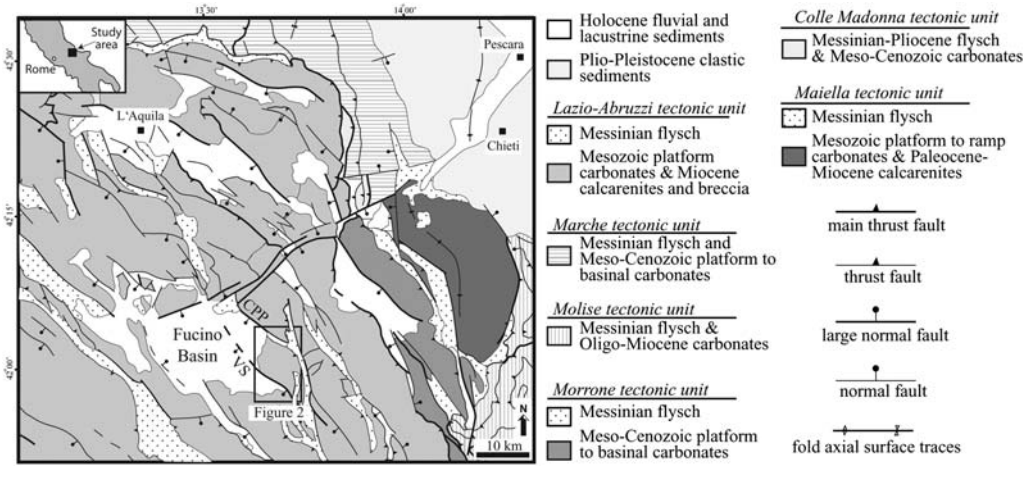

Fig. 1. Simplified tectonic map of central Apennines (after Vezzani & Ghisetti, 1998). The location map is in the inset, the legend on the right side. CPP, Celano–Pescina–Parasano normal fault zone; VS, Venere–Sperone normal fault zone.

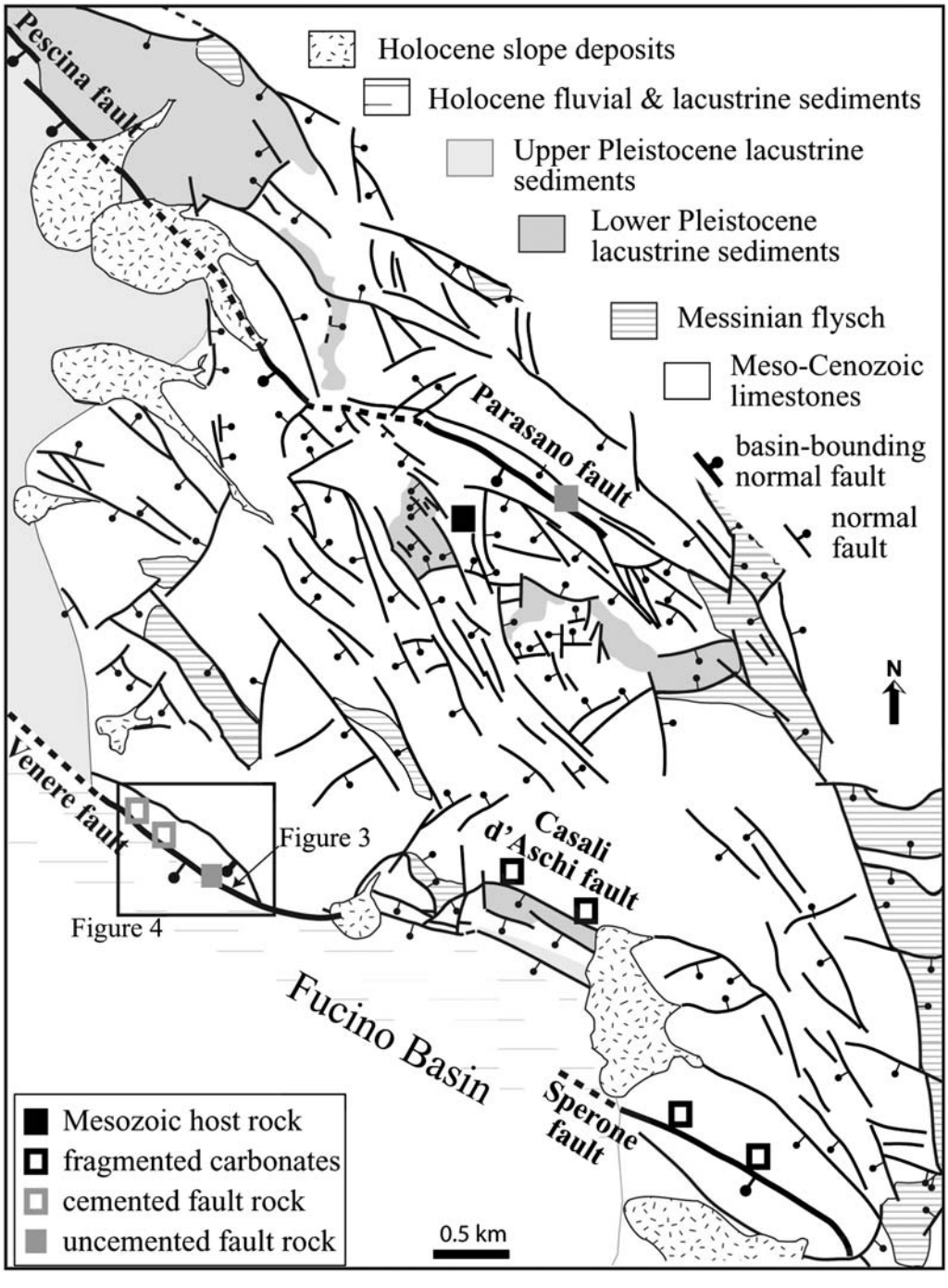

Fig. 2. Structural map of the relay ramp area bounded by the Celano–Pescina–Parasano (CPP) and the Venere–Sperone (VS) normal fault zones. The legend is on the upper right. Squares represent the hand-collected-specimens from along the normal fault zones for petrophysical and ultrasonic analyses.

from the damage zones of the Casali d'Aschi and Sperone faults, and on four fault rocks (two cement-supported and two matrix-supported) sampled from the Venere and Parasano fault cores (Fig. 2). Unfortunately, the pulverized carbonate rocks of the damage zone, which are broken into millimetre to centimetre thick fragments, could not be sampled for laboratory analyses. Each specimen, collected after removing 10–15 cm of weathered materials, was first cut for thin-sectioning, and then drilled to obtain cylindrical cores 3–5 cm long, and 2.54 cm in diameter for porosity (using a helium porosimeter based on the Boyle's law double-cell method), permeability (CMS-300 automated core measurement system) and ultrasonic analyses (pulse transmission technique at increasing confining pressures, cf. Prasad *et al.* 1999; Prasad & Nur 2003; and Vanorio *et al.* 2003). The orientation of the eight cylindrical core plugs with respect to the major slip surfaces is reported in Agosta *et al.* (2007). These analyses were also performed on a host rock sample, collected several hundreds of metres away from the CPP and VS fault zones, which was drilled parallel to bedding.

Cuttings of the two uncemented fault rock specimens recovered from the thin sectioning were used for mercury-injection capillary tests (using Micromeritics™ Auto Pore III 9420 instrumentation). The cuttings were first dried in a low temperature oven, and then injected with high-pressure mercury. The volume of mercury injected, monitored at 118 points from 11.3 to 4.06×10^5 MPa, was corrected for closure (i.e., mercury conformance to the sample surface). The breakthrough pressure was determined by picking the mercury–air capillary pressure, the pressure at which non-wetting fluids can form a throughgoing flow path through the rock, which corresponds to 10% of the cumulative intruded mercury (90% wetting phase saturation, Schowalter 1979). These data are used to estimate the resistance of a rock to invasion by gas and most oils (Sneider *et al.* 1997).

Internal properties of normal faults

The individual fault segments within the CPP and VS fault zones are several kilometres long, and have up to 600 m of cumulative throw (Cavinato *et al.* 2002). These fault zones, exhumed from 1–2 km depth since the Late Pliocene–Early Pleistocene, penetrate the central Apennines down to about 10–15 km (Ghisetti & Vezzani 1999, and references therein), and are seismically active as recorded by historical earthquakes (e.g., the $M_s = 7.0$, 1915 Avezzano earthquake, Boschi *et al.* 1997). Furthermore, the active tectonics of the area is recorded by many geomorphic features, such as fault scarps and triangular facets present in the Fucino basinal sediments and adjacent mountain fronts, respectively.

The focal mechanism of the 1915 Avezzano earthquake shows oblique extension, with a sub-horizontal T-axis oriented either east–west (Gasparini *et al.* 1985) or NNE–SSE (Basile & Valensise 1991). However, trench investigations indicate pure normal faulting for that event (Micchetti *et al.* 1996). In the longer period, an average throw slip rate of $0.4–1.0\ \mathrm{mm\,a^{-1}}$, and minor right-lateral components of slip, have been documented by the analysis of widespread fault scarps present in the Fucino area (Piccardi *et al.* 1999).

The area bounded by the CPP and VS fault zones forms a large relay ramp dissected by three different sets of normal faults (Fig. 2). The most prominent set consists of normal faults that strike NW, dip primarily to the SW and flank narrow, NW-elongated structural depressions. Based on the offset of Middle Miocene carbonate grainstones, the NW-striking faults produced an average throw of 400 m across the whole relay ramp. The other two sets of normal faults strike ENE and north, respectively. The ENE-striking faults dip mainly to the north, and mostly localize at the relay's edges. Faults striking north, which dip either to the east or to the west, abut those of the first two sets.

Structural properties

The internal architecture of the CPP and VS fault segments is made up of faulted and brecciated, metres thick basinal sediments in the hanging wall, and deformed thicker zones of platform carbonates in the footwall (Fig. 3). In the hanging wall, the Quaternary sediments dip generally to the SW, towards the basin, or less commonly to the NE, depending on the segmentation, relative geometry and amount of slip of the fault panels at depth (Cartwright *et al.* 1995; Gawthorpe *et al.* 2003). Locally, centimetres-thick slices of these sediments and slope scree have been accreted into the footwall, due to the basinward migration of the slip surfaces during faulting and exhumation. At depths greater than 1 km, where the normal faults are intra-carbonates (Cavinato *et al.* 2002), it is likely that the deformed carbonates are thicker in the hanging walls than in the footwalls (Berg & Skar 2005, and references therein).

The deformed carbonates have been studied in detail along the walls of five quarries that expose the Venere fault footwall in a three-dimensional view. There, the deformed carbonates include a 1 m-thick fault core and a *c.* 100 m-thick damage zone. The fault core comprises major slip surfaces and both matrix-supported (uncemented) and

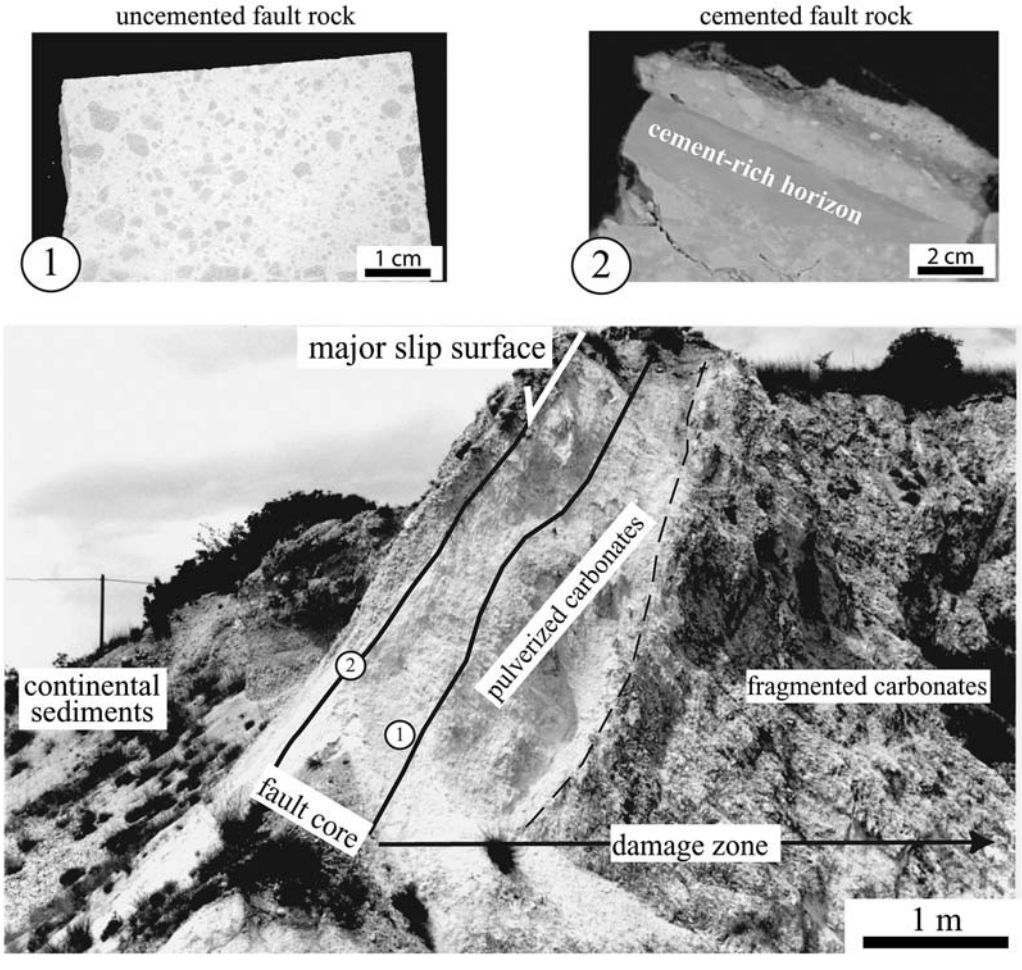

Fig. 3. Cross-sectional photographic view of the Venere fault, which juxtaposes the continental sediments of the hanging wall against the deformed carbonates. In the footwall, the fault zone comprises fragmented and pulverized carbonates (damage zone), and matrix- and cement-supported fault rocks (fault core). The polished sections of a matrix-supported (uncemented) fault rock sample, and of a cement-supported (cemented) fault rock sample, are shown on the upper left and right, respectively. The location of the two samples is reported in the photograph.

cement-supported (cemented) fault rocks (cf. Fig. 3). The slip surfaces define a strike range of N100–150E and a dip range of 40–65° S along the Venere fault. Both striations and slickenfiber orientations show predominant normal components of slip, with minor left- or right-lateral slip (surfaces oriented N100–110E have dextral components, those oriented N140–150E sinistral components). The uncemented fault rocks are made up of angular-to-subrounded survivor clasts embedded in fine-grained calcite matrix. The centimetres thick, cemented fault rocks localize primarily along the major slip surfaces, and contain sub-rounded survivor clasts embedded in low-Mg calcite cements (Agosta & Kirschner 2003). The micro veins present within these rocks, infilled with low-Mg calcite, are sub-parallel to the major slip surfaces (Agosta *et al.* 2007).

The damage zone is highly deformed in correspondence with the quarries to such a degree that the rock it contains may be classified as fragmented and pulverized, although the bedding is still discernable (Fig. 4). The degree of deformation intensity in this zone generally increases towards the fault core. Based on this trend, as measured by fracture spacing and grain-size distribution (Agosta & Aydin 2006), two main domains can be distinguished: (i) fragmented carbonates; and (ii) pulverized carbonates, which localize near the fault core. The former are crosscut by numerous

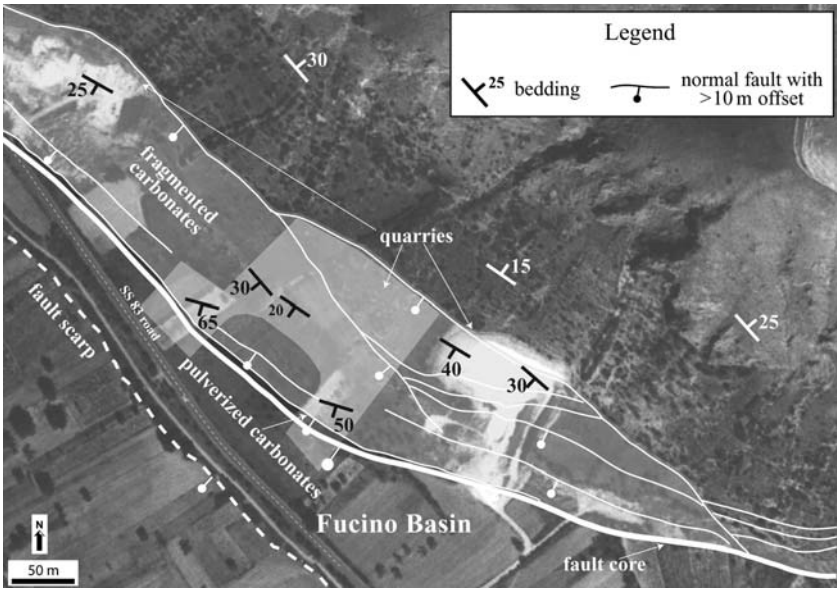

Fig. 4. Aerial distribution of the structural domains present in the footwall of the south-central portion of the Venere fault. The legend is on the upper right.

sets of closing mode (pressure solution seams), opening mode (joints and veins) and shearing mode fractures (sheared pressure solution seams, sheared joints, sheared veins). The pulverized carbonates contain several sets of pressure solution seams, joints, veins, sheared joints, and cataclastic shear bands.

Based on the rock type and on the fracture spacing, four different structural domains are distinguished within the Venere fault footwall: fragmented (domain A) and pulverized carbonates (domain B) in the damage zone, and uncemented (domain C) and cemented fault rocks (domain D) in the fault core. The distribution of these four structural domains across the Venere fault footwall shows an increase of deformation towards the hanging wall/footwall contact, with a pronounced lateral variability (Fig. 4). Both domains A and B are crosscut by small normal faults that have offsets up to several tens of metres. The small faults of the damage zone with the largest offset, shown in Figure 4, bind slivers of rocks with different dip domains; the dip angles vary from 20° SW to 65° SW, and are generally steeper near the fault core (cf. Fig. 4).

Petrophysical properties

The results of porosity, ϕ, and Klinkenberg permeability, k, measurements of the samples collected along the eastern side of the Fucino Basin (cf. Fig. 2) are plotted as a function of their relative structural position (Fig. 5). The ϕ of the fragmented samples (domain A) is higher relative to the host rock ϕ, increasing towards the fault core. This correlation, however, does not include the variations occurring in this fault domain due to the small faults and meso-scale fractures. The ϕ of the pulverized carbonates (domain B) is inferred to be 15% or higher based on the presence of cataclastic shear bands, which are common features in porous clastic rocks (Antonellini & Aydin 1994; Antonellini *et al.* 1994). In the uncemented fault rocks (domain C), the ϕ decreases relative to the inferred ϕ of the pulverized carbonates and drops down to 0.6% in the cemented fault rocks (domain D) that localize along the major slip surfaces.

The permeability measurements, gathered at a confining pressure (P_c) of 5.5 MPa, show that the fragmented rock samples have higher values relative to host and fault rock samples. The k values of the fragmented carbonates (domain A) range between 1.5×10^{-2} and 79.9 mD, consistent with an increase of permeability within this domain towards the fault core. The k-value of the pulverized carbonates (domain B) is projected to be higher than 1.5×10^{-2} mD. The measured k of the uncemented fault rocks (domain C) ranges between 0.12 and 0.14 mD. The cemented fault rock's k values (domain D) are lower than 1×10^{-4} mD, which is the lower bound of the instrument.

The P-wave velocity (V_p)-confining pressure relationship is indicative of the pore geometry

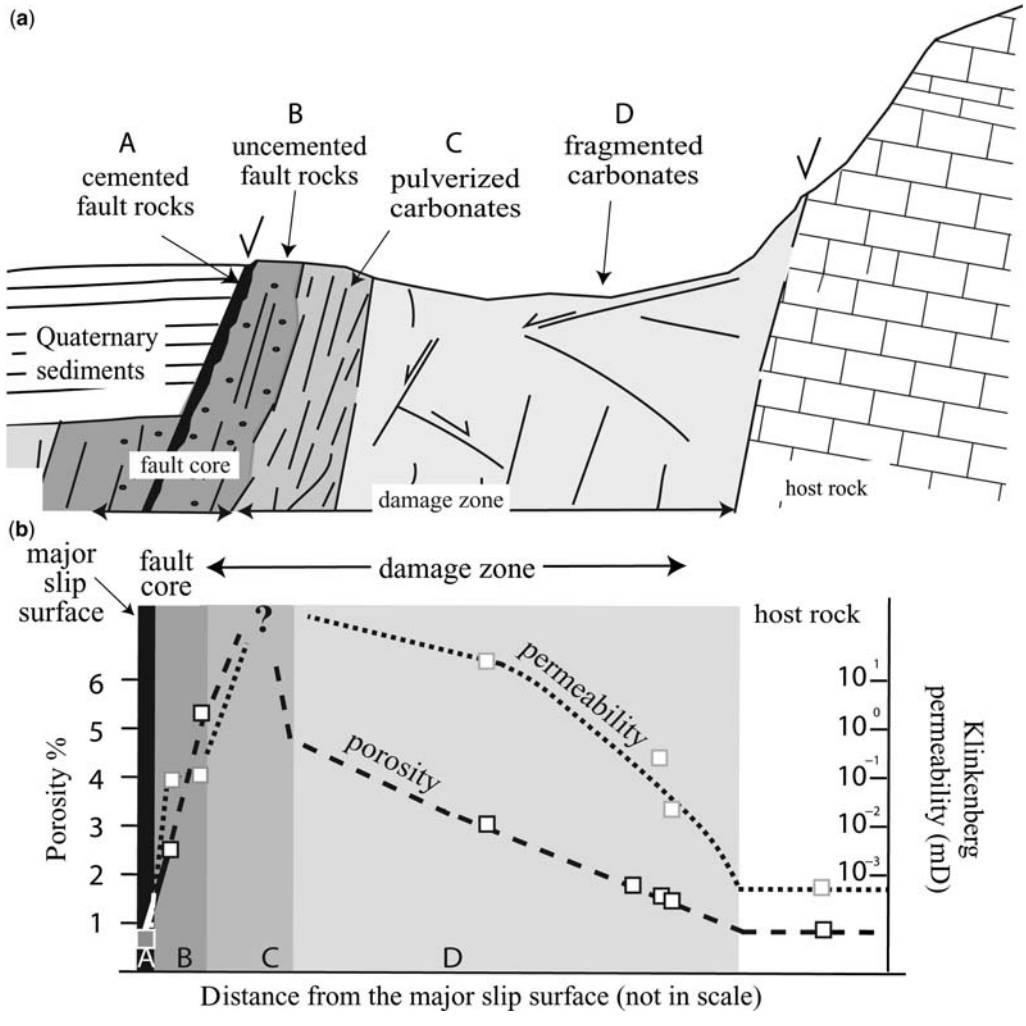

Fig. 5. (**a**) Schematic cross-section of the internal structural domains (A–D) present in the footwall of the basin-bounding normal faults. (**b**) Composite diagram of porosity (dashed line) and Klinkenberg permeability (dotted line) measured on samples collected from the four fault domains. The porosity value for the pulverized carbonates is inferred to be 15% or higher because of the presence of shear bands in these rocks (Antonellini & Aydin 1994; Antonellini *et al.* 1994). The permeability of the two cemented fault rocks is smaller than 1×10^{-4} mD, which is instrumental lower bound.

within the study rock samples (Fig. 6a). The V_p of samples collected from domain A rises significantly during the first increments of pressure, and plateaus at P_c *c.* 10 MPa consistent with pores with a high aspect ratio (e.g., crack-like). Conversely, the V_p of samples collected from domains C and D increases slightly during the first increments of pressure, and plateaus at P_c *c.* 5 MPa (Fig. 6b). This behaviour indicates that pores present in both uncemented and cemented fault rocks have a low aspect ratio (e.g., sub-spherical). The effect of porosity on V_p (Fig. 6c) shows the presence of moldic ϕ within the fault rocks. Three of the four fault rock data points, for given ϕ values, have a higher V_p relative to the best-fit curve published for the platform carbonates of Bahamas and the Maiella Mountain, central Italy (Anselmetti & Eberli 1993, 1997). Moldic ϕ is due to selective dissolution that does not affect the elastic frame of the rock, and thus enhances porosity but not permeability (Anselmetti & Eberli 2001). After microscopy analysis, the moulds localize within the survivor clasts of the fault rocks, and not in the matrix/cements that form the elastic frames of these rocks.

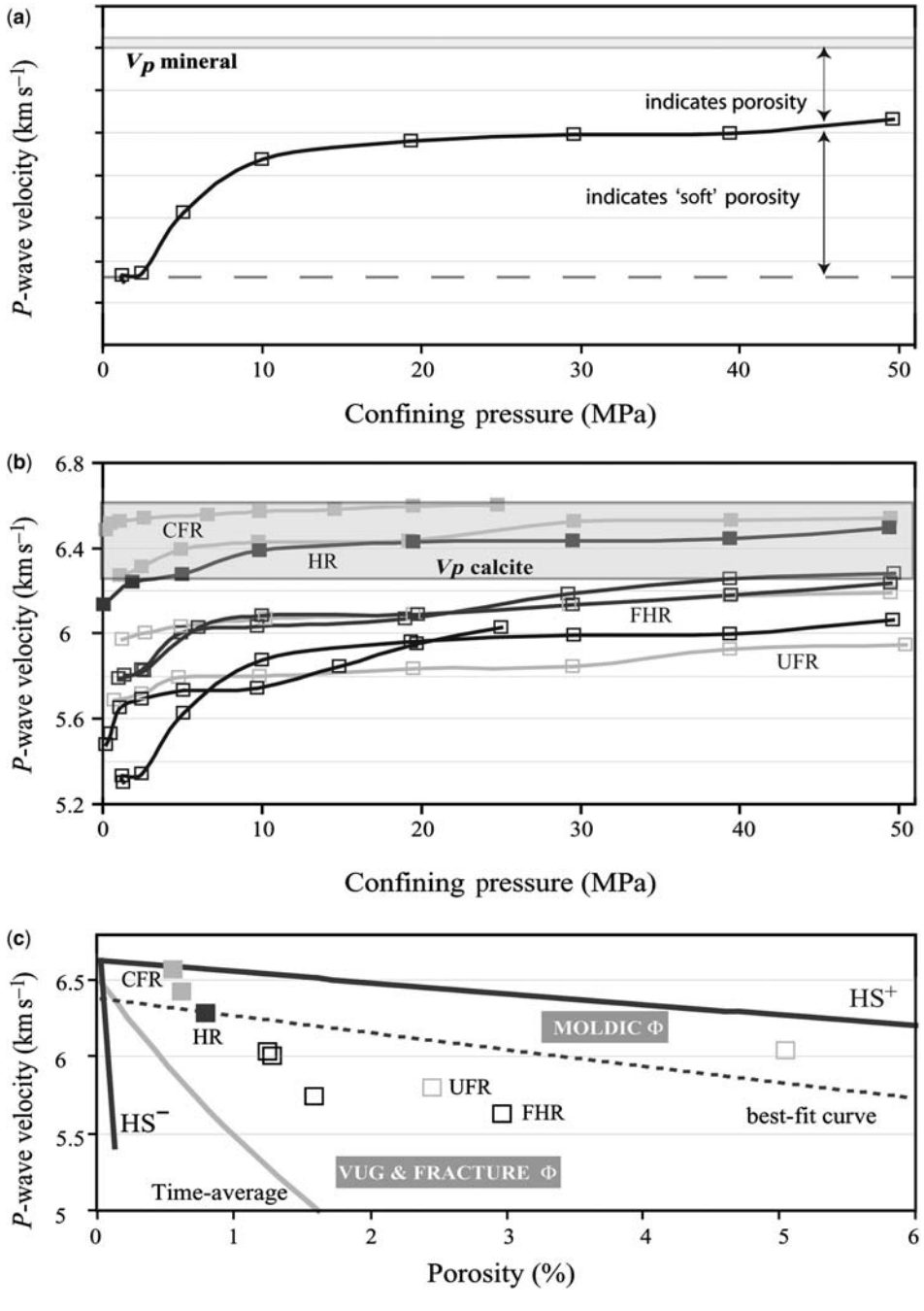

Fig. 6. (**a**) Idealized plot of *P*-wave velocity (V_p)-confining pressure (P_c) relation for a monomineralic rock; (**b**) $V_p - P_c$ relation for one sample of Mesozoic host rock, four samples of fragmented carbonates, two samples of uncemented fault rocks, and two samples of cemented fault rocks. The legend is shown in Figure 2. The grey area at the top of this plot represents the published values for calcite (Mavko *et al.* 1998). (**c**) Plot of the V_p–porosity relations measured at 5 MPa (legend in Fig. 2). The HS^+ and HS^- lines represent the Hashin–Shtrikman upper and lower bounds, respectively, the time-average line represents the *P*-wave velocity calculated using Wyllie's equation (Wyllie *et al.* 1956, 1958, 1963). The dashed line reports the power best-fit curve of V_p of undeformed carbonates from Bahamas and Maiella Mountain (Anselmetti & Eberli 1993, 1997).

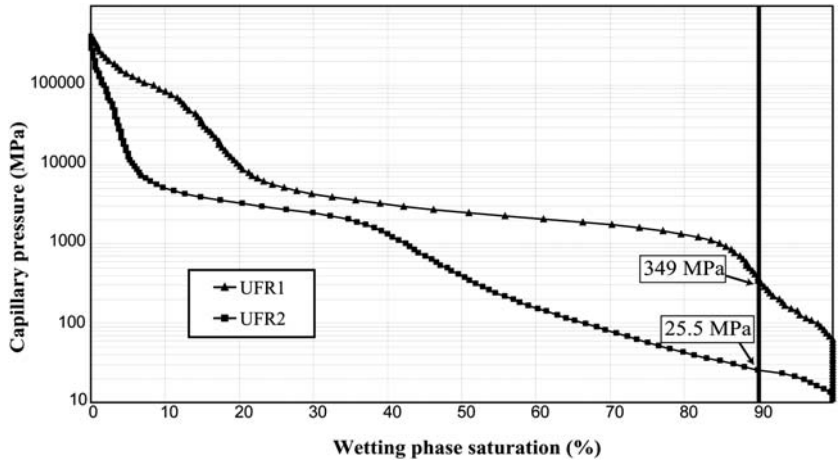

Fig. 7. Composite plot of drainage data computed from mercury-injection capillary tests of two uncemented fault rock samples, UFR1 and UFR2. A mercury–air capillary pressure corresponding to 10% of the cumulative intruded mercury is used to estimate breakthrough pressures.

A composite plot of the drainage data obtained for two uncemented fault rock samples (UFR1 and UFR2) represents the mercury–air capillary pressure as a function of the cumulative percent age intruded mercury up to a maximum applied 4.06×10^5 MPa (Fig. 7). The measured breakthrough pressure varies between 25.5 and 349 MPa. Based on these values, the sealing capacity is computed using representative fluid properties for both oil and gas and the two following equations (Sneider *et al.* 1997):

$$P_{c,h/w} = \left[\frac{(\sigma_{h/w}{}^* \cos\theta_{h/w})}{(\sigma_{Hg/air}{}^* \cos\theta_{Hg/air})}\right] P_{c,Hg/air} \quad (1)$$

and

$$h = P_{c,h/w}/\Delta\rho^* \; 0.433 \quad (2)$$

where P_c is the capillary breakthrough pressure, h is the maximum hydrocarbon height, σ is the interfacial tension between hydrocarbon and brine, θ is the contact angle, and $\Delta\rho$ is the difference in tension between hydrocarbon and brine. Subscripts h, w and Hg refer, respectively, to hydrocarbon, water and mercury. The input parameters used to compute the maximum sealable hydrocarbon column height are those provided by Sneider *et al.* (1997). The sealing potential of the two sampled uncemented fault rocks varies between 5.7 and 77 m for gas, and 10.4 and 140 m for oil. According to the Sneider seal classification (Sneider *et al.* 1997), these rocks form a Class-E seal (<15 m oil) and a Class-C seal (30–150 m oil), respectively.

The results of mercury-injection capillary analysis are also used to compute the pore radii distribution (Fig. 8). One sample is characterized by one main peak, which corresponds to a pore radius of 0.33 μm, whereas the other sample has two peaks that correspond to the pore radii of 0.27 μm and 29 μm. Since the higher pore radius in the latter sample (29 μm) is due to vugs and microcracks depicted in thin-section, the radius of 0.27 μm represents the pore size in this sample.

Discussion

Based on their structural and petrophysical properties, the carbonate footwalls of the basin-bounding normal faults contain two distinct units: (i) fault core (low ϕ and low k), and (ii) damage zone (high ϕ and high k). Taking into account the pore structure of the samples collected from these units, documented by ultrasonic analysis, the fault permeability is modelled as follows. The fault core is thought of as a granular medium composed of a bundle of tortuous, capillary tubes of constant length and cross-sectional area. The damage zone is modelled as an elastic cracked medium, in which all the fractures behave as open cracks and form the main control on porosity.

Calculation of matrix permeability for a granular medium

To compute the matrix permeability, k, of the granular fault core from known values of effective porosity ($\phi_{eff} = \phi_{total} - \phi_{moldic}$) and pore radii,

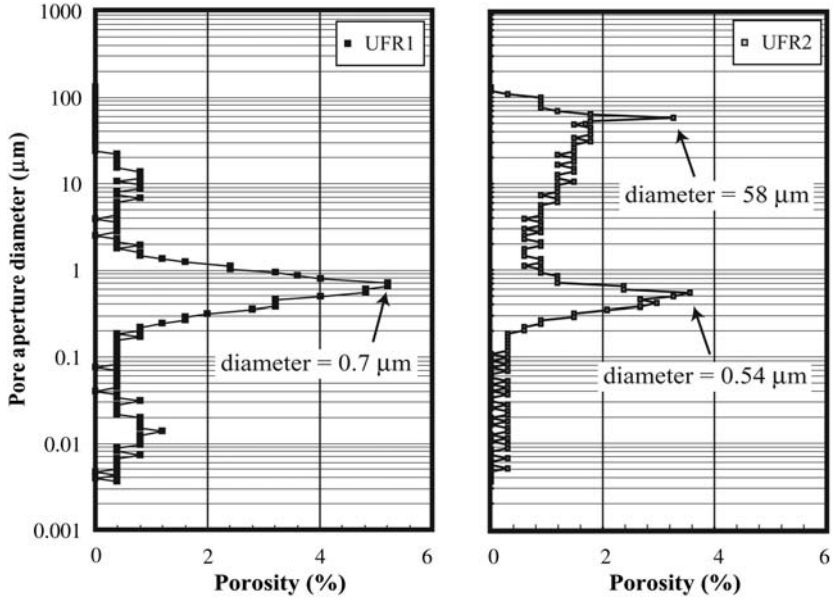

Fig. 8. Pore aperture distribution of the two uncemented fault rocks computed from capillary pressure tests. Sample UFR1 shows one main peak corresponding to a pore radius of 0.33 μm. Sample UFR2 shows two peaks (0.27 μm and 29 μm). The higher pore radius, 29 μm, represents small vugs present in the cuttings.

we use the Kozeny–Carmen correlation (Tiab & Donaldson 1996). The permeability is proportional to square of the radius of the individual capillary tubes, which is related to the pore size in the fault rocks. Considering the two uncemented fault rocks samples, by first calculating the wetted surface area per unit of pore volume, S_{vp}, and then the specific surface area of the porous material, S_{vgr}, k is computed as follows:

$$k = [1/(5^{*}S_{vgr}{}^{2})]^{*}[\phi_{eff}{}^{3}/(1-\phi_{eff})^{2}] \qquad (3)$$

where 5 represents the value of the Kozeny constant, K_z, reported by Carmen (1937) for tubes with a tortuosity coefficient of 2.5. Using this correlation, the two computed values, 0.09 and 0.16 mD, are quite similar to the measured Klinkenberg k values, 0.12 and 0.14 mD.

Calculation of matrix permeability of an elastic cracked medium

To compute the permeability of the elastic cracked damage zone, we assume that the open cracks are highly interconnected, and that the fluid flow occurs through the individual cracks in response to the pressure gradients. We use the Budiansky–O'Connell (1976) correlation to compute the fracture density, e, within the elastic cracked medium:

$$e = -(K_{air}/K_{rock} + 1)/\{(16/9) \cdot [(1-\nu_{rock})/(1-2\nu_{rock})]\} \qquad (4)$$

where K is the bulk modulus and ν the Poisson's ratio. These moduli are obtained from ultrasonic analysis (cf. table 1 in Agosta *et al.* 2007). Plugging the calculated e value into the power-law equation, following percolation theory we compute k (Zhang & Sanderson 1995):

$$k = -[Ap \times (e-dc)^{1.3}]/(\pi \cdot r^{2}) \times [\mu/(dh/dl)] \qquad (5)$$

where Ap is the anisotropy factor, dc the percolation threshold, r the radius of the core plugs, μ the water viscosity (0.862×10^{-3} Pas at 26.6 °C), and dh/dl is the hydraulic gradient (5 MPa m^{-1}). A value of percolation threshold, dc, is associated with each individual anisotropy factor. By changing the values of both Ap and dc, we can represent the different orientation that fractures can have relative to the direction of fluid flow: isotropic conditions ($Ap = 1$ and $dc = 0.047$), most favourable conditions for fluid flow ($Ap = 3$ and $dc = 0.06$) or

least favourable ($Ap = 0.33$ and $dc = 0.034$). The computed permeability values (7.4 – 64.8 mD) are similar to those measured in the laboratory (1.5×10^{-2} to 79.9 mD) only for samples with a large secondary porosity and high-aspect ratio pores (Agosta *et al.* 2006).

Fluid flow properties of normal fault zones

The overall permeability structure of the normal fault zones is thus consistent with a combined barrier–conduit to fluid flow (Fig. 9). At and near the land surface, this structure includes fault cores that act as seals for fluid flow (domains C and D). These seals, able to compartmentalize as much as 77 m of gas and 140 m of oil, are encompassed between two separate fluid conduits that localize within the deformed Quaternary sediments, and in the fragmented and pulverized carbonates (domains A and B). Of course, the sealing potential of the fault cores would be greater if the centimetres-thick, cemented fault rocks were taken into account. At depths where the normal faults are intra-carbonates, the permeability structure is inferred to include a central, thin barrier to fluid flow, the fault core, sandwiched between

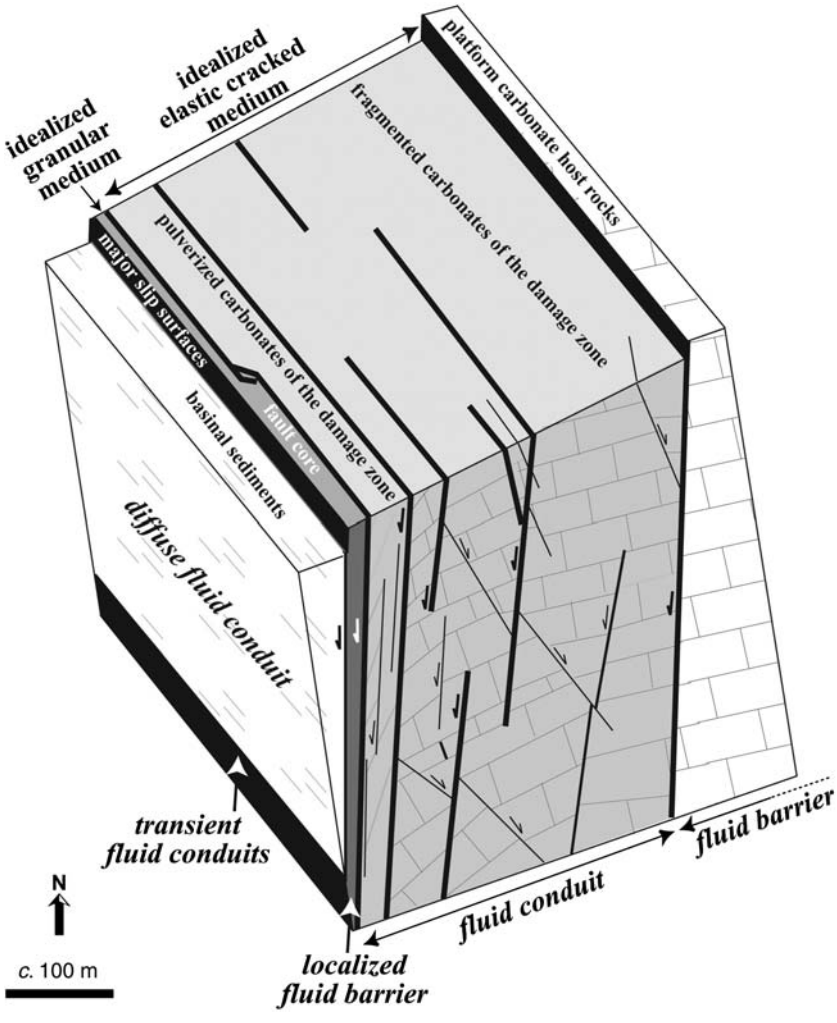

Fig. 9. Idealized barrier–conduit permeability structure of the basin-bounding normal faults. At and near the land surface, the fault cores act as seals for fluid flow and are sandwiched between two fluid conduits that localize within the deformed Quaternary sediments (fault hanging wall) and in the deformed carbonates of the damage zone (fault footwall).

two fluid conduits that localize within the carbonates damage zones of the hanging wall and the footwall.

The aforementioned fluid model, however, does not take into account two important factors that may affect the fluid flow properties of the normal fault zones: (i) the transient variation of the along-fault permeability in the fault core that occurs during seismic slip of the normal faults, and (ii) the impact of both small faults and meso-scale fractures on the fluid flow within the damage zones. The formation of fluid pathways within the fault cores, as indicated by calcite coating the major slip surfaces, is due to coseismic dilation and opening of cracks (Sibson 2000). This process may determine transients of high permeability in the fault core, forming fluid pathways primarily along the major slip surfaces that channel fluids either at the land surface (original meteoric water, Ghisetti *et al.* 2001; Agosta & Kirschner 2003), or at depths of 2–3 km (original CO_2-rich groundwater, Agosta *et al.* 2008). These diagenetic fluids eventually seal the open cracks, coat the slip surfaces, and cement the fault rocks, reducing therefore the fault core permeability in the interseismic periods.

The small faults and meso-scale fractures contained in the damage zone may enhance or reduce the fluid transmissibility depending on their internal architecture and structural arrangement. It has been documented that small faults made up of fragmented and brecciated rocks, joints, veins, sheared and opened pressure solution seams create fluid pathways in low-porosity rocks (Aydin 2000; Graham *et al.* 2006). In contrast, small faults that contain continuous cores of comminuted fault rocks, characterized by low values of ϕ and k, can form barriers to fluid flow. Since the internal architecture of the small faults present within the normal fault footwalls has not been documented in detail, the proposed model of fault permeability is thus reliable only to compute the matrix permeability. Further studies are therefore necessary, such those to calculate fault transmissibility (e.g., Walsh *et al.* 1998; Manzocchi *et al.* 1999) and upscaled fault permeability (e.g., Flodin 2003), to include these elements in the overall permeability model of the carbonate damage zones.

Conclusions

This eastern side of the Fucino Basin is bounded by two major normal fault zones that contain individual, several kilometers-long fault segments. These fault segments, exhumed from 1–2 km depth since the Late Pliocene–Early Pleistocene, have up to 600 m of cumulative throw, are seismically active and juxtapose Quaternary continental sediments of the hanging walls against deformed massive, platform carbonates of the footwalls. The platform carbonate host rocks are Mesozoic boundstones with low values of porosity ($<1\%$) and permeability ($<1 \times 10^{-4}$ mD).

The internal architecture of the carbonate fault footwalls comprises of metres-thick fault cores and hundreds of metres thick damage zones. The fault cores include matrix- and cement-supported fault rocks, and major slip surfaces. The damage zones include fragmented and pulverized carbonates, and several small faults with throws of up to tens of metres. The pulverized carbonates, which generally flank the fault cores, are up to few metres-thick. The principal structural elements present in the damage zone include several sets of opening mode (joints and veins), closing mode (pressure solution seams) and shearing mode fractures (sheared pressure solution seams, sheared joints/veins, cataclastic shear bands).

The fragmented samples analysed in the laboratory, which contain only a subset of the aforementioned structure elements, have high values of porosity and permeability (up to 3% and 79.9 mD, respectively). Based on the presence of cataclastic shear bands, the porosity of the pulverized carbonate rocks is inferred to be 15% or higher. The samples collected from the fault cores have porosity values that range from 0.6% (cemented fault rocks) and 5.2% (uncemented), and permeability values between $<1 \times 10^{-4}$ mD (cemented) and 0.14 mD (uncemented).

Based on the results of ultrasonic analysis, the fragmented carbonate samples contain pores with a high aspect ratio (e.g., crack like), whereas the fault rock samples pores with a low aspect ratio (e.g., sub-spherical). The effect of porosity on *P*-wave velocity shows the presence of moldic porosity in the latter samples. Microscopy analysis indicates that moulds localize within the survivor clasts, and not within the matrix and cements.

Both structural and petrophysical data suggest that the normal faults are characterized by an asymmetrical, combined barrier–conduit permeability structure. The fault cores form barriers for cross-fault fluid flow, which can compartmentalize as much as 77 m of gas and 140 m of oil. The fault cores are flanked by fluid conduits the localize within the metres-thick, brecciated sediments of the fault hanging walls, and in the hundreds of metres-thick fragmented and pulverized carbonates of the fault footwalls.

Based on their different pore structure, the fault core is modelled as a granular medium containing a bundle of tortuous, capillary tubes, whereas the damage zone is modelled as an elastic cracked medium in which all fractures are highly interconnected. The permeability of these two separate

carbonate fluid units is then computed from measured values of porosity, pore radii, and elastic moduli using the Kozeny–Carmen and Budiansky–O'Connell correlations. At depths greater than 1 km the normal faults are entirely confined within the platform carbonates, and characterized by a quite symmetrical permeability structure in which the central barrier, the fault core, is flanked by two fluid conduits present in the fragmented carbonates of the hanging wall (probably thicker) and of the footwall (thinner).

The fluid flow properties of normal faults are also controlled by other factors. The along-fault permeability may be modulated by the seismic cycle of the faults. The isotopic signature of calcite that mineralized from fault fluids shows the ingression within the faults of both meteoric water and CO_2-rich groundwater. These diagenetic fluids move primarily along the major slip surfaces, and eventually seals the open cracks, coat the slip surfaces, and cement the fault rocks. The fluid transmissibility of the carbonate damage zones is not only controlled by the matrix permeability, but also by small faults and meso-scale fractures. Further studies are therefore necessary to document how these structures affect the fluid flow properties of the faults.

The work presented in this paper forms part of the PhD dissertation defended by the author in January 2006. F.A. thanks his former supervisor, A. Aydin, for the continuous support and encouragement during his studies at Stanford University, and M. Prasad for the help and guidance during rock physics experiments. Comments and suggestions made by G. Cello, D. Sanderson and an anonymous reviewer helped to improve the quality of this manuscript.

References

AGOSTA, F. & AYDIN, A. 2006. Deformation mechanisms and structural architecture of a large normal fault in platform carbonates, Fucino Basin, central Italy. *Journal of Structural Geology*, **28**, 1445–1467.

AGOSTA, F. & KIRSCHNER, D. L. 2003. Fluid conduits in carbonate-hosted seismogenic normal faults of Central Italy. *Journal of Geophysical Research*, **108**, 2221, doi:101029/2002JB002013.

AGOSTA, F., PRASAD, M. & AYDIN, A. 2007. Physical properties of carbonate fault rocks, Fucino basin, central Italy: implications for fault seal in platform carbonates. *Geofluids*, **7**, 19–32.

AGOSTA, F., MULCH, A., CHAMBERALIN, P. & AYDIN, A. 2008. Geochemical traces of CO_2 emission from earth interior along normal faults in central Italy. *Geophysical Journal International* (in press).

ALVAREZ, W., ENGELDER, T. & GEISER, P. A. 1978. Classification of solution cleavage in pelagic platform carbonates. *Geology*, **6**, 263–266.

ANSELMETTI, F. & EBERLI, G. P. 1993. Controls on sonic velocity in carbonates. *Pure and Applied Geophysics*, **141**, 287–323.

ANSELMETTI, F. & EBERLI, G. P. 1997. Sonic velocity in carbonate sediments and rocks. *Geophysical Development Series*, **6**, 53–74.

ANSELMETTI, F. & EBERLI, G. P. 2001. *Sonic Velocity in Carbonates – a Combined Product of Depositional Lithology and Diagenetic Alterations.* Society for Sedimentary Geology Special Publications, **70**, 193–216.

ANTONELLINI, M. & AYDIN, A. 1994. Effect of faulting on fluid flow in porous sandstones – petrophysical properties. *American Association Petroleum Geologists Bulletin*, **78**, 355–377.

ANTONELLINI, M. & AYDIN, A. 1995. Effect of faulting on fluid flow in porous sandstones: geometry and spatial distribution. *American Association Petroleum Geologists Bulletin*, **79**, 642–671.

ANTONELLINI, M., AYDIN, A. & POLLARD, D. 1994. Microstructure of deformation bands in porous sandstones at Arches National Park. Utah. *Journal of Structural Geology*, **16**, 941–959.

ANTONELLINI, M., TONDI, E., AYDIN, A. & AGOSTA, F. 2007. Evolution of strike-slip faults in basinal carbonates of the Maiella Mt., central Italy. *Marine and Petroleum Geology*, doi:10.1016/j.marptgeo.2007.10.008.

AYDIN, A. 2000. Fractures, faults, and hydrocarbon entrapment, migration and flow. *Marine and Petroleum Geology*, **17**, 797–814.

BASILE, A. & VALENSISE, G. 1991. Contributo alla caratterizzazione della sismicita' dell'area marsicano-fucense. *Aree Sismogenetiche e Rischio Sismico in Italia*, ING-SGA, 197–214.

BERG, S. & SKAR, T. 2005. Controls on damage zone asymmetry of a normal fault zone: outcrop analysis of a segment of the Moab fault, SE Utah. *Journal of Structural Geology*, **27**, 1803–1822.

BIGI, G., COSENTINO, D., PAROTTO, M., SARTORI, R. & SCANDONE, P. 1992. *Structural Model of Italy*, scale 1:500,000, 6 sheets. CNR, Quaderni di Ricerca Scientifica, **114**.

BOSCHI, E., GUIDOBONI, E., FERRARI, G. & VALENSISE, G. 1997. *Catalogo dei forti terremoti in Italia dal 461 A.C. al 1990.* ING-SGA.

BOSI, C., GALADINI, F. & MESSINA, P. 1995. Stratigrafia Plio-Pleistocenica della conca del Fucino. *Il Quaternario*, **8**, 89–93.

BRUHN, R., PARRY, W. & THOMPSON, T. 1994. Fracturing and hydrothermal alteration in normal fault zone. *Pure and Applied Geophysics*, **142**, 609–644.

BUDIANSKY, B. & O'CONNELL, R. J. 1976. Elastic moduli of dry and saturated cracked solids. *International Journal of Solids Structures*, **12**, 81–97.

CAINE, J. S. & FORSTER, C. B. 1999. Fault zone architecture and fluid flow – Insights from field data and numerical modeling. *In*: HANEBERG, W. *ET AL.* (eds) *Faults and Subsurface Fluid Flow in the Shallow Crust.* American Geophysics Union Geophysical Monographs, **133**, 101–127.

CAINE, J. S., EVANS, J. P. & FORSTER, C. B. 1996. Fault zone architecture and permeability structure. *Geology*, **24**, 1025–1028.

CARMEN, P. C. 1937. Fluid flow through granular beds. *Transactions of the American Institute of Chemical Engineers*, **15**, 150–166.

CARTWRIGHT, J. A., TRUDGILL, B. & MANSFIELD, C. S. 1995. Fault growth by segment linkage: an explanation for scatter in maximum displacement and trace length data from Canyonlands Grabens of SE Utah. *Journal of Structural Geology*, **17**, 1319–1326.

CAVINATO, G. P., CARUSI, C., DALL'ASTA, M., MICCADEI, E. & PIACENTINI, T. 2002. Sedimentary and tectonic evolution of Plio-Pleistocene alluvial and lacustrine deposits of Fucino Basin (central Italy). *Sedimentary Geology*, **148**, 29–59.

CELLO, G. 2000. A quantitative structural approach to the study of active faults in the Apennines (Peninsula Italy). *Journal of Geodynamics*, **29**, 265–292.

CHESTER, F. M. & LOGAN, J. M. 1986. Composite planar fabric of gouge from the Punchbowl fault, California. *Journal of Structural Geology*, **9**, 621–634.

COWIE, P. A. & SCHOLZ, C. H. 1992. Growth of faults by accumulation of seismic slip. *Journal of Geophysical Research*, **97**, 11085–11095.

DE JOSSINEAU, G. & AYDIN, A. 2007. The evolution of the damage zone with fault growth in sandstone and its multiscale characteristics. *Journal of Structural Geology*, **112**, B12, B12401, doi:10.1029/2006JB004711.

FLODIN, E. 2003. *Structural evolution, petrophysics, and large-scale permeability of faults in sandstone, Valley of Fire, Nevada*. PhD thesis, Stanford University.

FLODIN, E., GERDES, M., AYDIN, A. & WIGGINS, W.D. 2005. Petrophysical properties and sealing capacity of fault rock from sheared-joint based faults, Aztec sandstone, Nevada. *In*: SORKHABI, R. & TSUJI, Y. (eds) *Faults, Fluid Flow, and Petroleum Traps*. American Association of Petroleum Geologists, Special Memoirs, **85**, 197–217.

GASPARINI, C., IANNACONE, G. & SCARPA, R. 1985. Fault-plane solutions and seismicity of the Italian peninsula. *Tectonophysics*, **117**, 59–78.

GAWTHORPE, R. L., JACKSON, C., YOUNG, I. M. J., SHARP, R., MOUSTAFA, A. R. & LEPPARD, C. W. 2003. Normal fault growth, displacement localization and the evolution of normal fault population: the Hammam Faraun fault block Suez rift, Egypt. *Journal of Structural Geology*, **25**, 883–895.

GHISETTI, F. & VEZZANI, L. 1999. Depth and modes of Pliocene-Pleistocene crustal extension of the Apennines (Italy). *Terra Nova*, **11**, 67–72

GHISETTI, F., KIRSCHNER, D. L., VEZZANI, L. & AGOSTA, F. 2001. Stable isotope evidence for contrasting paleofluid circulation in thrust and seismogenic normal faults of central Apennines, Italy. *Journal of Geophysical Research*, **106**, 8811–8825.

GRAHAM, B., ANTONELLINI, M. & AYDIN, A. 2003. Formation and growth of normal faults in carbonates within a compressive environment, *Geology*, **31**, 11–14.

GRAHAM, B., GIRBECCA, R., MESONJESI, A. & AYDIN, A. 2006. Evolution of fluid pathways through fracture controlled faults in carbonates of the Albenides fold-and-thrust belt. *American Association of Petroleum Geologists Bulletin*, **90**, 1227–1249.

KELLY, Y. S., PEACOCK, D. C. P. & SANDERSON, D. J. 1998. Linkage and evolution of conjugate strike-slip fault zones in platform carbonates of Somerset and Northumbria. *Journal of Structural Geology*, **20**, 1477–1493.

KIM, Y. S., PEACOCK, D. C. P. & SANDERSON, D. J. 2004. Fault damage zones. *Journal of Structural Geology*, **26**, 503–517.

LUCIA, F. J. 1999. *Carbonate Reservoir Characterization.* Springer, Berlin.

MANZOCCHI, T., WALSH, J. J., NELL, P. & YIELDING, G. 1999. Fault transmissibility multipliers for flow simulation models. *Petroleum Geoscience*, **5**, 53–63.

MARSHAK, S., GEISER, P. A., ALVAREZ, W. & ENGELDER, T. 1982. Mesocopic fault array of the northern Umbrian Apennine fold belt: geometry of conjugate shear by pressure-solution slip. *Geological Society of America Bulletin*, **93**, 1013–1022.

MAVKO, G., MUKERJI, T. & DVORKIN, J. 1998. *The Rock Physics Handbook.* Cambridge University Press, Cambridge.

MYERS, R. & AYDIN, A. 2004. The evolution of faults formed by shearing across joint zones in sandstones. *Journal of Structural Geology*, **26**, 947–966.

MICCHETTI, A., BRUNAMONTE, F., SERVA, L. & VITTORI, E. 1996. Trench investigations of the 1915 earthquake fault scarps (Abruzzo, central Italy): geological evidence of large, historical events. *Journal of Geophysical Research*, **101**, 5921–5936.

PEACOCK, D. C. P. & SANDERSON, D. J. 1995. Pull-aparts, shear fractures and pressure solution. *Tectonophysics*, **241**, 1–13.

PICCARDI, L., GAUDEMER, Y., TAPPONNIER, P. & BOCCALETTI, M. 1999. Active oblique extension in the central Apennines (Italy); evidence from the Fucino region. *Geophysical Journal International*, **2**, 499–530.

PRASAD, M. & NUR, A. 2003. Velocity and attenuation anisotropy in reservoir rocks. Expanded Abstracts, Society of Exploration Geophysics Annual Meeting, RP 2–3.

PRASAD, M., PALAFOX, G. & NUR, A. 1999. Velocity and attenuation characteristics of Daqing sandstones – effects of permeability on velocity and attenuation anisotropy. *American Geophysical Union*, Fall Meeting, EOS Transactions, **80**.

RAWLING, G., GOODWIN, L. & WILSON, J. 2001. Internal architecture, permeability structure, and hydrologic significance of contrasting fault-zone types. *Geology*, **29**, 43–46.

SALVINI, F., BILLI, A. & WISE, D. U. 1999. Strike–slip fault-propagation cleavage in carbonate rocks; the Mattinata fault zone, Southern Apennines, Italy. *Journal of Structural Geology*, **21**, 1731–1749.

SCHOLZ, C. H. 1990. *The Mechanics of Earthquakes and Faulting*. Cambridge University Press, Cambridge.

SCHOWALTER, T. 1979. Mechanics of secondary hydrocarbon migration and entrapment. *Geological Society of America Bulletin*, **63**, 723–760.

SHIPTON, Z. K. & COWIE, P. 2001. Damage zone and slip surface evolution over a micron to km scales in high-porosity Navajo sandstone, Utah. *Journal of Structural Geology*, **23**, 1825–1844.

SIBSON, R. H. 1977. Fault rocks and fault mechanisms. *Journal of the Geological Society of London*, **133**, 191–213.

SIBSON, R. H. 2000. Fluid involvement in normal faulting. *Journal of Geodynamics*, **29**, 469–499.

SNEIDER, R., SNEIDER, J., BOLGER, G. & NEASHAM, J. 1997. Comparison of seal capacity determinations – Core versus cuttings. *Geological Society of America Memoir*, **67**, 1–12.

TIAB, D. & DONALDSON, E. 1996. *Petrophysics – Theory and Practice of Measuring Reservoir Rock and Transport Properties*, Gulf Publishing Company.

TONDI, E., ANTONELLINI, M., AYDIN, A., MARCHEGIANI, L. & CELLO, G. 2006. The role of deformation bands and pressure solution in fault development in carbonate grainstones of Majella Mountain, central Italy. *Journal of Structural Geology*, **28**, 376–391.

VANORIO, T., PRASAD, M., NUR, A. & PATELLA, D. 2002. Ultrasonic velocity measurements in volcanic rocks – correlation with microtexture. *Geophysical Journal International*, **149**, 22–36.

VEZZANI, L. & GHISETTI, F. 1998. *Carta Geologica dell'Abruzzo.* SELCA, Firenze.

WALSH, J. J., WATTERSON, J., HEATH, A. E. & CHILDS, C. 1998. Representation and scaling of faults in fluid flow models. *Petroleum Geoscience*, **4**, 241–251.

WANG, Z. 1997. Seismic properties of carbonate rocks. *Geophysical Development Series*, **6**, 29–52.

WILLEMSE, E. J., PEACOCK, D. C. P. & AYDIN, A. 1997. Nucleation and growth of strike-slip faults in platform carbonates from Somerset, U.K. *Journal of Structural Geology*, **19**, 1461–1477.

WYLLIE, M., GREGORY, A. & GARDNER, L. 1956. Elastic wave velocities in heterogeneous and porous medium. *Geophysics*, **21**, 41–70.

WYLLIE, M., GREGORY, A. & GARDNER, L. 1958. An experimental investigation of factors affecting elastic wave velocities in porous medium. *Geophysics*, **23**, 459–493.

WYLLIE, M., GARDNER, L. & GREGORY, A. 1963. Studies of elastic wave attenuation in porous medium. *Geophysics*, **27**, 569–589.

ZHANG, X. & SANDERSON, D. 1995. Anisotropic features of geometry and permeability in fractured rock masses. *Engineering Geology*, **40**, 65–75.

$^{40}Ar/^{39}Ar$ dating of synkinematic white mica: insights from fluid–rock reaction in low-grade shear zones (Mont Blanc Massif) and constraints on timing of deformation in the NW external Alps

Y. ROLLAND[1], M. ROSSI[2,3], S. F. COX[4], M. CORSINI[1], N. MANCKTELOW[5], G. PENNACCHIONI[6], M. FORNARI[1] & A. M. BOULLIER[3]

[1]*Géosciences Azur, Université de Nice Sophia-Antipolis, CNRS, IRD, 28 Av. Valrose, BP 2135, 06103 Nice, France (e-mail: yrolland@unice.fr)*

[2]*PGP, University of Oslo, PO Box 1048, Blindern, 0316 Oslo, Norway*

[3]*LGCA-LGIT, OSUG, BP53, Université J. Fourier, 38041 Grenoble, France*

[4]*Department of Earth and Marine Sciences, and Research School of Earth Sciences, Australian National University, Canberra, ACT 0200, Australia*

[5]*Geologisches Institut, ETH Zürich, CH-8092 Zürich, Switzerland*

[6]*Dipartmento di Geoscienze, Via Giotto 1, 35137 Padova, Italy*

Abstract: This paper highlights the use of synkinematic white mica, biotite and phlogopite for the dating of deformation in ductile shear zones within crystalline rocks under low-grade metamorphic conditions. The Mont Blanc shear zones range from 1 mm to 50 m in width and have localized intense fluid flow, resulting in substantial differences in mineralogy and whole-rock geochemistry. On the basis of their synkinematic alteration assemblages and geographic distribution within the Mont Blanc Massif, three main metamorphic zones are distinguished within the network of shear zones. These are: (i) epidote $\pm$ white mica-bearing assemblages; (ii) chlorite–phlogopite-bearing assemblages; and (iii) white mica $\pm$ biotite $\pm$ calcite $\pm$ actinolite $\pm$ epidote-bearing assemblages. $^{40}Ar/^{39}Ar$ age spectra of biotite and phlogopite are complex, and reflect significant variations in chemical composition. In biotite, this is partly due to inheritance from precursor Variscan magmatic biotite. In contrast, new white mica grew at the expense of feldspar during Alpine deformation and its Ar spectra do not show any excess ^{40}Ar. On the SE side of Mont Blanc, ages of shear zone phengites have a narrow range of 15.8–16.0 $\pm$ 0.2 Ma, which is in the same age range as $^{40}Ar/^{39}Ar$ ages of minerals from kinematically related veins. The top-to-SE sense of shear is consistent with initiation of a Mont Blanc flower-structure within a dextral transpressional system by 16 Ma. On the NW side, mini-plateaux ages of 14.5 $\pm$ 0.3 and 23.4 $\pm$ 0.4 Ma are preserved in the same sample, suggesting the possibility of two phases of deformation. This is also supported by partly preserved ages of 18–36.6 Ma in biotites and phlogopites. Ages between 36 and 18 Ma might reflect ongoing top-to-NW thrusting, following Penninic Front activation, in a context of nappe stacking and crustal thickening. NW-directed thrusting on the NW side of Mont Blanc continued after 18 Ma, synchronous with SE-directed thrusting on the SE side of the massif. These divergent movements produced the overall pop-up geometry of the Mont Blanc Massif, which may correspond to a positive flower structure developed within a zone of regional dextral transpression extending SW from the Rhone valley into the Mont Blanc area.

Mid-crustal shear zones which breach crustal fluid reservoirs can be zones of intense fluid flow during orogenesis, due to deformation-induced permeability enhancement at high pore fluid pressures (e.g., Beach & Fyfe 1972; Beach 1980; Kerrich 1986; Cox *et al.* 1987; O'Hara 1988; Mc Caig *et al.* 1990; Cox 2005). Major redistribution of crustal fluids via transiently permeable shear zone networks may result in significant mass and heat transport. This in turn can control the stability of mineral assemblages which impact on the rheology of rocks through fluid-present softening reactions, and via effects of fluid pressures on effective normal stresses and frictional shear strength (e.g., Ferry & Gerdes 1998; Guermani & Pennacchioni 1998; Wibberley & McCaig 2000; Cox 2005).

A method for constraining the time of deformation and mineral growth/recrystallization in

From: WIBBERLEY, C. A. J., KURZ, W., IMBER, J., HOLDSWORTH, R. E. & COLLETTINI, C. (eds) *The Internal Structure of Fault Zones: Implications for Mechanical and Fluid-Flow Properties*. **299**, 293–315.
DOI: 10.1144/SP299.18 0305-8719/08/$15.00

shear zones is required to establish the pressure (P)–temperature (T)–time (t) histories during crustal deformation, and to obtain a more complete understanding of how coupling between fluid–rock reaction processes and deformation processes may influence crustal deformation (Ferry & Gerdes 1998; Streit & Cox 1998). The $^{40}Ar/^{39}Ar$ dating method is the most frequently used technique for dating low-grade ($T < 450\ ^{\circ}C$) synkinematic minerals (Kligfield *et al.* 1986; Wijbrans & McDougall 1986; Kelley 1988; Goodwin & Renne 1991; West & Lux 1993; Kirschner *et al.* 1996; Reddy *et al.* 1996), because U–Pb systems close at higher temperatures and the Rb–Sr is prone to resetting by post-deformation fluid circulation (e.g., Wickman *et al.* 1983). In theory, synkinematic minerals formed below their closure temperature retain their crystallization age (e.g., Dodson 1973) and it is generally accepted that direct dating of deformation by $^{40}Ar/^{39}Ar$ can be achieved if dynamic crystallization has occurred at or below the closure temperature of a given mineral (West & Lux 1993). However, the interpretation of $^{40}Ar/^{39}Ar$ ages obtained for low temperature (LT) shear zone minerals is still a matter of debate. $^{40}Ar/^{39}Ar$ ages of synkinematic minerals might date (1) a cooling age corresponding to a specific closure temperature depending on cooling rate and mineral chemistry (T_c; e.g., Dodson 1973), or (2) a crystallization age, which can approximate the deformation age if crystallization is syntectonic (e.g., Reddy & Potts 1999), or (3) the age of isotopic resetting due to fluid interaction, which can occur both above or below the usually accepted T_c (Villa *et al.* 1997; Villa 1998). Interpretations (1) and (2) are strictly different because the cooling age corresponds to the age at which the rock was cooled below the cooling temperature of the mineral analysed, for example 350–400 °C for white mica, whereas the crystallization age is not a function of the temperature.

In reality, $^{40}Ar/^{39}Ar$ ages might be even more complex, as minerals formed at high temperature (HT) and deformed below T_c might have their Ar-chronometer partly reset due to Ar loss (Hames & Hodges 1993; Hames & Cheney 1997), as suggested by analytical (Kramar *et al.* 2001) and experimental (Dunlap 1997; Dunlap & Kronenberg 2001) work. These studies have emphasized that Ar loss due to diffusion depends on the mineral size and structure, as well as strain intensity and deformation mechanisms. Micas are strongly anisotropic during deformation; they typically deform by dislocation glide parallel to [001] and kinking (Hames & Bowring 1994), as well as by dissolution–precipitation processes. In addition, grain boundary sliding may operate at HT, especially in shear zones (Gibson 1990). Reddy & Potts (1999) have found that deformation ages can be obtained in cases where deformation has led to a significant change in grain size as the result of dynamic recrystallization. However, $^{40}Ar/^{39}Ar$ dating of deformation in low-grade metamorphic systems has been most successfully achieved in cases where micas have grown during deformation, for example in pressure fringes (Sherlock *et al.* 2003). In this case, it may be possible to obtain ages for a specific shearing event and even derive estimates for slip rates in a given shear zone, following the approach of Müller *et al.* (2000).

In this paper, we present the results of $^{40}Ar/^{39}Ar$ dating of phyllosilicates (white mica, biotite and phlogopite) formed during the development of a low-grade shear zone network in the Mont Blanc Massif (western Alps). This field example allows comparisons to be made between several $^{40}Ar/^{39}Ar$ chronometers formed in the same moderate- to low-T system. The shear zones considered in this study of the Mont Blanc Massif were developed in a suite of relatively homogeneous granite protoliths which differ only in their grainsize (Rolland *et al.* 2003; Rossi *et al.* 2005). Various synkinematic, hydrothermal alteration assemblages have developed within the network of granite-hosted shear zones. The nature of the alteration assemblages and changes in rock chemistry during shear zone evolution depend largely on the fluid–rock ratios and chemistry of fluids that migrated through the shear zones under relatively similar *PT* conditions. The $^{40}Ar/^{39}Ar$ dates are discussed in relation to a model for the tectonic–metamorphic–fluid evolution of the Mont Blanc Massif, which is the subject of a larger study (see Rolland *et al.* 2003, 2007; Rossi *et al.* 2005).

Geological setting

Protolith

The Mont Blanc Massif is one of several Variscan 'External Crystalline massifs' within the western Alps (Fig. 1) and is composed of paragneisses, orthogneisses, migmatites and granites (Baggio 1958; Ayrton *et al.* 1987; Bussy 1990; Bonin *et al.* 1993). The gneisses have yielded ages of 453 ± 3 Ma, obtained by U–Pb on zircon (Bussy & von Raumer 1994). The Hercynian granite forms a 35×10 km calc-alkaline batholith dated at 300 ± 20 Ma by the Rb–Sr method (Baggio *et al.* 1967; Bussy *et al.* 1989) and at 300 ± 3 Ma by U–Pb on zircon (Bussy & von Raumer 1994). Several magmatic facies have been recognized, mainly based on grain size. The granite facies is porphyritic in the centre of the batholith and becomes very fine-grained near its NW and SE

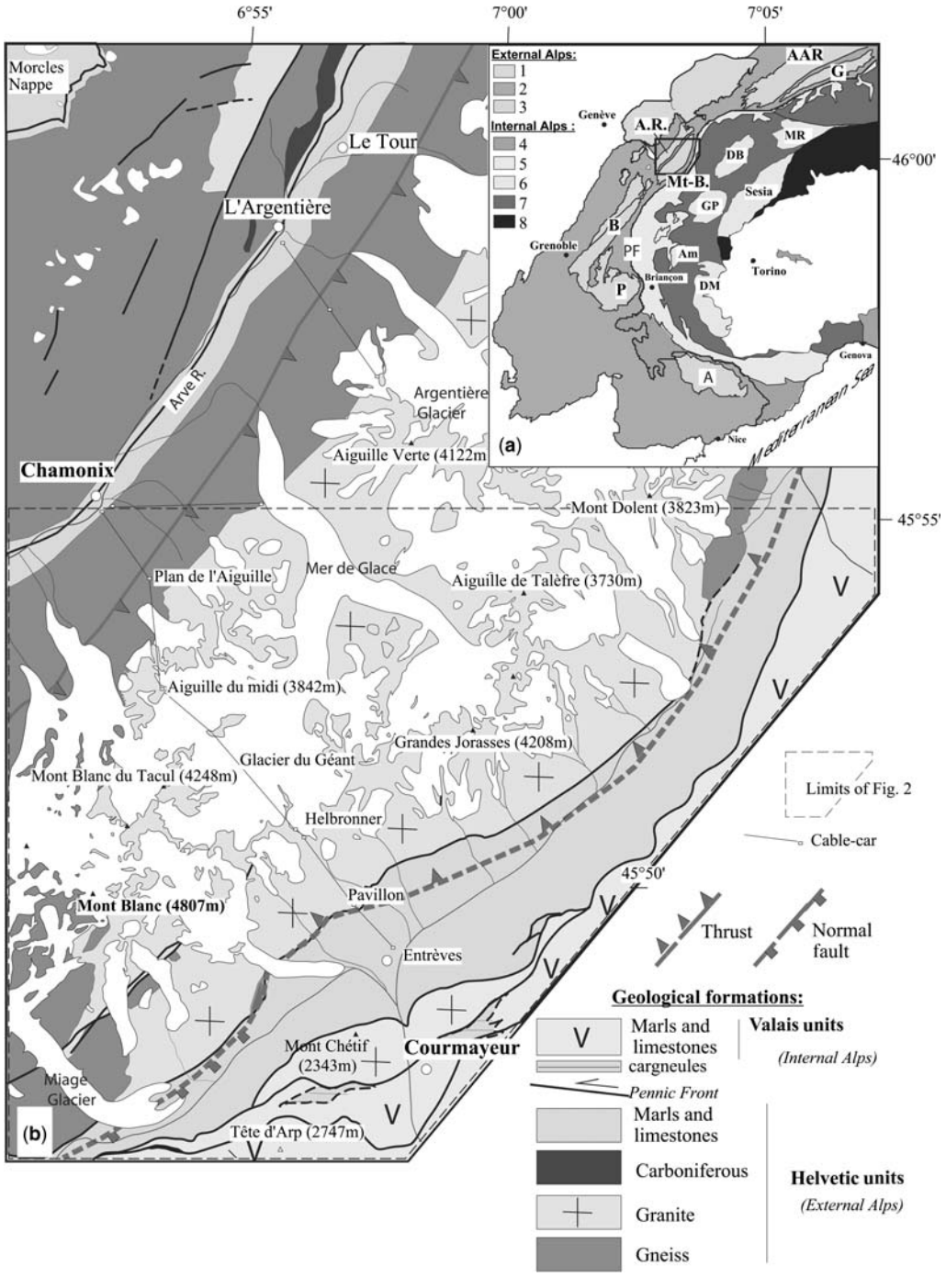

Fig. 1. (**a**) Geological map of the western Alps. 1, Pre-Alpine nappes; 2, Dauphinois/Helvetic zones; 3, External Crystalline massifs; 4, exotic flysch; 5, Briançonnais zone; 6, Internal Crystalline massifs; 7, Schistes Lustrés complex; 8, Austro-Alpine units of the western Alps. External Crystalline massifs: A, Argentera; AR, Aiguilles Rouges; B, Belledonne; G., Gotthard; Mt-B., Mont Blanc; P., Pelvoux. Internal Crystalline massifs: Am., Ambin; DB., Dent Blanche; GP, Gran Paradiso; MR, Monte Rosa; PF, Penninic Front. (**b**) Simplified geological map of the Mont Blanc Massif, modified after Ayrton *et al.* (1987). The dashed line frames the location of Figure 2.

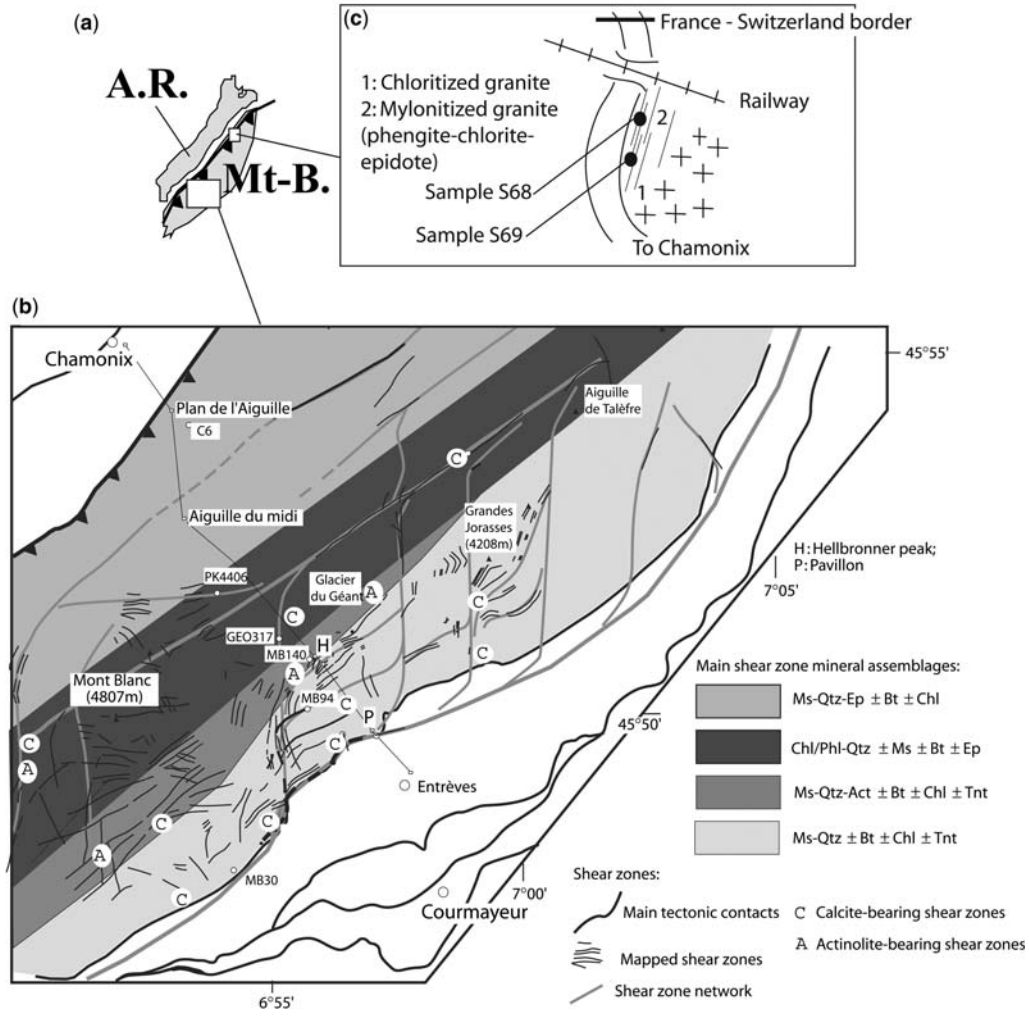

Fig. 2. (**a**) Location of studied areas in the Aiguilles Rouges–Mont Blanc Massifs. (**b**) Structural and metamorphic sketch map of the Mont Blanc Massif. Mineral abbreviations: Act, actinolite; Bt, biotite; Chl, chlorite; Ep, epidote; Ms, white mica; Phl, phlogopite; Qtz, quartz; Ttn, titanite; modified after Rossi *et al.* (2005). (**c**) Sketch of the structural location of samples S68–S69 in the northern part of the Mont Blanc massif, on the border between France and Switzerland.

intrusive contacts with the country rock (Baggio 1958; Marro 1988; Bussy 1990).

Alpine structures

The studied shear zone network in the Mont Blanc Massif has two main components on a regional scale. One trends N40–N60°E with a partly oblique dextral strike–slip sense of shear and the other trends north–south with a partly oblique sinistral strike–slip sense of shear (Fig. 2). The intrusive contacts of the granite were tectonically reactivated during the Cenozoic Alpine orogeny. The massif is bounded by a NW-vergent thrust on its NW side (e.g., Butler 1985; Belliere 1988) and by a SE-vergent thrust on its SE margin (Antoine *et al.* 1975), and lies within a zone where late (Neogene) regional dextral strike–slip shearing approximately parallel to the SW–NE elongation of the Mont Blanc Massif has also been reported (e.g., Gourlay & Ricou 1983; Hubbard & Mancktelow 1992; Bistacchi *et al.* 2000). The Mont Blanc Massif has been interpreted as: (1) the fold core of the recumbent Morles nappe (e.g., Ramsay 1981; Ramsay *et al.* 1983); (2) an actively extruding pop-up structure as suggested by the

fan-like distribution of faults within the granite (Bertini *et al.* 1985); (3) a back-steepened imbricate slice, with the current SE-directed thrust geometry on the internal side interpreted as an overturned normal fault originally 'accommodating extension on the dorsal culmination wall' (Butler 1985); (4) an uplifted block within a dextral transpressive zone, i.e., a positive flower structure (Gourlay & Ricou 1983; Hubbard & Mancktelow 1992); (5) a horst exhumed within the footwall of a late to recent normal fault on the SE side of the massif (Seward & Mancktelow 1994); and (6) a NW-verging thrust ramp structure with minor back-thrusting to the SE (Leloup *et al.* 2005). On the SE margin of the Mont Blanc, deformation has been shown to evolve with time from a brittle to a ductile style in individual shear zones, due to phyllosilicate recrystallization at the expense of feldspars during fluid-assisted deformation (see Guermani & Pennacchioni 1998). Fluid flow was localized predominantly in shear zones, as well as in kinematically related vein networks (Poty 1969; Marquer 1989; Rolland *et al.* 2003; Rossi *et al.* 2005).

Age of Alpine deformation

The age of shear zone development in the Mont Blanc Massif is poorly constrained. Dating of shear zone minerals has been attempted only for K-feldspar (Leloup *et al.* 2005), which was found to be only partly reset during Alpine (10–20 Ma?) deformation. Ar spectra of K-feldspar were shown to be discordant with step ages ranging between very young (4–20 Ma) and old (300 Ma), interpreted as partial resetting of K-feldspar during the Alpine event. Significant excess ^{40}Ar is interpreted by Leloup *et al.* (2005) to be due to ^{40}Ar inherited from the Variscan magmatic feldspar, which crystallized at *c*. 300 Ma (Bussy & von Raumer 1994). The Alpine white mica–chlorite–epidote–quartz–albite greenschist facies assemblage of the shear zones is interpreted to have been formed between 18 and 36 Ma on the basis of Rb–Sr whole-rock ages (Baggio *et al.* 1967). However, $^{40}Ar/^{39}Ar$ dating of biotite from undeformed granites, as well as foliation-defining biotite from weakly deformed granites, provided plateau ages from 22.8 ± 0.6 to 63.7 ± 1.9 Ma. This age range exceeds the range of realistic $^{40}Ar/^{39}Ar$ ages for Alpine tectonic events (Leloup *et al.* 2005). The onset of deformation in the External Crystalline Massifs of the Alps should post-date the onset of shearing on the Penninic Front at *c*. 35 Ma (Ceriani *et al.* 2001 and references therein). The Mont Blanc Massif is the basement to the Helvetic sedimentary sequence in the Morcles nappe. The youngest part of this sequence is the Taveyannaz sandstone, which contains andesitic blocks of Periadriatic magmatic age, i.e., *c*. 32 Ma (Steck 1984; Fischer & Villa 1990). Accordingly, deformation of the Mont Blanc Massif has to be younger than mid-Oligocene, and has usually been assumed to be late Oligocene or early Miocene (Gourlay 1986; Marro 1988). Therefore, excess or inherited ^{40}Ar components are suspected to be present in these >40 Ma samples, and result in apparent ages that are too old. K–Ar dating on minerals from Alpine veins that are kinematically related to shear zones yields ages in the range 15.2–18.3 Ma for adularia (hydrothermal K-feldspar), and in the range 13.4–15.2 Ma for muscovite (Leutwein *et al.* 1970). These ages are close to $^{40}Ar/^{39}Ar$ white mica ages of 14.6–18.5 Ma obtained within a thrust affecting the Mont Blanc sedimentary cover in the Morcles Nappe (Crespo-Blanc *et al.* 1995; Kirschner *et al.* 1996, 2003).

P–T estimates of ductile shear zone development

Fluid inclusion studies on granite-hosted vein quartz indicate formation temperatures of 350–400 °C (Poty 1969; Poty *et al.* 1974; Marshall *et al.* 1998). Shear zones were formed under mid-crustal greenschist facies conditions, as shown by estimates of pressure and temperature conditions for shear zone deformation around 0.5 ± 0.05 GPa and 400 ± 25 °C, determined on the basis of independent mineral equilibria (Rolland *et al.* 2003).

Structural and mineralogical setting of studied shear zones

A more detailed analysis of structural, mineralogical and geochemical relationships between the shear zones and the undeformed granite is presented in Rolland *et al.* (2003), Rossi (2005) and Rossi *et al.* (2005). The main features are summarized below.

Shear zone mineralogy

Three main hydrothermal alteration assemblages are recognized, with each main assemblage being developed in distinct geographic domains in the Mont Blanc Massif (Fig. 2b). These assemblages are: (1) white mica $\pm$ actinolite $\pm$ epidote $\pm$ calcite assemblages in the SE part of the massif; (2) chlorite + phlogopite-bearing assemblages in the central part of the massif; and (3) epidote-bearing assemblages in the NW part of the massif (Rolland *et al.* 2003; Rossi *et al.* 2005). The development of the different assemblages from a protolith of near-uniform composition is interpreted to relate to different intensities of fluid–rock interaction within the shear zones, as well as variations in the

chemistry of fluids migrating through different parts of the shear zone network. Each of the mineral assemblages can be found in cataclasites, mylonites and ultramylonites. Accordingly, variations in synkinematic mineral assemblages do not reflect the style or amount of deformation. In these shear zones, synkinematic phyllosilicates were sampled in strain-shadows and in adjacent foliation-defining mica-rich layers for $^{40}Ar/^{39}Ar$ dating (e.g., Fig. 3).

In white mica-bearing shear zones, from the SE domain of the massif, there is a progressive evolution in both space and time from cataclasites to mylonites. The transition from brittle to ductile behaviour occurs due to reaction weakening as feldspar is replaced by white mica. White mica forms during fluid–rock reaction during shearing at the expense of both plagioclase and, to a lesser extent, K-feldspar (e.g., MB71 in Fig. 4). Sense-of-shear in this domain is consistently top-to-SE (Fig. 3). White mica occurs at the rim or along fractures within both feldspars, which suggests that the following reactions were active (e.g., Wibberley & McCaig 2000 and references therein):

$$3NaAlSi_3O_8 + K^+ + 2H^+ = KAl_3Si_3O_{10}(OH)_2 + 6SiO_2 + 3\,Na^+$$
albite + K-bearing acidic fluid
= white mica + quartz + Na-bearing fluid (1)

$$3KAlSi_3O_8 + 2H^+ = KAl_3Si_3O_{10}(OH)_2 + 6SiO_2 + 2K^+$$
orthoclase + acidic fluid
= white mica + silica + K-bearing fluid. (2)

The reactions suggest that the fluid is initially acidic. Reaction (1) would lead to increasing Na^+ contents in the fluid and reaction (2) to increasing K^+ contents. These reactions result in SiO_2 depletion in the shear zone unless it is precipitated *in situ* (e.g., Wibberley & McCaig 1999), but do not require any large input of elements from outside the system. In the case of the Mont Blanc most shear zones are depleted in silica (Rolland *et al.* 2003), which shows that the system was relatively open, but not much matter precipitated from the fluid.

In the central domain of the massif, the deformation is mylonitic and no cataclasites are observed. The transition from undeformed granite to shear zones occurs over distances on the order of tens of metres and is more progressive than in the SE domain of the Mont Blanc Massif. Feldspars tend to deform in a brittle manner within a ductile quartz–phyllonite rich matrix. Chlorite forms mainly from the breakdown of biotite, and is also associated with the destabilization of plagioclase and K-feldspar (i.e., C33 and C46, Fig. 4). In individual large shear zones, phlogopite-rich and Mg-chlorite-rich

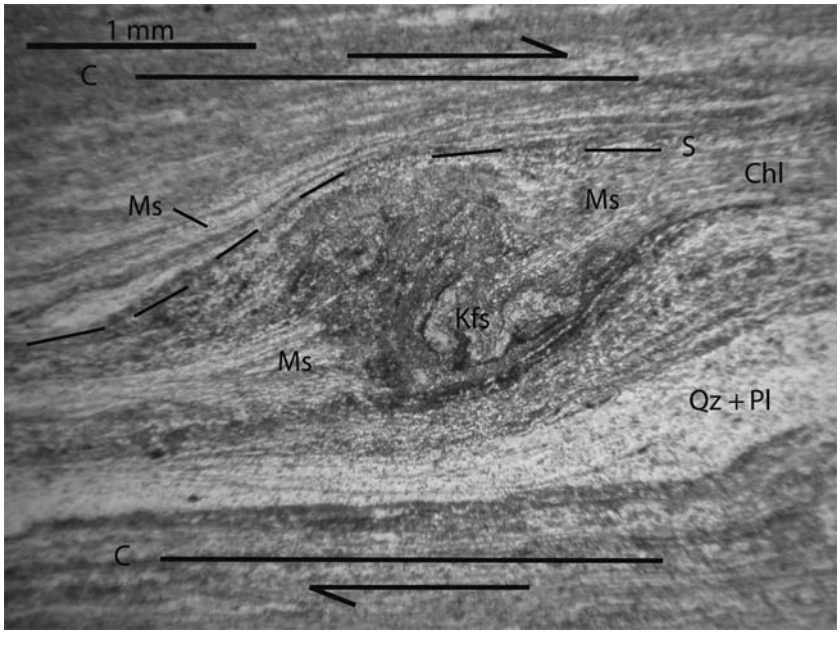

Fig. 3. Microphotograph of a phengite-bearing shear zone. Phengite aggregates in the pressure shadow formed at the expense of feldspar porphyroclasts. Note the C–S relationships in agreement with top-to-SE sense of shear.

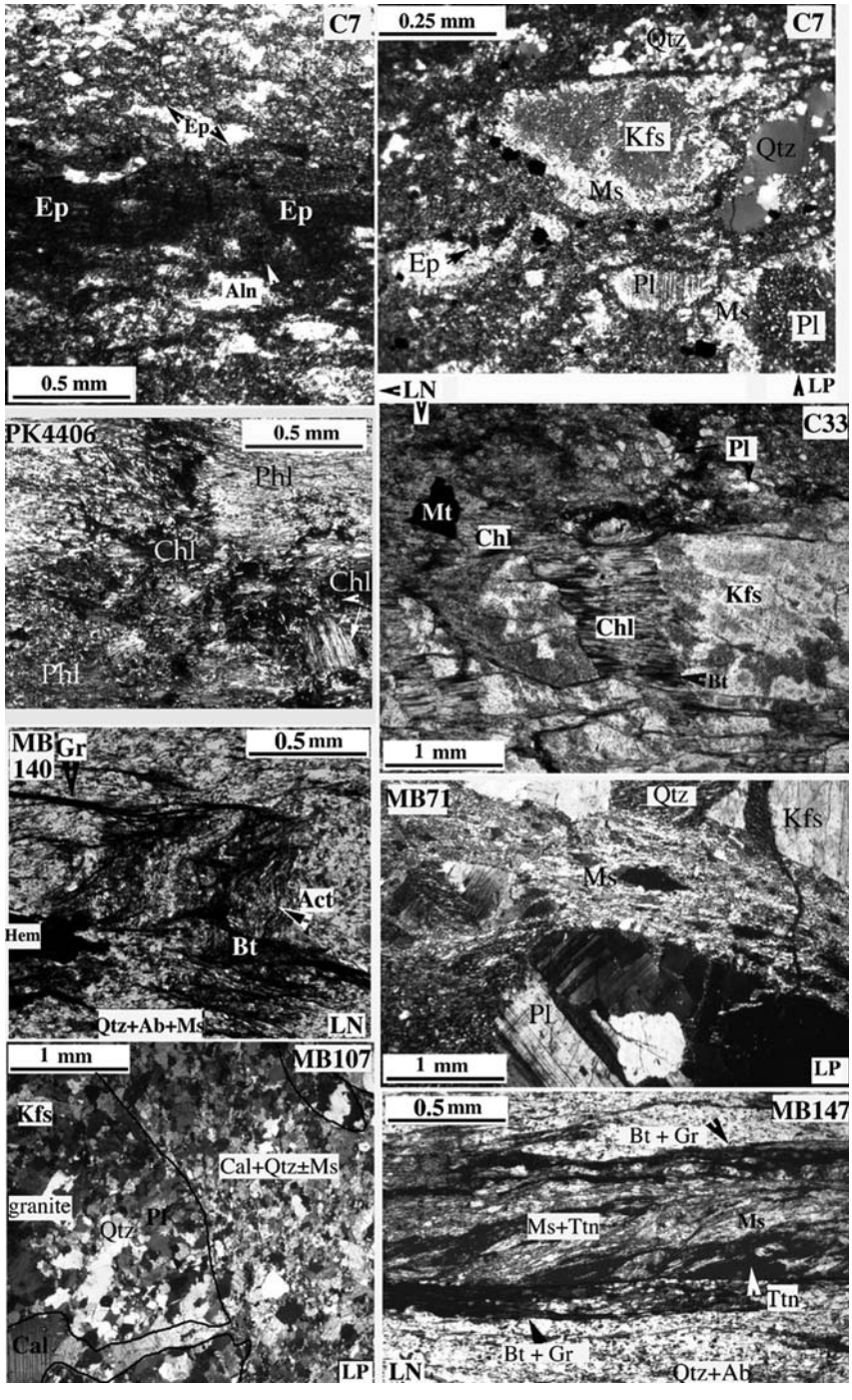

Fig. 4. Photomicrographs of representative mineral assemblages found in the Mont Blanc granite shear zones. Mineral abbreviations, as for Figure 2 and additionally: Ab, albite; Aln, Allanite; Cal, calcite; Gr, graphite; Hem, hematite; Kfs, K-feldspar; Mt, magnetite; Pl, plagioclase. LN, plane polarized light; LP, crossed polars.

domains can be distinguished. These domains are separated by a sharp, but extremely irregular alteration front (Rossi *et al.* 2005). On the basis of S–C fabrics, both top-to-NW and top-to-SE senses of shear are recognized. Accordingly, the bulk deformation pattern is interpreted to be approximately pure shear. The crystallization of chlorite and phlogopite requires substantial Mg-metasomatism during high flux fluid migration within these shear zones. In biotite-rich shear zones, relicts of brown Ti-rich, originally igneous biotite are locally preserved and partially recrystallized into metamorphic green low-Ti biotite by the following reaction:

$$\begin{aligned}&K_2Fe_3Mg_2Ti_{0.2}Si_{5.8}Al_2O_{20}(OH)_4\\&+0.4SiO_2+0.2Ca^{2+}+0.2OH^-\\&=K_2Fe_3Mg_2Ti_0Si_6Al_2O_{20}(OH)_4\\&+0.2CaTiOSiO_4+0.2H^+\\&\text{Ti-biotite}+\text{quartz}+\text{basic Ca-bearing fluid}\\&=\text{Ti-free biotite}+\text{titanite}+\text{acidic fluid.}\end{aligned}\quad(3)$$

In most phlogopite-rich samples, phlogopite porphyroblasts have inclusions of relict chlorite, which suggests the following prograde reaction (e.g., sample PK4406, Fig. 4):

$$\begin{aligned}&2FeMg_8Al_5Si_8O_{20}(OH)_{16}+14SiO_2\\&+0.5Fe_3O_4+3Fe^{2+}+10K^++9Mg^{2+}\\&+SO_4^{2-}+10H_2O=5K_2FeMg_5Si_6\\&Al_2O_{20}(OH)_4+0.5FeS_2+32H^+\\&\text{chlorite}+\text{magnetite}=\text{phlogopite}\\&+\text{pyrite}+\text{acidic fluid.}\end{aligned}\quad(4)$$

Samples for $^{40}Ar/^{39}Ar$ dating from phlogopite-rich shear zones in the central and central-east part of the massif were selected from the Mont Blanc tunnel sample collections of the Torino Museum of Natural Sciences (samples PK4406 and GEO317; Fig. 4).

In the NW domain of the Mont Blanc Massif, cataclasites are more common than mylonites. Cataclastic zones are epidote-bearing and there is little neo-crystallization of phyllosilicates and associated transition to ductile shear zones. Epidote forms at the expense of plagioclase, K-feldspar and biotite (e.g., C7, Fig. 4). Biotite crystals were sampled from top-to-NW shear zones (sample C6; Fig. 2) close to the main thrust that forms the NW border of the Mont Blanc Massif. $^{40}Ar/^{39}Ar$ dating of shear zone biotite complements biotite $^{40}Ar/^{39}Ar$ ages from undeformed granite already published by Leloup *et al.* (2005).

At the French-Swiss border a fine-grained white mica-bearing mylonite (samples S68–69; Figs 2a & 5) was collected within the same top-to-NW thrust zone bounding the Mont Blanc Massif. The fine-grained granite protolith is compositionally similar to the Mont Blanc granite. Deformation within this shear zone has already been described in detail by FitzGerald & Stünitz (1993). In this zone the main top-to-the NW thrust which bounds the Mont Blanc Massif has only one mesoscopically apparent mineral lineation and foliation. However, in thin-section, two foliations are present at a low angle to each other (S1 and S2, Fig. 5). One foliation overprints the other, with each foliation being associated with lattice and shape preferred orientations in phengite aggregates. As these two foliations clearly are not an S–C fabric, they are interpreted

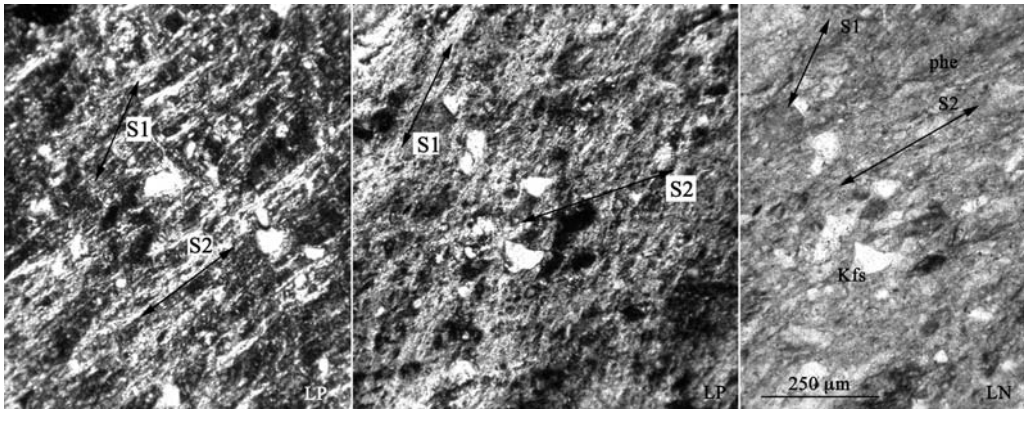

Fig. 5. Photomicrographs of the sample S68 collected At the French–Swiss border (Fig. 2a), within top-to-NW thrust zone bounding the Mont Blanc Massif. S1 and S2 refer to the two generations of phengite evidenced in thin section by rotating the thin section in plane polarized light. Mineral abbreviations: Kfs, K-feldspar; Phe, Phengite. LN, plane polarized light; LP, crossed polars.

as resulting from two separate shearing events. Unfortunately, the two fabrics occur together on such a fine scale that it is not possible to separate grains related to a specific foliation.

Shear zone mineral chemistry

Within individual shear zones, phyllosilicates (chlorite, white mica, biotite–phlogopite) have similar X_{Mg} (Mg/Mg + Fe) ratios, indicating good equilibrium between minerals of the synkinematic metamorphic assemblage. On a regional scale, variations in X_{Mg} of the phyllosilicates reflect the observed zoning in metamorphic mineral assemblages present in the shear zones. An inverse bell-shape profile of X_{Mg} values in phyllosilicates is found across the massif, with compositions of $X_{Mg} = 0.3–0.1$ at the rim to $X_{Mg} = 0.9–0.6$ in the core (Fig. 6). The high X_{Mg} domain coincides with a progressive increase in abundance of mafic minerals toward the central domain of the Mont Blanc Massif. The regional trend is not due to variation in the original composition of the Mont Blanc granite (Rolland *et al.* 2003). Instead, it is interpreted to reflect differences in fluid composition and fluid/rock ratio growth of the phyllosilicates in actively deforming shear zones.

Biotite X_{Mg} compositions in shear zones greatly exceed the range of values exhibited by primary igneous biotites in relatively undeformed granite (Fig. 6). Biotite X_{Mg} ratios in shear zones range between 0.9 and 0.1, whereas in the undeformed granite X_{Mg} values are approximately 0.4 ± 0.05 (2σ). Phlogopite with $X_{Mg} = 0.9$ occurs only in shear zones in the central domain of the massif. White mica compositions have homogeneous Si contents of 3.37 ± 0.08 (2σ) per formula unit, based on 84 measurements from samples throughout the massif. Chlorite has X_{Mg} values of 0.3 ± 0.1 near the rim of the massif, whereas high X_{Mg} (0.6 ± 0.1) chlorites are present in the central domain of the massif (Fig. 6 & Table 1).

The three types of alteration assemblages developed in the shear zone network are interpreted in part as a response to varying fluid fluxes across the massif, but they must also reflect the effects of varying fluid chemistry within different parts of the shear network. Chlorite and phlogopite assemblages are developed only in the central domain as a result of high fluid–rock ratios and Mg metasomatism. White mica developed at the expense of feldspars in the SE domain at moderate fluid–rock ratios. Epidote–biotite ± phengite bearing assemblages in the NW domain suggest limited fluid–rock interaction. This regional variation of alteration assemblages in shear zones provides an opportunity to compare the $^{40}Ar/^{39}Ar$ systematics in various micas (phengite, phlogopite and biotite) formed at similar depths but differing fluid–rock interaction environments. It also provides an opportunity to constrain the ages of formation of the various components of the shear network in the Mont Blanc Massif.

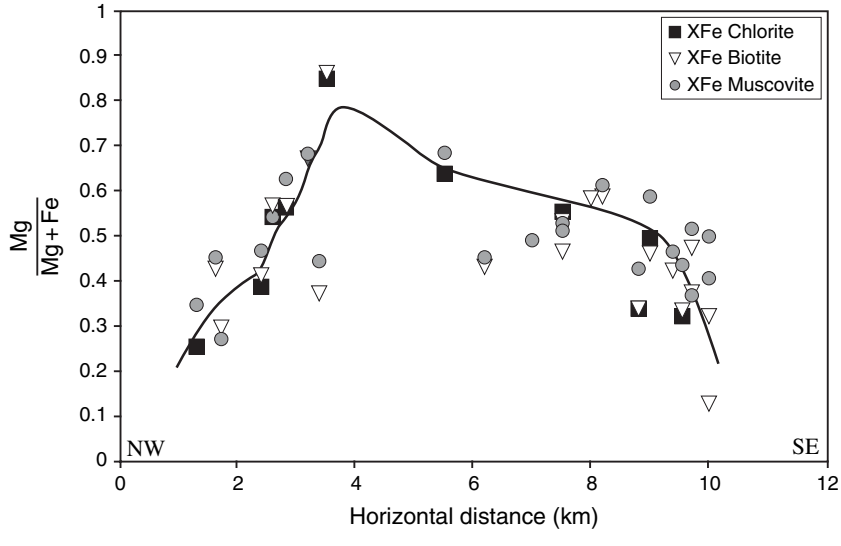

Fig. 6. Mineralogical variation of X_{Mg} (Mg/Mg + Fe) values across the Mont Blanc Massif shear zones. Values represent X_{Mg} in each mineral type v. distance. Modified after Rossi *et al.* (2005).

Table 1. *Representative analyses of some minerals from the Helbronner area*

Major oxides (wt%)		Mineral samples						
		Biotites			Chlorites			White micas
		MB140	MB02.55D		MB140	MB02.55D		MB140
SiO_2		37.33	34.88		26.26	24.53		48.14
TiO_2		0.87	1.01		0.09	0.04		0.09
Al_2O_3		15.29	16.63		19.81	19.19		26.98
FeO		17.35	23.75		23.09	32.84		3.98
MnO		0.49	0.50		1.21	1.13		—
MgO		11.84	8.06		16.82	10.89		2.83
CaO		0.55	0.00		—	0.07		0.29
Na_2O		—	0.06		—	0.02		—
K_2O		8.24	9.42		0.15	0.01		10.73
Total		91.96	94.30		87.43	88.72		93.04
X–Fe		0.45	0.62		0.41	0.63		0.44
	%vac	3.67	2.50	%Al	25.95	34.14	%Si	3.22
	%Si	86.69	73.41	%Si	67.39	62.23	%Al	61.77
	%Al	9.64	24.08	%diO	6.67	3.63	%Cel	35.01

Biotites: %vac, proportion of di-octaerdic biotites; %Si, proportion of the silica-rich biotites (phlogopite − annite); %Al, proportion of aluminium-rich biotites (siderophyllites and eastonite). Chlorites: %Al, proportion of aluminium-rich chlorites; %Si, proportion of silica-rich chlorites; %diO, proportion di-octaerdic chlorites. White micas: %Si, proportion of silica-rich muscovite; %Al, proportion of aluminium-rich muscovite; %Cel, proportion of celadonite. MB140, mylonite; MB147, ultramylonite; MB02.55Aa, episyenite; MB02.55D, fresh granite.

$^{40}Ar/^{39}Ar$ dating

This section presents new geochronological data obtained on the various sets of shear zones across the Mont Blanc Massif, described in the previous section 8. Results of the laser $^{40}Ar/^{39}Ar$ dating are given in Figures 7 & 8 and Table 2, and procedures are described in the Appendix.

Phengite dating

$^{40}Ar/^{39}Ar$ plateau and mini-plateau ages from shear zones on the SE side of the massif range from 15.8 to 16.0 $\pm$ 0.2 Ma (Fig. 7a–c). In all samples, the analysed white mica corresponds to a pure mineral, as shown by the corresponding $^{37}Ar_{Ca}/^{39}Ar_K$ ratio data, except for the highest temperature steps in which the Ca component may result from small mineral inclusions such as epidote (Table 2). Duplicate analyses on samples MB140 and MB94 were undertaken to check data reproducibility and the ages were identical within error (Fig. 7a & b). All three spectra have a staircase shape for lower temperature steps corresponding to 25–50% of cumulative ^{39}Ar, with lower $^{40}Ar/^{39}Ar$ ages at lower temperature. Inverse isochron plots for MB30 and MB94 are not well constrained because of very low $^{36}Ar/^{40}Ar$, close to detection limits, and a lack of spread in $^{39}Ar/^{40}Ar$ ratios. However, one inverse isochron diagram was obtained for MB140. It is relatively well constrained and yields a similar age to the plateau age (Fig. 8a).

Near the NW border of the Mont Blanc Massif, the $^{40}Ar/^{39}Ar$ spectra are more complex. Sample S69 does not show a plateau age, whereas S68 shows two mini-plateau ages at 14.3 $\pm$ 0.2 Ma (1σ) and 22.9 $\pm$ 0.9 Ma (2σ). In Figure 8d, the inverse isochron age of S68 calculated with the first three steps gives a similar age (within error) to the plateau age of 14.5 $\pm$ 0.3 Ma. The inverse isochron age obtained with the HT steps (6–8) is 23.4 $\pm$ 0.4 Ma, again similar within error to the plateau age for the same HT steps. Both isochron correlations provide $(^{40}Ar/^{36}Ar)_0$ ratios close to the atmospheric value of 295.5, which validates the use of this value in the model calculation of the apparent age steps. As shown on Figure 8f, Ca/K values are between 0.002 and 0.01 for the LT steps, which is within the range of values obtained by microprobe analysis. In HT steps, Ca/K ratios increase to values above those obtained by microprobe analysis, which suggests that other Ca-rich phase(s) may be present as contaminants.

Biotite and phlogopite dating

$^{40}Ar/^{39}Ar$ spectra from biotite and phlogopite (Fig. 7f–h) are more irregular. Dating of biotite from the NW part of the massif (sample C6) gives relatively flat Ar spectra with apparent ages

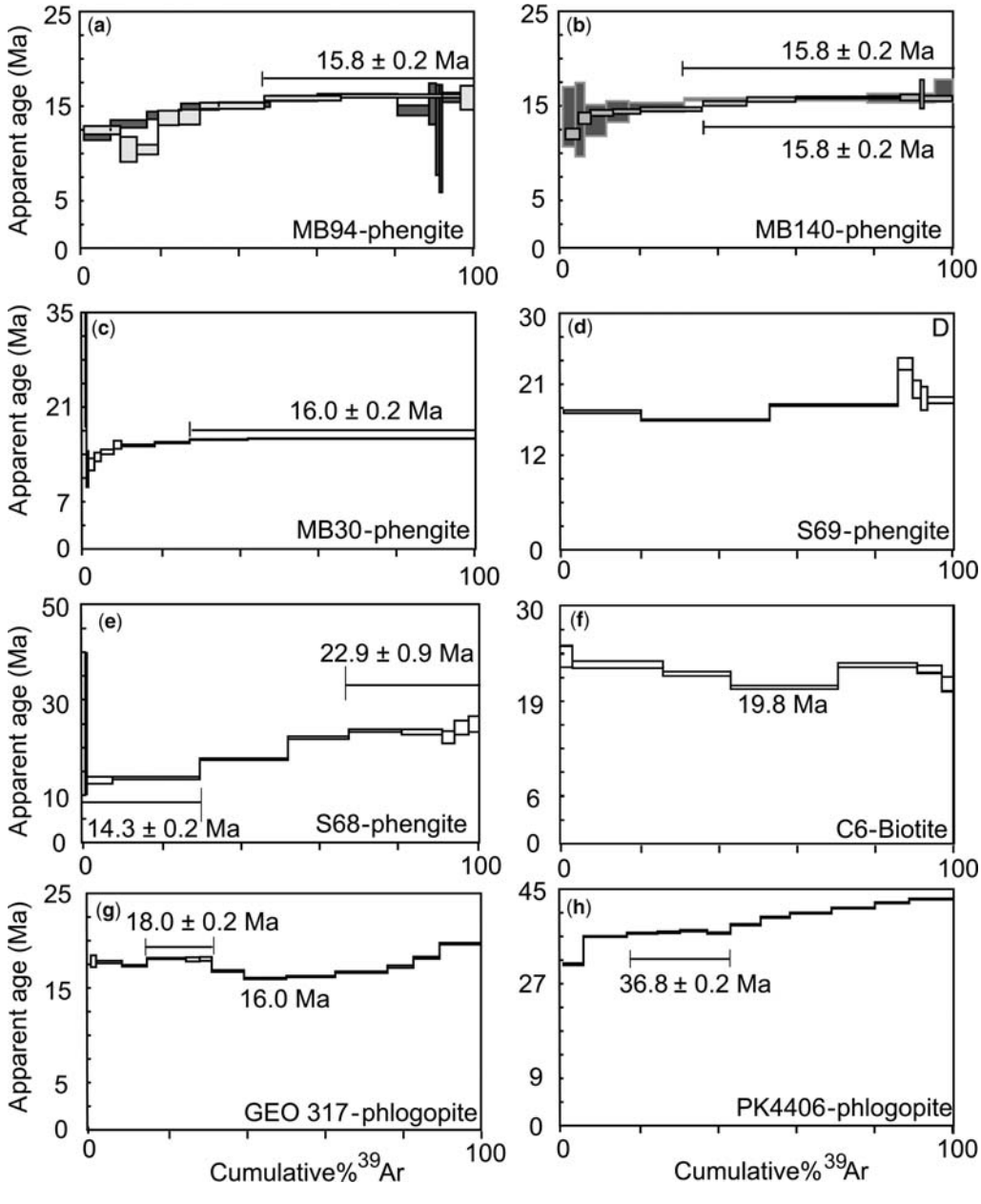

Fig. 7. $^{40}Ar/^{39}Ar$ age spectra obtained on mineral separates from shear zone samples of the Mont Blanc Massif (for locations see Fig. 2). Uncertainties on miniplateau and plateau ages are given at the 2σ-level.

between 19.8 and 24 Ma, but no plateau-age can be calculated. The inverse isochron diagram (Fig. 8b) gives an age of 21.8 ± 3 Ma. The 'U' shape of the spectra can be interpreted as an indication of excess ^{40}Ar, as is also suggested by an $(^{40}Ar/^{36}Ar)_0$ ratio slightly above the atmospheric value. The lower-age step (19.8 Ma) in the central part of the spectra age could therefore be considered a maximum age for sample C6.

$^{40}Ar/^{39}Ar$ spectra of phlogopite from the central-eastern part of the Mont Blanc Massif (sample GEO317, Fig. 7g) are irregular, with step ages between 16 and 20 Ma and a mini-plateau of 18.0 ± 0.2 Ma (1σ) for the LT steps. The inverse

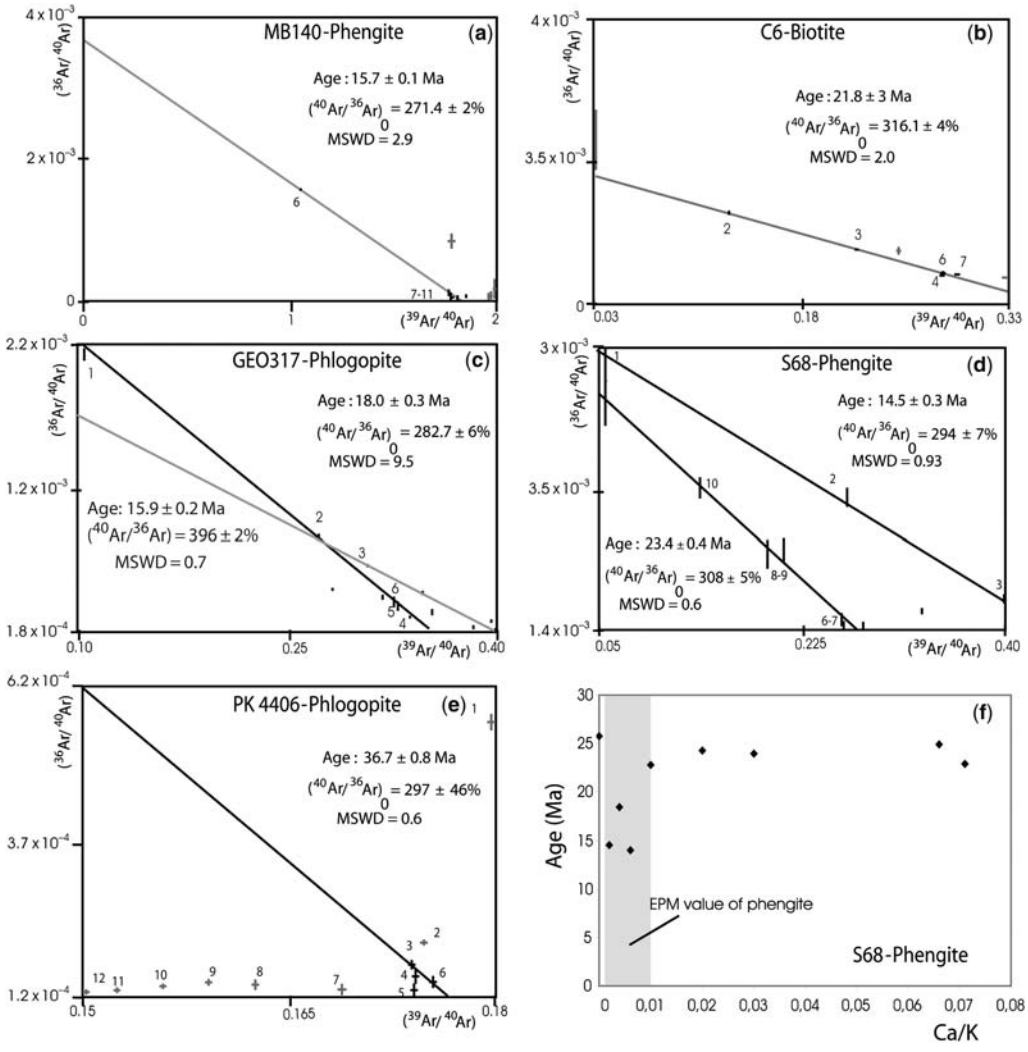

Fig. 8. (**a**–**e**) Inverse isochron diagrams of Mont Blanc shear zone samples. (**f**) Ca/K v. age diagram of phengite from sample S68. MSWD, mean square weighted deviation.

isochron (Fig. 8c) obtained with the same LT steps 1–6 gives the same age, 18.0 $\pm$ 0.3 Ma (2σ), with an $(^{40}Ar/^{36}Ar)_0$ ratio similar to the atmospheric value. An isochron age of 15.9 $\pm$ 0.3 Ma (2σ) is calculated for the rest of the spectra. This age is in agreement with the youngest step ages obtained on the $^{40}Ar/^{39}Ar$ spectra, as well as with the age of 15.8 Ma obtained in a neighbouring phengite-bearing shear zone (sample MB140). The older ages (>18 Ma) obtained on the HT part of the spectra might be explained by excess ^{40}Ar, as suggested by elevated $(^{40}Ar/^{36}Ar)_0$ ratios for the 15.9 Ma correlation isochron plot.

Sample PK4406 from the centre of the massif yielded a staircase spectra (Fig. 7h), except for a mini-plateau obtained in the LT steps at 36.8 $\pm$ 0.2 Ma (2σ). A similar age of 36.7 $\pm$ 0.8 Ma is obtained from the inverse isochron plot, using the same steps (3, 4, 6), and has an atmospheric $(^{40}Ar/^{36}Ar)_0$ ratio value. The staircase shape of the spectra at HT is consistent with the presence of excess ^{40}Ar, as shown (Fig. 8e) by increasingly lower ratios between the $^{40}Ar/^{36}Ar$ and $^{40}Ar/^{39}Ar$ values from step 6 to 12 on the inverse isochron plot.

In summary, for phlogopite-bearing shear zones, older $^{40}Ar/^{39}Ar$ ages are found in LT steps (18 Ma for GEO317, 36.6 Ma for PK4406) and excess ^{40}Ar is found in the HT steps.

Table 2. *Phengite, biotite and phlogopite $^{40}Ar/^{39}Ar$ dating results, from the Mont Blanc shear zones*

Step	Laser power (mW)	Furnace temp (°C)	Atmospheric cont (%)	^{39}Ar (%)	$^{37}Ar_{Ca}/^{39}Ar_K$	$^{40}Ar^*/^{39}Ar_K$	Age (Ma $\pm 1\sigma$)
Sample MB94 (1)							
1	413		20.417	9.37	0.022	0.438	12.464 ± 0.437
2	441		21.694	4.2	0.033	0.367	10.438 ± 1.317
3	450		22.243	5.47	0.031	0.366	10.417 ± 0.514
4	465		2.088	5.29	0.017	0.484	13.76 ± 0.765
5	481		4.262	5.43	0.016	0.487	13.854 ± 0.793
6	520		2.481	16.52	0.019	0.53	15.051 ± 0.326
7	545		1.901	19.6	0.015	0.558	15.849 ± 0.25
8	576		1.422	30.66	0.026	0.566	16.087 ± 0.182
9	800		6.42	3.46	0.184	0.56	15.9 ± 1.268
Sample MB94 (2)							
1	370		18.53	6.86	0.032	0.42	11.90 ± 0.48
2	388		2.70	9.31	0.031	0.46	13.13 ± 0.40
3	402		1.02	8.77	0.025	0.50	14.03 ± 0.41
4	422		0.00	9.64	0.033	0.53	14.95 ± 0.34
5	432		1.99	13.15	0.036	0.54	15.16 ± 0.25
6	439		0.47	12.15	0.030	0.56	15.83 ± 0.28
7	450		0.08	20.50	0.054	0.57	16.15 ± 0.16
8	455		8.98	8.10	0.069	0.51	14.55 ± 0.54
9	460		3.14	1.79	0.080	0.54	15.25 ± 2.18
10	473		16.63	0.90	0.114	0.44	12.50 ± 4.77
11	501		18.93	0.69	0.200	0.41	11.58 ± 5.67
12	800		0.85	8.13	0.239	0.56	15.93 ± 0.50
Sample MB140 (1)							
1	388		32.35	3.24	0.000	0.49	13.85 ± 3.15
2	410		8.12	2.34	0.010	0.48	13.56 ± 3.91
3	435		7.10	5.58	0.008	0.47	13.47 ± 1.66
4	450		1.67	5.78	0.000	0.51	14.41 ± 1.12
5	475		0.00	14.20	0.006	0.52	14.86 ± 0.49
6	506		1.28	46.92	0.004	0.55	15.70 ± 0.14
7	523		2.26	17.25	0.006	0.56	15.82 ± 0.48
8	700		0.00	4.70	0.015	0.59	16.61 ± 1.19
Sample MB140 (2)							
1	369		23.75	3.74	0.007	0.43	12.16 ± 0.56
2	388		4.74	2.84	0.004	0.49	13.78 ± 0.60
3	408		1.93	6.10	0.006	0.50	14.33 ± 0.31
4	425		1.76	6.65	0.004	0.51	14.44 ± 0.23

(*Continued*)

Table 2. *Continued*

Step	Laser power (mW)	Furnace temp (°C)	Atmospheric cont (%)	^{39}Ar (%)	$^{37}Ar_{Ca}/^{39}Ar_K$	$^{40}Ar^*/^{39}Ar_K$	Age (Ma $\pm 1\sigma$)
5	439		45.13	16.21	0.003	0.52	14.69 ± 0.19
6	443		1.86	11.50	0.002	0.54	15.27 ± 0.14
7	449		1.33	12.53	0.002	0.55	15.70 ± 0.16
8	455		1.38	26.81	0.004	0.56	15.89 ± 0.09
9	469		1.93	5.42	0.007	0.56	15.89 ± 0.26
10	469		0.00	0.75	0.009	0.57	16.15 ± 1.55
11	1111		3.24	7.44	0.027	0.55	15.75 ± 0.24
Sample S69							
1	379		9.92	19.86	0.000	2.57	17.52 ± 0.19
2	455		2.88	32.94	0.001	2.41	16.47 ± 0.10
3	500		1.71	32.87	0.000	2.69	18.35 ± 0.11
4	525		1.81	3.77	0.007	3.47	23.59 ± 0.76
5	580		—	2.11	0.028	2.99	20.37 ± 1.12
6	680		0.67	1.69	0.003	2.82	19.21 ± 1.48
7	1111		1.09	6.77	0.005	2.79	18.99 ± 0.40
Sample MB30							
1	415		16.51	0.28	0.000	3.89	26.45 ± 8.33
2	435		40.57	0.49	0.002	1.73	11.83 ± 2.66
3	503		25.22	1.54	0.000	1.83	12.52 ± 0.90
4	532		14.98	1.69	0.000	1.99	13.62 ± 0.65
5	555		9.60	3.28	0.000	2.11	14.38 ± 0.35
6	575		2.79	1.94	0.000	2.26	15.43 ± 0.60
7	605		3.61	8.56	0.000	2.25	15.32 ± 0.15
8	627		1.99	8.97	0.000	2.31	15.76 ± 0.11
9	649		1.37	14.89	0.000	2.37	16.19 ± 0.06
10	800		1.80	58.36	0.000	2.39	16.34 ± 0.04
Sample PK 4406							
1	565		17.903	5.15	0.000	4.522	30.733 ± 0.186
2	575		6.368	11.12	0.000	5.305	36 ± 0.1
3	581		5.208	7.85	0.000	5.399	36.63 ± 0.124
4	590		4.604	5.8	0.000	5.425	36.802 ± 0.169
5	605		3.886	6.95	0.000	5.469	37.099 ± 0.156
6	626		4.311	5.99	0.000	5.401	36.644 ± 0.143
7	649		3.914	7.71	0.000	5.641	38.254 ± 0.149
8	672		4.167	7.49	0.000	5.849	39.649 ± 0.138
9	692		4.289	10.69	0.000	5.969	40.454 ± 0.112
10	709		4.082	11.09	0.000	6.112	41.415 ± 0.102
11	726		3.874	8.79	0.000	6.263	42.423 ± 0.109
12	748		3.781	11.37	0.000	6.365	43.108 ± 0.106

Sample GEO317							
1	378		61.554	1.34	0.000	2.615	17.834 ± 0.621
2	423		24.658	6.66	0.000	2.602	17.749 ± 0.133
3	444		18.744	6.39	0.000	2.545	17.359 ± 0.089
4	460		8.324	10.01	0.000	2.658	18.125 ± 0.069
5	471		11.413	3.52	0.000	2.643	18.025 ± 0.224
6	491		10.56	3.08	0.000	2.65	18.073 ± 0.203
7	525		13.186	8.28	0.000	2.462	16.794 ± 0.102
8	555		7.504	10.82	0.000	2.346	16.008 ± 0.074
9	581		5.676	12.54	0.000	2.377	16.22 ± 0.074
10	604		6.262	13.39	0.000	2.445	16.68 ± 0.081
11	624		9.321	6.66	0.000	2.531	17.262 ± 0.128
12	678		12.352	6.68	0.000	2.669	18.205 ± 0.118
13	900		13.956	10.62	0.000	2.888	19.689 ± 0.091
Sample C8							
1		750	357.657	3.19	0.009	3.493	23.631 ± 1.372
2		850	167.573	22.95	0.001	3.342	22.612 ± 0.442
3		950	179.897	17.27	0.002	3.175	21.49 ± 0.288
4		1050	315.524	27.26	0.001	2.916	19.749 ± 0.212
5		1150	844.847	19.98	0.001	3.33	22.535 ± 0.277
6		1250	2492.416	6.21	0.005	3.257	22.045 ± 0.46
7		1400	1246.793	3.13	0.009	2.977	20.156 ± 0.888
Sample S68							
1		650	78.935	0.33	0.000	3.761	25.72 ± 14.638
2		750	44.566	6.67	0.006	2.044	14.026 ± 0.756
3		850	13.509	22.06	0.002	2.115	14.51 ± 0.242
4		950	9.763	22.4	0.004	2.686	18.408 ± 0.2
5		1000	5.307	15.36	0.010	3.337	22.836 ± 0.301
6		1050	5.464	13.5	0.020	3.546	24.259 ± 0.345
7		1100	7.214	10.31	0.030	3.504	23.974 ± 0.537
8		1150	28.362	3.13	0.071	3.348	22.912 ± 1.216
9		1300	27.273	3.6	0.066	3.646	24.937 ± 1.512
10		1450	47.642	2.64	0.275	3.741	25.586 ± 1.615

Discussion

In the literature, $^{40}Ar/^{39}Ar$ ages on phyllosilicates are most often interpreted as cooling ages (Dodson 1973), with a closure temperature (T_c) of *c*. 350 °C for white mica and *c*. 300 °C for biotite. However, for low-grade shear zones, this need not necessarily be the case. In this context, minerals are either (i) newly crystallized at the expense of feldspars, or (ii) strained and partly recrystallized during fluid-present shearing. If recrystallization is incomplete, a number of studies have shown that the K–Ar isotopic system is not totally reset (e.g., Kramar *et al.* 2001 and references therein). This is true even if the rocks were buried for a long time at temperatures above the assumed closure temperature for the K–Ar system, and even if the deformation was strongly mylonitic (Kramar *et al.* 2001). As a result, $^{40}Ar/^{39}Ar$ ages from phyllosilicates in shear zones could represent (1) the time of syntectonic crystallization, (2) the time of cessation of fluid circulation, (3) the time of cooling through the closure temperature (T_c), (4) a geologically meaningless age reflecting excess or inherited ^{40}Ar, or (5) some indeterminate combination of any of these. In the Mont Blanc Massif, application of the $^{40}Ar/^{39}Ar$ chronometer to several different minerals (white mica, biotite and phlogopite) formed during shear zone development by differing amounts of fluid–rock interaction under similar low-T metamorphic conditions provides a chance to critically assess the geological significance of the ages obtained.

Significance of biotite and phlogopite $^{40}Ar/^{39}Ar$ ages

Leloup *et al.* (2005) published five biotite plateau ages from undeformed or slightly deformed Mont Blanc granite, ranging between 22.8 ± 0.6 and 63.7 ± 1.9 Ma. They interpreted these results as cooling ages, except for the older ages, which they considered to have no tectonic significance. In biotite and phlogopite, it is unclear if the old plateau ages are due to (1) significant tectonic events (e.g., cooling through T_c or mineral nucleation at $T \geq 350$ °C), (2) excess ^{40}Ar due to ^{40}Ar incorporation during deformation, or (3) excess ^{40}Ar due to Ar inheritance from magmatic minerals. These three points are now discussed separately.

(1) The fact that biotite shows a range of ages suggests that they do not reflect simple cooling through T_c following Alpine greenschist facies metamorphism. The older Alpine ages reported in the external NW Alps are Upper Eocene–Oligocene (35–30 Ma), and coincide with the activation of the Penninic Front (Ceriani *et al.* 2001). The external part of the Alps was first involved in Alpine orogenesis at around 35–32 Ma and metamorphic peak conditions could not have been attained before this time. All ages obtained in the current study are close to or younger than this age and therefore could be geologically meaningful. For instance, the LT part of the staircase $^{40}Ar/^{39}Ar$ spectra and the corresponding inverse isochron plots yield similar ages, without any evidence for excess ^{40}Ar, of *c*. 18 Ma in sample GEO317 and *c*. 37 Ma in sample PK4406. The 37 Ma age is close to published ages for early NW thrusting along the Penninic Front (Ceriani *et al.* 2001; Dumont *et al.* 2004), while the 18 Ma age is in the range of other phengite ages obtained in the Mont Blanc Massif and the neighbouring external Alps (see below).

(2) It is known that excess ^{40}Ar preferentially partitions into biotite rather than muscovite (Kelley 2002 and references therein). Thus, biotite and phlogopite might be a 'sink' for excess ^{40}Ar during fluid–rock interaction. $^{40}Ar/^{39}Ar$ biotite age spectra obtained in this study and in Leloup *et al.* (2005) generally show slight U shapes, which could indicate the presence of excess ^{40}Ar (e.g., Arnaud *et al.* 1995; Scaillet 1996). Phlogopite spectra obtained in this study are quite irregular, with old age components (>36.6 Ma for sample PK4406; and ≥ 18.0 Ma for sample GEO317). The inverse isochron plots for both biotite and phlogopite indicate slight (C6, GEO317) to significant excess ^{40}Ar (PK4406). The presence of excess Ar could be related to the growth of phlogopite at the expense of chlorite [reaction (4)], which involves intense Mg-metasomatism with high fluid–rock ratios.

(3) As shown by Rossi *et al.* (2005), the Alpine deformation affects the granite protolith heterogeneously. With increasing deformation in shear zones, pre-existing magmatic minerals are progressively recrystallized under greenschist facies conditions (0.5 GPa and 400 °C; Rolland *et al.* 2003). Under such P–T conditions with incomplete recrystallization of biotite, inherited ^{40}Ar could be partially preserved during Alpine deformation. The $^{40}Ar/^{39}Ar$ biotite age must therefore be considered to be a maximum age. The spread of biotite plateau ages from 22.8 ± 0.6 to 63.7 ± 1.9 Ma obtained in undeformed granite by Leloup *et al.* (2005) could well be due to such partial ^{40}Ar inheritance. In the shear zones, (low-Ti)

metamorphic biotite recrystallizes at the expense of (high-Ti) magmatic biotite [reaction (3)]. Unexpelled ^{40}Ar inherited from magmatic biotites is the most likely source of excess Ar, as indicated by older ages obtained in the undeformed granite. Biotites from mylonites, with more intense fluid–rock reaction, yield ages of *c*. 22 Ma, which are within the age range of older phengite ages (sample S68, from the NW part of the massif). If excess ^{40}Ar was introduced by fluids percolating along shear zones, the most deformed rocks should appear older than undeformed rocks ($>c$. 300 Ma, Bussy & von Raumer 1994). As this is not the case, it is probable that the excess ^{40}Ar is inherited from the magmatic biotite.

Significance of white mica $^{40}Ar/^{39}Ar$ ages

In contrast to biotite and phlogopite, the Ar spectra obtained for white micas show no evidence of excess ^{40}Ar. Similar ages are obtained on geographically distinct shear zones and on duplicate analyses from the same shear zone.

Explanation for the LT staircase shape of Ar spectra In the SE part of the massif, white mica from samples MB30, 94 and 140 show systematic staircase shapes in the lower-temperature part of Ar spectra. These patterns could be explained by several processes, two of which are considered in detail here.

(1) The patterns could reflect mixtures and intergrowths between different generations of white mica (Villa *et al.* 1997) or between white mica and other phyllosilicates present as intergrowths, such as paragonite (Boundy *et al.* 1997), illite (DeJong *et al.* 2001) or chlorite (Lo & Onstott 1989). However, different hand-picked white mica separates from the same samples and different samples from separate shear zones have given similar age estimates. Furthermore, electron-microprobe traverses within phengite aggregates have not shown any compositional zoning or the presence of any other K-rich mineral within the aggregates. It is therefore unlikely that the younger ages obtained for the lower temperature steps of the Ar spectra could be due to the presence of mineral inclusions, or to a low-temperature, younger phengite generation in the samples from the SE part of the massif (Fig. 7a–c).

(2) The patterns could be due to Ar loss, interpreted to result from partial re-opening of the K–Ar system after crystallization (Berger 1975; Hames & Cheney 1997; McDougal & Harrison 1999). For example, this could be due to post-crystallization deformation of micas (Kramar *et al.* 2001; Mulch *et al.* 2002) or to the effect of late fluids (e.g., Kirschner *et al.* 1996; Villa 1998). Examples of partial Ar resetting due to deformation typically involve large porphyroclasts bordered by microshears (Kramar *et al.* 2001; Mulch *et al.* 2002). This is not the case in SE Mont Blanc massif shear zones, where pressure shadow mica aggregates show no microstructural evidence for subsequent deformation. However, analysis of microtextures in samples MB94 and MB140 from the SE Mont Blanc Massif area and geochemical changes associated with deformation in shear zones from this area indicate that large volumes of fluid have circulated within these shear zones (Rolland *et al.* 2003; Rossi *et al.* 2005). Fluid flow occurred even during the later brittle evolution, as shown by more discrete calcite-bearing, quartz-free veins and quartz-rich cataclasites. Furthermore, present-day high rates of groundwater flow on the order of several cubic metres per second per unit length of fault were measured in the continuation of the MB140 and MB94 shear zones in the underlying Mont Blanc tunnel as it was excavated (Maréchal & Perrochet, 2001). It follows that, in the SE Mont Blanc Massif, the Ar loss observed in the lower temperature steps could be interpreted as being due to post-kinematic fluid circulation (e.g., Kirschner *et al.* 1996).

$^{40}Ar/^{39}Ar$ spectra with LT and HT mini-plateaux In the NW part of the massif, sample S68 shows an irregular Ar spectra, with two miniplateaux at LT (14.3 ± 0.2 Ma) and HT (22.9 ± 0.9 Ma). Unlike phengites from the SE part of the massif, the staircase shape is interpreted as reflecting two disctinct events, with the ^{40}Ar loss ascribed to a superposed crystallization event and not to post-kinematic fluid circulation. Textural observations from sample S68 show that two foliations are present, in agreement with a two-phase evolution and the development of two phengite generations at (1) *c*. 23 Ma and (2) *c*. 14 Ma, respectively. In similar Alpine settings, such spectra were interpreted by Kirschner *et al.* (1996) and Markley *et al.* (1998) to reflect superposed shearing events within the same zone. This possibility is also supported by the presence of U-shaped Ca/K ratios, interpreted by Wijbrans & McDougall (1986) and DeJong (2003) as being due to the presence of chemically

inhomogeneous mica that was incompletely recrystallized during a younger deformation event.

Cooling or nucleation age? In large crystals (*c*. 500 μm), the closure temperature T_c for the K–Ar white mica system (*c*. 350–450 °C) is slightly above that of phlogopite (*c*. 300–350 °C, e.g., Villa 1998; West & Lux 1993). For a cooling rate of 25 °C Ma^{-1} deduced from the age of 16 Ma obtained by phengite Ar–Ar dating and the temperature of 400 °C obtained by thermobarometry, we recalculate T_c for the size of mica grains in the analysed shear zone aggregates (*c*. 50 μm) with the diffusion parameters of Hames & Bowring (1994). This yields an estimate of $T_c = 338$ °C for white mica and $T_c = 278$ °C for biotite and phlogopite. If we assume that $^{40}Ar/^{39}Ar$ ages are cooling ages, white mica should be older than biotite and phlogopite. In the case of the Mont Blanc Massif, white mica ages are much younger than biotite and phlogopite ages. For a cooling rate of 25 °C Ma^{-1}, a difference in T_c of 50 °C would lead to an age difference of 2 Ma, far above the error span of ±0.2 Ma. In contrast, biotite and phlogopite ages are systematically older than phengite by more than 2 Ma. Thus, the consistent ages obtained between different phengite samples more likely represent the age of synkinematic crystallization during a short-lived shearing event, rather than cooling ages. However, if the ages obtained for phengite were cooling ages, then the phengite could still only have grown at a temperature slightly above T_c, because the maximum temperature reached in the Mont Blanc Massif during Alpine deformation was around 400 °C. In this case, $^{40}Ar/^{39}Ar$ dating of phengite provides a minimum age of deformation, but, because of the fast cooling rate of *c*. 25 °C Ma^{-1} the cooling age should be only *c*. 2 Ma younger than the crystallization age.

Age of deformation in the Mont Blanc massif

As discussed above, phengite develops by feldspar breakdown [reactions (1) and (2)] and crystallizes in strain shadows and foliation domains around feldspar porphyroclasts, parallel to the stretching lineation (on average pitching W70° on a N45°E–70N foliation plane, see also Guermani & Pennacchioni 1998). The asymmetric development of these strain shadows (Fig. 3) is consistent with the overall kinematic indicators indicating top-to-SE sense of shear on the SE side and top-to-NW on the NW side of the Mont Blanc Massif, with a smaller dextral component (lineations plunge 60–90°; Rossi *et al.* 2005). The age of the three analysed shear zones from the SE area (i.e., MB94, MB140 and MB30) varies by less than 0.2 Ma, i.e., it is effectively the same within error. Top-to-SE motion therefore initiated at or before *c*. 16 Ma on the SE side of the Mont Blanc Massif (if the 18 Ma phengite age is interpreted as a cooling age, with rapid cooling of *c*. 25 °C Ma^{-1}, see above). This result is in agreement with previous K–Ar ages from horizontal vein minerals which are kinematically related to the shear zones, yielding 15.2–18.3 Ma on adularia and 13.4–15.2 Ma on muscovite (Leutwein *et al.* 1970).

Deformation in the central-western part of the Mont Blanc Massif is less well constrained, but two ages of 22.9 ± 0.9 and 14.3 ± 0.2 Ma were obtained on sample S68. As discussed above, these two ages may represent two deformation phases in the same shear zone. As only top-to-NW sense of shear has been observed in this shear zone, it is likely that both deformation events are due to thrusting towards the NW. The LT miniplateau age of 14.3 Ma is relatively close to the age of 15.8 Ma obtained from shear zones on the SE side of Mont Blanc Massif and to the K–Ar ages obtained by Leutwein *et al.* (1970) on kinematically related veins. The age of 22.9 Ma for the higher-temperature mini-plateau from this phengite sample is close to younger biotite ages (22.8 ± 0.6 Ma) obtained in the 'undeformed granite' by Leloup *et al.* (2005), and also close to that for biotite sampled from a shear zone close to the thrust on the NW border of the Mont Blanc Massif (21.8 ± 3 Ma). The $^{40}Ar/^{39}Ar$ ages of samples S68 and S69 therefore suggest that this NW-directed thrusting was first active at around 22–23 Ma, but was probably later reactivated, with movement continuing down to *c*. 14 Ma. Near-simultaneous deformation on both sides of the massif at 14–16 Ma is in agreement with the interpretation of the Mont Blanc Massif as a pop-up structure, as proposed earlier by Von Raumer (1974) and Bertini *et al.* (1985). However, as noted above, there is also evidence for an overall dextral component to deformation on both sides of the Mont Blanc Massif (Gourlay & Ricou 1983; Hubbard & Mancktelow 1992; Bistacchi *et al.* 2000; Rossi *et al.* 2005), which would suggest that this pop-up is more of a positive flower structure within a dextral transpressive zone, although the dextral component need not be large (Rossi *et al.* 2005). Based on the *P–T–t* data, the massif has been exhumed at a continuous rate of *c*. 1 mm/year since 16 Ma, which is the rate obtained using both $^{40}Ar/^{39}Ar$ data and FT data (Seward & Mancktelow 1994; Leloup *et al.* 2005). Based on these new data and the lack of any jump in FT ages across the Mont Blanc Massif, we propose that the tectonic context of the Mont Blanc Massif has not changed significantly since 16 Ma.

Significance of Mont Blanc deformation ages in the framework of the western Alps

The ages older than 16 Ma can be related to deformation during nappe transport (cf. age data on the Morcles Nappe from Kirschner *et al.* 1996). Nappe transport in the external Alps probably began with activation of the Penninic Front and related thrusts (Ceriani *et al.* 2001), subsequent to deposition of the Taveyannaz sandstone around 32 Ma (Fischer & Villa 1990). In the Mont Blanc Massif, an apparent age of 36.6 Ma is obtained in sample PK4406 phlogopites, but this age is probably not geologically meaningful, due to some excess ^{40}Ar component. Most $^{40}Ar/^{39}Ar$ ages, such as the S68 phengite age of 22.9 ± 0.9 Ma, the younger biotite ages from Leloup *et al.* (2005) and our biotite–phlogopite data (sample C6 biotite, GEO 317 phlogopite), indicate an early phase of top-to-NW thrusting starting at 23–24 Ma and continuing to around 16–18 Ma. This phase of thrusting is correlated with the emplacement of the Morcles/Doldenhorn nappe (Crespo-Blanc *et al.* 1995; Kirschner *et al.* 1999, 2003). The younger ages around 16 Ma are interpreted as representing the transition to a phase of backfolding and backthrusting in the Alps, as already proposed by Hunziker *et al.* (1992) and Kirschner *et al.* (2003). This later period is also also associated with truncation of nappes in the Rhone Valley by the dextral transcurrent Rhone–Simplon fault (Steck 1984; Mancktelow 1992; Burkhard 1990; Steck & Hunziker 1994). The transpressive pop-up structure of the Mont Blanc developed within the westward continuation of this Rhone–Simplon dextral fault system (Hubbard & Mancktelow 1992), which has been active since *c*. 18 Ma (Grasemann & Mancktelow 1993).

Conclusions

Constraining the age of ductile deformation events in the middle to upper crust (e.g., in the Mont Blanc massif) necessitates dating minerals that crystallized during deformation at or below their closure temperature T_c. The P–T–t data for key deformation events can be obtained by combining thermobarometry with $^{40}Ar/^{39}Ar$ dating on newly grown minerals that have crystallized synkinematically and actually provide the kinematic indicators to determine the sense-of-shear (e.g., asymmetric pressure shadows or S–C structures). In this study, direct dating of shear zone deformation was undertakern for a set of synkinematic minerals (white mica, biotite and phlogopite) formed at 0.5 ± 0.05 GPa and 400 ± 25 °C in the Mont Blanc Massif shear zone network, which is interpreted to represent a dextral transpressive pop-up system.

Biotite and phlogopite crystals preserve significant amounts of inherited and possibly excess ^{40}Ar, but some geologically significant ages have been obtained in the LT part of Ar spectra, ranging between 36.6 and 18.0 Ma. In the NW part of the massif, $^{40}Ar/^{39}Ar$ biotite ages are locally similar to phengite ages, ranging between 21.8 and 22.9 Ma. In contrast, in the SE part of the massif, white mica (phengite) provides undisturbed younger ages, with no evidence for excess ^{40}Ar. The absence of any excess ^{40}Ar in phengite is ascribed to the nucleation of phengite at the expense of feldspars during low to moderate fluid/rock ratio deformation. In contrast, biotite nucleates on and replaces pre-existing magmatic biotite. Phlogopite may have incorporated some excess ^{40}Ar during high fluid–rock ratio deformation. In the case of multiple shearing events within a single shear zone, the $^{40}Ar/^{39}Ar$ phengite age provides either (1) disrupted age spectra, with step ages ranging between the maximum age of the second tectonic event and the minimum age of the first event (sample S69), or (2) miniplateaux, which could possibly represent the age of each event (sample S68). In the case of single events, well-defined single plateau ages are obtained, such as in the SE part of the Mont Blanc Massif. In this area, ages are all within 15.8–16.0 Ma, in agreement with ages previously determined on vein mineral assemblages whose formation was associated with shear zone development. Partial ^{40}Ar loss could be associated with late fluid circulation, but does not significantly affect the estimated plateau ages. In conclusion, phengite can be a good tool for estimating deformation ages in structurally well-defined low-grade shear zones, if carefully constrained by a combination of field observation, microstructural analysis, geochemistry and geothermobarometry.

This research was supported partly by an Australian Research Council grant. The authors wish to thank G. Féraud for his help with $^{40}Ar/^{39}Ar$ laser dating, the Torino Museum of Natural Sciences for providing samples from the Mont Blanc tunnel, and K. DeJong and S. Sherlock for their careful and stimulating reviews.

Appendix: analytical techniques

Locations of the samples dated by $^{40}Ar/^{39}Ar$ are provided in Table 3. Mineral compositions were determined by electron probe microanalysis (EPMA). The analyses were carried out at 15 kV and 1 nA using a Jeol 6400 scanning electron microscope (SEM) equipped with an Oxford Instrument light EDS detector and Link ISIS SEMquant software, at the ANU Electron Microscopy Unit. Natural

Table 3. *GPS coordinates (UTM-WGS84) and tunnel location of samples dated by $^{40}Ar/^{39}Ar$*

Sample	GPS (N)	GPS (E)
C6	5084725	335411
MB30	5076035	336641
MB94	5077445	339523
MB140	5079122	339420
S68 & S69	5101734	341103
PK4406	4.406 km in Mont Blanc tunnel (from entrance on the French side)	
GEO317	6.334 km in Mont Blanc tunnel (from entrance on the French side)	

samples were used as standards. Representative mineral analyses are presented Table 1. The textural relationships between the minerals in each assemblage suggest a series of reactions occurring during deformation. Reactions (1)–(4) are written assuming Al mobility, as supported by mass-balance calculations in Rossi *et al.* (2005). The mineral formulae used are approximated following representative EPMA analyses (Table 1).

Geochronology of synkinematic micas was undertaken by laser $^{40}Ar/^{39}Ar$ dating. Results are presented in Table 2. White mica was analysed by EPMA to check that mineral compositions are homogeneous from core to rim. Grain aggregates less than 1 mm were separated by hand-picking under a binocular microscope, to avoid altered grains. The samples were then irradiated in the nuclear reactor at McMaster University in Hamilton (Canada), in position 5c, along with Hb3gr hornblende neutron fluence monitor, for which an age of 1072 Ma is adopted (Turner *et al.* 1971). The total neutron flux density during irradiation was 9.0×10^{18} neuton/cm^2. The estimated error bar on the corresponding $^{40}Ar^*/^{39}Ar_K$ ratio is $\pm 0.2\%$ (1σ) in the volume where the samples were set.

Analyses of small amounts of mica aggregates (1 aggregate of *c*. 500μm and 2–4 mg: samples MB30, MB94, MB140, GEO317 and PK4406) were undertaken by step heating with a 50 W CO_2 Synrad 48-5 continuous laser beam. Measurement of isotopic ratios was done with a VG3600 mass spectrometer, equipped with a Daly detector system. Detailed procedures are given in Jourdan *et al.* (2004). The typical blank values for extraction and purification of the laser system are in the ranges 4.2–8.75, 1.2–3.9 and 2–6 cc STP for masses 40, 39 and 36, respectively. Analyses of larger mica populations (10 aggregates of *c*. 500 μm and *c*. 20–40 mg: samples S68 and C8) were undertaken with a furnace step-heating technique using a double-vacuum high-frequency furnace and a mass spectrometer composed of a 120° MASEE tube, a Baur–Signer GS98 source and a Blazers electron multiplier. Heating lasted 20 min for each temperature step, followed by 5 min for clean-up of the released gas, before introducing the gas into the spectrometer. Ar isotopes were of the order 100–2000, 100–1000 and 2–200 times the blank for masses 40, 39 and 36, respectively. All measurements were undetaken at the University of Nice (Géosciences Azur). For both Ar-dating techniques, the mass-discrimination was monitored by regularly analysing air pipette volume. Decay constants are those of Steiger & Jäger (1977). Uncertainties on apparent ages are given at the 2σ level and do not include the error on the $^{40}Ar^*/^{39}Ar_k$ ratio of the monitor.

The criteria generally used in the laboratory for defining a 'plateau' age are the following: (1) it should contain at least 70% of total ^{39}Ar released; (2) there should be at least three successive step-heating fractions in the plateau; (3) the integrated age of the plateau (weighted average of apparent ages of individual fractions comprising the plateau) should agree with each apparent age of the plateau with a 2σ error. In this study, we also consider plateaux smaller than 70% of total ^{39}Ar, because the lower temperature age spectra are generally lowered by a ^{39}Ar loss effect.

References

ANTOINE, P., PAIRIS, J. L. & PAIRIS, B. 1975. Quelques observations nouvelles sur la structure de la couverture sédimentaire interne du massif du Mont Blanc, entre le Col du Ferret (frontière italo-suisse) et la Tête des Fours (Savoie, France). *Géologie Alpine*, **51**, 5–23.

ARNAUD, N. O. & KELLEY, S. P. 1995. Evidence for excess argon during high pressure metamorphism in the Dora Maira Massif (Western Alps, Italy), using an ultra-violet laser ablation microprobe ^{40}Ar–^{39}Ar technique. *Contributions to Mineralogy and Petrology*, **121**, 1–11.

AYRTON, S., BARFÉTY, J. C., BELLIÈRE, J., GUBLER, Y. & JEMELIN, L. 1987. *Carte géologique de Chamonix* (1/50 000). BRGM, Orléans.

BAGGIO, P. 1958. Il granito del Monte Bianco e le sue mineralizzazioni uranifere. *Studi e ricerche della divisione geomineraria CNRN Roma*, **1**, 1–130.

BAGGIO, P., FERRARA, G. & MALADORA, R. 1967. Results of some Rb/Sr age determinations of the rocks of the Mont Blanc tunnel. *Bolletino dellà Società Geologica Italiana*, **86**, 193–212.

BEACH, A. 1980. Retrogressive metamorphic processes in shear zones with special reference to the Lewisian complex. *Journal of Structural Geology*, **2**, 257–263.

BEACH, A. & FYFE, W. S. 1972. Fluid transport in shear zones at Scourie, Sutherland: evidence of overthrusting? *Contributions to Mineralogy and Petrology*, **36**, 175–180.

BELLIERE, J. 1988. On the age of mylonites within the Mont Blanc massif. *Geodinamica Acta*, **2**, 13–16.

BERGER, G. W. 1975. $^{40}Ar/^{39}Ar$ step heating of thermally overprinted biotite, hornblende and potassium feldspar from Eldora, Colorado. *Earth and Planetary Science Letters*, **26**, 387–408.

BERTINI, G., MARCUCCI, M., NEVINI, R., PASSERINI, P. & SGUAZZONI, G. 1985. Patterns of faulting in the Mont Blanc granite. *Tectonophysics*, **111**, 65–106.

BISTACCHI, A, EVA, E., MASSIRONI, M. & SOLARINO, S. 2000. Miocene to Present kinematics of the NW-Alps: evidences from remote sensing, structural analysis, seismotectonics and thermochronology. *Journal of Geodynamics*, **30**, 205–228.

BONIN, B., BRÄNDLEIN, P. *ET AL.* 1993. Late Variscan magmatic evolution of the Alpine basement. *In*: VON RAUMER, J. F. & NEUBAUER, F. (eds) *Pre-Mesozoic Geology in the Alps*, Springer, Heidelberg, 171–201.

BOUNDY, T. M., HALL, C. M., LI, G., ESSENE, E. J. & HALLIDAY, A. N. 1997. Fine-scale isotopic heterogeneities and fluids in the deep crust: a $^{40}Ar/^{39}Ar$ laser ablation and TEM study of muscovites from a granulite–eclogite transition zone. *Earth and Planetary Science Letters*, **148**, 223–242.

BURKHARD, M. 1990. Aspects of the large-scale Miocene deformation in the most external part of the Swiss Alps (Subalpine Molasse to Jura fold belt). *Eclogae Geologicae Helvetiae*, **83**, 559–583.

BUSSY, F. 1990. *Pétrogenèse des enclaves microgrenues associées aux granitoïdes calco-alcalins: exemple des massifs varisque du Mont Blanc (Alpes occidentales) et miocène du Monte Capanne (Ile d'Elbe, Italie)*. Mémoires de Géologie de l'Université de Lausanne, **7**.

BUSSY, F. & VON RAUMER, J. F. 1994. U–Pb geochronology of Palaeozoic magmatic events in the Mont Blanc crystalline massif, Western Alps. *Schweizerische Mineralogische and Petrographische Mitteiling*, **74**, 514–515.

BUSSY, F., SCHALTEGGER, U. & MARRO, C. 1989. The age of the Mont Blanc granite (Western Alps): a heterogeneous system dated by Rb–Sr whole-rock determinations on its microgranular enclaves. *Schweizerische Mineralogische und Petrographische Mitteilung*, **69**, 3–13.

BUTLER, R. W. H. 1985. The restoration of thrust systems and displacement continuity around the Mont Blanc massif, NW external Alpine thrust belt. *Journal of Structural Geology*, **7**, 569–582.

CERIANI, S., FÜGENSCHUH, B. & SCHMID, S. M. 2001. Multi-stage thrusting at the 'Penninic Front' in the Western Alps between Mont Blanc and Pelvoux massifs. *International Journal of Earth Science*, **90**, 685–702.

COX, S. F. 2005. Coupling between deformation, fluid pressures and fluid flow in ore-producing hydrothermal systems at depth in the Earth's crust. *Economic Geology 100th Anniversary Volume*, 39–75.

COX, S. F., ETHERIDGE, M. A. & WALL, V. J. 1987. The role of fluids in syntectonic mass transport, and localization of metamorphic vein-type ore deposits. *Ore Geology Reviews*, **2**, 65–86.

CRESPO-BLANC, A., MASSON, H., SHARP, Z., COSCA, M. & HUNZIKER, J. 1995. A stable and $^{40}Ar/^{39}Ar$ isotope study of a major thrust in the Helvetic nappes (Swiss Alps): evidence for fluid flow and constraints on the nappe kinematics. *Geological Society of America Bulletin*, **107**, 1129–1144.

DEJONG, K. 2003. Very fast exhumation of high-pressure metamorphic rocks with excess ^{40}Ar and inherited ^{87}Sr, Betic Cordilleras, southern Spain. *Lithos*, **70**, 91–110.

DEJONG, K., FÉRAUD, G., RUFFET, G., AMOURIC, M. & WIJBRANS, J. R. 2001. Excess argon incorporations in phengite of the Mulhacén complex: submicroscopic illitization and fluid ingress during late Miocene extension in the Betic zone, south-eastern Spain. *Chemical Geology*, **178**, 159–195.

DODSON, M. H. 1973. Closure temperature in cooling geochronological and petrological systems. *Contributions to Mineralogy and Petrology*, **40**, 259–274.

DUMONT, T., HEYMES, T., ROLLAND, Y. & AUTHEMAYOU, C. 2004. Early Oligocene N–NW thrusting in the External Alps before the onset of westward indentation. *2nd Swiss Geoscience Meeting*, Lausanne.

DUNLAP, W. J. 1997. Neocrystallization or cooling? $^{40}Ar/^{39}Ar$ ages of white micas from low-grade mylonites. *Chemical Geology*, **143**, 181–203.

DUNLAP, W. J. & KRONENBERG, A. K. 2001. Argon loss during deformation of micas: constraints from laboratory deformation experiments. *Contributions to Mineralogy and Petrology*, **141**, 174–185.

FERRY, J. M. & GERDES, M. L. 1998. Chemically reactive fluid flow during metamorphism. *Annual Reviews in Earth and Planet. Science*, **26**, 255–287.

FISCHER, H. & VILLA, I. M. 1990. Erste K/Ar- und $^{40}Ar/^{39}Ar$-Hornblende-Mineralalter des Taveyannaz-Sandsteins. *Schweizerische Mineralogische und Petrographische Mitteilung*, **70**, 73–75.

FITZ GERALD, J. D. & STÜNITZ, H. 1993. Deformation of granitoids at low metamorphic grade. I: reactions and grain size reduction. *Tectonophysics*, **221**, 269–297.

GIBSON, R. G. 1990. Nucleation and growth of retrograde shear zones: an example from the Needle mountains, Colorado, USA. *Journal of Structural Geology*, **12**, 339–350.

GOODWIN, L. B. & RENNE, P. R. 1991. Effects of progressive mylonitization on Ar retention in biotites from the Santa Rosa mylonite zone (California), and thermochronologic implications. *Contributions to Mineralogy and Petrology*, **108**, 283–297.

GOURLAY, P. 1986. La déformation du socle et des couvertures delphino-helvétiques dans la région du Mont Blanc (Alpes occidentales). *Bulletin de la Société Geologique de France*, **8**, 159–169.

GOURLAY, P. & RICOU, L. E. 1983. Le jeu décrochant dextra Tardif de la suture de Chamonix (Alpes françaises et suisses). *Comples Rendu de la Academie de Sciences Paris*, **296**, 927–932.

GRASEMANN, B. & MANCKTELOW, N. S. 1993. Two-dimensional thermal modelling of normal faulting: the Simplon Fault Zone, Central Alps, Switzerland. *Tectonophysics*, **225**, 155–165.

GUERMANI, A. & PENNACCHIONI, G. 1998. Brittle precursors of plastic deformation in a granite: an example from the Mont Blanc massif (Helvetic, western Alps). *Journal of Structural Geology*, **20**, 135–148.

HAMES, W. E. & BOWRING, S. A. 1994. An empirical evaluation of the argon diffusion geometry in muscovite. *Earth and Planetary Science Letters*, **124**, 161–167.

HAMES, W. E. & CHENEY, J. T. 1997. On the loss of $^{40}Ar^*$ from muscovite during polymetamorphism. *Geochimica Cosmochimica Acta*, **61**, 3863–3872.

HAMES, W. E. & HODGES, K. V. 1993. Laser $^{40}Ar/^{39}Ar$ evaluation of slow cooling and episodic loss of ^{40}Ar from a sample of polymetamorphic muscovite. *Science*, **261**, 1721–1723.

HUBBARD, M. & MANCKTELOW, N. S. 1992. Lateral displacement during Neogene convergence in the western and central Alps. *Geology*, **20**, 943–946.

HUNZIKER, J. C., DESMONS, J. & HURFORD, A. J. 1992. *Thrirty-two Years of Geochronological Work in the Central and Western Alps: a Review on Seven Maps*. Mémoires de Géologie de l'Université de Lausanne, **13**, 1–59.

JOURDAN, F., FÉRAUD, G., BERTRAND, H., KAMPUNZU, A. B., TSHOSO, G., LE GALL, B., TIERCELIN, J. J. & CAPIEZ, P. 2004. The Karoo triple junction questioned: evidence for Jurassic and Proterozoic $^{40}Ar/^{39}Ar$ ages and geochemistry of the giant Okavango dyke swarn (Botswana). *Earth and Planetary Science Letters*, **222**, 989–1006.

KELLEY, S. P. 1988. The relationship between K–Ar mineral ages, mica grain sizes and movement on the Moine Thrust Zone, NW Highlands, Scotland. *Journal of the Geological Society London*, **145**, 1–10.

KELLEY, S. P. 2002. Excess argon in K–Ar and Ar–Ar geochronology. *Chemical Geology*, **188**, 1–22.

KERRICH, R. 1986. Fluid infiltration into fault zones: chemical, isotopic, and mechanical effects. *Pure and Applied Geophysics*, **124**, 225–268.

KIRSCHNER, D. L., COSCA, M., MASSON, H. & HUNZIKER, J. 1996. Staircase $^{40}Ar/^{39}Ar$ spectra of fine-grained white mica: timing and duration of deformation and empirical constraints on argon diffusion. *Geology*, **24**, 747–750.

KIRSCHNER, D. L., MASSON, H. & COSCA, M. A. 2003. An $^{40}Ar/^{39}Ar$, Rb/Sr, and stable isotope study of micas in low-grade fold-and-thrust belt: an example from the Swiss Helvetic Alps. *Contributions to Mineralogy and Petrology*, **145**, 460–480.

KLIGFIELD, R., HUNZIKER, J., DALLMEYER, R. D. & SCHAMEL, S. 1986. Dating deformation phases using K–Ar and $^{40}Ar/^{39}Ar$ techniques: results from the Northern Apennines. *Journal of Structural Geology*, **8**, 781–798.

KRAMAR, N., COSCA, M. A. & HUNZIKER, J. C. 2001. Heterogeneous $^{40}Ar^*$ distributions in naturally deformed muscovite: *in-situ* UV–laser ablation evidence for microstructurally controlled diffusion. *Earth and Planetary Science Letters*, **192**, 377–388.

LELOUP, P. H., ARNAUD, N., SOBEL, E. R. & LACASSIN, R. 2005. Alpine thermal and structural evolution of the highest external crystalline massif: the Mont Blanc. *Tectonics*, **24**, TC4002, doi:10.1029/2004TC001676.

LEUTWEIN, F., POTY, B., SONET, J. & ZIMMERMAN, J. L. 1970. Age des cavités à cristaux du granite du Mont Blanc. *Comples Rendu de la Academie de Sciences Paris*, **271**, 156–158.

LO, C. H. & ONSTOTT, T. C. 1989. ^{39}Ar recoil artifacts in chloritized biotite. *Geochimica Cosmochimica Acta*, **53**, 2697–2711.

MANCKTELOW, N. S. 1992. Neogene lateral extension during convergence in the Central Alps: evidence from interrelated faulting and backfolding around the Simplonpass (Switzerland). *Tectonophysics*, **215**, 295–317.

MARÉCHAL, J. C. & PERROCHET, P. 2001. Theoretical relation between water flow rate in a vertical fracture and rock temperature in the surrounding massif. *Earth and Planetary Science Letters*, **194**, 213–219.

MARKLEY, M. J., TEYSSIER, C., COSCA, M. A., CABY, R., HUNZIKER, J. C. & SARTORI, M. 1998. Alpine deformation and $^{40}Ar/^{39}Ar$ geochronology of synkinematic white micas in the Siviez–Mischabel Nappe, western Penninic Alps, Swizerland. *Tectonics*, **17**, 407–425.

MARQUER, D. 1989. Transferts de matières et déformation des granitoïdes. Aspects méthodologiques. *Schweizerische Mineralogische und Petrographische Mitteilung*, **69**, 13–33.

MARRO, C. 1988. Organisation géochimique et organisation du granite du Mont Blanc et de deux leucogranites. *Schweizerische Mineralogische und Petrographische Mitteilung*, **68**, 521–529.

MARSHALL, D., PFEIFER, H. R., HUNZIKER, J. C. & KIRSCHNER, D. 1998. A pressure–temperature–time path for the NE Mont Blanc massif: fluid-inclusion, isotopic and thermobarometric evidence. *European Journal of Mineralogy*, **10**, 1227–1240.

MCCAIG, A. M., WICKHAM, S. M. & TAYLOR, H. P. 1990. Deep fluid circulation in Alpine shear zones, Pyrenees, France: field and oxygen isotope studies. *Contributions to Mineralogy and Petrology*, **106**, 41–60.

MCDOUGALL, I. & HARRISON, M. T. 1999. *Geochronology and Thermochronology by the $^{40}Ar/^{39}Ar$ method*, 2nd edn. Oxford University Press, Oxford.

MULCH, A., COSCA, M. A. & HANDY, M. R. 2002. *In-situ* UV-laser $^{40}Ar/^{39}Ar$ geochronology of a micaceous mylonite: an example of defect-enhanced argon loss. *Contributions to Mineralogy and Petrology*, **142**, 738–752.

MÜLLER, W., MANCKTELOW, N. S. & MEIER, M. 2000. Rb–Sr microchrons of synkinematic mica in mylonites an example from the DAV fault of the Eastern Alps. *Earth and Planetary Science Letters*, **180**, 385–397.

O'HARA, K. 1988. Fluid flow and volume loss during mylonitization: an origin for phyllonite in an overthrust setting, North Carolina, USA. *Tectonophysics*, **156**, 21–36.

POTY, B. 1969. *La croissance des cristaux de quartz dans les filons sur l'exemple du filon de la Gardette (Bourg d'Oisans) et des filons du massif du Mont Blanc*. PhD thesis, Université de Nancy.

POTY, B., STADLER, H. A. & WEISBROD, A. M. 1974. Fluid inclusion studies in quartz from fissures of the Western and Central Alps. *Schweizerische Mineralogische und Petrographische Mitteilung*, **54**, 717–752.

RAMSAY, J. G. 1981. Tectonics of the Helvetic nappes. *In*: MCKLAY, K. R. & PROCE, N. J. (eds) *Thrust and Nappe Tectonics*. Geological Society of London Special Publications, **9**, 293–309.

RAMSAY, J. G., CASEY, M. & KLIGFIELD, R. 1983. Role of shear in development of the Helvetic fold-thrust belt of Switzerland. *Geology*, **11**, 439–442.

REDDY, S. M. & POTTS, G. J. 1999. Constraining absolute deformation ages: the relationship between deformation mechanisms and isotope systematics. *Journal of Structural Geology*, **21**, 1255–1265.

REDDY, S. M., KELLEY, S. P. & WHEELER, J. 1996. A $^{40}Ar/^{39}Ar$ laser probe study of micas from the Sesia Zone, Italian Alps: implications for metamorphic and deformation histories. *Journal of Metamorphic Geology*, **14**, 493–508.

ROLLAND, Y., CORSINI, M., ROSSI, M., COX, S. F., PENNACCHIONI, G., MANCKTELOW, N. & BOULLIER, A. M. 2007. Comment on the dating of Alpine deformation by Ar–Ar on syn-kinematic mica in mid-crustal shear zones of the Mont Blanc Massif (paper by Leloup *et al.*). *Tectonics*, **26**, TC2015, doi:10.1029/2006TC001956.

ROLLAND, Y., COX, S. F., BOULLIER, A. M., PENNACCHIONI, G. & MANCKTELOW, N. 2003. Rare Earth and trace element mobility and fractionation in mid-crustal shear zones: insights from the Mont Blanc Massif (Western Alps). *Earth and Planetary Science Letters*, **214**, 203–219.

ROSSI, M. 2005. *Déformation, transferts de matière et de fluide dans la croûte continentale: application aux massifs cristallins externes des Alpes*. PhD thesis, Université de Grenoble.

ROSSI, M., ROLLAND, Y., VIDAL, O. & COX, S. F. 2005. Geochemical variations and element transfer during shear zone development and related episyenites at middle crust depths: insights from the study of the Mont Blanc Granite (French-Italian Alps). *In*: BRUHN, D. & BURLINI, L. (eds) *High-strain Zones: Structure and Physical Properties*. Geological Society of London Special Publications, **245**, 373–396.

SCAILLET, S. 1996. Excess ^{40}Ar transport scale and mechanism in high-pressure phengites; a case study from an eclogitized metabasite of the Dora–Maira nappe, Western Alps. *Geochimica Cosmochimica Acta*, **60**, 1075–1090.

SEWARD, D. & MANCKTELOW, N. S. 1994. Neogene kinematics of the central and western Alps: evidence from fission-track data. *Geology*, **22**, 803–806.

SHERLOCK, S., KELLEY, S. P., ZALASIEWICZ, J. A., SCHOFIELD, D. I., EVANS, J. A., MERRIMAN, R. J. & KEMP, S. J. 2003. Precise dating of low-temperature deformation: Strain-fringe analysis by ^{40}Ar-^{39}Ar laser microprobe. *Geology*, **31**, 219–222.

STECK, A. 1984. Structures de déformations tertiaires dans les Alpes centrales (transversale Aar–Simplon–Ossola). *Eclogae Geologicae Helvetiae*, **77**, 55–100.

STECK, A. & HUNZIKER, J. C. 1994. The tertiary structural and thermal evolution of the Central Alps – compressional and extensional structures in an Orogenic belt. *Tectonophysics*, **238**, 229–254.

STEIGER, R. H. & JÄGER, E. 1977. Subcomission on geochronology: convention of the use of decay constants in geo- and cosmochronology. *Earth and Planetary Science Letters*, **36**, 359–362.

STREIT, J. E. & COX, S. F. 1998. Fluid infiltration and volume-change during mid-crustal mylonitization of Proterozoic granite, King Island, Tasmania. *Journal of Metamorphic Geology*, **16**, 197–212.

TURNER, G., HUNEKE, J. C., PODOSE, F. A. & WASSERBURG, G. J. 1971. $^{40}Ar/^{39}Ar$ ages and cosmic ray exposure ages of Apollo 14 samples. *Earth and Planetary Science Letters*, **12**, 15–19.

VILLA, I. M. 1998. Isotopic closure. *Terra Nova*, **10**, 42–47.

VILLA, I. M., RUGGIERI, G. & PUXEDDU, M. 1997. Petrological and geochronological discrimination of two white-mica generations in a granite cored from the Larderello–Travale geothermal field (Italy). *European Journal of Mineralogy*, **9**, 563–568.

VON RAUMER, J. F. 1974. Kristallization und gefugebildung im Mont Blanc granit. *Schweizerische Mineralogische und Petrographische Mitteilung*, **47**, 499–579.

WEST, D. P. & LUX, D. R. 1993. Dating mylonitic deformation by the $^{40}Ar–^{39}Ar$ method: an example from the Norumbega Fault Zone, Maine. *Earth and Planetary Science Letters*, **120**, 221–237.

WIBBERLEY, C. A. J. & MCCAIG, A. M. 2000. Quantifying orthoclase and albite muscovitisation sequences in fault zones. *Chemical Geology*, **165**, 181–196.

WICKMAN, F. E., ABERG, G. & LEVI, B. 1983. Rb–Sr dating of alteration events in granitoids. *Contributions to Mineralogy and Petrology*, **83**, 358–362.

WIJBRANS, J. R. & MCDOUGALL, I. 1986. $^{40}Ar/^{39}Ar$ dating of white micas from an Alpine high-pressure metamorphic belt on Naxos (Greece) – the resetting of the argon isotopic system. *Contributions to Mineralogy and Petrology*, **93**, 187–194.

Assessment of thermal circulations in strike–slip fault systems: the Terme di Valdieri case (Italian western Alps)

A. BAIETTO[1], P. CADOPPI[1,4], G. MARTINOTTI[1], P. PERELLO[2], P. PERROCHET[3] & F.-D. VUATAZ[5]

[1]*DST, Dipartimento di Scienze della Terra, Università di Torino, Via Valperga Caluso 35, 10125, Torino, Italy (e-mail: alessandro.baietto@unito.it)*

[2]*SEA Consulting Srl, Via Cernaia 27, 10121, Torino, Italy*

[3]*CHYN, Centre d'Hydrogéologie, Université de Neuchâtel, Rue Emile-Argand 11– CP 158 CH-2009 Neuchâtel, Switzerland*

[4]*CNR-IGG, Istituto di Geoscienze e Georisorse, Sezione di Torino, Via Valperga Caluso 35, 10125, Torino, Italy*

[5]*CREGE, Centre for Geothermal Research, c/o CHYN, Rue E.-Argand, CP 158, CH-2009 Neuchâtel, Switzerland*

Abstract: Individual faults, faults linking at depth in flower structure zones and jogs bounded by faults are common structural elements in strike–slip fault systems and can play an important role in controlling thermal fluid flows. This paper explores the influence of these structures on the thermal circulations and fluid outflows of Terme di Valdieri, in the crystalline basement of the Argentera Massif (western Alps). In this site, thermal waters upwell at the tip of a NW-trending right-lateral fault, but exactly which structures control infiltration of meteoric waters and deep circulation is not clear from field surveys. Three-dimensional thermohydraulic numerical models calculated in steady-state and in transient regimes are presented for three alternative hypotheses. These account for circulations occurring: (i) within a single fault and adjoining host rocks; (ii) in faults intersecting at depth; and (iii) in faults interacting by means of a permeable step-over. The simulations show that advective flows can coexist with convective flows in models (i) and (iii), provided that the fault permeabilities are higher than 2×10^{-13} m^2, while advection prevails in model (ii) at all values of permeability. Model (iii) achieves the best fit to the data under the assumption of advective and convective flows. This finding provides a first quantitative estimate of the importance of jog structures bounded by strike–slip faults in favouring thermal outflows. Moreover, the numerical results suggest that thermal convection can coexist with advection also in mountainous settings.

Faults profoundly affect the patterns and rates of fluid flow in present-day flow systems in the upper seismogenic crust (Yeamans 1983; Sibson 1987; Henley & Adams 1992; Hickman *et al.* 1995; Curewitz & Karson 1997; Benoit 1999). Fluids flowing within large faults control the mobilization, transport and deposition of chemical species and influence heat transfer through the crust (Cox *et al.* 2001; Jaboyedoff & Pastorelli 2003). The thermal effect of fault-related fluid circulations can account for the deposition of ores at anomalously shallow depths (Bethke & Marshak 1990; Garven *et al.* 1993) and the emergence of hot springs (Alföldi *et al.* 1985; Forster & Smith 1989). The quantitative assessment of the structural influence of fault zones on thermal flow systems requires an accurate conceptual model of fault zone structure coupled to data regarding the hydraulic properties (e.g., permeability, porosity and storativity) of both the fault zone and the adjacent rock masses (Evans *et al.* 1997; Barton *et al.* 1995; Caine *et al.* 1996; Parry 1998; Sibson 2001). However, these parameters are difficult to assess due to their spatial and temporal variability and the scarcity of direct measurements (Smith 1980; Sibson 1994).

In order to obtain insights into fault-related thermal flow systems, several researchers have applied hydrogeological numerical modelling to a range of tectonic contexts, for example to extensional sedimentary basins (López & Smith 1995; Wisian & Blackwell 2004; McKenna & Blackwell 2004), to accretionary wedges (Henry 2000; Cutillo *et al.* 2003), and to oceanic spreading centres (Fehn & Cathles 1979; Travis *et al.* 1991). In general, these models aim to determine the conditions allowing high surface heat flows and high temperatures both in reservoirs and at

From: WIBBERLEY, C. A. J., KURZ, W., IMBER, J., HOLDSWORTH, R. E. & COLLETTINI, C. (eds) *The Internal Structure of Fault Zones: Implications for Mechanical and Fluid-Flow Properties*. **299**, 317–339.
DOI: 10.1144/SP299.19 0305-8719/08/$15.00

springs as a function of the structural and hydraulic properties attributed to fault zones and hosting rocks. Despite the common association between strike–slip faults and hydrothermal systems (Sibson 1987; Henley & Adams 1992), quantitative documentation of fluid and heat flow patterns in these tectonic contexts has received relatively little attention (Kasameyer *et al.* 1984).

It is uncertain what controls are exerted on thermal circulations by structures that commonly occur in contexts of wrench tectonics (e.g., single fault strands, coalescing faults, step-over faults). This is an important aspect of the problem because there is evidence that active outflow sites and preserved hydrothermal deposits are most commonly located at the terminations of individual faults and where multiple faults interact (Sibson 1987; Curewitz & Karson 1997). Moreover, while numerical simulation applied to sedimentary basins has contributed to the recognition of thermal processes driven by both advective and convective flows (López & Smith 1995, 1996; Garven *et al.* 2001; Simms & Garven 2004; Thornton & Wilson 2007), this remains to be verified in strike–slip fault-related thermal systems developed in basement rocks.

This study refers to a thermal outflow site located in the Argentera Massif (western Italian–French Alps), where several groups of hot springs, with temperatures of 30–70 °C and flow rates of 2–50 kg s^{-1}, emerge along regional NW–SE strike–slip faults (Fig. 1; Perello *et al.* 2001; Baietto 2007). As in all the other geothermal systems of the Alps (e.g., Vuataz 1982; Rybach 1995; Perello 1997; Martinotti *et al.* 1999; Pastorelli *et al.* 1999, 2001; Marini *et al.* 2000),

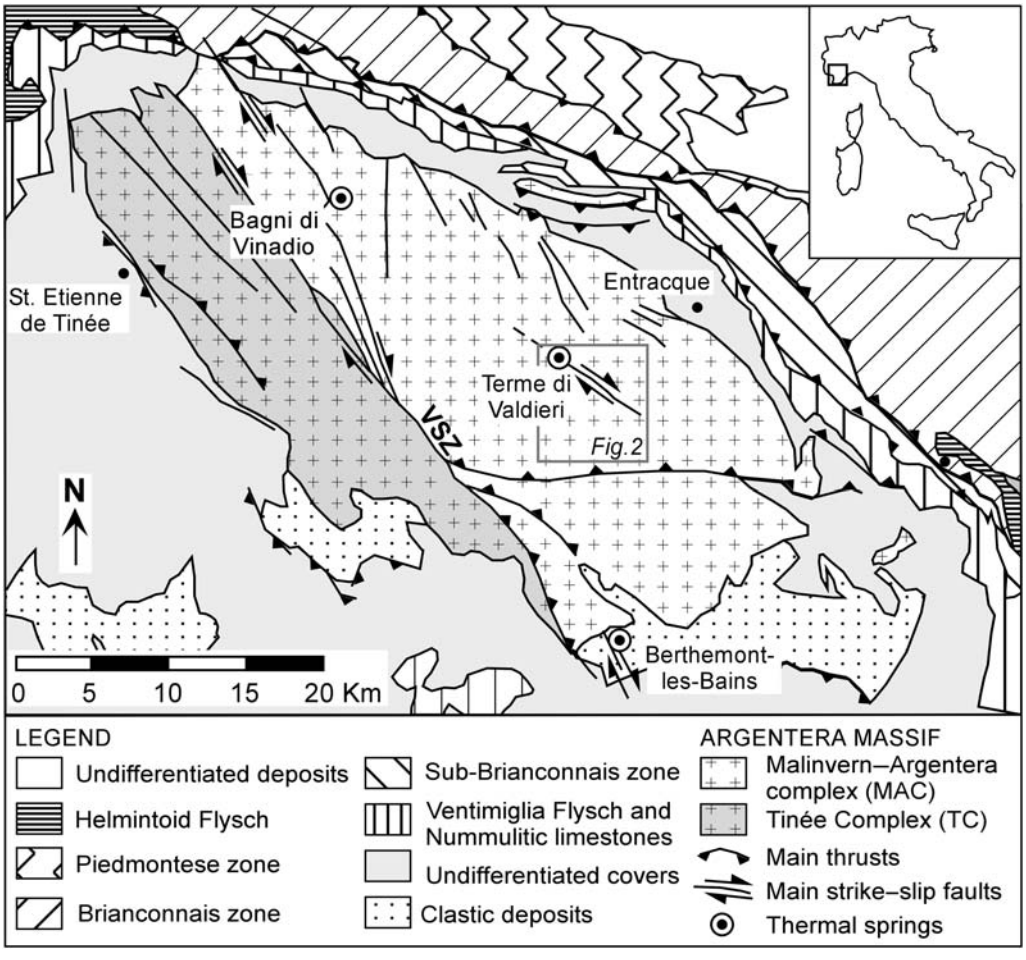

Fig. 1. Sketch map of the Argentera Massif and adjoining regions. VSZ, Valletta Shear Zone. Groups of thermal springs are located at the margins of NW–SE strike–slip faults at Bagni di Vinadio (I), Terme di Valdieri (I) and Berthemont-Les-Bains (F), exhibiting maximum outlet temperatures of 60, 70 and 30 °C, respectively.

the Argentera thermal discharges originate from the circulation at depth of meteoric waters that heat up and rapidly upwell to surface, in a region where active cooling of igneous bodies is absent. One of the most interesting among the Argentera thermal sites is represented by the Terme di Valdieri springs, a group of hot-water springs that discharge at the tip of a main strike–slip fault zone called the Lorusa Fault (Figs 1 & 2). Structural surveys have pointed out that the Lorusa Fault forms a channel which permits the final upwelling of the hot waters. However, the routes facilitating the penetration of cold water into the system and the nature of their circulation patterns remain unknown. In particular, it is not clear whether the Lorusa Fault acts as a unique pathway where fluids infiltrate, circulate while exchanging heat with rocks and upwell to the surface, or whether the circulation is partitioned among several strike–slip faults that are hydraulically connected through intersecting strands or through a permeable step-over. The purpose of this paper is therefore to explore the mechanisms of heat and fluid transport through the Valdieri faults using thermohydraulic numerical modelling in which some of the geometrical complexity related to strike–slip fault systems is taken into account. Sets of 3D numerical simulations of heat and fluid transport were carried out in steady-state and transient regimes to examine and compare the responses of the hot spring parameters as a function of the structural configuration and hydraulic properties attributed to the Valdieri faults and surrounding host rocks. These simulations yield insights into the conditions favouring the coexistence of advective flows governed by topographic gradients and convective flows driven by fluid density gradients in a strike–slip setting. Given the Alpine setting of the study area, the mechanisms governing water and heat transport along faults and the thermal state of the upper crust are also of strategic importance in both geothermal energy exploration and development and in the forecasting of risk related to underground engineering projects (e.g., deep tunnels).

Structural and hydrogeological setting of the Valdieri sector

The Argentera Massif (AM), the southernmost of the Alpine external massifs (others being Aar-Gothard, Aiguilles Rouges, Mount Blanc, Belledonne, Grandes Rousses and Pelvoux), is a slice of the European plate crystalline basement which crops out owing to its uplift and to the subsequent erosion of the overlying Mesozoic sedimentary succession (Helvetic–Dauphinois cover, HDC; Fig. 1). This massif represents one of the zones of the Western Alps with the highest concentration of thermal discharges. The main AM springs are located at Bagni di Vinadio (I), Terme di Valdieri (I), and Berthemont-Les-Bains (F; Fig. 1), exhibiting maximum outlet temperatures of 70, 60 and 30 °C respectively. The massif consists mainly of two gneissic complexes: to the east, the Malinvern–Argentera Complex (MAC), and to the west, the Tinée Complex (TC; Fig. 1). They are separated by a steep NW–SE striking mylonitic belt known as the Valletta Shear Zone (VSZ; Faure-Muret 1955; Bogdanoff 1986). This pre-Alpine structural element was reactivated by both ductile and brittle deformation during the Alpine Orogeny (Fry 1989). The TC is similar to the MAC in that it consists mainly of migmatitic gneisses related to pre-Alpine, high-grade metamorphism (Malaroda *et al.* 1970; Bogdanoff 1986). Fission-track analyses (Bigot-Cormier *et al.* 2000) reveal differential uplifts of the MAC and TC blocks. In the last 3.5 Ma, the MAC was characterized by a faster exhumation than the TC, with apparent uplift rates of *c.* 1.3 mm a^{-1}. According to Tricart (2004), the recent uplift of the AM results from the onset of a transpressive tectonic regime with dextral wrench faulting along the southern branch of the Alpine arc, close to the internal–external arc boundary.

In the area surrounding Terme di Valdieri, which forms part of the MAC, the main rock types are igneous rocks and migmatitic gneisses, the former consisting of medium- to coarse-grained granites and leucocratic aplites, and the latter, biotite-rich embrechites and leucocratic anatexites (Fig. 2a). The migmatitic gneisses outcrop mainly in the northern part of the mapped sector, whereas in the southern part, granite is prevalent. Close to the Terme di Valdieri site, the migmatitic gneisses crop out and overlie the granites at shallow depths. A main system of NW–SE strike–slip faults of Alpine age showing en-echelon geometries and evidence of right-lateral displacement cut pervasively through the migmatitic gneisses and granites in the area surrounding Valdieri (Perello *et al.* 2001). Subsidiary ENE–WSW striking faults characterized by left-lateral movements are associated with the main system. The springs of Terme di Valdieri discharge alongside the river bed of the Valletta Valley (Fig. 2a) next to the northwestern tip of a kilometre-scale NW–SE fault zone, the Lorusa Fault. Close to the thermal outlets, rock alterations and sulfide mineral deposits associated with the Lorusa Fault zone attest to the presence of earlier hydrothermal activity (Perello *et al.* 2001).

South of the Lorusa Fault, other kilometre-scale, NW-trending faults cross-cutting the Terme di Valdieri sector include the Cougne Fault, the S. Giovanni Fault, and the Valcuca Fault (cf. Fig. 2). Because their dips vary from SW to NE, these faults define an overall upward diverging

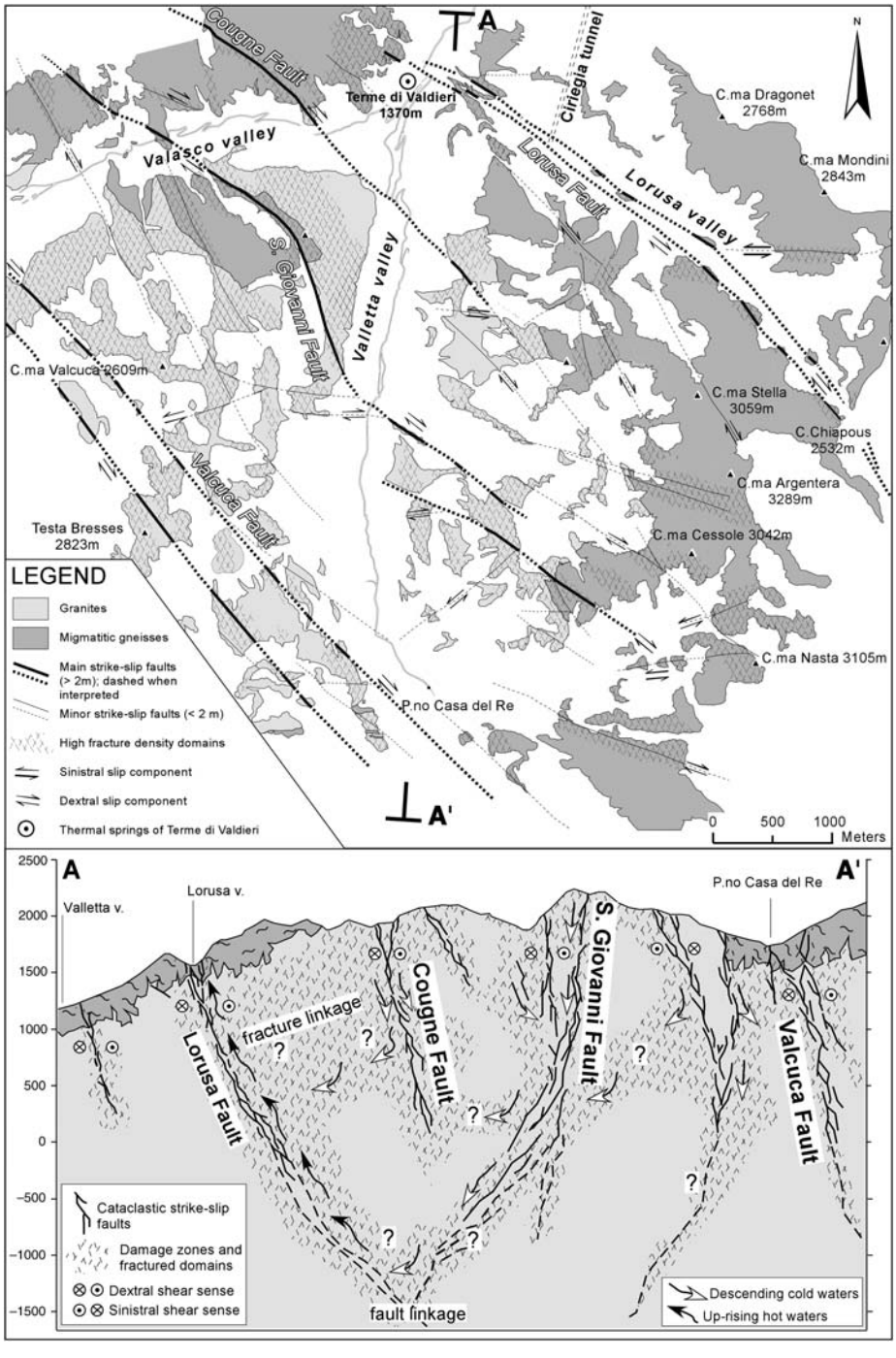

Fig. 2. Structural map (upper part, **a**) of the area surrounding the Terme di Valdieri springs. This area is pervasively cut by NW–SE strike–slip faults with right-lateral slip components and by subsidiary ENE–WSW striking faults with left-lateral slip. The Valdieri springs emerge through the damage zone at the northwestern tip of the Lorusa fault, a 7 km long NW–SE strike–slip fault characterized by a cataclastic core and fractured damage zones. A cross-section (lower part, **b**) along the A–A′ trace shows possible patterns of hydrothermal circulation. The occurrence of fault and fracture linkages can influence the descent of cold waters and the upwelling of hot waters.

geometry. Kinematic evidence associated with these faults indicates that this sector can be interpreted as a flower structure that developed in a context of right-lateral transpressive displacement (Baietto 2007). The faults probably converge at depth into a single shear zone, as suggested by existing flower structure models (Woodcock & Fischer 1986).

As for the Valdieri hot springs, it seems that an important role in hot-water outflow could be played by the particular geometrical configuration defined by the Lorusa and Cougne faults. The tip-line of the Lorusa Fault lies close (*c*. 2 km) to the inferred tip-line of the Cougne Fault. At the local scale, these two structures define a right-contractional step which corresponds to an area of intense fracturing which coincides with the thermal discharges of Valdieri.

As a consequence of different concentrations of oriented phyllosilicates, brittle deformation associated with the faults in the migmatitic gneisses and in the granites resulted in different fault architectures. The structure of the strike–slip faults which developed within the migmatitic gneisses is characterized, moving from the inner to the outer part of the fault zone, by a narrow phyllonitic gouge zone (where most of the slip is accommodated), by an intermediate zone of foliated cataclasites, and by an outer domain of highly fractured rocks. The gouge, cataclasite and fractured zones have thicknesses, respectively, of 0.1–2, 0.5–5 and 1–10 m. In contrast, within the granites, brittle deformation is accommodated by several discrete shear planes composing a pervasive network of fractures broadly distributed over the mapped area (Fig. 2b). These planes, which are concentrated in domains hundreds of metres thick, have fracture spacings ranging from a few centimetres to a metre and an aperture of a few millimetres. At various spacings, these domains enclose NW–SE-trending metre-width cataclastic zones.

Conceptual models of thermal circulation

Conceptual models of the groundwater flow system were arrived at by studying the physical and chemical properties of the hot springs and the geometrical and hydraulic characteristics of the fault zones in the Terme di Valdieri sector. These models constituted the basis for constructing numerical models that were then tested against data and used to assess the possible hydrodynamic properties of the Terme di Valdieri system. The Valdieri springs have a maximum outlet temperature of 70 °C (Baietto 2007). Mass balance calculations performed on the water temperatures and flow rates of the Valletta River provided an estimate of the bulk thermal discharge of *c*. 50 kg s^{-1}. The thermal waters have pH values of 9 and salinities of 0.2–0.4 g l^{-1}. Analyses of stable isotopes indicate a pure meteoric origin and, according to geothermometric calculations, the meteoric waters equilibrated at temperatures between 90 and 150 °C with hydrothermal minerals (Perello 1997; Perello *et al.* 2001; Baietto 2007). A temperature of 150 °C corresponds to depths of 5–6 km, assuming a geothermal gradient of 30 or 25 °C km^{-1} respectively, which are typical for the western Alps (Jaboyedoff 1999).

The meteoric origin of the fluids and mountainous setting of the Argentera Massif suggest that the process driving the Valdieri thermal flow is primarily controlled by advective flow related to differences in topographic elevation. The Valdieri springs are located at 1370 m, while adjoining summits reach 3000 m and have a mean elevation of 2600 m. However, two other processes might potentially influence the bulk geothermal system: thermal convection and pressure-driven flow after faulting. Thermal convection is created by fluid density gradients associated with changes in temperature, salinity and pressure (Evans & Raffensperger 1992). In their numerical simulations, Forster & Smith (1989) and López & Smith (1995) investigated the role played by factors such as fault and host rock permeability, regional heat flux, fault length and depth, relief, and geometry of the water table in influencing advective as opposed to convective heat transfer regimes within faults in mountainous regions. Up to now, it has not been clear to what extent the thermal flow is governed by regional topographic gradients or by thermal convection along the strike of the Valdieri faults. Numerical modelling is therefore used here to highlight the conditions which can favour the occurrence of these processes.

Pressure-driven flow after faulting can also control the hydrodynamics of faulted systems (Neuzil 1995; Faulkner & Rutter 2001; Garven *et al.* 2001). This process may result from the combination of conditions leading to fluid overpressures (e.g., decrease of porosity or increase of fluid volume over time) and tectonic loads (Bredehoeft & Hanshaw 1968). Earthquakes and swarm activity can account for fluid redistribution in response to the local generation of overpressure through fault-fracture meshes, but the level of overpressure that can accumulate depends on the tectonic setting, the localized stress state, and the extent of inherited brittle architecture (Sibson & Scott 1998). In the present case, despite the fact that the Argentera Massif is located in one of the most seismically active parts of the Alpine range (Calais *et al.* 2000), the largest instrumental earthquakes recorded in recent years occurred along the northern

margin of the Ligurian basin, south of the massif ($M_L = 6.0$, 1989; $M_L = 4.5$, 1995; Ritz 1991; Courboulex *et al.* 1998). Within the Argentera Massif, the Valletta Shear Zone was proposed as the locus of two relevant earthquakes in 1938 ($M_L = 5.1$) and 1959 ($M_L = 5.3$; Ghafiri 1995), but the last 50 years have been characterized only by low-magnitude earthquakes ($M_L < 3$; RSNI database). Owing to the low intensity of recent seismicity affecting the Argentera Massif (Larroque *et al.* 2001), and to the fact that transient effects associated with fault rupture in the crystalline basement are thought to vanish rapidly (Phillips 1991), it is reasonable to exclude the hypothesis that mechanisms such as pressure-driven flow after faulting can substantially influence the hydrodynamic behaviour of the Valdieri thermal system. For these reasons, this process is not considered in the simulations.

The definition of the geometries and structural architectures of fault zones by means of detailed field investigations has not been able to resolve the thermal circulation in the Valdieri area. The scant hydrogeological data available for this area are consistent with a range of alternative hypotheses concerning fluid and heat flow patterns. In the final part of its pathway, the thermal flow is confined to the borders of the Lorusa Fault, located in the shallower part within the gneisses and in the deeper part within the granites (Fig. 2b). The core zone of this fault constitutes an impermeable barrier to cross-flow circulation, allowing upward fluid flow and discharge at the Terme di Valdieri site. At *c*. 1 km east and at an altitude of 100 m below the Valdieri hot springs, the Lorusa Fault is intersected by the Ciriegia exploration tunnel (Fig. 2a). At this point, the reported inflows were 20 kg s^{-1} at a temperature of 20 °C, which is indicative of an apparent geothermal gradient of 20 °C km^{-1} (Bortolami & Grasso 1969) that can be attributed to downflowing cold waters. Data relative to the tunnel compared with those of the thermal springs help to define a scenario in which the hot waters of Valdieri ascend vertically close to the tip of the Lorusa Fault and concentrate a hot anomaly in the neighbourhood of the spring discharges without affecting the rest of the zone. However, whether the final part of the thermal water flow is reasonably well constrained, where cold waters penetrate and circulate, remains unknown. A crucial factor not yet revealed by field surveys is the degree of hydraulic connectivity among the different faults. This uncertainty involves the possibility either that the Lorusa Fault crosscuts other fault zones at depth, or that regions of enhanced permeability connect the Lorusa Fault with other permeable fault zones. Based on field evidence, three main conceptual models involving different fluid flow patterns are proposed as alternative descriptions of the Terme di Valdieri circulation. These include a single conduit model (model 1), a fault intersection model (model 2) and a fault interaction model (model 3).

In model 1, the thermal flow is focused within the Lorusa Fault, which acts as a single permeable channel allowing infiltration of cold waters, circulation and upward migration of heated waters towards the surface. Depending on the relative permeability of the Lorusa Fault and host rocks, either the damage zone of the Lorusa Fault may constitute the region where most of the fluids circulate and where heat transfer processes occur, or the thermal flow may be pervasively distributed through permeable fracture networks within the granites surrounding the fault. In the latter case, fluids would infiltrate pervasively through fracture networks (fracture linkage; cf. Fig. 2b) developed within the granites and migrate in tortuous pathways towards the Lorusa Fault, where they would focus and emerge at the springs. In models 2 and 3, the thermal flow is partitioned between several conduits corresponding to the borders of main NW–SE striking faults. In this case (cf. Fig 2b), additional amounts of heated waters may be driven to the Lorusa Fault, either by the intersection of this structure with the S. Giovanni Fault, or by the interaction generated by the Lorusa Fault with the Cougne Fault. In model 2, the Lorusa and S. Giovanni Faults crosscut at depth and both constitute permeable channels where fluids infiltrate. Under the influence of pressure gradients, meteoric waters are driven at depth toward the Lorusa Fault and then up to the Terme di Valdieri springs. In model 3, it is assumed that the zone of intense fracturing observed between the Lorusa and Cougne Faults which corresponds to a contractional step constitutes a permeable bridge interconnecting the thermal circulations that occur within the two faults.

Methodology and boundary conditions of numerical models

The alternative hydrogeological hypotheses proposed for the Valdieri geothermal system were investigated using 3D thermo-hydraulic numerical simulations. These were carried out by integrating increasing degrees of geometrical complexity into a base model, thus finally allowing the different thermal flow hypotheses to be compared. The use of 3D rather than 2D modelling allowed the authors to account more fully for the lateral thermal effects of the geothermal system under study, thus providing a more realistic representation of the heat flow field through the area. The hypotheses concerning thermal flow were investigated

through the three discretization geometries illustrated in Fig. 3. These include a base model where only the Lorusa Fault is taken into account (model 1; Fig. 3a & b), a model where the Lorusa Fault is crosscut at depth by the S. Giovanni Fault (model 2; Fig. 3c), and a model where the Lorusa Fault is in hydraulic connection with the Cougne Fault through a permeable jog (model 3; Fig. 3d). The location of the hot springs is shown in Figure 3a. In the base discretization geometry, the Lorusa Fault is represented by a vertical slab 200 m wide and 7 km long, which is enclosed within a block of host rocks 9.4 km long and 5 km wide. The length of this model was fixed to the SE by the southern tip of the fault and to the NW by the mountain ridge, while its width was varied according to the hypothesis under test. In model 1, the width is 5 km and is constrained to the NE by the Cougne Fault, which in this case is considered as not contributing to the active thermal flow. In model 2, the width is 7.5 km and the NE limit corresponds to the outer border of the S. Giovanni fault. In model 3, the width is 5 km (as for model 1) and the NE limit is marked by the Cougne Fault, which in this case is considered as being involved in the thermal flow. The maximum thickness of the three blocks modeled is fixed at 5.5 km, assuming that this value represents the approximate depth at which thermal water equilibration occurs (*c*. 150 °C, if a gradient of 30 °C km^{-1} is

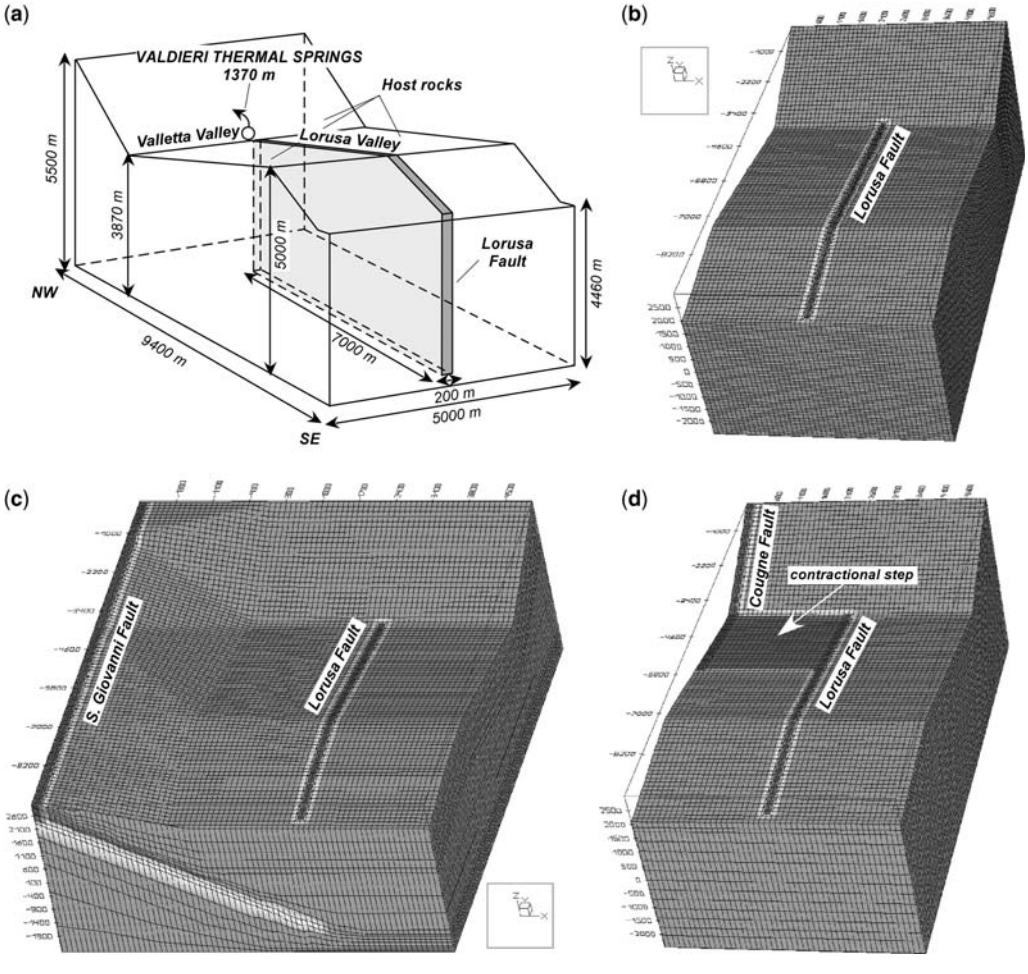

Fig. 3. 3D geometry and dimensions used for the numerical simulations. (**a**) Dimensions of the base geometry of model 1. A vertical fault plane, 200 m wide and 7 km long, representing the damage zone of the Lorusa Fault, is enclosed within a block of host rocks. The maximum thickness of the modeled block is fixed at 5.5 km, assuming that this value represents approximately the depth at which thermal water equilibration occurs. Discretized elements of model 1 (**b**), model 2 (**c**) and model 3 (**d**) are shown.

assumed; Perello *et al.* 2001). In all the geometries, the elements are composed of cubic cells with a horizontal size of 100 × 100 m within the protolith rocks. To provide sufficient resolution of both thermal and flow regimes along the faults, the cell size is halved (50 × 50 m) in those areas. The computer software used to perform the simulations is the three-dimensional Galerkin finite-element program, FeFlow® 5.1 (Diersch 1998).

The simulation results were calibrated by comparing the numerical outputs with spring temperatures of 70 °C and flow rates of 50 kg s^{-1} (*c.* 4320 m^3/day). As an additional condition, it was sought to achieve a close fit between the simulated temperatures and the 20 °C reading that was taken within the Ciriegia tunnel connected to the Lorusa Fault. It must be emphasized that after the drilling of the tunnel in 1960, no significant perturbation was recorded in subsequent years at the springs. Tests on the sensitivity of the thermal flow system to the presence of the tunnel were carried out for all three model geometries by introducing in an appropriate location a fluid sink of 15 kg s^{-1} for a time span of 100 years. In all models tested, the presence of the tunnel itself did not cause any significant perturbation to the thermal circulation (*c.* 1 °C variation at the springs), so this factor was not considered further in the simulations.

In general, modelling was performed in two stages: (1) thermo-hydraulic simulations were first carried out in a steady-state regime; (2) these results were then taken as initial conditions for a coupled fluid flow and heat transport simulation in a transient regime. This procedure implicitly assumes that a circulation system was already active and that it accounted for a steady-state pressure–temperature distribution. Despite considerable uncertainty regarding this assumption, adopting initial steady-state conditions is a convenient approach that allows comparison of the temporal responses of the thermal circulation in the different systems modelled (cf. also McKenna & Blackwell 2004). Three-dimensional computations, especially those performed in transient regimes, are time-consuming. A simulation timespan of 10 000 years was chosen as it allowed a relatively high number (*c.* 100) of tests on transient-regime models to be performed.

The thermo-hydraulic behaviour of fault-related geothermal systems is commonly affected by processes that can involve either an increase or a decrease in fault permeability (Parry 1998) or the creation of fluid density and viscosity dependencies on temperature and salinity (Simms & Garven 2004). These processes result in changes to the groundwater flow patterns over time. Therefore, transient-regime as opposed to steady-state simulations provide, in principle, better approximations of thermal flow systems. To understand fully how temporal variations in permeability occur within a thermal system, a good characterization of the processes underlying these variations should first be attempted.

Microstructural observations suggest that the Lorusa Fault has been affected by repeated episodes of cataclasis, fluid influx and cementation, reflecting cycles of permeability increase and decrease (Baietto 2007). However, the kinetics of crack sealing with respect to the rate of geodynamic processes occurring in the Valdieri sector are unknown. The assessment of these parameters would require modelling of the sensitivity of crack sealing to various parameters, as performed by Gratier *et al.* (2003), but this exercise is beyond the scope of the present study. Instead, permeability was assumed to be constant over time, and transient-regime simulations were performed by solving coupled fluid and heat flow equations, which in turn permitted verification of the natural conditions giving rise to thermal convection. The mass conservation equation for the fluid phase is

$$\frac{\partial(\phi\rho)}{\partial t} + \nabla \cdot \rho\mathbf{q} = 0 \tag{1}$$

where ϕ is the porosity of the medium (dimensionless), ρ is the fluid density (kg m^{-3}), ∇ is the divergence operator and $\mathbf{q}$ is the flux vector (m s^{-1}). The latter quantity obeys Darcy's law,

$$\mathbf{q} = -\frac{\mathbf{k}}{\mu}(\nabla p + \rho\mathbf{g}) \tag{2}$$

where $\mathbf{k}$ is the permeability tensor of the medium (m^2), $\mathbf{g}$ is the acceleration due to gravity (m s^{-2}), μ the dynamic fluid viscosity (kg $m^{-1}s^{-1}$), and p the pore pressure (N m^{-2}). In the context of coupled flow and heat transport processes, both fluid density and viscosity vary with temperature T according to the appropriate constitutive laws $\rho = \rho(T)$ and $\mu = \mu(T)$ as given in equation (4). The conservation equation for advective–dispersive–diffusive transport of thermal energy is

$$[\phi(\rho c)\mathrm{l} + (1-\phi)(\rho c)\mathrm{s}]\frac{\partial T}{\partial t} + (\rho c)\mathrm{l}\mathbf{q} \cdot \nabla T = \nabla \cdot [\phi\Lambda\mathrm{l} + (1-\phi)\lambda\mathrm{s}\mathrm{I}]\nabla T \tag{3}$$

where (ρc)l and (ρc)s are the volumetric heat capacities (J m^{-3} K^{-1}) of the liquid and solid phases, respectively. In equation (3), $\lambda s\mathbf{I}$ (J $m^{-1}s^{-1}$ K^{-1}) is the thermal conduction tensor of the solid phase (assumed isotropic), and

Λl ($\mathrm{J\,m^{-1}s^{-1}\,K^{-1}}$) the hydrodynamic thermal dispersion tensor of the fluid phase. Equations (1) and (2) can be further developed to yield a governing flow equation in terms of pore pressure. Introducing the arbitrary temperature T_0, at which $\rho_0 = \rho$ ($\mathrm{T_0}$) and $\mu_0 = \mu$ (T_0), Darcy's law in equation (2) can be re-written as

$$\mathbf{q} = -\frac{\mathbf{k}\rho_0 g}{\mu_0}\frac{\mu_0}{\mu}\left(\nabla\frac{p}{\rho_0 g} + \frac{\rho}{\rho_0}\nabla z\right) = -\mathbf{K}_0\frac{\mu_0}{\mu}\left(\nabla H_0 + \frac{(\rho-\rho_0)}{\rho_0}\nabla z\right) \qquad (4)$$

where $\mathbf{K}_0 = \mathbf{k}\rho_0 g/\mu_0$ ($\mathrm{m\,s^{-1}}$) is the hydraulic conductivity tensor at $T = T_0$ and $H_0 = \mathrm{p}/\rho_0 g + z(\mathrm{m})$ is a notional hydraulic head, also at T_0. To allow the use of more conventional hydrogeological parameters such as hydraulic conductivity and specific storage, the equivalent hydraulic head formulation in equation (4) is used in this paper. The only coupling laws considered are temperature-dependent functions for both fluid viscosity and density. Fluid salinity is not considered owing to the low salinity of the Valdieri waters ($<0.4\ \mathrm{g\,l^{-1}}$; Perello *et al.* 2001). To compute the fluid viscosity, a polynomial expression for the hydraulic conductivity correction factor, μ_0/μ, derived from Mercer & Pinder (1974) is introduced in equation (4). To express the variation of fluid density with temperature, a conventional form is: $\rho(T) = \rho_0[1 - \beta(T)(T-T_0)]$, where $\beta(K^{-1})$ is the volumetric thermal fluid expansion coefficient and ρ_0 the reference fluid density. In a geothermal context where large temperature variations can be expected and buoyancy forces dominate, β varies widely. In the present simulation, a calculation of a non-linear temperature-dependent expansion coefficient β is included, based on the physically 'exact' fluid density curve measured in the range 0–100 °C (Perrochet & Tacher 1997). The temperature and pressure fields obtained from steady-state simulations are used with the boundary conditions to solve equations (3) and (4) simultaneously. In the calculations, the so-called 'Boussinesq approximation' is adopted as usual for most density-dependent transport phenomena (Bird *et al.* 1960). This allows a simplification of the coupled nonlinear systems of mass and energy balance equations, but without the elimination of intrinsic coupling mechanisms which are significant for thermal convection. Automatic time-step control was carried out by the Adams–Brashfort/Trapezoidal-rule predictor–corrector scheme. Sequential Picard iteration between flow and heat transport is used to accommodate the nonlinearities resulting from variable-density flow.

A description of flow through fractured systems would require exact information about each individual fracture, which in practice is almost never available. Hence, in practice such environments can be only described in terms of *equivalent porous media*. This type of assumption was adopted here and is widely employed when simulating faulted systems (e.g., Garven *et al.* 2001; Simms & Garven 2004; Wisian & Blackwell 2004; McKenna & Blackwell 2004). Simulation parameters used in this work are shown in Table 1; note that the term 'fault' is used for all faults that are taken into account in each of the model geometries considered, including the jog in model 3. Many of these parameters and boundary conditions were based by necessity on generalized assumptions and simplifications. Sensitivity studies were used mainly to determine the effect on the hot-spring response of varying the fault and host rock permeability, but sensitivity tests were also carried out on some other parameters, such as basal heat flux, host rock porosity and infiltration rates, as described later in this paper.

Table 1. *Typical simulation parameters used in the three geometries modelled*

Parameter	Value
Fault permeability	1×10^{-12} to 1×10^{-15} $\mathrm{m^2}$
Host rock permeability	1×10^{-13} to 1×10^{-18} $\mathrm{m^2}$
Fault porosity	0.1
Host rock porosity	0.01–0.1
Solid thermal conductivity	3.0 $\mathrm{J\,m^{-1}\,K^{-1}\,s^{-1}}$
Solid thermal capacity	2.28×10^{6} $\mathrm{J\,m^{-3}\,K^{-1}}$
Fault infiltration rate	1.7×10^{-4} m/day
Host rock infiltration rate	1.7×10^{-5} m/day
Basal heat flow	80–100 $\mathrm{mW\,m^{-2}}$
Altitudinal temperature gradient	0.004 °C $\mathrm{m^{-1}}$
Heat production	2.5μW $\mathrm{m^{-3}}$
Longitudinal thermal dispersivity	10
Transverse thermal dispersivity	100

Permeabilities in the range of 10^{-18}–10^{-12} m^2 were used in these simulations because these values can be considered as representative of most rocks of the upper continental crust (Manning & Ingebritsen 1999). To reproduce the tendency of the Valdieri faults to act as partial barriers to fluid crossflow (Baietto 2007), these faults were assigned one order of difference in magnitude between the permeability oriented parallel to the fault and the permeability oriented normal to the fault surface. The permeability of both faults and host rocks is assumed to be isotropic along the vertical direction. More likely situations in which bulk rock permeability decreases with depth (e.g., exponentially, cf. Ingebritsen and Manning 1999) will be investigated in subsequent modelling. A constant and isotropic thermal conductivity of 3.0 W m^{-1} K^{-1} was applied to the bulk of the modelled block, because this is representative for granitic rocks (Chapman & Furlong 1992). The heat capacity of the modelled rock mass was set to 2.28×10^6 J m^{-3} K^{-1} and the heat production to 2.5 μW m^{-3}, which are typical values for a granitic crust (Rybach 1981). Porosity was set at 0.1 through the fault zone, while in the host rocks it was varied from 0.01 to 0.1, which is a representative range for moderately to intensely fractured crystalline rocks (Brace *et al.* 1966). The conductivity, diffusivity, density and heat capacity (solid and fluid) are kept constant over time and are assumed to be independent of temperature.

Concerning the hydraulic boundary conditions, the lateral boundaries of the three models were set as impermeable to fluid and heat flow. In all models, a free-surface computation has been applied to the upper topographic boundary. This approach provides an appropriate condition to reproduce reasonable recharge patterns through the system (Forster & Smith 1989). The FeFlow software provides an advanced method which is based on 3D moving meshes, allowing for more accurate and rigorous modelling of heat processing compared with a computation based on fixed grids (Diersch 1998). Even if the recharge rates in the Terme di Valdieri zone are unknown, this approach enables constraint of the water table by incorporating the imposed infiltration rates into the computations. In all models, a hydraulic head corresponding to an altitude of 1370 m was imposed at the lowermost part of the topographic surface to reproduce the river running through the Valletta valley. On the rest of the upper boundary, infiltration rates of 1.7×10^{-4} and of 1.7×10^{-5} m/day were assigned at the surface of faults and of host rocks respectively. These values were selected after estimation procedures based on average rainfall in the Valdieri area (about 1400 mm a^{-1}; Regione Piemonte database) and on preliminary sensitivity tests aimed at evaluating the consistency of the fluid pressure field with respect to the Ciriegia tunnel. Furthermore, these conditions are also consistent with the infiltration rates that Forster & Smith (1989) used in their models to simulate the groundwater flow in a mountainous setting similar to that of Terme di Valdieri. However, since these infiltration values are based only on indirect evaluations, the sensitivity of these values to changes of up to an order of magnitude was analysed and is discussed below.

A Cauchy-type temperature condition controlled by heat transfer coefficients is imposed along the fault trace and at the valley bottom (1370 m). This condition allows for the continuity of the heat flux across the boundary and control of surface temperatures by rising groundwater. On the upper surface of the host rocks, temperatures are fixed according to an altitudinal gradient of 0.004 °C m^{-1}. The Valdieri station has a reference mean temperature of 7 °C. Basal heat flows (BHF) of 80 and 100 mW m^{-2} were imposed at the lowest altitude of the models. These values seem appropriate for the region of Valdieri, where high exhumation rates (*c.* 1.3 mm a^{-1}) have been recorded for the past 3.5 Ma (Bigot-Cormier *et al.* 2000). Jaboyedoff & Pastorelli (2003) estimated that regions undergoing exhumation at rates of 1 mm a^{-1} can have heat flow densities on the order of the values here attributed to Valdieri.

Model 1: single-conduit v. fracture network model

In this model, the Lorusa Fault is assumed to constitute the main channel for fluid flow. Accordingly, a focused flow occurs if most of the fluid flows through this fault and a negligible contribution comes from the surroundings (i.e., the single-conduit model). Conversely, fluid flows pervasively if the permeability of the fractured host rocks is sufficiently high to allow advection from the surroundings. In this case, the circulation in the Lorusa Fault can result from the combination of fluids infiltrating directly from the fault surface and fluids migrating in from the fault zone wallrocks (i.e., the fracture network model). As can be deduced from Figure 3a, the amount of fluid flow directed towards the Lorusa Fault from the host rock depends both on the capability of the fault to draw fluids and of the host rocks to allow fluids to circulate. In other words, focused as opposed to pervasive flows are expected to occur as the result of different host rock and fault equivalent permeabilities. Sets of steady-state and transient-regime simulations are performed here

to investigate dependencies among specific heat and fluid flow regimes on different fault and host rock permeabilities.

Steady-state simulation

Figure 4a & b shows contours in permeability space of the percentages of fluid and heat fluxes discharging at springs, compared respectively with the total fluid fluxes penetrating across the topographic surface and with the heat fluxes imposed at the base of the model. These diagrams provide a first approximation to constraints on the sensitivity of spring temperatures and discharges to fault permeability (k_f) and host rock permeability (k_{hr}). Since the contours express relative percentages, Fig. 4a & b holds true for BHF values of both 80 and 100 mW m^{-2}. Figure 4a shows evidence of the dependency of the proportion of total fluid discharged at the spring on the host rock permeability. For $k_{hr} = 1 \times 10^{-16}$ m^2, the fluid discharge exceeds 90% of total mass, whereas for permeabilities lower than 1×10^{-16} m^2, the amount of fluid discharged decreases to values of 30–40% of total mass. This variation is related both to the limited fluid recharge capacity of the host rock – because infiltration is constrained by hydraulic head – and to the fact that as the water table rises, increasing amounts of fluid flow out of the system instead of reaching the springs. For values of k_{hr} higher than 1×10^{-16} m^2, owing to the reduced permeability difference between the host rock and the fault, the draining effect of the fault decreases, with a consequent decrease in the amount of fluid upwelling at the springs. Conversely, discharge rates are less affected by k_f. This can be explained by the fact that the infiltrations imposed at the fault surface percolate within the fault, with relatively little dispersion into the surroundings. At values of k_f lower than 5×10^{-14} m^2, the fluid discharge is reduced because of the decreased drainage capacity of the fault. In terms of absolute fluid rate, a discharge peak of 1205 m^3/day is reached at $k_{hr} = 1 \times 10^{-16}$ m^2 and $k_f = 1 \times 10^{-12}$ m^2, with 80% of the fluid supply derived from the host rock. However, this is about 3.6 times less than the expected rate for the Valdieri springs, and thus this condition does not provide the required quality of fit.

The contours shown in Figure 4b indicate that the percentage of heat discharged at the springs depends both on the host rock and on the fault zone permeability. The maximum percentage of heat reaching the springs exceeds 50% of the total available heat in the permeability range 3×10^{-17} to 3×10^{-16} m^2, for the host rock, and 2×10^{-13} to 8×10^{-13} m^2, for the fault itself. Compared with the contour distribution of the fluid discharges, a more restricted k_f range is required in order to achieve a heat flux peak of waters released at the spring. In fact, at lower fault and host rock permeabilities, fluid flow to the fault is limited, and a greater proportion of basal heat flow is transferred by conduction to the surrounding rock, while at higher fault and host rock permeabilities, the amount of discharged heat is less because a larger volumetric flux stores most of the thermal energy imposed at the base of the system. Within the

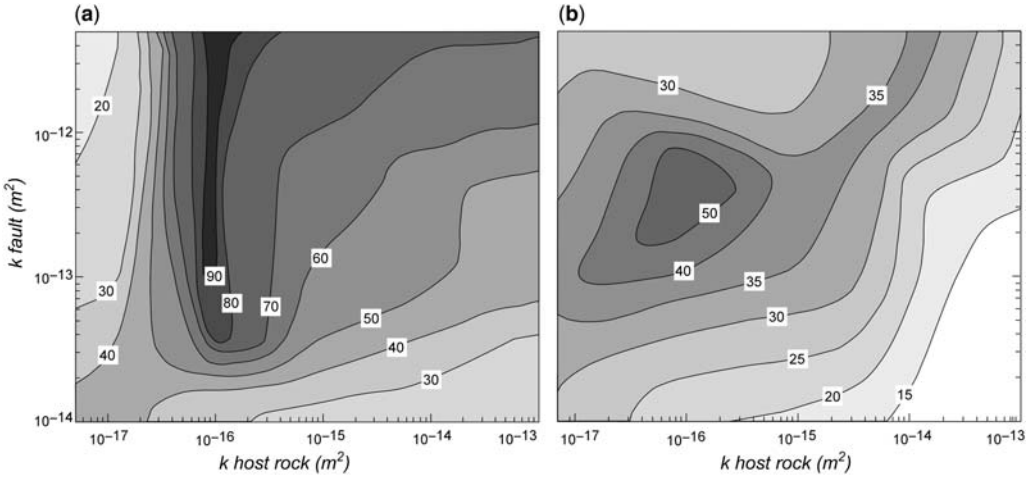

Fig. 4. Results of steady-state simulations using model 1. (**a**) Contours indicating the percentage of fluid flux discharging at the springs relative to the infiltration rates imposed on the upper (topographic) boundary of the system. (**b**) Contours indicating the percentage of heat flux discharging at the springs relative to the bulk heat flux imposed on the system. Plots are expressed on a logarithmic scale as a function of the fault and host rock permeabilities.

50% contour, at a BHF of 80 mW m^{-2}, the peak water temperature is 52 °C, while at 100 mW m^{-2}, the peak temperature increases to 62 °C.

Figure 5a illustrates the distribution of isotherms across the fault profile obtained with a BHF of 80 mW m^{-2}, $k_f = 2 \times 10^{-13}$ m^2 and $k_{hr} = 1 \times 10^{-16}$ m^2. At the fault base, the steady-state solution indicates that temperatures are approximately 130 °C, with a maximum ΔT of 15 °C with respect to the surrounding rocks. Under the same conditions, and with a heat flux of 100 mW m^{-2}, the temperature at the fault base increases to 160 °C (Fig. 5b). The latter result gives a thermal distribution through the fault which is reasonably consistent with the temperature of 150 °C that was estimated for the base of the reservoir, and with the 20 °C encountered within the Ciriegia tunnel. However, the steady-state solutions predict spring discharges that are not consistent with the measured spring rates. Since the imposed calibration procedure requires a simultaneous fit of both discharge rates and temperatures with those measured at the springs (i.e., $T = 70$ °C; $Q = 4320$ m^3/day), the hydraulic and thermal numerical results cannot be improved independently simply by increasing or decreasing the rate of fluid penetration through the system. For instance, if the infiltration rates are increased by one order of magnitude (i.e., 1×10^{-4} and 1×10^{-3} m/day, respectively, on top of the host rocks and in the fault), the expected value of 4320 m^3/day can be attained at the springs (for $k_f = 2 \times 10^{-13}$ m^2 and $k_{hr} = 1 \times 10^{-16}$ m^2). However, in this case the outlet spring temperatures would be too low, reaching only 40 and 51 °C respectively for BHF of 80 and 100 mW m^{-2}. In addition, in both cases, the isotherms would remain excessively depressed by comparison with the temperatures found in the Ciriegia tunnel and the temperatures expected at the base of the system.

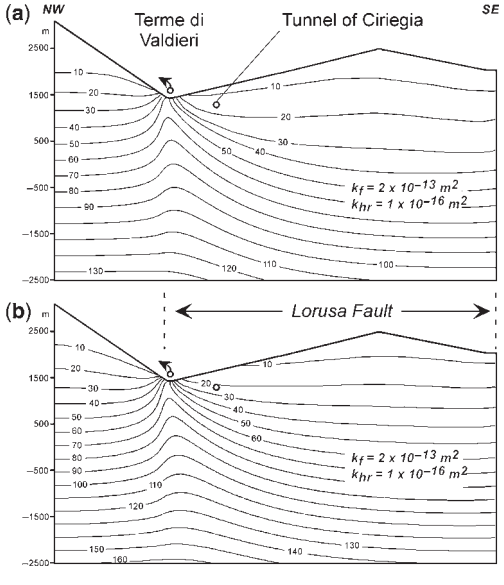

Fig. 5. Steady-state distribution of isotherms across the fault profile obtained for permeabilities of 2×10^{-13} and 1×10^{-16} m^2 of the fault (k_f) and host rock (k_{hr}), respectively. Isotherm distribution obtained with a basal heat flow of 80 (**a**) and 100 mW m^{-2} (**b**).

Transient-regime simulation

The transient-regime simulations show that, at sufficiently high fault permeabilities, convective circulation can occur in the Lorusa Fault. Similarly to the results shown in Figure 4b, the transient results are examined using as a reference the contours in permeability space of the heat flux percentages discharging at the spring site with respect to the total heat fluxes imposed on the models. Figure 6a–6d shows the contours for simulation times of 10, 100, 1000 and 10 000 years, respectively, at a BHF of 80 mW m^{-2} (solutions with a BHF of 100 m W m^{-2} are discussed later). After 10 years (Fig. 6a) from circulation onset, the heat flux distribution in the permeability space changes noticeably compared with the steady-state distribution, with a proportion of heat delivered at springs as high as 20% of the applied heat. The region where this peak occurs is between fault permeabilities of 7×10^{-14} and 3×10^{-14} m^2 and host rock permeabilities of 2×10^{-16} and 1×10^{-16} m^2, indicating that the peak region has both been restrained and has shifted toward lower permeabilities in the fault zone. The shift in position and magnitude of the heat flux peak within the permeability field reflects the perturbation recorded by the steady-state flow system owing to the introduction of temperature dependencies on density and viscosity. After 100 years (Fig. 6b), the heat flux peak records a further decrease in magnitude (max. 14%) and a further shift in spatial permeability distribution. However, it should be noted that, for k_f higher than 5×10^{-13} m^2, increasing amounts of groundwater are discharged at the springs. A peak of discharged heat (33%) occurs at $k_f = 1 \times 10^{-12}$ m^2 and $k_{hr} = 2 \times 10^{-17}$ m^2. For k_{hr} higher then 3×10^{-16} m^2, the heat discharge decreases because of a greater proportion of cold shallow waters flowing in from the host rock towards the fault and then upwelling at the springs. After 1000 years (Fig. 6c), the peak region broadens and the contour distribution indicates a dependency of heat discharge maxima on fault permeability. Amounts exceeding 80% of the imposed heat flux are obtained for a

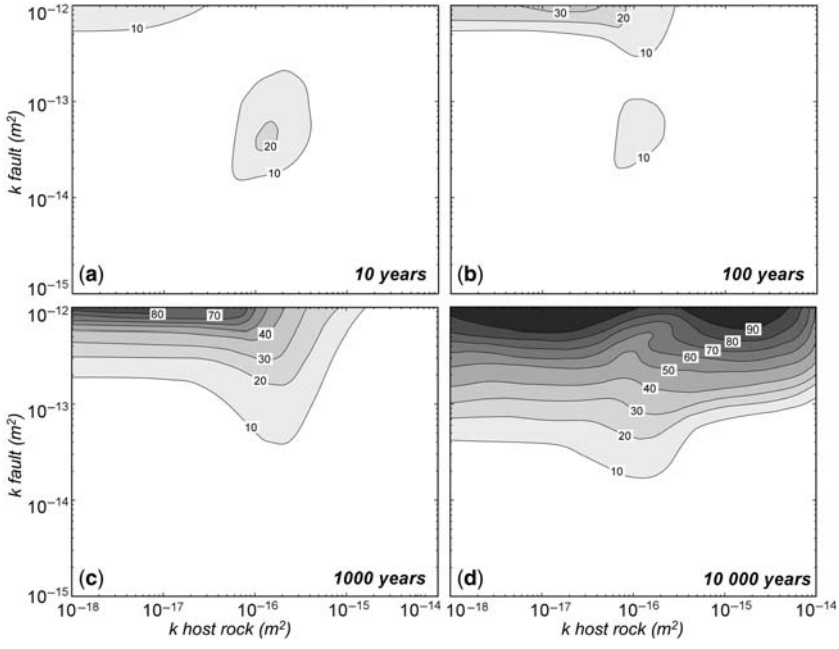

Fig. 6. Transient-regime results for model 1, plotted in permeability space. The contours represent the heat flux percentages discharging at the spring site with respect to the total heat fluxes imposed on the models after (**a**) 10, (**b**) 100, (**c**) 1000 and (**d**) 10 000 years since circulation onset.

$k_f = 1 \times 10^{-12}$ m^2, while the positive peak can be rapidly decreased by 10% if the permeability is decreased by an order of magnitude. Increased effects of discharged heat occur for k_{hr} in the range of 4×10^{-16} and 5×10^{-17} m^2, due to the enhanced capability of the host rocks to convey, at these permeabilities, a large amount of heated fluids along the fault plane. After 10 000 years (Fig. 6d), the region containing peaks of heat discharges further broadens towards lower fault permeabilities, and the proportion of discharged heat increases compared with previous stages.

These results were also analysed to estimate the influence of the fault and host rock permeability on the types of fluid flow and heat transfer regimes that occur within the geothermal system. Figure 7 shows the regions in the permeability field where advection, conduction and convection are the dominant processes within the fault and host rocks at BHF values of 80 and 100 mW m^{-2}. The transition between an advective regime and a convective regime was identified by completing a series of simulations at constant host rock permeability and variable fault permeabilities. For BHF values of 80 and 100 mW m^{-2}, conduction is the predominant heat transfer process within the host rocks

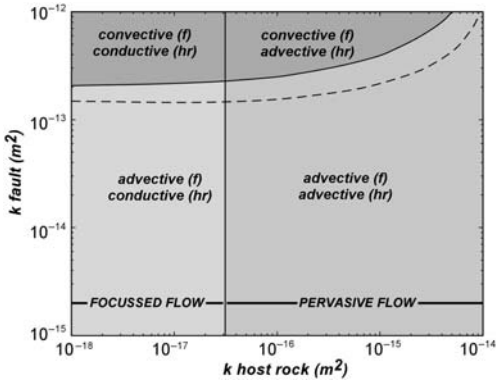

Fig. 7. Thermal regimes of the fault (f) and of the host rocks (hr) plotted in permeability space for model 1. At permeability less than 3×10^{-17} m^2, the host rocks transfer the heat by conduction and the thermal circulation is mainly focused within the damage zone of the Lorusa Fault. Above this value, the thermal circulation results from a combination of focused flow within the fault and pervasive flow through fractures within the host rocks. The region where thermal convection occurs within the fault zone is represented in dark grey (BHF = 80 mW m^{-2}). The dotted line represents the boundary of this field for a BHF = 100 mW m^{-2}.

only at permeabilities lower than 3×10^{-17} m^2, while at higher values, advection becomes the dominant process. This makes it possible to distinguish between two fields where the fractures within the host rock are, or are not, hydraulically connected. At permeability values below 3×10^{-17}m^2, heat is transferred predominantly by conduction as most fractures are not connected, while above this value, advection prevails, reflecting the fact that the fractures have attained a percolation threshold so that pervasive flow occurs. In this regime, the proportion of fluids flowing from the host rocks to the fault plane and finally discharged at the springs becomes a function of the fault drainage capability. For example, this capability was estimated by comparing the total cumulative amount of spring discharges during 10 000 years of thermal activity for a fixed k_{hr} of 1×10^{-16} m^2 and a variable k_f in the range from 5×10^{-15} to 5×10^{-13} m^2. At $k_f = 5 \times 10^{-15}$ m^2 the drainage is negligible; at $k_f = 5 \times 10^{-14}$ m^2 the fault draws 27% of the fluid mass circulating in the surrounding country rock; this percentage increases to 57 and 71% if the k_f is increased to 1×10^{-13} and 5×10^{-13} m^2, respectively. Accordingly, the maximum distance of drainage from the fault increases from 1100 m ($k_f = 5 \times 10^{-14}$ m^2) to 1500 m ($k_f = 1 \times 10^{-13}$ m^2) and to 2100 m (5×10^{-13} m^2).

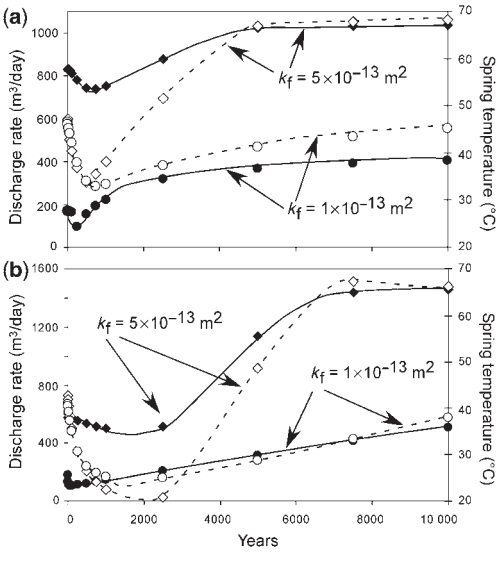

Fig. 8. Maximum flow rates and temperatures of waters discharging at springs v. time in years, plotted for $k_f = 1 \times 10^{-13}$ and 5×10^{-13} m^2 and host rock permeabilities of (**a**) 1×10^{-17} and (**b**) 1×10^{-15} m^2 using model 1. The BHF is 80 mW m^{-2}. Symbols (•) and (◆) represent water discharges, while (○) and (◇) represent maximum spring temperatures.

Within the fault, the transition between advection and convection was identified by completing a series of simulations at constant host rock permeability and variable fault permeabilities. Figure 7 shows that as the host rock permeability is increased, the convective cells onset within the fault at slightly higher fault permeabilities. At $k_{hr} = 1 \times 10^{-18}$ m^2, this onset occurs at $k_f = 2 \times 10^{-13}$ m^2, while at $k_{hr} = 5 \times 10^{-18}$ m^2, it occurs at $k_f = 1 \times 10^{-12}$ m^2. The effect of increasing the BHF from 80 to 100 mW m^{-2} is to expand the convective field toward lower values of fault permeability and higher values of host rock permeability. Figure 8a and b provides an illustration of the spring flow rate and temperature variation over time for two cases: (a) $k_f = 1 \times 10^{-13}$, $k_f = 5 \times 10^{-13}$ m^2, and $k_{hr} = 1 \times 10^{-17}$, and (b) $k_{hr} = 1 \times 10^{-15}$ m^2 with the other values unchanged, illustrating the difference in spring response to advective and convective flow systems. It can be noticed that: (i) a negative trend in flow rates and temperatures occurs during the initial stages of circulation, and the negative trend in temperature is more pronounced at higher fault permeability; (ii) at higher fault and host rock permeabilities (Fig. 8b), the negative temperature anomaly persists for a longer period than at lower permeabilities; (iii) after 10 000 years, the thermal and hydraulic spring outputs are mainly contingent on fault permeabilities, such that an enhancement in k_f from 1×10^{-13} to 5×10^{-13} m^2 brings about a marked increase in the discharge temperatures and flow rates for both the modelled host rock permeabilities; and (iv) quasi-steady-state configurations are attained at lower host rock permeabilities. During initial periods of simulated circulation [points (i) and (ii)], the flow rates and temperatures decrease because of the bulk rearrangement of the circulation patterns related to the introduction of density and viscosity dependencies on temperature. This negative anomaly lasts for a longer time at higher host rock permeabilities, because the springs discharge proportionally higher amounts of cold water which infiltrates in from the nearby host rocks. The considerable increment in discharge temperature and discharge flow rate [point (iii)] recorded by increasing the fault permeability from 1×10^{-13} to 5×10^{-13} m^2 reflects the efficiency of the convective circulations (active within the fault at 5×10^{-13} m^2) in bringing a larger amount of fluid and heat toward the surface. By contrast, the onset of a convective circulation is not achieved with an imposed k_f of 1×10^{-13} m^2, resulting in lower proportions of heat and flow reaching the surface. More stable configurations [point (iv)] arise at lower host rock permeability because the self-rearrangement of the circulation patterns

occurs mainly within the fault plane. Figure 9 shows the isotherm distribution along the Lorusa Fault at 2500 years and 10 000 years for $k_f = 5 \times 10^{-13}$ m^2 and $k_{hr} = 1 \times 10^{-15}$ m^2 respectively. Moreover, the efficiency of the convective circulations in conveying heat toward the surface can be estimated by inspection of Figure 10, which shows the isosurface corresponding to a temperature of 70 °C at 10 000 years for different fault permeabilities and for a fixed host rock permeability of 1×10^{-17} m^2. As k_f varies from 1×10^{-14} to 1×10^{-13} m^2, the hot plume located below the spring site is slightly amplified. As k_f varies from 1×10^{-13} to 5×10^{-13} m^2, the isosurface changes dramatically in shape owing to the development of convection that gives rise to a positive thermal anomaly that intercepts the topographic surface at the spring site.

Despite the detailed characterization of the hydraulic and thermal state of the Valdieri system model, none of the combinations of fault and host rock permeabilities in the regimes shown in Figure 7 satisfies the required conditions for calibration. In fact, the simulated spring discharges are underestimated with respect to the expected values of flow rates measured at Valdieri, even considering the highest-performing case: at $k_{hr} = 1 \times 10^{-15}$ m^2 and $k_f = 1 \times 10^{-12}$ m^2, after 7500 years from circulation onset, the spring temperature ($T_{sim} = 69$ °C) fulfills the calibration condition ($T = 70$ °C), while the discharge rate ($Q_{sim} = 2248$ m^3/day) represents only about half the expected value ($Q = 4320$ m^3/day). In the convective flow region, moderate, but still insufficient improvements in the results are obtained for models based on a BHF of 100 mW m^{-2}. In summary, this discussion has revealed that the numerical models representing combinations of a single-conduit geometry surrounded by hydraulically connected fracture networks do not give a reasonable description of the Terme di Valdieri circulation system.

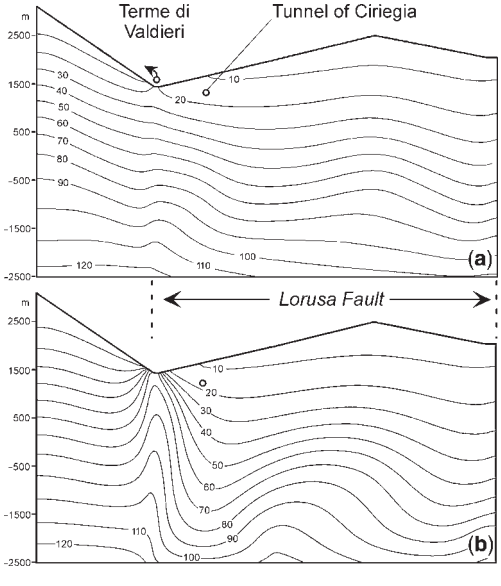

Fig. 9. Isotherm distribution across the Lorusa Fault obtained for $k_f = 2 \times 10^{-13}$ m^2 and $k_{hr} = 1 \times 10^{-15}$ m^2 using model 1. (**a**) Distribution after 2500 years and (**b**) after 10 000 years.

Model 2: fault intersection

This scenario includes the interception at depth of the Lorusa Fault by the S. Giovanni Fault (Fig. 2), and both structures contribute to the thermal flow feeding the Terme di Valdieri springs. The two faults show a comparatively similar proportion of damage/core zone, which suggests that they share broadly equivalent hydraulic properties. Ideally, pressure gradients due to the higher topographic elevation of the S. Giovanni Fault with respect to the Lorusa Fault would drive fluids through the two faults and then up to the surface at the thermal springs. The model geometry represented in Figure 3c was used for performing sensitivity tests of the Lorusa and S. Giovanni fault permeabilities on spring temperatures and flow rates. Since this model aims mainly to identify the impact of fault linkage on the bulk thermal system, simulations were carried out with a fixed host rock permeability of 1×10^{-15} m^2 and with an equal permeability value and a constant infiltration rate of 1.7×10^{-4} m day^{-1} assigned to both

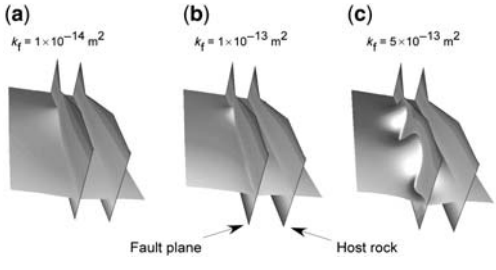

Fig. 10. Isosurface corresponding to a temperature of 70 °C (at $t = 10\,000$ years) obtained using model 1 for a fixed host rock permeability of 1×10^{-17} m^2 and fault permeabilities of (**a**) 1×10^{-14} m^2, (**b**) 1×10^{-13} m^2 and (**c**) 5×10^{-13} m^2. Heat fringes traced along the fault plane and within the host rock are also displayed. It can be noticed that the onset of convective circulation cells occurs between 1×10^{-13} and 5×10^{-13} m^2 and that the effects of convection strongly perturb the thermal state of the surrounding protolith rocks.

faults in each simulation run. Figure 11 shows the evolution over time of spring flow rate and temperature, with $k_f = 1 \times 10^{-13}$, $k_f = 5 \times 10^{-13}$ m^2, and $k_{hr} = 1 \times 10^{-15}$. Compared with the trends shown in Figure 8, this diagram shows that the two faults intercepting at depth increase the bulk discharge, but decrease the maximum temperature. After 10 000 years, at $k_f = 1 \times 10^{-13}$ m^2, the discharge rate is approximately 800 m^3/day at a temperature of 46 °C. If a $k_f = 5 \times 10^{-13}$ m^2 is imposed, the discharge rate doubles owing to the increased drainage from the S. Giovanni Fault of the fluids flowing adjacent of this zone, but the temperature rises only to 42 °C. This behaviour occurs because fluids infiltrating through the S. Giovanni Fault contribute to a relatively rapid increase (in a few tens of years) of the total fluid flow within the Lorusa Fault, but remove more heat at the base of the thermal system when compared with the case where the two faults were not linked (cf. Fig. 8b). The advective perturbation caused by the fluid flow within the S. Giovanni Fault inhibits the onset of convective circulations in the Lorusa Fault, which results in lower discharge temperatures. Figure 12a & b illustrate the isotherm distribution within the Lorusa Fault at $k_f = 5 \times 10^{-13}$ m^2 at 2500 and 10 000 years respectively. At both simulation times, the presence of the S. Giovanni Fault causes a separation of the isotherm distribution above the zone of linkage, with apparent geothermal gradients of *c*. 15 °C km^{-1}, and below the zone, with apparent geothermal gradients exceeding 40 °C km^{-1}. It must be remarked that no significant improvement of the numerical results with respect to the calibration conditions was achieved by varying fault or host rock permeabilities. Moreover, assuming a BHF = 100 mW m^{-2}, it does not lead to a definitive solution of the problem, because it results in spring temperatures which are slightly increased (maximum 57 °C over 10 000 years), but still distant from the required values. Even simulations carried out with lower permeabilities for the S. Giovanni Fault with respect to the Lorusa Fault produced no significant improvement. In summary, these results indicate that a fault linkage scenario has difficulty explaining the measured values at the Terme di Valdieri springs.

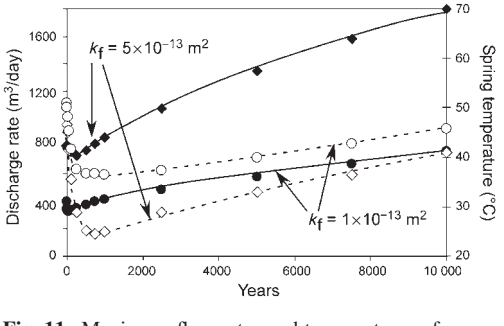

Fig. 11. Maximum flow rates and temperatures of waters discharging at springs v. years, plotted for fault permeabilities of 1×10^{-13} and 5×10^{-13} m^2 and host rock permeabilities of 1×10^{-15} m^2 using model 2. The BHF is 80 mW m^{-2}. Symbols (•) and (◆) represent water discharges, while (○) and (◇) represent maximum spring temperatures.

Model 3: fault interaction

The springs of Terme di Valdieri are sited in an area of fracturing that corresponds to a contractional step-over developed by the interaction of the Lorusa Fault with the Cougne Fault. As with model 2, the thermal flow can be partitioned between two faults that act as separate channels. However, in this case, waters circulating in the two systems can come into contact through the jog rather than by direct fault linkage. This implies that the resulting thermal flow system would depend not only on the hydraulic properties of the Lorusa and Cougne Faults, but also on the specific hydraulic properties, such as the fracture hydraulic connectivity, of the breakdown region between these two faults. The model geometry represented in Figure 3d was used as a basis for

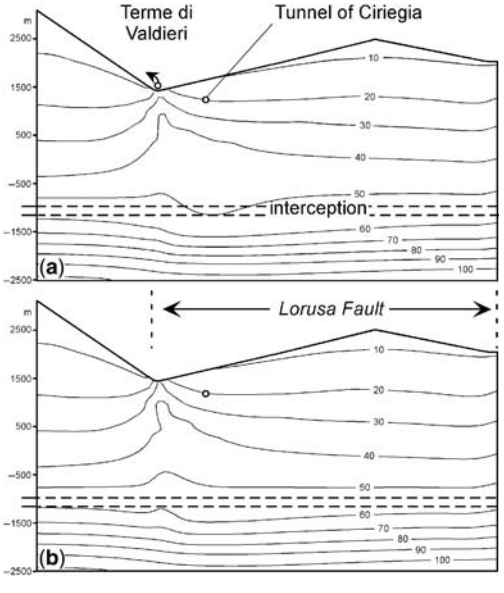

Fig. 12. Isotherm distribution across the Lorusa Fault obtained for $k_f = 5 \times 10^{-13}$ m^2 and $k_{hr} = 1 \times 10^{-15}$ m^2 using model 2. (**a**) Distribution after 2500 years and (**b**) after 10 000 years.

performing sensitivity tests for the Lorusa Fault, the Cougne Fault, and the effect of jog permeabilities on spring temperatures and flow rates. Figure 13 shows the differences in response of spring temperatures and discharges due to advective as opposed to convective flows. As in the previous models, fault permeability was set equal to 1×10^{-13} and 5×10^{-13} m^2, while the host rock permeability was kept fixed at 1×10^{-15} m^2. Accordingly, the permeability of the region corresponding to the step-over was set equal to that attributed to the faults. After 500 years, at $k_f = 1 \times 10^{-13}$ m^2, the springs record a linear increase of temperatures and discharges that attain, at 10 000 years, values of 64 °C and 1900 m^3/day. By contrast, at $k_f = 5 \times 10^{-13}$ m^2, the highest spring temperatures and discharges are obtained at *c*. 2000 years, while decreases of over 20 °C and 200 m^3/day occur at 10 000 years with respect to the peak temperature and flow rates respectively. In the latter case, the abrupt increase of the spring heat flux discharge is attributed to the onset of convective cells within the Lorusa Fault and in the adjoining step-over. After 2000 years, the convective cells continue to expand within the fault plane, bringing about a thermal perturbation relative to the surrounding country rock. However, the lateral migration of the convective flows results in a decrease of the heat flux discharges at springs. Assuming these conditions, the spring temperatures and discharges as modelled fulfill the calibration requirements of the Terme di Valdieri springs at *c*. 1500–1800 years. The isotherm distributions at 2500 and 10 000 years in the Lorusa Fault are shown in Figure 14, and Figure 15 provides a snapshot of the 3D spatial distribution of the 70 °C isotherm at 1500 years.

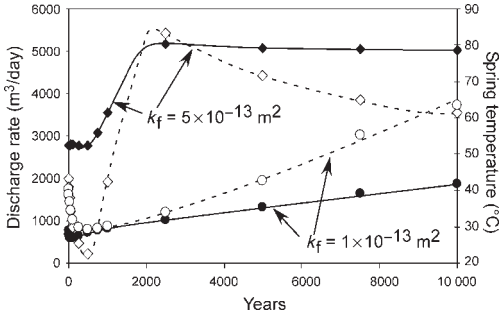

Fig. 13. Maximum flow rates and temperatures of waters discharging at springs v. years, plotted for fault permeabilities of 1×10^{-13} and 5×10^{-13} m^2 and host rock permeabilities of 1×10^{-15} m^2 using model 3. The BHF is 80 mW m^{-2}. Symbols (•) and (◆) represent water discharges, while (○) and (◇) represent maximum spring temperatures.

It is of interest to note that the thermal state of the jog region is highly perturbed, with a negative anomaly close to the Cougne Fault and a sharp positive anomaly close to the western end of the Lorusa Fault. The shape of this latter anomaly fits well with the field location of the Terme di Valdieri springs.

To check the consistency of this scenario, the sensitivity of the modelling results was checked against variations in the most uncertain assigned parameters by keeping $k_f = 5 \times 10^{-13}$ m^2 and $k_{hr} = 1 \times 10^{-15}$ m^2. Through these analyses, it was found that the effect of increasing the infiltration rates through the Lorusa Fault, the Cougne Fault and the step-over region more than three-fold (to 5×10^{-4} m/day) is reflected in a delay of 4000 years in the time interval at which the peak of spring temperatures and discharges occurs. Under this condition, the convective circulation is capable of beginning, providing results that are still consistent with those required by calibration. However, by further increasing the infiltration rate, the thermal convection is inhibited by advective circulation, and satisfactory results are never obtained in the 10 000 year time-range. Similarly, an analysis of the sensitivity of host rock porosity on the thermal system was performed, indicating that porosities of 0.01 instead of 0.1 cause a reduction of the simulated spring temperatures of at most 3 °C.

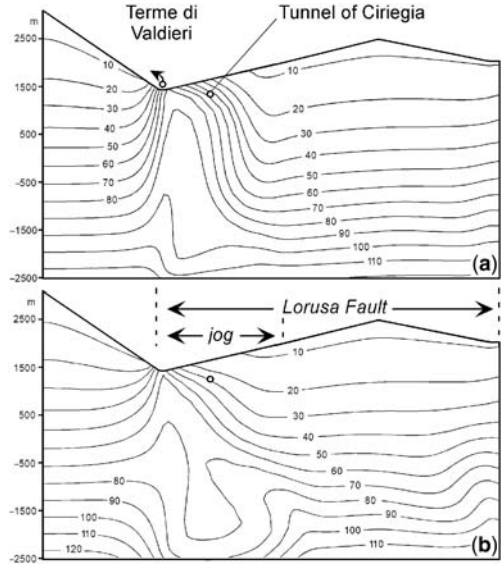

Fig. 14. Isotherm distribution across the Lorusa Fault obtained for $k_f = 5 \times 10^{-13}$ m^2 and $k_{hr} = 1 \times 10^{-15}$ m^2 using model 3. (**a**) Distribution after 2500 years and (**b**) after 10 000 years.

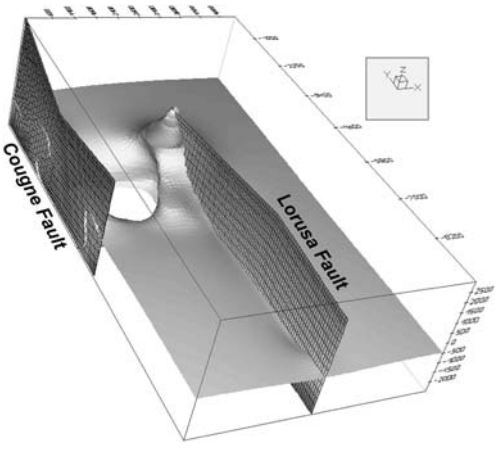

Fig. 15. Isosurface corresponding to a temperature of 70 °C (at $t = 1500$ years) visualized for a permeability of the Lorusa Fault, Cougne Fault, and jog of 5×10^{-13} m^2 and a host rock permeability of 1×10^{-15} m^2. Notice that, within the jog, a sharp transition occurs between a negative thermal anomaly located next to the Cougne Fault and a positive anomaly concentrated next to the Lorusa Fault. The latter is related to the upwelling and discharge of waters at the Terme di Valdieri springs.

Discussion

The simulations show that the type of structural configuration crucially affects the temporal variation of hot spring temperatures and discharges, in addition to the host rock and fault permeabilities. For the Terme di Valdieri flow system, a satisfactory fit between the numerical outputs and the measured spring temperatures of 70 °C and discharges of 50 kg s^{-1} is obtained only if the fault interaction scenario of model 3 is assumed. This scenario postulates that meteoric waters infiltrating through the Lorusa Fault and the Cougne Fault are transferred to the permeable jog structure where they finally upwell to the Valdieri springs. On the other hand, sensitivity tests carried out on fault and host rock permeabilities using model 1 and model 2 provided spring discharges and temperatures that are remarkably different than those required by the calibration specifications. Validation of model 3 was also possible both through increasing the recharge rate, one of the most unconstrained parameters, by up to three times (up to 200 mm a^{-1}) and by decreasing the porosity of host rocks by a factor of 10 (to 0.01).

By studying relationships between active hot springs and faults in a variety of tectonic settings, Curewitz & Karson (1997) have documented the common occurrence of hot springs in zones of fault interaction. In these zones, stress concentration promotes active fracturing and enhanced fluid flow despite clogging by hydrothermal mineral precipitates (Segall & Pollard 1980; Scholz & Anders 1994). For example, the strong localized enhancement of vertical permeability in a dilational jog is interpreted by Sibson (1987) to be the factor sustaining the powerful hydrothermal Salton Sea system of the southern San Andreas Fault. In the Argentera Massif, Perello *et al.* (2001) also proposed that the location of the thermal springs of Bagni di Vinadio (*c.* 17 km north of Valdieri) is attributable to the zone of enhanced fracturing that corresponds to a dilational step-over bounded by two NW-trending right-lateral faults. In this work, the numerical validation of a fault interaction model obtained through comparison of the different hypotheses provides a first quantitative constraint on the role played by jogs in controlling the location of thermal discharges. However, in the Terme di Valdieri sector, there is a lack of field and seismological evidence supporting the hypothesis that the contractional step-over bounded by the Lorusa and Cougne Faults represents a still-active structure with permeability dynamically maintained by fault propagation and active fracturing. Freshly exposed fracture surfaces in granite and the low salinity of fluids (Fancelli & Nuti 1978; Michard *et al.* 1989; Baietto 2007) suggest that clogging by hydrothermal minerals could not be efficient at filling fractures and at reducing permeability over relatively short periods (e.g., hundreds of years, Fournier 1991), as is indeed the case in many other geothermal settings (Elders *et al.* 1979; Sibson 1987). This circumstance could suggest that the Valdieri thermal flow system has not been affected by substantial decreases in permeability, even over thousands of years, and that the Lorusa and Cougne faults have been inactive during this period. Moreover, in this work, permeability within the jog was considered as isotropic and homogeneous across the whole region. Future numerical models applied in similar structural contexts should also take into account variations of fracture distribution and permeability gradients within the jog regions.

In the three model geometries considered, spring discharges with temperatures higher than ambient temperatures were produced by either advective or convective flows. However, the numerical results have shown that thermal convection is a requirement for providing water flow rates and temperatures such as those measured at the Terme di Valdieri springs. In a context like the Alps, thermal circulations have always been attributed to advective flows controlled by topographic gradients (Vuataz 1982; Rybach 1995; Perello 1997; Martinotti *et al.* 1999; Pastorelli *et al.* 1999, 2001; Perello *et al.* 2001). The results of this work

demonstrate that, provided permeabilities are adequate, thermal convection can develop in mountainous settings in combination with advective flows. Diagenetic processes, brine migration and ore deposition in many sedimentary basins (Prats 1966; Raffensperger & Vlassopoulos 1999; Garven *et al.* 2001; Thornton & Wilson 2007) and the upwelling of hot springs in the Basin and Range Province (López & Smith 1995) are some of the processes that are thought to be controlled by coexisting convective and advective flows (i.e., mixed convection).

In the Valdieri setting, convective circulations begin at fault permeabilities higher than 2×10^{-13} and 1×10^{-13} m^2 (at BHF values of 80 and 100 mW m^{-2} respectively) and at host rock permeabilities lower than 5×10^{-15} m^2. This permeability range is consistent with that indicated by López & Smith (1995) for the onset of convection in the Basin and Range province. However, the Valdieri simulations have also shown that the geometry of the flow system strongly influences the field where convection can occur. In fact, while this process activates in models 1 and 3 for the permeability ranges noted above, in model 2, convection in the Lorusa Fault is inhibited by the fluids downflowing from the S. Giovanni Fault. The effect of convection in the thermal system can be evaluated by comparing for all three models the cumulative heat (J) discharged at springs over 10 000 years, assuming $k_f = 5 \times 10^{-13}$ m^2 (Fig. 16). It can be seen that the difference in heat discharges in the three models increases over time. This reflects the onset of convective cells in models 1 and 3 (at *c*. 800 a) which results in an accelerated increase in heat discharge that does not occur in model 2. Moreover, this difference is also caused by the more vigorous convection occurring in model 3 with respect to model 1. At the Terme di Valdieri springs, the occurrence of granitic bodies located beneath migmatitic gneisses might represent an additional factor that can favor convective flows at shallow depths. In fact, the state of fracturing of the granites where large rock volumes are involved, as opposed to the fracturing within the migmatitic gneisses which is mostly concentrated along localized damage zones, creates the conditions for pervasive flows and focused flows, respectively. Thus, migmatitic gneisses sited above granites at the spring site, on the one hand can prevent massive infiltrations of cold meteoric waters (as would be expected in the case of outcropping granites), and on the other can promote the onset of thermal convective circulation within the granites. Similarly, in their thermohydraulic models in a mountainous setting, Forster & Smith (1988*a* & *b*) observed that a low-permeability layer was needed to allow thermal convection to occur without being suppressed by overlying topographically-driven flow.

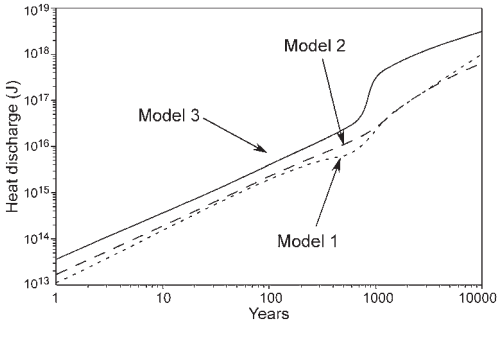

Fig. 16. Cumulative heat discharge at the Terme di Valdieri springs for the three models considered.

The fault interaction model (model 3) was validated by imposing a $k_f = 5 \times 10^{-13}$ m^2 to the Lorusa and Cougne Faults and to the jog inbetween. This remarkably high permeability with respect to the damage zones bounding the two faults falls within the range of permeability values obtained from laboratory tests (10^{-16}–10^{-11} m^2; Evans *et al.* 1997) and *in situ* tests (10^{-17}–10^{-11} m^2; Istok 1989; Phillips 1991; National Research Council 1996) of damage zones in faulted crystalline rocks in different geological settings. Moreover, the fault permeability values obtained by numerical modeling are consistent with the permeabilities obtained from slug tests that were performed in the St Anna borehole (Darcy 1997). This borehole, *c*. 1200 m deep, was drilled at *c*. 10 km to the NW of Valdieri in the Valletta Shear Zone, a NW-trending fault with hydraulic characteristics similar to those of the Lorusa and Cougne Faults. The tests indicated fault damage zone permeabilities greater than 10^{-14} m^2 (Baietto 2007).

With respect to host rock permeability, validation of model 3 was achieved through the adoption of a broad range of permeability values, in either the conductive or the advective field. This indicates that, for transient fluid and heat flows, the heat discharge at the springs is much more dependent on the fault than on the host rock permeability. However, it could be expected that the possible occurrence of pervasive flow around the fault zones could have important consequences for water–rock interaction and mineralization. If a large proportion of groundwater is directed towards the fault zone, the various chemical species brought into solution by water–rock interactions along the flow path will reach the fault zone, where they can promote processes such as hydrothermal alteration and mineral deposition.

In summary, simulation results show that thermal circulations in strike–slip fault systems can develop in contexts of single faults, of multiple faults linked at depth, or of faults connected by jogs. It might be useful to remember that, within the Alps, post-Oligocene tectonic activity led to the widespread development of these structural elements in both the internal and external portions of the mountain chain (Hubbard & Mancktelow 1992; Bistacchi & Massironi 2000; Tricart 2004; Giglia *et al.* 1996). However, the upwelling of hot springs and the occurrence of active thermal flow systems related to these features is much less commonly observed. Rough topography is a factor that promotes the infiltration of cold waters and the subsequent upwelling of waters with temperatures higher than ambient at valley bottoms (Forster & Smith 1988*a* & *b*; Jaboyedoff 1999; Pastorelli *et al.* 1999). However, the upwelling of thermal springs is often likely to be obliterated by low-permeability valley fills or by infiltration of cold waters from river beds. Numerical modelling of Valdieri reveals new constraints on this aspect, showing that permeable jogs sited at valley bottoms and hydraulically connected with strike–slip faults might represent a reasonable requirement for obtaining high spring temperatures and discharges. On the contrary, thermal systems that are controlled by single strike–slip faults or faults connected at depth could not be efficient enough to drive the upwelling of thermal springs.

One shortcoming of these models is the assumption, ignoring any information that could indicate the possible lifetime of the Terme di Valdieri flow system, of a steady-state solution as the initial condition for all transient-regime simulations. If this assumption were reasonable, the simulations show that the time required to attain the calibration conditions is *c*. 1500 years. In principle, this could ideally represent the period since the last seismic event caused an increase in fault and jog permeabilities through fracturing by fault displacement and stress concentration.

Conclusions

Comparison of the numerical solutions obtained for thermal circulation scenarios using a single fault, faults intersecting at depth and faults interacting through a permeable jog have provided a better understanding of the influence exerted by these structures. This applies both to the bulk fluid and heat patterns within geothermal systems and to the temporal variations of heat discharge at springs. A satisfactory calibration of the numerical results with the measured temperature of 70 °C and discharges of 50 kg s^{-1} was obtained by assuming a fault jog interaction context. In this framework, the thermal discharges at Terme di Valdieri can be seen to be controlled by circulations that occur both in the Lorusa Fault and in the Cougne Fault, that interact by means of a permeable step-over located at the bottom of the valley. Simulations of circulation in a single fault (i.e., the Lorusa Fault) and in faults that intersect at depth (i.e., the Lorusa and San Giovanni Fault) provided heat discharges that are not nearly as high as those provided by a jog context. The reason for this is that the enhanced permeability in the jog region favours the onset of vigorous convective circulations. Once the onset occurs, the spring temperatures and flow rates of springs increase rapidly, attaining the values required by the model calibration at *c*. 1500 years under the assumption of a initial steady-state flow condition. After this period, owing to the lateral expansion of the convective cells within the fault plane, the heat flux discharge slightly decreases. Thermal convection can also develop within single faults, but it seems to be less efficient in drawing high heat fluxes into springs than convection developed in jog and fault contexts. This finding demonstrates that thermal convection is a viable process that can occur in strike–slip fault systems within basement that can also coexist with advective flows in mountainous regions. Assuming for the geological setting of Valdieri a basal heat flow of 80 mW m^{-2}, the requirements for the development of convection are a fault permeability higher than 2×10^{-13} m^2, a host rock permeability lower than 5×10^{-15} m^2, and infiltration rates lower than 200 mm a^{-1}. If higher values of basal heat flow are assumed, the convective region expands in permeability space. Moreover, under these conditions, convection within the fault and the jog can develop in cases where heat transfer in the host rock is predominantly of either conductive or advective type, that is, for host rock permeabilities lower or higher than 3×10^{-17} m^2, respectively. By contrast, simulations of thermal flows occurring in faults that intercept at depth have shown that the development of thermal convection in this setting is inhibited by advective perturbation at the base of faults. In this setting, the cumulative heat flux discharged at springs is remarkably lower than that produced in the other contexts. Finally, the use of numerical modelling for comparing spring response under different structural configurations provides a first quantitative estimate of the importance of jog structures in controlling the localization of thermal discharges in strike–slip fault systems. This finding opens up new perspectives in the field of geothermal exploration, particularly considering the currently increased interest in renewable sources of energy. It must be emphasized that, despite large

uncertainties in the factors that can exert substantial control on the water circulation within geothermal systems, numerical modelling can be appropriately used with some degree of confidence as a tool for checking the consistency of structural hypotheses.

We are grateful to J. Imber and R. Holdsworth for the constructive review, which helped to improve the quality of the manuscript. The Centre d'Hydrogéologie de l'Université de Neuchâtel (CHYN) is acknowledged for the use of the Feflow package. This research has been financially supported by Italian MIUR (Ministero dell'Istruzione, dell'Università e della Ricerca), grants awarded to P. Cadoppi.

References

ALFÖLDI, L., GÁLFI, J. & LIEBE, P. 1985. Heat flow anomalies caused by water circulation, *Journal of Geodynamics*, **4**, 199–217.

BAIETTO, A. 2007. *Fault-related thermal circulations in the Argentera Massif (south-western Alps)*. PhD thesis, Earth Science Department, University of Turin.

BARTON, C. A., ZOBACK, M. D. & MOOS, D. 1995. Fluid flow along potentially active faults in crystalline rocks. *Geology*, **23**, 683–686.

BENOIT, W. R. 1999. Conceptual models of the Dixie Valley, Nevada, geothermal system. *Geothermal Resources Council Transactions*, **23**, 505–511.

BETHKE, C. M. & MARSHAK, S. 1990. Brine migrations across North America – the plate tectonics of groundwater. *Annual Reviews of Earth and Planetary Sciences*, **18**, 287–315.

BIGOT-CORMIER, F., POUPEAU, G. & SOSSON, M. 2000. Dénudation différentielles du massif cristallin externe alpin de l'Argentera (Sud-Est de la France) révélées par thermochronologie traces de fission (apatites, zircons). *Comptes Rendus del' Academie des Sciences de Paris, Earth and Planetary Sciences*, **330**, 363–370.

BIRD, R. B., STEWART, W. E. & LIGHTFOOT, E. N. 1960. *Transport Phenomena*, Wiley, New York.

BISTACCHI, A. & MASSIRONI, M. 2000. Post-nappe brittle tectonics and kinematic evolution of the northwestern Alps: an integrated approach. *Tectonophysics*, **327**, 267–292.

BOGDANOFF, S. 1986. Evolution de la partie occidentale du Massif cristallin externe de l'Argentera. Place dans l'arc Alpin. *Géologie de France*, **4**, 433–453.

BORTOLAMI, G. & GRASSO, F. 1969. Osservazioni geologico-applicative sul cunicolo d'assaggio del traforo del Ciriegia e considerazioni sull'intero tracciato. *Procedures of I International Congress: 'Problemi tecnici nella costruzione di gallerie'*, 111–126.

BRACE, W. F., PAULDING, B. W. & SCHOLZ, C. H. 1966. Dilatancy in the fracture of crystalline rocks. *Journal Geophysical Resources*, **71**, 3939–3953.

BREDEHOEFT, J. D. & HANSHAW, B. B. 1968. On the maintenance of anomalous fluid pressures; 1, thick sedimentary sequences. *GSA Bulletin*, **79**, 1097–1106.

CAINE, J. S., EVANS, J. P. & FORSTER, C. B. 1996. Fault zone architecture and permeability structure. *Geology*, **24**, 1025–1028.

CALAIS, E., GALISSON, L. *ET AL*. 2000. Crustal strain in the Southern Alps, France, 1948–2000. *Tectonophysics*, **319**, 1–17.

CHAPMAN, D. S. & FURLONG, K. P. 1992. Thermal state of the continental crust. *In*: FOUNTAIN, D. M., ARCULUS, R. J. & KAY, R. W. (eds) *Continental Lower Crust: Developments in Geotectonics.* Elsevier, Amsterdam, **23**, 179–199.

COX, S. F., KNACKSTEDT, M. A. & BRAUN, J. 2001. Principles of structural control on permeability and fluid flow in hydrothermal systems. *Reviews in Economic Geology*, **14**, 1–24.

COURBOULEX, F., DESCHAMPS, A. *ET AL*. 1998. Source study and tectonic implications of the Ventimiglia (border of Italy and France) earthquake (M_L= 4.7). *Tectonophyisics*, **290**, 245–257.

CUREWITZ, D. & KARSON, J. 1997. Structural settings of hydrothermal outflow: fracture permeability maintained by fault propagation and interaction. *Journal of Volcanology and Geothermal Research*, **79**, 149–168.

CUTILLO, P. A., SCREATON, E. J. & GE, S. 2003. Three-dimensional numerical simulation of fluid flow and heat transport within the Barbados Ridge accretionary complex. *Journal of Geophysical Research*, **108**, 2555, doi:10.1029/2002JB002240.

DARCY, J. 1997. La nouvelle liaison routiere Nice-Cuneo et le Tunnel du Mercantour. *Tunnels et ouvrages souterrains*, **139**, 46–50.

DIERSCH, H.-J. G. 1998. *FeFlow® – Finite Element Subsurface Flow & Transport Simulation System.* Wasy Software GmbH.

ELDERS, W. A., HOAGLAND, J. R., MCDOWELL, S. D. & COBO, J. M. 1979. Hydrothermal mineral zones in the geothermal reservoir of Cerro Prieto. *Geothermics*, **8**, 201–209.

EVANS, D. G. & RAFFENSPERGER, J. P. 1992. On the stream function for variable-density groundwater flow. *Water Resources Research*, **28**, 2141–2145.

EVANS, J. P., FORSTER, C. B. & GODDARD, J. V. 1997. Permeability of fault-related rocks, and implications for hydraulic structure of fault zones. *Journal of Structural Geology*, **19**, 11, 1393–1404.

FANCELLI, R. & NUTI, S. 1978. Studio geochimico delle sorgenti termali del Massiccio Cristallino dell'Argentera (Alpi Marittime). *Boll. Soc. Geol. It.*, **97**, 115–130.

FAULKNER, D. R. & RUTTER, E. H. 2001. Can the maintenance of overpressured fluids in large strike–slip fault zones explain their apparent weakness? *Geology*, **29**, 503–506.

FAURE-MURET, A. 1955. Etudes géologiques sur le massif de l'Argentera. *In*: BOILLOT, G. (ed.) *Les Marges continentales actuelles et fossiles autour de la Mercantour et ses enveloppes sédimentaires*. Mémoires pour servir à l'explication de la carte géologique détaillé de la France. Imprimerie Nationale, Paris.

FEHN, U. & CATHLES, L. 1979. Hydrothermal convection at slow-spreading midocean ridges. *Tectonophysics*, **55**, 239–260.

FORSTER, C. & SMITH, L. 1988*a*. Groundwater flow systems in mountainous terrain, 1, numerical modelling technique. *Water Resources Research*, **24**, 999–1010.

FORSTER, C. & SMITH, L. 1988*b*. Groundwater flow systems in mountainous terrain, 2, controlling factors. *Water Resources Research*, **24**, 1011–1023.

FORSTER, C. & SMITH, L. 1989. The influence of groundwater flow on thermal regimes in mountainous terrain: a model study. *Journal of Geophysical Research*, **85**, 1867–1875.

FOURNIER, R. O. 1991. The transition from hydrostatic to greater than hydrostatic fluid pressure in active hydrothermal systems in crystalline rocks. *Geophysical Research Letters*, **18**, 955–958.

FRY, N. 1989. Southwestward thrusting and tectonics of the western Alps. *In*: COWARD, M., DIETRICH, D. & PARK, R. G. (eds) *Alpine Tectonics*. Geological Society, London, Special Publications, **45**, 83–111.

GARVEN, G., GE, S., PERSON, M. A. & SVERJENSKY, D. A. 1993. Genesis of stratabound ore deposits in the midcontinent basins of North America, 1, The role of regional groundwater flow. *American Journal of Science*, **293**, 497–568.

GARVEN, G., BULL, S. W. & LARGE, R. R. 2001. Hydrothermal fluid flow models of stratiform ore genesis in the McArthur Basin, Northern Territory, Australia. *Geofluids*, **1**, 289–311.

GHAFIRI, A. 1995. *Paléosismicité de failles actives en contexte de sismicité modérée: application à l'évaluation de l'aléa sismique dans le Sud-Est de la France*. PhD thesis, Univ. Paris XI.

GIGLIA, G., CAPPONI, G., CRISPINI, L. & PIAZZA, M. 1996. Dynamics and seismotectonics of the West-Alpine arc. *Tectonophysics*, **267**, 143–175.

GRATIER, J. P., FAVREAU, P. & RENARD, F. 2003. Modeling fluid transfer along California faults when integrating pressure solution crack sealing and compaction processes. *Journal of Geophysical Research*, **108**, 2104, doi:10.1029/2001JB000380.

HENLEY, R. W. & ADAMS, D. P. M. 1992. Strike–slip fault reactivation as a control on epithermal vein-style gold mineralization. *Geology*, **20**, 443–446.

HENRY, P. 2000. Fluid flow at the toe of the Barbados accretionary wedge constrained by thermal, chemical and hydrogeologic observations and models. *Journal of Geophysical Research*, **105**, 25855–25872.

HICKMAN, S., SIBSON, H. R. & BRHUN, R. 1995. Introduction to special section: mechanical involvement of fluids in faulting. *Journal of Geophysical Research*, **100**, B7, 12.831–12.840.

HUBBARD, M. & MANCKTELOW, N. S. 1992. Lateral displacement during Neogene convergence in the western and central Alps. *Geology*, **20**, 943–946.

INGEBRITSEN, S. E. & MANNING, C. E. 1999. Geological implications of a permeability–depth curve for the continental crust. *Geology*, **27**, 1107–1110.

ISTOK, J. 1989. *Groundwater Modelling by Finite Element Method*, Vol. 13. American Geophysical Union, Water Resources Monograph, Washington, DC.

JABOYEDOFF, M. 1999. Modèles thermiques simples de la croûte terrestre: un regard sur les Alpes. *Bullettin de la Société Vaudoise des Sciences Naturelles*, **86**, 229–271.

JABOYEDOFF, M. & PASTORELLI, S. 2003. Perturbation of the heat flow by water circulation in a mountainous framework. Examples from the Swiss Alps. *Eclogae Geologicae Helvetiae*, **96**, 37–47.

KASAMEYER, P., YOUNKER, L. & HANSON, J. 1984. Development and application of a hydrothermal model for the Salton Sea Geothermal Field, California. *Bulletin of the Geological Society of America*, **95**, 1242–1252.

LARROQUE, C., BÉTHOUX, N. *ET AL*. 2001. Active and recent deformation at the Southern Alps–Ligurian basin junction. *Geologie en Mijnbouw*, **80**, 255–272.

LÓPEZ, D. L. & SMITH, L. 1995. Fluid flow in fault zones: Analysis of the interplay of convective circulation and topographically driven groundwater flow. *Water Resources Research*, **31**, 1489–1503.

LÓPEZ, D. L. & SMITH, L. 1996. Fluid flow in fault zones: influence of hydraulic anisotropy and heterogeneity on the fluid flow and heat transfer regime. *Water Resources Research*, **32**, 3227–3235.

MALARODA, R., CARRARO, F., DAL PIAZ, G. V., FRANCESCHETTI, B., STURANI, C. & ZANELLA, E. 1970. Carta geologica del Massiccio dell'Argentera alla scala 1:50 000 e note illustrative. *Memoire della Società Geologica Italiana*, **9**, 557–663.

MANNING, C. E. & INGEBRITSEN, S. E. 1999. Permeability of the continental crust: implications of geothermal data and metamorphic systems. *Reviews of Geophysics*, **37**, 127–150.

MARINI, L., BONARIA, V., GUIDI, M., HUNZIKER, J. C., OTTONELLO, G. & VETUSCHI ZUCCOLINI, M. 2000. Fluid geochemistry of the Acqui Terme–Visone geothermal area (Piemonte, Italy). *Applied Geochemistry* **15**, 917–935.

MARTINOTTI, G., MARINI, L., HUNZIKER, J. C., PERELLO, P. & PASTORELLI, S. 1999. Geochemical and geothermal study of springs in the Ossola-Simplon Region. *Eclogae Geologicae Helvetiae*, **92**, 295–305.

MCKENNA, J. R. & BLACKWELL, D. D. 2004. Numerical modelling of transient Basin and Range extensional geothermal systems. *Geothermics*, **33**, 457–476.

MERCER, J. W. & PINDER, G. F. 1974. *Finite Element Analysis of Hydrothermal Systems, Finite Element Methods in Flow Problems*. University of Alabama Press, Tuscaloosa, AL.

MICHARD, G., GRIMAUD, D., D'AMORE, F. & FANCELLI, R. 1989. Influence of mobile ion concentrations on the chemical composition of geothermal waters in granitic areas, example of hot springs from Piemonte (Italy). *Geothermics*, **18**, 729–741.

National Research Council 1996. *Rock Fractures and Fluid Flow*. Washington, DC.

NEUZIL, C. E. 1995. Abnormal pressures as hydrodynamic phenomena. *American Journal of Science*, **295**, 742–786.

PARRY, W. T. 1998. Fault-fluid compositions from fluid inclusion observations and solubilities of fracture-sealing minerals. *Tectonophysics*, **290**, 1–26.

PASTORELLI, S., MARINI, L. & HUNZIKER, J. C. 1999. Water chemistry and isotope composition of the Acquarossa thermal system, Ticino, Switzerland. *Geothermics*, **28**, 75–93.

PASTORELLI, S., MARINI, L. & HUNZIKER, J. C. 2001. Chemistry, isotope values (δD, δ^{18}O, $\delta^{34}S_{SO4}$) and temperatures of the water inflows in two Gotthard tunnels, Swiss Alps. *Applied Geochemistry*, **16**, 633–649.

PERELLO, P. 1997. *Interazioni tra strutture tettoniche, fenomeni di sollevamento rapido recente e emanifestazioni*

geotermiche a bassa entalpia nelle Alpi occidentali. Studio di quattro località tipo: Settore Ossolano, Alta Valle d'Aosta, Settore Vallesano, Massiccio dell'Argentera. PhD thesis, Earth Science Department, University of Turin, Italy.

PERELLO, P., MARINI, L., MARTINOTTI, G. & HUNZIKER, J. C. 2001. The thermal circuits of the Argentera Massif (western Alps, Italy): an example of low-enthalpy geothermal resources controlled by Neogene alpine tectonics. *Eclogae Geologicae Helvetiae*, **94**, 75–94.

PERROCHET, P. & TACHER, L. 1997. *Mathematical modeling of hydro-thermal processes in Mururoa Atoll*. Research Report GEOLEP-EPFLDGC, University of Lausanne.

PHILLIPS, O. M. 1991. *Flow and Reactions in Permeable Rocks*. Cambridge University Press, New York.

PRATS, M. 1966. The effect of horizontal fluid flow on thermally induced convection currents in porous mediums. *Journal of Geophysical Research*, **71**, 4835–4837.

RAFFENSPERGER, J. & VLASSOPOULOS, D. 1999. The potential for free and mixed convection in sedimentary basins. *Hydrogeology Journal*, **7**, 505–520.

RITZ, J-F. 1991. *Evolution du champ de contrainte dans les Alpes du Sud depuis la fin de l'Oligocène, implications sismotectoniques*. PhD thesis, Université Montpellier II.

RYBACH, L. 1981. Geothermal systems, conductive heat flow, geothermal anomalies. *In*: RYBACH, L. & MUFLLER, L. J. P. (eds) *Geothermal Systems*. Wiley, New York, 3–36.

RYBACH, L. 1995. Thermal waters in deep Alpine tunnels. *Geothermics*, **24**, 631–637.

SCHOLZ, C. H. & ANDERS, M. H. 1994. The permeability of faults. *In*: HICKMAN, S. H., SIBSON, R. H. & BRUHN, R. (eds) *Proceedings of Workshop LXIII on the Mechanical Involvement of Fluids in Faulting*. USGS Open file report, **94–228**, 247–253.

SEGALL, P. & POLLARD, D. D. 1980. Mechanics of discontinuous faults. *Journal of Geophysical Research*, **85**, 4337–4350.

SIBSON, R. H. 1987. Earthquake rupturing as a mineralizing agent in hydrothermal systems. *Geology*, **15**, 701–704.

SIBSON, R. H. 1994. Crustal stress, faulting and fluid flow. *In*: PARNELL, J. (ed.) *Geofluids: Origin, Migration and Evolution of Fluids in Sedimentary Basins*. Geological Society, London, Special Publications, **78**, 69–84.

SIBSON, R. H. 2001. Seismogenic framework for hydrothermal transport and ore deposition. Structural controls on ore genesis. *Reviews in Economic Geology*, **14**, 25–50.

SIBSON, R. H. & SCOTT, J. 1998. Stress/fault controls on the containment and release of overpressured fluids: examples from gold-quartz vein systems in Juneau, Alaska, Victoria, Australia, and Otago, New Zealand. *Ore Geology Reviews*, **13**, 293–306.

SIMMS, M. A. & GARVEN, G. 2004. Thermal convection in faulted extensional sedimentary basins: theoretical results from finite-element modelling. *Geofluids*, **4**, 109–130.

SMITH, D. A. 1980. Sealing and nonsealing faults in Louisiana Gulf Coast salt basin. *American Association of Petroleum Geologists Bulletin*, **64**, 145–172.

THORNTON, M. M. & WILSON, A. M. 2007. Topography-driven flow versus buoyancy-driven flow in the U. S. mid-continent: implications for the residence time of brines. *Geofluids*, **7**, 69–78.

TRAVIS, B. J., JANECKY, D. R. & ROSENBERG, N. D. 1991. Three-dimensional simulation of hydrothermal circulation at mid-ocean ridges. *Geophysical Research Letters*, **18**, 1441–1444.

TRICART, P. 2004. From extension to transpression during the final exhumation of the Pelvoux and Argentera massifs, Western Alps. *Eclogae Geologicae Helvetiae*, **97**, 429–439.

VUATAZ, F.-D. 1982. *Hydrogéologie, géochimie et géothermie des eaux thermals de Suisse et des regions alpines limitrophes*. Matériaux pour la Géologie de la Suisse, Série Hydrologie, **29**, Kümmerly & Frey, Berne.

WISIAN, K. W. & BLACKWELL, D. D. 2004. Numerical modelling of Basin and Range geothermal systems. *Geothermics*, **33**, 713–741.

WOODCOCK, N. H. & FISCHER, M. 1986. Strike–slip duplexes. *Journal of Structural Geology*, **8**, 725–735.

YEAMANS, F. 1983. *Basin and Range Geothermal Hydrology: an Empirical Approach*. Special Report. Geothermal Resources Council, **13**, 159–174.

Permeability structure and co-seismic thermal pressurization on fault branches: insights from the Usukidani fault, Japan

SEBASTIEN BOUTAREAUD[1], CHRISTOPHER A. J. WIBBERLEY[2], OLIVIER FABBRI[1] & TOSHIHIKO SHIMAMOTO[3]

[1]*EA 2642, Université de Franche-Comte, 16 route de Gray, 25030 Besançon cédex, France (e-mail: sebastien.boutareaud@univ-fcomte.fr; olivier.fabbri@univ-fcomte.fr)*

[2]*Géosciences Azur CNRS, Université de Nice-Sophia Antipolis, 250 rue Albert Einstein, 06560 Valbonne, France*

[3]*Division of Earth and Planetary Sciences, Graduate School of Science, Kyoto University, Kyoto 606-8502, Japan*

Abstract: Detailed mapping of complex fault zones shows that secondary faults often branch off the principal slip zone. However, the effect of secondary branch faults on the hydrodynamic behaviour of fault zones has not yet been examined, largely because of a lack of hydraulic data and because numerical or analogue modelling of splay faulting is a complex issue. This contribution investigates the thermal pressurization process in cases of slip along a principal slip zone and along splay faults branching off the principal displacement zone. The study is based on porosity and permeability data presented in this paper from the principal and secondary slip zones of an active, clay-rich gouge-bearing strike–slip fault, the Usukidani fault of SW Japan. Modelling constrained by these data suggests that thermal pressurization is a viable process only as long as the rupture remains located in the central gouge zones or in mature splay fault gouge zones. Splaying of the rupture into surrounding microbreccias or into immature or newly generated splay faults of higher permeability will release fluid pressure or inhibit the generation of coseismic excess fluid pressures by thermal pressurization. The modelling results suggest that secondary fault branches can play a key role in controlling fluid pressurization during faulting. Hence, complete investigation of active fault zones needs to include secondary faults and their corresponding hydraulic behaviour, in order to establish the influence of such structures on earthquake mechanics.

Earthquakes in the brittle crust are considered to result from dynamic slip-weakening processes in the fault zone following an initial stage of slip over a critical distance D_c of the order of 1 m or less (Ide & Takeo 1997; Scholz 2002; Mikumo *et al.* 2003; Fukuyama *et al.* 2003*a*). Based on theoretical or experimental studies and analyses of fossil earthquake rupture zones exposed at the Earth's surface, several mechanisms have been proposed to account for dynamic slip weakening. These mechanisms include frictional melting (McKenzie & Brune 1972; Sibson 1980; Cardwell *et al.* 1978; Kanamori & Heaton 2000; Hirose & Shimamoto 2003, 2005), fluid thermal pressurization (Sibson 1973; Lachenbruch 1980; Mase & Smith 1985, 1987; Andrews 2002; Wibberley 2002; Wibberley & Shimamoto 2003, 2005; Noda & Shimamoto 2005), acoustic fluidization (Melosh 1979, 1996), elastohydrodynamic lubrication (Brodsky & Kanamori 2001) and dynamic unloading effects (Weertman 1980; Brune *et al.* 1993; Ben-Zion & Andrews 1998; Bouissou *et al.* 1998; Mora & Place 1999). Among these possible mechanisms, thermal pressurization has received a lot of attention in the last few years due to recent findings that narrow, water-saturated gouge zones often delimit the most recent slip boundaries in active faults observed at the surface and in cores (e.g., Lockner *et al.* 1999; Tsutsumi *et al.* 2004; Noda & Shimamoto 2005). Thus, frictional heating is likely to efficiently heat up the pore water in the gouge, generating excess fluid pressures which in turn decrease the effective shear strength. Recent permeability measurements of gouge slip zones in active and exhumed faults (e.g., Lockner *et al.* 1999; Wibberley & Shimamoto 2005; Noda & Shimamoto 2005) have verified the feasibility of this process. Besides, detailed structural mapping of complex fault zones has shown that secondary faults often branch off the principal displacement zone. However, the effect of secondary branch faults on thermal pressurization has not yet been examined, probably because numerical or analogue modelling of splay faulting in fault zones is a complex issue (e.g., Poliakov *et al.* 2002). Nevertheless, fault branches can play a key

From: WIBBERLEY, C. A. J., KURZ, W., IMBER, J., HOLDSWORTH, R. E. & COLLETTINI, C. (eds) *The Internal Structure of Fault Zones: Implications for Mechanical and Fluid-Flow Properties*. **299**, 341–361.
DOI: 10.1144/SP299.20 0305-8719/08/$15.00

role either in inhibiting or promoting fluid pressurization. Since secondary branch faults are commonly found along exhumed outcrops of seismogenic faults, their hydraulic properties need to be determined in order to evaluate their effect on dynamic slip weakening by thermal pressurization.

This paper presents results of porosity and permeability measurements obtained on the principal and secondary slip surfaces of an active, clay-rich gouge-bearing strike–slip fault, the Usukidani fault of SW Japan. These porosity and permeability values constrain calculations of hydraulic diffusivities of the displacement zones and determine the conditions under which rupture branching off the principal slip zone may or may not significantly inhibit thermal pressurization and dynamic slip weakening. Before addressing the hydraulic properties of the Usukidani fault, we present a synthesis of permeability data obtained in and around core zones of active strike–slip faults. This synthesis allows the study to be put into a wider context, relevant to strike–slip fault zones in general, beyond the example studied in this paper. Note that we restrict this synthesis to faults crossing low-porosity rocks such as plutonic or medium- or high-grade metamorphic rocks. Indeed, the case analysed here concerns an active strike–slip fault crossing highly compacted silicified volcanic tuffs characterized by a very low porosity.

Synthesis of hydraulic properties of seismic faults

Most kilometre-scale mature (long-lived) exhumed faults typically consist of a *core zone* along which the latest displacements occurred, bordered on one or both sides by a fractured *damage zone* passing progressively or abruptly to the non-deformed or weakly deformed *host rock* or *protolith* (Chester & Logan 1986; Caine *et al.* 1996 and references therein). The core zone, whose thickness seldom exceeds 1m, is commonly composed of highly comminuted material with variable amounts of clay minerals. In the damage zone, the protolith is commonly strongly fractured and altered following extensive fluid–rock interactions. This zonation has also been reported from kilometre-scale active faults. More precisely, several kilometre-scale active faults are characterized by a narrow and continuous unconsolidated or poorly consolidated clay-rich gouge layer surrounded by damage zones of variable widths. Indeed, when observed on outcrops, in trenches or through drilling, the uppermost, near-surface, part of seismogenic faults reveals a strong localization of slip along a planar zone consisting of a few centimetre-thick unconsolidated clayey gouge termed the *principal slip zone* (PSZ; Sibson 2003). The boundaries between the PSZ and the surrounding rocks are sharp surfaces which often bear striations. The PSZ generally maintains good lateral continuity at the scale of the outcrop and between outcrops, typically being between 1 and 20 cm thick. In several instances, the gouge is partly or totally foliated, but remains poorly consolidated. Examples have been described in California (Chester *et al*. 1993), in Japan (Lin 2001; Lin *et al.* 2001*a*; Wibberley & Shimamoto 2003, 2005; Tsutsumi *et al.* 2004; Noda & Shimamoto 2005), Taiwan (Lin *et al.* 2001*b*) and New Zealand (Sibson *et al.* 1981; Warr & Cox 2001). Such PSZs are interpreted as the location of the most recent displacements, and can thus be considered as the expression of the seismic rupture at or close to the surface of the Earth, between 0 and several kilometres depth (Sibson 2003).

A review of permeability profiles obtained across inactive or active faults shows that the highest permeability values are typically found in the damage zones (particularly for crystalline rocks), the lowest values are obtained in the core zone and intermediate values come from the protolith (Evans *et al.* 1997; Seront *et al.* 1998; Lockner *et al.* 1999; Faulkner & Rutter 1998, 2000, 2001; Morrow *et al.* 1984; Wibberley 2002; Wibberley & Shimamoto 2003; Tsutsumi *et al.* 2004; Uehara & Shimamoto 2004; Mizoguchi *et al.* 2000; Mizoguchi 2004). In addition to the experimental protocols and pressure ranges which vary between studies, the permeability values depend on the clay content, the proportion and size distribution of clasts, the possible sealing of fractures or cracks by secondary minerals and the orientation of the samples with respect to the structural components of the studied faults (open fractures and foliation). In particular, across-fault permeabilities, that is permeabilities of samples oriented perpendicularly to gouge foliation, are one to three orders of magnitude smaller than the permeabilities of samples parallel to the foliation (Evans *et al.* 1997; Seront *et al.* 1998; Faulkner & Rutter 1998, 2000, 2001; Faulkner 2004).

Measurements carried out on samples from strike–slip active faults in low-porosity host rocks with a clayey PSZ show that, for effective confining pressures in the range 80–180 MPa, and for pore pressures of 10–20 MPa, the permeability values obtained from the core zone vary between 10^{-21} and 10^{-17} m^2, those from the damage zones between 10^{-17} and 10^{-15} m^2 and those from the protolith range from 10^{-18} and 10^{-16} m^2 (Fig. 1; Morrow *et al.* 1984; Faulkner & Rutter 1998, 2000, 2001; Mizoguchi *et al.* 2000; Wibberley 2002; Wibberley & Shimamoto 2003; Mizoguchi 2004; Tsutsumi *et al.* 2004; Uehara & Shimamoto 2004; Noda & Shimamoto 2005).

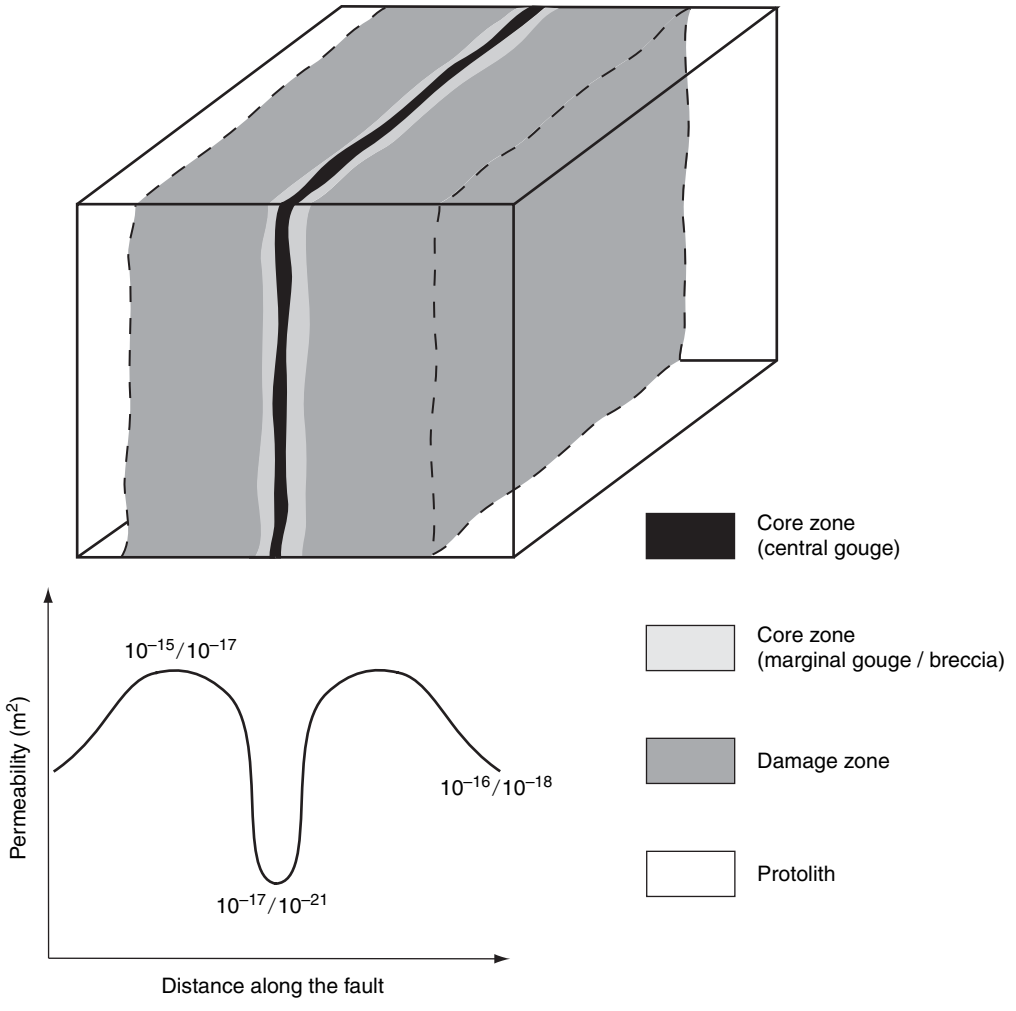

Fig. 1. Schematic permeability profile across an active strike–slip fault after Faulkner & Rutter (1998, 2000, 2001) for mica schists, carbonate sediments and volcanic rocks; Morrow *et al.* (1984), Wibberley (2002), Wibberley & Shimamoto (2003), Uehara & Shimamoto (2004) for gneisses, mylonitic gneisses rocks and metapelitic schists; Noda & Shimamoto (2005) for pelitic rocks; Mizoguchi *et al.* (2000) and Mizoguchi (2004) for conglomerates and granitic rocks; Tsutsumi *et al.* (2004) for sandstone, shale, chert and volcanic rocks. The permeability values are close to values obtained at high effective pressures (of about 100 MPa).

Geological setting of the Usukidani fault

The vertical N55°E-striking Usukidani fault is located in the western part of Honshu, Japan, about 50 km north of Hiroshima (Figs 2 & 3). It belongs to the western Chugoku fault system which consists of prominent NE–SW master faults and short second-order NW–SE faults commonly abutting against the previous ones (Kanaori 1990, 2005; Fabbri *et al.* 2004). The western Chugoku fault system was probably formed in Cretaceous to Paleogene times in response to distributed strike–slip deformation between the Median Tectonic Line (MTL) and a poorly defined fault zone located along the Japan Sea coast, the Southern Japan Sea fault zone (SJSFZ). The formations affected by the western Chugoku fault system include Permian metamorphic and sedimentary rocks, Jurassic sedimentary rocks and Cretaceous acidic pyroclastic deposits locally intruded by late Cretaceous granites and granodiorites (Yamada *et al.* 1985).

Several faults of the western Chugoku system are active today, as attested by shallow earthquakes with magnitudes between 5 and 6.8 and with focal

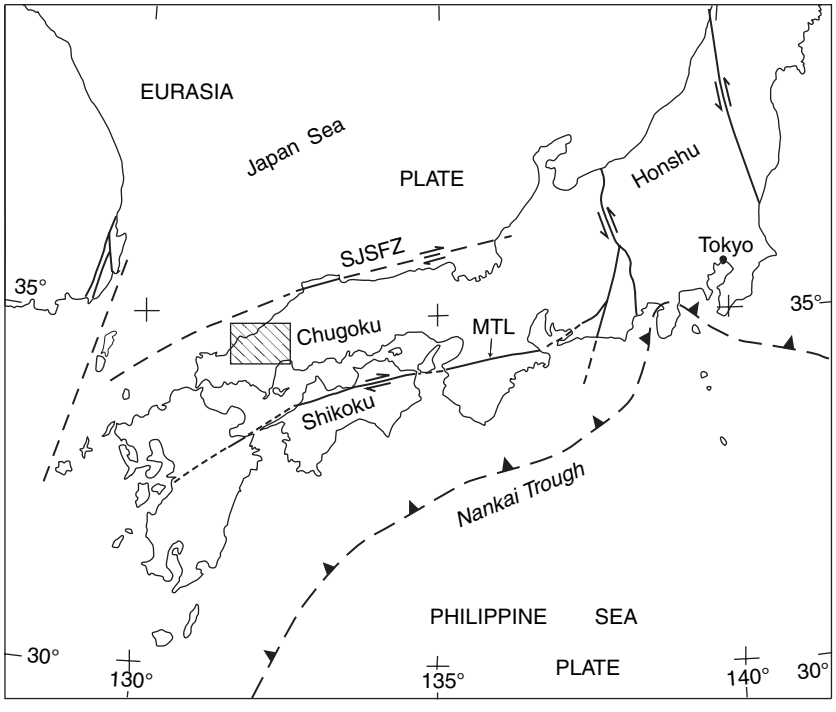

Fig. 2. Geodynamical setting of the western Chugoku fault system. The area covered by the shaded box indicates the position of Figure 3.

depths ranging from 8 to 12–15 km (Fig. 3; Kanaori 1997, 2005; Okada 2004). Displaced ridges or valleys testify to an active right-lateral motion along the NE–SW first-order faults. Focal mechanisms of earthquakes generated along these faults also indicate a right-lateral slip along the NE–SW nodal planes (Research Group for Active Faults of Japan 1991; Fukuyama *et al.* 2000).

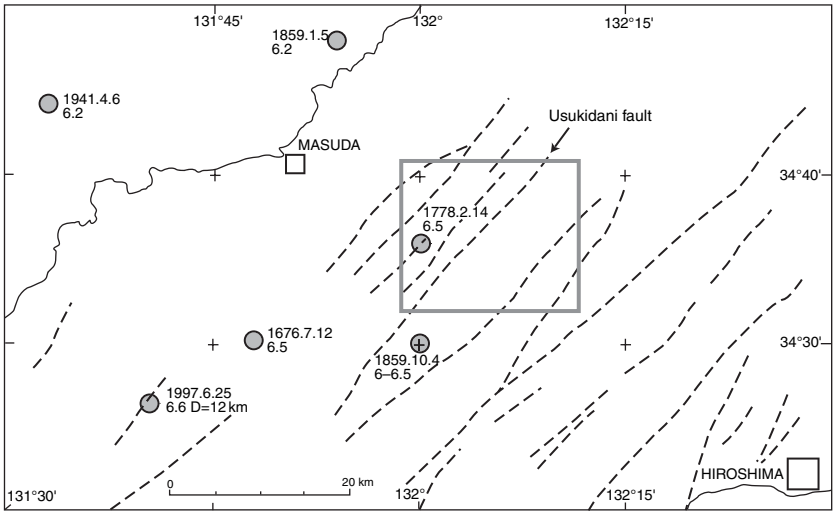

Fig. 3. Seismotectonic context of the study area, with circles corresponding to crustal seismic events. The boxed area indicates the position of Figure 4.

Second-order NW–SE faults do not show any clear displaced topographical features. However, in the easternmost part of the Chugoku region, the 2000 M_w 6.6–6.8 Tottori earthquake (focal depth *c*. 15 km) nucleated on a NNW–SSE fault without any surface expression (Fukuyama *et al.* 2003*a*). The well-constrained focal mechanism indicates an almost pure left-lateral sense of slip (Sagiya *et al.* 2002). Inversion of seismological data further indicates that most of the co-seismic displacement occurred in the upper 6 km of the crust (Semmane *et al.* 2005). Right-lateral slip along NE–SW faults and left-lateral slip along NW–SE faults agree with the directions of the principal components of the present-day stress field, namely a horizontal east–west-trending σ_1 axis and a horizontal north–south-trending σ_3 axis (Ichikawa 1971; Huzita 1980; Tsukahara & Kobayashi 1991).

The Usukidani fault cross-cuts late Cretaceous rhyolitic and dacitic secondary silicified tuffs and tuff breccias (Hikimi and Abu Groups; Yamada *et al.* 1985). It corresponds to an alignment of valleys and depressions which can be followed on aerial photographs along more than 40 km. Based on this pronounced geomorphological expression, the Research Group for Active Faults of Japan (1991) classified the Usukidani fault as potentially active. The epicentres of two magnitude 6–6.5 historical earthquakes (14 February 1778 and 4 October 1859) are located at about 5 km from the fault trace (Fig. 3; Research Group for Active Faults of Japan 1991), but there is no proven relationship between these events and displacement along the Usukidani fault.

Internal structure of the Usukidani fault in the study area

The internal structure of the Usukidani fault zone was investigated along a continuous section where nearly the entire width of the fault zone is exposed (Figs 4 & 5). The fault zone around this locality cuts through rhyolitic tuff protolith. At this locality, the Usukidani fault zone consists of a 10 m wide damage zone which includes three gouge zones.

Protolith

The protolith consists of a coarse secondary silicified tuff with feldspar phenocrysts embedded in a siliceous matrix inside which rare micas can be recognized. Flow surfaces are not uncommon in the region, but could not be recognized in the vicinity of the Usukidani fault. Away from the fault, the protolith tuff is moderately jointed, and most of the joints are of cooling type. In the vicinity of the fault, joints become numerous and tectonic joints prevail over cooling joints. Secondary minerals such as quartz or calcite commonly fill the joints.

Damage zone

The damage zone consists predominantly of a coarse breccia composed of intensely fractured and strongly altered welded tuff with clay minerals, quartz, calcite and laumontite filling the fractures. Close to the core zones, the alteration is more intense, as attested by clay minerals replacing feldspar phenocrysts, especially along fractures.

Core zones

Three distinct core zones can be distinguished in the section across the fault zone (Figs 5 & 6). They consist of unconsolidated or poorly consolidated clay gouge zones flanked by fine fault breccia zones. Among these gouge zones, the one located to the southeast contained the principal slip zone, because its boundaries with the adjacent breccia are sharp and planar, and because of its clear lateral continuity at the scale of the outcrop (Fig. 6). Conversely, the two other clay gouge zones display less sharp and less regular boundaries and their thicknesses show a high variability (Fig. 7b). They are considered as secondary slip zones (SSZ) and are presumed to merge laterally, along strike or along dip, with the PSZ. This assumption is supported by the observation, at an outcrop located 7 km northeast of the study area, of a similar pattern of gouge slip zones (one principal zone to the SE and two secondary zones to the NW), clearly showing the merging of one secondary zone with the principal one.

The PSZ consists of a planar vertical strip of clay gouge striking N55°E and whose thickness ranges from 4.2 to 13.6 cm, with a mean value of 8 cm (averaged on 26 measurements; Fig. 7a). It is separated from the adjacent fine fault breccia or from a marginal foliated gouge by two striated vertical planes striking N55°E $\pm$ 2°. The rake of the striation is less than 10° northeastwards. The PSZ gouge is composed of unconsolidated grey clay showing a finely spaced vertical foliation striking 30° or less counterclockwise of the trend of the PSZ, in agreement with the right-lateral sense of slip reported for the Usukidani fault (Kanaori 1999). XRD analyses of grey clay gouge samples show that it is composed of quartz, K-feldspar, plagioclase, calcite, kaolinite and mixed illite–smectite layers.

The PSZ gouge is flanked by a marginal poorly consolidated blue foliated clayey gouge and by moderately consolidated fine clay-rich fault breccia. The fine breccia likely results from cataclasis and circulation of hydrothermal fluids. Both processes probably contributed to the alteration of

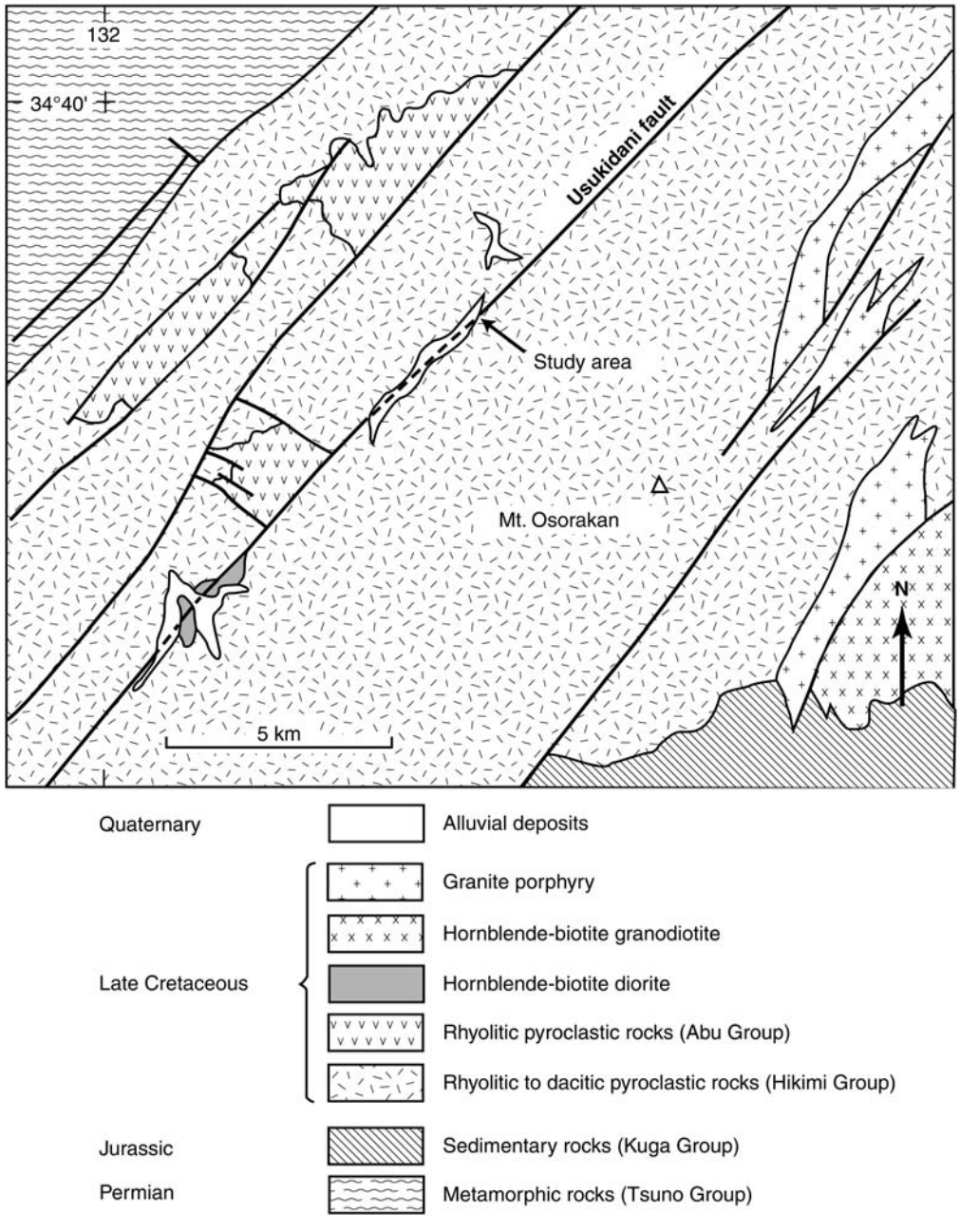

Fig. 4. Simplified geological map of the Usukidani fault and location of the studied outcrop.

the original protolith and its enrichment in clay minerals. A strand of the marginal foliated gouge penetrates the fine fault breccia and pinches out along a fracture striking 10–20° clockwise to the trend of the PSZ (Fig. 5b; area located to the right, or southwest, of sample 18). This pattern suggests that ancient ruptures may have propagated sidewards off the line of the main fault.

The zonation of the secondary displacement zone SSZ-1 is similar to that of the PSZ (Fig. 5c). It includes a narrow central unconsolidated grey clay gouge zone bounded by two vertical striated

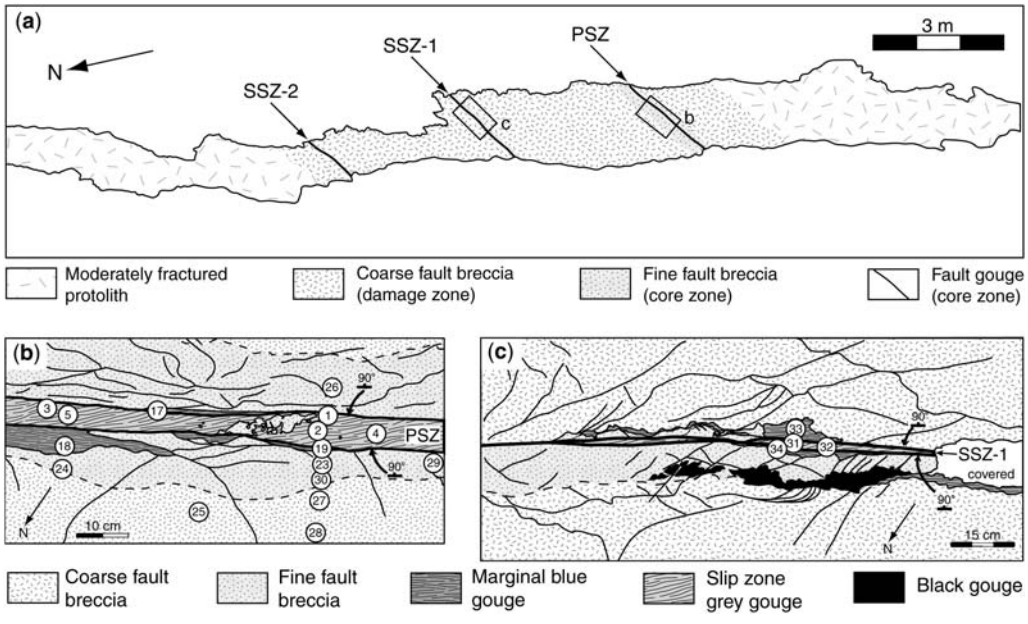

Fig. 5. (**a**) Structural sketch map of the Usukidani fault zone. (**b**) Detail of the principal slip zone PSZ. (**c**) Detail of the secondary slip zone SSZ-1.

planes striking N55°E ± 15° and whose thickness ranges from 0.2 to 22.5 cm, with a mean value of 5.6 cm (averaged on 35 measurements; Fig. 7b). XRD analyses show that the grey clayey gouge is composed of the same minerals as the PSZ gouge. As for the PSZ, the rake of the striation on the bounding planes is between 0 and 10° either northeastwards or southeastwards. Remnants of poorly consolidated foliated blue clayey gouge are observed between the striated planes and the thick marginal clayey fault breccia zones. Unlike the PSZ, remnants of consolidated black gouge are also found between the fine fault breccia and the coarse fault breccia.

Porosity and permeability measurements

Field sampling, sample preparation and measurement procedures

Cylindrical gouge samples were collected in three mutually perpendicular directions: parallel to both the gouge foliation and the striation (∥ ∥), parallel to the gouge foliation and perpendicular to the striation (∥⊥), and perpendicular to both the gouge foliation and the striation (⊥ ⊥). It is important to note that, given the narrowness of each gouge zone, sampling perpendicular to the foliation and the striations (⊥ ⊥ orientations) was very difficult and only a few such samples could be retrieved. Hence the most complete porosity and permeability dataset was obtained for vertical samples (∥⊥orientations), which were the easiest samples to extract from the outcrop with minimum damage to the gouge microfabric. The dataset used in the modelling will therefore correspond to ∥⊥orientations.

The samples were obtained by hammering 20 mm-diameter stainless steel or copper tubes into the gouge zones. The 3–5 cm long samples were then immediately pushed out into a heat-retractable polyolefin jacket sealed using a hair-drier in order to minimize sample disturbance during transportation. In the laboratory, samples were oven dried at 60–80 °C for one week to eliminate pore water, then cut to the desired length (1–2 cm) before being further oven dried for a second week. Care was taken to ensure that the original pore structure of the clayey gouge or breccia samples was not significantly modified by sampling nor altered during laboratory preparation and oven drying.

The porosities of gouge and breccia samples were measured with a simple pore-pressure decay method with a fixed volume of pore-fluid reservoir, using the intra-vessel deformation fluid-flow apparatus, an oil medium triaxial machine, in Kyoto University. This method assumes that mineral grains are rigid and that their compressibility is

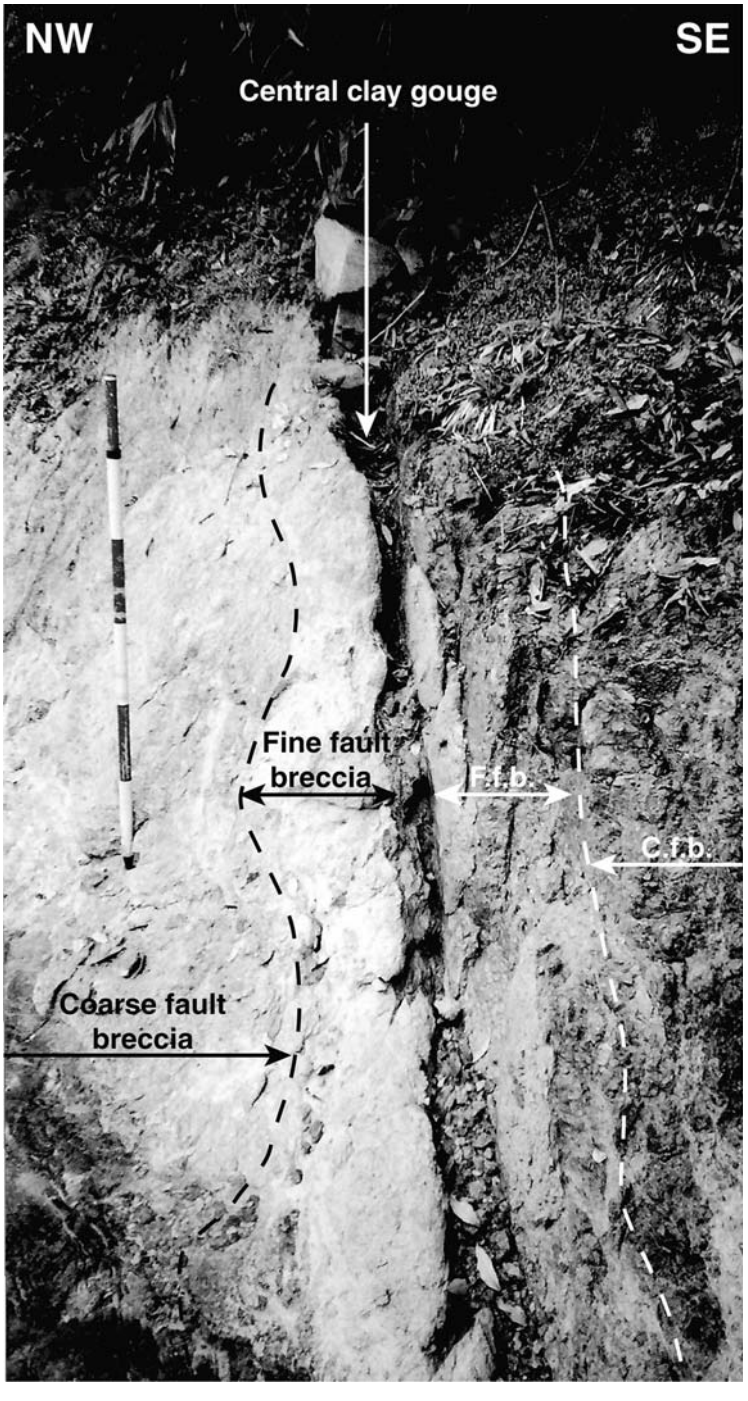

Fig. 6. Lateral view of the PSZ towards the northeast, showing its lateral continuity. Scale bar length is 1.20 m.

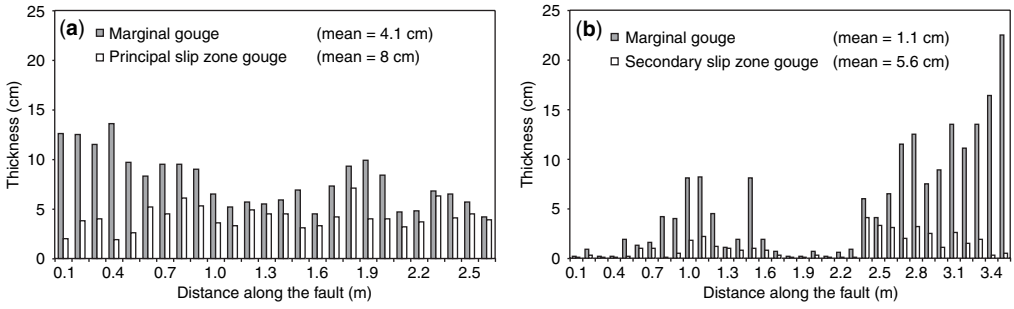

Fig. 7. Along-strike measured variations of the thickness of the PSZ gouge and the marginal gouge (**a**), and the SSZ-1 gouge and the marginal gouge (**b**).

negligible compared with that of the pores. Nitrogen was used as the pore fluid, and oil used as the confining pressure medium. The nitrogen pressure upstream of the sample did not exceed 1 MPa. Porosities were measured at several confining pressures following first an increasing pressure path (from 10 to 100 MPa by 10 or 20 MPa steps) and then a decreasing path (from 100 to 10 MPa with similar pressure steps). The increasing effective confining pressure paths are assumed to simulate increasing depths and hence increasing lithostatic load from 0.4 km (10 MPa) to 4 km (100 MPa), whereas the decreasing paths are considered to reflect a progressive increase of pore fluid pressure for a given depth.

Permeabilities were measured with the same intra-vessel deformation fluid-flow apparatus as for the porosity measurements. A constant differential pore pressure was applied to the top of the specimen with air-drained conditions at the downstream end. The flow rate was monitored by a flowmeter capable of detecting flow rates between 0.05 and 5000 ml min^{-1}. As for the porosity measurements, permeabilities were first measured following an increase in effective confining pressure (from 5 to 100 MPa, with 5, 10 or 20 MPa pressure steps) and then following a decrease in effective confining pressure (from 100 to 10 MPa). The maximum effective confining pressure obtained (100 MPa) corresponds to lithostatic load conditions expected at about 6 km depth with a hydrostatic fluid pressure.

Results

The results of the seven porosity runs and the 34 permeability runs are given in Tables 1 & 2, along with the orientations of the samples. The values obtained on representative samples, including the samples from the different zones for which thermal pressurization will be tested, are plotted as a function of P_e on Figures 8 & 9.

Porosity of central and marginal clayey gouges and marginal breccias

During increasing pressure paths, porosity values of central and marginal clayey gouges decrease from 25–40% at $P_e = 10$ MPa down to 23–34% at $P_e = 100$ MPa (Table 1 and Fig. 8a). During subsequent decreasing pressure paths, the porosity values tend to recover initial values. The porosities of the marginal fault breccia evolve from 10–18% at $P_e = 10$ MPa to 8–9% at $P_e = 100$ MPa (Fig. 8b). As already noted by David *et al.* (1994), porosity variations as a function of P_e generally follow an exponential law of the form:

$$n = n_0 \times \exp\left[-\alpha \times (P_e - P_0)\right] \qquad (1)$$

where n_0 is the porosity at a reference pressure P_0, here fixed at zero.

More precisely, for the decreasing confining pressure paths (decreasing effective pressure), the equations in Figure 8, derived from best-fit trends, will be used in the modelling to calculate porosity values from given P_e values.

Permeability of fault gouges and fault breccias

During increasing pressure paths (confining paths), permeability values of central and marginal clayey gouges decrease from 5.5×10^{-17} to 1.06×10^{-14} at $P_e = 20$ MPa down to 2.95×10^{-19} to 4.16×10^{-16} at $P_e = 100$ MPa (Table 2). During subsequent decreasing pressure paths (deconfining paths), the permeability values increase but without returning to their initial values, illustrating the effect of permanent compaction. Indeed, these values at $P_e = 20$ MPa are one to two orders of magnitude lower than the starting values (Fig. 9). With respect to sample orientation, the permeability values show the following

Table 1. *Summary of porosity measurements and of estimates of n_0, α, β_0 and χ coefficients (for deconfining paths). PSZ is for principal slip zone and SSZ for secondary slip zone*

Fault rock zone	Fault rock type	Sample number	Sample orientation	Porosity		Reference porosity n_0 at $P_e = 0$	Porosity-pressure sensitivity coefficient α (MPa^{-1})		Reference compressibility β_0 (Pa^{-1}) at $P_e = 0$		Bulk compressibility-pressure sensitivity coefficient χ (MPa^{-1})
				P_e (20 MPa)	P_e (100 MPa)	Deconfining path	Deconfining path		Deconfining path		Deconfining path
PSZ	Central gouge	4	$\parallel\perp$	0.389	0.337	0.375	0.0011		7×10^{-10}		2×10^{-8}
PSZ	Central gouge	16	$\perp\perp$	0.386	0.237	0.351	0.0041		1×10^{-8}		4×10^{-8}
PSZ	Fine fault breccia	24	$\perp\parallel\perp$	0.141	0.899	0.108	0.0022		7×10^{-10}		5×10^{-8}
PSZ	Fine fault breccia	25	$\parallel\perp$	0.135	0.810	0.120	0.0042		8×10^{-10}		4×10^{-8}
PSZ	Fine fault breccia	29	$\parallel\perp$	0.146	0.859	0.104	0.0020		4×10^{-10}		4×10^{-8}
SSZ-1	Central gouge	31	$\parallel\perp$	0.382	0.319	0.357	0.0012		6×10^{-10}		2×10^{-8}
SSZ-1	Central gouge	32	$\parallel$	0.303	0.227	0.270	0.0019		9×10^{-10}		3×10^{-8}

hierarchy: $k_{\perp\perp} < k_{\parallel\parallel} < k_{\parallel\perp}$, a hierarchy which is particularly clear at $P_e = 100$ MPa (Fig. 9).

In a similar way, during confining paths, the permeability values of the marginal fine clayey fault breccia decrease from 8.5×10^{-16} to 1.6×10^{-15} at $P_e = 20$ MPa down to 7.22×10^{-18} to 4.16×10^{-16} at $P_e = 100$ MPa (Table 2). During subsequent deconfining paths, the permeability values increase but without returning to their initial values. Their values at $P_e = 20$ MPa are about two orders of magnitude lower than the starting values (Fig. 9e). Given the fact that all samples from the marginal breccia were cored with the same orientation ($\parallel\perp$ orientation), the dependency of permeability with orientation cannot be considered here.

As initially noted by David *et al.* (1994), the permeability values follow equations of the form:

$$k = K_0 \times \exp\left[-\gamma \times (P_e - P_0)\right] \tag{2}$$

where K_0 is the permeability at a reference pressure P_0, here fixed at zero.

More precisely, for the decreasing confining pressure paths (decreasing effective pressure), the equations in Figure 9, derived from best-fit trends, will be used in the modelling to calculate permeability values (in m^2) from P_e values.

Analysis of the influence of branching faults on thermal pressurization

General considerations

The basic condition for thermal pressurization to occur in a slip zone is that the hydraulic diffusion length d_h of the constitutive material be significantly smaller than the half-width $w/2$ of the heated zone. The hydraulic diffusion length, which can also be defined as the distance of propagation of a fluid pressure from a source at time t, can be related to the hydraulic diffusivity by the equation (Lachenbruch 1980):

$$d_h(t) = (4 \times D_h \times t)^{1/2}. \tag{3}$$

The hydraulic diffusivity, D_h, depends on the permeability, k, and the storage capacity per unit sample volume, β_c, of the material constituting the fault zone and on the fluid viscosity, η, according to the equation:

$$D_h = k/(\eta \times \beta_c). \tag{4}$$

The values of k at a given effective pressure P_e can be derived by using the equations relating k and P_e obtained by best-fit trends (see above and

Table 2. *Summary of permeability measurements and of estimates of K_0 and γ coefficients*

Fault rock zone	Fault rock type	Sample number	Sample orientation	Permeability (m^2)		Permeability-pressure coefficient γ (MPa^{-1})	
				P_e (20 MPa)	P_e (100 MPa)	Confining path	Deconfining path
PSZ	PSZ gouge	1	∥ ⊥	3.92×10^{-15}	1.24×10^{-16}	0.0547	0.0081
PSZ	PSZ gouge	2	∥ ⊥	2.14×10^{-15}	7.00×10^{-18}	0.0738	0.0203
PSZ	PSZ gouge	3	∥ ⊥	1.54×10^{-15}	5.77×10^{-18}	0.0731	0.0162
PSZ	PSZ gouge	4	∥ ⊥	1.58×10^{-15}	4.74×10^{-18}	0.0725	0.0213
PSZ	PSZ gouge	5	∥ ⊥	8.39×10^{-16}	9.04×10^{-19}	0.0843	0.0342
PSZ	PSZ gouge	6	∥ ∥	1.55×10^{-15}	2.80×10^{-17}	0.0538	0.0140
PSZ	PSZ gouge	7	∥ ∥	2.84×10^{-16}	1.75×10^{-18}	0.0606	0.0222
PSZ	PSZ gouge	8	∥ ∥	6.30×10^{-16}	8.49×10^{-18}	0.0587	0.0140
PSZ	PSZ gouge	9	∥ ∥	2.05×10^{-16}	1.83×10^{-19}	0.0907	0.0248
PSZ	PSZ gouge	10	⊥ ⊥	4.68×10^{-16}	3.78×10^{-18}	0.0680	0.0164
PSZ	PSZ gouge	11	⊥ ⊥	3.50×10^{-16}	3.18×10^{-18}	0.0673	0.0147
PSZ	PSZ gouge	12	⊥ ⊥	3.45×10^{-16}	2.87×10^{-18}	0.0652	0.0151
PSZ	PSZ gouge	13	⊥ ⊥	5.66×10^{-16}	2.30×10^{-18}	0.0733	0.0242
PSZ	PSZ gouge	14	⊥ ⊥	7.43×10^{-16}	1.99×10^{-18}	0.0786	0.0177
PSZ	PSZ gouge	15	⊥ ⊥	2.00×10^{-16}	1.20×10^{-18}	0.0718	0.0211
PSZ	PSZ gouge	16	⊥ ⊥	5.50×10^{-17}	7.42×10^{-19}	0.0503	0.0173
PSZ	Marginal gouge	17	∥ ⊥	1.06×10^{-14}	2.91×10^{-17}	0.0779	0.0177
PSZ	Marginal gouge	18	∥ ⊥	4.21×10^{-15}	1.01×10^{-17}	0.0813	0.0207
PSZ	Marginal gouge	19	∥ ⊥	5.67×10^{-16}	6.64×10^{-19}	0.0257	0.0874
PSZ	Marginal gouge	20	∥ ∥	3.13×10^{-15}	5.97×10^{-18}	0.0862	0.0277
PSZ	Marginal gouge	21	∥ ∥	2.09×10^{-15}	1.50×10^{-18}	0.0898	0.0217
PSZ	Marginal gouge	22	∥ ∥	4.48×10^{-16}	2.95×10^{-19}	0.0978	0.0239
PSZ	Fine fault breccia	23	∥ ⊥	5.28×10^{-16}	1.14×10^{-17}	0.0587	0.0160
PSZ	Fine fault breccia	24	∥ ⊥	2.11×10^{-16}	7.22×10^{-18}	0.0514	0.0096
PSZ	Fine fault breccia	25	∥ ⊥	3.03×10^{-16}	1.01×10^{-17}	0.0535	0.0129
PSZ	Fine fault breccia	26	∥ ⊥	6.60×10^{-15}	4.16×10^{-16}	0.0414	0.0078
PSZ	Fine fault breccia	27	∥ ⊥	8.50×10^{-16}	3.07×10^{-17}	0.0474	0.0088
PSZ	Fine fault breccia	28	∥ ⊥	3.29×10^{-16}	5.36×10^{-18}	0.0585	0.0144
PSZ	Fine fault breccia	29	∥ ⊥	4.34×10^{-16}	1.38×10^{-17}	0.0524	0.0137
PSZ	Fine fault breccia	30	∥ ⊥	1.60×10^{-15}	4.64×10^{-17}	0.0534	0.0112
SSZ-1	SSZ-1 gouge	31	∥ ⊥	4.69×10^{-16}	1.04×10^{-18}	0.0797	0.0140
SSZ-1	SSZ-1 gouge	32	∥ ⊥	8.62×10^{-16}	2.65×10^{-18}	0.0855	0.0140
SSZ-1	Marginal gouge	33	∥ ⊥	3.96×10^{-16}	3.06×10^{-18}	0.0736	0.0149
SSZ-1	Marginal gouge	34	∥ ⊥	7.70×10^{-16}	1.15×10^{-17}	0.0626	0.0155

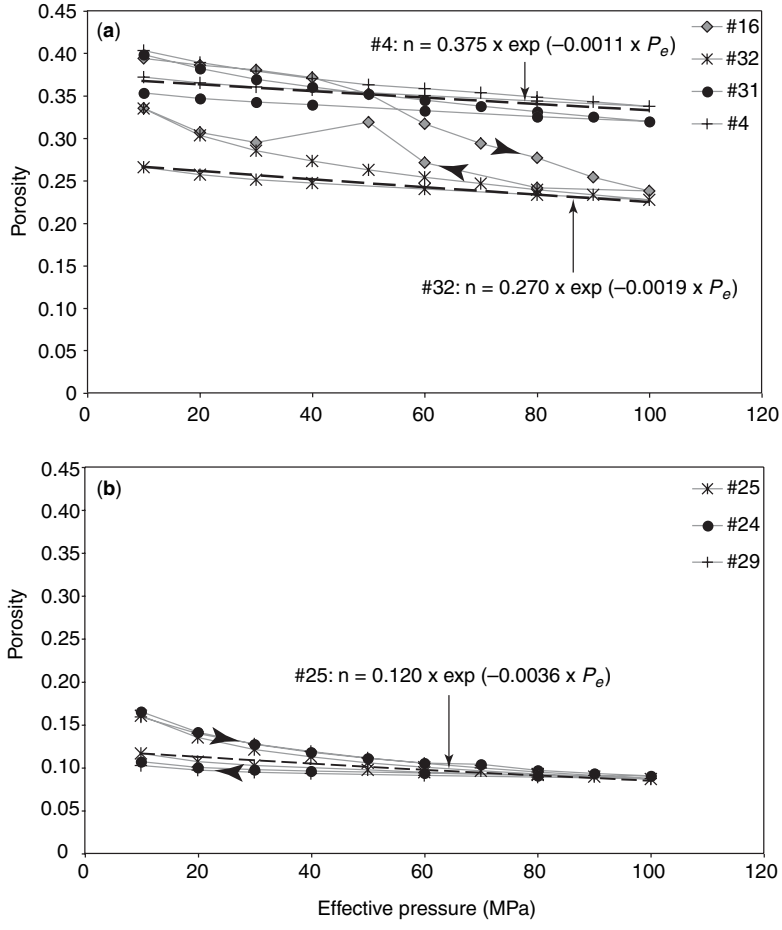

Fig. 8. Evolution of porosity with increasing/decreasing effective confining pressures for gouges (**a**) and fault breccias (**b**) from the principal and secondary slip zones of study area. Samples 4 and 16 are gouges from PSZ. Samples 31 and 32 are gouges from SSZ-1. Samples 24, 25 and 29 are from the PSZ marginal fine fault breccias. All samples except 16 are located on Figure 5b and c, and are vertical, that is parallel to the gouge foliation and perpendicular to the striation ($\parallel \perp$ orientations). Sample 16 is perpendicular to the gouge foliation. Also given are the equations of the best-fit curves (dashed lines) for decreasing effective pressure paths for samples 4, 32 and 25. In the equations, P_e is expressed in MPa.

Fig. 9). The storage capacity per unit sample volume β_c is related to the porosity n of the material, to the compressibilities β_f of the fluid and β_s of the mineral grains, and to the sample bulk framework compressibility β_b by the following equation:

$$\beta_c = n \times (\beta_f - \beta_s) + (\beta_b - \beta_s). \qquad (5)$$

The compressibilities of water (Table 3) and mica (1.2×10^{-11} Pa^{-1}) will be taken for β_f and for β_s, respectively. The values of β_b for different effective pressures P_e were derived by finding the volume change per unit confining pressure decrease and dividing this change by the sample volume at the start of the confining pressure step (see details in Wibberley 2002). The calculated β_b are then plotted as a function of P_e and a linear extrapolation is made in order to obtain equations relating theoretical β_b values to P_e for each sample (Fig. 10). These equations are of the form:

$$\beta_b = \beta_0 \times \exp\left[-\chi \times (P_e - P_0)\right] \qquad (6)$$

where β_0 is a compressibility at a reference pressure P_0, here fixed at zero.

More precisely, for the decreasing confining pressure paths (decreasing effective pressure), the

equations in Figure 10 derived from best-fit trends will be used in the modelling to calculate compressibility values from given P_e values.

Choice of parameters

In addition to physical constants given in Table 3, the following parameters are needed for the modelling: porosity and permeability, fault zone thickness and depth of deformation.

Ideally, the permeability values to be used for modelling should be the ones corresponding to samples oriented perpendicularly to the slip zones. However, as stated above, the data obtained on samples with that ideal orientation are incomplete. The most complete dataset corresponds to samples oriented vertically, i.e. parallel to the slip zones and perpendicular to the striation ($\parallel \perp$ orientations). Representative samples for each zone are sample 4 (PSZ gouge), sample 25 (PSZ marginal fine breccia) and sample 32 (SSZ-1 gouge). For each sample, the porosity and permeability at a given effective confining pressure P_e will be calculated using the equations corresponding to these samples as determined above.

Although the most complete dataset collected corresponds to samples cored in the $\parallel \perp$ orientation, in the case of clay gouges, these data show permeabilities one to three orders of magnitude higher than the $\perp \perp$ samples. Hence the best-fit equation, based on data from the $\parallel \perp$ direction, will overestimate the permeability perpendicular to the foliation, which is the suitable direction of fluid pressure dissipation from the heated slip zone towards adjacent high permeable breccia. We therefore selected gouges in the centre of the slip zones (numbers 4 and 32) as the most representative ones, and reduced their permeability values by one order of magnitude for the modelling in order to account for this anisotropy. For the breccia permeabilities, we chose an average permeability trend.

The equations relating P_e to n, k or β_b were obtained by best-fitting of experimental data pertaining to the deconfining path (decrease of P_e from 100 to 10 MPa; Figs 8–10), as described above, in order to simulate effective pressure decrease. We assume the effective pressure law in its simplest form in order to model pore fluid pressure increase, corresponding to the phenomenon expected to occur during thermal pressurization.

The thickness of the fault zone, either gouge or breccia, is another parameter which needs to be taken into consideration. The values used for the PSZ and SSZ-1 gouges are average values derived from direct measurements carried out on the outcrop (Fig. 7). They are 80 mm for the PSZ central gouge and 56 mm for SSZ-1 central gouge. The thickness of the marginal fine breccia is difficult to measure with accuracy on the outcrop because the limits between this breccia and the surrounding coarse breccia are unclear. Estimates range from 50 to 700 mm. In order to test the possible effects of a rupture propagating from the PSZ into the marginal fine breccia, modelling of breccia pressurization will be done for a 50 mm thick zone, which may correspond to a mean thickness of the zone supposed to accommodate the slip.

The 2000 Tottori earthquake, whose hypocentral depth is estimated at 10–15 km (Semmane *et al.* 2005) can be considered as a representative event of the Chugoku region. Modelling of strong motion displacement records and GPS coseismic data reveal two areas of large slip amplitudes: a shallow one, between 0 and 2 km, and a deeper one, between 4 and 6 km (Semmane *et al.* 2005). The thermal pressurization process will be tested at 6 km, that is the depth at which the rupture propagating upward from depth starts to induce a significant amount of slip.

Modelling approach

Our modelling assumes a planar slip zone (thickness $2w$) of finite hydraulic diffusivity, D_h, surrounded by a material of infinite hydraulic diffusivity, so that the fluid pressure can be assumed to remain hydrostatic at all times at the limits of the shear zone. Our second assumption is to ignore the effect of heat loss, justified because, for typical thermal diffusivities, the thermal diffusion length scale is much smaller than the thickness of the gouge central slip zone (Lachenbruch 1980; Mase & Smith 1987). A third assumption is that dilatancy does not occur in the slip zone: for poroelastic dilatancy to occur during pore fluid pressure rises, the low matrix compressibility in comparison to that of water will inhibit dilatancy (Wibberley 2002); for shear dilatancy, dilatancy angles measured in clay materials are typically very small, and dilatancy in coarse granular materials decreases to zero at shear strains of about 0.1–0.5 (e.g., Mandl *et al.* 1977), i.e., after only a small amount of the total shear strain suffered during seismic slip on a narrow zone.

The modelling approach balances the rate of fluid pressure increase by frictional heating with the rate of fluid pressure decrease by excess pressure dissipation, to determine the net change in fluid pressure through time. The rate of frictional heating ($\mathrm{d}T/\mathrm{d}t$) of the pore water in the slip zone is determined by the shear stress, τ, the relative slip velocity, $2V$ (assumed constant in this modelling at 0.5 m s^{-1}) and the width of the shear zone, assuming that all

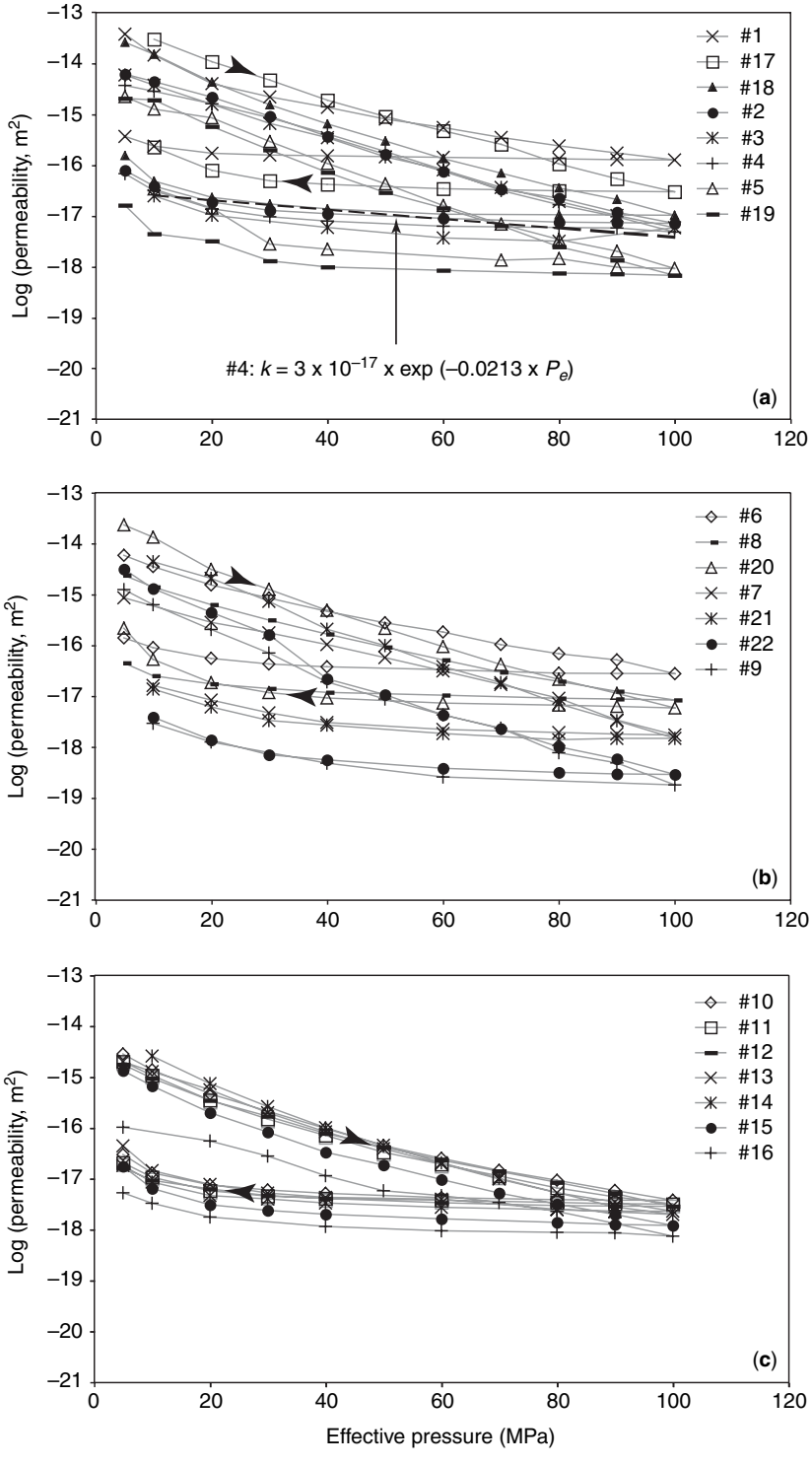

Fig. 9. (*Continued*).

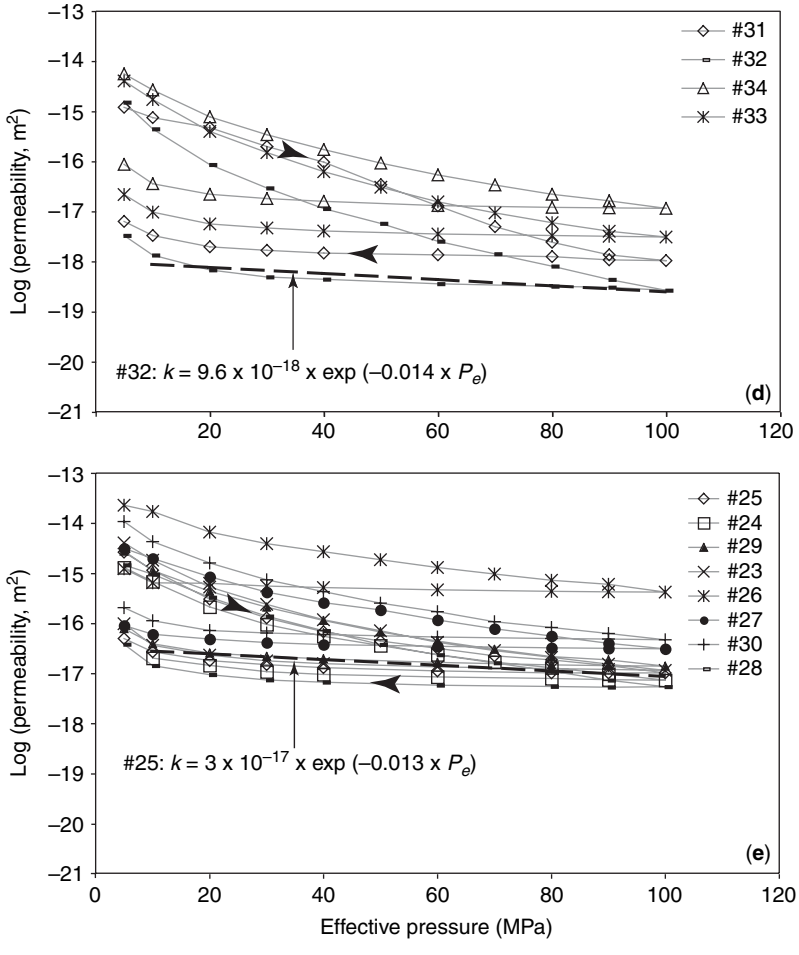

Fig. 9. (*Continued*) Evolution of permeability with increasing/decreasing effective confining pressures for gouges and breccias from the principal and secondary slip zones of study area. (**a**) Samples from PSZ gouges with $\parallel\perp$ orientations. (**b**) Same as (a), with $\parallel\parallel$ orientations. (**c**) Same as (a), with $\perp\perp$ orientations. (**d**) Samples from SSZ-1 gouges with $\parallel\perp$ orientations. (**e**) Samples from PSZ marginal breccias with $\parallel\perp$ orientations. Also given are the equations of the best-fit curves (dashed lines) for decreasing effective pressure paths for samples 4, 32 and 25. In the equations, P_e is expressed in MPa.

the frictional work is transformed into heat:

$$\frac{\mathrm{d}T}{\mathrm{d}t} = \frac{\tau \times V}{\rho \times c \times w} \tag{7}$$

where $\tau = \mu \times (\sigma_\mathrm{n} - P_{(\mathrm{t})})$, ρ is the density of the material (assumed to be 2500 kg m^{-3}), c is the specific heat capacity (assumed to be 1000 J kg^{-1} K^{-1}), μ is the coefficient of friction (assumed to remain constant at 0.4), σ_n is the normal stress (assumed to equal the overburden pressure) and P is the fluid pressure in the slip zone. Starting with the 'undrained' extreme case of no fluid escape, the water pressure will rise at a rate related to the thermal expansivity, α_w, and

Table 3. *Water properties used in the thermal pressurization modelling*

Water expansivity	α_w	0.0015	K^{-1}
Water specific heat capacity	c	1000	J kg^{-1} K^{-1}
Water compressibility	β	4.3×10^{-10}	Pa^{-1}

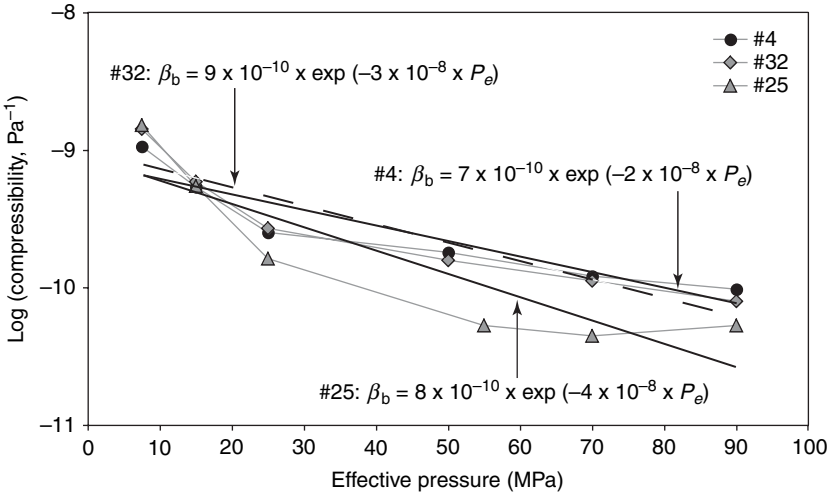

Fig. 10. Calculated sample bulk framework compressibility β_b as a function of the effective confining pressure P_e and best-fit equations (continuous and dashed lines) for the three samples representative of PSZ gouge (4), SSZ-1 central gouge (32) and PSZ marginal fine breccia (25). In the equations, P_e is expressed in MPa.

compressibility, β_w, of water:

$$\frac{d\Delta P}{dt} = \frac{\alpha_w}{\beta_w} \times \frac{dT}{dt} = \frac{\alpha_w}{\beta_w} \times \frac{\mu \times (\sigma_n - P_{(t)}) \times V}{\rho \times c \times w}. \quad (8)$$

Following classical solutions for heat diffusion as an analogue for fluid pressure diffusion (Carslaw & Jaeger 1959), the rate of fluid pressure dissipation in the centre of the shear zone can be estimated as:pt?>

$$\frac{d\Delta P}{dt} = -D_h \times \Delta P \times \left(\frac{\pi}{2w}\right)^2 \times \exp\left[-D_h \times \left(\frac{\pi}{2w}\right)^2 \times t\right]. \quad (9)$$

The rate of thermal pressurization is the difference between the rate of pressure build-up due to frictional heating and the rate of pressure dissipation due to fluid flow and is obtained by subtracting equation (9) from equation (8). Integration of the result with respect to time allows calculation of the fluid pressure evolution. Note that the rate of thermal pressurization depends upon the actual excess fluid pressure at any one point in time [equation (9)], and hence the effective normal stress. As thermal pressurization occurs, the effective normal stress will decrease; hence the rate of frictional heating will decrease [equation (7)]. The fluid pressure can therefore never exceed lithostatic pressure in the model.

The modelling calculates, as a function of time: (1) the increase of pore fluid pressure inside a slip zone of given width due to co-seismic frictional heating of the pore fluid in the gouge zone; and (2) the corresponding shear stress evolution through time, assuming Amonton law with the effective normal stress being the difference between normal stress and fluid pressure. Thermal pressurization is considered to be fully efficient in the cases for which the effective normal stress is reduced to zero in a short span of time (of the same order as the earthquake duration).

Results of numerical analyses

We calculate the evolution through time of the shear stress expected for three representative rock types of the Usukidani fault: PSZ central gouge (sample number 4), SSZ-1 central gouge (sample 32) and PSZ marginal fine fault breccia (sample 25) at depths of 6 km (Fig. 11). Thermal pressurization appears to be efficient for the two PSZ and SSZ-1 gouges, and stress drop is predicted to occur to $1/e$ of its initial value over timescales of the order of 1 s. For minimum widths, for instance of 5 mm (Fig. 12), the thermal pressurization is less efficient, yet the shear stress is nevertheless reduced by one order of magnitude, although it does not reach zero.

Unlike the PSZ or SSZ-1 gouges, the hydraulic properties of the PSZ marginal breccia do not allow the pore fluid pressure to rise sufficiently to counteract the normal stress, at least for the 50 mm thickness used in the modelling (Fig. 11b). For larger thicknesses (1 m or more), the effective normal stress

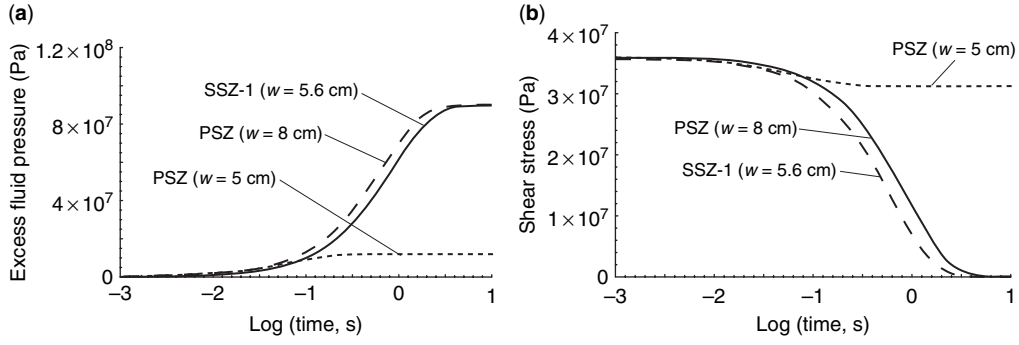

Fig. 11. Results of modelling of the thermal pressurization process for gouge or breccia showing the effects of frictional heating during seismic slip at a depth of 6 km, for respectively PSZ gouge ($w = 8$ cm), SSZ-1 gouge ($w = 5.6$ cm), PSZ marginal fine fault breccia (w estimated at 5 cm). (**a**) Predicted fluid pressure against time. (**b**) Corresponding shear stress variation with time.

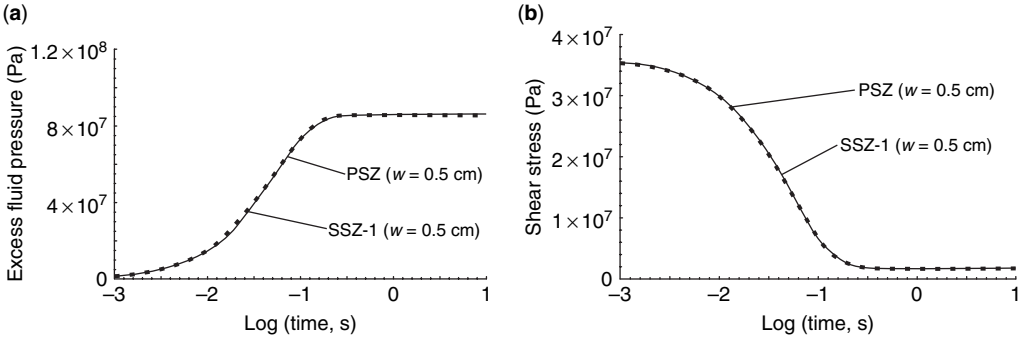

Fig. 12. Same as Figure 11 for a 0.5 cm thickness value of PSZ and SSZ-1 gouge zones.

(and hence shear stress) would decrease to zero, but only after significantly longer periods of time than typical earthquake slip durations.

Calculations carried out on the same samples with the same thicknesses at a depth of 4 km show that thermal pressurization is less efficient than at 6 km. In particular, the pore pressure rise for the PSZ and SSZ-1 gouges is not sufficient to counteract the normal stress. Conversely, at a depth of 8 km, if thermal pressurization does still not occur for the marginal breccia samples, it becomes efficient for the hypothetical thin PSZ and SSZ-1 gouges.

Discussion

Fluid flow properties of the Usukidani fault zone

The permeability values obtained for the clay gouges of the Usukidani fault zone at an effective pressure of 100 MPa (Table 2, Fig. 9) fall mid-way in the range of previously reported data for clay gouges, being closest to those reported for the Neodani and Hanaore faults, Japan (Tsutsumi *et al.* 2004; Noda & Shimamoto 2005). At Usukidani, typical values are 10^{-16}–10^{-19} m^2 for the central clay gouge and 10^{-15}–10^{-17} m^2 for the marginal fine fault breccia. Nevertheless, a wide range in clay gouge permeability values exists in the literature, which can be explained by: (1) differences in microstructure and clay mineralogy of the gouge zones, influenced by structural history, reworking into the gouge zones of clasts of adjacent material, and strain localization, and/or (2) differences in sampling procedures and experimental methodologies. This is also true for porosity values of clay gouges, although the number of studies reporting porosity data for natural clay gouges is far fewer than for permeability. Porosity measurements reported here in the range of 23–32% at effective pressures of 80–100 MPa (Table 1, Fig. 8) are similar to those reported by Noda & Shimamoto (2005) but

significantly higher than the porosities of 4–9% measured for fault gouges from the Median Tectonic Line (Wibberley & Shimamoto 2005).

Individual cores of clay gouge along the Usukidani fault zone yielded permeability values varying between one and three orders of magnitude, depending on the orientation of the cores (see above: $\parallel\parallel$, $\parallel\perp$ or $\perp\perp$ orientations). More precisely, the permeability values show the following hierarchy, which is quite clear at $P_e = 100$ MPa (Fig. 9a–c): $k_{\perp\perp} < k_{\parallel\parallel} < k_{\parallel\perp}$. Similar dependencies between the permeability values and the sample orientations have already been reported by other studies carried out on gouges with internal anisotropies (Seront *et al.* 1998; Faulkner & Rutter 1998, 2001; Wibberley & Shimamoto 2005). These studies have also found the same hierarchy as the one stated above.

Gouge permeability is expected to decrease with depth due to the effect of compaction. For permeability–pressure data matched closely by an exponential decrease law, the compaction coefficient, γ, illustrates the permeability dependence on pressure. Typical values of γ for Usukidani fault rocks are $0.04\ \mathrm{MPa}^{-1}$ for fine fault breccia and $0.1\ \mathrm{MPa}^{-1}$ for clay gouges. Upon deconfinement, permeability recovers to values one to three orders of magnitude lower than initial values, illustrating the importance of permanent compaction. This deconfinement represents a decrease in effective pressure, presumed to have a similar effect on permeability as an increase in fluid pressure.

Thermal pressurization

Previous investigations of the thermal pressurization process as a slip-weakening mechanism have shown that it is highly affected by several factors such as the slip rate, the depth and the width of the deformation zone (Andrews 2002; Noda & Shimamoto 2005; Wibberley & Shimamoto 2005). The slip rate determines the rate of frictional heating and the rate of fluid pressure build-up. However, in order to compare the different modelling cases, the relative sliding velocity in our models is fixed at $0.5\ \mathrm{m\ s}^{-1}$, which is in the range of seismological studies (Scholz 2002).

The depth determines the hydraulic transport properties and controls the normal stress. Calculations performed for parameters appropriate to a depth of 6 km yielded estimates for the amount of shear stress drop on the fault of around 36 MPa for both the PSZ and the SSZ-1 for fully effective thermal pressurization (Fig. 11a & b), slightly larger (half an order of magnitude) than that considered typical for large earthquakes (in the order of 10 MPa). When the microbreccia properties are used as the parameters in the thermal pressurization modelling, pressurization and consequent shear stress drop occur to a much lesser extent, and over much longer time scales, than those compatible with significant coseismic stress drop. This difference in hydrodynamical behaviour is directly related to the contrast in material hydraulic properties, which depends on the clast-size supported framework, clast-size distribution and amount of clay.

The width of the slip zone controls the rate of frictional heating and the rate of thermal pressurization. Calculations carried out on the same samples for different deformation zone widths show that thermal pressurization is not effective for $w < 1$ mm (c.f the representative cases for PSZ and SSZ-1 in Fig. 12a & b), which implies that the half-width of the slip zone is lower than the hydraulic diffusion length (Lachenbruch 1980), and that pressurized fluid loss can no longer be neglected. This suggests that the variation in slip zone width can lead to an important heterogeneity in fluid pressure distribution along the fault, which could result in critical variations in the degree and rate of slip weakening, and hence could dramatically affect the way in which thermal pressurization progresses, influencing the dynamic fault motion (Wibberley & Shimamoto 2005).

A fault is expected to be less stable for a small slip weakening distance D_c (Scholz 2002), which is seismically estimated between 0.01 and 1 m (Ide & Takeo 1997; Fukuyama *et al.* 2003*b*). This implies that earthquake instabilities should appear for a slip weakening time between 0.02 and 2 s if we assume a constant slip velocity of $0.5\ \mathrm{m\ s}^{-1}$. The numerical analysis presented in this paper suggests that thermal pressurization would lead to a stress drop on PSZ or SSZ-1 to $1/e$ of its initial value over time scales of the order of 1 s, this timescale being consistent with seismological data.

Our modelling results predict fault stress drops and slip weakening times in broad agreement with seismological studies. Based on a constant slip rate and constant mean width values of the gouge zones (80 mm for PSZ central gouge, and 56 mm for SSZ-1 central gouge), our numerical analyses suggest that the thermal pressurization should be effective at 6 km depth, regardless of the path (PSZ or SSZ-1) followed by the rupture. However, rupture branching off these zones into adjacent high-permeability fine breccia will lead to fluid pressure decrease and inhibition of thermal pressurization as a slip weakening process (as must have once happened when SDZ-1 was initially generated). Although it is difficult to incorporate the along-strike difference in properties from the PSZ to the high-permeability fine breccia into modelling the overall slip response in such a

case of branching, we speculatively suggest that the fault will be locally controlled by the strongest points, i.e., such high-permeability branch structures, which may act as seismic asperities. Along with the control exerted by the width of the slip zone on the feasibility of thermal pressurization, this mechanism may explain why complete dynamic stress drop is unlikely to occur in natural earthquakes.

Conclusion

Based on porosity and permeability data obtained from the principal and secondary slip zones of the Usukidani fault, our modelling shows that thermal pressurization is a viable process to account for dynamic slip weakening, as long as the rupture remains located within the PSZ and SSZ-1 gouges and these gouge zones maintain good lateral continuity along the fault. If the rupture splays from the gouge slip zone and propagates through the marginal fine fault breccia, as could happen along small faults branching off the PSZ (e.g., Fig. 5b, NW side), coseismic excess fluid pressure will no longer be trapped, and will rapidly bleed off into the breccia, thus cancelling dynamic weakening.

The possibility of thermal pressurization occurring along secondary as well as along principal slip zones is probably a common feature of many crustal earthquakes. A notable example of such a complex propagation could be represented by the 1992 Landers event in California in which the rupture of the earthquake first propagated along a major fault, then shifted along a secondary fault before jumping to a third fault (Sowers *et al.* 1994). Indeed, if rupture propagates into an 'immature' branch fault or microbreccia zone characterized by a hydraulic diffusivity higher than that of the principal slip zone, excess fluid pressure can dissipate from this main zone, thus inhibiting pressurization. On the contrary, transfer of slip to 'mature' branching faults (such as SSZ-1 in the case of the example presented here), with a hydraulic diffusivity similar to or lower than the main slip zone, will not impede fluid pressurization unless the branching faults are significantly narrower than about 5–10 mm.

Partial inhibition of thermal pressurization by propagation of the rupture into an adjacent fine breccia or into an immature splay fault may explain why coseismic stress drops do not generally reach zero. This implies that a complete investigation of the hydraulic behaviour of active faults should also include secondary or higher order faults, if the geological exposure conditions permit.

This research was funded by the Ministry of Education, Sciences, Sport and Culture, Grant-in-Aid for Scientific Research (B), 163101127, 2004–2007 to Y. Kanaori, a French–Japanese Doctoral College scholarship to S. Boutareaud, a CNRS PICS grant to A. M. Boullier and INSU grants (DyETI program) to O. Fabbri. Permeability and porosity measurements were carried out at Kyoto University. We express our sincere thanks to Y. Aizawa for help with laboratory measurements, to K. Iwamura for logistical support and to Y. Kanaori, H. Noda, H. Sone and W. Tanikawa for fruitful discussions, and Z. Shipton and A. Tsutsumi for thoughtful reviews.

References

ANDREWS, D. J. 2002. A fault constitutive relation accounting for thermal pressurization of pore fluid. *Journal of Geophysical Research*, **107**, doi:10.1029/2002JB001942.

BEN-ZION, Y. & ANDREWS, D. J. 1998. Properties and implications of dynamic rupture along a material interface. *Bulletin of the Seismological Society of America*, **88**, 1085–1094.

BOUISSOU, S., PETIT, J. P. & BARQUINS, M., 1998. Experimental evidence of contact loss during stick-slip: possible implications for seismic behaviour. *Tectonophysics*, **295**, 341–350.

BRODSKY, E. E. & KANAMORI, H. 2001. Elastohydrodynamic lubrication of faults. *Journal of Geophysical Research*, **106**, 16357–16374.

BRUNE, J. N., BROWN, S. & JOHNSON, P. A. 1993. Rupture mechanism and interface separation in foam rubber models of earthquakes: a possible solution to the heat flow paradox and the paradox of large overthrusts. *Tectonophysics*, **218**, 59–67.

CAINE, J. S., EVANS, J. P. & FORSTER, C. B. 1996. Fault zone architecture and permeability structure. *Geology*, **24**, 1025–1028.

CARDWELL, R. K., CHINN, D. S., MOORE, G. F. & TURCOTTE, D. L. 1978. Frictional heating on a fault zone with finite thickness. *Geophysical Journal of the Royal Astronomical Society*, **52**, 525–530.

CARLSLAW, H. C. & JAEGER, J. C. 1959. *Conduction of Heat in Solids*. Oxford University Press, New York.

CHESTER, F. M. & LOGAN, J. M. 1986. Implications for mechanical properties of brittle faults from observations of the Punchbowl Fault zone, California. *Pure and Applied Geophysics*, **124**, 79–106.

CHESTER, F. M., EVANS, J. P. & BIEGEL, R. L. 1993. Internal structure and weakening mechanism of the San Andreas Fault. *Journal of Geophysical Research*, **98**, 771–786.

DAVID, C., WONG, T. F., ZHU, W. & ZHANG, J. 1994. Laboratory measurement of compaction-induced permeability change in porous rocks: implications for the generation and maintenance of pressure excess in the crust. *Pure and Applied Geophysics*, **143**, 425–456.

EVANS, J. P., FORSTER, C. B. & GODDARD, J. V. 1997. Permeability of fault-related rocks, and implications for hydraulic structure of fault zones. *Journal of Structural Geology*, **19**, 1393–1404.

FABBRI, O., IWAMURA, K., MATSUNAGA, S., COROMINA, G. & KANAORI, Y. 2004. Distributed strike–slip faulting, block rotation and possible intracrustal vertical decoupling in the convergent zone of SW Japan. *In*: GROCOTT, J., MCCAFFREY, K. J. W., TAYLOR, G. & TIKOFF, B. (eds) *Vertical Coupling and Decoupling in the Lithosphere*. Geological Society, London, Special Publications, **227**, 141–165.

FAULKNER, D. R. 2004. A model for the variation in permeability of clay-bearing gouge with depth in the brittle crust. *Geophys. Res. Lett.*, **31**, L19611, doi:10.1029/2004GLO20736.

FAULKNER, D. R. & RUTTER, E. H. 1998. The gas-permeability of clay-bearing fault gouge at 20 °C. *In*: JONES, G., FISHER, Q. & KNIPE, R. J. (eds) *Faulting, Fault Sealing and Fluid-flow in Hydrocarbon Reservoirs*. Geological Society, London, Special Publications, **147**, 147–156.

FAULKNER, D. R. & RUTTER, E. H. 2000. Comparison of water and argon permeability in natural clay-bearing fault gouge under high pressure at 20 °C. *Journal of Geophysical Research*, **105**, 16415–16426.

FAULKNER, D. R. & RUTTER, E. H. 2001. Can the maintenance of overpressured fluids in large strike–slip fault zones explain their apparent weakness? *Geology*, **29**, 503–506.

FUKUYAMA, E., ISHIDA, M. *ET AL*. 2000. *NIED seismic moment tensor catalogue January–December 1997*. Technical Note of the National Research Institute for Earth Science and Disaster Prevention, **205**.

FUKUYAMA, E., ELLSWORTH, W. L., WALDHAUSER, F. & KUBO, A. 2003*a*. Detailed fault structure of the 2000 western Tottori, Japan, earthquake sequence. *Bulletin of the Seismological Society of America*, **93**, 1468–1478.

FUKUYAMA, E., MIKUMO, T. & OLSEN, B. 2003*b*. Estimation of the critical slip-weakening distance: Theoretical background. *Bulletin of the Seismological Society of America*, **93**, 1835–1840.

HIROSE, T. & SHIMAMOTO, T. 2003. Fractal dimension of molten surfaces as a possible parameter to infer the slip-weakening distance of faults from natural pseudotachylytes. *Journal of Structural Geology*, **25**, 1569–1574.

HIROSE, T. & SHIMAMOTO, T. 2005. Growth of molten zone as a mechanism of slip weakening of simulated faults in gabbro during frictional melting. *Journal of Geophysical Research*, **110**, B05202, doi:10.1029/2004JB003207.

HUZITA, K. 1980. Role of the Median Tectonic Line in the Quaternary tectonics of the Japanese Islands. *In*: ICHIKAWA, K. (ed.) *Median Tectonic Line of Southwest Japan*. Memoirs of the Geological Society of Japan, **18**, 129–153.

ICHIKAWA, M. 1971. Reanalysis of mechanisms of earthquakes which occurred in and near Japan, and statistical studies on the nodal plane solutions obtained. *Geological Magazine*, **35**, 207–274.

IDE, S. & TAKEO, M. 1997. Determination of constitutive relations of fault slip based on seismic wave analysis. *Journal of Geophysical Research*, **102**, 27379–27391.

KANAMORI, H. & HEATON, T. H. 2000. Microscopic and macroscopic physics of earthquakes. *In*: RUNDLE, J. B., TURCOTTE, D. L. & KLEIN, W. (eds) *GeoComplexity and the Physics of Earthquakes*. AGU Geophysical Monographs, **120**, 147–163.

KANAORI, Y. 1990. Late Mesozoic–Cenozoic strike–slip and block rotation in the inner belt of southwest Japan. *Tectonophysics*, **177**, 381–399.

KANAORI, Y. 1997. Seismic risk assessment of active fault systems in the western Chugoku district of southwest Japan. *Journal of Natural Disaster Science*, **19**, 9–29.

KANAORI, Y. 1999. Reactivation of cataclastic belts and formation of fault gouge in the western Chugoku region. *Gekkan Chikyu (The Earth Monthly)*, **21**, 22–29.

KANAORI, Y. 2005. *Active Faults in Yamaguchi Prefecture: for the Mitigation of Earthquake Disaster*. Kinmiraisha, Nagoya (in Japanese).

LACHENBRUCH, A. H. 1980. Frictional heating, fluid pressure, and the resistance to fault motion. *Journal of Geophysical Research*, **85**, 6097–6112.

LIN, A. 2001. S–C fabrics developed in cataclastic rocks from the Nojima fault zone, Japan, and their implications for tectonic history. *Journal of Structural Geology*, **23**, 1167–1178.

LIN, A., SHIMAMOTO, T. *ET AL*. 2001*a*. Comparative study of cataclastic rocks from a drill core and outcrops of the Nojima fault zone, on Awaji Island, Japan. *The Island Arc*, **10**, 368–380.

LIN, A., OUCHI, T., CHEN, C. F. & MARUYAMA, T. 2001*b*. Co-seismic displacements, folding and shortening structures along the Chelungpu surface rupture zone during the 1999 Chi-Chi (Taiwan) earthquake. *Tectonophysics*, **330**, 225–244.

LOCKNER, D. NAKA, H., TANAKA, H., ITO, H. & IKEDA, R., 1999. Permeability and strength of the Nojima core samples from the Nojima fault of the 1995 Kobe earthquake. *In*: ITO, H., FUJIMOTO, K., TANAKA, H. & LOCKNER, D. (eds) *Proceedings of the International Workshop on the Nojima Fault Core and Borehole Data Analysis*. Preliminary Report, 147–152.

MANDL, G., DE JONG, L. N. J. & MALTHA, A. 1977. Shear zones in granular material. *Rock Mechanics*, **9**, 95–144.

MASE, C. W. & SMITH, L. 1985. Pore-fluid pressures and frictional heating on a fault surface. *Pure and Applied Geophysics*, **122**, 583–607.

MASE, C. W. & SMITH, L. 1987. Effects of frictional heating on the thermal, hydrologic, and mechanical response of a fault. *Journal of Geophysical Research*, **92**, 6249–6272.

MCKENZIE, D. P. & BRUNE, J. N. 1972. Melting on fault planes during large earthquakes. *Geophysical Journal of the Royal Astronomical Society*, **29**, 65–78.

MELOSH, J. 1979. Accoustic fluidization: a new geologic process? *Journal of Geophysical Research*, **84**, 7513–7520.

MELOSH, J. 1996. Dynamic weakening of faults by accoustic fluidization. *Nature*, **379**, 601–606.

MIKUMO, T., OLSEN, K. B., FUKUYAMA, E. & YAGI, Y. 2003. Stress-breakdown time and slip-weakening distance inferred from slip-velocity functions on earthquake faults. *Bulletin of the Seismological Society of America*, **93**, 264–282.

MIZOGUCHI, K. 2004. *High-velocity frictional behaviour of Nojima fault gouge and its implications for seismogenic fault motion*. Doctoral Thesis, the Graduate School of Science, Kyoto University.

MIZOGUCHI, K., HIROSE, T. & SHIMAMOTO, T. 2000. Permeability structure of the Nojima fault at Funaki, Hokudan-Cho, Japan. *The Earth Monthly*, **31**, 58–65 (in Japanese).

MORA, P. & PLACE, D. 1999. The weakness of earthquake faults. *Geophysical Research Letters*, **26**, 123–126.

MORROW, C. A., SHI, L. Q. & BYERLEE, J. D. 1984. Permeability of fault gouge under confining pressure and shear stress. *Journal of Geophysical Research*, **89**, 3193–3200.

NODA, H. & SHIMAMOTO, T. 2005. Thermal pressurization and slip-weakening distance of a fault: An example of the Hanaore fault, Southwest Japan. *Bulletin of the Seismological Society of America*, **95**, 1224–1233.

OKADA, Y. 2004. *Map of Japanese Earthquakes*. Shoseki, Tokyo, (in Japanese).

POLIAKOV, A. N. B., DMOWSKA, R. & RICE, J. R. 2002. Dynamic shear rupture interactions with fault bends and off-axis secondary faulting. *Journal of Geophysical Research*, **107**, 2295, doi:10.1029/2001 JB000572, ESE 6-1-6-18.

Research Group for Active Faults of Japan. 1991. *Active Faults in Japan. Sheet Maps and Inventories*, revised edn, Tokyo University Press, Tokyo (in Japanese with English abstract).

SAGIYA, T., NISHIMURA, T., HATANAKA, Y., FUKUYAMA, E. & ELLSWORTH, W. L. 2002. Crustal movements associated with the 2000 western Tottori earthquake and its fault model. *Bulletin of the Seismological Society of Japan*, **54**, 523–534.

SCHOLZ, C. H. 2002. *The Mechanics of Earthquakes and Faulting*. Cambridge University Press, London.

SEMMANE, F., COTTON, F. & CAMPILLO, M. 2005. The Tottori earthquake: a shallow earthquake with no surface rupture and slip properties controlled by depth. *Journal of Geophysical Research*, **110**, B03306, doi:10.1029/2004JB003194.

SERONT, B., WONG, T. F., CAINE, J. S., FORSTER, C. B., BRUHN, R. L. & FREDRICH, J. T. 1998. Laboratory characterization of hydrodynamical properties of a seismogenic normal fault system. *Journal of Structural Geology*, **20**, 865–881.

SIBSON, R. H. 1973. Interactions between temperature and pore fluid pressure during earthquake faulting and a mechanism for partial or total stress relief. *Nature*, **243**, 66–68.

SIBSON, R. H. 1980. Power dissipation and stress levels on faults in the upper crust. *Journal of Geophysical Research*, **85**, 6239–6247.

SIBSON, R. H. 2003. Thickness of the seismic slip zone. *Bulletin of the Seismological Society of America*, **93**, 1169–1178.

SIBSON, R. H., WHITE, S. H. & ATKINSON, B. K. 1981. Structure and distribution of fault rocks in the Alpine Fault Zone, New Zealand. *In*: MCCLAY, K. R. & PRICE, N. J. (eds) *Thrust and Nappe Tectonics*. Geological Society, London, Special Publications, **9**, 275–292.

SOWERS, J. M., UNRUH, J. R., LETTIS, W. R. & RUBIN, T. D. 1994. Relationship of the Kickapoo Fault to the Johnson Valley and Homestead Valley faults, San Bernardino County, California. *Bulletin of the Seismological Society of America*, 528–536.

TSUKAHARA, H. & KOBAYASHI, Y. 1991. Crustal stress field in central and southwest Japan. *Journal of the Seismological Society of Japan*, **44**, 221–231.

TSUTSUMI, A., NISHINO, S., MIZOGUCHI, K., HIROSE, T., UEHARA, S., SATO, K., TANIKAWA, W. & SHIMAMOTO, T. 2004. Principal fault zone width and permeability of the active Neodani fault, Nobi fault system, Southwest Japan. *Tectonophysics*, **379**, 93–108.

UEHARA, S. & SHIMAMOTO, T. 2004. Gas permeability evolution of cataclasite and fault gouge in triaxial compression and implications for changes in fault-zone permeability structure through the earthquake cycle. *Tectonophysics*, **378**, 183–195.

WARR, L. N. & COX, S. J. 2001. Clay mineral transformations and weakening mechanisms along the Alpine Fault, New Zealand. *In*: HOLDSWORTH, R. E., STRACHAN, R. A., MAGLOUGHLIN, J. F. & KNIPE, R. J. (eds) *The Nature and Significance of Fault Zone Weakening*. Geological Society, London, Special Publications, **186**, 85–101.

WEERTMAN, J. 1980. Unstable slippage across a fault that separates elastic media of different elastic constants. *Journal of Geophysical Research*, **85**, 1455–1461.

WIBBERLEY, C. A. J. 2002. Hydraulic diffusivity of fault gouge zones and implications for thermal pressurization during seismic slip. *Earth Planets Space*, **54**, 1153–1171.

WIBBERLEY, C. A. J. & SHIMAMOTO, T. 2003. Internal structure and permeability of major strike-slip fault zones: the Median Tectonic Line in Mie Prefecture, Southwest Japan. *Journal of Structural Geology*, **25**, 59–78.

WIBBERLEY, C. A. J. & SHIMAMOTO, T. 2005. Earthquake slip weakening and asperities explained by thermal pressurization. *Nature*, **436**, 689–692.

YAMADA, N., HIGASHIMOTO, S. & MIZUNO, K. 1985. *Hiroshima Map 1:200,000*, **NI-53-33**. Geological Survey of Japan.

Index

Faults are primary focuses of both fluid migration and deformation in the upper crust. The recognition that faults are typically heterogeneous zones of deformed material, not simple discrete fractures, has fundamental implications for the way geoscientists predict fluid migration in fault zones, as well as leading to new concepts in understanding seismic/aseismic strain accommodation. This book captures current research into understanding the complexities of fault-zone internal structure, and their control on mechanical and fluid-flow properties of the upper crust. A wide variety of approaches are presented, from geological field studies and laboratory analyses of fault-zone and fault-rock properties to numerical fluid-flow modelling, and from seismological data analyses to coupled hydraulic and rheological modelling. The publication aims to illustrate the importance of understanding fault-zone complexity by integrating such diverse approaches, and its impact on the rheological and fluid-flow behaviour of fault zones in different contexts.